Science and Technology of Electroceramic Thin Films

edited by

Orlando Auciello

MCNC,
Electronics Technology Division,
Research Triangle Park, North Carolina, U.S.A.

and

Rainer Waser

Institut für Werkstoffe der Elektrotechnik,
RWTH Aachen University of Technology,
Aachen, Germany

N00014-94-1-0430

19960722 094



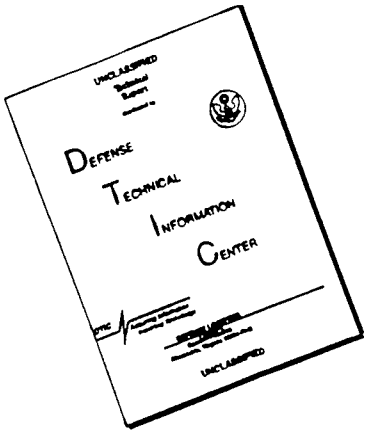
Kluwer Academic Publishers

Dordrecht / Boston / London

Published in cooperation with NATO Scientific Affairs Division

DTIC QUALITY INSPECTED 1

DISCLAIMER NOTICE



THIS DOCUMENT IS BEST QUALITY AVAILABLE. THE COPY FURNISHED TO DTIC CONTAINED A SIGNIFICANT NUMBER OF PAGES WHICH DO NOT REPRODUCE LEGIBLY.

MCNC

Electronic and Information Technologies

July 8, 1996

Mr. Wallace Smith
Scientific Officer Code: 331
Office of Naval Research
Ballston Tower One
800 North Quincy Street
Arlington, VA 22217-5660

Re: ONR Grant No. N00014-94-1-0430,
MCNC Contract No. C94-5010-020

Dear Mr. Smith:

Please find enclosed two copies of the proceedings for the above agreement. One copy was forwarded to your attention February 1995 by Dr. Orlando Auciello. If you have any questions, please contact Dr. Auciello at (919) 248-1872 or me at (919) 248-9217.

Sincerely,

Alicia M. Durham
Contracts Specialist

cc: Grant Administrator, 1 copy
DTIC, 1 copy

3021 Cornwallis Road • PO Box 12889 • Research Triangle Park, NC 27709-2889 • 919-248-1800 • Fax 919-248-1455

Proceedings of the NATO Advanced Research Workshop on
Science and Technology of Electroceramic Thin Films
Villa del Mare, Italy
June 20–24, 1994

A C.I.P. Catalogue record for this book is available from the Library of Congress.

ISBN 0-7923-3332-2

Published by Kluwer Academic Publishers,
P.O. Box 17, 3300 AA Dordrecht, The Netherlands.

Kluwer Academic Publishers incorporates the publishing programmes of
D. Reidel, Martinus Nijhoff, Dr W. Junk and MTP Press.

Sold and distributed in the U.S.A. and Canada
by Kluwer Academic Publishers,
101 Philip Drive, Norwell, MA 02061, U.S.A.

In all other countries, sold and distributed
by Kluwer Academic Publishers Group,
P.O. Box 322, 3300 AH Dordrecht, The Netherlands.

Printed on acid-free paper

All Rights Reserved
© 1995 Kluwer Academic Publishers and copyright holders as specified on appropriate pages within
No part of the material protected by this copyright notice may be reproduced or utilized in any form or by any means, electronic or mechanical, including photocopying, recording or by any information storage and retrieval system, without written permission from the copyright owner.

Printed in the Netherlands

TABLE OF CONTENTS

Preface ix
Report on the NATO/ARW xi
Acknowledgments xvi

PULSED LASER ABLATION-DEPOSITION AND CHARACTERIZATION OF FERROELECTRIC METAL OXIDE HETEROSTRUCTURES 1
R. Ramesh, O. Auciello, V.G. Keramidas and R. Dat

LOW ENERGY ION BOMBARDMENT INDUCED EFFECTS IN MULTI-COMPONENT ELECTROCERAMIC THIN FILMS 23
S.B. Krupanidhi

GROWTH AND PROPERTIES OF $Pb(Mg_{1/3}Nb_{2/3})O_3$ - $PbTiO_3$ AND $Pb(Zr,Ti)O_3$ THIN FILMS BY PULSED LASER DEPOSITION 53
A. Safari, C. Tantigate and J. Lee

WAVELENGTH DEPENDENCE IN PULSED LASER DEPOSITION OF ZnO THIN FILMS 67
D. Craciun and V. Craciun

ORGANOMETALLIC CHEMICAL VAPOR DEPOSITION OF LEAD ZIRCONATE TITANATE 75
M. de Keijser, P.J. van Veldhoven and G.J.M. Dormans

ALKOXIDE PRECURSORS FOR FERROELECTRIC THIN FILMS 85
M.I. Yanovskaya, N.YA. Turova and L.I. Solov`Yova

DEPOSITION OF UNDOPED AND DOPED Pb $(Mg,Nb)O_3$ - $PbTiO_3$, $PbZr_xTi_{1-x}O_3$, ALKALINE EARTH TITANATE AND LAYERED PEROVSKITE THIN FILMS ON Pt AND CONDUCTIVE OXIDE ELECTRODES BY SPIN - ON PROCESSING: CORRELATION OF GROWTH AND ELECTRICAL PROPERTIES 99
M. Klee, U. Mackens, J. Pankert, W. Brand and W. Klee

RELATIONSHIPS BETWEEN FERROELECTRIC 90^o DOMAIN FORMATION AND ELECTRICAL PROPERTIES OF CHEMICALLY PREPARED $Pb(Zr,Ti)O_3$ THIN FILMS 117
B.A. Tuttle, T.J. Garino, J.A. Voigt, T.J. Headley, D. Dimos and M.O. Eatough

CHARACTERIZATION OF SOL-GEL $Pb(Zr_xTi_{1-x})O_3$ THIN FILM CAPACITORS WITH HYBRID (Pt, RuO_2) ELECTRODES 133
H.N. Al-Shareef, O. Auciello and A.I. Kingon

ORGANICALLY MODIFIED SOL-GEL PRECURSORS FOR FERROELECTRIC DEPOSITION BY SPIN COATING 147
P. Gaucher, J. Hector and J. C. Kurfiss

PREPARATION AND PROPERTIES OF CALCIUM MODIFIED LEAD TITANATE THIN FILMS 157
M.L. Calzada, F. Carmona, R. Sirera and B. Jimenez

MICROSTRUCTURE OF LEAD TITANATE-BASED THIN FILMS 167
L. Pardo, J. Ricote and M.L. Calzada

STOICHIOMETRY AND PHASE STRUCTURE OF SOL-GEL DERIVED PZT-BASED THIN FILMS 177
M. Kosec, Y. Huang, E. Sato, A. Bell, N. Setter, G. Dražič, S. Bernik and T. Beltram

LIQUID PHASE EPITAXY OF $Na_{1-y}K_yTa_{1-x}Nb_xO_3$ on $KTaO_3$ SUBSTRATES 187
Z. Sitar, R. Gutmann and P. Günter

PULSE SWITCHING CHARACTERIZATION OF FERROELECTRIC THIN FILMS 201
P.K. Larsen, R. Cuppens and G.J.M. Dormans

POLARIZATION, CONDUCTION, AND BREAKDOWN IN NON-FERROELECTRIC PEROVSKITE THIN FILMS 223
R. Waser

ANOMALOUS LOGARITHMIC DEPENDENCIES IN D.C. BREAKDOWN OF FERROELECTRIC THIN FILMS 249
J. F. Scott

THE SHAPE OF THE HYSTERESIS CURVE OF FERROELECTRIC SINGLE CRYSTALS AND CERAMICS 261
G. Arlt

FAST TRANSIENT MEASUREMENTS ON ELECTROCERAMIC THIN FILMS 269
G.W. Dietz, M. Schumacher and R. Waser

THE INFLUENCE OF DOPANTS ON THE LEAKAGE CURRENT IN PZT THIN-FILM FERROELECTRIC CAPACITORS 279
D.J. Wouters, G. Willems, G. Groeseneken, H.E. Maes, K. Brooks and R. Klissurska

PHOTO-INDUCED STORAGE AND IMPRINTING IN $(Pb,La)(Zr,Ti)O_3$ THIN FILMS 291
D. Dimos, W. L. Warren and B. A. Tuttle

DEPLETION, DEPOLARIZING EFFECTS AND SWITCHING IN FERROELECTRIC THIN FILMS 301
A.K. Tagantsev, M. Landivar, E. Colla, K. G. Brooks and N. Setter

NONSTOICHIOMETRY, DEFECTS, AND CHARGE TRANSPORT IN PZT 315
M. V. Raymond and D. M. Smyth

X-RAY DIFFRACTION LINE PROFILE ANALYSIS OF ZnO THIN FILMS DEPOSITED ON Al-SiO_2-Si SUBSTRATES 327
P. Sutta, Q. Jackuliak, V. Tvarozec and I. Novotny

ELECTRON EMISSION FROM FERROELECTRICS 335
H. Gundel

INTEGRATION OF FERROELECTRIC THIN FILMS FOR MEMORY APPLICATIONS 353
H. Achard and H. Mace

PROCESSING AND DEVICE ISSUES OF HIGH PERMITTIVITY MATERIALS FOR DRAMS 373
B.E. Gnade, S.R. Summerfelt and D. Crenshaw

FERROELECTRIC THIN FILMS FOR CAPACITOR AND SENSOR APPLICATIONS 383
R. W. Whatmore, P. Kirby, A. Patel, N. M. Shorrocks, T. Bland and M. Walker

PIEZOELECTRIC AND FERROELECTRIC DEVICES: POTENTIAL AND ISSUES 399
M. Sayer, D.A. Barrow, R. Noteboom, E.M. Griswold and Z. Wu

INTEGRATED FERROELECTRIC MICROELECTROMECHANICAL SYSTEMS 413
D. L. Polla

FUNDAMENTAL PROPERTIES AND SOME APPLICATIONS OF SOL-GEL CERAMIC THIN FILMS 427
A.S. Sigov, V.I. Petrovsky, E.F. Pevtsov, K.A. Vorotilov and A.S. Valeev

$SrTiO_3$ THIN FILMS FOR OXYGEN SENSORS 439
J. Gerblinger and H. Meixner

INDEX 455

PREFACE

The basic and applied science of electroceramic thin films constitute one of the fast interdisciplinary evolving fields of research worldwide. A major driving force for the extensive research being performed in many Universities and Industrial and National Laboratories is the promise of applications of electroceramic thin films into a whole new generation of advanced microdevices that may revolutionize various technologies and create new multibillion dollar markets. Properties of electroceramic thin films that are being intensively investigated include electrical conductivity, ferroelectricity, piezoelectricity, pyroelectricity, electro-optic activity, and magnetism. Perhaps the most publicized application of electroceramics is that related to the new high temperature superconducting (HTSC) materials, which has been extensively discussed in numerous national and international conferences, including NATO/ASI's and ARW's. Less glamorously publicized applications, but as important as those of HTSC materials, are those involving the other properties mentioned above, which were the subject of this ARW. Investigation on ferroelectric thin films has experienced a tremendous development in recent years due to the advent of sophisticated film synthesis techniques and a substantial improvement in the understanding of the related materials science and implementation of films in various novel devices. A major driving force behind the progress in this interdisciplinary field of research is the promise of the development of a new generation of non-volatile memories with long endurance and fast access time that can overcome the problems encountered in the semiconductor non-volatile memory technology. Researchers have also rediscovered the utility of ferroelectric materials as high dielectric constant capacitors, which opens new possibilities for manufacturing planar, very high density DRAM memories. Ceramic conductors can be applied to ohmic, voltage-dependent, and thermally sensitive resistors; fast-ion conductors; and humidity and gas sensors. Piezoelectricity is being exploited in micromachines such as accelerometers, displacement transducers, and actuators such as those required for inkjet printers, for video-recording head positioning and for micromachining metals. Pyroelectricity can be utilized in the fabrication of high sensitivity infrared detectors, while electro-optic activity can be used in color filter devices, displays, image storage systems, and optical switches for integrated optical systems. The applications of electroceramic thin films mentioned above are only a part of a more extensive list, which indicates the relevance of these materials in the new technological era of a modern society. Most materials science and device issues related to electroceramic thin films are discussed in various national and international conferences where researchers interact through formal presentations and informal discussions, which in general do not give an opportunity for detailed analysis of the issues that are most critical for the advancement of the science of electroceramic thin films and devices. The field of research on electroceramic thin films and related devices has reached a state of development in which substantial progress has been made. However, there are some critical materials and device issues that need to be solved for the realization of commercially available devices.

The format of this NATO/ARW was designed to facilitate extensive scientific discussions. Key speakers reviewed the most relevant topics, making critical assessments of the current state of knowledge. Invited speakers presented recent advances on "hot" topics, and several participants presented papers related to new research. Each session concluded with extensive discussions in round table format, which permitted a fruitful and spirited interchange of ideas.

An important aspect of our NATO/ARW was that we were able to support the participation of several scientists from Eastern European Countries and contribute in this manner to the beginning of the new era of scientific cooperation between East and West promoted by NATO.

Orlando Auciello
North Carolina, 1994

Rainer Waser
Aachen, 1994

REPORT ON THE NATO/ARW

The NATO/ARW was divided in three sessions which included comprehensive reviews, invited papers on "hot" topics, contributed papers on new research, and extensive round table discussions following each session. In addition, a night session was dedicated to the discussion of highly speculative ideas. The three main subjects of the NATO/ARW in which this book is also organized are described below:

(1) Synthesis of ferroelectric thin films and their integration into heterostructures with metal and metal oxide electrodes. Presentations included characterization of films composition, microstructure, and electrical properties and their relationships. The discussions included consideration of various deposition techniques such as pulsed laser ablation deposition (PLAD), ion beam sputter-deposition (IBSD), metalorganic chemical vapor deposition (MOCVD), and sol-gel synthesis. Descriptions on the state of the art hardware and critical analyses of the basic principles of each thin film deposition technique were presented.

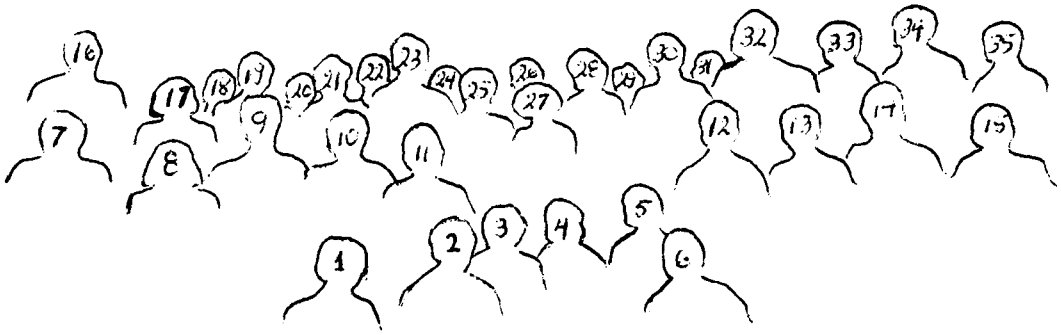
(2) Electrical characterization of ferroelectric capacitors and modeling, including pulse switching characterization of ferroelectric thin films, modeling of voltage dependent dielectric losses for ferroelectric MMIC devices, polarization, conduction, and breakdown in non-ferroelectric perovskite thin films, induced strain responses in ferroelectric, and relaxor ferroelectric and phase switching thin films. In addition, two comparatively new topics were discussed in this Session, namely, *in situ*, real-time analysis of ferroelectric /conductive oxide layers during growth by a new time-of-flight ion beam surface analysis technique, and electron emission from the surface of ferroelectric cathodes.

(3) Materials integration and application to devices, including discussions of ferroelectric thin films for sensor applications, integration of ferroelectric thin films for memory applications, fundamental properties and applications of sol-gel ceramic thin films, processing and device issues of high permittivity materials for DRAM memories, ferroelectric and piezoelectric devices: issues and potentials, and integrated ferroelectric microelectromechanical systems.

The NATO/ARW was attended by professionals, postdoctoral, and students from thirteen countries, including: Australia, Belgium, Canada, France, Germany, Italy, The Netherlands, Russia, Slovakia, Spain, Switzerland, United Kingdom, and The United States of America.

The main objective of the ARW was to bring together experts in the field of electroceramic thin films to discuss the status of the field and future directions in research and development. The highly interdisciplinary nature of the ARW allowed participants to interchange ideas in an environment rarely available in other international conferences.

SCIENCE AND TECHNOLOGY OF
ELECTROCERAMIC THIN FILMS

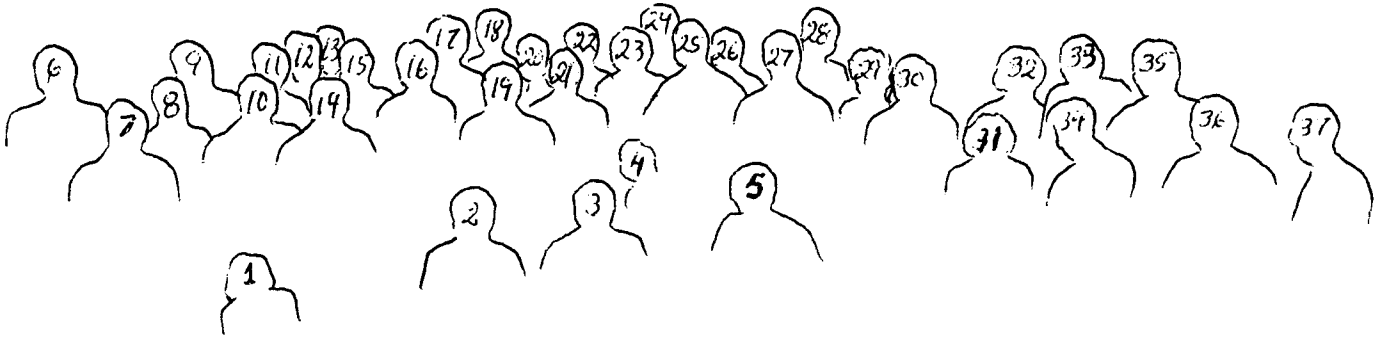


33) G. Dietz, 34) Z. Sitar, 35) B.A. Tuttle,
25) L. Pardo, 26) J.F. Scott, 27) M.L. Calzada, 28) A.S. Sigov, 29) R.W. Whatmore,
30) G. Montesperelli, 31) H. Gundel, 32) J. Gerblinger,
16) P.K. Larsen, 17) M.I. Yanovskaya, 18) V. Craciun, 19) B.E. Gnade, 20) A.K. Tagantsev,
21) M. Kosec, 22) M. de Keijser, 23) D. Polla, 24) S.K. Dey,
7) P. Sutta, 8) M. Klee, 9) H. Achard, 10) D.J. Wouters, 11) G. Arlt, 12) D. Dimos,
13) A.I. Kingon, 14) M. Sayer, 15) P. Kirby,
1) R. Waser, 2) S.B. Krupanidhi, 3) R. Ramesh, 4) H.N. Al-Shareef, 5) S.B. Desu, 6) O. Auciello

participants not present in the picture

L.E. Cross, P. Gaucher, A. Safari, D.M. Smyth





32) M.I. Yanovskaya, 33) P. Sutta, 34) L. Pardo, 35) M. Sayer, 36) G. Arlt, 37) A.K. Tagantsev,
23) H. Gundel, 24) P. Gaucher, 25) H. Achard, 26) A.S. Sigov, 27) G. Dietz, 28) Z. Sitar,
29) M. Kosec, 30) P. Kirby, 31) M.L. Calzada,
15) D.J. Wouters, 16) J.F. Scott, 17) J. Gerblinger, 18) M. de Keijser, 19) S.B. Krupanidhi,
20) H.N. Al-Shareef, 21) R.W. Whatmore, 22) S.B. Desu,
6) P.K. Larsen, 7) R. Ramesh, 8) B.A. Tuttle, 9) D. Dimos, 10) V. Craciun, 11) G. Montesperelli,
12) D.L. Polla, 13) B.E. Gnade, 14) A. Safari,
1) M. Klee, 2) R. Waser, 3) O. Auciello, 4) Gundel, 5) A.I. Kingon

participants not present in the picture

L.E. Cross, S.K. Dey, D.M. Smyth

ACKNOWLEDGMENTS

The Directors of the NATO/ARW acknowledge the financial support of NATO, through the Scientific Affairs Division, the Advanced Research Projects Agency (USA), and the Office of Naval Research (USA). The directors are grateful to all program administrators and/or directors, and all the personnel in the Agencies mentioned above, who contributed with their work, in one way or another, to the success of this ARW. Last but not least, the Directors acknowledge the excellent organization of the Hotel Villa del Mare and its personnel, whom provided an excellent service and warm attention that contributed to the scientific and social success of the NATO/ARW.

PULSED LASER ABLATION-DEPOSITION AND CHARACTERIZATION OF FERROELECTRIC METAL OXIDE HETEROSTRUCTURES

R. RAMESH,[1] O. AUCIELLO,[2,3]
V.G. KERAMIDAS[1] AND R. DAT[3]
1. Bellcore, Red Bank, NJ 07701.
2. MCNC, Electronics Technology Division Research Triangle Park, NC 27709-2889,
3. N.C. State University, Department of Materials Science and Engineering, Raleigh, NC 27694-7179

ABSTRACT. Materials integration strategies investigated by the NCSU-MCNC and Belcore groups have demonstrated that PZT-based heterostructure capacitors involving conductive oxide or hybrid metal-conductive oxide electrodes have negligible or no fatigue, long polarization retention and small tendency to imprint. The work reviewed involves the synthesis of heterostructure capacitors using the pulsed laser ablation deposition technique (PLAD). The properties observed for PZT-based heterostructure capacitors make them suitable for non-volatile ferroelectric memories. However, further work is necessary, particularly in producing small size capacitors ($\leq 1\ \mu m^2$), to determine if scaling down to dimensions compatible with high density memories will introduce undesirable effects.

The work discussed shows that PLAD will remain a very useful technique for fundamental research, but extensive work is necessary to make it a viable method for device fabrication on large area substrates.

1. Introduction

1.1. BACKGROUND INFORMATION

There is currently a strong research and development effort directed at producing a commercially viable solid state, nonvolatile ferroelectric memory (FRAM) technology. Many laboratories are focusing their work on integrating sub-micron thin ferroelectric capacitors of, for example, $Pb(Zr_xTi_{1-x})O_3$ (PZT), with the mature silicon based transistor technology to yield capacitor-transistor based memory architectures [1-5], as schematically illustrated in Fig.1. This figure also shows the perovskite unit cell of the ferroelectric PZT and the variety of interfaces (structural, chemical, electronic and ionic) that arise during the fabrication and integration of these metal oxide heterostructures on a Si substrate.

O. Auciello and R. Waser (eds.), Science and Technology of Electroceramic Thin Films, 1-22.
© 1995 *Kluwer Academic Publishers. Printed in the Netherlands.*

Realization of a commercially viable ferroelectric memory technology has been hampered by one or a combination of problems related to either the reliable performance of the PZT ferroelectric capacitor or to the growth and processing of capacitors that translate to high density memory elements. The electrode-ferroelectric interface is very crucial in determining the reliability characteristics of the ferroelectric capacitor, such as fatigue, which is the loss of switchable polarization when subjected to repeated bipolar pulses. Fatigue can be overcome for all practical purposes by replacing **metallic** Pt electrodes with **metal oxide** electrodes such as RuO_2 [6-9] or any of the large number of perovskite metal oxides such as Y-Ba-Cu-O [10,11] and La-Sr-Co-O [12-14] among others. Similarly, internal interfaces in the ferroelectric, such as domain walls and grain boundaries and microstructural defects such as oxygen vacancies influence the ferroelectric properties. In another approach, a layered ferroelectric material, termed as "Y1", which corresponds to the family of bismut-based oxides (e.g. $SrBi_2Ta_2O_9$) [15], has also yielded capacitor structures with non-volatile ferroelectric memory compatible properties. We shall not discuss or compare the properties of the results presented in this review with those of the "Y1" material.

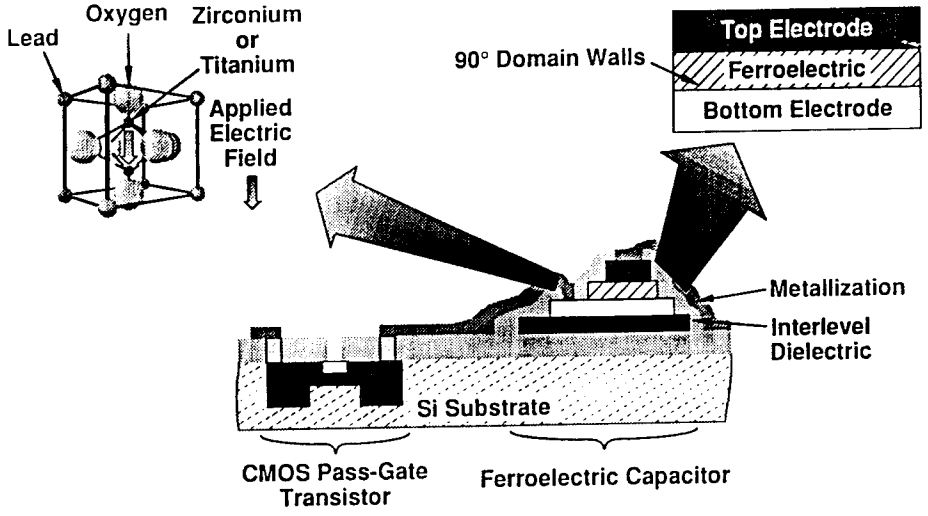


Figure 1. Schematic of capacitor - transistor based memory architecture, the perovskite unit cell of the ferroelectric PZT, and the variety of structural, chemical, electronic and ionic interfaces that arise during the fabrication and integration of these metal oxide heterostructures on a Si substrate.

In order to integrate these ferroelectric and other metal oxide heterostructures into a commercially viable memory technology several aspects have to be considered. Firstly, a scalable deposition process (i.e., ability to grow on 6" wafers) such as chemical vapor deposition (CVD) or sputter-deposition is essential. The film synthesis technique has to provide also the ability to grow thin films on non-planar surfaces with good conformal coverage. Secondly, a reliable etching technology has to be available to fabricate the

memory elements of the desired size. Finally, the memory elements need to function in a reliable fashion over conventionally accepted performance conditions of write and read voltages, usage temperature, etc. The success of ferroelectric non-volatile memories will depend critically on whether the materials integration problems are solved in a timely and cost-effective fashion with respect to other competing technologies.

Several issues need to be addressed to achieve a reliable integration of ferroelectric and associated multi-component metal oxides with Si-CMOS devices, including growth processes, etching processes, device design and fabrication, and reliability testing of the prototype capacitor structures. Direct growth of the lead-based compounds on Si (or SiO_2/Si) at high temperatures leads to the formation of very stable binary silicates such as lead silicate. Indeed, this is generally true if the film contains any of the highly reactive Group I or II cations (such as Ba, Ca, K, etc.), although much needs to be experimentally proven regarding this observation. Consequently, integration of such metal oxides on Si requires novel approaches to provide chemical isolation of the overlayers from the substrate and also yield the desired crystallographic phase and orientation in the ferroelectric layer. These last two issues are critical to the engineering of interfaces and stack structure in PZT-based heterostructure capacitors, and they are being intensively investigated in the authors' laboratories, using novel materials integration approaches.

1.2. THE PULSED LASER ABLATION-DEPOSITION TECHNIQUE

Desirable features of a deposition technique for producing multicomponent oxide thin films and heterostructures include: 1) a capability for producing stoichiometric films, 2) a high deposition rate, 3) ability to produce conformal deposition, and 4) scalability to cover large area substrates with uniform composition and thickness. The PLAD method is very good in terms of the two first features, but it may have problems in relation to conformal deposition, as in any other directional vapor deposition technique, although investigation on conformality of PLAD films has not been reported yet. In addition, the PLAD method is not as easily scalable as other techniques such as sputter-deposition and CVD. PLAD is very suitable to perform preliminary experiments to rapidly explore the viability of materials integration strategies, the consequences of the complicated interface chemistry in heterostructures and the effect of various process and microstructural variables on the ferroelectric's performance. However, it is relevant to consider the capabilities and limitations of PLAD to have a proper perspective of what can be achieved with this method.

A schematic of the PLAD process for the growth of metal oxide heterostructures is depicted in Fig. 2. PLAD has achieved popularity, primarily in the oxide thin film deposition community, through the demonstration of the growth of very high quality thin films and heterostructures. Thin films of the desired material and composition are deposited by the ablation of material from solid target surfaces by a short laser pulse. Typically, an ultra-violet (e.g., 248 nm) excimer laser with a pulse width of a few nanoseconds is used for this purpose, although other types of lasers (for example, frequency tripled YAG laser) have also been used. The instantaneous interaction of the pulsed laser beam with the target produces a plume of material that is very forward directed and is transported towards the heated substrate that is placed directly in the line of this plume. The spatial and temporal evolution of the ablated plume are quite complicated and are not discussed in this review. The reader interested in the subject can consult recent work in the literature [16-20].

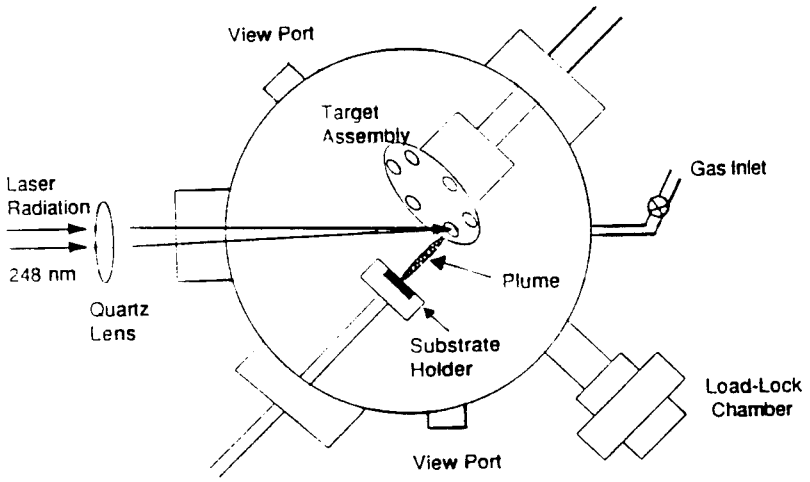


Figure 2. Schematic of the PLAD process for the growth of metal oxide heterostructures.

Under appropriate deposition conditions, the composition of the thin film is the same as that of the target within a small central area of the film, but is non-stoichiometric outside this central area. The ability of producing stoichiometric films is perhaps the main intrinsic advantage of PLAD, in comparison with other techniques such as sputtering when using multicomponent oxide PZT targets. For sputter-deposition of PZT films, enrichment of Pb in the PZT target is necessary to compensate for preferential sputtering. The compositional congruency in the central part of the ablated plume is translated to the film depending, among other factors, on the substrate temperature, the interface chemistry between the substrate surface and the film and, the oxygen partial pressure during deposition. An advantage of PLAD, as implemented by various groups, is that multiple targets can be loaded inside the chamber, before deposition, on a rotating holder that allows sequential exposure of different targets to the laser beam, thereby enabling the in-situ growth of heterostructures and superlattices with relatively clean interfaces. For example, a versatile rotating target holder with capability for target exchange through a load-lock system, to allow for target polishing without breaking vacuum, has been designed and built by one of the authors [21]. The heterostructures can be cooled in a variety of ambients after the deposition is completed. Finally, other advantages include a rapid throughput of films that is useful in process optimization and the ability to include in-situ processing such as etching through the use of a load-lock and etching chamber in conjunction with the deposition chamber.

The PLAD technique has some deficiencies that need to be overcome. The first is that uniform coating of large area wafers (i.e., $\geq$ 6" diameter) has still not been routinely demonstrated. This will require not only the uniform heating of large area wafers but also the deposition of material with uniform thickness and composition over the whole surface. The second issue that remains to be demonstrated is the ability to carry out conformal growth. Finally, films with complete absence of particulates have yet to be

demonstrated, although the particulate density and size distribution can be reduced considerably through the use of high density targets and/or the implementation of velocity selectors [18].

The synthesis of films and heterostructures described in this review was performed using pulsed laser ablation-deposition (PLAD) systems involving excimer laser beams (λ = 248 nm, 1-3 Hz, 1-2 J/cm^2) directed at a position inside the deposition chamber where PZT and other perovskite oxide targets (e.g., YBCO and LSCO) were sequentially positioned under the laser beam by means of rotating target holders with capability for continuous rotation of each target during laser ablation [see ref. 21 for example). PZT layers were synthesized using stoichiometric PZT targets, while YBCO and LSCO films were produced by ablation of stoichiometric $YBa_2Cu_3O_{7-x}$ and $La_{0.5}Sr_{0.5}CoO_3$ targets. In all cases, the layers were deposited in an oxygen ambient (100-300 mTorr), and at substrate temperatures in the range 550-675 °C.

1.3. MATERIALS INTEGRATION STRATEGIES

The materials integration strategies discussed in this review are illustrated with examples primarily from research currently in progress in our laboratories, although most of the conclusions are quite relevant to those obtained from other research laboratories. Wherever appropriate, results from other research groups relevant to this topic will also be discussed. Details of the laser deposition conditions used for the work discussed in this review can be found elsewhere [10-14, 20, 21]. This review is dedicated to discuss only current general results, conclusions, and future research and development work. The discussion in this review is centered around the LSCO / PLZT / LSCO heterostructure capacitor, because this system is not only interesting from the fundamental thin film science point of view, but also has a very strong chance of being used in a commercial memory technology in the future. The compositions of the PZT and PLZT ferroelectric layers typically investigated in our programs include $Pb(Zr_{0.47}Ti_{0.53})O_3$ [14], $Pb_{0.9}La_{0.1}Zr_{0.2}Ti_{0.8}O_3$ (10/20/80) [12,13], $Pb_{1.0}Zr_{0.2}Ti_{0.8}O_3$ (0/20/80) [12,13]; $PbZr_{0.5}Ti_{0.5}O_3$(0/50/50) [12,13] although the whole range of compositions in the PLZT phase diagram can and have been grown by PLAD.

Following the general introduction presented in this section, a description is presented in subsequent sections, about the key advances made in the field of ferroelectric film growth by PLAD, through the use of the approaches discussed above, namely the use of anisotropic perovskite templates and metallic oxide electrodes to influence the phase stability and orientation distribution as well as the ferroelectric properties of the test capacitors. Work performed in our laboratories, during the last two years, has been focused on using **perovskite metallic oxides** as top and bottom electrodes instead of Pt. The perovskite oxide electrodes, processed under optimized conditions, yield capacitors that show negligible or no bipolar fatigue at least up to 10^{12} cycles [12-14]. Two different types of perovskite oxide electrodes have been discussed, namely, the layered superconducting Y-Ba-Cu-O (YBCO) [10,11] and the cubic metallic La-Sr-Co-O (LSCO) [12-14]. These perovskite oxides have room temperature resistivities of the order of a few hundred μΩ-cm (for example, epitaxial LSCO has a resistivity of 90 μΩ-cm at room temperature). In comparison, Pt has a resistivity in the range of 5-20 μΩ-cm at room temperature. In an attempt to lower the effective sheet resistance of the bottom electrode while maintaining the good fatigue characteristics of the LSCO-based capacitors, heterostrucutre LSCO/PLZT/LSCO capacitors were grown on epitaxial or highly [001]

oriented Pt. The integration of these capacitors with metal oxide electrodes on Si can be accomplished using a novel approach that involves the growth of a thin layer of an anisotropic perovskite **template** layer such as bismuth titanate (BTO) on the thermally oxidized Si wafer prior to the deposition of a Pt layer and subsequent LSCO/PLZT/LSCO capacitor heterostructure [12,13]. The BTO template layer grows with a preferred c-axis texture, even on an amorphous surface such as SiO_2/Si. It not only provides a good chemical barrier between the overlayers and the Si wafer but also provides a perovskite-like surface (since it is c-axis oriented and hence the a-b plane is exposed) for the subsequent growth of the cubic perovskite layers. The perovskite structure and crystal chemistry of the BTO template layer is advantageously used to nucleate the [001] orientation of a perovskite phase both in LSCO and PZT layers preferentially over other competing orientations of the perovskite phase and other competing phases. Figure 3 illustrates schematically both these concepts.

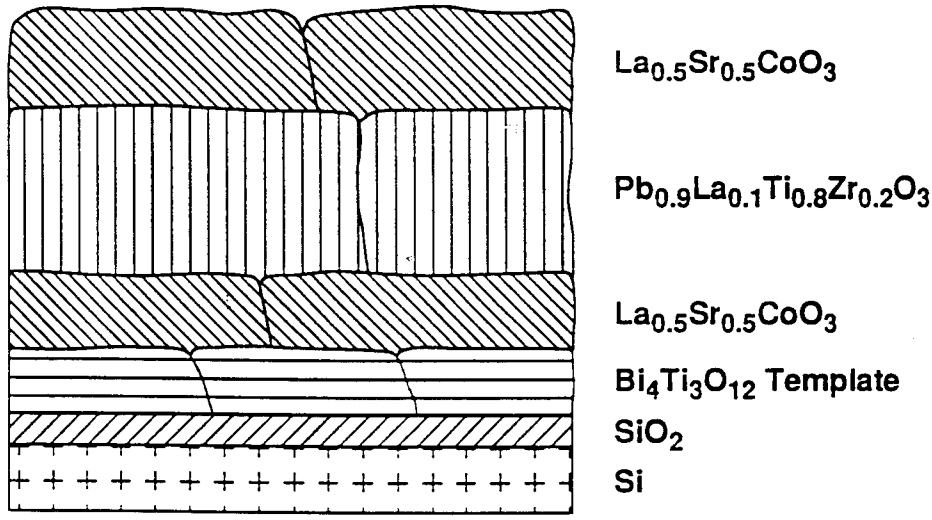


Figure 3 Schematic demonstrating the concept of BTO layer-induced oriented perovskite phase in electrode and PZT layers.

2. Structure and Microstructure of PZT-Based Capacitors

2.1. EPITAXIAL PZT-BASED CAPACITORS

Both LSCO and PZT (PLZT) materials are cubic at the growth temperature, which is typically in the range of 550-670°C, depending upon the substrate. PZT and PLZT undergo a cubic-tetragonal (or cubic-rhombohedral) transformation upon cooling to room temperature. A large part of the work discussed here have been performed using [100] oriented single crystal $LaAlO_3$ substrates, since this material is very closely lattice matched to both LSCO and PLZT (within a few %). Very high quality heterostructures

have been grown on these substrates, as evidenced by x-ray diffraction pole figure scans (which is discussed in a later section) and electron microscopy studies. X-ray θ-2θ scans of the LSCO/ PLZT show that the PLZT layer is typically c-axis oriented. The degree of alignment of the c-axis depends on the PLZT composition and the post-deposition cooling conditions. PLZT(10/20/80) compositions yield only c-axis oriented films while the 0/20/80 composition has a stronger propensity to yield a mixture of c-axis and a-axis (i.e., c-axis in the substrate plane) oriented films. The volume fraction of the film with the c-axis normal to the substrate increases as the cooling rate from deposition temperature increases.

Transmission electron microscopy studies of the films grown on $LaAlO_3$ substrates confirm the x-ray diffraction results with respect to their crystalline quality. Planar sections reveal the presence of only low angle grain boundaries and dislocations. The presence of 90° domain walls have been demonstrated in 0/20/80 films, both by x-ray diffraction (i.e., the presence of a-axis oriented regions) and by diffraction contrast electron microscopy (Fig. 4). These domains appear to nucleate at the interface between the electrode and the ferroelectric film, as illustrated in the cross-section micrograph in Fig. 5. The growth crystallography of these films on $LaAlO_3$ is the cause for the 45° angle these domain walls make with the substrate normal. On the other hand, 10/20/80 films have very little 90° domains, if any. This observation is consistent with x-ray diffraction data which shows a completely c-axis oriented film. This difference can be understood in terms of two facts : (i) the c/a ratio for the PLZT 10/20/80 films is much smaller than for the PLZT 0/20/80, and the a-axis lattice parameter is much better matched to the LSCO layer; (ii) the saturation polarization value is also much smaller for the PLZT 10/20/80 (and consequently the depolarizing field is also much smaller). In films with the 0/20/80 composition, the tendency to form 90° domains is primarily driven by the desire to lower the depolarizing field, which can happen if the polarization direction is in-plane; however, this is opposed by the larger mismatch of the c-axis lattice parameter with that of LSCO or the $LaAlO_3$ substrate. It is also clear that the presence of 90° domain walls is deleterious to the ferroelectric performance, as will be shown later.

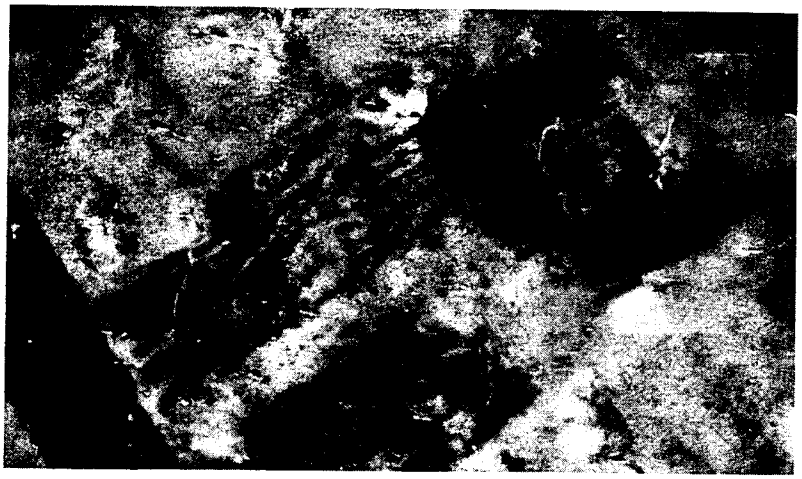


Figure 4. A planar section transmission electron micrograph illustrating the formation of 90° domain boundaries in a PZT thin film.



Figure 5. A cross-section TEM image showing the nucleation of 90° domain walls at the electrode - ferroelectric interface.

As outlined in the introduction, growth of PZT layers on either YSZ-buffered Si or SiO_2/Si is accomplished through the use of a bismuth titanate template layer. The efficiency of this layer in controlling the phase stability and PLZT layer orientation can be established from x-ray diffraction patterns. Figure 6 shows the effect of using the BTO template layer on the crystalline quality of PLZT-based heterostructure capacitors grown on [100]YSZ/Si substrates.

In Fig. 6 (a), the x-ray diffraction pattern show the existence of predominant [110] PLZT and LSCO peaks along with the [002] YSZ peak, although one might expect to see the [00l] peaks instead. The reason for this is the intrinsic mismatch between the LSCO (a=3.83 Å) lattice parameter and that of YSZ ($a/\sqrt{2}$=3.64 Å; mismatch of 4.7%). This, in conjunction with the inherent lack of structural anisotropy in the cubic perovskites, leads to a situation where the growth of the LSCO layer is predicated by the minimization of the growth surface energy. In general, this is accomplished by the stacking of the planes with the highest atomic density (i.e., the close-packed planes). In the case of the perovskites, (110) type planes exhibit the highest atomic denisty and consequently the films have a predominant [110] surface normal texture. It is relevant to notice that weak [001] and [002] diffraction peaks are also observed in Fig. 6(a). The BTO template layer dramatically alters the orientation of the PLZT layer because of its intrinsic structural anisotropy. When the BTO layer is deposited at the appropriate substrate temperature, it grows with a strong preferred [001] direction normal to the substrate, i.e., the a-b plane is the lowest energy surface. A thin layer, sufficient to cover the YSZ substrate surface can subsequently provide a perovskite-like surface for the subsequent growth of the cubic layers. The distinct effect of such a template layer on the orientation of the LSCO/PLZT/LSCO ferroelectric heterostructure is demonstrated in the x-ray scan in Fig. 6(b), where the main noticeable feature is the complete absence of the [110] diffraction peak. The reader may note that this is not completely unique to BTO; indeed, earlier research on high temperature superconductors (such as YBCO) had already demonstrated the growth of high quality c-axis oriented YBCO thin films on the same YSZ/Si substrate. While the difference in structural quality may itself be of fundamental interest for researchers interested in the growth mechanisms, the films with and without

the template layer show a dramatic difference in ferroelectric properties, which is discussed in the next section. Transmission electron microscopy studies show that the LSCO and the PLZT layers in the PLZT/LSCO/BTO/YSZ hetrostructure are very highly c-axis oriented with very little, if any, large angle grain boundaries.

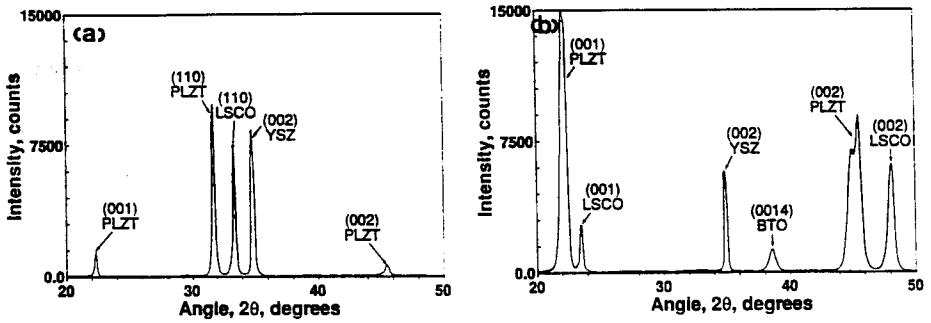


Figure 6. (a) X-ray diffraction pattern of a PLZT/LSCO/YSZ heterostructure, showing the existence of predominant [110] PLZT and LSCO peaks along with the [002] YSZ peak. (b) X - ray pattern of a PLZT/LSCO/BTO/YSZ heterostructure showing the highly preferred [001] PLZT orientation induced by the BTO template layer [12].

Figure 7 shows a micrograph of all the layers in this complicated heterostructure and shows that the BTO layer is c-axis oriented and has a high density of stacking defects, which is well known in these layered perovskites. High resolution images of the LSCO/BTO, Fig. 8 (a) and PLZT/LSCO, Fig. 8 (b), interfaces show no indication of possible interfacial reactions. The PLZT/LSCO interface is highly defective, primarily due to interface dislocations as a consequence of the lattice mismatch.

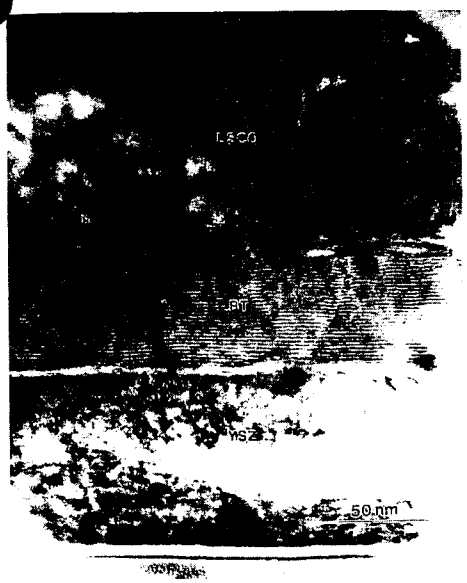


Figure 7. TEM cross-section micrograph of a PLZT / LSCO / BTO / YSZ hetrostructure showing the presence of a high density of stacking defects in all the layers.

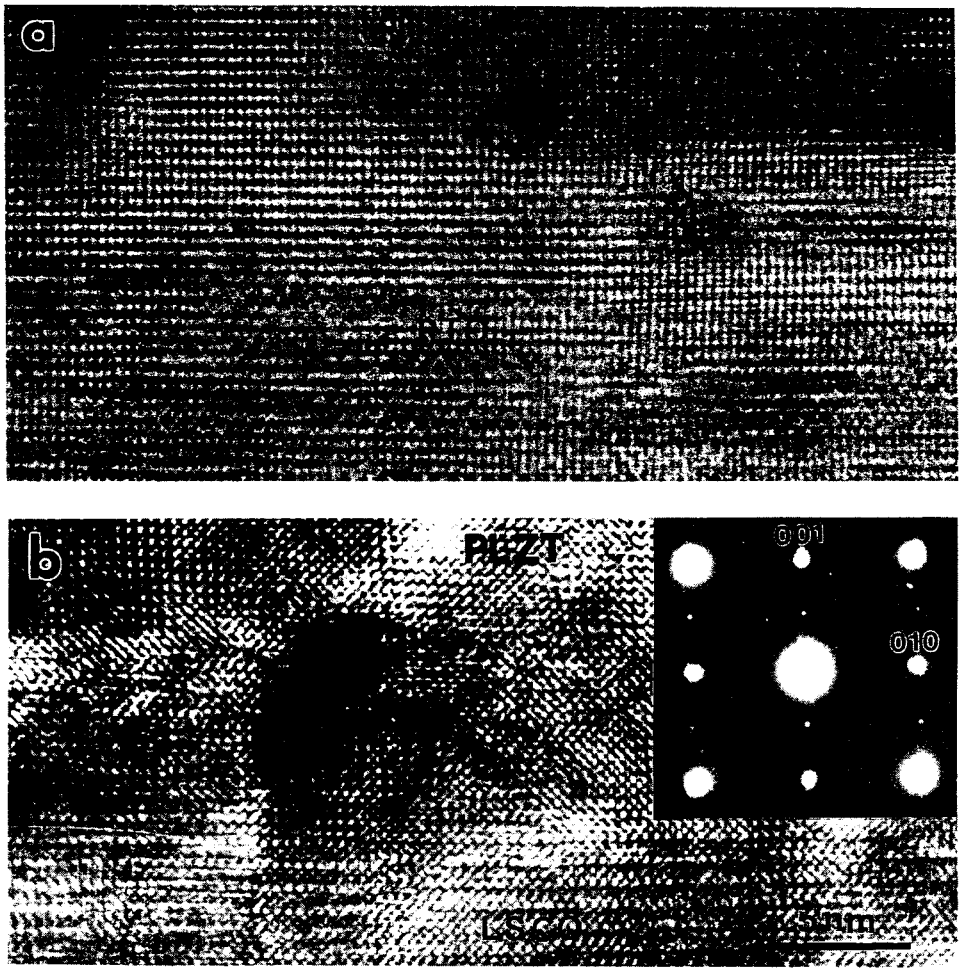


Figure 8. High resolution TEM micrographs of:
a) LSCO/BTO and b) PLZT/LSCO heterostructures.

The ideal demonstration of the effect of the BTO crystallographic anisotropy on its growth is through the studies of BTO growth on SiO_2/Si. The presence of the thermal oxide on Si is important since it will form the basis for fabricating the pass-gate transistors in the Si-CMOS wafer. At first glance, it should be expected that the BTO layer would be completely polycrystalline when grown on an amorphous surface such as SiO_2; however, this is not the case. At the appropriate growth temperature, the BTO layer grows completely c-axis oriented, although the film has very little crystallographic long-range correlation in the plane. The BTO layer provides a template with a perovskite structure to control the subsequent growth of the LSCO/PLZT/LSCO stack promoting the growth of the PLZT layer with [001[orientation, as illustrated in the x-ray diffraction pattern in Fig. 9. Rocking measurements about the [002] PLZT peak show a width of

about 1.0-1.2°, which is larger than that obtained for PLZT layers on $LaAlO_3$ and YSZ/Si substrates. The efficacy of BTO template layer to control the orientation of the over-layer is further demonstrated by the fact that even metals, such as Pt (fcc; a=3.92 Å) can be grown on a BTO template with a prefered [001] orientation when deposited at the appropriate substrate temperature (400-500 °C). In this case, although there is no intrinsic similarity in the structural chemistry of Pt and BTO, the fundamental lattices of the two materials match very well (BTO $a=5.41/\sqrt{2}$; $b=5.45/\sqrt{2}$). As will be demonstrated later, the BTO layers and the subsequent perovskite layers grown on top of it are all randomly oriented in the plane of the film. The crystallographic and chemical characteristics of the grain boundaries present in these oriented heterostructures still remain to be understood and is an interesting field of study.

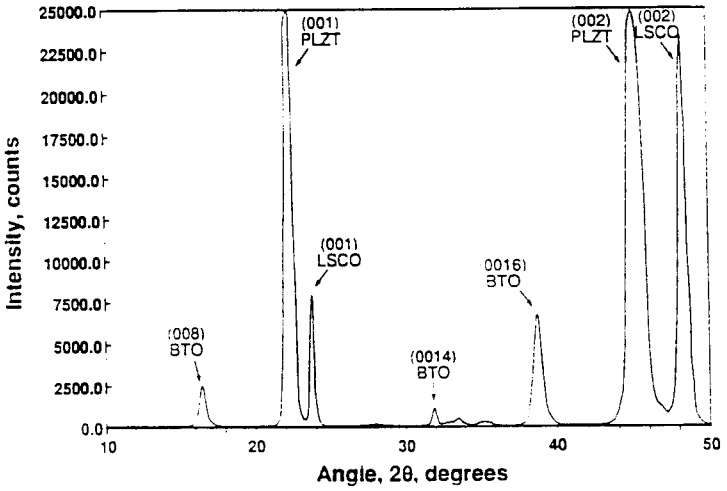


Figure 9. X-ray pattern of an LSCO/PLZT/LSCO/BTO heterostructure grown on a SiO_2/Si substrate, at 600 °C, showing the preferred [001] orientation of the PLZT layer induced by the BTO template [13].

Figure 10 shows a Bragg X-ray scan from a heterostructure that is similar to that schematically illustrated in Fig. 1, but has a [001] Pt layer (~ 800 Å thick) grown on the BTO template layer before the growth of the LSCO/PLZT/LSCO heterostructure capacitor. As it can be seen in Fig. 10, only the [002] Pt peak is observed with a very strong intensity. The inset in Fig. 10 shows, for comparison, the Bragg scan of a PLZT/Pt heterostructure grown without the BTO template laver, indicating that it is weakly [111] oriented. X-ray pole figure scans of LSCO/PLZT/LSCO heterostructures grown on the three types of substrates discussed here are shown in Fig. 11. In this experiment, the pole figure is obtained about the [101] PLZT diffraction peak. In the case of films grown on $LaAlO_3$ and YSZ/Si substrates, a strong four-fold intensity distribution is observed, indicating that there is a significant degree of orientational locking of the in-plane [010] and [100] directions on these substrates. On the other hand, the films grown on SiO_2/Si appear to be completely random in the plane of the film. The effect of these microstructural differences on the ferroelectric properties are discussed in Section.3.

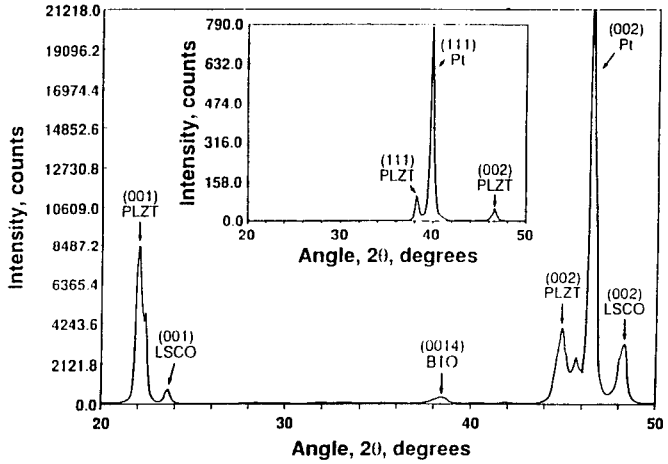


Figure 10. An X-ray Bragg scan from an LSCO/PLZT/LSCO/Pt/BTO heterostructure grown on a SiO_2 / Si substrate, at 600 °C, showing the preferred [001] orientation of the whole structure induced by the BTO template. The inset shows a similar X - ray scan from a PLZT / Pt heterostructure without the BTO template [13].

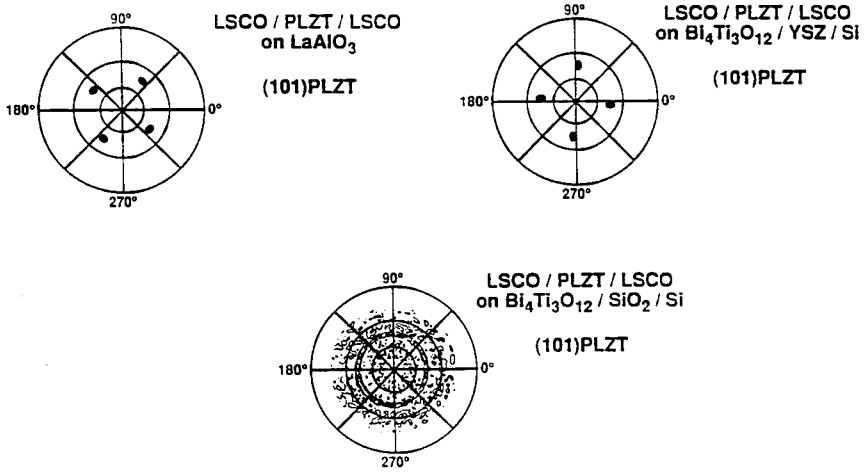


Figure 11. X-ray pole figure scans of LSCO/PLZT/LSCO heterostructures grown on $LaAlO_3$, YSZ/Si and SiO_2/Si.

2.2. POLYCRYSTALLINE PZT-BASED CAPACITORS

Recent work in our laboratories [14] demonstrated that polycrystalline LSCO/PLZT/LSCO heterostructure capacitors grown on Si substrates have as good long term electrical properties (e.g. negligible or no fatigue) as those characteristics of the

highly oriented capacitors discussed in Section 2.1., the main difference being that the polycrystalline capacitors present lower absolute values of remanent polarization [14] than those characteristic of the highly oriented capacitors. The relevance of these results relates to the possibility of simplifying the fabrication of the capacitors for non-volatile memories. For example, heterostructure LSCO/PZT/LSCO capacitors were produced on $Pt/Ti/SiO_2/(100)Si$ substrates using the PLAD technique in such a way that all layers of the capacitor were deposited in-situ without breaking vacuum [14], at 600 °C, in an oxygen background pressure of 300-900 mTorr. The Pt and Ti layers were deposited in a separate system using e-beam evaporation, which produced (111) Pt layers with a columnar structure perpendicular to the substrate surface. An XRD pattern of an $LSCO/PZT/LSCO/Pt/Ti/SiO_2/Si$ structure is shown in Fig. 12, which demonstrates that the PZT film is polycrystalline with a partial (111) orientation and contains the perovskite phase only. The polycrystalline nature of the PZT-based capacitors grown directly on Pt is contrasted against the highly oriented PZT-based capacitors grown on Si with an intermediate BTO layer, as discussed in Section 2.1.

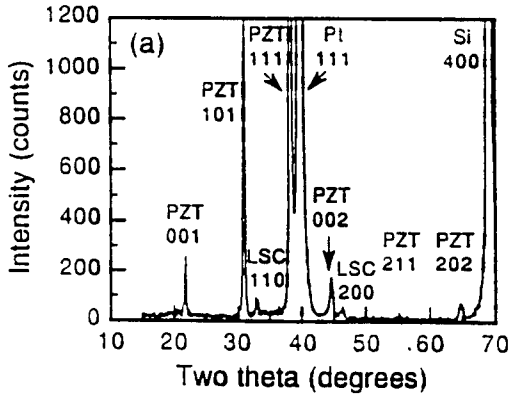


Figure 12. XRD spectrum of an $LSCO/PZT/LSCO/Pt/Ti/SiO_2/Si$ heterostructure, showing the polycrystalline nature of the PZT layer [14].

3. Electrical Properties of PZT-based heterostructure capacitors

3.1. SHORT AND LONG TERM ELECTRICAL PROPERTIES

3.1.1. *Highly Oriented PZT-Based Capacitors*

The main reason for the considerable interest in growing PZT-based heterostructure capacitors with oxide or hybrid metal-metallic oxide electrodes is the recent demonstration of very desirable ferroelectric properties using such structures. Many of the details of the ferroelectric properties of LSCO/PLZT/LSCO capacitors produced by the PLAD method can be found in the recently published literature [12-14]. In this review, only the salient features and some particular aspects of films prepared by the PLAD technique are discussed. The PZT-based capacitors used for the electrical tests discussed in this section

were fabricated using blanket bottom electrodes and a combination of a photolithographic lift-off procedure in conjunction with either wet etching or dry ion beam milling to pattern the top electrodes. Capacitors with 600 to 2 μm diameter were fabricated using the methods mentioned above. The details of device fabrication are described in earlier papers. The electrical tests were performed mainly using the ferroelectric tester RT66A from Radiant Technologies, primarily in the pulsed testing mode to simulate as close as possible the memory operation. For example, the differential pulsed remanent polarization, DP, defined as switched polarization, P* - nonswitched polarization, P^ is in general twice the conventionally measured remanent polarization, Pr, which can be measured from the hysteresis loop.

Figure 13 shows a family of pulsed hysteresis loops of an LSCO/PLZT/LSCO capacitor grown on $LaAlO_3$. Typically, pulsed remanent polarization values in the range of 25-35 $\mu C/cm^2$ were obtained at room temperature, with an applied field of 5V. The coercive field of the PZT-based capacitors with oxide electrodes, which is also an important memory element design variable, is typically in the range of 0.7-1.5V. The field dependence of the hysteresis properties is illustrated in Fig. 13. The film resistivity at 5V is typically in the range of $5x10^9$ - $5x10^{10}\Omega$-cm, a value which is considerably higher compared to those obtained in the early days of the use of these metal oxide electrodes. This result can be attributed to better control over the deposition parameters, including the film thickness.

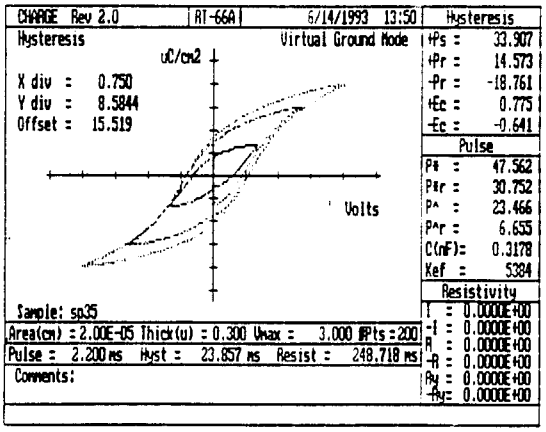


Figure 13. Family of pulsed hysteresis loops obtained from a highly oriented LSCO/PLZT/LSCO capacitor grown on $LaAlO_3$.

Figure 14 shows the pulsed remanent polarization and film resistivity as a function of temperature, for the same capacitor for which the hysteresis loops are shown in Fig. 13, measured with an applied voltage of 5V. This temperature dependence is expected, since we are approaching the Curie temperature. Concurrently, there is more thermal

activation for point defects such as oxygen and lead vacancies to move, thus contributing to transport in the film. Ferroelectric hysteresis properties for films grown on YSZ/Si are very similar to that on $LaAlO_3$.

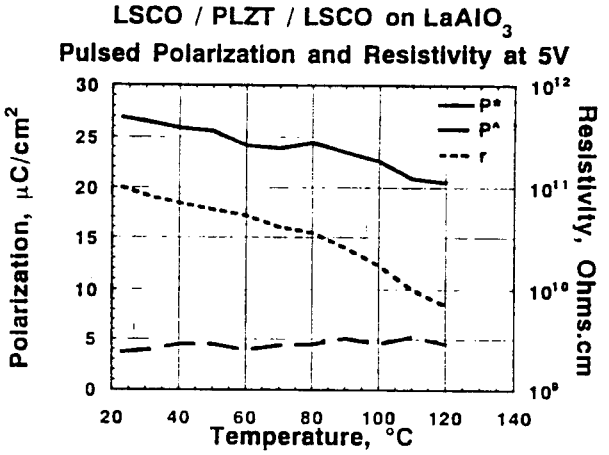


Figure 14. Pulsed remanent polarization and resistivity vs. temperature curves for the same LSCO/PLZT/LSCO capacitor for which hysteresis loops are shown in Fig. 13.

Figure 15 shows pulsed hysteresis loops for a LSCO/PLZT/LSCO heterostructure grown on SiO_2/Si with the BTO template and a Pt under-layer. The overall trend is very similar to that of the capacitors on $LaAlO_3$, with the difference being that the coercive fields are slightly larger and the pulsed remnant polarization is smaller (typically in the range of 15-20 $\mu C/cm^2$ at 5V). It should be noted, however, that these values are more than sufficient for nonvolatile memory operation, if they satisfy the reliability requirements. Consequently, very detailed pulsed testing of the capacitors described above is being performed to understand the effect of process variables and microstructure on the key reliability parameters. The initial work was focused on finding solutions to the problem of bipolar fatigue in PZT-based capacitors. As outlined in the introduction, it has been found that using metallic oxide electrodes instead of the conventional Pt electrodes makes a dramatic difference in the fatigue characteristics. This is illustrated in Fig. 16, for the case of a LSCO/PLZT/LSCO capacitor grown on $LaAlO_3$. In capacitors grown under the optimum conditions, we do not observe any significant fatigue even after 10^{12} cycles. These results are very promising, considering that fact that capacitors with Pt electrodes typically fatigue and lose more than 50% of their initial polarization after just 10^8 cycles, as shown in Fig. 16. This marked difference in fatigue characteristics with the type of electrode (i.e., Pt or metal oxide) is observed irrespective of the crystalline quality of the PLZT thin film. It is important to note that although many research groups have demonstrated similar fatigue results using metallic oxide electrodes,

a clear and rigorous understanding of the cause for this difference in fatigue behavior is still not available.

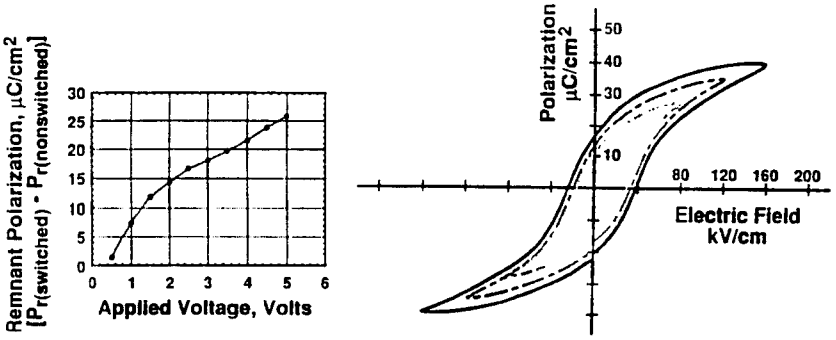


Figure 15. Pulsed hysteresis loops for an LSCO / PLZT / LSCO heterostructure capacitor grown on a SiO_2/Si substrate with the BTO template and a Pt under-layer [13].

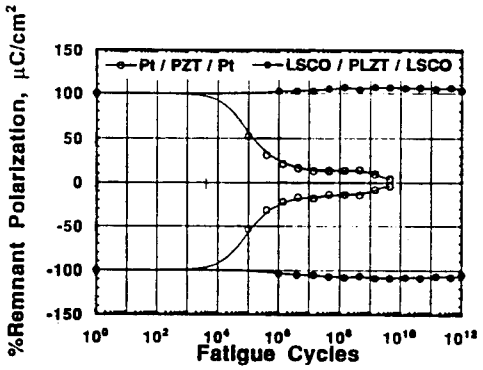


Figure 16. Results of a fatigue test on an LSCO / PLZT /LSCO capacitor grown on a $LaAlO_3$ substrate and compared with that of a Pt / PLZT / LSCO capacitor on $LaAlO_3$.

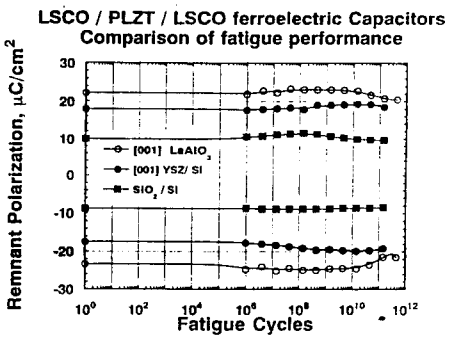


Figure 17. Comparison of fatigue characteristics of LSCO/PLZT/LSCO capacitors grown on $LaAlO_3$, BTO / YSZ / Si and Pt / BTO / SiO_2 / Si.

The capacitors grown on YSZ/Si and SiO_2/Si show essentially identical fatigue behaviour, as illustrated in Fig. 17 (compare with Fig. 16) for a 50 μm diameter capacitor grown on SiO_2/Si with the Pt underlayer. These heterostructures also show similar fatigue characteristics when tested at 100°C. Results of fatigue experiments at 100°C on the same capacitor are also presented in Fig. 17. The almost complete absence of any loss in pulsed remanent polarization under these testing conditions is quite desirable for the ultimate use of these capacitor structures in nonvolatile memories.

3.1.2. *Polycrystalline PZT-Based Capacitors*

The main difference in the short and long term electrical properties between PZT-based polycrystalline and highly oriented capacitors with oxide electrodes, discussed in this review, are that the polycrystalline capacitors exhibit slimmer hysteresis loops with lower remanent polarization (compare Figs. 18(a) and 18(b)). However, both the polycrystalline and highly oriented PZT-based capacitors described here exhibit practically no fatigue when tested up to about 10^{10} polarization switching cycles (Fig. 19). These results further confirm that the film crystallinity plays a minor role vis-a-vis fatigue compared to the nature of the interfaces between the electrode and the ferroelectric.

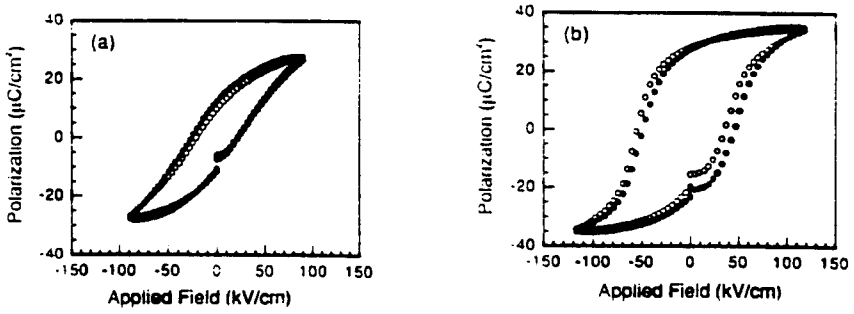


Figure 18. (a) hysteresis loop [(•) before and (o) after fatigue] of a polycrystalline LSCO/PZT/LSCO capacitor deposited on a Pt/Ti/SiO_2/Si substrate; (b) hysteresis loop [(•) before and (o) after fatigue] of a highly oriented LSCO/PZT/LSCO capacitor deposited on a (100) MgO substrate presented for comparison [14].

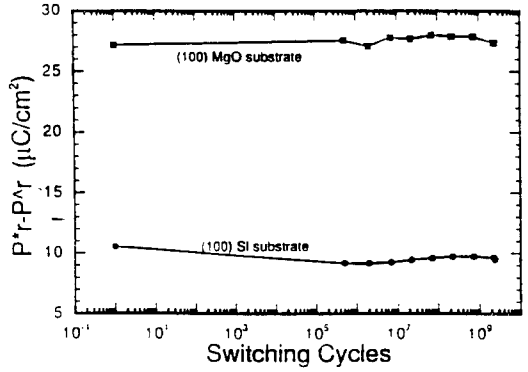


Figure 19. Fatigue data for polycrystalline (on Si) and highly oriented LSCO/PZT/LSCO on (100) MgO heterostructure capacitors produced by the PLAD technique [14].

Another important parameter related to the reliable electrical behavior of a capacitor for non-volatile memories is the polarization retention as a function of time after a capacitor has been polarized in one logic state. The "ON" state retention results for oriented and polycrystalline PZT films are compared in Fig. 20 of Ref. [14]. Both curves follow a log-linear relationship with a constant decay rate. By extrapolation, the polycrystalline PZT capacitors will maintain a minimum of 2 $\mu C/cm^2$ of switched polarization after a cumulative aging period of $1x10^{10}$ seconds ($3x10^2$ years!). Therefore, retention is a parameter that is currently under control for both highly oriented and polycrystalline PZT-based capacitors with oxide electrodes.

In summary, polycrystalline PZT-based capacitors with hybrid LSCO-Pt electrodes fabricated on Si exhibit excellent fatigue and retention characteristics at room temperature, demonstrating that it may not be absolutely necessary to have oriented PZT in order to achieve fatigue-free ferroelectric capacitors. This result, coupled with the fact that Pt/Ti adheres well to SiO_2 and is stable in an oxygen ambient, makes the integration of ferroelectric PZT capacitors with Si much simpler for fabricating PZT-based non-volatile memories. In addition, resistivity measurements indicate that the hybrid LSC/Pt electrode have much lower resistivity than the pure LSCO electrode, which would improve the device performance. However, considerable further testing under a variety of operating conditions are required to verify this completely.

4. Imprint in PZT-Based PLAD Capacitors

As discussed in Section 3, issues pertaining to fatigue and retention have received considerable attention over the past few years. With regards to imprint in ferroelectric capacitors, there is not a consensus as to what constitutes a reliable imprint test, since this phenomena has not received much attention. Researchers have not agreed either on whether imprint represents a "write" or a "read" error. From a device point of view, the key aspect of imprint is that it constitutes a "write" error, which in our view is explained as follows: If a written and previously imprinted states are in opposite directions (e.g., up and down, respectively), the written (up) state will, as a function of time, show a tendency to revert to the imprinted (down) state. Hence, the written state will, after some time, assume the complementary (down) orientation of the intended (up) logic state causing a "write" error. If it is assumed that the capacitor is read non-destructively, the write error will be easily verified. However, if the capacitor is read destructively, the original state which had been written "up" and subsequently imprinted to the "down" state will correctly be read as a "down" state as long as the applied electric field is greater than the coercive field. If the applied field is less than the coercive field, the imprinted dipoles will not switch causing a read error. The process by which imprint manifests itself is via the reversal of ferroelectric domains (possibly due to space charge, defect dipoles, charge at trap sites, or other mechanisms).

In thin film PZT ferroelectric capacitors, the self reversal effect has been investigated and found to be dependent on the time between the write and read pulses and on the length of the write pulse [22]. Recently, work was discussed related to the imprint properties of Sol-Gel PZT capacitors, using a sequence of fatigue-related bipolar, positive unipolar, and negative unipolar pulses [23]. More recently, the NCSU-MCNC group performed detailed measurements of imprint in PZT-based capacitors produced by PLAD [24]. The work discussed in Ref. [24] and recently reviewed in a book chapter [25], differs from previous

investigation in the following ways: (a) the imprint results were not affected by fatigue effects, since fatigue-free capacitors were used for the tests; (b) the effects of retention loss and imprint were separately identified; (c) the test methodology and instrumentation were much simpler than in prior work; (d) alternative test sequences were provided; and (e) the tendency to imprint was accelerated by a DC bias rather than by temperature, where pyroelectric effects may influence the measurement.

The imprint test methodology used in the work discussed in Refs. [24, 25] involves testing the imprint characteristics of ferroelectric capacitors using either a DC bias or an asymmetric AC signal to accelerate the process and determine the "rate of imprint". This term was used to describe the rate of approach towards imprint failure [24]. In analyzing the experimental data, polarization retention effects were identified and separated from the rate of imprint, since it is relevant to try to understand these effects separately to better interpret their combined effects which may determine the time it takes for device failure to occur.

In the work described in Refs. [24, 25], pulse trains such as that shown in Fig. 20 were applied to ferroelectric capacitors causing some dipoles to be imprinted in the "up" state. When the first read signal was applied, the dipoles switched "down" and -P* (the switched polarization was measured). During the interval between the two read pulses shown in Fig. 20, some dipoles returned back to the "up" (imprinted, preferred) state. The second read pulse switched the "imprinted" dipoles back to the "down" state and -P^ was recorded. The criteria adopted was that if $|-P^*-(-P^\wedge)| < 2\ \mu C/cm^2$, then an imprint failure has occurred. It should be noted that the above criterion is the same as that which has been established for fatigue and retention failures. Thus, a distinction is required in order to be able to identify a particular failure mode. In the case of fatigue and retention tests, the switched (P^* and P^*_r) and non-switched ($P^\wedge$ and $P^\wedge_r$) polarizations will decrease with time (including the possibility that $P^\wedge$ and $P^\wedge_r$ may remain constant). The distinction between these failure modes is determined by the device history, i.e., whether failure is due to switching cycle effects or simply time-related effects. The evaluation of retention using the pulse sequence of Fig. 20 without the DC bias shows loss of switchable polarization.

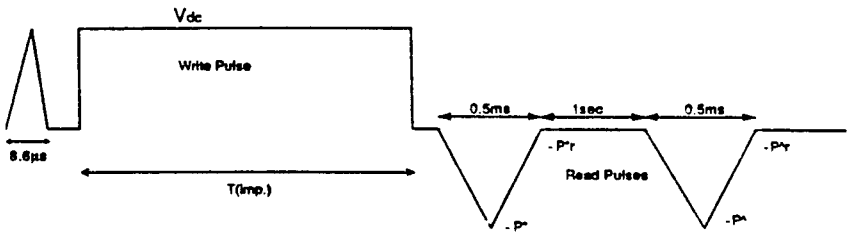


Figure 20 . Voltage wave form used to test for an imprinted state that is in the opposite direction of the read voltage [24].

A failure by imprint (without loss of retained polarization), as measured using a pulse sequence such as that of Fig. 20, should show an increase in $P^\wedge$ and $P^\wedge_r$, while the switched components (P^* and P^*_r) should stay constant. When the loss of retained polarization is simultaneously occurring during an imprint failure, the switched polarizations should decrease and the non-switched components should increase with time.

These features were observed in imprint tests of PLAD PZT-based capacitors, as shown in Fig. 21.

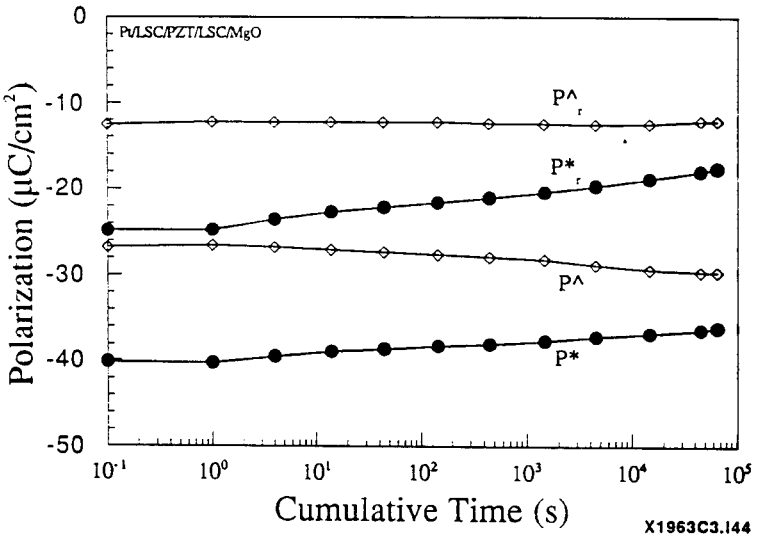


Figure 21. Imprint characteristics of an LSCO/PZT/LSCO/MgO capacitor using a DC bias = 5 volts and read voltage of -3 volts [24].

Imprint tests performed for heterostructure LSCO/PZT/LSCO capacitors on sapphire and GaAs also revealed [26], as for the capacitors on MgO and Si discussed above, that failure due to imprinting would not occur until 10^{13}-10^{14} seconds of operating time, under the present test conditions.

Based on the imprint test results briefly discussed above and in more detail in Refs. [24, 25], it appears that failures by imprint/retention loss mechanisms are not an issue for the type of capacitors that were evaluated (including size), at least under the test conditions used in the work described here. However, because the failure mechanism is not understood, extrapolations of this type have limited applicability. In addition, it is very important to perform imprint tests on capacitors much smaller than those used in the tests reported here, i.e., tests should be performed with micron and submicron-size capacitors to fully evaluate possible imprint effects on capacitors that will be used in high density non-volatile memories. Further work is obviously necessary to better understand the implications of imprint on the operation of ferroelectric non-volatile memories.

5. Conclusions

Pulsed laser ablation deposition (PLAD) is a very versatile technique to perform fundamental and applied research related to developing materials integration strategies for thin film-based devices.

Work on materials integration by the NCSU-MCNC and Bellcore has demonstrated that PZT-based heterostructure capacitors involving conductive oxide or hybrid metal-conductive oxide electrodes have negligible or no fatigue, long polarization retention and very small tendency to imprint. These properties make PZT-based heterostructure

capacitors suitable for non-volatile ferroelectric memories. However, further work is necessary, particularly in relation to producing small size capacitors ($\leq$ 1 μm), to determine if scaling down to dimensions compatible with high density memories will not introduce undesirable effects.

6. Acknowledgments

We wish to gratefully acknowledge the support of Dr. Jane Alexander, ARPA through contracts at Bellcore (N00014-93-C-0127) and at NCSU and MCNC (N00014-93-1-0591). We have benefited from many discussions with numerous colleagues around the world and we would like to acknowledge each and every one of them. Specifically we wish to acknowledge the on-going interactions with J.T.Evans, Jr. (Radiant Technologies), A.Kingon (NCSU), W.E.Warren and G.Pike (Sandia), Dr. J.Lee (Bellcore) and Professor E.Goo (University of Southern California).

7. References

1. Carrano, J., Sudhama, C., Lee, J., Tasch, A., Shepherd, W.H. and Abt, N. (1991), *IEEE Trans. Ultrasonics, Ferroelectrics and Freq. Control* **38**, 690.
2. Evans, J.T. and Womack, R. (1988), *IEEE J. Solid State Circuits* **23**, 1171 .
3. Scott, J.F. and Paz de Araujo, C.A.(1989),*Science* **246**, 1400.
4. Dey, S. and Zuleeg, R. (1990), *Ferroelectrics* **108**, 37.
5. *Proceedings of the 3th International Symposium on Integrated Ferroelectrics* (1991), C.A. Paz de Araujo (ed.), University of Colorado Press, Colorado Springs. Also, *Proceedings of the 4th International Symposium on Integrated Ferroelectrics* (1992), C.A. Paz de Araujo (ed.), University of Colorado Press, Colorado Springs.
6. Kwok, C.K., Vijay, D.P., Desu, S. B., Parikh, N.R., and Hill, E.A. 1992), *Proceedings of the 4th Intern. Symp. on Integrated Ferroelectrics*, C.A. Paz de Araujo (ed.), University of Colorado Press, Colorado Springs, p. 412.
7. Al-Shareef, H.N., Bellur, K.R., Auciello, O., and Kingon, A.I. (1993), *Proc. 5th Intern. Symp. on Integrated Ferroelectrics*, C.A. Paz de Araujo (ed.),University of Colorado Press, (in press).
8. Auciello, O., Gifford, K.D. and Kingon, A.I. (1994), *Appl. Phys. Lett.* **64**, 2873. .
9. Gifford, K.D., Auciello, O. and Kingon, A.I. (1994), *Integrated Ferroelectrics* (in press).
10. Ramesh, R., Inam, A., Wilkens, B., Chan, W.K., Hart, D.L., Luther, K. and Tarascon, J.M. (1991), *Science* **252**, 944.
11. Ramesh, R., Chan, W.K., Wilkens, B., Gilchrist, H., Sands, T., Tarascon, J.M., Keramidas, V.G., Fork, D.K., Lee, J. and Safari, A. (1992), *Appl. Phys. Lett.* **61**, 1537.
12. Ramesh, R., Gilchrist, H., Sands, T., Keramidas, V.G., Haakenaasen, R., and Fork, D.K. (1993), *Appl. Phys. Lett.* **63**, 3592.
13. Ramesh, R., Lee, J., Sands, T., Keramidas, V.G., and Auciello, O. (1994), *Appl. Phys. Lett.* **64**, 2511.
14. Dat, R., Lichtenwalner, D.J., Auciello, O. and Kingon, A.I. (1994), *Appl. Phys. Lett.* **64**, 2673.

15. Scott, J.F. (1994), *in "Science and Technology of Electroceramic Thin Films", this NATO/ARW book, pp.* .
16. Kelly, R. and Miotello, A. (1994), in D.B. Chrisey and G.K. Hubler (eds.), *Pulsed Laser Deposition of Thin Films*, John Wiley & Sons, Inc., New York, pp. 55.
17. Geohegan, D.B., (1994), Ibid, pp. 115.
18. Chen, L.C. (1994), Ibid, pp. 167.
19. Saenger, K.L. (1994), Ibid, pp. 199.
20. Lichtenwalner, D.J., Auciello, O., Dat, R. and Kingon, A.I. (1994), *J. Appl. Phys.* **74**, 7497.
21. Auciello, O., Emerick, J., Duarte, J. and Illingworth, A. (1993), *J. Vac. Sci. Technolo.* **A11**, 267.
22. Benedetto, J.M., Moore, R.A. and McLean, F.B. (1994), *J. Appl. Phys.* **75**, 460.
23. Mihara, T., Watanabe, H. and Paz de Araujo, C.A. (1993), *Jpn. J. Appl. Phys.* **32**, 4168.
24. R. Dat, D.J. Lichtenwaler, O. Auciello, and A.I. Kingon, (1994), *Integrated Ferroelectric* (in press).
25. Auciello, O., Dat, R. and Ramesh, R. (1994), in *"Electroceramic Thin Films: Basic Processes and Applications,"* C.A. Paz de Araujo, J.F. Scott, and G.W. Taylor (eds.), Grodon and Breach Publishers, New York (in press).
26. Dat, R., Lichtenwalner, D.J., Auciello, O. and Kingon, A.I. (1994), *J. Mater. Res.* (submitted).

LOW ENERGY ION BOMBARDMENT INDUCED EFFECTS IN MULTI-COMPONENT ELECTROCERAMIC THIN FILMS

S.B. KRUPANIDHI
206 Materials Research Laboratory
Department of Engineering Science & Mechanics
The Pennsylvania State University
University Park, PA 16802, USA

ABSTRACT. This paper is focused on discussing low energy ion bombardment-induced effects on the growth processes, composition, microstructure, and properties of electroceramic thin films grown by ion beam sputter-deposition and pulsed laser ablation-deposition.

1. Introduction

With most sputter deposition techniques, intrinsic energetic particle bombardment of depositing films is generally observed, however this bombardment is usually uncontrollable. In plasma based deposition techniques such as magnetron sputter deposition, the fluence and the energy of the sputtering species are interdependent, while relatively larger amounts of unwanted bombardment is unavoidable. Controlled bombardment of a growing thin film has long been recognized as an important approach in modifying the growth process, microstructure and properties of resultant films. Although the benefits of controlled low-energy ion bombardment are well known, its application has been mostly limited to the deposition of single-component or single-cation (such as metal, semiconductor and simple oxide) films. However, we have successfully applied such low energy oxygen ion bombardment to complex oxide ferroelectric thin films such as $Pb(Zr,Ti)O_3$, $(Pb,La)TiO_3$ and $(Ba,Sr)TiO_3$.

Several physical vapor growth techniques were explored while a low energy ion bombardment during growth process has been introduced accordingly. More specifically, low energy ion beam using a Kaufman source in case of multi-ion-beam reactive sputter (MIBERS) deposition, low pressure dc glow discharge in case of excimer laser ablation and an electron cyclotron resonance plasma source for providing high density of bombarding ions, are used in the present investigations. The presence of such low energy bombarding environment during the growth of complex electroceramic thin films enhanced the crystallization process, reduced growth temperature, improved electrical behavior (short and long terms) and also aided modulating the nature of conduction mechanisms. The present paper describes the involvement of a variety of these approaches during the development of multi-component ferroelectric oxide thin films, such as $Pb(Zr,Ti)O_3$, $(Pb,La)TiO_3$, $(Ba,Sr)TiO_3$, and $SrTiO_3$ and the effect of bombardment is quantified in terms of describing the properties.

O. Auciello and R. Waser (eds.). Science and Technology of Electroceramic Thin Films, 23-51.
© 1995 *Kluwer Academic Publishers. Printed in the Netherlands.*

2. Thin Film Growth And Low Energy Assistance Approaches

2.1. MULTI-ION BEAM REACTIVE SPUTTER (MIBERS) DEPOSITION : KAUFMAN SOURCE BASED ION BEAM ASSISTANCE

The ion beam sputter-deposition technique with concurrent low energy ion bombardment offers the following unique features:[1,2] a) independent control of flux density and energy of the sputtered species, b) lower operating pressures during thin film growth ensures better quality of films, and c) the possibility of independently controlled low energy ion bombardment (usually with reactive oxygen species) of the growing films. Besides incorporating reactive oxygen species in the films, this sort of bombardment also offers additional benefits such as increasing adatom mobility, providing extra energy to supplement thermal energy to the species during nucleation thus allowing the reduction of the crystallization temperature.

Very recently, few alternative attempts are evident in the literature involving ion beam sputter deposition to grow ferroelectric thin films[3,4]. A multi-ion beam sputter deposition approach has been devised in our laboratory.[5] Considering PZT films as a typical example, three independent metal targets of Pb, Zr and Ti were individually sputtered by high energy focused ion beam sources; the schematic illustration of the system is shown in Fig. 1. Three individual metal targets about 7.5 cm diameter were coordinately arranged so that a flat profile of sputtered species was obtained. A fourth ion source was used to bombard the growing film which was operated in defocused mode for obtaining a broad beam and was arranged to achieve a bombarding angle of 35° with respect to the normal of the substrate surface. An ion flux density measurement probe was placed adjacent to the substrates to measure the flux density of bombarding ions at the substrate. This measurement, in conjunction with the atomic flux density determined from the thickness monitor, establishes the ion/atom ratio which is critical to achieve reproducible bombarding effects.

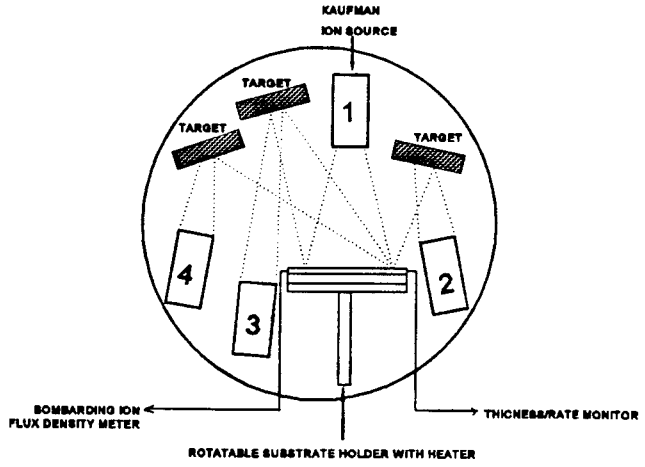


Figure 1. Schematic of the MIBERS system with low energy ion beam assistance.

The deposition rates of individual targets were measured as a function of ion beam voltage, while the ion beam current and oxygen partial pressures were kept constant. The beam voltage determines the energy of the sputtered ions which is to be kept above a threshold level necessary to initiate sputtering of each metal. Small quantities of molecular oxygen were bled into the chamber during the deposition to create a reactive environment for the oxidation of the sputtered metal species. By adjusting the powers on individual targets, stoichiometric PZT films could be grown over large areas (4" diameter). Significant uniformity in the homogeneous distribution of composition and thickness was achieved. A variation in compositional homogeneity of < 5% and thickness of < 7% was reproducibly obtained over a diameter of 4".

PZT(50/50) films were deposited on Pt-coated Si or bare Si substrates by the MIBERS system at room temperature and at a deposition rate about 18 Å/min. During the deposition, the growing films were directly bombarded by a low-energy oxygen ion (O_2^+/O^+) beam from a 3-cm Kaufman ion source in single grid configuration. The beam was directed to the substrates with an angle of incidence at about 25° from the normal of substrate surface. To compensate for the Pb resputtering by the direct bombardment and maintain nearly the same Pb content in the deposited films, the Pb flux was increased by 12-19 % excess (relative to the case of non-bombardment) depending on bombarding conditions. This was done by increasing the voltage and current of the sputtering ion beam of the Pb target. To comparatively study the effects of bombardment, non-bombarded films were also deposited under otherwise the same conditions. It needs to be mentioned that here the word "non-bombarded" means without direct ion bombardment. The intrinsic bombardment effect of ion beam sputter deposition due to the backscattered ions and sputtered neutrals, which in the present case have energies of about 10 eV as measured,[6] is not specified, since it is common in both cases (with and without direct bombardment). The as-grown films were annealed at temperatures from 550 to 700 °C in an oxidizing ambient to achieve crystallization, and were then characterized in terms of structure, morphology and electrical properties to examine the bombardment effects.

2.2. UV EXCIMER LASER ABLATION : LOW PRESSURE DC GLOW DISCHARGE

Laser induced vaporization (also called laser ablation) is another film deposition technique in which a plume of ionized and ejected material is produced by high intensity laser irradiation of a solid target. Most commonly, UV excimer lasers are being employed for this purpose and the wavelength of the radiation is tuned by the lasing gas composition, such as ArF (193 nm), KrF (248 nm), KCl (222 nm), XeF (351 nm) and XeCl (308 nm). KrF (248 nm) has been most dominantly employed due to its high energy laser pulse output. Pulse to pulse variations are on the order of 5%, while the pulse durations can be 10-25 ns with repetition rates of up to 500 Hz.[7] The process of laser ablation mainly consists of three regions, a) interaction of the laser beam with target, b) interaction of the laser beam with evaporated materials and c) adiabatic plasma expansion and deposition of thin films. Figure 2 shows the schematic of our laser ablation system arrangement. The output of a KrF excimer laser beam at 5 Hz and 248 nm was used in the present work. The beam is focused by a UV grade plano-convex lens and was brought into the vacuum chamber through a quartz port. The incoming beam was incident onto the target at an angle of 45°.

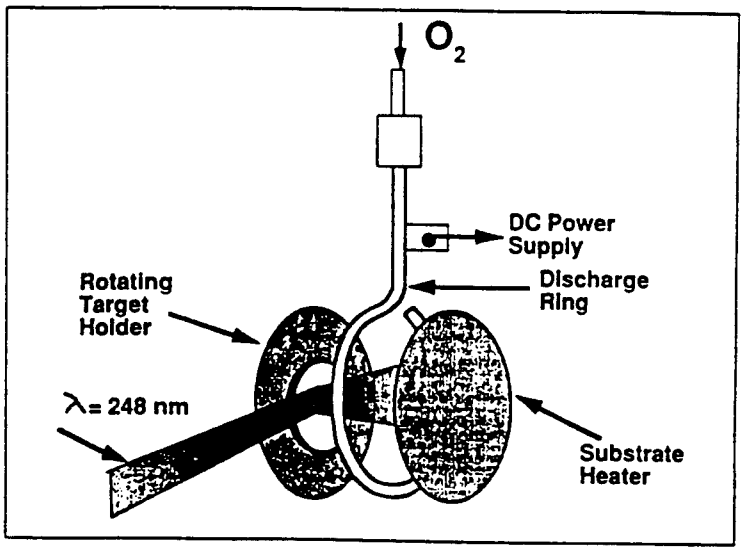


Figure 2. Excimer laser ablation with DC glow discharge.

The ablation of the material is always perpendicular to the target surface irrespective of the angle of incidence of laser beam and the generated plasma is composed of neutrals, ionized atomic and mostly molecular species. This technique has been popularly employed for the successful deposition of high T_c superconductors and currently being exploited for the growth of device quality *in-situ* stoichiometric ferroelectric thin films, such as $Bi_4Ti_3O_{12}$[8] and PZT.[9] Inspite of a few limitations of the technique, such as the occurrence of particulates on the surface of the film and the thickness unevenness, the laser ablation offers several advantages, such as, a) composition of the film can be similar to that of target, even for complex multicomponent systems, b) deposition in relatively high oxygen partial pressures, c) low crystallization temperatures because of the high excitation energy of the photofragments in the laser produced plasma, d) high deposition rates and e) materials with high melting temperatures can be deposited.

During the excimer laser deposition of complex electroceramic thin films, a dc glow discharge plasma was introduced between the target and substrates. The discharge voltage was varied between 0 + 500 V. Such plasmas have been shown to activate the available oxygen resulting in a higher chemical reactivity as well as imparting low energy bombardment. It was seen that the presence of low field discharge in low pressure oxygen environment (1 mTorr) enhanced the dielectric permittivity by almost a factor of 2 and also caused a reduction in the necessary growth temperatures to about 500°C.

2.3. ELECTRON CYCLOTRON RESONANCE (ECR) PLASMA ASSISTED GROWTH

In semiconductor device fabrication processes, plasma reactions by glow discharge at a low temperature, has become an important research subject in recent years,[10] while the frequency of the glow discharge has been changed from dc to microwave regions. Electron Cyclotron Resonance (ECR) plasma stream-enhanced deposition is an emerging

technology and allows the deposition of high quality thin films at relatively lower substrate temperatures.[11] Thus significant process improvement is achieved by enhancing the plasma excitation efficiency and by the acceleration effect of ions with moderate energies on the deposition reaction, using a microwave ECR source and plasma extraction by a divergent magnetic field. Besides the efforts of depositing simple oxides[12] which are optically clear. Most recently, efforts are also evident to deposit ferroelectric complex oxide thin films[13] and we, at MRL/Penn State, are also involved in developing this approach to grow device quality ferroelectric thin films at lower processing temperatures.[14]

The deposition sources (up to three) were arranged with an oblique angle with respect to the ECR source, as shown in Fig. 3 and a certain degree of uneven distribution of the deposited species were noticed without ECR plasma. The results indicate that besides imparting intrinsic low energy bombardment, the efficient coupling of ECR plasma either to magnetron or ion-beam sputtered species offered a highly uniform composition distribution over large areas. The high density of ECR plasma even at low operating pressures may be responsible for controlling the uniform distribution of deposited species, particularly minimizing the scattering of species of large Z numbers. However, the applied ECR power should be compatible with the deposition rates of the species to realize its effect.

During this process the growing film is affected by the presence of energetic species which arise from the plasma. It would be desirable if these energetic species could be controlled during the deposition process. In the present study, species were supplied to the substrate by RF planar magnetron sputtering. A sintered ceramic compound target was used as a raw material source. The magnetron mode of operation was employed to enhance the sputtering process. In this type of configuration a magnetic field is imposed in such a way that the electrons are trapped in a region near the target surface. Since there is a high density of electrons near the target surface, a gas atom entering this electron cloud has a greater probability of becoming ionized. This increased efficiency means that a lower gas pressure is required to maintain the sputtering process and allows for a greater compatibility between rf magnetron and ECR plasma stream.

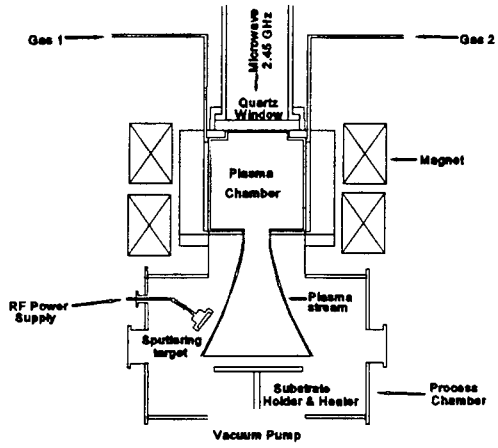


Figure 3. ECR plasma source coupled to an RF magnetron cathode.

The attractive features of ECR plasma stream for the deposition of ferroelectric thin films, include a) low temperature deposition process, b) even at very low pressures, the plasma density in an ECR plasma is much higher than the conventional capacitive RF plasma, c) the wide operating pressure range of 10^{-5} - 10^{-1} Torr, offers high flexibility, and d) the ions arriving at the sample are of low energy, in the range of 5 - 50 eV, to enhance the adatom mobility.

3. Controlled Low Energy Oxygen Ion Bombardment Induced Effects in Multi-Component Oxide Thin films

3.1. KAUFMAN SOURCE : LOW ENERGY (50-100 eV) AND MEDIUM RANGE ION FLUX DENSITIES

Low-energy oxygen ion bombardment was successfully used to modify and enhance the physical properties of MIBERS deposited $Pb(Zr,Ti)O_3$ (PZT) thin films. In the following sections, the bombardment induced effects are systematically described. Figure 4 shows the percentage of resputtered Pb out of the total Pb species arriving to the growing PZT films as a function of the bombardment energy of the secondary ion beam at constant ion flux and deposition rate. It is obvious from the figure that if the direct bombardment is applied, it is necessary to increase Pb flux onto the substrates to compensate for the ongoing resputtering. With a single ceramic target, there is no convenient way to make such a compensation. Therefore, it is very difficult, if not impossible, to introduce an effective ion bombarding assistance into the single ion beam / single target configuration for growing stoichiometric ferroelectric PZT films. However, with the MIBERS technique compensating for such preferential resputtering is no longer a problem, since different components are sputtered independently from different targets by respective ion sources, so that the arrival flux of each component can be easily adjusted.

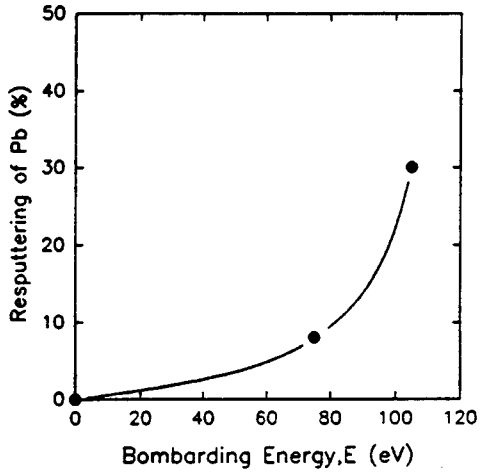


Figure 4. Bombarding energy versus resputtered Pb content.

3.1.1. Crystallization Enhancement

The first obvious effect of the bombardment is the reduction in crystallization temperature. As seen in Fig. 5, films grown with the bombardment at ion energy of 75 eV and ion beam current of 3 mA show dominant perovskite phase after annealing at 550 °C for 2 h, while films grown without the bombardment assume only the pyrochlore phase by the same annealing. Similar phase formation behavior was observed for those films deposited *in-situ* crystalline at 475 °C. This bombardment induced enhancement in crystallization was expected, since similar results have been widely reported for other materials.[15,16] The same effect was also observed for PZT films on bare Si substrates. It has been found that usually excess amount of Pb as high as 20-25 % is needed for PZT(50/50) films on bare Si substrates to attain the perovskite phase by post-deposition annealing. Figure 6 (a) indicates that the perovskite phase is difficult to obtain in the non-bombarded PZT films of near-stoichiometric Pb content (about 3% excess Pb) on bare Si substrates. But the bombarded films of the same kind and by the same annealing assume dominant perovskite phase, as shown in Fig. 6 (b). Such crystallization enhancement may in part be attributed to enhanced adatom mobility by the bombardment. Muller visualized the possible mechanism of this effect in molecular dynamics simulations of crystal growth.[16] Low energy ion bombardment provides local atomic rearrangement allowing atoms to relax into lower energy sites. In the present case, although the as-grown films are mainly amorphous, it is quite possible that nucleation may have been initiated during deposition by these local atomic rearrangement and relaxation, so that some micro-crystallites have already existed in the as-grown films although they are too small to be detected by x-ray diffraction (XRD). In addition, enhanced incorporation of oxygen in the films by the reactive oxygen ion (O_2^+/O^+) bombardment, as similarly reported,[17] may be another reason for this crystallization enhancement. It has been noted that sufficient oxygen concentration is crucial for PZT films in forming and maintaining the perovskite structure.[18] Also, it is worth mentioning that the bombarded as-grown films tend to store more excess free energy due to the bombardment. The release of such energy can significantly promote nucleation and crystallization of the amorphous films.[19]

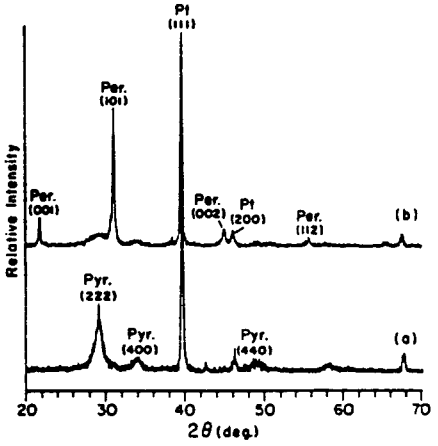


Figure 5. XRD data of PZT films on Pt/Si substrates: a) non-bombarded and b) *in situ* bombarded.

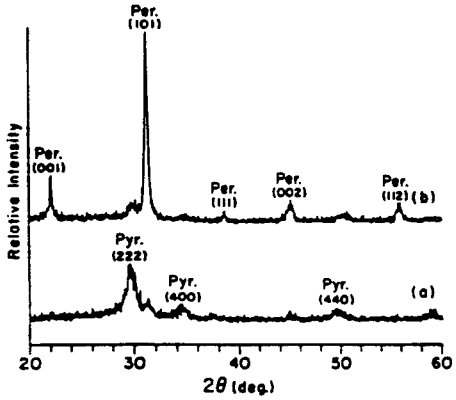


Figure 6. XRD data of PZT films on bare Si substrates: a) non-bombarded and b) *in situ* bombardment.

3.1.2. Inducing Preferred Orientation

Figure 7 indicates that while non-bombarded films usually exhibits a random orientation with the XRD pattern similar to those of randomly oriented PZT ceramics, bombarded films can assume preferred (100) orientation. The degree of such preferred orientation seems highly dependent on the bombardment conditions such as ion/atom ratios (Figs. 7 (b) and (c)). It was observed that the difference in Pb content between these two kinds of films is very small (nominally the same in the as-grown films, by Rutherford backscattering spectrometry). Also, it can be noted that the preferred orientation induced by the effect of Pb content (as seen in the previous part) may not assume such a high degree of orientation as seen here, and usually is accompanied with the formation of a second phase. Therefore, the bombardment effect is thought to be the major reason for the preferred orientation in this case. The bombardment effect on preferred orientation has often been attributed to the occurrence of recrystallization associated with ion channeling effect.[20] Since there was no appreciable *in-situ* crystallization in the present case, it is thought that this preferred orientation might initiate from the possible *in-situ* nucleated micro-crystallites (as mentioned above) which acted as seeds for the following crystallization. The other possible reasons are associated with bombardment induced anisotropic stress[21] and the bombarding energy stored in the as-grown amorphous films[22] which may tend to cause a preferred orientation of film upon instantaneous release during post-deposition annealing.

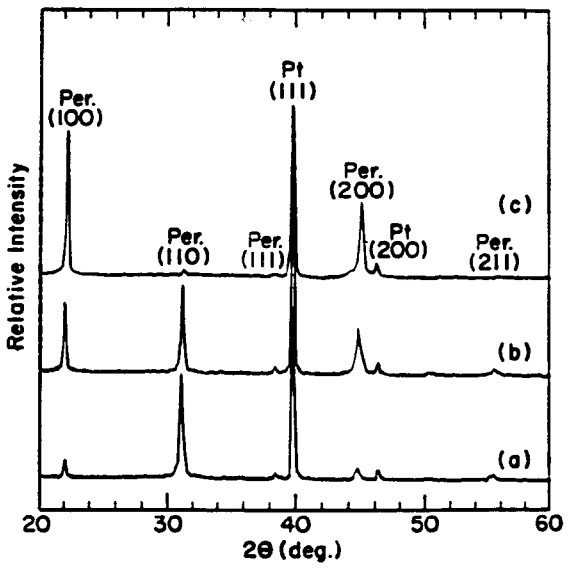


Figure 7. XRD patterns for PZT films under different bombarding conditions: a) non-bombardment, b) bombarded (I/A = 1.1), and c) bombarded (I/A = 1.4).

3.1.3. Densification and Surface Smoothing

Scanning electron microscopy showed that the films grown with assisted bombardment attained denser structure and smoother surface than the non-bombarded ones, although both have some common features such as clustering attributable to low-temperature deposition and fine grain size due to the intrinsic bombardment effect of the ion beam sputter deposition.[14] According to molecular dynamics simulations, the densification by off-normal incident ion beam bombardment is thought to be a natural consequence of the bombardment.[17] The surface smoothness would, of course, be improved with film density. Besides, enhanced adatom mobility makes a significant contribution to smoothing the surface.[17] The other aspect of the surface smoothing might be a consequence of resputtering. Since the sputter yield is strongly dependent on the angle of incidence of sputtering species, the result of energetic bombardment during deposition is often that topographical features which protrude up from the rest of the surface plane are more rapidly etched than the flat surface, resulting in a smoother and more featureless films.[22] This is true if the substrate is rotated continuously, as in the present work. However, if the substrate is fixed one can still develop strong topography of cones, for example, with orientation along the ion beam direction even if it is not grazing angle.[23]

3.1.4. Modification of Electrical Properties

3.1.4.1. Remanent Polarization and Coercive Field. As a natural consequence of structural modification, the impact of the low-energy oxygen ion bombardment on the electrical properties of the films is profound. Figure 8 shows the evolution of both remanent polarization (P_r) and coercive field (E_c) of both kinds of the films with annealing temperature (T_a). A common trend is that, within the temperature range shown, P_r always increases with T_a while E_c initially drops and afterwards flatten out, which may be attributed to the development of the crystallinity of perovskite phase. The significant feature shown in the figure, however, is that for each T_a the bombarded films have higher P_r and lower E_c than the non-bombarded films. The following reasons can be noted responsible for this superiority of the bombarded films: a) better crystallinity for each corresponding T_a since the bombarded films started to form perovskite phase at lower temperature, b) higher degree of (100) orientation, and c) better electrode-film interfaces attributed to denser and smoother film surfaces.

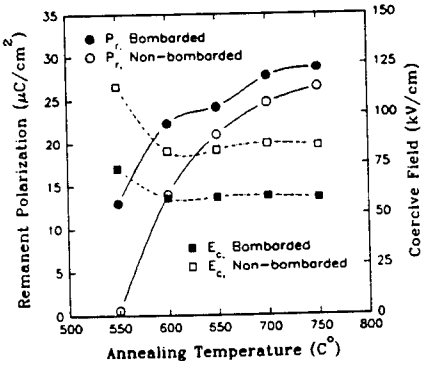


Figure 8. Effect of bombardment on the evolution of polarization.

3.1.4.2. Dielectric Response. Figure 9 shows the change of room-temperature low-field dielectric constant and dielectric loss of both kinds of films with annealing temperature T_a. In general, after completing perovskite formation ($T_a \geq 600$ °C) these films have relatively high dielectric constant (in the range of 700-1200) and low dissipation factor (0.02-0.03) which are comparable to those of bulk ceramic PZT of the same composition.[24] It can also be seen from Fig. 9 that for T_a below 650 °C the bombarded films have higher dielectric constant than the non-bombarded films, being consistent with the fact of reduction in crystallization temperature of perovskite phase in the bombarded films. While the dielectric constant of non-bombarded films keeps increasing with annealing temperature, the dielectric constant of bombarded films decreases with annealing temperature above 600 °C and becomes smaller than that of non-bombarded films for higher temperatures. This could be attributed to the development of larger degree of (100) orientation in the bombarded films which tends to lower the dielectric constant.[25] In almost all cases, the bombarded films have lower dielectric loss than the non-bombarded films.

3.1.4.3. Leakage Current. Figure 10 shows the results of measurements of I-V response of both the bombarded and non-bombarded films, annealed at 600 °C for 2 h. Several interesting differences can be noted between the bombarded films and the non-bombarded films: (a) The ohmic resistivity of the bombarded films (~3×10^{11} Ω-cm) is about one order of magnitude higher than that of the non-bombarded films (~3×10^{10} Ω-cm). (b) The onset voltage of the space-charge-dominant conduction is much higher for the bombarded films (~12 V) than for the non-bombarded films (~10 V). (c) The bombarded films have much higher dielectric breakdown strength compared with the non-bombarded films (~770 kV/cm versus ~350 kV/cm, under the indicated measurement conditions). It was also found that for films annealed at higher temperatures, these differences become less significant while the values of the non-bombarded films approaches those of the bombarded films. These differences may be due to the difference in the microstructure and the degree of non-stoichiometry between these two kinds of films, and are being under further investigation.

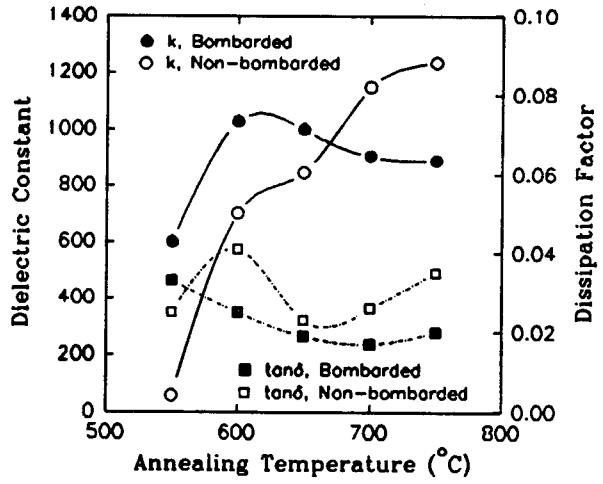


Figure 9. Dielectric response with bombarding conditions.

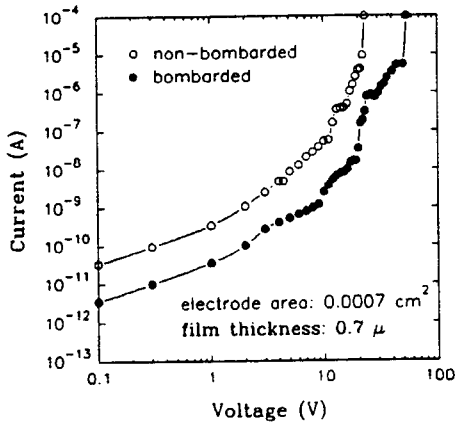


Figure 10. Leakage current behavior with bombarding conditions.

3.1.4.4. Time Dependent Dielectric Breakdown. The time dependent dielectric breakdown (TDDB) of the ferroelectric films is believed to have close relation to the I-V behavior since both of them are due to the motion of charge carriers.[26] Figure 11 shows the TDDB characteristics of the above mentioned films annealed at 680 °C for 2 h. As expected, the bombardment induced effect on TDDB is extremely large. Under the same dc field of 450 kV/cm, the non-bombarded films break down in about 50 min, while the bombarded films can last for 925 min.

Low-energy oxygen ion bombardment during growth also has positive effect on the TDDB behavior. Figure 12 shows the TDDB of $BaTiO_3$ films with and without bombardment deposited at room temperature and annealed at 700 °C for 2 hrs. Initially, the same increasing rate of leakage current can be seen for both films. However, the leakage currents increase rapidly for non-bombarded films after 780 min. stressing at 0.5 MV/cm, while the current for bombarded films still increase slowly. The difference have been attributed to the denser microstructure and possibly the low-energy oxygen ions reacted more strongly with metal ions for bombarded films and thus reduce the concentration of oxygen vacancies.[27]

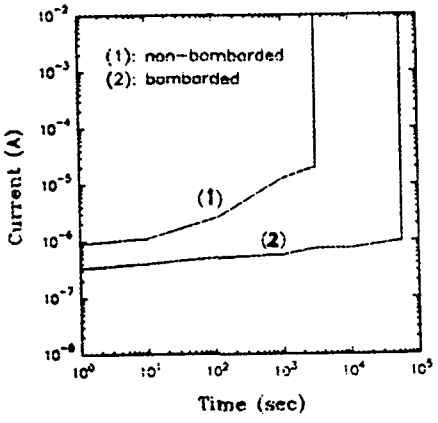


Figure 11. TDDB behavior of PZT films.

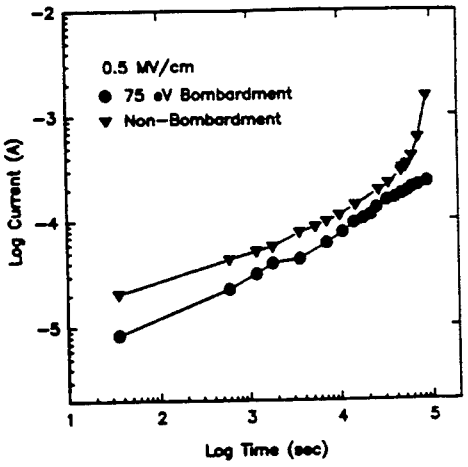


Figure 12. TDDB behavior of $BaTiO_3$ films.

3.2. USING C DC GLOW DISCHARGE: VERY LOW ENERGY (5-20 eV) AND LOW ION FLUX DENSITY

Few critical parameters were chosen to examine the effect caused by the presence of low pressure dc glow discharge, more specifically pertinent to the memory applications, involving ferroelectric thin films. Electrical behavior of PZT films was also re-examined, after they were subjected to a fatigue test, to observe the impact of dc glow discharge.

3.2.1. Time Dependent Dielectric Breakdown (TDDB)

TDDB was studied in the present work in MFM configuration for the films deposited with and without the presence of dc glow discharge. Figure 13 shows the TDDB results obtained on the films deposited without glow discharge. As the stress increased, the breakdown time (t_{BD}) decreased. The t_{BD} for 3 V stress was around 2000 s and decreased to less than 1800 s when the stress voltage was increased to 10 V. The TDDB data for the films deposited in the presence of glow discharge are also shown in Figure 13. The t_{BD} was about 4000 s for a voltage stress of 3 V and it decreased to about 3600 s when the stress was increased to 10 V.

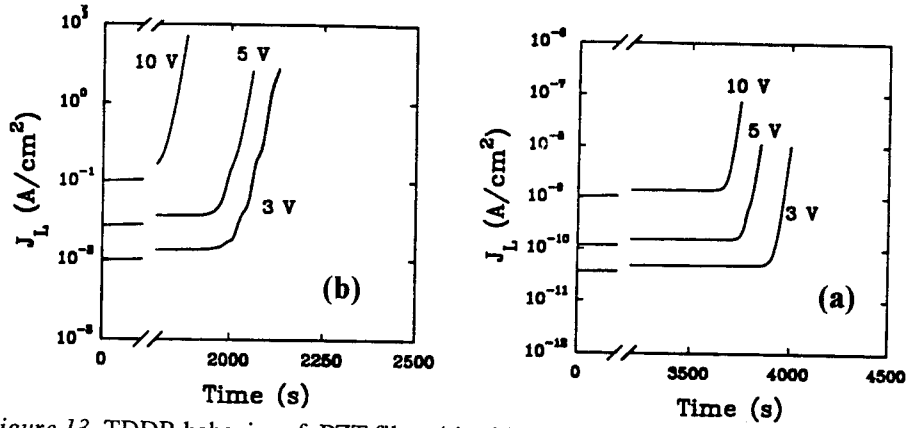


Figure 13. TDDB behavior of PZT films (a) with and (b) without DC glow dischage.

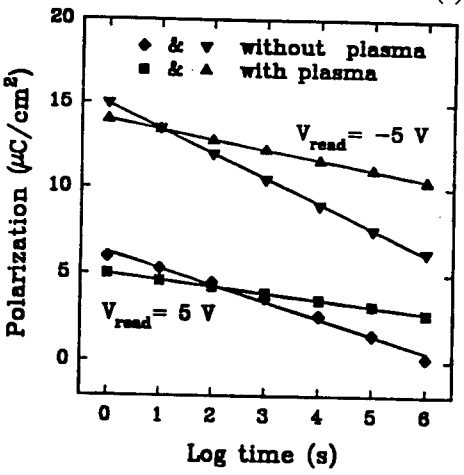


Figure 14. Retention in PZT films deposited with and without plasma.

3.2.2. Retention

The results obtained from the retention experiments on the films deposited with and without plasma are shown in Figure 14. When amplitude of the write and read voltages are the same i.e., 5 V, the polarization of the capacitors for both the logic states is linear with time and showed very little loss of polarization when tested up to six decades of time. This would indicate that the retention is practically infinite. However, when tested under more realistic conditions, in which the read voltage is typically smaller than the write voltage, the capacitors showed a stronger drop of polarization.[28]

3.2.3. Fatigue

Capacitors produced by depositing PZT films using glow discharge-assisted deposition with V_D = 0 and 300 V respectively, were subjected to fatigue testing using a pulsed Radiant Technologies, RT66A, tester. The effect of fatiguing on P_r is presented in Fig. 15, which shows the effect of fatigue on the two PZT films deposited on platinum coated silicon substrate. The films deposited with V_D = 300 V showed excellent stability in P_r up to $10^{10.5}$ cycles. The films deposited with no plasma showed a strong decline in P_r beyond 10^9 cycles.

3.2.4 Effect of Fatigue on Electrical Properties

3.2.4.1. Dielectric Behavior. Figure 16 shows the dielectric constant and dissipation factor as a function of frequency in post-fatigued films deposited with no plasma and a discharge voltage of 300 V. Films deposited with no plasma revealed a drop in dielectric constant measured at 100 KHz from 400 to about 300 or 25 %. Whereas the drop in films deposited with plasma was from 865 to about 730. It appears the films deposited in presence of activated oxygen showed smaller reduction in dielectric constant. Also the increase in dissipation factor in the films deposited with no activated oxygen was higher than in the films deposited with plasma.

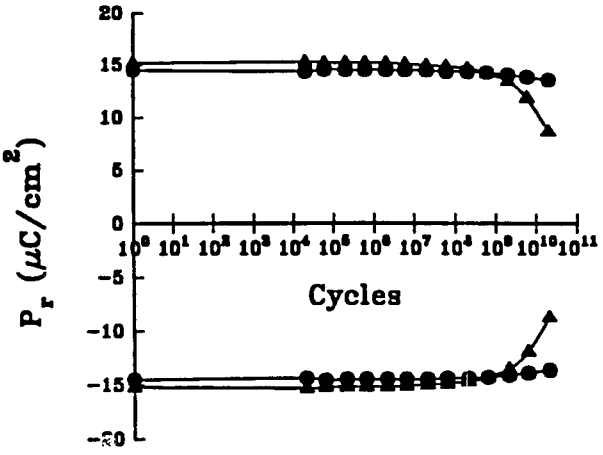


Figure 15. Fatigue in PZT films with and without Plasma.

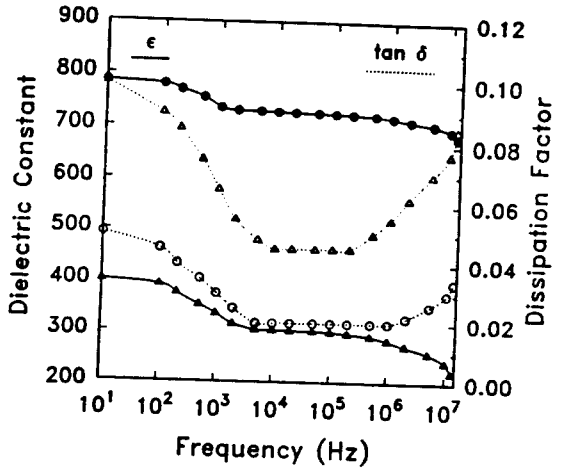


Figure 16. Dielectric response of post-fatigued PZT films.

3.2.4.2. I-V Characteristics. The effect of fatigue on the current-voltage characteristics in MFM structures are shown in Figs. 17 and 18. For the films deposited without the plasma (Fig. 17) the leakage current density (J) showed a clear increase after fatigue. The films deposited with V_D=300 V (Fig. 18) also showed similar increase in J but by smaller magnitude. It is worth mentioning that, by examining the slopes of the J-V curves, the PZT films deposited under no plasma conditions, entered space charge region at relatively lower voltages, after they have been subjected to a fatigue cycling of up to 10^{10} cycles. However, similar tests performed on the films deposited at a discharge voltage of 300 V indicates no such tendency of films entering space charge region.[29]

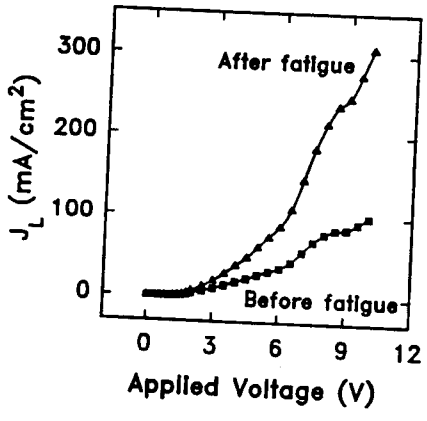


Figure 17. I-V behavior of post-fatigued PZT films without discharge.

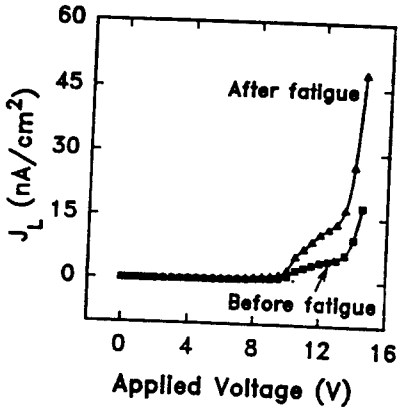


Figure 18. I-V behavior of post-fatigued PZT films within a glow discharge.

3.3. ECR PLASMA SOURCE ASSISTANCE: LOW ENERGY (5-50 eV) AND HIGH ION FLUX DENSITY

To illustrate the effect of ECR plasma during the development of electroceramic thin films, $SrTiO_3$ was chosen as the candidate for study. Conventional processing of DRAM gate dielectrics employs vacuum techniques in which planar or three dimensional capacitor structures are fabricated on the silicon substrate. The crystalline structure and the composition are extremely sensitive properties which influence the electrical behavior of complex oxide thin films. In the case of $SrTiO_3$ films deposited at a temperature of 400 °C, ECR plasma assistance enhanced crystallinity, as evidenced by the increase in peak intensities. It was seen that beyond an ECR power of 100 W, no appreciable enhancement in crystallinity was noticed indicating an optimal power. Such enhancement in crystallinity is also reflected in the improved composition of $SrTiO_3$ films. The Sr/Ti ratio increased from 0.75 to approximately 1.0 with the presence of ECR plasma. The improvement in crystallinity and stoichiometry in the presence of ECR plasma can be understood in terms of bombardment by a high density of species with moderate energies between 15 and 30 eV and effective transport and incorporation of activated oxygen and ionic species to the growing film during deposition. These factors result in increased adatom mobility due to low energy bombardment by a high density of species and improved reaction kinetics on the substrate surface due to the presence of activated species in the plasma.

3.3.1. Leakage current behavior

Figure 19 illustrates the effect of ECR plasma presence on the leakage current behavior of $SrTiO_3$ with applied electric field, which is an essential requirement for high permittivity dielectric thin films meant for developing DRAM type devices.

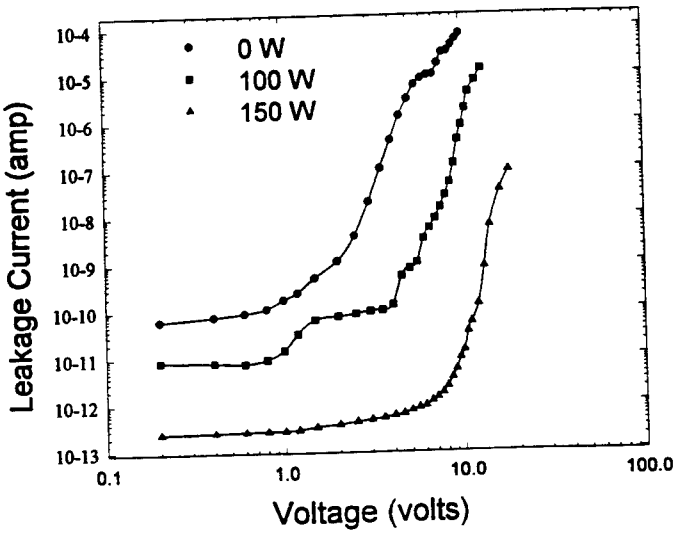


Figure 19. Leakage current behavior of $SrTiO_3$ thin films deposited in the presence of an ECR plasma.

The I-V curve shows a near ohmic behavior in the low field region followed by an increase in current with higher electric fields, which may be attributed to the onset of a bulk limited space charge conduction process. This behavior is similar to that observed in films produced with other physical vapor growth processes described in this paper. However, two features noticeable in Fig. 19 are that the leakage current in the near-ohmic region is reduced with the ECR plasma power and that the voltage for the space charge onset is shifted to higher values for films produced with higher ECR plasma powers. These effects may be explained in terms of the ECR plasma presence improving the oxidation kinetics of the compounds via an effective incorporation of oxygen and making films more insulating.

3.3.2. Time Dependent Dielectric Breakdown

Figure 20 shows the time dependent dielectric breakdown response for $SrTiO_3$ films under an applied constant electric field of 200 kV/cm. This level of field was chosen intentionally to drive the films to near space charge conditions and observe the breakdown behavior. It can be concluded from Fig. 20 that with the inclusion of ECR plasma during the growth process, the TDDB extended to much longer durations, up to $5x10^4$ seconds, whereas the breakdown in the films without ECR plasma occurred at much earlier times (about 10^3 seconds). This behavior once again can be ascribed to ECR plasma induced near perfect stoichiometry, denser grain-grain boundary structure and better oxygen incorporation. Several physical models have been presented in the literature to explain TDDB behavior, and our results appear to lean in support of oxygen vacancy dependent behavior.

3.3.3. Charge Storage Density

Dielectric layers meant for DRAM type devices are expected to offer better charge storage densities in comparison with the conventional gate dielectrics such as SiO_2. Figure 21 shows the variation of charge storage density with applied electric fields for films deposited under different ECR plasma conditions. The charge storage varies linearly with applied field and the magnitude improved with increasing ECR power. It is also worth noticing that the films exhibited no breakdown even up to fields of 250 kV/cm and offered charge storage as high as 40 $fC/\mu m^2$. These characteristics further establish the property enhancement via energetic particle bombardment. It was shown earlier that the presence of ECR plasma improved the structure and composition, both of which contribute to improvement in the dielectric behavior of dielectric thin films. The improved charge storage density with ECR plasma reflects from the improved dielectric constant.

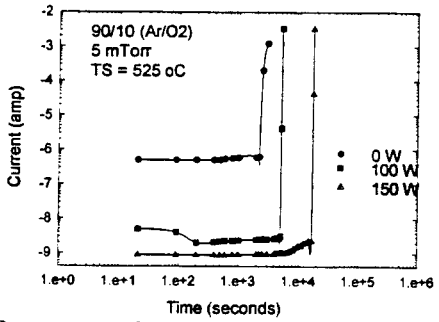


Figure 20. TDDB response of $SrTiO_3$ films deposited with an ECR plasma.

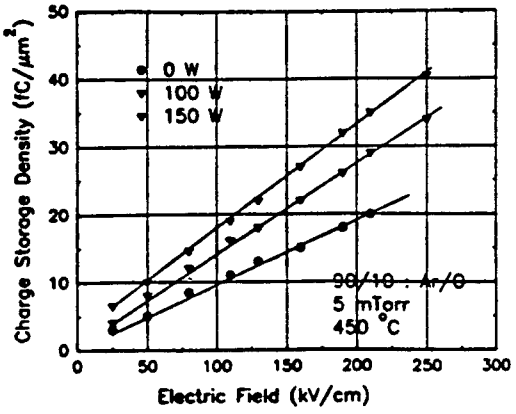


Figure 21. Charge storage density of $SrTiO_3$ films with an ECR plasma.

3.4. INFLUENCE OF BOMBARDMENT ON THE NATURE OF THE I-V CHARACTERISTICS

3.4.1.Varistor Type Characteristics: Films Bombarded During Growth

Figure 22 shows a typical J-E curve which is usually observed for PZT films grown in the presence of low energy reactive ion bombardment. More strikingly, this type of curve features a strong nonlinear J-E dependence. Five regions can be distinguished by using the non-linearity coefficient, a, which is defined as the slope of lnJ-lnE plot ($J = CE^{\alpha}$ and α = dlnJ / dlnE, where C is a constant). Linear J-E dependence (ohmic conduction) is observed only at very low fields (region I, 0-4 kV/cm). In the wide intermediate field region, a continuously decreases from nearly 1 to nearly 0 as the field increases (region II, ~170 kV/cm). In other words, in this region the conductivity of the films steadily decreases as the field increases. This is contrary to the common phenomenon that the conductivity is enhanced as the field is increased. At higher fields (above ~170 kV/cm), the films behave much like varistors: a prebreakdown region (region III) is followed by a breakdown region (region IV) and then an upturn (region V). (Here we follow the particular terminology in varistors, such that some terms may bear different meanings than those commonly used. For instance, "breakdown" here means the breakdown of grain boundaries rather than the failure of the whole specimen.) The breakdown region is characterized by a high α (~50) and a significant increase in current (over 4 orders of magnitude) within a small range of field (less than 0.1 order of magnitude). In the upturn region, the a on the average becomes close to unity again. All of these features indicate a strong varistor nature of these films, which may only be explained in grain boundary effects. Thus this type of conduction falls into the category of grain boundary limited conduction (GBLC).

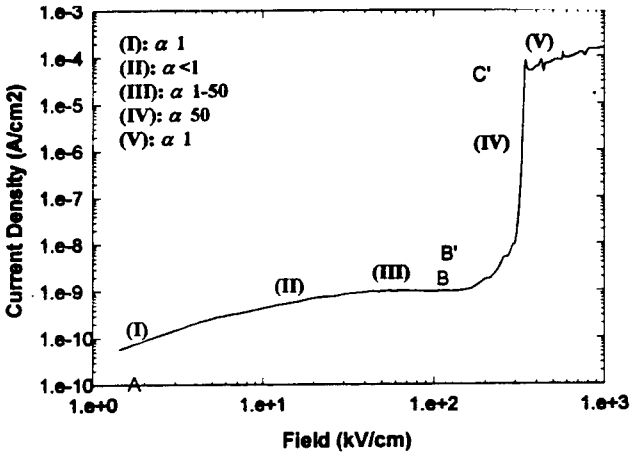


Figure 22. Typical J-E curve of PZT films grown under low energy ion bombardment.

3.4.2.Space Charge Limited Conduction (SCLC): Films Non-Bombarded During Growth. Figure 23 shows another typical J-E curve which is observed in some moderately-annealed films. Unlike the previous type, the long-term segment (AB) and the short-term segment (B'C') in this case do not meet one another, indicating the coexistence of polarization and time-dependent dc degradation effects between B and B'. An approximate transitive arc (BB') is therefore needed to connect the two segments. This type of J-E curve clearly exhibits four different α regions; however changes in α are less dramatic than those in the previous case. In the low field region, the α is close to unity (region I, 0-30 kV/cm). Followed is the transition region where the α varies from approximately 2 to 3.5 (region II, 30-100 kV/cm). The next is a region characterized by an α of about 9 (region III, 100-130 kV/cm). At higher fields, the α becomes 2 to 3.5 again (region IV, above 130 kV/cm). This type of J-E curve can be easily modeled in terms of space charge limited conduction (SCLC) theory: region I follows Ohm's law; region II corresponds to the shallow trap square law; region III seems to be the region of trap filled limit (TFL); and region IV corresponds to the trap free square law.

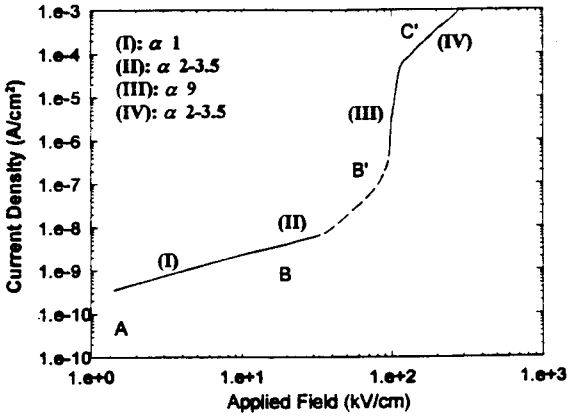


Figure 23. Typical J-E Curve of PZT films grown without bombardment.

3.4.3. Conduction Through PZT Films

3.4.3.1.Low Field Region. Like any other polycrystalline samples, the ultra-fine-grain PZT films can be considered as a series array of grains, grain boundaries and electrode interfaces. The field dependence of conductivity, or the J-E characteristics, of the films is a combined response of these three parts. Variations in the influences of different parts give rise to variations in J-E characteristics.

Both types of films (bombarded and non-bombarded) show ohmic conduction in the low field region (Figs. 22 and 23), indicating a near-ohmic contact at the electrode/film interfaces in both cases. Since the work function of unmodified PZT (about 3.5 eV)[30] is much smaller than that of either electrode material (5.1 eV for Au and 5.7 eV for Pt),[31] the contact must be hole-injecting to the film in nature, i.e. ohmic contact with respect to holes.[31,32] Even though the work functions of both the electrode and the film could possibly be altered due to the presence of surface states, the nature of the contacts could hardly be changed,[33] especially in the present case in which the differences in initial work functions are so large. The fact that these samples exhibit an ohmic contact for holes confirms p-type conduction in the PZT films and is consistent with the previous assumption.

In the ohmic conduction region, the resistivity is approximately $2x10^{13}$ Ω-cm for grain boundary limited conduction (GBLC) films and $4x10^{12}$ Ω-cm for SCLC films, both of which are higher than that of bulk unmodified PZT ceramics of similar composition (10^{11}-10^{12} Ω-cm).[34] The higher resistivity in the film case could be attributed to the depletion of the ultra-fine grains as well as the grain boundary barriers, and is consistent with observations by other researchers. It is worthwhile to emphasize that here the depletion is due to the multiple grain boundary interfaces rather than the electrode/film contacts. This assertion reconciles the two seemingly contradictory observations: ohmic contact at electrode/film interfaces but depletion throughout the film bulk.

A comparison between the two types of films shows that GBLC films exhibit almost one order of magnitude higher resistivity than SCLC films . This is due to the higher resistive grain boundaries in GBLC films, as indicated in the above sections. In all cases, the resistance of the films comes from the series contribution of grains and grain boundaries (given that the electrode/film contacts are ohmic). In the case of GBLC, pronounced grain boundary barriers make a predominant contribution to the series resistance of the films. Conduction through the grain boundaries at low voltages is probably due to thermally activated excitation of the charge carriers and may consequently be described by[35]

$$\sigma = \sigma_0 \exp(-\phi_b / k_B T) \qquad (2)$$

where ϕ_b is the barrier height, and σ_0 is the conductivity in the absence of barriers. In the case of SCLC films, the grain boundary barriers, if any, are not so pronounced, and thus make a contribution to the series resistance which is comparable to that of the grains.

3.4.3.3. High Field Region. The field-induced increase in the height of grain boundary barriers for GBLC films has a limit when the polarization of the film reaches saturation. Further increase in fields beyond the saturation level does not cause any further decrease in k and increase in the barrier height, but leads the grain boundary barriers to be overcome.

Correspondingly, current rises dramatically within a narrow field range, giving rise to the breakdown region in Fig. 22. Several mechanisms may account for the breakdown of the grain boundary barriers.[36] Among them a tunneling process seems most likely in the present case, based on the following reasoning. As seen in Fig. 22, the resistivity of GBLC films just before breakdown (at the junction of region I and region II) is about $2x10^{14}$ Ω-cm, which is approximately 50 times the resistivity of SCLC films in the ohmic conduction region. This means that the grain boundaries (before breakdown) are much more resistive than the grains, and consequently bear almost all the applied field. Noting that the breakdown takes place at fields higher than 10^2 kV/cm (Fig. 22) and assuming that grain boundaries take up approximately 10 % of the film thickness, the breakdown field can be estimated to be higher than 10^3 kV/cm. Such a high value of the breakdown field is consistent with tunneling.[37] For a simple rectangular barrier and neglecting image forces, the tunneling process takes the form

$$J = 3.39 \times 10^{-2} (E^2 / \phi_b) \exp(-7.22 \times 10^7 \phi_b^{3/2} / E) \qquad (4)$$

where J is the current density in A/cm^2, E is the field in V/cm, and ϕ_b is the barrier height in eV. Hence

$$\alpha = d\ln J / d\ln E = 2 + 7.22 \times 10^7 \phi_b^{3/2} / E \qquad (5)$$

For a rough estimation, assuming $\phi_b \sim 0.5$ eV and $E \sim 1x10^3$ kV/cm, we get $\alpha \sim 30$, which is in rough agreement with the observed values. Better estimation needs the knowledge of temperature dependence of the leakage current, from which the value of ϕ_b can be determined by Eqs. (2) and (3). Once again, it should be noted that in the present case the word breakdown specifies being overcome of the grain boundary barriers rather than the failure of the whole specimen. Beyond the breakdown field, the grain boundaries exhibit a finite resistivity, which is much smaller than the resistivity before breakdown. The series combination of the finite grain boundary resistivity and grain resistivity gives rise to the upturn region (Fig. 22, region V).

For SCLC films, the J-E characteristics are relatively simple and can be described as SCLC with shallow traps (Fig. 23). In region II, the shallow trap square law:

$$J = 9 \mu k \varepsilon_0 \theta E^2 / 8 L \qquad (6)$$

applies, where μ is the mobility of the charge carriers, L is the film thickness, θ is the ratio of the total density of free carriers (holes in the present case) to the trapped carriers. After the applied field forces all the traps to become filled, another square law, the trap free square law:

$$J = 9 \mu k \varepsilon_0 \theta E^2 / 8 L \qquad (7)$$

applies (region IV). The two regions are separated by the voltage of trap filled limit, V_{TFL}, given by:

$$V_{TFL} = e N_t L^2 / 2 k \varepsilon_0 \qquad (8)$$

where the N_t is the density of traps. The actual J-E characteristics (Fig. 23), however, do not exactly follow these equations. The deviations can be attributed to the scattered distribution of the trapping levels. Because of the large amount of structural and chemical disorders presented in the ultra-fine-grained films, the traps do not have a uniquely defined environment and thus there would be a broad smearing out of the energy level of the traps, which results in the observed deviations.

It is worth mentioning that in p-type films the trapping is due to hole-trapping states, which are donor type impurities or defects. In other words, the nature of the trapping states is the same in both types of films. What makes the distinction is the position and energy distributions of the trapping states, which are highly correlated to the grain boundary segregation and in turn to processing conditions. If the trapping states are highly segregated at grain boundaries and tightly trap charge carriers, substantial potential barrier will set up at the boundaries, and thus the film will show varistor-like, or GBLC characteristics; if the trapping states are not highly segregated at grain boundaries such that the grain boundary barriers are not appreciable, or the segregation does not result in potential barriers at all, the film will appear to be homogeneous and show trap-influenced SCLC.

3.4.4. Conduction Through (Ba,Sr)TiO_3 Thin Films

$(Ba,Sr)TiO_3$ films were prepared in a variety of processing conditions, and a comparative work is done for films between and Nb doped and bombarded conditions. Fig. 24, compares the I-V characteristics of undoped-nonbombarded, 10 mol % Nb-doped-non-bombarded and undoped-bombarded films deposited at T_S = 400 and annealed at 700 °C for 8 hrs.

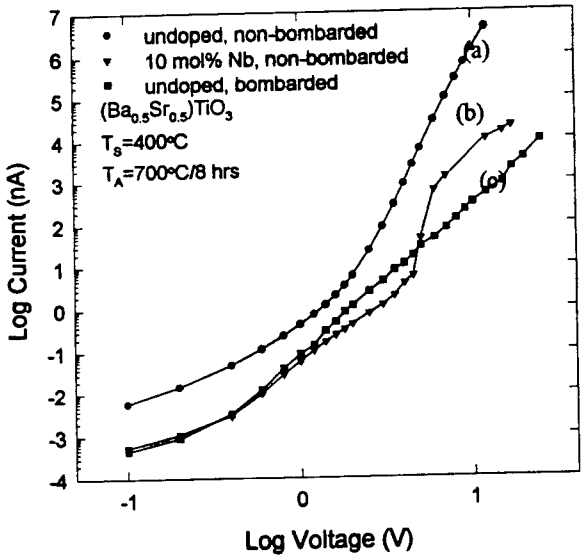


Figure 24. Comparisons of I - V characteristics of (a) undoped-non-bombarded, (b) 10 mol% Nb doped-non-bombarded, and (c) undoped-bombarded BST films deposited at T_S = 400 °C and annealed at 700 °C for 8 hrs.

There are two regimes in curve (a) type: $\alpha \sim 1$, which represents Ohmic conduction behavior; and $\alpha \sim 7.5$-10. Apparently, there are some common features between these films prepared by two very different deposition processes, which we will discuss later. Curve (b) type behavior resembled the ideal I-V characteristics of SCLC with a discrete set of shallow traps.[38] The conduction mechanism of our films is most likely of the SCLC type. Curve (b) type behavior in Fig. 24 suggests that heavy donor-doped films deposited at higher substrate temperatures have discrete shallow traps, possibly a donor state of Nb_{Ti}. The near vertical regime (iii) which has a slope of 16 corresponds to a trap-filled limit (TFL) law and is preceded by a trap-distributed region (ii) (slope = 2.6 ~ 3), which is followed by a discrete trap-free but trap-distributed regime (iv) (slope = ~ 3). Such a discrete trap embedded in a background of distributed traps was also seen in organic molecular crystals of anthracene by Helfrich and Mark[39] and by Adolph et. al.[40]

For undoped films deposited at T_S = 400 °C, there was no such near vertical regime, indicating the absence of discrete-traps (either shallow or deep traps). The non-linearity at high electric fields was believed to be due to the distributed-traps induced by the unavoidable acceptor impurities in titanate perovskite systems. These acceptor impurities may come from the target or the sputtering chamber. The microstructures of films deposited at T_S = 400 °C and annealed at 700 °C maintain columnar structure and contain small number of grain boundaries for both undoped and Nb-doped films. The difference between undoped and Nb-doped films thus must be attributed to the differences in chemistry, i.e. doping effect.

The I-V curves for bombarded films consists of two regimes, with ohmic regime at low voltage (<0.4 V) and non-ohmic regime with slope of ~ 3.5 at voltages higher than 0.6 V. This result is very promising, because the undoped films bombarded under conditions of 75 eV and 1.6 ion/atom arrival ratio has much lower leakage current than non-bombarded films at high electric field. For example, the leakage current of bombarded films is 4 orders of magnitude lower than non-bombarded films at 10 V (0.25 MV/cm). The bombardment also has comparable effect of donor-doping below ~ 5V, and ~1 order of magnitude lower leakage current than doped films at voltage higher than 6 V. The much smaller slope (~3.5) at high field of I-V characteristics for bombarded films may be attributed to the structure disorder induced by the oxygen ion bombardment as well as the intensive reaction of oxygen ions with metal ions at high deposition temperatures.

Low-energy oxygen ion bombardment has shown no marked effect on the slopes of I-V characteristics of bombarded $(Ba,Sr)TiO_3$ (BST) films as compared to similar films deposited at R.T. and annealed at 700 °C for 2 hrs. The only difference is that the leakage current is about 0.7 order of magnitude lower for bombarded films than no-bombarded films. The lower leakage current for bombarded films may be associated with the effective reaction between oxygen and metal ions during deposition, and thus probably results in more oxidized films. For films deposited at higher substrate temperatures, however, preliminary data show that there is large difference in the slopes of I-V characteristics of bombarded and non-bombarded films.

Comparison of BST films derived by chemical routes and physical vapor growth process combined with low energy oxygen ion bombardment revealed a close relationships among processing, structure and property, which is schematically illustrated in Fig. 25. The microstructures of BST thin films could be classified into three types: (a) Type I structure with multi-grain through the film thickness. (b) columnar structure (Type II) which remained even after high temperature annealing and (c) highly dense columnar structure encouraged via low energy ion bombardment. Depending on the

microstructure, one may realize different time-domain responses, followed by different nature of conduction mechanisms.

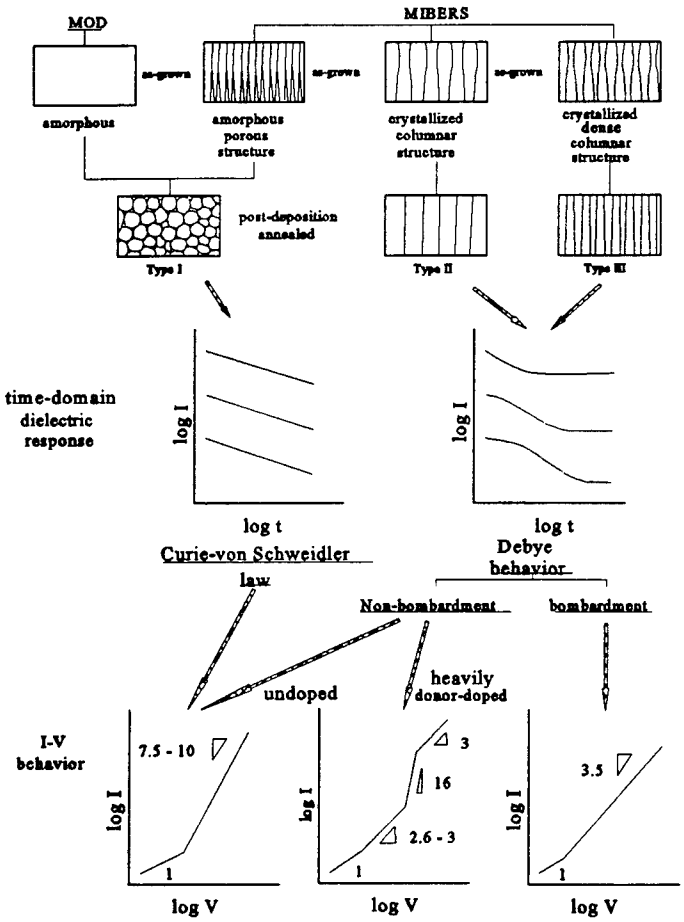


Figure 25. A qualitative comparison of process-structure - nature of conduction mechanisms for complex oxide films such as (Ba,Sr)TiO_3.

Two types of I-V characteristics could be seen in non-bombarded films depending on the chemistry of the films (doped or undoped) and substrate temperature during deposition. Only the films doped with higher donor concentration and deposited at high substrate temperatures (400 °C) showed bulk limited space-charge conduction with discrete shallow traps embedded in trap-distributed background at high electric fields. Bombarding the films at higher substrate temperatures (400 °C) undoubtedly improved the density, reduced the trap density and improved the time dependent dielectric breakdown behavior. Such low energy reactive ion bombardment exhibited comparable/better effect on the leakage behavior and transport mechanisms with that of high donor doping.

4. Optimization of Bombardment Conditions

After the effects of bombardment were qualitatively scanned, several bombardment-sensitive properties were chosen, and the dependencies of such properties on the bombardment parameters (ion beam flux and voltage) were investigated, using a Kaufman ion source, in order to define an optimal range of bombardment conditions. For this purpose, the films were deposited with similar thickness ranging from 1700 to 2100 Å. While all the other deposition parameters were fixed the same, the bombarding ion energy (E_b) and beam flux (I_b) were changed, one at a time, from run to run to render different bombardment conditions. The I_b was changed by adjusting the current of ion source filament only, without varying the O_2 flow, so that the oxygen partial pressure of the deposition chamber was kept the same at 0.01 Pa for all the runs. From the values of I_b and the measured deposition rates, the ion/atom arrival ratio was calculated as one of the parameters expressing the bombardment effects.[41] Electron probe microanalysis (EPMA) showed that most of such deposited films have nearly the same Pb content (about 3% excess relative to the stoichiometry of PZT perovskite phase), except for a few deposited at too high E_b or I_b which are slightly Pb deficient. The as grown films were annealed under the same condition (580 °C for 20 min). All the crystallized films assumed pure perovskite phase in X-ray diffraction (XRD).

4.1. ION FLUX

Figure 26 shows the XRD intensity ratio $I_{(100)}/(I_{(100)}+I_{(100)})$ of the crystallized films as a function of the ion/atom ratio. For clarity, it is worth mentioning that in the present case "ion" denotes both O_2^+ and O^+, and "atom" includes Pb, Zr and Ti. It is noted from Fig. 27 that the degree of (100) orientation increases monotonically within the range of ion/atom ratio from 0 to about 1.4, gradually from 0 to 1.0, and sharply from 1.0 to 1.4. Afterwards, however, the degree of orientation decreases steeply with ion/atom ratio. The trend of the evolution of preferential orientation with ion/atom ratio in the region lower than 1.4 is consistent with the behavior of low-energy ion bombardment modifying properties in general, and confirms the strongly flux-dependent nature of the bombardment effect. It is of interest to note that there is a highly sensitive range between 1.0 and 1.4 of ion/atom ratio, which may be of particular importance in practice of property modifications. The abnormal steep decrease in the degree of (100) orientation in the higher ion/atom ratio region (>1.4) can be attributed to the deviation in the film stoichiometry, namely the resputtering-induced Pb deficiency by the high ion flux, as revealed by EPMA.

Figure 27 shows the P_r and E_c values as functions of the ion/atom ratio. Basically, the curve of P_r versus ion/atom ratio follows a trend similar to that of orientation in Fig. 27, although it increases more steadily over the entire lower ion/atom region (from 0 to 1.3). It may be noted, however, that the peak position of ion/atom ratio is shifted to about 1.3, compared to 1.4 for the preferential orientation. This discrepancy may be stress related, since the films deposited at ion/atom ratio near 1.4 seemed highly stressed, as seen from our stress measurements and also evidenced by the fact that thicker films (about 5000 Å) of this condition tended to buckle off after crystallization. It has been noted that the stress and preferential orientation are often highly correlated. The further decrease in P_r with ion/atom>1.4 is again thought to be the consequence of Pb deficiency.

It can also be seen from Fig. 27 that the E_c changes with ion/atom ratio the other way against the P_r. This fact is of great significance as it allows optimum conditioning to attain as high P_r and as low E_c as possible simultaneously.

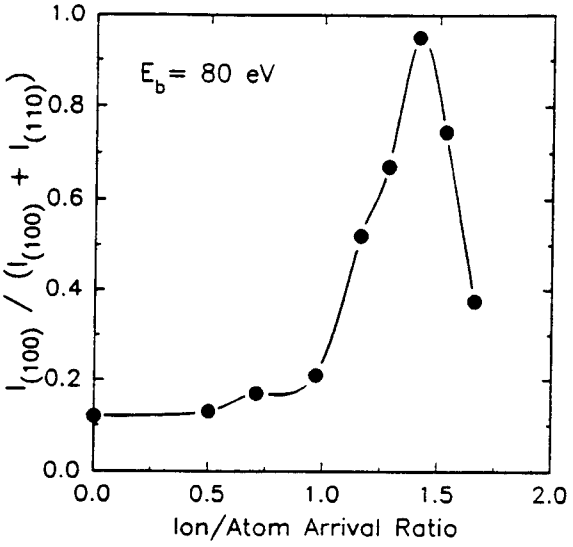


Figure 26. Variation of orientation of PZT films with varying I / A ratio.

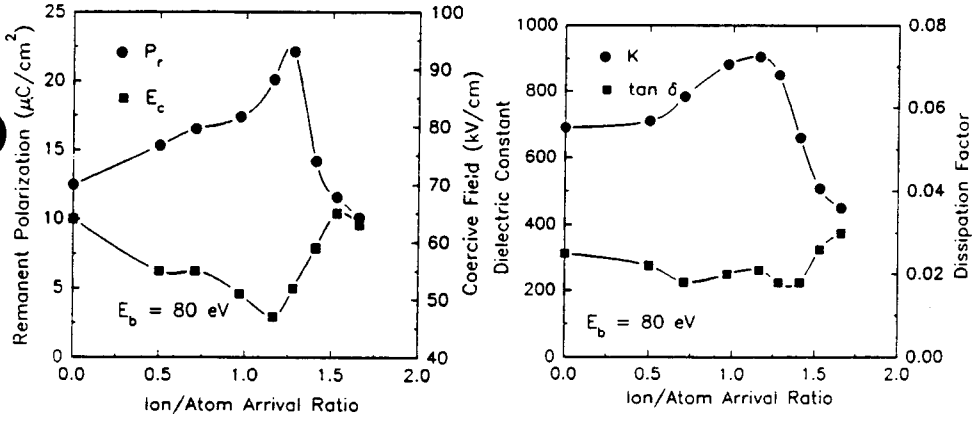


Figure 27. Variation of (a) polarization and (b) dielectric constant with ion / atom ratio.

The dielectric constant (k) of the films at 100 kHz also showed a strong dependence on the ion/atom ratio, while the dissipation factor (tan ∂) remained in the vicinity of 0.02 (Fig. 27). Again, the k curve roughly mimics the P_r curve or orientation curve, except for a little further shift in the peak position towards the lower ion/atom side and some

broadening of the peak. Comprehensively, the ion/atom ratio for optimum combination of P_r, E_c and k in the present conditions seems within the range from 1.0 to 1.3. Relative to the non-bombarding case (zero point of ion/atom ratio), the increments in P_r and k could be about 60% and 25% respectively, while the reduction in E_c could be about 20%.

4.2. ION ENERGY

While the ion/atom ratio was kept constant at 1.28, the bombardment effect was also studied in terms of P_r and E_c versus the bombarding ion energy E_b. The results are summarized in Fig. 28. It is shown that for E_b from 60 eV to 80 eV, P_r had almost equally high values of about 20-22 $\mu C/cm^2$, while beyond 80 eV it continuously decreases as E_b increases. Therefore, it seems that, within the range of experimental condition explored in the present work, the bombarding energies between 60 and 80 eV are optimal to realize effective property modification. Higher E_b was not suitable because it led to significant Pb resputtering, which may have resulted in less effective bombardment for desirable modification[17] as well as Pb deficiency in the films (observed by EPMA in the case of 110 eV).

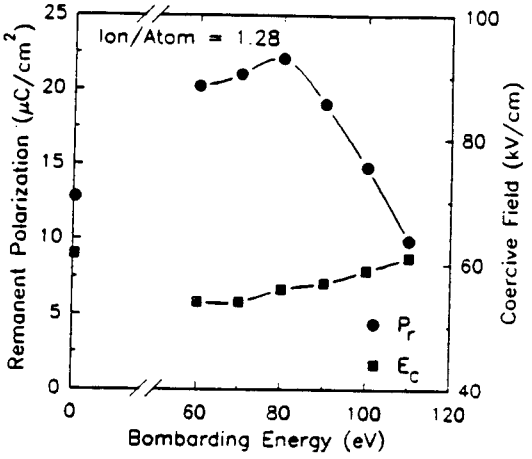


Figure 28. Variation of remanent polarization and coercive fields with ion energy.

5. Summary

A variety of approaches of introducing controlled low energy ion bombardment has been attempted such that the physical and electrical properties are modified/enhanced. The choice of approaches is primarily based upon varied bombarding ion flux densities, while the bombarding energies were kept under 80 eV. The DC glow discharge is a weak plasma and provided low ion flux density, where as the ECR source offered very high flux density of ions even at pressures as low as 10^{-5} torr and the Kaufman source stands in

the intermediate range. A qualitative comparison is made for $SrTiO_3$ thin films, assisted by all approaches of low energy ion bombardment listed in the present work and the results are shown in Table 1.

TABLE 1. Comparison of bombarding conditions and the resultant selective electrical properties of $SrTiO_3$ thin films of 4000 A thick, deposited on Pt coated Si Substrates.

Approach	Bombard Energy (eV)	Ion/Atom Ratio	Leakage Current (amps)	TDDB E = 0.25 (MV/cm)	Charge Density ($fC/Um^{2)}$
Kaufman Source	50 - 80	1.0 - 1.4	5×10^{-13}	10^5 secs	40
DC Glow Discharge	5 - 20	0.2 - 0.4	2×10^{-10}	5×10^3secs	32
ECR Plasma	5 - 50	1.3 - 1.8	10^{-13}-10^{-14}	10^5 secs	45

It may be seen that the leakage current behavior and dielectric breakdown improved significantly for the films deposited with high density bombarding ions. In case of ablation with dc glow discharge, it is known that excimer laser ablation offers high rate of deposition rate which is accompanied by a weak plasma. This results in a low ion/atom ratio and the effect of low energy ion bombardment is visible to a lesser extent.

Low - energy oxygen ion bombardment involving a Kaufman source, during $Pb(Zr,Ti)O_3$ film growth was found to have a pronounced effect on the growth process, structure and electrical properties of PZT thin films, evidenced by reduced perovskite formation temperature, induced preferential orientation, improved film morphology and enhanced electrical properties. Some properties are strongly dependent on the bombarding ion flux (characterized by ion/atom ratio) and energy, and therefore can be quantified to figure out optimal range of the bombardment conditions. The ion/atom ratios between 1.0 and 1.3 and the bombarding ion energies ranging from 60 to 80 eV were found to be optimal to realize desirable property modification in Pb-based perovskites. Relative to the non-bombarded case, the bombardment could increase the P_r and k by up to 60 % and 25 % respectively, and reduce the E_c by about 20 %. The improved properties also include crystallization temperature, switching characteristics, I-V behavior and time dependent dielectric breakdown.

The role of O_2 ion bombardment may be understood in terms of ; (a) the presence of activated oxygen species for a enhanced chemical reaction among the sputtered species and (b) additional low energy bombardment to affect the grain growth process. However, the observed effects may be due to the combination of bombarding energy, atomic and ion flux densities, momentum transfer and the enhanced chemistry, which are yet to be resolved.[41] Out of these three possibilities, in the present work, the bombarding energy was kept under 80 eV and the contribution towards property modification may not be

significant. The momentum transfer[42] may be possible with the compounds consisting of elements with atomic weights comparable to Ar or Oxygen ions. In the present work, most of inorganic compounds are made of relatively heavier elements. The ion/atom ratio of the incident accelerated ion flux to the flux of deposited thermal particles appeared to be more fundamentally responsible for the observed property modification/enhancement.[43] It will be essential to establish a much clearer understanding of low energetic ion-surface interactions, such that it is anticipated to offer a great potential for coupling low energy ion assistace in both physical vapor or chemical vapor (e.g., MOCVD) growth processes and engineer physical and electrical properties of multicomponent electroceramic thin films for a variety of applications.

6. REFERENCES

1. Harper, J.M.E., Cuomo, J.J., Gambino, R.J. and Kaufman, H.R. (1984), in *Ion Bombardment Modification of Surfaces: Fundamentals and Applications*, O. Auciello and R. Kelly (Eds). Elsevier Science Publishers, B.V. Amsterdam.
2. Cuomo, J.J., Rossnagel, S.M. and H.R. Kaufman (eds) (1989), *"Handbook of Ion Beam Processing Technology", Noyes Publications, New Jersey.*
3. Auciello, O., Glifford, K. and Kingon, A.I. (1994), *Appl. Phys. Lett.* **64**, 2873.
4. Krupanidhi, S.B., Hu, H., Kumar, V. (1992), *J. Appl. Phys.* **71**, 376.
5. Krupanidhi, S.B., Hu, H. and Kumar, V. (1992), *Ceramic Transactions*, Vol. **25** .
6. Fox, G.R., Krupanidhi, S.B., More, K.L. and Allard, L.F. (1992), *J. Mater. Res.*
7. Singh, R.K. and J. Narayan (1990), *Phys. Rev.* **B41**, 8843.
8. Buhay, H., Sinharoy, S., Kasner, W.K., Francombe, M.H., Lampe, D.R. and Stepke, E. (1991), *Appl. Phys. Lett.* **58**, 1470 .
9. Roy, D., Krupanidhi, S.B. and Dougherty, J. (1991), *J. Appl. Phys.* **69**, 7930.
   Dat, R., Lichtenwalver, D.J., Auciello, O. and Kingon, A. I. (1994), *Appl. Phys. Lett.* **64**, 2673.
   Ramesh, R., Lee, J., Sands, T., Keramidas, V.G. and Auciello, O. (1994), *Appl. Phys. Lett.*, **64**, 2511.
10. Beach, D.B. (1990), *IBM J. Res. Dev.* **34**, 6, 795.
11. Ohkubo, M. (1988), *Jpn. J. Appl. Phys.* **27**, L1271.
12. Machida, K. and Oikawa, H. (1986), J. Vac. Sci. Technol. **B4**, 818.
13. Okuyama, M., Togan, Y. and Hamakawa, Y., (1988), *Appl. Surf. Sci.* **33/34**, 625.
14. Belsick, J.R. and Krupanidhi, S.B. (1993), *J. Appl. Phys.* **74**, 6851.
15. Kay, E., Rossnael, S.N., Roy, R.A., Yee, D.S., Muller K.H. and Bradley, R.M. (1989), in *Handbook of Ion Beam Processing Technology*, edited by J.J. Cuomo, S.M. Rossnagel and H.R. Kaufman (Noyes, Park Ridge, NJ, pp.170.
16. Muller, K.H. (1989), in *Handbook of Ion Beam Processing Technology*, edited by J.J. Cuomo, S.M. Rossnagel, and H.R. Kaufman (Noyes, New Jersey , pp.241
17. Harper, J.M.E., Cuomo, J.J. and Hentzell, H.T.G. J. (1985), *Appl. Phys.* **58**, 550.
18. Castellano, R.N. and Feinstein, L.G. (1979), *J. Appl. Phys.* **50**, 4406.
19. Krishnaswamy, S.V., Messier, R., Swab, P., Tongson, L.L. and Vedam, K. (1981), *J. Electron. Mater.* **10**, 433.

20. Yu, L.S. , Harper, J.M.E., Cuomo, J.J. and Smith, D.A. (1986), *J. Vac. Sci. Technol.* **A4**, 443.
21. Hoffman, D.W. (1983), *Thin Solid Films* **107**, 353.
22. Messier, R., Takamori, T. and Roy, R. (1972), *J. Non. Cryst. Solids* **8-10**, 816.
23. Jaffe, B., Cook, W.R. and Jaffe, H. (1971), *Peizoelectric Ceramics*, Academic, New York, pp. 142.
24. Burfoot, J.C. and Taylor, G.W. (1979), *Polar Dielectrics* (Macmillan, London, pp.36.
25. Melnick, B.M., Paz de Araujo, C.A., MacMillan, L.D., Carver, D.A. and Scott, J.F. (1991), *Ferroelectrtics* **116**, 79.
26. Lehovec, K. and Shirn, G.A. (1962), *J. Appl. Phys.* **33**, 2036.
27. Roy, D. and Krupanidhi, S.B. (1994), *J. Appl. Phys.* (in press).
28. Roy, D. and Krupanidhi, S.B., (1994), *J. Appl. Phys.* (in press)..
29. Bernacki, S.E. (1992), *Mater. Res. Soc. Symp. Proc.* **243**, 135.
30. Weast, R.C. and Astle, M.J. (1981), *CRC Handbook of Chemistry and Physics, 62nd Edition* CRC, Boca Raton. FL, E-79.
31. Lampert, M.A. and Mark, P. (1970), *Currnet Injection in Solids* (Academic, New York, Chapter 1.
32. Sharma, B.L.(1981), in *Semiconductors and Semimetals,* Academic, New York, Vol **15**, Chapter 1.
33. Tredgold, R.H. (1966), *Space Charge Conduction in Solids*, Elsevier, Amsterdam, Chapter 4.
34. Jaffe, B., Cook, W.R. and Jaffe, H. (1971), *Piezoelectric Ceramics* , Academic, New York, p.155.
35. Phillip, H.R. and Levinson, L.M. (1976), *J. Appl. Phys.* **47**, 3177.
36. Mahan, G.D., Levenson, L.M. and Phillip, H.R. (1979), *J. Appl. Phys.* **50**, 2799.
37. Simmons, J.G. (1963), *J. Appl. Phys.* **34**, 1793.
38. Seuter, A.M.J.H. (1974), *Philips Res. Rep. Suppl.* **3**, 50.
39. Helfrich, W. and Mark, P. (1963), *Z. Phys.* **171**, 527.
40. Adolph, J., Baldinger, E., Czaja, W. and Granacher, I. (1963), *Phys. Lett.* **6**, 137.
41. Krupanidhi, S.B. (1992), *J. Vac. Sci. & Tech.* **A10**, 1569.
42. Roy, R.A., Catanie, P., Saenger, K.L., Cuomo, J.J. and Lossy, R.L. (1993), *J. Vac. Sci. Technol.* **B11**, 1921.
43. Petrov, I., Adibi, F., Greene, J.E., Hultment, L. and Sundgren, J.E. (1993), *Appl. Phys. Lett.* **63**, 36.

GROWTH AND PROPERTIES OF $Pb(Mg_{1/3}Nb_{2/3})O_3$ - $PbTiO_3$ AND $Pb(Zr,Ti)O_3$ THIN FILMS BY PULSED LASER DEPOSITION

A. SAFARI, C. TANTIGATE AND J. LEE*
Department of Ceramic Science and Engineering,
Rutgers, The state University of New Jersey,
Piscataway, NJ 08855, USA

ABSTRACT. $Pb(Zr,Ti)O_3$ (PZT) and $Pb(Mg_{1/3}Nb_{2/3})O_3$ - $PbTiO_3$ (PMN - PT) thin films have been prepared by pulsed laser deposition. Substrate temperature and oxygen pressure were varied to obtain thin film with perovskite structure. Perovskite formation was favored with a substrate temperature in the range of 535 °C to 575 °C and oxygen pressure of about 200 mTorr. Control of Pb and Mg content are important in the formation of perovskite in PZT and PMN-PT thin films respectively. Ferroelectric properties and reliability characteristics, especially fatigue, were studied of PZT thin films for nonvolatile memory applications. The crystalline quality of the PZT films and the electrode materials (metal or conductive oxides) for thin film capacitors were varied and tested as fatigue parameters. The electrode material had more of an effect on fatigue than the crystalline quality of the films. Photo-induced effects of PZT films under UV illumination were studied to investigate a possible fatigue mechanism. Examination of the photo-induced effect within a framework of polarization screening suggest that fatigue in PZT is closely related to charged defects. For PMN-PT thin films, the heterostructures of PMN-PT/ $La_{0.5}Sr_{0.5}CoO_3$ (LSCO) or $Y_1Ba_2Cu_3O_{7-x}$ (YBCO) film were prepared on MgO(100) substrates to evaluate the dielectric properties. The values of the dielectric constant ranged from 2300 to 3100 at 1 kHz with the dielectric loss below 5% for films of all compositions. The highest dielectric constant was obtained with the 0.9 PMN-0.1 PT composition.

1. Introduction

Recently, ferroelectric thin films have attracted much attention for their potential applications in piezoelectric, pyroelectric, electro-optic and especially ferroelectric memory devices due to the nonvolatility inherent in ferroelectricity [1]. These devices require a varying range of properties in the films. The spontaneous polarization and high dielectric constant characteristic of ferroelectric materials are used for non-volatile random access memories (FRAM) [2-5] or dynamic random access memories (DRAM) [6,7]. These properties depend on the deposition technique and the various processing parameters. Pulsed laser deposition has shown to be a promising technique for thin films of oxide materials, particularly of $YBa_2Cu_3O_{7-x}$ [8]. Ferroelectric thin films such

* Present address : Bellcore, Red bank, NJ 07701, USA

O. Auciello and R. Waser (eds.), Science and Technology of Electroceramic Thin Films, 53-65.
© 1995 *Kluwer Academic Publishers. Printed in the Netherlands.*

as $BaTiO_3$ [9,10], $PbZr_xTi_{1-x}O_3$(PZT) [11-15] and $Bi_4Ti_3O_{12}$ [16-18] have recently been synthesized by pulsed laser deposition.

To date, PZT thin films have been extensively studied for dielectric, piezoelectric and memory applications due to a wide range of electrical properties. Current studies on PZT thin films are primarily directed to non-volatile memory applications. However, relaxor materials provide several unique properties, compared to normal ferroelectric materials such as PZT and $BaTiO_3$, including a high dielectric constant and broadened dielectric maxima at the transition temperature. $Pb(Mg_{1/3}Nb_{2/3})O_3$ (PMN) is the most well known relaxor material which exhibits a high dielectric constant, high electrostrictive coefficient and diffuse phase transition near -15°C [19-20]. To modify the Curie temperature, solid-solutions of $Pb(Mg_{1/3}Nb_{2/3})O_3$ - $PbTiO_3$ (PMN - PT) have been reported [21]. The ferroelectric properties of PMN-PT compositions cover a wide range of applications which are dependent on the amount of PT in the formulation. A large induced electrostrictive strain can be obtained from compositions which contain small amounts of PT. The piezoelectric effect becomes significant for compositions near the morphotropic phase boundary, where the PT content is approximately 35% [22]. PMN and PMN-PT thin films have become attractive for microelectronic applications. Several researchers have investigated the development of PMN-PT thin films for memory (DRAM,FRAM) and microactuator applications [23-24].

Important electrical properties of ferroelectric thin films for nonvolatile memory applications are remanent polarization, coercive field, fatigue and retention. Among these, fatigue is a significant indicator of the reliability for FRAM devices which use a destructive readout operation, i.e., the switching of polarization for each read/write operation. Fatigue is expected to be dependent on composition, structure, crystalline quality (epitaxial or polycrystalline), electrode materials and microstructure of the film. Recently, metal-oxide electrodes, e. g., $Y_1Ba_2Cu_3O_x$ and RuO_2, were used as electrodes for Pb(Zr, Ti)O_3 (PZT) thin films, yielding PZT capacitors which exhibited superior fatigue resistance [25,26]. In this paper, we report in situ film growth of PZT films near the morphotrophic phase boundary (Zr/Ti=52/48) and (1-x)PMN-xPT (x=0 - 0.4). Several experiments have been carried out using different metal-oxide substrates and different top and bottom electrodes to investigate the effect of crystalline quality on fatigue and compare it with the effect of electrode materials (metal or metal-oxide). Photo-induced effects in PZT films were studied in order to investigate a possible fatigue mechanism.

2. Experimental

PZT (Zr/Ti=58/42) and (1-x)PMN-xPT, where x= 0, 0.1, 0.3, 0.35 and 0.4 mole, targets were prepared by solid solution reaction. For PZT, PbO, TiO_2 and ZrO_2 were calcined at 800°C and sintered at 1250°C/1hr. PMN-PT was prepared via the columbite process by prereaction of $MgCO_3$ and Nb_2O_5 at 1050°C/6 hrs and calcined with stoichiometric PbO and TiO_2 at 850°C/ 4 hrs. Pellets of 1" diameter were prepared and sintered at 1250°C for 1.5 hrs. The target density was about 95% theoretical density. Targets were then placed at a distance of 6 cm from the substrate holder.

MgO(100) , $SrTiO_3$(100) and r-plane sapphire were used as a substrate materials. The substrates were attached to a heater plate by silver paste. Each substrate was heated up to 600 °C for 30 minutes under 2 mTorr to clean the substrate surface of hydrocarbon residues. Films were prepared at different substrate temperatures and oxygen pressures. A KrF laser, operating at 248 nm with a repetition rate of 6 Hz, was focused onto the target.

The laser energy was set at 2 J/cm^2, which is just sufficient to remove the ions or molecules from the target and deposit onto the substrate. The deposition was set at 5000 pulses. After deposition, films were cooled down under an oxygen pressure of 600 Torr.

The thickness of the films was measured by a profilometer. X-ray diffraction was used to evaluate the perovskite phase formation. The elemental analysis of the films was characterized by Rutherford back-scattering spectrometry (RBS).

For evaluation of the dielectric properties of the films, conductive oxides of $Y_1Ba_2Cu_3O_x$(YBCO) or $La_{0.5}Sr_{0.5}CoO_3$ (LSCO) were used as the bottom electrode. The LSCO films were first deposited on the MgO(100) substrate for 2500 pulses at 150 mTorr of oxygen pressure and a substrate temperature of 575 °C. In the case of YBCO, the deposition was carried out at a substrate temperature of 700 °C under an oxygen pressure of 120 mTorr. After the deposition of the electrode, PZT or PMN-PT film was deposited, followed by the deposition of YBCO or sputtered Pt on top of PZT or PMN-PT thin films. The thickness of bottom electrode and the films were 2500 Å and 5000 Å respectively. The diameter of the Pt top electrode was 0.6 mm.

3. Results and Discussion I : PZT Thin Films

Films were deposited on MgO(100) substrate as a function of substrate temperature and oxygen pressure. Figure 1 shows x-ray diffraction patterns of PZT films deposited on MgO at an oxygen pressure of 200 mTorr and substrate temperatures between 550 °C and 625 °C. The films had an oriented perovskite structure in a narrow window of the substrate temperatures around 575 °C. At substrate temperatures below 500 °C, a pyrochlore phase was dominant. Upon increasing the substrate temperature, the perovskite phase began to develop, and became the only phase in the film at 575 °C. The full width at half maximum (FWHM) of the x-ray rocking curve for the (002) peak of the PZT film was 1.5°. Up to 600 °C, stoichiometry in the films was preserved. Increasing substrate temperatures caused the Pb content in the films to decrease leading to an oriented pyrochlore structure, as shown in Figure 1. To find the effect of the ambient oxygen pressure on the structure of the films, the oxygen pressure was varied between 10 and 600 mTorr, with a substrate temperature of 575 °C. The perovskite phase was obtained in stoichiometric films deposited at oxygen pressures of 60 - 600 mTorr. However, the films deposited at 10 mTorr were Pb deficient and had a mixed pyrochlore and perovskite structure.

To obtain various crystalline qualities of the PZT films, YBCO films were grown on $SrTiO_3$(100), MgO(100) or r-plane sapphire at different substrate temperatures from 550 °C to 760°C. Figure 2 shows x-ray diffraction patterns from PZT/YBCO heterostructures. YBCO films deposited on $SrTiO_3$ (100) at 760 °C were c-axis oriented. PZT films deposited on these YBCO films had a highly oriented perovskite structure. Full width at half maximum (FWHM) of the x-ray rocking curve for the (002) peak of the PZT films and (005) peak of the YBCO films were 0.98° and 0.32°, respectively. Using MgO substrates instead of $SrTiO_3$, the YBCO films deposited above 700°C were also c-axis oriented, and subsequently deposited PZT films were highly oriented. The FWHM of the PZT and YBCO films were 0.81° and 0.52° respectively. However, when the deposition temperature for the YBCO film on MgO were reduced to 550°C, the YBCO films started to develop a (103) peak, indicating that an appreciable fraction of polycrystalline or misoriented material existed in the c-axis oriented films. PZT films deposited on these YBCO films were polycrystalline, slightly textured to [100] (see Figure 2). YBCO

films deposited on sapphire were polycrystalline, as were the PZT films deposited on these YBCO films.

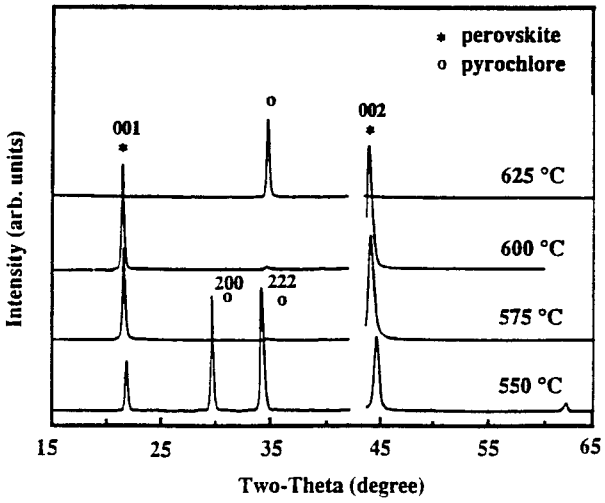


Figure 1. X - ray diffraction patterns of the PZT films deposited on MgO(100) at different substrate temperatures, (a) 550 °C, (b) 575 °C, (c) 600 °C and (d) 625 °C.

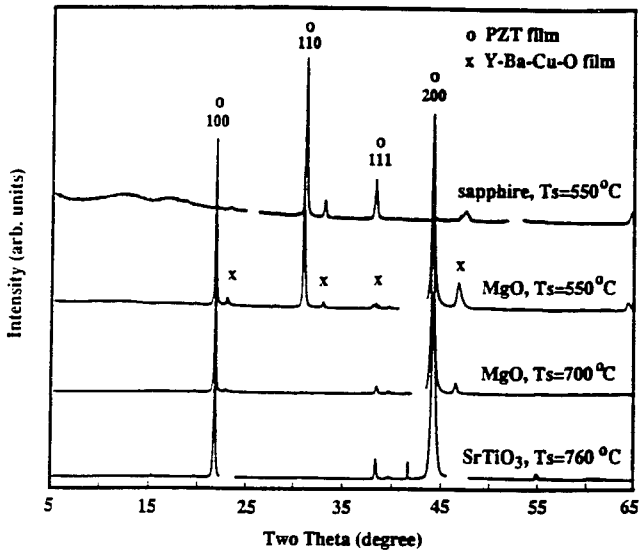


Figure 2. X - ray diffraction patterns of PZT / YBCO films on different substrate materials and temperatures. Substrate temperature for the deposition of YBCO films on $SrTiO_3$ (100) was 760 °C, those on MgO (100) were 550 °C and 700 °C, and that on r - plane sapphire was 550 °C. Substrate temperature for the deposition of PZT films was 575 °C.

Epitaxial or highly oriented PZT films with a Pt top electrode had remanent polarizations of 35-45 $\mu C/cm^2$ and coercive fields of 55-60 kV/cm. These remanent polarization values are comparable to those of epitaxial PZT films deposited by rf magnetron sputtering while the coercive fields values are much lower than those of the rf sputtered films [27]. On the other hand, polycrystalline PZT films had a low polarization which is comparable to those of rapidly annealed PZT films deposited by reactive magnetron sputtering [28] or post-annealed PZT films deposited by pulsed laser ablation [13]. The hysteresis loops obtained from the epitaxial PZT films were asymmetric due to an internal bias field. The internal bias fields were estimated to be 10 - 15 kV/cm. This large internal bias field was observed in highly oriented PZT films with a Pt top and YBCO bottom electrode, and were directed toward the bottom electrode. On the other hand, polycrystalline PZT films with Pt top electrodes had only slightly asymmetric loops. The reduced internal bias field might be due to the polycrystalline nature of the PZT films.

Epitaxial or highly oriented PZT films underwent a large decrease in polarization, dropping to about half of the initial value at 10^9 cycles. On the other hand, randomly oriented polycrystalline PZT films showed less fatigue, dropping to 65 % of the initial value after the same number of cycles. In contrast, when epitaxial or polycrystalline PZT films had YBCO films as both the top and bottom electrode, they showed quite a different fatigue behavior from the PZT films which had Pt top electrodes, as shown in Figure 3. These PZT films had a low remanent polarization (~18 $\mu C/cm^2$) but significantly improved fatigue behavior regardless of whether they were epitaxial or polycrystalline. These results suggest that the electrode material has a strong effect on fatigue. Moreover, the epitaxial PZT films with YBCO top electrodes showed nearly symmetric hysteresis loops. In other words, epitaxial PZT films with both top and bottom electrodes of YBCO had a low internal bias field compared to those with a Pt top electrode. In the PZT films with a Pt top electrode, Pt and YBCO electrodes are expected to develop different contacts at each electrode-PZT interface. These asymmetric interfaces may react differently with charged defects (in our films possibly Pb or oxygen vacancies) or related space charges (and/or defect dipoles) which have been considered to create the internal bias field [29-31]. This would result in the asymmetric behavior (large internal bias field) observed in the epitaxial or oriented PZT films with Pt top electrode. These charged defects can be also closely related to fatigue via the screening effect of polarization in the metal-PZT interface region.

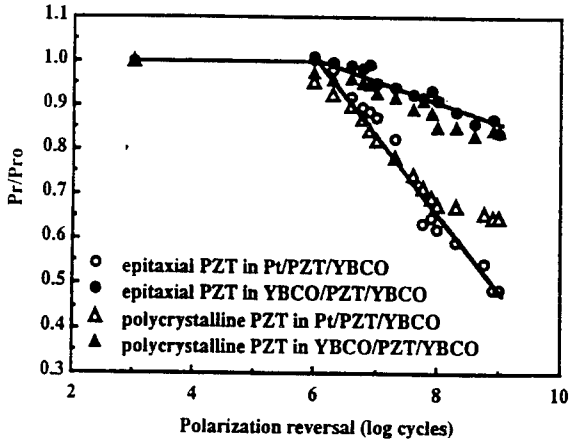


Figure 3. Fatigue characteristics of epitaxial and polycrystalline PZT films with Pt or YBCO top electrode. PZT films in PZT/YBCO/$SrTiO_3$ and PZT/YBCO/sapphire are epitaxial and polycrystalline films, respectively.

In order to investigate a possible mechanism of fatigue of PZT films, the role of defects using a polarization screening model was examined. The polarization screening is an essential phenomenon in the stabilization of ferroelectrics. The charged state of the defects is an important factor in the polarization screening and can be studied using a light source since photons will create non-equilibrium photocarriers in materials and in turn change the charged state of the defects. A He-Cd laser was used to create the non-equilibrium photocarriers in the PZT films.

First dielectric hysteresis loops of PZT films were measured in the dark state and during exposure to UV light from a He-Cd laser (λ=325 nm). Figure 4 shows the hysteresis loops of an epitaxial PZT film before and after exposure to the UV light. The remanent polarization of the film was increased upon the light illumination. The He-Cd laser has a wavelength of 325 nm, corresponding to a photon energy of 3.8 eV. Since the bandgap of PZT materials is 3.6 eV [32], illumination of the UV light will induce non-equilibrium photocarriers to the conduction band in PZT films through the band-band transition. The absorption coefficient of PZT films at the wavelength of 325 nm is estimated to be 7.5 x 10^4 cm^{-1} [32], corresponding to the optical penetration depth of ~1300 Å. Therefore, the non-equilibrium photocarriers will affect PZT films (5000 Å thick) mostly near the Pt-PZT interface. After relaxation and recombination, the non-equilibrium photocarriers are trapped at defect centers which are already involved in the screening process of the spontaneous polarization. As a result, the screening condition is changed. From the previous results on the fatigue of PZT films with conducting oxide electrodes, oxygen vacancies are the most probable defects in PZT films. The ionized defects are the charged defect centers which screen the polarization and, upon light illumination, trap the excited photocarriers. This results in neutralizing the charged defect. Finally, the neutralized defects temporarily are not involved in the screening process. Instead, the spontaneous polarization must be screened in the electrode. In other words, the polarization screened by the charged defects can be reoriented under switching electric field, which results in the increased remanent polarization upon illumination of the UV light, as shown in figure 4. Photo-induced improvement in the hysteresis loop was also observed in PZT films after exposure to band-gap light with a bias voltage [33]. However, the remanent polarization immediately decreased when the light was turned off. This temporal behavior may be due to the non-equilibrium nature of the trapped charges and their fast relaxation to the ground state.

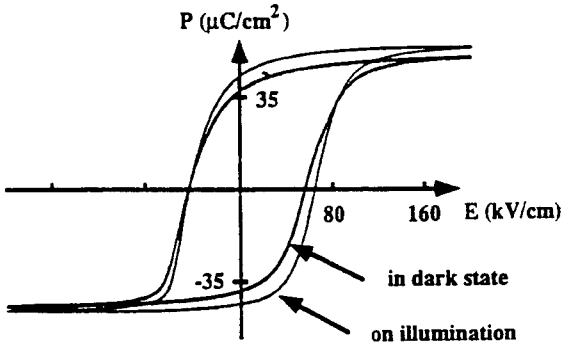


Figure 4. Polarization-electric field (P-E) hysteresis loop of a PZT film in the dark state and upon He-Cd laser illumination.

The He-Cd laser (λ=325 nm) was illuminated on the top electrode of PZT films during fatigue. Figure 5 shows the fatigue behavior of PZT films under the He-Cd laser light. When exposed to the UV light, PZT films exhibited less loss of polarization than in the dark state. PZT films in the dark state had 50 % of the initial polarization. On the other hand, PZT films with a 400 Å thick Pt electrode exposed to the UV light had 70 % of the initial polarization after 10^9 cycles. As the thickness of the Pt top electrode is reduced from 400 Å to 300 Å, the PZT films had 80 % of the initial polarization after 10^9 cycles. Transmission of the UV light in the Pt film (200 Å) was estimated to be 10 % of incident illumination [34]. Based on this estimation, the Pt films with a thickness of 400 Å and 300 Å are expected to transmit 1% and 3 % of incident light, respectively. The dependence of fatigue behavior on the thickness of the Pt top electrode indicates that fatigue is affected by light intensity (i.e., non-equilibrium photocarriers excited by the UV light).

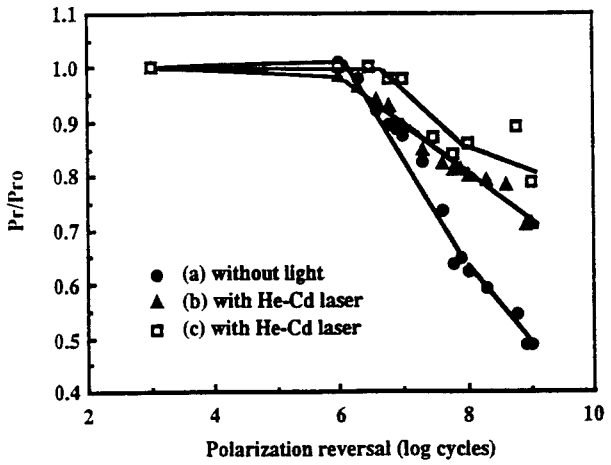


Figure 5. Fatigue of PZT films (a) in the dark state with 400 Å Pt top electrode, and upon He-Cd laser illumination with (b) 400 Å and (c) 300 Å Pt top electrodes. P_{ro} and P_r represent remanent polarizations of fresh and fatigued PZT film capacitors, respectively.

In the above model, the amount of increased polarization upon UV light exposure shown in figure 4 is related to the concentration of charged defects involved in the internal screening causing fatigue in PZT films. Therefore, the quantity of the increased polarization upon UV light exposure was measured with cycling. In this experiment, the polarization of epitaxial PZT films was first measured in the dark state. After each measurement in the dark state, the PZT film was exposed to UV light and the remanent polarization was measured. The light was then turned off and cycling was continued. Figure 6 shows that the amount of increased polarization in epitaxial PZT films exposed to the UV light increases with cycling, indicating that more charged defects are involved in fatigue with cycling through the internal screening of polarization. The internal screening as a cause of fatigue is most likely to occur at domain-boundaries or film-electrode interfaces since domain-boundaries and interfaces are the most probable sites where the defects are trapped and become immobile.

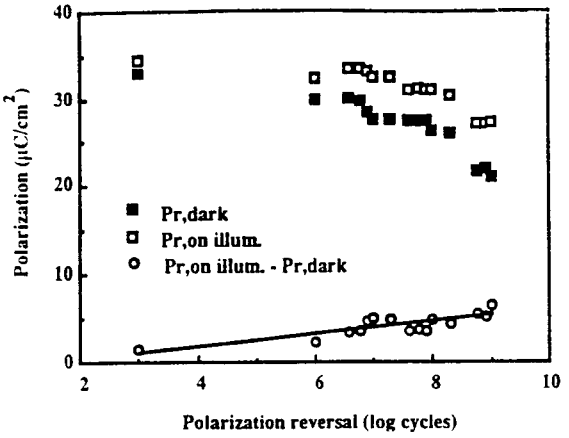


Figure 6. Fatigue of a PZT film in the dark state, while the measurements were done in the dark state and upon He-Cd laser illumination.

4. Results and Discussion II : PMN-PT Thin Films

XRD patterns of PMN films deposited in situ on MgO(100) at a substrate temperature in the range of 500 °C to 600 °C are shown in Figure 7. The XRD patterns show an amorphous phase at substrate temperatures below 535°C and an oriented (100) perovskite phase at 535°C and 550°C. A mixture of perovskite and pyrochlore phases appear at a substrate temperature above 575°C. The amount of pyrochlore phase increases from 2% to 5% as the substrate temperature increases from 575°C to 600°C. A similar study has been carried out for the composition of 0.9 PMN -0.1PT, 0.7PMN-0.3PT, 0.65PMN-0.35PT and 0.6PMN-0.4PT. To obtain the perovskite phase for compositions with a higher amount of PT, the substrate temperature was shifted to 575°C. However, for compositions near the morphotropic phase boundary, the perovskite phase was obtained at temperature as low as 535°C. A summary of the perovskite phase formation with different PMN-PT composition are shown in Figure 8.

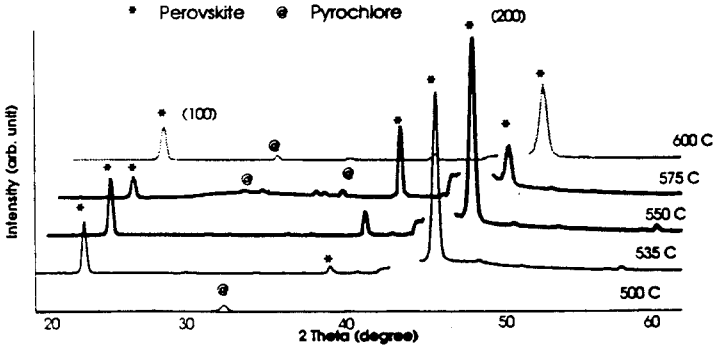


Figure 7. XRD pattern of PMN films prepared at various substrate temperature and oxygen pressure of 200 mTorr.

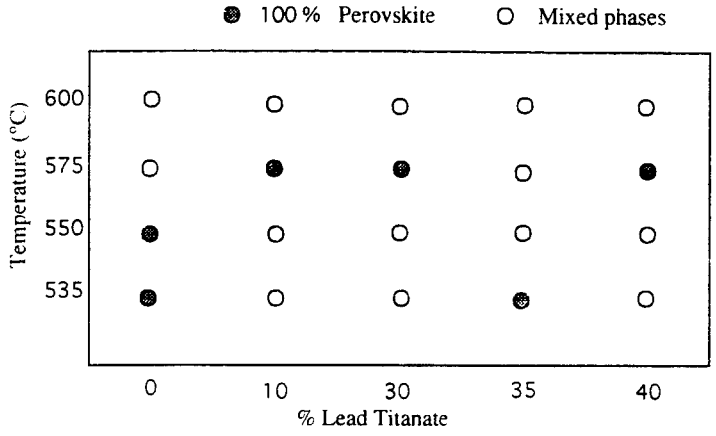


Figure 8. Effect of composition and substrate temperatures on the perovskite / pyrochlore formation of PMN-PT thin films prepared at substrate temperature of 200 mTorr.

Figure 9 shows the XRD patterns of PMN films prepared at a temperature of 535°C and an oxygen pressure between 50 to 600 mTorr. Pure perovskite was obtained at about 200 mTorr, while at pressures below 50 mTorr only pyrochlore was detected. A mixture of perovskite and pyrochlore phases was formed using oxygen pressures higher than 200 mTorr. The PMN-PT compositions also yield the same result.

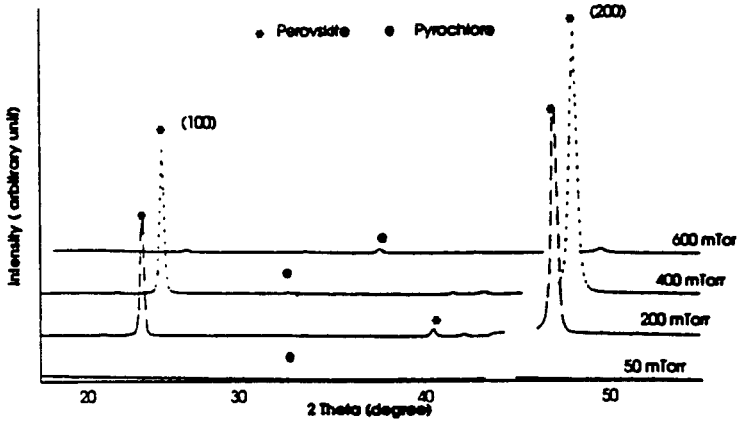


Figure 9. XRD pattern of PMN films prepared at substrate temperature of 535°C under various oxygen pressure.

Composition of the films was determined by Rutherford back scattering spectrometry (RBS) and are shown in Table I. It was found that the fraction of Mg in the film was sensitive to the substrate temperature but the fraction of Pb and Nb ions in the films was constant. It has been reported for most Pb based materials that the fraction of Pb in the film is deficient when deposited at high temperature and low oxygen pressures (<100 mTorr) [35]. However, stoichiometric PZT thin films can be obtained at a substrate

temperature of 575 °C and an oxygen pressure between 60 and 600 mTorr [36]. Although lead loss during the sintering process is very critical to form the perovskite phase, there was no significant of Pb loss for thin films when deposited at substrate temperatures lower than 600 °C [14]. For the deposition of thin films , the volatility of the ion must be considered. The temperature to produce a pressure of 10 mTorr of Pb^{2+} and Mg^{2+} are about 715 °C and 440 °C respectively [37]. Therefore it is likely that Mg ions are more volatile than Pb-ions in this substrate temperature range. In preparation of PMN thin films, it is difficult to avoid the pyrochlore phase formation, which is nonferroelectric and detrimental to the dielectric properties. The pyrochlore phase appears when the PMN compound is PbO or MgO deficient. Excess additions of MgO and PbO were found to enhance the perovskite formation in bulk ceramics [18]. As shown in Table I the highest ratio of Mg/Nb can be obtained with a substrate temperature of 535 °C. At this temperature the pure perovskite phase of PMN is obtained while at higher substrate temperatures the Mg/Nb ratio decreased and the pyrochlore phase began to form.

TABLE 1. Elemental analysis of PMN thin films prepared at various substrate temperatures.

Substrate temperature (°C)	Mg/Nb	Crystalline phase
535	0.45	perovskite
575	0.37	perovskite + pyrochlore
600	0.37	perovskite + pyrochlore

The dielectric constant and dissipation factor of the films with several different PMN-PT compositions are measured at room temperature and are shown in Table II. The dielectric loss of all films are less than 5%. The 0.9PMN - 0.1PT composition exhibited the highest dielectric constant because the Curie temperature is near to room temperature. The temperature dependence of dielectric constant for the oriented (100) PMN films are displayed in figure 10. The PMN-PT exhibited a broad transition temperature which is a characteristic of relaxor ferroelectric material.

TABLE 2. Dielectric properties of PMN-PT thin films measure at 1 kHz at room temperature.

Composition	Bulk ceramic		Thin film	
	K	Loss (%)	K	Loss (%)
PMN	13060	0.1	2300	5.0
0.9 PMN - 0.1 PT	17290	6.0	3120	4.8
0.65 PMN - 0.35 PT	3153	2.0	2170	5.0

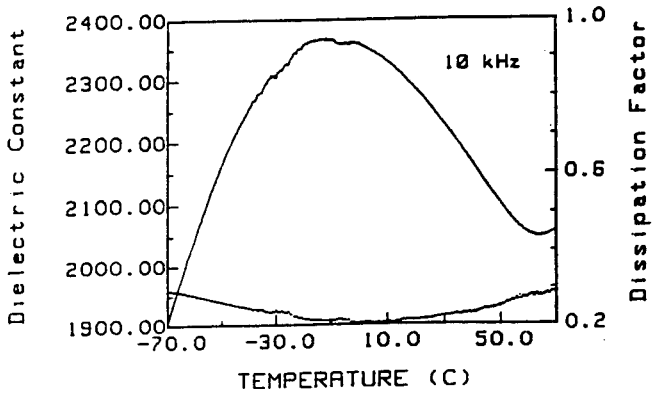


Figure 10. Plot of dielectric constant vs temperature for PMN film.

5. Conclusions

Oriented perovskite PZT, PMN and PMN-PT films were prepared on MgO(100), $SrTiO_3$(100) and r-plane sapphire substrates at 535 °C - 575 °C under an oxygen pressure of approximately 200 mTorr. It was found that the Pb content affects the perovskite phase formation of PZT films while the Mg content has an important effect on perovskite formation of PMN-PT films. The electrode material was found to be more detrimental to fatigue resistance than the crystalline quality of the PZT film. Examination of the photo-induced effect suggested that fatigue in PZT films was related to the charged defects involved in fatigue cycling.

The highest dielectric constant, measured at room temperature at 1 kHz, was obtained with 0.9PMN-0.1PT. The dielectric constant measured in relaxor films were much lower than in those measured in bulk ceramics of the same composition. The variation of dielectric constant as a function of temperature showed the characteristics of a diffuse phase transformation.

6. References

1. Francombe, M. H. and Krishnaswany, S. (1990), *J. Vac. Sci. Technol.* **A8**, 1382.
2. Eaton, S. S., Butler, D. B., Parris, M., Wilson, D. and Mcneillie, H. (1988) *Proc. IEEE Inter. Solid State Circuits Conference, San Francisco, CA, published by IEEE, Piscataway, NJ*, pp. 130. Evans, J. T. and Womack, R. (1988), *IEEE J. Solid State Circuits* **23**, 1171. Womack, R. and Tolsch, D. (1989), *Proc. IEEE Inter. Solid State Circuits Conf., San Francisco, CA, published by IEEE, Piscataway, NJ*, pp. 242. Moazzami, R., Hu, C. and Shepherd (1990), *W.IEEE Electron Device Lett.* **11**, 454 .
3. See for example, *Proc. of 3rd Inter. Symp. on Integrated Ferroelectrics, Ed. C. A. Paz de Araujo, Univ. of Colorado, Colorado Springs, CO*, April 1991.
4. Scott, J. F. and Paz de Araujo, C. A. (1989), *Science* **246**, 1400. Dey, S. and Zuleeg, R. (1990), *Ferroelectrics* **108**, 37.

5. Ramesh, R., Inam, A. , Wilkens, B., Chan, W. K., Hart, D. L., Luther, K. and Tarascon, J. M. (1990), *Science* **252**, 944. Buhay, H., Sinharoy, S., Kasner, W., Francombe, M. H., Lampe, D. R. and Stepke, E. (1991), *Appl. Phy. Lett.* **58**, 1470 .
6. Carrano, J., Sudhama, C., Lee, J., Tasch, A. and Miller, W. (1989), *IEEE-IEDM* **89**, 255. Carrano, J., Sudhama, C., Lee, J., Tasch, A., Shepherd, W. H. and Abt, N. (1991), *IEEE Trans. Ultrasonics, Ferroelectrics and Freq. Control* **38**, 690.
7. Miyasaka, Y., Sakuma, T., Matsubara, S., Watanabe, H. and Koyama, K. (1992), *Proc. of 4th Inter. Symp. on Integrated Ferroelectrics, Monterey, CA*, in press.
8. Wu., X. D., Inam, A., Venkatesan, T., Chang, C. C., Chase, E. W., Barboux, P., Tarascon, J. M. and Wilkens, B. (1988), *Appl. Phys. Lett.* **52**, 754.
9. Davis, G. M. and Gower, M. C. (1989), *Appl. Phys. Lett.* **55**, 112.
10. Norton, M., Scarfone, C., Li, J., Carter, C. B. and Mayer, W. (1991), *J. Mater. Res.* **6**, 2023.
11. Saenger, K. L., Roy, R. A., Etzold, K. F. and Cuomo, J. J. (1990), *Mat Res. Soc. Symp. Proc.* **200**, 115.
12. Kidoh, H., Ogawa, T., Morimoto, A. and Shimizu, T. (1991), *Appl. Phys. Lett.* **58**, 2910
13. Roy, D., Krupanidhi, S. B. and Doughty, J. P. (1991), *J. Appl. Phys.* **69**, 7930.
14. Horwitz, J. S., Grabowski, K. S., Chrisey, D. B. and Leuchtner, R. E. (1991), *Appl. Phys. Lett.* **59**, 1565.
15. Ramesh, R., Inam, A., Chan, W. K., Tillerot, F., Wilkens, B., Chang, C. C., Sands, T., Tarascon, J. M. and Keramidas, V. G. (1991), *Appl. Phys. Lett.* 59, 3542.
16. Buhay, H., Sinharoy, S., Lampe, D., Stepke, E., Kasner, W. H. and Francombe, M. H. (1991), *Proc. of IEEE The International Symp. on Applications of Ferroelectrics, University of Illinois at Urbana-Champaign, June 1990 (IEEE, Piscataway, NJ,*), pp. 1139. *Appl. Phys. Lett.* **58**, 1470.
17. Ramesh, R., Luther, K. Wilkins, B. Hart, D. L., Wang, E., Tarascon, J.M., Inam, A., Wu, X.D., and Venkatesan, T. (1990), *Appl. Phys. Lett.* **57**, 1505.
18. Buhay, H., Sinharoy, S., Francombe, M. H., Kasner, W. H., Talvacchio, J., Park, B. K., Doyle, N. J., Lampe, D. R. and Polinsky, M. (1991), *Proceedings of 3rd International Symposium on Integrated Ferroelectrics, Colorado Springs,* (ISIF, Colorado Springs, CO, pp. 62.
19. Nomura, S. and Uchino, K. (1983), *Ferroelectrics* **50**, 197.
20. Swartz, S.L., Shrout, T.R., Schultze, W.A. and Cross, L.E. (1984), *J. Amer. Ceram. Soc.* **67**., 311
21. T.R.Shrout and J. Fielding, (1990), *Ultrasonics Symposium*, 711.
22. Choi, S.W., Shrout, T.R., Jang, S.J and Bhalla, A.S. (1989), *Ferroelectrics* 100, 29.
23. Francis, L.F., Oh, Y-J. and Payne, D.A. (1990), *J. Mat. Sci.* **25**, 5007.
24. Francis, L. F. and Payne, D.A. (1991), *J.Am.Ceram.Soc.* **74** (12), 3000.
25. Ramesh, R., Chan, W. K., Wilkens, B., Gilchrist, H., Sands, Tarascon, J. M. V. Keramidas, G., Fork D. K., Lee J. and Safari, A. (1992), *Appl. Phys. Lett.* **61**, 1537.
26. Berstein, S. D., Wong, T. Y., Kisler, Y., and Tustison, R. W. (1992), *Proc. of 4th Inter. Symp. on Integrated Ferroelectrics*, Paz de Araujo, C.A. (ed.), in press. Nasby, R. D. and Rodgers, M. S., ibid.
27. Takayama, R. and Tomita, Y. (1989), *J. Appl. Phys.* **65**, 1666

28. Vasant Kumar, C. V. R., Sayer, M., Pascual, R., Amm, D. T., Wu, Z. and Swanston, D. M. (1991), *Appl. Phys. Lett.* **58**, 1161.
29. Lambeck, P. V. and Jonker, G. H. (1978), *Ferroelectrics* **22**, 729.
30. Carl, K. and Hardtl, K. H. (1978), *Ferroelectrics* **17**, 473.
31. Takahashi, M. (1970), *Jpn. J. Appl. Phys.* **9**, 1236.
32. Peng, C. H., Chang, J.F. and Desu, S. B. (1991), *Mat. Res. Soc. Proc.* **243**, 21.
33. Dimos, D. D, Warren, W. L. and B. A. Tuttle, B. A. (1993), *Mat. Res. Soc. Proc.* **310**, 87 .
34. Brody, P. S. and Rod, B. J., (1991), *Proc. 3rd Intern. Symp.; Integrated Ferroelectrics,* Colorado Springs, Colorado, pp. 291.
35 Chang, S.S., Nishioka, M., Fulrath, R.M. and Pask, J.A. (1991), *Am. Ceram. Soc. Bull.* **60**, 484.
36. Lee, J., Safari, A. and Pfeffer , R.L. (1992), *Appl. Phys. Lett.* **61**, 1643.
37. Honig, R.E. (1962), *RCA Rev* **23**, 567.
38. Teowee, G. and Uhlmann, D.R. (1993), *Mater. Res. Soc. Symp. Proc.* ***310***, pp. 415.

WAVELENGTH DEPENDENCE IN PULSED LASER DEPOSITION OF ZnO THIN FILMS

D. CRACIUN AND V. CRACIUN
Institute of Atomic Physics,
Laser Department,
Bucharest, Romania

ABSTRACT. The properties of thin ceramic films such as ZnO and CeO_2 grown by the pulsed laser deposition (PLD) technique have been reported to depend on the wavelength of the laser used for ablation. Under otherwise identical deposition conditions, the quality of the ZnO layers grown by the KrF laser (λ=248 nm) was always noticed to be better than that of the layers grown by the frequency-doubled Nd:YAG laser (λ=532 nm). The temperature profile inside the irradiated targets, obtained by solving a one-dimensional heat diffusion equation, indicated a strong superheating effect of the melted material for the case of Nd:YAG laser irradiation. This effect can lead to microexplosion with an adverse effect on the quality of the grown layers and thus account for the different film qualities observed.

1. Introduction

ZnO thin films, combining interesting properties such as high optical transmittance in the visible region (energy band-gap, E_g = 3.24 eV), good electrical conductivity and, when c-axis oriented, large piezoelectric and piezooptic coefficients [1], have been employed in many important applications: pressure or gas sensors, surface acoustic wave transducers, varistors, liquid crystal displays, and solar cells [2-8]. As the piezo and opto-electric properties strongly depend on the degree of c-axis orientation, many techniques such as sputtering [3, 7, 9], chemical vapour deposition [10], sol-gel [11], chemical spraying [12], electron plasma sputtering [13], ion-beam assisted deposition [14], electron beam evaporation [15] or reactive evaporation [16] have been employed for the growth of high quality c-axis oriented ZnO layers at substrate temperatures as low as possible.

The use of the pulsed laser deposition (PLD) method for the growth of ZnO films was first reported more than 10 years ago [17, 18]. Recently, there have been further reports published describing the use of PLD method to obtain ZnO [19-23]. Some of these ZnO films grown by PLD at substrate temperatures below 350° C have been shown to exhibit structural properties amongst the best yet reported [22, 23]. However, these studies have also shown [19, 21-23] that higher quality ZnO films are usually obtained when employing a KrF laser for ablation rather than a frequency doubled Nd:YAG laser. In this paper theoretical support for this observed wavelength dependence is presented as temperature profile results obtained by solving the heat diffusion equation for each set of laser irradiation conditions.

O. Auciello and R. Waser (eds.), Science and Technology of Electroceramic Thin Films, 67-74.
© 1995 *Kluwer Academic Publishers. Printed in the Netherlands.*

2. Theory

An interesting question raised by several PLD studies was why the quality of ceramic films like ZnO [19, 21-23], CeO_2 [24] and YBCO [25] grown under identical deposition conditions by UV lasers has always been better than that of those grown by longer wavelength lasers. A possible answer to this question is provided by the results obtained when solving the usual one dimensional heat diffusion equation with boundary conditions describing the laser target interaction [26-29]:

$$\rho Cp(T)\frac{\partial T(x,t)}{\partial t} = \frac{\partial}{\partial x}(K(T)\frac{\partial T(x,t)}{\partial x}) + (1 - R(T))I(t)\alpha(T)\exp(-\alpha(T)x) \quad (1)$$

$$(K(T)\frac{\partial T(x = 0,t)}{\partial x}) = 0 \quad (2)$$

$$T(x \to \infty,t) = 300K \quad (3)$$

Where ρ, Cp(T), R(T), and α(T) refer to the temperature dependent density, heat capacity, reflectivity, and absorption coefficient. I(t) is the time-dependent intensity for each laser type used. When the target surface reached the boiling temperature, T_b, a new surface boundary condition, taking into account the heat loss associated with the evaporated material was used [29, 30]:

$$(K(T)\frac{\partial T(x = 0,t)}{\partial x}) = Lb\rho\frac{dx}{dt} \quad (4)$$

where L_b is the latent heat of boiling.

3. Results and Discussions

Equations 1-4 were solved by a finite difference method [29], in a reference frame moving with the liquid/vapour interface. Because the thermo-physical and optical properties of ZnO are not known for temperatures above 1300 K, these unknown parameters were adjusted to obtain a good fit between the model estimations and the measured ablation depths for different laser fluences reported in the literature [23]. The parameters determined in this way are listed in Table 1 and the comparison between the measured and estimated ablation depth data is shown in Fig. 1.

In the absence of any data relating the boiling temperature, T_b, to the vapour pressure for ZnO, we "clamped" it at a value slightly higher (10 K) than that corresponding to the

atmospheric pressure, T^{o}_{b} = 2300 K. As can be seen in Fig. 2, the temperature profile shape remains qualitatively unchanged when a variation of the boiling temperature of 300° C above the 2310 K value was allowed.

It is worth mentioning that a good fit as that shown in Fig. 1 requires a jump in the value of the reflectivity when ZnO melts. As the liquid ZnO was found to be a good electrical conductor [1], such a jump could be associated with a semiconductor-metal transition, as in the case of Si. Secondly, the log-type dependence of the ablation depth vs fluence requires the introduction of a plasma shielding factor [31, 32]. To the best of our knowledge, the absorption coefficient for laser radiation of a ZnO plasma has not yet been measured. To circumvent this lack of experimental data, we used an empirical term added to the reflection coefficient:

$$R = R_0 + R_1(1-\exp(-\Delta x / x_0)) \qquad (5)$$

where Δx is the quantity of ablated material estimated by the model and R_1 and x_0 are two fitting parameters.

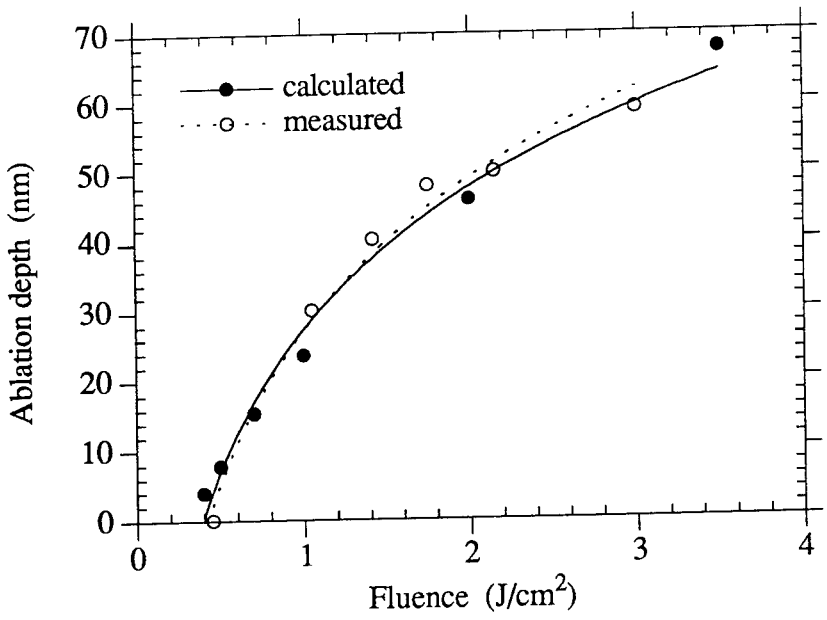


Figure 1. ZnO ablation depth versus excimer laser fluence. The measured data are taken from Ref. 23.

TABLE 1. ZnO parameters used for calculations

Density ($g\ cm^{-3}$)	5.6	
Melting Temperature (K)	2300	
Evaporation Temperature (K)	2310	
Latent Heat of Fusion ($J\ g^{-1}$)	971.6	
Latent Heat of Vaporization ($J\ g^{-1}$)	7656.1	
Thermal Conductivity ($W\ cm^{-1}\ K^{-1}$)	$0.58 - 1.1\ 10^{-3}\ T + 3.93\ 10^{-7}\ T^2$	
	0.038 $T > 1300$ K	
	0.076 $T > 2300$ K	
Heat Capacity ($J\ g^{-1}\ K^{-1}$)	$0.5156\ (11.71 + 1.2\ 10^{-3}\ T - 2.18\ 10^{5}\ T^{-2})$	
	0.744 $T > 2300$ K	
Absorption Coefficient (cm^{-1})	$2.55\ 10^{5} + 250\ T$	
	$5\ 10^{5}$ $T > 1200$ K	
Reflectivity	$0.17 + 10^{-4}\ T$	(solid)
	0.6	(liquid)
	$0.6 + 0.35\ [1-\exp(-\Delta x/7.5)]$	(vapour)

As one can notice from Fig. 1, the agreement between the experimental data and model predictions is very good. For a laser fluence of 2.1 J/cm^2, the shielding factor was found to be around 0.29. Knowing that the attenuation of the laser intensity due to plasma absorption can be written as [32]:

$$I = I_0 \exp(-\alpha_p v (t_p - t_f)) \qquad (6)$$

where α_p and v are the plasma absorption and, respectively, expanding velocity and t_p and t_f are the plasma appearance and pulse ending time, one obtains, using $v = 10^5$ cm/s, a value for $\alpha_p = 50\ mm^{-1}$, in good agreement with other measured data for ceramic materials like Si_3N_4 [32].

The temperature profile inside the irradiated target at the onset of melting, $T(0) = T_b$, and when the first 7 nm of the target material were completely removed, estimated for the same laser fluences as those used in Ref. 23 are shown in Fig. 2. Also shown are the temperature profiles estimated with a variable T_b. The target surface morphology after the ablation process, reproduced from ref 23, is shown in Fig. 3.

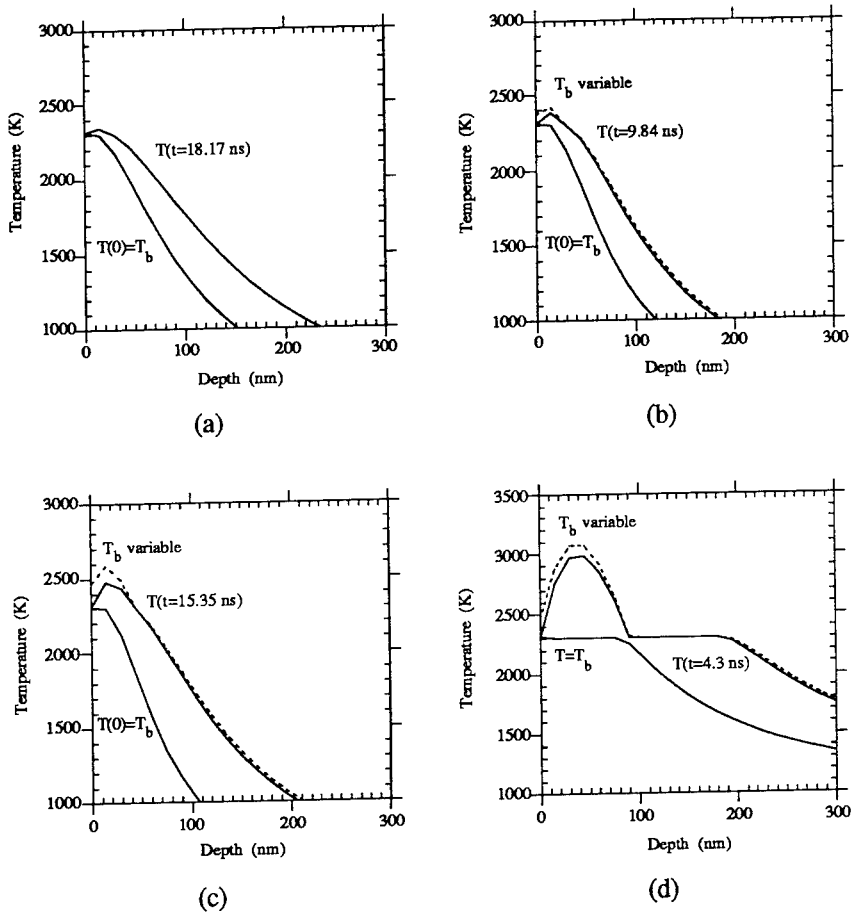
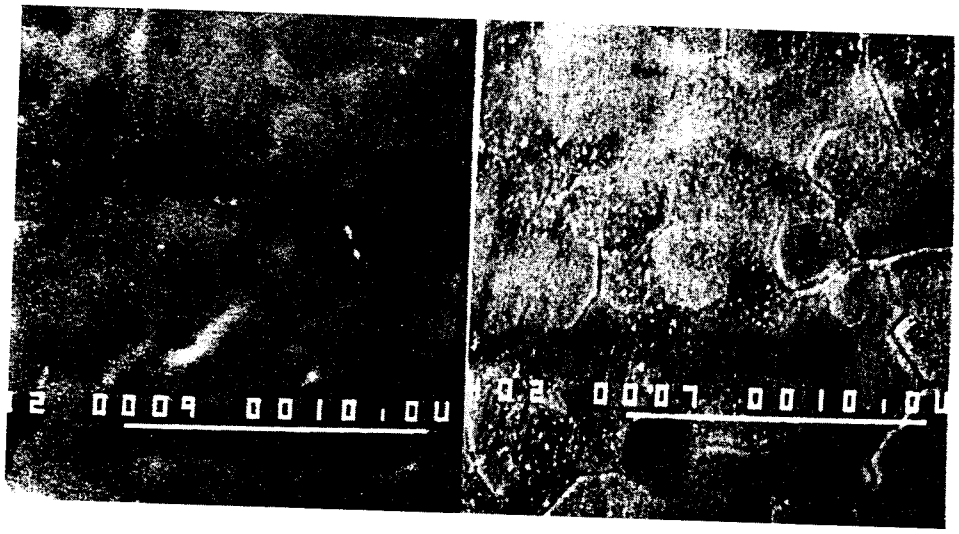
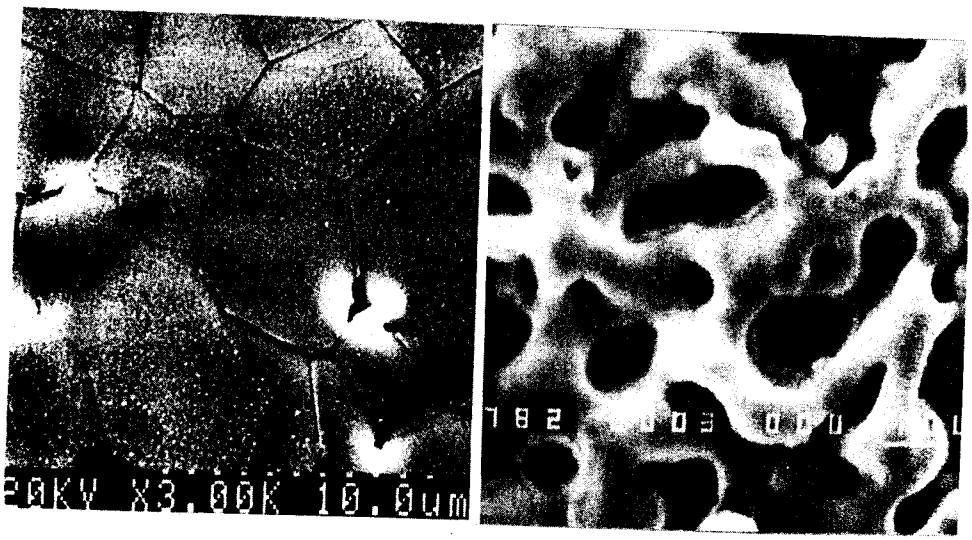


Figure 2. Temperature profiles estimated at the moment when the surface temperature reached the boiling point and when 7 nm (only 1.5 nm for case a) of target material were ablated (laser fluences as those shown in Fig. 3) The dotted line correspond to the model with T_b allowed to increase by 300 K.

For low fluence values such as 0.7 J/cm^2, just above the plasma formation threshold (see Fig. 1 & 3a), the target surface melted, but the quantity of ablated material was too low to form a dense plasma. The deposition process is more akin to the thermal evaporation than ablation and the quality of the grown layer has been notice to be poor [23]. For fluences between 1.5 to 2.5 J/cm^2, approximately 30 to 55 nm of target material was ablated during the action of a single laser pulse. The target surface morphology after ablation, as shown in Fig. 3b, exhibited a very smooth surface. Under these laser irradiation conditions the temperature profile peaked at the target surface (see Fig. 2b) or very close to it. The ablation front is planar and the best quality films can be grown within this fluence range.



(a) (b)



(c) (d)

Figure 3. SEM micrographs of the target surface after laser irradiation for different incident fluences (in J/cm^2): (a) 0.7 (b) 2.1 (c) 3.5, KrF laser irradiation, and (d) 2.1 Nd:YAG laser (reproduced from ref 23).

Further increase of the laser fluence above 3 J/cm^2 resulted in a target morphology exhibiting a recrystallization process (see Fig. 3c), with grain sizes significantly higher than those initially present. One can also notice the appearance of small craters or holes on the surface. The simulated temperature profile begins to change its shape, the maximum value being displaced well inside the depth of the sample (see Fig. 2c). Such a superheating effect can lead to microexplosions within the melted material with subsequent adverse effects on eventual film quality [26-28,30]. This behavior effectively limits the laser fluence one can use for growth of high quality ZnO films.

In the case of Nd:YAG laser irradiation, because of the high optical transparency of the target material at 532 nm (extinction coefficient, $k = 10^{-3}$ as experimentally determined from the recorded optical transmittance spectra [21]) and the resulting volume absorption of laser energy, the superheating effect appears at much lower fluences, in fact at levels just above the ablation threshold, and is more pronounced (see Fig. 2d; actually, it is unrealistic to assume an overheating of the liquid by more than few hundreds of K). As shown in Fig. 3d, the target surface was heavily affected by microexplosions, preventing high quality films from being grown with this wavelength.

In conclusion, the strong superheating effect of the liquid target material evidenced by the temperature simulations for ablation with laser photon energies less than the target material optical bandgap can explain the poorer quality of the grown ZnO films. The model employed, being quite general can be easily applied to predict the temperature profiles in other useful target materials once the ablation data versus fluence are known.

It is also worth noting that a heavily damaged surface morphology exhibits strongly non-uniform optical absorption. The incident laser beam can be trapped inside these cavities, similar to the well known light-pipe or key-hole effect in laser welding and drilling [30], the local absorptivity being practically equal to 1. The subsequent ablation process firstly appears in these regions, fact that can further deepen the cavities.

4. Acknowledgment

Parts of this work were initiated during an EEC scholarship (for DC) at University College London, Electronic and Electrical Department, UK.

5. References

1. Bornstein New Series, Volume 17b (1982), O. Madelung (ed.), Springer Verlag, Berlin, Heidelberg, New York.
2. Pizzini, S., Butta, N., Narducci, D., and Palladino, M. (1989), *J. Electrochem. Soc.* **136**, 1945.
3. Aeugle, T., Bials, H., Heneka, K., and Pleyer, W. (1991),*Thin Solid Films* **201**, 293.
4. Hikernell, F. S. (1985) , *IEEE Trans. Sonics Ultrasonics* **SU-32**, 621.
5. Cao, Z. C., Wu, R. J., and Song, R. S. (1994), *Mat. Sci. Eng.* **B22**, 261.
6. Yoo, J. B., Fahrenbruch, A. L., and Bube, R. H. (1990), *J. Appl. Phys.* **68**, 4694.
7. Itoh, T. and Suga, T. (1994), *Appl. Phys. Lett.* **64**, 37.
8. Shih, W.-C. and Wu, M.-S. (1994), *J. Crystal Growth* **137**, 319.
9. Pol, F. C. M. van de, Blom, F. R., and Popma, Th. J. A. (1991), *Thin Solid Films* **204**, 349.

10. Wenas, W. W., Yamada, A., Konagai, M., and Takahashi, K. (1994), *Jpn. J. Appl. Phys.* **33**, L283.
11. Tang, W. and Cameron, D. C. (1994), *Thin Solid Films* **238**, 83.
12. Olivera, M. dela L., Maldonado, A., and Asomoza, R. (1993), *Thin Solid Films* **229**, 196.
13. Manabe, Y. and Mitsuyu, T. (1990), *Jpn. J. Appl. Phys.* **29**, 334.
14. Zhang, D. H. and Brodie, D. E. (1994), *Thin Solid Films* **238**, 95.
15. Kuroyanagi, A. (1989), *Jpn. J. Appl. Phys.* **28**, 219.
16. Jin, M. and Ying, L. S. (1994), *Thin Solid Films* **237**, 16.
17. Sankur, H. and Cheung, J. T. (1983), *J. Vac. Sci. Technol.* **A1**, 1806.
18. Nakayama, T. (1983), *Surface Sci.* **133**, 101.
19. Ianno, N. J., McConville, L., Shaikh, N., Pittal, S. and Snyder, P. G. (1992), *Thin Solid Films* **220**, 92.
20. Maruyama, K., Endo, S., Sasaki, G., Kamata, K., Nishino, J., and Kuchitsu, K. (1992), *J. Mat. Sci. Lett.* **11**, 1588.
21. Amirhaghi, S., Craciun, V., Beech, F., Vickers, M., Tarling, S., Barnes, P. and Boyd, I. W. (1993), Mater. Res. Soc. Proc., B. Braren, J. J. Dubovski, D. P. Norton (eds.), Pittsburgh, **Vol. 285**, 489.
22. Amirhaghi, S., Craciun, V., Craciun, D., Elders, J. and Boyd, I. W. (1994), J. Electron. Mat (in press).
23. Craciun, V., Amirhaghi, S., Craciun, D., Elders, J., Gardeniers, J. G. E. and Boyd, I. W. (1994), E-MRS Spring Meeting, Strasbourg (in press).
24. Amirhaghi, S., Beech, F., Craciun, V., Sajjadi, A., Vickers, M., Tarling, S., Barnes, P. and Boyd, I. W. (1992), Mater. Res. Soc. Proc., D. T. Shaw, C. C. Tsuei, T. R. Schneider, and Y. Shiohara (eds.), Pittsburgh, **Vol. 275**, 501.
25. Koren, G. Gupta, A., Baseman, R. J., Lutwyche, M. I. and Laibowitz, R. B. (1989), *Appl. Phys. Lett.* **55**, 2450.
26. Gagliano, F. P. and Paek, U. C. (1974), *Appl. Optics* **13**, 274.
27. Dabby, F. W., Paek, U. C. (1972), *IEEE J. Quantum Electr.* **QE-8**, 106.
28. Singh, K. R., Bhattacharya, D, and Narayan, J. (1990), *Appl. Phys. Lett.* **57**, 2022.
29. Crank, J. (1984) *Free and moving boundary problems*, Oxford University Press, Oxford.
30. Gagliano, F. P. and Zaleckas, V. J. (1972) Laser processing fundamentals in S. S. Charschan (ed.) *Lasers in industry*, Van Nostrand Reinhold Company, N. Y., 138.
31. Tokarev, V., Marine, W., Lunney, J. G. and Sentin, M. (1994), *Thin Solid Films* **241**, 129.
32. Maruo, H., Miyamoto, I., and Ooie, T. (1993), in Proc. of LAMP'92, Nagoya, 293.

ORGANOMETALLIC CHEMICAL VAPOR DEPOSITION OF LEAD ZIRCONATE TITANATE

M. DE KEIJSER, P.J. VAN VELDHOVEN AND G.J.M. DORMANS
Philips Research Laboratories Eindhoven,
Prof. Holstlaan 4, 5656 AA Eindhoven,
The Netherlands.

ABSTRACT. The deposition of $PbZr_xTi_{1-x}O_3$ by organometallic chemical vapor deposition (OMCVD) on 100 mm platinized silicon wafers is described.

Two types of electrodes were used, Pt and Pt/RuO_2., and the growth and properties of the $PbZr_xTi_{1-x}O_3$ films were investigated. Although ferroelectric capacitors with good properties are obtained with conventional Pt-based electrodes, the use of oxide electrodes like RuO_2, may be advantageous. It will be shown that the microstructure of the $PbZr_xTi_{1-x}O_3$ is strongly dependent on the nature of the bottom electrode.

In the second part, some results of the ferroelectric properties of $PbZr_xTi_{1-x}O_3$ films with Pt electrodes that are integrated with CMOS will be presented. It will be shown that uniform deposition can be achieved over large areas and that a good step coverage can be obtained. Good ferroelectric properties are obtained for fully integrated $PbZr_xTi_{1-x}O_3$ films that allow the proper functioning of memory cells.

1. Introduction

The integration of ferroelectric materials in microelectronic devices requires the deposition of films on large area substrates. For applications explicitly making use of the ferroelectric properties of these materials (e.g. non-volatile memories, piezo- and pyroelectric sensors and actuators) ferroelectric capacitors need to be made. In this case the film has to be deposited on an electrode. The most frequently used electrode material until now is platinum which is one of the few materials that can withstand the high temperatures and oxidising conditions that are present during $PbZr_xTi_{1-x}O_3$ deposition. Alternatively, oxidic conductors like ruthenium dioxide, RuO_2, can be used. Such electrodes are compatible with $PbZr_xTi_{1-x}O_3$ processing and good ferroelectric properties can be obtained with these electrodes [1]. In the first part of this paper the properties of $PbZr_xTi_{1-x}O_3$ films deposited by organometallic chemical vapor deposition (OMCVD) on silicon wafers with Pt- as well as RuO_2 electrodes will be given. In the second part results relevant for the integration of the OMCVD ferroelectric films with CMOS will be given.

O. Auciello and R. Waser (eds.), Science and Technology of Electroceramic Thin Films, 75-84.
© 1995 *Kluwer Academic Publishers. Printed in the Netherlands.*

2. Experimental

Details of the OMCVD apparatus and the deposition conditions of the $PbZr_xTi_{1-x}O_3$ are given elsewhere [2]. In short, the $PbZr_xTi_{1-x}O_3$ films were deposited at 675°C, using a fixed ratio of the precursor- and oxygen partial pressures yielding a deposition rate of about 0.8 μm/hr.

The Pt bottom electrodes were obtained by sputter deposition of a thin Ti adhesion layer followed by a Pt layer of about 70 nm thickness on oxidized silicon wafers. The sputtered Pt films were used as electrodes for the deposition of $PbZr_xTi_{1-x}O_3$ directly, or they were coated with RuO_2 prior to the deposition of the ferroelectric thin film. This deposition of RuO_2 thin films was done by OMCVD in a second set-up capable of handling up to 100 mm wafers. The precursor was biscyclopentadienylruthenium, $Ru(C_2H_5)_2$, which was evaporated at 65°C. Deposition temperatures were between 300-500°C and the deposition rate was approximately 0.5 μm/hr.

The chemical composition of the films was measured using x-ray fluorescence (XRF). This technique, combined with a for thin film analysis dedicated software package, enabled the determination of the metals ratios within 2% accuracy. Uniformity both in composition and in thickness was estimated by XRF measurements on several positions over the wafer. The thickness of the $PbZr_xTi_{1-x}O_3$ was also measured using optical spectroscopy. The crystallinity of the $PbZr_xTi_{1-x}O_3$ film was examined with x-ray diffraction (XRD) using CuKa radiation.

3. Results

3.1. $PbZr_xTi_{1-x}O_3$ ON Pt AND RuO_2 ELECTRODES

The influence of the bottom electrode on the microstructure of the $PbZr_xTi_{1-x}O_3$ film was investigated by using the same deposition conditions for the ferroelectric films on the platinum and on the RuO_2 electrodes. In Figure 1 the thickness of $PbZr_xTi_{1-x}O_3$ films deposited onto these substrates is plotted versus the position on the wafers. The thickness was measured with optical spectroscopy and was confirmed by XRF. For both substrates the variation in thickness is below 5%. It appears that the film on the RuO_2 electrode is some 10% thicker than the one on the platinum electrode.

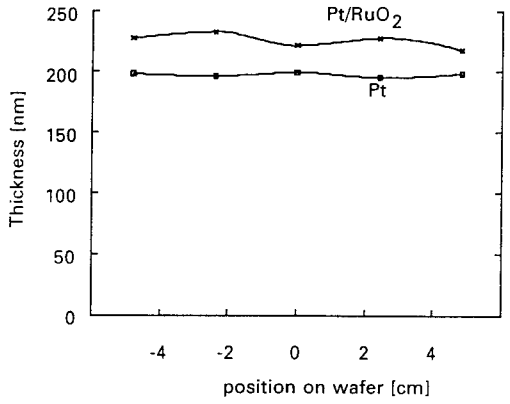


Figure 1. Thickness distribution of $PbZr_xTi_{1-x}O_3$ films on Pt and Pt/RuO_2 electrodes as determined by optical spectroscopy.

Figure 2(a) shows a scanning electron microscopy (SEM) image of a typical surface morphology of a polycrystalline $PbZr_xTi_{1-x}O_3$ film of 0.2 μm thickness with x=0.30 deposited at 675°C on a platinized SiO_2/Si wafer. The morphology is rather rough and individual crystallites can be observed. The estimated average crystallite size is 0.25 μm. These crystallites are faceted, pointing at a three-dimensional growth of the film with some crystal planes growing faster than others. A rather dense film seems to have formed however. The morphology of the Pt electrode after removal the $PbZr_xTi_{1-x}O_3$ by wet-etching is shown in Figure 2(b). It should be noted that during the process of OMCVD the Pt electrode is annealed. A slightly rough surface is observed without any etch residues from the ferroelectric film. In comparison with the morphology of the Pt electrode before deposition of the $PbZr_xTi_{1-x}O_3$ a small increase in surface roughness was observed.

On the same electrode but this time provided with a 100 nm RuO_2 film the morphology of the $PbZr_xTi_{1-x}O_3$ film is markedly different. In this case no individual crystallites are observed. The ferroelectric film has a characteristic periodic structure, see Figure 3(a). After etching of the $PbZr_xTi_{1-x}O_3$ thin film the RuO_2 electrode shows a rather flat surface morphology (Figure 3(b)) with even less structure than the electrode with Pt only, Figure 2(b). It seems that the RuO_2 film reduces the roughness of the platinum electrode. This absence of surface structure has an influence on the morphology of the $PbZr_xTi_{1-x}O_3$ and may be the cause for the observed structure. On RuO_2 films that deliberately were deposited with some surface roughness by increasing the deposition temperature, the structure in the ferroelectric film was less than observed on the smoother RuO_2 electrodes, see Figure 3(a). $PbZr_xTi_{1-x}O_3$ thin films with a comparable structure to that of Figure 3(a) were observed for films deposited onto platinum electrodes using a modified sol-gel process [3]. Deposition of $PbZr_xTi_{1-x}O_3$ on smooth as deposited Pt electrodes yields films with a relatively rough and inhomogeneous structure. Annealing the Pt electrodes resulted in the formation of hillocks which served as nucleation centres for the $PbZr_xTi_{1-x}O_3$ growth. Deposition of $PbZr_xTi_{1-x}O_3$ onto these substrates yielded homogeneous films with a smooth surface morphology.

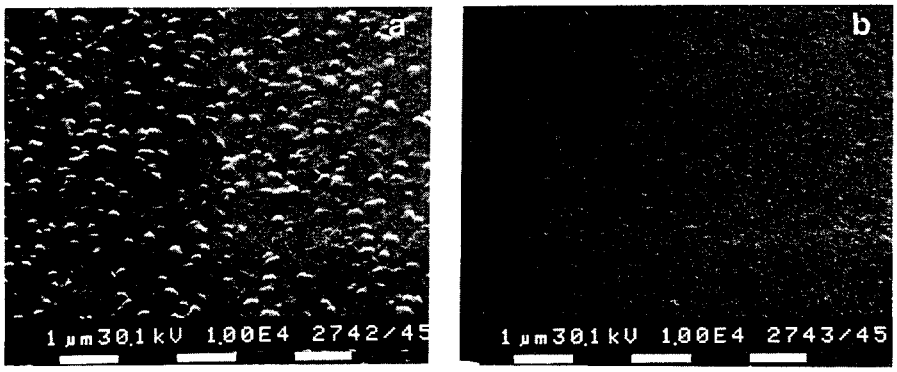


Figure 2. SEM of a typical surface morphology of a polycrystalline $PbZr_xTi_{1-x}O_3$ film on a Pt electrode (a); and morphology of the Pt electrode after removal of the $PbZr_xTi_{1-x}O_3$.

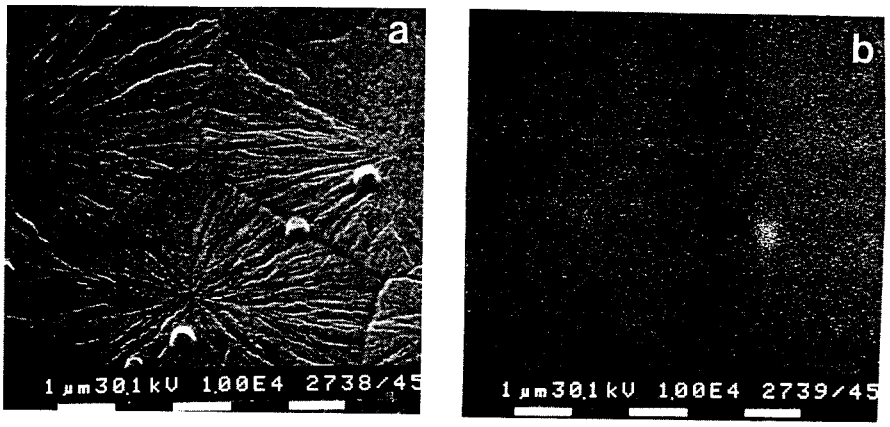


Figure 3. SEM of a typical surface morphology of a polycrystalline $PbZr_xTi_{1-x}O_3$ film on a Pt / RuO_2 electrode (a); and morphology of the Pt/RuO_2 electrode after removal of the $PbZr_xTi_{1-x}O_3$.

The XRD pattern of the $PbZr_xTi_{1-x}O_3$ thin film from Figure 2 is presented in Figure 4. As expected for x=0.30, the diffraction pattern can be indexed by a tetragonal structure, although the splitting of the (00*l*) and (*h*00) lines is less than for large grained powders. A third reflection located between the (00*l*) and (*h*00) reflections indicates that some spread in x is present in the film. The cause of this effect is not clear yet. Clearly the $PbZr_xTi_{1-x}O_3$ has a (111) preferential orientation. This is due to the fact that $PbZr_xTi_{1-x}O_3$ of this composition only has a small mismatch with Pt. Since the latter electrode crystallizes mainly in the (111) orientation, see the largest peak in this pattern around $2\theta = 40°$, this orientation is also favored in the ferroelectric thin film.

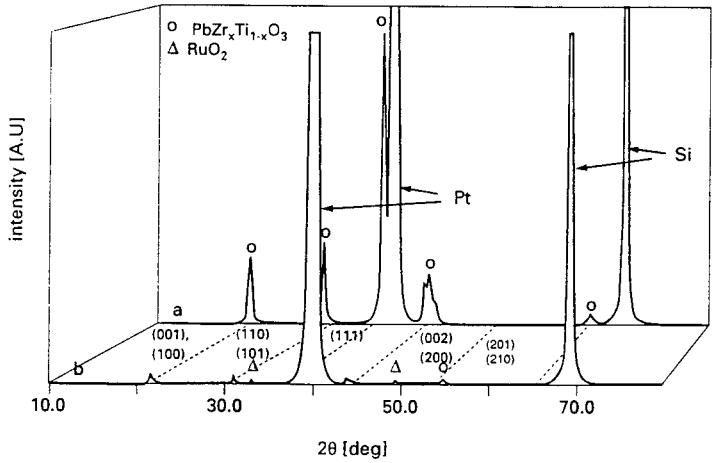


Figure 4. XRD patterns of $PbZr_xTi_{1-x}O_3$ films on Pt (a) and RuO_2 (b) electrodes.

For comparison, the XRD pattern of a $PbZr_xTi_{1-x}O_3$ film deposited using the same conditions on a RuO_2 coated Pt-electrode is included in Figure 4. Obviously the diffraction intensities of the latter are much lower than for the film deposited onto the Pt. This seems to indicate that the film on the RuO_2 is crystallized to a lesser extent than the $PbZr_xTi_{1-x}O_3$ on the Pt electrode. The difference in diffraction intensity may be due to the presence of amorphous $PbZr_xTi_{1-x}O_3$ or to a preferential orientation of the $PbZr_xTi_{1-x}O_3$ on the Pt electrode compared to the film on the RuO_2. A second difference between the two patterns is the absence of the strong (111) reflection of the $PbZr_xTi_{1-x}O_3$. This is attributed to the fact that the (111)Pt now is covered with a randomly oriented RuO_2 film. Also the mismatch between the $PbZr_xTi_{1-x}O_3$ and the RuO_2 lattices is larger.

Ferroelectric capacitors were made by rf-sputter deposition of a blanket platinum film onto the $PbZr_xTi_{1-x}O_3$. The stacks then were structured into ferroelectric capacitors by reactive ion etching. Hysteresis loops were measured using conventional Saywer-Tower circuitry operated at 1 kHz on capacitors of 10^4 μm^2.

Hysteresis loops at several field-strengths for the capacitors with the Pt and the RuO_2 bottom electrodes are presented in Figure 5. In the case of the platinum bottom-electrode a square shaped loop is observed with values for the remanent polarization and coercive-field strength of 36 $\mu C/cm^2$ and 100 kV/cm respectively. The loops saturate at a field strength of about 200 kV/cm (i.e. 4 V). In the case of the RuO_2 bottom electrode comparable hysteresis loop are obtained. Both the values for the remanent polarization and coercive field-strength are somewhat lower, 33 $\mu C/cm^2$ and 85 kV/cm, respectively. It is interesting to note the asymmetry of the hysteresis loop. With the RuO_2 bottom electrode on the positive side of the electric-field scale the values for E_c increase when the measuring field-strength increases. On the negative side of the electric-field scale this effect is not observed and the value for E_c saturates when the measuring field is increased. This behavior is attributed to the asymmetry between the two electrodes (Pt and RuO_2).The values for the remanent polarization are for both capacitors about the same.

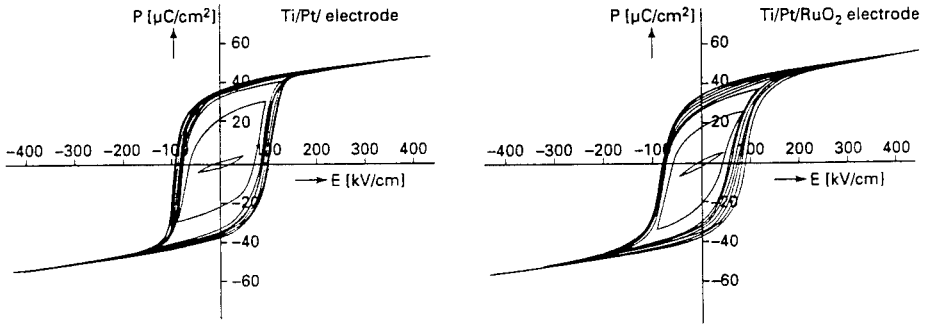


Figure 5. Hysteresis loops of $PbZr_xTi_{1-x}O_3$ films on Pt (a) and RuO_2 (b) electrodes. In both cases a Pt top electrode was used.

The rather high values measured for the coercive field-strength, both for the Pt as well as for the RuO_2 bottom electrodes, as compared to values for bulk ceramic material, may have several causes. An important observation is that, for metallic electrodes, the apparent E_c decreases with increasing film thickness. This observation may point at an imperfect crystal structure for very thin films [4], intrinsic stress [5] or an interface effect between the electrode and the $PbZr_xTi_{1-x}O_3$ film [6]. The latter two effects may be influenced by the use of RuO_2 electrodes since its chemical and structural nature is different from that of Pt.

The use of RuO_2 top electrodes is interesting but since such electrodes are difficult to synthesize using OMCVD they are not included in the present work [7].

3.2. NON-VOLATILE MEMORIES

For memory applications ferroelectric films should meet a number of device oriented requirements. These include demands on the deposition technique such as the capability of depositing uniform films over large areas with a good step coverage as well as demands on the capacitor properties. It will be shown that OMCVD can produce films that meet the specified needs. In this section only Pt electrodes are considered.

The uniformity of $PbZr_xTi_{1-x}O_3$ films over 100 and 150 mm wafers is presented in Figure 6. It demonstrates that both variations in Pb/(Zr+Ti) as well as Zr/(Zr+Ti) are below 5%. It should be noted that the deposition conditions yielding optimal uniformity over 100 mm wafers are different from those which give the optimal result over the 150 mm wafers.

The deposition of $PbZr_xTi_{1-x}O_3$ over a structured platinized silicon wafer is shown in Figure 7. It appears that OMCVD is capable of depositing layers conformally over such structures. Only in the trenches the film thickness is somewhat smaller but this is mainly due to a reduced thickness of the sputtered Pt electrode.

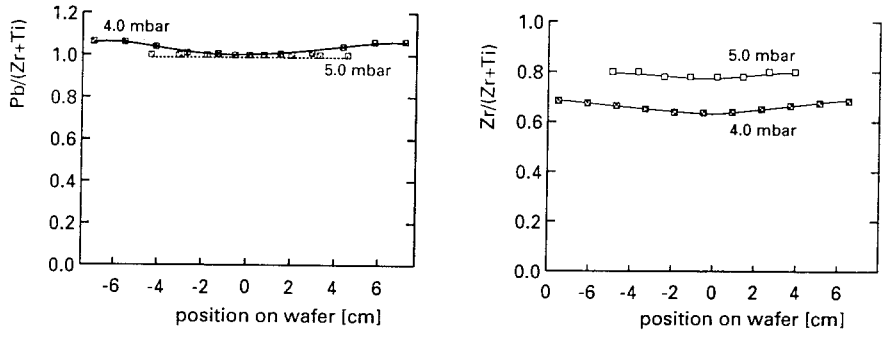


Figure 6. Uniformity of the composition of $PbZr_xTi_{1-x}O_3$ films over 100 and 150 mm Pt coated substrates.

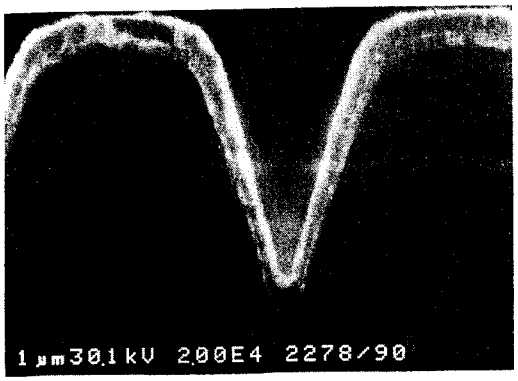


Figure 7. Deposition of $PbZr_xTi_{1-x}O_3$ over a structured Pt coated substrate.

At present, for high density memories the operating voltage is nominally 3.3 V. However the voltage available for switching of the ferroelectric capacitor will be about 2 V. This requires thin films with a small coercive field-strength. Using OMCVD, films were produced that could be switched using pulses of 1.5 V amplitude [8]. In principle an even lower switching voltage may be obtained by reducing the thickness of the ferroelectric film and improving the interface properties. The latter can for example be achieved by making use of the mentioned RuO_2 electrodes (notice the lower value for E_c in the previous paragraph).

Further requirements to the ferroelectric capacitors include a virtually unlimited number of read- and write cycles, a data retention of at least 10 years and a switching time in the range 10-100 ns.

The endurance is a point of major importance for non-volatile memory applications. It is determined by the degradation of ferroelectric properties caused by polarisation reversals. This degradation, or fatigue, is a property of the complete capacitor structure, i.e. it is determined by the ferroelectric thin film properties, the electrodes and test conditions. In Figure 8 the influence of switching voltage on the endurance is presented. It was demonstrated that for films deposited using OMCVD and switched with a voltage of 1.5 V, the difference in switched charge between a switching and a non-switching pulse still was sufficiently large after 10^{11} switching cycles [2]. Clearly, the use of a lower switching voltage leads to a better endurance. This effect has been observed before [8].

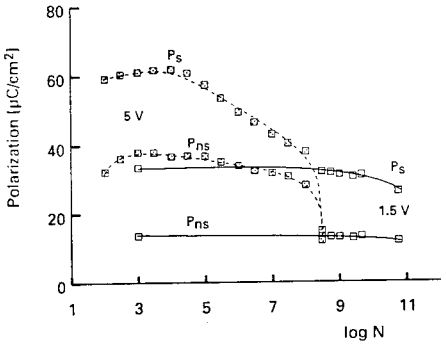


Figure 8. Endurance at different switching voltages. The drawn curves are a guide to the eye.

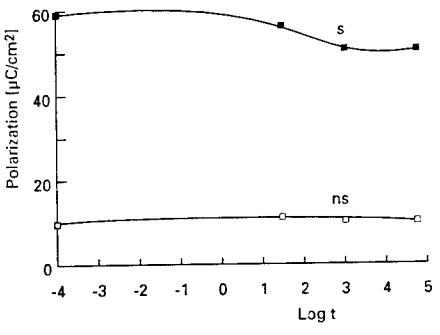


Figure 9. Retention of a capacitor with Pt electrodes. The drawn curves are a guide to the eye.

Obviously, the quality of the $Pt/PbZr_xTi_{1-x}O_3/Pt$ capacitors with OMCVD ferroelectrics, approaches the regime where application of such films in ferroelectric random access memories is possible. If the Pt electrodes are replaced by RuO_2 films this endurance behavior may even improve [1].

The retention of the ferroelectric capacitor is its capability of maintaining the polarization with time. In some cases a considerable retention-loss of a ferroelectric capacitor is observed. This effect, caused by a partial back-switching of ferroelectric domains, is undesirable for memory operation. The result of such an experiment on a ferroelectric capacitor with a large difference between the switching and non-switching response is presented in Figure 9. The delay time between the write- and read pulse was varied between 10^{-4} and 6 x 10^4 s. No large retention-loss is observed here. The ratio between the switched- and non-switched pulses is about 6 and is almost constant over more than eight decades of delay times.

In Figure 10 the switching and non-switching response of a ferroelectric capacitor is presented. The switching time is only a few nanoseconds for this 2000 μm^2 capacitor and is determined by the measurement set-up. The switching time is inversely proportional to the capacitor area. Switching times below 1 ns have been reported [9].

The successful integration of $PbZr_xTi_{1-x}O_3$ films grown by OMCVD with CMOS technology was reported by Dormans *et al.* [10]. Both the CMOS part as well as the ferroelectric capacitors were only slightly affected by the processing. The proper functioning of ferroelectric memory cells was demonstrated. In Figure 11 the hysteresis loops measured at 1 kHz with amplitudes of 3, 5 and 8 V for a fully integrated capacitor with a 300 nm $PbZr_{0.5}Ti_{0.5}O_3$ film is shown.

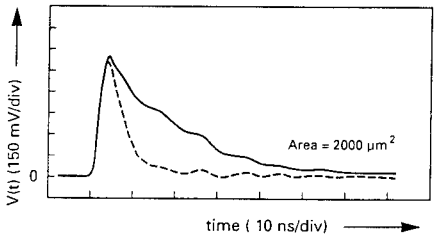


Figure 10. Switching behavior of a capacitor with Pt electrodes.

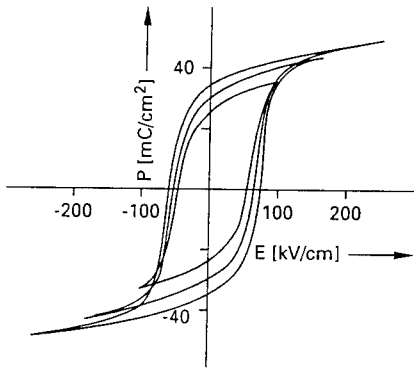


Figure 11. Hysteresis loops for a ferroelectric capacitor with Pt electrodes.

The memory cells could be operated at only 3 V with 20 ns pulse widths and the endurance using platinum electrodes exceeded 10^{13} read-write cycles using supply voltages of 4-6 V.

4. Summary

It was shown that the microstructure of $PbZr_xTi_{1-x}O_3$ deposited onto Pt electrodes is different from that deposited onto RuO_2/Pt electrodes. A marked difference between the Pt and RuO_2 electrode is that the surface of the latter is much smooth and therefore only a limited number of nucleation centres will be available. This may result in an enhanced surface mobility leading to the observed patterns in the $PbZr_xTi_{1-x}O_3$ film. On the relatively rough Pt surface the number of nucleation sites is much higher. The adsorbed species are trapped more rapidly and a film consisting of many individual crystallites will be formed. Also on the (111) oriented Pt electrode a distinct seeding effect is observed which translates into a strong (111) preferential orientation of the $PbZr_xTi_{1-x}O_3$.

XRD data show that also the crystallinity of the films on the RuO_2 electrodes is much less that for the films deposited onto Pt electrodes. It is not clear what the cause of this effect is.

Despite these large differences in microstructure the hysteresis loops of the capacitors are comparable. It cannot be excluded however that the observed differences in structure have a significant influence on properties of the capacitors e.g. the fatigue and retention behavior.

Uniform deposition of $PbZr_xTi_{1-x}O_3$ can be obtained over 100 and 150 mm substrates. It has been shown that with OMCVD ferroelectric capacitors can be made, using Pt electrodes, that meet the requirements for their application in high density memories. For the integration of $PbZr_xTi_{1-x}O_3$ with CMOS Pt electrodes are most widely used. Endurance data as well as retention measurements of $PbZr_xTi_{1-x}O_3$ on Pt electrodes indicate that these films are of sufficiently high quality for application in thin film devices such as ferroelectric memories. Ferroelectric capacitors with Pt electrodes and with $PbZr_xTi_{1-x}O_3$ films grown by OMCVD were successfully integrated with CMOS devices without serious degradation of the CMOS part nor of the ferroelectric capacitors.

5. Acknowledgements

The authors would like to thank W.A. Groen, R.B.F. Janssen, P.K. Larsen and G.A.C.M. Spierings for their assistance. Part of this work has been carried out under the FELMAS project. This support from the European Commission is gratefully acknowledged.

6. References

1. Peng, C.H. and Desu, S.B. (1992), *Appl. Phys. Lett.* **61,** 16.
2. De Keijser, M., Dormans, G.J.M., and Van Veldhoven, P.J. (1993), *Mat. Res. Soc. Symp. Proc.* **310,** 223.
3. Spierings, G.A.C.M., Van Zon, J.B.A., Larsen, P.K., and Klee, M. (1993), *Integrated Ferroelectrics* **3,** 283.

4. Funakubo, H., Hioki, T., Otsu, M., Shinozaki, K., and Mizutani, N. (1993), *Jpn. J. Appl. Phys.* **32,** 4175.
5. Sakashita, Y., Segawa, H., Tominaga, K., and Okada, M. (1993), *J. Appl. Phys.* **73,** 7857.
6. Larsen, P.K., Taylor D.J., Dormans, G.J.M., and Van Veldhoven, P.J. (1994), *J. Appl. Phys.* In press.
7. De Keijser, M., Dormans, G.J.M., and Van Veldhoven, P.J. (1993), *paper presented at the 5th International Symposium on Integrated Ferroelectric*, Colorado Springs.
8. Larsen, P.K., Cuppens, R., and Spierings, G.A.C.M. (1992), *Ferroelectrics* **128,** 265.
9. Larsen, P.K., Kampschöer, G.L.M., Ulenaers, M.J.E., Spierings, G.A.C.M., and Cuppens, R (1991), *Appl. Phys. Lett.* **59,** 611.
10. Dormans, G.J.M., Larsen, P.K., Spierings, G.A.C.M., Dikken, J., Ulenaers, M.J.E., Cuppens, R., Taylor, D.J., and Verhaar, R.D.J. (1994), *paper presented at the 6th International Symposium on Integrated Ferroelectrics*, Monterey.

ALKOXIDE PRECURSORS FOR FERROELECTRIC THIN FILMS

M.I. YANOVSKAYA,[1] N.YA. TUROVA[2]
AND L.I. SOLOV`YOVA[3]
1. Karpov Institute of Physical Chemistry,
Obukha st. 10, Moscow, 103064, Russia
2. Moscow State University, Chemical Department,
Vorobjovy Hills, 119899 Moscow, Russia
3. NIPIM
Lenina Prosp. 106-A, Tula, 300600, Russia

ABSTRACT. Preparation of alkoxides, their physico-chemical properties and structures are discussed. Formation of complex oxoalkoxides as true precursors of oxides is proved by the data of direct X-ray structural analysis and solubility diagrams in the three-component systems. The influence of hydrolysis conditions on crystallization of oxides and morphology is studied. Examples of application of alkoxides for preparation of barium titanate, magnesium titanate, bismuth oxide, PZT-powders and thin films are given.

1. Introduction

Synthesis of oxides from solutions has been intensively studied recently as a promising route to oxides (so called sol-gel method). The alcoholic derivatives of metals - metal alkoxides - $M(OR)_n$ are the most commonly used precursors in sol-gel chemistry. This is due to the fact that metal alkoxides have a series of important advantages in comparison with the derivatives of other chemical classes. Firstly, metal alkoxides can be purified by distillation or sublimation to very high extents due to their volatility; their solubility in organic solvents allows recrystallization as another method of purification. In addition, metal alkoxides are hydrolyzed to form colloids containing no foreign anions, which explains unique stability of such sols. M-O-M bonds - the main structural units of oxides already exist in initial alkoxides. In the course of hydrolysis, linear, planar and three-dimensional networks of future oxide phases are formed; branching of the network is accompanied by formation of sols which are gradually transformed to gels. The pronounced tendency to form M-O-M bonds in all directions of decomposition of metal alkoxides (hydrolysis, thermolysis, low temperature decomposition with elimination of ethers) is the peculiarity of the derivatives of this class, which determines their special place as precursors of oxides in modern technologies. Application of metal alkoxides is especially fruitful in synthesis of complex oxides: synthesis of bi- and polymetallic alkoxides ensures homogeneity of the alkoxy-derived complex oxides at the atomic level.

Synthesis of ferroelectric oxide materials from metal alkoxides comprises the following stages:

O. Auciello and R. Waser (eds.), Science and Technology of Electroceramic Thin Films, 85-97.
© 1995 *Kluwer Academic Publishers. Printed in the Netherlands.*

1) synthesis of alkoxides;
2) preparation of the initial solutions;
3) hydrolysis of solutions in organic solvents;
4) thermal treatment of the hydrolysis products for evaporation of solvents and crystallization.

In the present report we shall try to summarize the approaches we use for these four main stages of synthesis of ferroelectric materials from metal alkoxides.

2. Synthesis of Alkoxides

Development of preparation of oxide materials from alkoxides requires inexpensive and simple enough routes for synthesis of alkoxides themselves. The following metal alkoxides are important for preparation of ferroelectrics: alkaline, alkaline-earth, magnesium, lead, rare-earth, titanium, zirconium, niobium, tantalum, molybdenum, and tungsten. However, ferroelectric materials usually contain different elements as dopants, thus, practically all metal alkoxides are used for preparation of ferroelectric materials.

Having revised the numerous (but sometimes unreliable) literature data on synthesis of metal alkoxides, we have in many cases optimized the old techniques and suggested the new method for their synthesis. There are two main techniques suitable for laboratory as well as commercial applications.

The most commonly used commercial route for synthesis of alkoxides is the exchange reaction [1]:

$$MCl_n + nNaOR \longrightarrow M(OR)_n + nNaCl\downarrow$$

M = In, Y, La, Ti, Ge, Bi, V^{IV}, VO^{2+}+, VO^{3+}, Nb^{V}, NbO^{3+}, W^{VI}, $[M'0]^{4+}$ and $[M'O_2]^{2+}$ (M' = Mo, W), Fe^{3+}

We modified the technique considerably [2-5]. The alkoxides were obtained with almost quantitative yields (in contrast to 20-30 % yields reported earlier), which was achieved due to elimination of the parallel process of interaction of strong Lewis acids MCl_n with alcohols. For this purpose, the chlorides were introduced into the alcoholic solutions of NaOR with cooling and vigorous stirring in hydrocarbon or ether either in the form of solutions or as suspensions. Destruction of the intermediate alkoxochlorides was achieved by prolonged refluxing or complete elimination of the solvent.

The other method widely used by us comprises anodic oxidation of metals in the alcoholic media in the presence of electroconductive additives such as R_4NBr, LiCl, etc. It was successfully used for preparation of both soluble $M(OR)_n$ (M = Sc, Y, La and Ln, Ti, Zr, Hf, Nb^{V}, Ta^{V}; R = Et, i- Pr, n-Bu, $MeOC_2H_4$), $M(OC_2H_4OMe)_n$ (where M = Fe^{III}, Co, Ni), $MO(OR)_4$ (where M = Mo, W; R = Me, Et, i-Pr) [6,7] as well as insoluble alkoxides such as $Bi(OMe)_3$, $Cr(OR)_3$ (R = Me, Et, $MeOC_2H_4$), $V(OR)_3$, $Ni(OR)_2$ (R=Me, n-Bu, i-Pr), $M(OC_2H_2OMe)_2$ (M = Be, Cu) [4, 8, 9]. One of the most significant advantages of this route lies in application of pure metals (not the unstable and expensive anhydrous halogenides) as initial reagents; besides the reaction volumes are decreased considerably. It is very important for commercial applications that the method is highly efficient, gives no wastes (the only byproduct is gaseous hydrogen) and makes

AUCIELLO

possible the organization of continuous production. The electrochemical synthesis of metal alkoxides is now performed on a commercial scale in NIPIM (Tula, Russia).

For synthesis of solutions containing two or more alkoxides for ferroelectric applications it is very convenient to introduce alkaline or alkaline earth metals in the form of metals into the alcoholic solutions of $M(OR)_n$ (M = Ti, Zr, Nb, etc.; R = Et, i-Pr, Bu). It will be demonstrated below that the properties of thus prepared solutions differ greatly from the properties of solutions prepared by mixing of two alkoxides in alcohols.

The recent significant progress in sol-gel technology is associated with application of 2-alkoxyethoxides, the derivatives of ethylene glycol monoethers - HOC_2H_4OR (R = Me, Et). The methoxyethoxides of Na, Mg, Ca, Sr, Ba, Y, La, Ln, Sn, Zr, Hf, Bi, V(IV), Mo(VI), W(VI), Fe(III), Co, Ni, etc. are easily soluble in $MeOC_2H_4OH$, THF and hydrocarbons (while the corresponding alkoxides are often polymeric and poorly soluble); they are essentially more stable to hydrolysis and oxidation and form stable sols in excess of water [10].

Methoxyethanol proved the most convenient solvent for electrochemical synthesis [11]. It is interesting that in many cases current yields of metal dissolution are higher than 100%, which means that alongside with electrochemical dissolution chemical oxidation also occurs. Dissolution of metals in methoxyethanol may be successfully used for synthesis of solutions containing two or three elements. In many cases, conductivity of alkali and alkaline-earth methoxyethoxide solution is enough for anodic disolution of transition metals. In these cases, alkaline and alkaline-earth methoxyethoxides act as conductive additives in the processes of dissolution of transition metals, no other conductive additive is necessary. Complex oxides listed in Table 1 were obtained from such solutions.

TABLE 1. Anodic solution of transition metals with alkali and alkaline-earth methoxyethoxides as conductive additives.

Anode	Conductive additive	Complex oxide obtained from solution
Ti	$Ba(OC_2H_4OCH_3)_2$	$BaTiO_3$
Ti	$Mg(OC_2H_4OCH_3)_2$	$MgTiO_3$
Nb	$LiOC_2H_4OCH_3$	$LiNbO_3$
Mo	$NaOC_2H_4OCH_3$	Na_xMoO_3

Preparation of perovskites $BaM^{II}_{1/3}M^{V}_{2/3}$($M^{II}$ = Zn, Co, Ni; M^{V} = Nb, Ta) is another interesting example of application of the electrochemically synthesized solutions. In the case of M^{II} = Mg it is possible to dissolve Mg in solutions of niobium and tungsten alkoxides in methoxyethanol. The other metals M^{II} listed above cannot be dissolved in this way. However, the above mentioned metals readily undergo anodic dissolution in the presence of barium and niobium (or tantalum) alkoxides in methoxyethanol. Thus, prepared solutions were used for application of perovskite films and hydrolysis for preparation of powders.

3. Preparation of Initial Solutions for Synthesis of Ferroelectric Materials Solubility Diagrams in the Three-Component Systems

At first it seemed that the molecular distribution of the components in the initial solution ensures homogeneity of the future oxide phases. However, later it turned out that different hydrolysis rates of $M(OR)_n$ may be a certain obstacle. Even if bimetallic complexes are formed in solutions, homogeneity of future oxide phases on the atomic scale may be only achieved if the stoichiometry of alkoxy-complexes in solutions and in the future oxide phase comply. Below we shall discuss formation of some bimetallic complexes which are of special interest in the synthesis of important ferroelectric materials - titanates, zirconates, niobates and tantalates of alkaline and alkaline-earth elements.

In order to define the composition of the bimetallic alkoxides, which are formed in solutions or solid state - solubility diagrams in the three-component systems $M(OR)_n$ - $M'(OR)_m$ - L (L - ROH, ether, hydrocarbons, etc.) have been studied. These data allow us to optimize the conditions for preparation of the solutions both for synthesis of $MM'(OR)_n$ and for hydrolysis of alkoxides as well as to establish the composition of the complexes in solutions. More than 50 systems have been studied [12-14]:

$M(OR)_n$ - $Al(OR)_3$ - L; M =Li, Na, Mg, Ba; L = ROH, THF;
$M(OR)_n$ - $Ti(OR)_4$ - L; M = Mg, Ca, Ba, Al; L = ROH, THF, C_6H_6;
$M(OR)_3$ - $Zr(OR)_4$ - L; M = Ba. Y, Sc, La, Al; L = ROH, THF;
$M(OR)_n$ - $Nb(OR)_5$ - L; M = Li, Ba, Sc, La; L = ROH, THF;
$M(OR)_n$ - $Ta(OR)_5$ - ROH; M = Li, Ba;
$M(OR)_n$ - $Fe(OR)_3$ - L; M = Li, Na, Ba, Y; L = ROH;
$M(OEt)_n$ - $WO(OEt)_4$ - EtOH; M = Na, Bi;
$M(C_2H_4OMe)_n$ - $MoO_2(OC_2H_4OMe)_2$ - $MeOC_2H_4OH$, M = Na, Bi.

The compositions of the main bimetallic complexes found in the altkoxide solutions are presented in Table 2.

TABLE 2. Comparison of the composition of alkoxide - complexes and oxide phases

System	Main bimetallic alkoxide in solution	Isolated bimetallic oxoalkoxide	Oxide phase of interest
$Ba(OR)_2$-$Ti(OR)_4$-ROH R=Et, i-Pr, Bu	$BaTi_4(OR)_{18}$	$BaTiO(OPr\text{-}i)_4$	$BaTiO_3$
$Mg(OR)_2$-$Ti(OR)_4$-ROH R=Me,Et,Bu	no complexes	$MgTiO(OBu)_4$	$MgTiO_3$
$Ba(OPr\text{-}i)_2$-$Zr(OPr\text{-}i)_4$-i-PrOH	$BaZr_4(OPr\text{-}i)_{18}$	$BaZrO(OPr\text{-}i)_4$	$BaZrO_3$
LiOEt-$Nb(OEt)_5$-EtOH	$LiNb(OEt)_6$	$LiNbO(OEt)_4$	$LiNbO_3$
$Ba(OR)_2$-$Nb(OR)_5$-ROH R=Et, i-Pr	$BaNb_2(OR)_{12}$	$BaNbO(OEt)_5$	$BaNb_2O_6$
$Ba(OR)_2$-$Ta(OR)_5$-ROH R=Et, i-Pr	$BaTa_2(OR)_{12}$	$BaTaO(OEt)_5$	$BaTa_2O_6$

It is clear from these data that the compositions of the bimetallic alkoxides in solutions and complex oxides may comply (as in the cases of $LiNbO_3$, $BaNb_2O_6$, $BaTa_2O_6$) or not (as in the cases of $BaTiO_3$ or $MgTiO_3$). On the other hand, in many cases bimetallic oxoalkoxides are formed in these systems, which are true precursors of complex oxides. It is interesting that in contrast to the generally recognized opinion no bimetallic alkoxides with 1:1 ratio were found in the systems with alkaline-earth metals. On the other hand 1:1 ratio of cation seems to be especially characteristic of oxoalkoxides. The M-O-M' bonds in the structures of oxoalkoxides are presented in the course of formation of complex oxide via hydrolysis and future thermal treatment. Formation of oxoalkoxides increases drastically the solubility in the systems thus changing considerably the solubility diagrams (Fig. 1). It should be emphasized that a very small extent of decomposition of alkoxides to oxoalkoxides changes considerably the properties of solutions.

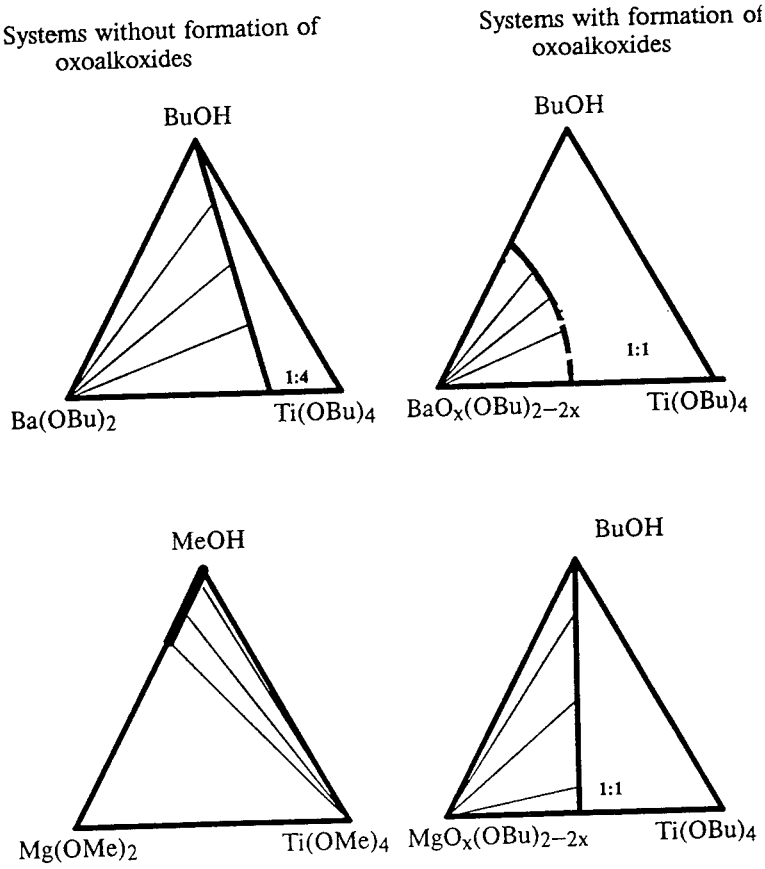


Figure 1. Solubility diagrams in the three-component systems

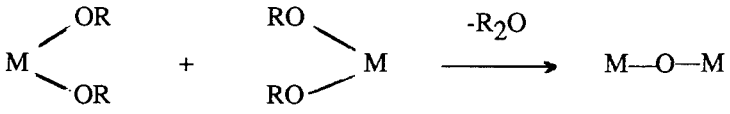
In many cases it is possible to distinguish between alkoxides and oxoalkoxides only after X-ray structural analysis of single crystals is performed. Practically all the

complexes mentioned in Table 2 were isolated and characterized by us by means of X-ray structural analysis of their single crystals (except for the liquid complexes; the structure of $LiNb(OEt)_6$ was solved by Payne and coworkers [15]). Chemical analysis in most cases is useless because oxoalkoxides are often solvated by alcohols. This is the reason why formation of oxoalkoxides in the alcoholic systems became the focus of studies only recently and practically no data concerning the origin of oxoalkoxides have been hitherto available.

3.1. THE ORIGIN OF OXO-GROUPS IN METAL ALKOXIDES

The first known oxoalkoxides - $Ti_7O_4(OEt)_{20}$, $Nb_8O_{10}(OEt)_{20}$ and $Zr_{13}O_8(OMe)_{36}$ [16] were isolated in the course of controlled hydrolysis of metal alkoxides. However, it turned out afterwards that the same products may be obtained in the course of the careful thermal decomposition of the latter, when prceautions for complete elimination of even traces of water were taken [17, 18].

These results suggest that the hydrolysis decomposition mechanism is rather complicated and includes for instance such stages as ether elimination:



This type of decomposition is especially characteristic of Mo and W derivatives. Their decomposition in the series:

$$M(OR)_6 \xrightarrow{-R_2O} MC(OR)_4 \xrightarrow{-R_2O} MO_2(OR)_2 \quad M = Mo, W$$

occurs rcadily. It is noteworthy that this process occurs in the organic solvcnt without any thermal treatmcnt under conditions of complete isolation from water:

$$NaOR + WO(OR)_4 \longrightarrow Na_2WO_4 + R_2O$$

$$NaOR + MoO2(OR)_2 \longrightarrow Na_2MoO_4 + R_2O$$

Another way which leads to formation of oxoalkoxides comprises oxidation of OR^- groups of ionic alkoxides by oxygen. It is interesting that these reactions have never been mentioned in the modern literature on sol-gel chemistry, although Le Berre [20] back in 1961 has shown that alkaline alkoxides react with oxygen to form peroxides. Decomposition of the latter is accompanied by carbon chain rupture. Studying simple and complex Ba and Sr alkoxides we have shown that the presence of oxo-groups in their molecules is due to oxidation by traces of O_2 (dissolved in alcohols or present as

admixtures in the gas phase). The first oxidation products contain -OOR or -OOH groups; in the decomposition of the latter by the radical mechanism water, oxo- and formate groups appear in the coordination sphere of the metal atom. The yellow color of the partially oxidized samples is due to free radicals with the unpaired electron delocalized in the system of the conjugated double bonds. The samples isolated from the colored solutions always contain fomate groups and the solvating alcohols [13]. This reaction is characteristic only for molecules with considerable polarization of M-OR bonds: alkaline, alkaline-earth, rare-earth derivatives (which dissociate in solutions in accordance with the scheme; $M(OR)_n \sim M^{n+} + nOR^-$, as far as it is OR^- ion which reacts with O_2). The tendency to oxidation is especially pronounced in the case of methoxyethoxides. According to Caulton [21] even the most careful elimination of moisture and oxygen does not allow to crystallize barium methoxyethoxide, instead oxoalkoxide $Ba_6(\mu\text{-}O)(OR)_{10}4ROH$ crystallizes. It is noteworthy that methoxides and tert-butoxides do not undergo oxidation at all.

Among more "acidic' alkoxides of the transition metal elements only derivatives of lower oxidation states react with O_2:

$$M(OR)_{n-1} \xrightarrow{O_2} MO_x(OR)_{n-2x}$$

Transformations of this type always occur at some extent in the process of electrochemical synthesis of alkoxides;

$$M + nROH \longrightarrow M(OR)_n \xrightarrow{+e} M(OR)_{n-1} \xrightarrow{O_2} MO_x(OR)_{n-2x}$$

Oxoalkoxides are usually readily eliminated from the alkoxides due to higher volatility of the latter. This way of formation of oxoalkoxides plays the most important role in reactions of alkaline-earth metals and magnesium with solutions of transition metal alkoxides, which is usually applied for introduction of these metals in solutions, e.g. in synthesis of perovskites:

$$Ti(OR)_4 \xrightarrow{[H]} Ti(III) \xrightarrow{O_2} TiO_x(OR)_{4-2x}$$

$$\uparrow$$

$$(M(Mg, Ba, Sr) + ROH)$$

Properties of such solutions differ considerably from the properties of solutions obtained by dissolving of two alkoxides.

As a conclusion for this section we would like to emphasize that practically all the known ways to decompose alkoxides proceed via formation of oxoalkoxides with M-O-M bonds - the basis for subsequent oxide formation.

3.2. THE ROLE OF OXOALKOXIDES IN PREPARATION OF $BaTiO_3$

One of the most interesting examples illustrating the role of oxoalkoxides in the synthesis of complex oxides is preparation of barium titanate from metal alkoxides. The rate of alkoxide decomposition with formation of bimetallic oxoalkoxides increases drastically with the lowering of the concentration of Ba-Ti - containing solutions and with introduction of the Ba component in the form of metal. However, it is refluxing of solutions which is the most important condition for the increase of the yield of oxoalkoxides in solution. It turns out that the phase purity of $BaTiO_3$ which is formed on thermal treatment of the residues after evaporation of alcohols under vacuum is determined by the extent of decomposition of bimetallic alkoxide to oxoalkoxide. Now the essence of the operation of refluxing of solutions before application for preparation of films or hydrolysis for powder preparation becomes clear: it leads to formation of oxoalkoxides in solutions.

While hydrolysis of metal alkoxides shows very little promise for production of barium titanate in the form of powders (application of large quantities of Ba-metal in technology is practically impossible) this method can be very useful for preparation of $BaTiO_3$ thin films. Our results for the studies of reaction in the alkoxide solutions suggest that preparation of film-forming solutions by two different methods:

(1) mixing of two alkoxides $Ba(OR)_2$ and $Ti(OR)_4$

(2) dissolution of Ba in solutions of $Ti(OR)_4$ in alcohols

results in different chemical compositions of solutions, which affect the phase composition of $BaTiO_3$ films. X-ray diffraction patterns of the films obtained by the first method exhibit peaks corresponding to Ba_2TiO_4 and polytitanates [22]. The second method leads to $BaTiO(OR)_4$ as the main reaction product, which ensures formation of pure $BaTiO_3$ phase in the films [23]. The films demonstrated high values of dielectric constants ε=380 ($\rho = 8.6 \times 10^{12}$ Ω.cm, E_B = 9.3 V/cm). A ferroelectric phase transition was registered only in the films annealed at temperatures higher than 900 °C.

3.3. THE ROLE OF OXOALKOXIDES IN PREPARATION OF $MgTiO_3$

In the case of synthesis of $MgTiO_3$ the solubility diagrams in the three- component systems $Mg(OR)_2$-$Ti(OR)_4$-ROH (R = Me, Et, n-Bu) demonstrated that formation of soluble oxoalkoxide with the Mg:Ti ratio of 1:1 occurs only in the butoxide system (Fig. 1). Thus, this is the only system suitable for preparation of $MgTiO_3$. The easiest way for preparation of solutions for hydrolysis is interaction of Mg with the butanolic solutions of titanium butoxide:

$$Mg + Ti(OBu)_4 + BuOH \longrightarrow MgTiO_x(OBu)_{6-2x} + H_2$$

which comprises the following reactions:

$$Mg + BuOH \longrightarrow Mg(OBu)_2 + H_2$$
$$Ti(OBu)_4 + [H] \longrightarrow Ti(OBu)_3 + BuOH$$
$$Ti(OBu)_3 + O_2 \text{ (dissolved in BuOH)} \longrightarrow TiO_x(OBu)_{4-2x}$$
$$TiO_x(OBu)_{4-2x} + Mg(OBu)_2 \longrightarrow MgTiOx(OBu)_{6-2x}$$

Reaction begins and procceds vigorously only if absolute BuOH with concentration of water ~ 0.05 % is used. In the course of magnesium dissolution, the reaction mixture turns dark green due to reduction of $Ti(OBu)_4$. The reaction mixture becomes colorless on absorption of oxygen during cooling. On the other hand, if prior to introduction of Mg into the reaction medium titanium butoxide is refluxed for about an hour with aqueous BuOH containing ~1% of water, oxobutoxide is formed, which is much more "acidic" than butoxide and thus reacts readily with Mg. The solutions are very stable and suitable for further applications. The reaction scheme is approximately the same for all reactions of Mg-metal with solutions of transition metal alkoxides used in preparation of solutions for the synthesis of perovskites.

4. The Influence of Hydrolysis Conditions on the Properties of Oxides

The hydrolysis conditions may affect the phase formation of oxides as well as the morphological characteristic of the powders. Thus, we have previously shown that crystallization of Bi_2MoO_6 and Bi_2O_3 - WO_3 solid solutions may occur in the course of hydrolysis of the alkoxide solutions at room temperature [24l.

The importance of introduction of Bi in the ferroelectric materials made us study hydrolysis of $Bi(OEt)_3$. It turned out that the crystallization temperature of a-Bi_2O_3 from the hydrolysis product is strongly dependent on the hydrolysis conditions. Thus, if $Bi(OEt)_3$ solution in benzene is hydrolyzed at slightly enhanced temperature and the hydrolysis product is dried in air, crystallization occurs only at 450 °C. On the other hand, if hydrolysis is performed at 100 °C in excess of water, the product dried at 100°C is highly crystalline a-Bi_2O_3 and therefore needs no further thermal treatment. Ether Et_2O was found alongside with EtOH in hydrolysis products of $Bi(OEt)_3$, which means that water enhances the low-temperature decomposition of alkoxides to crystalline oxides with elimination of ethers. This fact may explain the data of Hirano [25], who suggested to perform all operations of thermal treatment of the sol-gel films under the water vapor flow.

Another example concerns formation of different phases of complex oxides under different conditions of hydrolysis of the alkoxide solutions. Preparation of $MgTiO_3$ requires hydrolysis of the alcoholic solutions at room temperature. Increase of tlle hydrolysis temperature above 50 °C results in hydrolytic decomposition of the product by the excess of water, and the powder annealed at 800 °C demonstrates the peaks of $MgTi_2O_5$ alongside with $MgTiO_3$ in the X-ray patterns.

However, it is morphology of the powder particles which is most considerably affected by the hydrolysis conditions. Most techniques which are suggested for preparation of morphologically umiform powders comprise application of dilute solutions, they are very inefficient and time consuming. Working in close coopeation with technologists we tried to make our techniques suitable for further technological applications. By carefully choosing the hydrolysis conditions we prepared highly uniform powders of TiO_2, ZrO_2, ZrO_2-Y_2O_3, $BaTiO_3$[26]. Barium titanate powders with a narrow particle size distribution (mean particle size ~ 0.25 μm), sintered at 1280 °C into dense cerarnic capacitors with $e \approx 3500$ - 5000 (f = 1 kHz). They are also used for sintering of a group of capacitors with high temperature stability of dielcctric constant - X 7 R, $e \approx 3000$ (f = 1 kHz), and capacitors with low sintering temperature (1150 °C). In addition, this method was also

extended and used for preparation of solid solutions $BaTi_{0.9}Zr_{0.1}O_3$ with the dielectric constant in the temperature of phase transition 40000, as well as for preparation of doped $BaTiO_3$ (e.g. $BaTiO_3$ + 0.2 mol.% Y_2O_3) - powders for semiconducting $BaTiO_3$ ceramics. The specific conductivity of the ceramic samples was enhanced by this operation from 10^{-11} for the undoped to 10^{-3} $W^{-1} \cdot cm^{-1}$ for the doped ceramic samples.

5. Preparation of PZT Films from Alkoxide Solutions

Lead acetate trihydrate was used as the sourcce of lead in preparation of solutions for PZT films. Different techniques for dehydration of lead acetate were used.

(1) Lead acetate trihydrate melts at 80-90 °C. On evacuation of this melt, water is readily eliminated leaving dense residue. This method is very efficient and quick; however, the product is not quite homogeneous: as far as reaction is a heterogeneous process.

(2) Lead acetate trihydrate is dissolved in methoxyetanol. Water-methoxyethanol azeotrope is distilled off at 60-120 °C. In order to perform complete dehydration this operation is repeated several times; the residual water content in the reaction mixture is 0.3-0.6 mass %. Prolonged thermal treatment necessary in this route of dehydration leads to partial substitution of acetate by methoxyethoxide groups and formation of Pb-O-Pb bonds. These reactions are very hard to control, which leads to certain irreproducibility of the properties of solutions.

(3) Xylene is added to the solution of lead acetate in methoxyethanol. In this case, xylene-containing azeotropes are distilled off at a considerably lower temperature, thus diminishing the role of the above mentioned side reactions. On the other hand, the residual water content is about 1.0 mass %.

(4) Lead acetate trihydrate is dissolved in acetic anhydride which is introduced in the stoichiometric ratio in accordance with the following reaction:

$$Pb(CH_3COO)_2 \cdot 3H_2O + 3C_4H_6O_3 \longrightarrow Pb(CH_3COO)_2 + 6CH_3COOH$$

Acetic acid is distilled off under vacuum (P = 2-3 mm Hg, t = 3045 °C). The residue is dissolved in methoxyethanol, concentration of water in such solutions is in the level of 0.1-0.2 mass %. The absence of side reactions makes these solutions highly reproducible and absolutely stable.

Titatinium and zirconium were introduced in solutions by electrochemical dissolution of metals in methoxyethanol. Such solutions were very stable and easy to handle. No changes in physico-chemical characteristics were registered in solutiions stored for more than a year. A typical hysteresis loop for the film is presented in the Fig. 2.

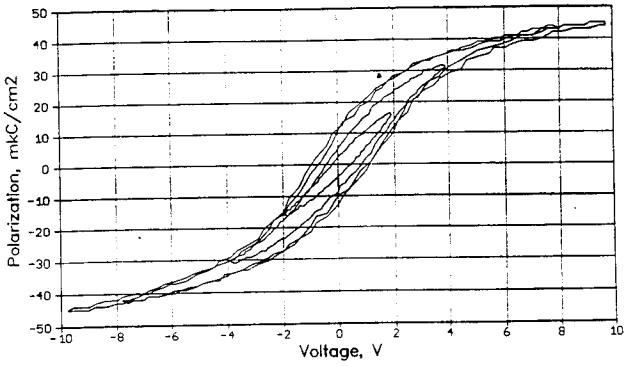


Figure 2. Typical dielectric hysteresis for the film $Pb_{1.1}Zr_{0.53}Ti_{0.47}O_3$(0.22 μm). This films were integrated into the test chips with the following characteristics:

TABLE 3. Typical characteristics of the PZT films (electrochemically synthesized solutions were used for films preparation)

Chemical composition	$Pb_{1.1}Zr_{0.52}Ti_{0.48}O_3$
Phase	Perovskite
Thickness	0. 18-0.25 μm
Structure	Si-SiO_2-Ti-Pt-PZT-Pt
Remanent polarization	10-20 μC]cm^2
Coercive voltage	0.5-1.5 V
Operating voltage	5-8 V
Breakdown voltage	> 20 V
Polarization switching time	< 10 ns
Number of switching cycles	> 10^8

6. Conclusions

Preparation of complex oxides from metal alkoxides requires comprehensive understanding of all chemical reactions which comprise the route for their preparation - from synthesis of alkoxides via preparation of the alcoholic solution and hydrolysis to the influence of chemistry on the properties of oxide materials.

7. Acknowledgment

The research described in this publication was made in part by grant N mpr 000 from the International Science Foundation

8. References

1. Feld, R and Cowe, P.L. (1965), *The Organic Chemistry of Titanium*, Butterworths, London.
2. Kozlova, N.I., Turova, N.Ya., Turevskaya, E.P. (1982), *Sov. J. Coord. Chem.* **8**, 339.
3. Turova, N.Ya. and Rogova, T.V. (1987), *Synthesis of Metal Alkoxides*, USSR *Patent # 1310381*; *Chem. Abstr.* **107**, 153.
4. Kucheiko, S.I., Kesslcr, V.G. and Turova, N.Ya. (1987), *Sov. J. Coord. Chem.* **13**, 586.
5. Turova, N.Ya and Rogova, T.V. (1983), *Sov. J. Coord. Chem.* **9**, 685.
6. Shreider, V.A., Turevskaya, E.P., Kozlova, N.I. and Turova, N.Ya. (1981), *Inorg. Chem. Acta* **53**, L73.
7. Kucheiko, S.I., Turova, N.Ya. and Shreider, V.A. (1985), *Zh. Obsch. Khim.* (Russia) **55**, 2412.
8. Rogova, T.V. and Turova, N.Ya. (1985, *Sov. J. Coord. Chem.* **11**, 448.
9. Turevskaya, E.P., Kozlova, N.L, Yanovskaya, M.I. and Turova, N.Ya. (1989), *Sverkfprovodimost (Russia)* **2**, 30.
10. Turova, N.Ya., Turevskaya, E.P., Kesslcr, V.G., Kozlova, N.A. (1992), *Russ.. Inorg. Chem.* **37**, 50.
11. Yanovskaya, M.I., Solov'yova, L.L, Kovsman, E.P., Obvintseva, I.E., Vorotilov, K.A. and Turova, N.Ya. (1994), *Integrated Ferroelectric*, (in press).
12. Novosyolova, A.V., Turova, N.Ya., Turevskaya, E.P. and Yanovskaya, M.L (1979), *Inorg. Materials (Russia)* **15,** 1055.
13. Turevskaya, E.P., Yanovskaya, M.L, Limar, V.K. and Turova, N.Ya. (1993), *Russ. J. Inorg. Chem.* **38**, 563.
14. Turevskaya, E.P., Turova, N.Ya., Kessler, V.G., Yanovsky, A.I. and Struchkov, Yu.T. (1993), *Russ. J. Inorg. Chem.* **38**, 875.
15. Eichorst, D., Payne, D.A., Wilson, S.R., Howard, E. (1990), *Inorg. Chem.* **29**, 1458.
16. Bradley, D.C., Mehrotra, R.C. and Gaur, D.P. (1978), *Metal Alkoxides*, Academic Press, London-New-York.
17. Shmid, R., Mosset, A. and Galy, J. (1991), *J. Chem. Soc. Dalton Trans.*, 1999.
18. Kesser, V.G., Turova, N.Ya., Yanovsky, A.I. and Struchkov, Yu.T. (1991), *Russ. J. Inorg. Chem.* **36**, 949.
19. Kozlova, N.L, Kessler, V.G. and Turova, N.Ya. (1989), *Sov. J. Coord. Chem.* **15**, 867.
20. Le Berre, A. (1961), *Bull. Soc. Chim. France*, pp. 1198.
21. Caulton, K.G., Chisholm, M.N., Drake, S.R. and Huffman, J.C. (1990), *Chem. Soc. Chem. Commun.*, pp. 1498.
22. Yanovskaya, M.I., Turevskaya, E.P., Turova, N.Ya. and Novosyolova, A.V. (1981), *Inorg. Materials* (Russia) **17**, 307.
23. Vorotilov, K.A., Orlova, E.V., Petrovsky, V.I., Yanovskaya, M.I., Turevskaya, E.P. and Turova, N.Ya. (1991), *Ferroelectrics* **123**, 261.
24. Yanovskaya, M.I., Turevskaya, E.P., Kessler, V.G., Obvintseva, I.R and Turova, N.Ya. (1992), *Ferroelectrcs* **1**, 343.
25. Hirano, S. (1993), *7th International Workshop on Glasses and Ceramics from Gels*, Abstracts D5.

26. Yanovskaya, M.I., Kotova, N.M., Golubko, L.A., and Kovsman, E.P. (1994), *J. Sol-Gel Science and Technology* **2**, 569.

DEPOSITION OF UNDOPED AND DOPED Pb (Mg,Nb)O_3 - $PbTiO_3$, $PbZr_xTi_{1-x}O_3$, ALKALINE EARTH TITANATE AND LAYERED PEROVSKITE THIN FILMS ON Pt AND CONDUCTIVE OXIDE ELECTRODES BY SPIN-ON PROCESSING: CORRELATION OF GROWTH AND ELECTRICAL PROPERTIES

M. KLEE, U. MACKENS, J. PANKERT, W. BRAND, AND W. KLEE*
Philips GmbH Forschungslaboratorien, Aachen,
Weibhausstr. 2, *52066 Aachen, Germany*
* *Fachhochschule Niederrhein, Adlersstr. 32, 47798 Krefeld, Germany*

ABSTRACT. Spin-on processes for lead based perovskite thin films, alkaline earth titanate thin films and thin films with layered perovskite structure are discussed. The growth of these systems on Ti/Pt and on conducting oxide electrodes, which have been produced by spin-on processing is reported. The ferroelectric and dielectric properties of the thin films dependent on thin film composition are presented.

1. Application of Perovskite Films

The unique properties of perovskite-based thin films, ferroelectricity, pyroelectricity and piezoelectricity together with small volume, large geometrical flexibility and integration into semiconductor processes are the basis for new microelectronic devices. The ferroelectric properties of $PbZr_xTi_{1-x}O_3$, $Bi_4Ti_3O_{12}$ and $BaMgF_4$ are used in ferroelectric non-volatile random access memories [1,2,3]. Piezoelectric $PbZr_xTi_{1-x}O_3$ films in combination with silicon micromachining are developed for thin film pressure sensors, microactuators and ultrasonic micromotors [4,5]. Undoped as well as La doped $PbTiO_3$ and $PbZr_{0.4}Ti_{0.6}O_3$ films deposited on Si and MgO single crystal substrates by spin-on processing are studied in combination wilh micromachining technologies for substrate etching to produce pyroelectric infrared sensor arrays [6,7]. Another important thin film material for pyroelectric detectors is the $PbSc_{0.5}Ta_{0.5}O_3$, which, however, due to the high reaction temperature of 900 °C can only be deposited on sapphire substrates without bottom electrode [8]. Additionally, $PbZr_xTi_{1-x}O_3$ and $Ba_xSr_{1-x}TiO_3$ thin films have received much attention as storage capacitor dielectric for ultra-high density dynamic random access memories, because of their high charge storage capacity, low leakage currents and high breakdown strength [9,10]. The electro-optic properties, especially of lanthanum doped $PbZr_xTi_{1-x}O_3$ films are studied by several groups for optical modulators and waveguides [11,12].

O. Auciello and R. Waser (eds.), Science and Technology of Electroceramic Thin Films, 99-115.
© 1995 *Kluwer Academic Publishers. Printed in the Netherlands.*

2. Electrode Materials For Perovskite Thin Films

Most perovskite thin films are deposited on Si-substrates with a thin Pt layer, which is either sputter deposited or evaporated on top of a thin Ti layer. The Ti layer serves as an adhesion layer for the Pt electrode. Several studies on the deposition of Pt electrodes by sputtering [13,14,15] have shown that the Pt growth and especially the hillock formation of the Pt films during annealing determines the growth and electrical properties of the perovskite films. All research studies world wide have, however, shown that even with optimized Pt bottom as well as top electrodes and optimized $PbZr_{0.53}Ti_{0.47}O_3$ thin films, the ferroelectric layers show a fatigue, if the polarization is switched in an electrical field. Several authors report on a decrease of the switched polarization by more than 50% after 10^4-10^8 polarization cycles. The origin of the fatigue of the ferroelectric cells is not yet clear. It has been proposed that a thin blocking layer with a low relative permittivity formed at the interface of the Pt electrode and the PZT film causes the fatigue in the ferroelectric cells [16, 17]. To improve the endurance of the devices, oxide electrodes such as RuO_x, In_2O_3-SnO, $SrRuO_3$, $La_xSr_{1-x}CoO_3$, and $YBa_2Cu_3O_{7-x}$ [15,18,19,20] are studied. With reactively sputtered RuO_x bottom electrodes, a strong improvement of the endurance has been found for PZT cells [18], however, higher leakage currents are reported [21]. A diffusion of RuO_x along the grain boundaries of PZT thin films is discussed with the formation of a conducting lead ruthenate phase [22]. TEM studies of the electrode PZT interface for PZT films deposited on sputtered RuO_x electrodes have been carried out by Bursil et al [23]. These data, however, give no indications for interdiffusion of RuO_x into PZT. Although conductive oxide electrodes are an important step forward to improve the fatigue of thin ferroelectric PZT cells. there are only a few reports on conductive oxide thin films produced by spin-on techniques.

2.1. SOL-GEL PROCESSING OF CONDUCTIVE OXIDE THIN FILMS

In order to improve the fatigue of PZT ferroelectric memory cells, conductive oxide electrodes such as RuO_x and $La_xSr_{1-x}CoO_3$ were grown by spin-on processes on Si substrates. RuO_x layers grown by spin-on processing show, similarly to sputtered RuO_x layers, a rutile structure with a primitive tetragonal cell and lattice constants a=0.451 nm ± 0.005 nm and c=0.308 nm ± 0.005 nm. Conductive perovskite films such as $La_xSr_{1-x}CoO_3$ show a cubic lattice constant with a=0.383 ± 0.005 nm. An X-ray diffraction pattern of a polycrystalline $La_xSr_{1-x}CoO_3$ film grown on a Si substrate is shown in Fig. 1.

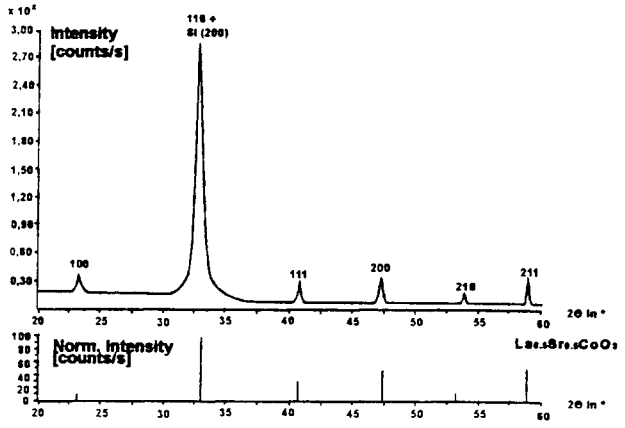


Figure 1. X - ray diffraction pattern of a $La_x Sr_{1-x} Co O_3$ film grown on a Si - substrate by spin-on processing.

The spin-on process gives rise to smooth, dense polycrystalline conductive oxide films as shown in Fig. 2. On top of these conductive oxides, PZT thin films could be grown (see Fig. 3).

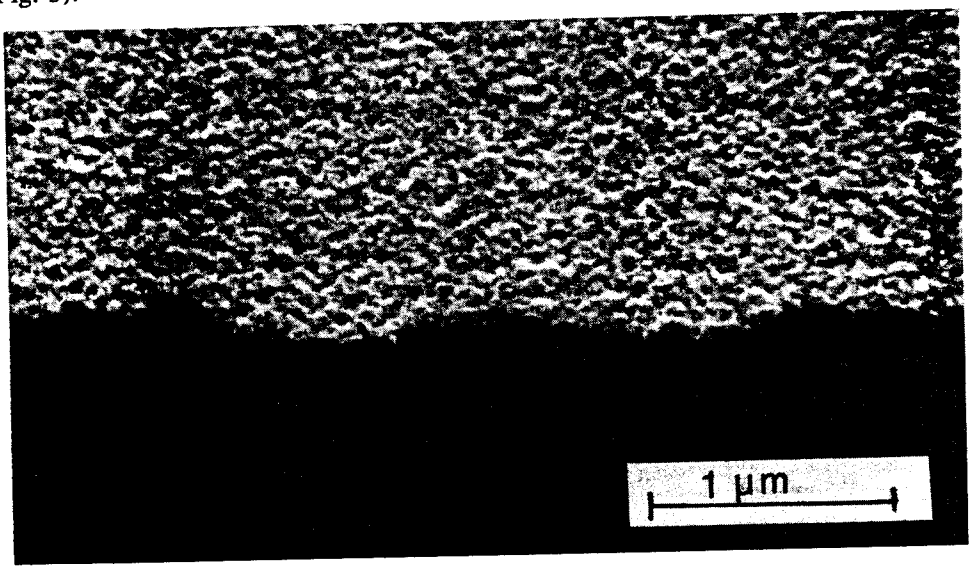


Figure 2. SEM micrograph of a conductive oxide electrode deposited by spin-on processing on a Si substrate.

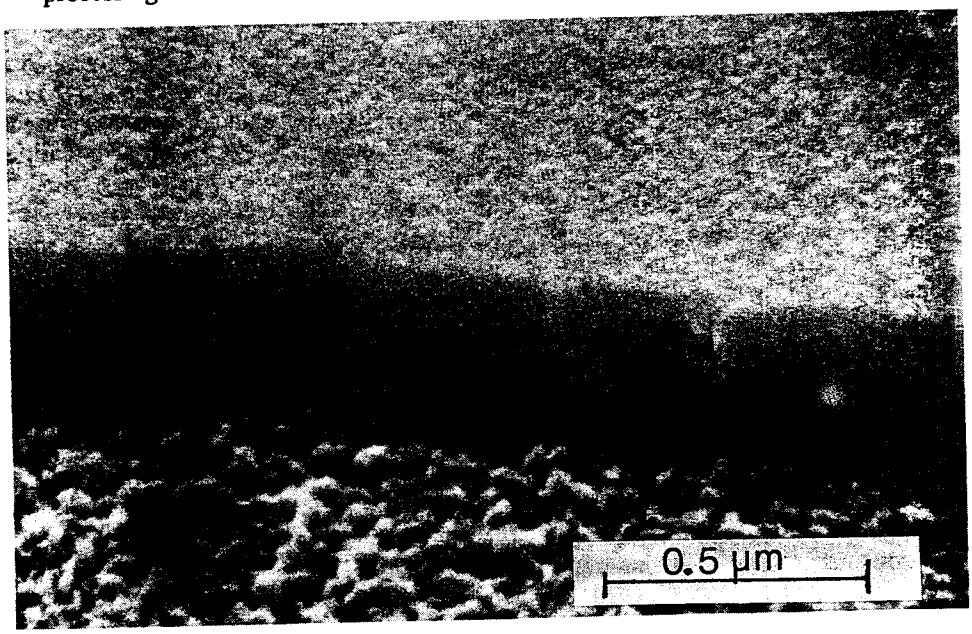


Figure 3. SEM rnicrograph of a PZT thin film grown on a conductive oxide film using a spin-on processing.

4. Spin - on Processing of Undoped and Doped $PbTiO_3$, $PbZr_xTi_{1-x}O_3$, $Pb(Mg,Nb)O_3$ - $PbTiO_3$, Alkaline Earth Titanate and Layered Perovskite ($Bi_4Ti_3O_{12}$, $SrBi_2Ta_2O_9$, $SrBi_2NbTaO_9$) Films

4.1. PREPARATION AND STRUCTURAL CHARACTERIZATION OF UNDOPED AND DOPED $PbZr_xTi_{1-x}O_3$ AND $PbTiO_3$ THIN FILMS

Thin $PbZr_xTi_{1-x}O_3$ with various zirconium-titanium ratios as well as with several dopants e.g. Nb, Zn, and La, are studied world wide by means of sol-gel processes [24]. Usually, lead acetate-tri-hydrate, titanium-teta-iso-propoxide and zirconium-tetra-n-propoxide are reacted in methoxyethanol as reported by Blum et al. [25], Budd et al. [26, 27]. Reaction of dehydrated lead acetate with titanium- zirconium methoxyethoxides results in Pb-Ti-Zr-oxo-methoxyethoxides as shown by Dey et al. [28] by means of FTIR and NMR spectroscopy. It is assumed that in the oligomeric species the bidentate ligand methoxyethanol is bridging between titanium and zirconium atoms as well as between lead atoms. Thin film deposition is carried out after prehydrolysis of these precursors with H_2O/HNO_3. Numerous modifications of this process have been reported. Schwartz et al. [29] and Yi et al. [30] developed modified sol-gel processes. Stabilization agents such as acetic acid and acetylacetone are used. The methoxyethanol solvent has been exchanged by other less toxic alcohols such as methanol. It has been found that the major part of the alkoxy groups in the metal alkoxides is replaced by acetate groups so that oligomeric Pb - Zr - Ti - oxo - alkoxy - acetates $PbZr_{0.5}Ti_{0.5}O_x(O_2C_2H_3)_yOR_z$ (with $z << y$) as stable precursors are formed.

Other groups studied the addition of drying agents such as ethylene glycol or dimethyformamide [31,32] to improve precursor chemistry and especially the drying behavior of the films. A precursor route based on diol systems has been developed to deposit relatively thick PZT films with thicknesses of 0.5 μm in one coating. Lead acetate-tri-hydrate is reacted with zirconium-n-propoxide and titanium-di-isopropoxide-bis-acetylacetonate in diols such as 1,3 propanediol [331. In addition to sol-gel and modified sol-gel precursors, also an MOD (metallo-organic decomposition) process is used by several groups to grow perovskite thin films such as $PbZr_xTi_{1-x}O_3$. In these systems, salts of long chain carboxylic acids e.g. Pb 2-ethylhexanoate are mixed with metal alkoxides such as titanium-n-butoxide and zirconium-n-butoxide in solvents such as butanol. After decomposition of the spin-on processed films at 600-700 °C, perovskite films are formed (see Ref. [34, 35]).

We investigated the sol-gel process reported by Budd et al [26,27,28] as well as a modified sol-gel and an MOD process to grow undoped and lanthanum, manganese, niobium and yttrium doped $PbZr_xTi_{1-x}O_3$ and $PbTiO_3$ films. In our modified sol-gel process as described in more detail in Ref. [31,32,33], lead acetate was reacted with titanium-iso-propoxide and zirconium-n-propoxide in methoxyethanol. The solutions were hydrolized with H_2O/HNO_3. Undoped and doped $PbZr_xTi_{1-x}O_3$ and $PbTiO_3$ films have been grown by spin-on processing on Ti/Pt and conducting oxide electrodes. Scanning electron microscopy (SEM) and transmission electron microscopy (TEM) studies in plan-view and cross section (XTEM) were carried out to characterize grain size, film morphology and defect structures. TEM studies on a series of thin films have shown that two types of thin films can be grown dependent on processing [36,37]. High temperature pretreatments at 550-600 °C after each spin-on process give rise to a columnar growth of

thin $PbTiO_3$ and $PbZr_xTi_{1-x}O_3$ films with column width of 70-250 nm. Due to the crystallization into the perovskite phase, after each spin-on process, the layers grow epitaxially on top of each other as has been found by means of HRTEM studies [37]. In these columnar films, typically a lamellar domain configuration predominates (see Fig. 4b). The standard firing process for PZT thin films reported by many groups, however, consists of a low temperature pretreatment at 200-350 °C on e.g. a hot-plate after each spin-on process. This gives rise to a quite different thin film growth. Amorphous layers are formed after each spin-on process. The amorphous stack is crystallized into the perovskite phase in the final annealing. The crystallization of the amorphous stack into the perovskite phase gives rise to films with a coarse-grained morphology. The grains within these films show grain sizes of 200-900 nm and are not epitaxially related. Within the relatively large PZT grains a banded domain configuration (see Fig. 4a) similar to the domain configurations reported for bulk ceramics was found.

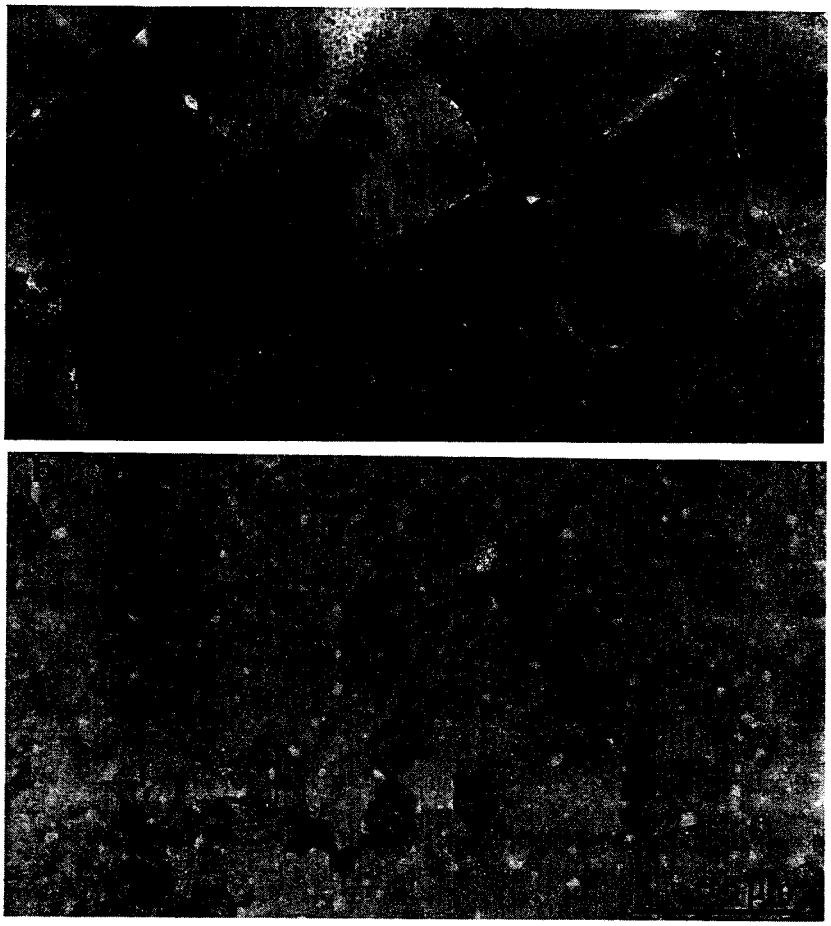


Figure 4. Plan - view TEM image of a $PbZr_xTi_{1-x}O_3$ film:
a) 300°C pretreatment after each spin-on, final annealing at 700 °C;
b) 600°C pretreatment after each spin-on, final annealing at 700 °C

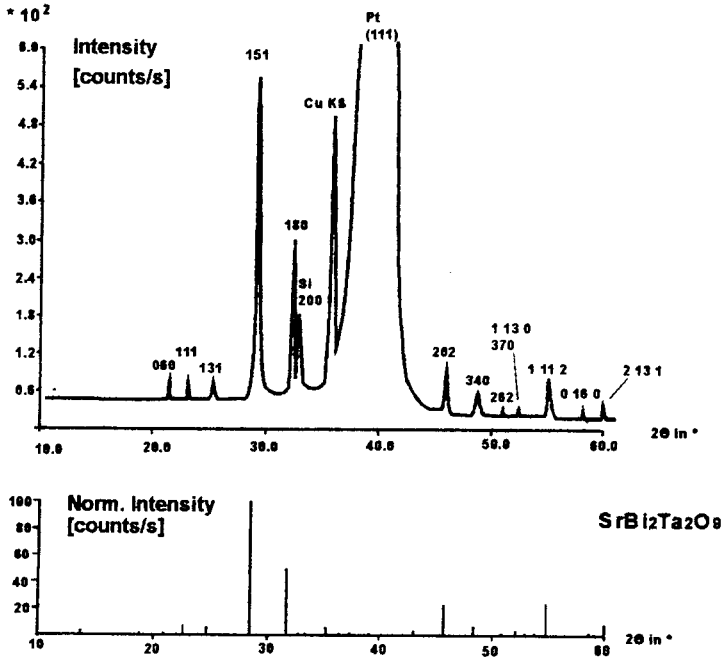


Figure 5. X-ray diffraction pattern of a $SrBi_2Ta_2O_9$ films grown on a $Si / SiO_2 / Ti / Pt$ substrate.

4.2. PREPARATION AND STRUCTURAL CHARACTERIZATION OF LAYERED PEROVSKITE FILMS ($Bi_4Ti_3O_{12}$, $SrBi_2Ta_2O_9$, $SrBi_2NbTaO_9$)

Although PZT thin films are so far the preferred material system for ferroelectric memory cells, other ferroelectric systems are studied in order to improve the endurance and to obtain fatigue-free ferroelectric cells. We investigated in more detail the spin-on processes for layered perovskites such as $Bi_4Ti_3O_{12}$, $SrBi_2Ta_2O_9$ and $SrBi_2TaNbO_9$, which has been described as ceramic materials by Smolenskii et al. in 1961 [47]. These thin films were deposited by means of MOD processes on Si substrates with a Ti/Pt bottom electrode. The technique is similar to the MOD process used for PZT thin films as described in more detail in Ref. [38]. Bismuth and alkaline earth salts of long chain carboxylic acids such as Sr- and Bi- ethylhexanoates were dissolved in alcohols together with titanium, niobium and tantalum alkoxides. Polycrystalline layered perovskite films were formed after spin-coating and firing at 650-800 °C. A random growth of the crystals on top of the Ti/Pt electrode with an orthorhombic primitive cell with a = 0.544 ± 0.002 nm b=0.541 ± 0.002 nm, c=3.284 ± 0.004 nm for the $Bi_4Ti_3O_{12}$ films was found. The $SrBi_2Ta_2O_9$ layers crystallize also orthorhombically with a=0.582 ± 0.002 nm, b=2.509 ± 0.004 nm, c=0.526 ± 0.002 nm. An X-ray diffraction pattern of a $SrBi_2Ta_2O_9$ film is shown in Fig. 5.

4.3. PREPARATION AND STRUCTURAL CHARACTERIZATION OF $Pb(Mg,Nb)O_3$-$PbTiO_3$ THIN FILMS

Almost all activities on spin-on processes report on the deposition of PZT and doped PZT systems. Only a few groups are studying more complex thin film systems such as the relaxor materials. Patel et al. investigated $PbSc_{0.5}Ta_{0.5}O_3$ films [39, 40]. Francis et al. [41] report on the growth of $Pb(Mg_{0.33}Nb_{0.67})O_3$-$PbTiO_3$ films. Magnesium was reacted with niobium ethoxide in ethanol to form magnesium-niobium ethoxide. This is followed by reaction with lead acetate, dehydrated in methoxyethanol, to form a Pb-Mg-Nb methoxyethoxide solution. The Pb-Mg-Nb solution was mixed with a 1 M stock Pb-Ti solution in the required amounts to obtain various compositions of $Pb(Mg_{0.33}Nb_{0.67})_xTi_{1-x}O_3$ films with x = 0 - 1. The solutions were prehydrolized with H_2O/HNO_3 or NH_4OH. It was stressed that especially the addition of benzoic acid improves the perovskite crystallization and the film morphology. Although the precursors are reacted to form a complex Pb-Mg-Nb-Ti species, Francis et al. report that the $Pb(Mg_{0.33}Nb_{0.67})_xTi_{1-x}O_3$ systems have to be fired at temperatures of 700-850 °C to obtain single perovskite phases. Especially for those films with high mangnesium+niobium content (x > 0.6) a minimum Pb-excess of 10-15 % has to be added to the precursor solution to compensate for PbO losses. Low reaction temperatures and low lead excesses give always rise to a pyrochlore second phase in amounts of 10 up to 50 % besides the perovskite phase. Udayakumar et al. [42] report on the reaction of magnesium ethoxide, niobium ethoxide and titanium-iso-propoxide in methoxyethanol. This is followed by reaction of the products with lead acetate, dehydrated in methhoxyethanol. After distillation, the solution is prehydrolized with H_2O/NH_4OH. Also, here the authors report that especially with high magnesium+niobium content (x = 0.9), reaction temperatures of 800-850 °C have to be used to grow perovskite layers without a pyrochlore phase. Generally, the pyrochlore phase formation as intermediate phase is a crucial step in the growth of relaxor thin films. We used our modified sol-gel process to grow $Pb(Mg,Nb)O_3$-$PbTiO_3$ thin films with magnesium+niobium content x > 0.6 at temperatures of 650 °C on Pt electrodes. These layers are single perovskite films with a homogeneous, dense columnar microstructure and column width of 150-200 nm (see Fig. 6, 7).

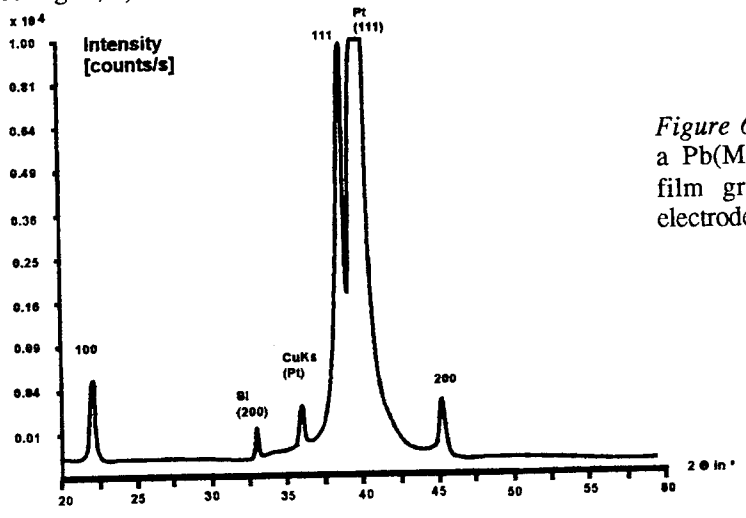


Figure 6. XRD pattern of a $Pb(Mg,Nb)O_3$-$PbTiO_3$ film grown on a Ti/Pt electrode at 650 °C.

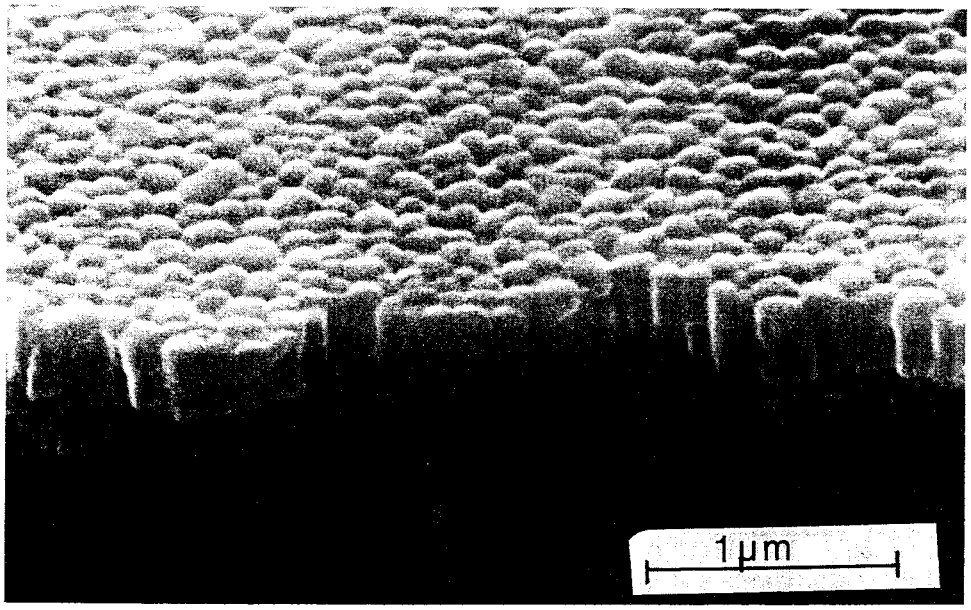


Figure 7. SEM micrograph of a $Pb(Mg,Nb)O_3$-$PbTiO_3$ film deposited on a Si / SiO_2 / Ti / Pt substrate.

4.4. PREPARATION AND STRUCTURAL CHARACTERIZATION OF UNDOPED AND DOPED $BaTiO_3$, $SrTiO_3$ THIN FILMS

Spin-on processes are an important deposition technique to grow also alkaline earth titanate thin films such as $BaTiO_3$, $SrTiO_3$, $Ba_xSr_{1-x}TiO_3$; these thin film systems are investigated by several groups as thin film storage capacitors for high density dynamic random access memories. We developed a sol-gel process for $BaTiO_3$, $Ba_xSr_{1-x}TiO_3$ and $SrTiO_3$ thin films. Barium and/or strontium iso-propoxides or ethoxides were reacted with titanium alkoxides [43, 45, 46]. After hydrolysis with H_2O/HNO_3 or H_2O/NH_4OH we formed polycrystalline alkaline earth titanate thin films by spin-on processing and firing at 700-750 °C. Frey et al. [44] reported on a similar process using barium- and titanium-methoxyethoxides in methoxyethanol as precursor system. Also, here modifications of the sol-gel process have been successfully applied to grow thin $BaTiO_3$ and $SrTiO_3$ films. In our modified sol-gel process metal carboxylates such as metal acetates for the two valent ions and titanium alkoxides for the four valent ions are dissolved in alcohols and were hydrolized with H_2O. Additionally, we investigated an MOD process to grow alkaline earth titanate films. Here, salts of long chain carboxylic acids of barium and strontium were mixed with metal alkoxides of titanium in organic solvents [45,46]. To dope all these three precursor systems with acceptors or donors e.g. Ni, La, Nb, metal alkoxides, metal acetates or metal β-dicetonates were homogeneously mixed with the 0.2-0.5 M sol-gel, modified sol-gel or MOD precursor solutions.

Spin-coating and firing of the films at 700-750 °C after each spin-on process gives rise to dense fine-grained films. As can be derived from SEM micrographs, alkaline earth titanate films grow always with a polycrystalline morphology and crystal sizes of 60-100 mn (see Fig. 8).

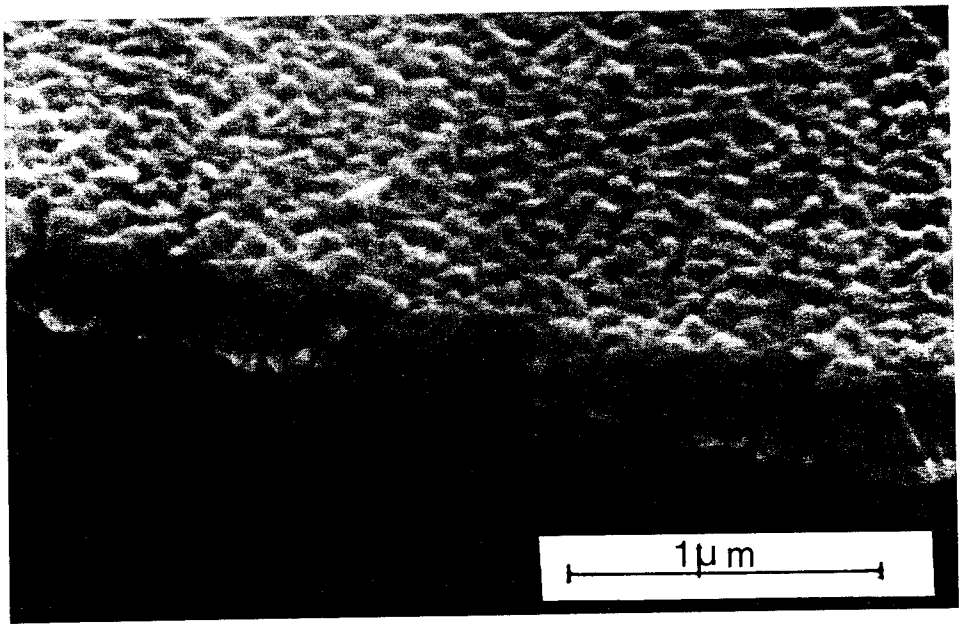


Figure 8. SEM micrograph of a $BaTiO_3$ film grown on Ti / Pt electrode by amodified sol-gel process.

5. Electrical Properties of Undoped and Doped $PbTiO_3$, $PbZr_xTi_{1-x}O_3$, $Pb(Mg,Nb)O_3$-$PbTiO_3$, Alkaline Earth Titanate and Layered Perovskite Films ($Bi_4Ti_3O_{12}$, $SrBi_2Ta_2O_9$, $SrBi_2NbTaO_9$)

5.1. FERROELECTRIC PROPERTIES AND DC CONDUCTIVITY OF $PbZr_xTi_{1-x}O_3$ (x = 0.35-0.65) FILMS ON Ti/Pt AND CONDUCTIVE OXIDE ELECTRODES

In chapter 4 it was shown that thin film processing has a strong influence on growth, morphology and domain configuration of PZT layers. From the ceramic data one can expect that the ferroelectric properties of $PbZr_xTi_{1-x}O_3$ can be tailored by controlling grain size and domain configuration. As described in more detail in Refs. [36, 37], large grained PZT films with grain sizes of 200-900 nm show a banded domain configuration and ferroelectric properties similar to bulk ceramics. For fine-grained columnar PZT films with a lamellar domain configuration the absolute values of the remanent polarization are

smaller compared with data for large-grained films. In fine-grained columnar films, however, the saturation remanent polarization can be achieved at lower electrical fields. For the application of PZT thin films in high density dynamic random access memories, fine-grained films are desirable, since the lateral grain size should be smaller than the dimensions of the ferroelectric capacitors. We therefore restrict ourselves to the fine-grained columnar films. Fine grained columnar $PbZr_{0.53}Ti_{0.47}O_3$ films deposited on Ti/Pt electrodes with a thickness of 0.2 and 0.4 nm show remanent polarizations of P_r = 19-23 $\mu C/cm^2$ and coercive fields of E_C=52-65 kV/cm (see Figs. 9 (a) and (c)). Similar ferroelectric data have been obtained, if the PZT films were deposited on conductive oxide electrodes, which were produced by spin-on processing (see Figs. 9 (b) and (d)).

Studies on the endurance of the ferroelectric cells carried out by means of hysteresis measurements revealed for 0.4 μm thick $PbZr_{0.33}Ti_{0.47}O_3$ layers grown on conductive oxide electrodes an improvement of the endurance compared with the films grown on Ti/Pt electrodes. In Fig. 10 (a), the virgin hysteresis loop and the hysteresis loop measured after 10^8 polarization cycles are shown for a PZT (53/47) thin film with a thickness of approximately 0.2 μm grown on a Ti/Pt electrode. The measurements demonstrate that the PZT thin film on the metal electrodes show a fatigue. In Fig. 10 (b), the data are demonstrated for a 0.2 μm thick PZT (53/47) film grown on a conductive oxide electrode.

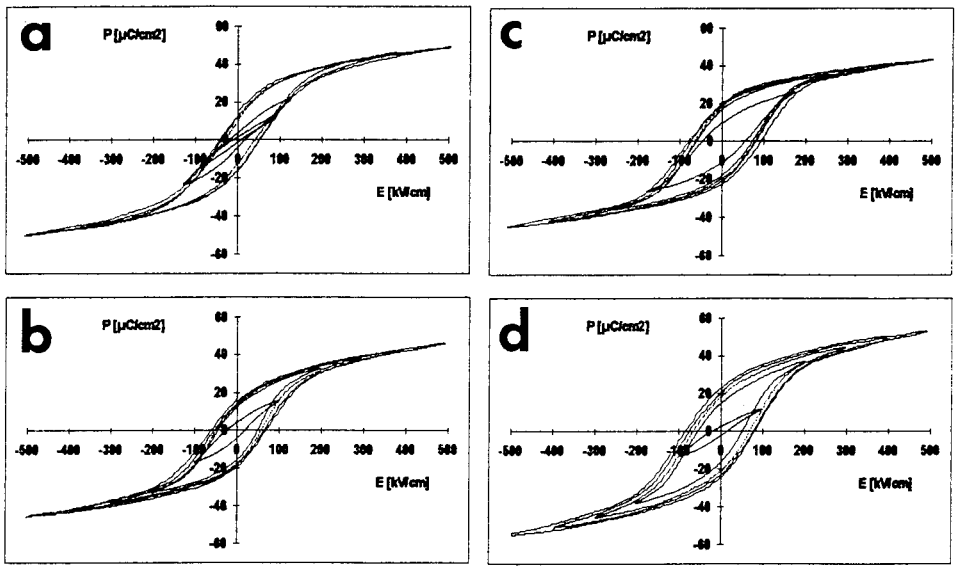


Figure 9. Hysteresis loops for $PbZr_{0.33}Ti_{0.47}O_3$ films. a) on Pt (film thickness 0.4 μm); b) on RuO_x (film thickness 0.4 μm); c) on Pt (film thickness 0.2 μm) d) on RuO_x (film thickness 0.2 μm).

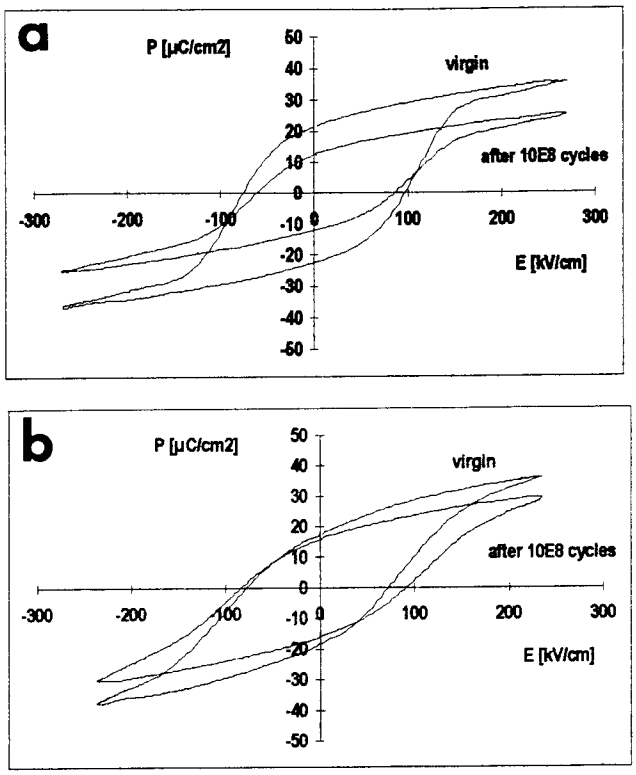


Figure 10. Virgin hysteresis loops and hysteresis loops after 10^8 polarization cycles for a 0.2 µm thick PZT thin film switched with 5 V. a) film on Ti / Pt electrode; b) film on conductive oxide electrode.

As can be derived from the loop measured after 10^8 polarization cycles, an improvement of the endurance is obtained if the PZT films are deposited on a conductive oxide electrode, produced by spin-on processing. These data agree with those reported for PZT thin films grown on conductive oxide electrodes deposited by laser ablation or sputtering.

PZT thin films for non-volatile memories are usually characterized with respect to switching time, fatigue and retention. For a high reliability of the ferroelectric cells, especially if used as storage capacitors in e.g. ultra-high density dynamic random access memories, one has also to pay attention to the dc conductivity of the thin films. We investigated the dc conductivity as a function of time for PZT thin films deposited on Ti/Pt and conductive oxide electrodes. To reach a steady state within 150 seconds our measurements were carried out at 150 °C. In Figs. 11 (a), (b), and (c), the dc conductivity σ (current density-field ratio J/E (S/cm)) is given as a function of time on a log-log scale. The measurements were carried out on 0.4 µm thick films with an applied voltage of 0.42 V and 1 V, which corresponds with field strengths of 10 kV/cm and 25 kV/cm, respectively.

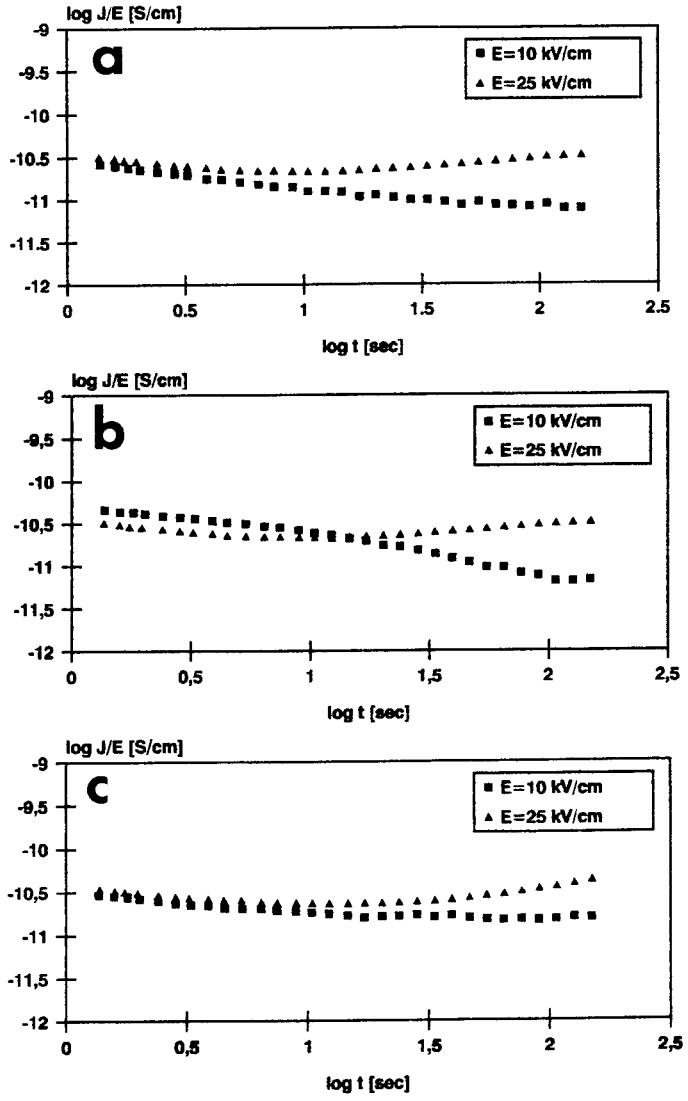


Figure 11. DC conductivity σ (current density - field ratio J/E) as a function of time on a log-log scale (T = 150 °C). a) $PbZr_{0.53}Ti_{0.47}O_3$ film (Ti/Pt bottom electrode, NiCr / Au top electrode); b) $PbZr_{0.53}Ti_{0.47}O_3$ film (RuO_X bottom electrode, NiCr / Au top electrode); c) $PbZr_{0.53}Ti_{0.47}O_3$ film (Ru_X bottom electrode, Pt top electrode).

The data in Fig. 11 (a), for a 0.4 μm thick $PbZr_{0.53}Ti_{0.47}O_3$ film deposited on a Ti/Pt electrode with a NiCr/Au top electrode, revealed $\sigma = 6.8 \times 10^{-12}$ S/cm after 150 s, if a dc field of 10 kV/cm is applied and $\sigma = 2.2 \times 10^{-11}$ S/cm if a dc field of 25 kV/cm is

applied. From the time dependence, one derives that at 150 °C a steady state has been reached, so that under these conditions the real dc conductivity of the films can be determined. In Fig. 11 (b), the data are presented for a $PbZr_{0.53}Ti_{0.47}O_3$ film deposited on a conductive oxide electrode produced by spin-on processing. We used again NiCr/Au as top electrode. Similar conductivity data were obtained for our films deposited on a conductive oxide electrode ($\sigma = 7.6 \times 10^{-12}$ S/cm at 10 kV/cm after 150 s and $\sigma = 3.3 \times 10^{-11}$ S/cm at 25 kV/cm). These results are in contrast to the data reported by Kingon et al. [21], where higher leakage currents were observed for PZT films grown on RuO_x electrodes. This might be due to the fact that we used a sol-gel processed conductive oxide bottom electrode instead of a sputter-deposited one. In Fig. 11 (c), one can find the data obtained for a 0.4 µm thick $PbZr_{0.53}Ti_{0.47}O_3$ film deposited on a conductive oxide electrode with a Pt electrode sputtered on top of the PZT layer. It can be seen that the dc conductivity is for these films in the same order as for the films with a Ti/Pt or RuO_x bottom electrode and NiCr/Au top electrode.

5.2. FERROELECTRIC PROPERTIES OF LAYERED PEROVSKITE FILMS

The ferroelectric properties of $Bi_4Ti_3O_{12}$ films and $SrBi_2Ta_2O_9$ films have also been characterized by means of hysteresis measurements and pulse measurements. For $Bi_4Ti_3O_{12}$ single crystals, a strong anisotropy is reported with P_s=50 µC/cm^2 along the a-axis and P_s= 4 µC/cm^2 along the c-axis. The data given for bulk $SrBi_2Ta_2O_9$ ceramics [48] show low polarization values with P_s = 5 µC/cm^2. Investigations of our ferroelectric $Bi_4Ti_3O_{12}$, $SrBi_2Ta_2O_9$ as well as $SrBi_2TaNbO_9$ films, which were randomly grown on top of Ti/Pt electrodes revealed remanent polarizations of P_r=3-10 µC/cm^2. The switched polarizations, which are a factor of three smaller than those for PZT films give rise to only a slight fatigue in these layered perovskites. The fatigue data for a $Bi_4Ti_3O_{12}$ film are presented in Ref. [38].

5.3. FERROELECTRIC AND PYROELECTRIC PROPERTIES OF LANTHANUM, MANGANESE DOPED $PbTiO_3$ FILMS

Lead based perovskite thin films are not only investigated because of their ferroelectric properties. Several groups are studying the pyroelectric properties of perovskite thin films for pyroelectric sensors or thermal image arrays. We investigated the ferroelectric and pyroelectric properties of lanthanum, manganese doped $PbTiO_3$ thin films, because of their low relative permittivities and reasonable pyroelectric coefficients. Approximately 0.4-1.0 µm thick $PbTiO_3$ films doped with La, Mn grown in our modified sol-gel process show relative permittivities of 240-320, square hysteresis loops with remanent polarizations of P_r=29 µC/cm^2 and coercive field strength of E_C=72 kV/cm (see Fig. 12). Measurements of the pyroelectric properties for 1.0 µm thick doped $PbTiO_3$ films revealed pyroelectric coefficients at room temperature of $dP/dT = 1.9 \times 10^{-4}$ C/Km^2. The measurement was performed during slow heat up and cool down of the samples (2 K/min) and integration of the released charge with a Keithley 617 electrometer. Samples were poled 24 h before measuring and showed no significant difference in pyroelectric

coefficient between up and down ramps. These data agree well with the bulk ceramic data ($dP/dT = 2.0 \times 10^{-4}$ C/Km^2).

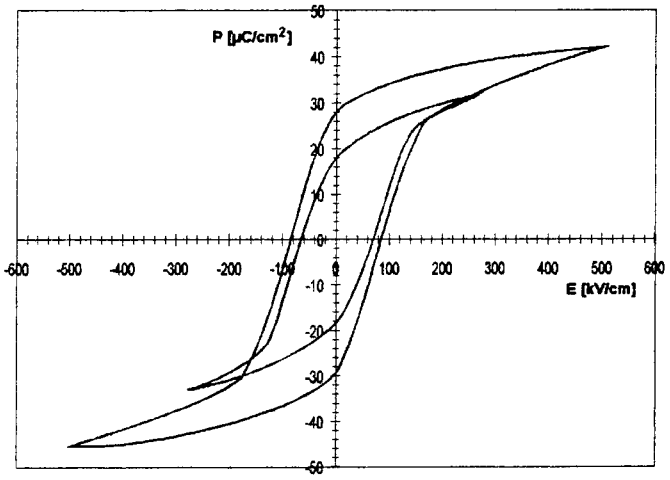


Figure 12. Hysteresis loops of a 1.0 µm thick $PbTiO_3$ films doped with La and Mn. Deposition of the film on a $Si/SiO_2/Ti/Pt$ substrate.

Together with a fairly low loss angle, $\tan \delta = 1\%$, this leads to a figure of merit

$$F_D = \frac{dP}{dT} \frac{1}{c \sqrt{\varepsilon \tan \delta}} = 1.6 \times 10^{-5} \text{ Pa}^{-1/2}$$

Here we have assumed a heat capacity of $C = 2.7 \times 10^6$ J/Km^3. The figure of merit is comparable to sputtered lanthanum doped $PbTiO_3$ films [49], but not has high as the figure of merit for the $PbSc_{0.5}Ta_{0.5}O_3$ thin films reported by Patel et al. [39] and Whatmore et al. [40]. The doped $PbTiO_3$ films can be grown at temperatures of 550-650 °C, so that integration in Si processes is possible. $PbSc_{0.5}Ta_{0.5}O_3$ thin films, however, have to be fired at temperatures of up to 900 °C to avoid the formation of a pyrochlore second phase. $PbSc_{0.5}Ta_{0.5}O_3$ thin films are therefore up to now deposited only on sapphire substrates without bottom electrode [39,40]. Additionally, pyroelectric $PbSc_{0.5}Ta_{0.5}O_3$ films need, in contrast to the pyroelectric $PbTiO_3$ system, a large dc field for operation of the pyroelectric detector.

5.4. ELECTRICAL PROPERTIES OF $Pb(Mg,Nb)O_3$-$PbTiO_3$, $BaTiO_3$ AND $SrTiO_3$ FILMS

$Pb(Mg,Nb)O_3$-$PbTiO_3$ thin films with a columnar growth produced in our modified sol-gel process show relative permittivites of 1300-1800 and dielectric losses tan δ = 1.5-3%.

Similarly to the data reported by Francis et al. [41], we found a strong dependence of the permittivity from the film thickness. From SEM micrographs we derive that the increase of the relative permittivities is caused by an increase of the column height in the layers with increasing thickness; the colurm width, however, remains with increasing thickness of the layers constant at approximately 150-200 nm. A similar dependence of the relative permittivity from the thickness has been found for thin $BaTiO_3$ films with relative permittivities of 300-800, dielectric losses of 1-3 % and thicknesses of 0.2-0.8 µm. For undoped and doped $SrTiO_3$ films, the relative permittivities ranged between 195-235 (tan δ = 0.3-1.3 %) and showed no dependence on the layer thickness, which was varied from 0.2 µm up to 0.8 µm. The low relative permittivities in $BaTiO_3$ and $Pb(Mg,Nb)O_3$-$PbTiO_3$ films compared with bulk ceramics are in all cases caused by the small grain sizes of the materials with grain sizes of 60-200 nm. As a result, an improvement of the temperature characteristic of the thin film capacitors compared with the bulk ceramics has been found. This holds for PMN as well as for $BaTiO_3$ thin films. For these thin film systems, the variation of the capacitances is smaller than ± 10 % in the temperature range of -55 up to 125°C. A comparison of the thin film data with bulk ceramics is shown in Fig. 13.

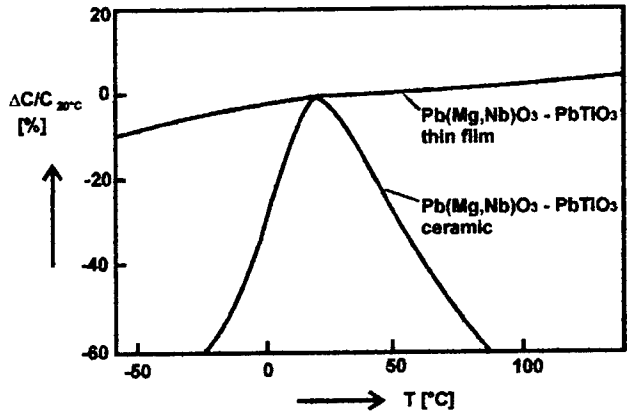


Figure 13. Relative capacitance as a function of temperature for a thin$Pb(Mg,Nb)O_3$ - $PbTiO_3$ film. In the diagram, data for a $Pb(Mg, Nb)O_3$ - $PbTiO_3$ ceramic are included.

6. Conclusions

Sol-gel, modified sol-gel and MOD spin-on processes for perovskite films such as undoped and doped $PaZr_xTi_{1-x}O_3$ films, $PbTiO_3$ films, alkaline earth titanate, $Bi_4Ti_3O_{12}$, $SrBi_2Ta_2O_9$ and $Pb(Mg_{0.33}Nb_{0.67})O_3$-$PbTiO_3$ films were discussed. It was

demonstrated that spin-on processes can also be used to grow conductive oxide layers. The growth of the perovskite layers by means of modified sol-gel processes on Pt and conductive oxide electrodes was presented in more detail and the dielectric, ferroelectric and pyroelectric properties of the layers were summarized.

7. Acknowledgements

We gratefully acknowlege the technical assistance by H. Knüfer, W. Moors and the structural characterization carried out by Dr. A. De Veirman (TEM studies), B. Krafczyk, D. Bausen (SEM and XRD analysis). Thanks are due to Dr. P.K. Larsen for helpful discussions.

8. References

1. Larsen, P.K, Cuppens, R. and Spierings, G C.A.M. (1992), *Ferroelectrics* **128**, 265.
2. Bondurant, D.W. (1991), *Fenoelectrics* **116**, 364.
3. Lampe, D.R., Adams, D.A., Sinharoy, S., and Buhay H. (1992), *Proc. 4th Int. Symp. on Integr. Ferroelectrics*, Paz de Araujo, C.A. (ed.), pp. 99.
4. Hsueh, C.-C., Tarnagawa, T., Ye, C., Helgerson, A. and Polla, D.L. (1993), *Integrated Ferroelectrics* **3**, 21.
5. Udayakumar R.K., Chen J., Brook K.G., Cross L.E., Flynn A.M. and Ehrlich, D.J. (1991), *Mat. Res. Soc. Symp.* **243**, Kingon, A.I., Myers, E.R., Tuttle, B. (eds.), pp. 49.
6. Bell A., Huang Y., Daglish M., Paul O., Nernirovsky Y., Nemirovsky, A., Setter, N. (1994), *Proc. of the 6th Int. Symp. on Integrated Ferroelectrics* , Paz de Araujo, C.A. (ed.), in press.
7. Choi, J.R., Lee, D.H., Nam, H.J., Cho, S.M., Lee, J. H., Kim, K.Y. (1994), *6th Int Symp. on Integrated Ferroelectric,* Paz de Araujo, C.A. (ed.), in press.
8. Patel, A., Shorrocks, N. and Whatmore, R. (1991), *Mat Res. Symp. Proc.* **243**, Kingon, A.I., Myers, E.R., Tuttle, B. (eds.), pp. 67.
9. Fazan, P.C. (1994), *Integrated Ferroelectrics*, in press.
10. Moazzarni, R. (1994), *6th Int. Symp. on Integr. Ferroelectrics*, Monterey, in press.
11. Baude, P.F., Ye, C., Tamagawa, T. and Polla, D. (1993), *J. Appl. Phys.* **73**, 7960.
12. Swartz, S.L. and Wood, N.E. (1992), *Condensed Matter News* **1**, 4.
13. Spierings, G. C. A.M., van Zon, J.B.A., Klee, M. and Larsen, P.K. (1992), *Proc. of 4th Int. Symp. on Integr. Ferroelectrics*, Paz de Araujo, C.A. (ed.), pp. 280.
14. Eichhorst D.J., Blanton T.N. Bames C.L and Bosworth L.A. (1994), *Integrated Ferroelectrics*, in press.
15. Al-Shareef, H.N., Gifford, K.D., Rou, S.H., Hren, F.D., Auciello, O. and Kingon, A.I. (1993), *Integrated Ferroelectrics* **3**, 321.
16. Larsen, P.K., Dormans, G.J.M., Taylor, D.J. and Veldhoven, P.J. (1994) , *J. AppL Phys.*, in press.
17. Melnick, B.M., Paz de Araujo, C.A. (1994), *Integrated Ferroelectrics*, in press.
18. Kwok, C.K., Viray, D.P., Desu, S B., Parikh, N.R. and Hil, E.A. (1992), *Integrated Ferroelectrics*, pp. 412

19. Ramesh, R., Dutta, B., Ravi, T.S., Lee, J., Sands, T. and Keramidas, V.G. (1994), *Appl. Phys. Lett.* **64**, 12, 1588.
20. Tiwari, P., Zheleva, T. and Narayan, J. (1993), *AppL Phys. Lett* **63**, 1, 30.
21. Chen, X.,Kingon, A.I, Bellur, K.,Auciello, O., and AI-Shareef, H.N. (1994), *Integrated Ferroelectrics*, in press.
22. Al-Shareef, H.N., Auciello, O., and Kingon, A. I. (1994), "Science and Technology of electroceramic Thin Films," Auciello, O. and Waser, R. (eds.), NATO/ARW Series E (this issue), in press.
23. Bursil, L.A., Reany, I, Vijay, D.P., and Desu, S.B. (1994), *J. Appl. Phys.* **75**,3, 1521.
24. Watanabe, H., Mihasu, T., Yoshimori, H. and Paz de Araujo, C.A. (1992) *Integrated Ferroelectrics*, 346.
25. Blum, S.B and Gurkowich, S.R. (1985) *J. Mat. Sci.* **20**, 4479.
26. Budd, K.D., Dey, S.K. and Payne, D. A. (1985), *Proc. Ceram. Proc.* **36**, 107.
27. Budd, K.D., Dey, S.K. and Payne, D. A. (1986), *Mat. Res. Soc. Symp. Proc.* **73**, pp. 711.
28. Coffman, P.R., Dey, S.K. (1994), *Proc. of the 5th Int. Symp. on Integrated Ferroelectrics*, in press.
29. Schwartz, R W., Assink, R. A. and Headley ,T. J (1991), *Mat. Res. Symp. Proc.* **243**, Kingon, A.I., Myers, E.R., Tuttle, B. (eds.), pp. 245.
30. Yi, G. and Sayer , M. (1991), *Ceramic. Bull* . **70**, 7, 1173.
31. Chang, D., Chok, Y., Hisieh ,W., Lin, P. and Tseng, T. (1993), *J. of Mat. Scie.* **28**, 6691.
32. Sanchez, L.E., Dion, D.T., Wu, S.Y. and Naich, I.K. (1991), *Ferroelectrics* **116**, 1.
33. Calzada, M. L. and Milne, S.J. (1993), *J. Mat. Sc. Lett.* **12**,1221.
34. Zhu, W. and Vest, R. (1992), *Ferroelectrics* **134**, 331.
35. Klee. M., Eusemann, R., Waser, R., Brand, W. and van Hal, H. (1992), *J. Appl. Phys.* **72**,1566.
36. Klee, M., De Veirman, A., Taylor, D.J. and Larsen, P.K. (1994), *Integrated Ferroelectrics* **4**, 197..
37. Klee, M., De Veirman, A. and Mackens, U. (1993), *Philips J. Res.* **47**, 263.
38. Klee, M. and Larsen, P.K. (1992), *Ferroelectrics* **133**, 92.
39. Pattle, A., Shorocks, N. and Whatmore, R. (1992), *Ferroelectrics* **134**, 343.
40. Whatmore, R. (1992), *Ferroelectrics* **133**, 35.
41. Francis, L.F . and Payne, D.A. (1991), *J. Am. Ceram. Soc.* **74**, 12, 3000.
42. Udayakumar, K.R., Chen, J., Schuele, P.J., Cross, L.E., Kumar, V. and Kupanidhi, S.B. (1992), *Appl. Phys. Lett.* **60**, 10, 1187.
43. Hennings, D., Klee, M., Waser, R. (1991), *Adv. Materials* **3**, 334.
44. Frey, M.H. and Payne, D.A. (1993), *Appl. Phys. Lett.* **63** , 20, 2753.
45. Klee, M. and Waser, R. (1992), *Mat. Res. Soc. Symp.* **234**, 437.
46. Waser, R. and Klee, M. (1992), *Integrated Ferroelectrics* **2**, 23.
47. Smolenskii, G.A., Iompov, V.A. and Agranovskaya, A.T. (1961), *Soviet Physics-Solid State* **3** (3), 651.
48. Mitsui, T., and Nomura, S., (1981), *Landolt-Bornstein, Ferroelektrika und verwandte Materialien* **16**, 230.
49. Watton, R. (1994), *Integrated Ferroelectrics* **4**, 175.

RELATIONSHIPS BETWEEN FERROELECTRIC 90° DOMAIN FORMATION AND ELECTRICAL PROPERTIES OF CHEMICALLY PREPARED $Pb(Zr,Ti)O_3$ THIN FILMS

B.A. TUTTLE, T.J. GARINO, J.A. VOIGT, T.J. HEADLEY, D. DIMOS AND M.O. EATOUGH
Sandia National Laboratories, Albuquerque,NM 87185, USA

ABSTRACT. The manner in which underlying substrate technology affects 90° domain formation and resultant ferroelectric properties of chemically prepared $Pb(Zr,Ti)O_3$ (PZT) thin films is described. For otherwise identically processed PZT films deposited on Pt coated substrates, remanent polarization is a monotonic function of the thermal coefficient of expansion of the substrate. We have determined that this behavior is the result of the 90° domain formation that occurs as the film is cooled through the transformation temperature. Specifically, PZT film stress in the vicinity of the Curie point controls 90° domain assemblages within the film. PZT films under tension at the transformation temperature are preferentially a-domain oriented; whereas, films under compression at the transformation temperature are c-domain oriented. From X-ray diffraction measurements of PZT thin films as a function of electric field, we show that electrical switching of 90° domains is severely limited. Thus, the formation of these 90° domains in the vicinity of the Curie point is a dominant factor in the determination of PZT film dielectric properties. Chemically prepared PZT thin films that have essentially random crystallite orientation, but preferential a-domain orientation, have low remanent polarization (24 $\mu C/cm^2$) and high dielectric constant (1000). Conversely, PZT films of similar crystallite orientation, but of preferential c- domain orientation, have large remanent polarizations (37 $\mu C/cm^2$) and low dielectric constants (700). These results are consistent with single crystal properties of tetragonally distorted, simple perovksite ferroelectrics. Further, we have determined for our films that grain size - 90° domain relationships appear similar to those in the bulk. The effect of grain size on 90° domain formation and postulated changes in electrical properties with grain size are discussed.

1. Introduction

Ferroelectric thin films, such as $Pb(Zr,Ti)O_3$, are under intense investigation because of their potential impact for a wide array of next generation applications. These applications include ferroelectiric nonvolatile memories, pyroelectric detectors, decoupling capacitors, piezoelectric micromotors and optical storage disks. The various figures of merit for

O. Auciello and R. Waser (eds.). Science and Technology of Electroceramic Thin Films, 117-132.
© 1995 *Kluwer Academic Publishers. Printed in the Netherlands.*

ferroelectric thin films, which determine the performance of the aforementioned devices, are in many instances proportional to the polarization that can be achieved. For this reason, remanent polarization is often used in this paper as a measure of ferroelectric thin film quality. The polarization measured for a ferroelectric thin film depends on several factors, which include phase purity, microstructural quality, crystallite orientation, grain size and the type of substrate used for deposition. A particularly intriguing issue is determining why the substrate has such a major effect on ferroelectric thin film properties. Remanent polarizations of otherwise identically processed, single phase perovskite PZT films with similar crystallite orientations can vary by a factor of ten depending on the substrate used for deposition. In this paper, we demonstrate that stress at the transformation temperature strongly influences 90^{o} domain assemblage and orientation, which in turn, determines the measured dielectric properties of PZT thin films.

Several research organizations [1-3] have reported on the difference of electrical properties of otherwise similarly processed PZT thin films that were deposited on different substrates. Previously, Tuttle and coworkers [1], demonstrated that two PZT 60 / 40 films (rhombohedral symmetry) with a similar degree of highly preferential (111) crystallite orientation deposited on platinum coated sapphire and silicon substrates, differed by a factor of two in remanent polarization. The remanent polarization of the PZT 60/40 film deposited on sapphire was 40.6 ± 3.8 $\mu C/cm^2$; whereas, the remanent polarization of the PZT 60/40 film deposited on silicon was 20.2 ± 1.9 $\mu C/cm^2$. Kingon and coworkers [2] have shown that PZT films deposited on RuO_2 coated MgO substrates have greater polarization than similar films deposited on Pt coated silicon substrates. Speck, Ramesh and coworkers [3] have demonstrated that (001) oriented PZT 20/80 films deposited by pulsed laser deposition have significantly higher remanent polarizations (60 $\mu C/cm^2$ compared to 5 $\mu C/cm^2$) than similarly processed films with (100) orientation. While the high remanent polarization films were deposited on YBCO coated $LaAlO_3$ substrates, the low remanent polarization films were deposited on YBCO coated Si substrates.

Grain size is a parameter that has substantial influence on 90^{o} domain assemblage in bulk ferroelectrics. Traditionally, bulk ferroelectrics were thought to have a critical grain size [4] below which no 90^{o} domains are formed. This critical grain size for bulk $BaTiO_3$ ceramics below which no 90^{o} domains are formed has been reported to be in the range of 0.75 μm [5] to 1.0 μm [4]. Demczyk and coworkers [6], reported that $(Pb_{0.8}La_{0.2})TiO_3$ ceramics, with 4mm crystal symmetry similar to the PZT thin films in this study, show no evidence of 90^{o} domain formation for grain sizes below 0.3 μm. Arlt [7] has reported that for fine grain ceramics, elementary 90^{o} domain twinning occurs. Elementary 90^{o} domain twinning occurs in the grain size range of approximately 0.3 μm to 1.0 μm for PZT ceramics, and consists of single 90^{o} domain lamallae that extend across the width of the grain. In this grain size range, domain width decreases with the square root of the grain size. For larger grain size materials, such as, commercial piezoelectric materials with grain sizes on the order of 10 μm, intersecting, complex 90^{o} domain patterns are developed. Arlt [8] has described these patterns as a spatial domain configuration which is almost free of polarization charge.

The critical grain size, which marks the boundary between the formation of single 90^{o} domain lamallae and no presence of 90^{o} domains, is proportional to the

stress generated as the ferroelectric cools through the transformation temperature. The equilibrium domain width d* given by eq. (1) [6],

$$d^* = (32\pi\,\alpha\,) / (\varepsilon^2 E) \qquad (1)$$

where α is the domain wall energy, on the order of 10^{-3} J/cm^2, ε is the transformation strain, and E is Young's modulus. The transformation strain, ε, is given by

$$\varepsilon = [(c/a)^2 - 1] / (c/a)^2 \qquad (2)$$

where c and a are the lattice parameters of the unit cell. From the above treatment as c/a increases, the transformation strain increases and the equilibrium domain width decreases. Thus, it is expected that ceramics with larger anisotropy will have smaller critical grain size. One must caution that many factors [10] are involved in determination of the critical grain size and these simple relationships may not hold, especially when comparing different families of ferroelectrics.

Recently, there have been a number of exemplary efforts [9,10] to rigorously determine the 90^o domain populations for PZT and $PbTiO_3$ thin films as a function of substrate technology and thermal processing. Speck and coworkers [9] have considered the following parameters that affect 90^o domain formation in $PbTiO_3$ thin films: lattice parameter mismatch between substrate and film, thermal expansion coefficient difference, film thickness and depolarization field behavior. Above an effective critical film thickness, 90^o domain formation will occur to minimize overall film stress. Below this thickness, the lattice parameter mismatch is accomodated by misfit dislocations and 90^o domains do not form. Domain stability maps were developed which indicated that the population of **a** and **c** domains in the film critically depends on the stress state of the film above the Curie point. For $PbTiO_3$ films deposited on MgO substrates, if complete strain relaxation occurred in quickly cooled films, **a-c** monodomain structure was predicted. However, if the film strain was not completely relaxed at the growth temperature, it would be possible to obtain a significant a-domain population despite the coefficient of thermal expansion mismatch. Erbil and coworkers [11], calculated the **c** domain population for $PbTiO_3$ thin films deposited on $KTaO_3$ substrates with and without strain relaxation at the growth temperature. These results were in good agreement with the c domain populations measured for a series of films of different thickness ranging from 20 nm to 600 nm.

For our work, we have emphasized a parameter space that is a subset of the general treatment given by the above two authors. That is, our film thickness was chosen to be similar to those of many PZT films reported on in the literature and also similar to the thickness anticipated for many near term applications. We have standardized our film thickness at 300 nm and our substrate lattice parameters are either that of Pt (0.393 nm) or MgO (0.425 nm). Thus, our films are considerably thicker than the calculated critical thickness and under appropriate thermal conditions, 90^o domains should readily form. The substrate-film lattice mismatches at the growth temperature of 650 ^{o}C are 3.2% and 1.9% for Pt with PZT 40/60 and PZT 20/80 films, respectively, For PZT 40/60 and

PZT 20/80 films deposited on MgO, the substrate-film lattice parameter mismatches are 5.0% and 6.4%, respectively at 650 ^{o}C. The paraelectric state lattice parameters of 0.4048 nm and 0.3995 nm were used [12] for the PZT 40/60 and PZT 20/80 films, respectively.

3. Experimental Procedure

PZT 60/40, PZT 40/60, and PZT 20/80 thin films were fabricated using a modification of the hybrid solution deposition procedure [12] developed by Yi, Wu and Sayer. The 0.4 M solutions were synthesized using an inverted mixing order process [13] for which the Zr and Ti alkoxides were blended first before the addition of the Pb precursor. Excess Pb (5 mol%) was added to enhance formation of the perovskite phase and improve electrical properties. The thin films were deposited by spin coating at 3000 rpm for 30 s. Following deposition, each thin film layer was heat treated at 300 ^{o}C for 5 min on a hot plate. Typically, three film layers were deposited to attain a final thickness of approximately 300 nm after crystallization. Crystallization treatments ranged from 500 ^{o}C to 650 ^{o}C for 30 min in air or flowing oxygen. While a heating rate of 7500 ^{o}C/min was used for rapid thermal processing, heating rates of 50 ^{o}C/min were used for conventional furnace treatments. For stress measurements, a heating rate of 10 ^{o}C/min was used.

Approriate development of the underlying substrate technology allowed fabrication of PZT thin films of systematically varying crystallite orientation, 90^{o} domain configurations and grain size. From these films, the impact of each of these three parameters on PZT film dielectric properties could be determined. Relationships between 90^{o} domain assemblage and dielectric properties were clearly demonstrated for a series of four different PZT 40/60 films that were fabricated with multiple crystallite orientations. Two PZT 40/60 films were deposited on Pt coated MgO substrates and two PZT 40/60 films were deposited on Pt coated Si substrates using a 50 nm adhesion layer of Ti. Pt layers which were 200 nm and 100 nm thick were deposited at ambient on the Si and MgO substrates, respectively. For other experiments, PZT films deposited directly on epitaxially finished MgO substrates had a high degree of (001) crystallite orientation, and the 90^{o} domain assemblage depended on the processing temperature and cooling rate. Our highly (001) oriented PZT 40/60 films, for which we later discuss electrical measurements, were fabricated by the deposition at 620 ^{o}C of highly (100) oriented Pt on a (100) MgO substrate. For PZT films of rhombohedral symmetry, deposition at 550 ^{o}C of Pt on SiO_2/Si substrates resulted in a highly oriented (111) Pt film on which oriented (111) PZT 60/40 films were fabricated.

Stress in PZT films as a function of thermal history was monitored by wafer curvature using a laser reflectance technique [14]. The initial (100) MgO substrates that were 1 mm thick were ground to 75 μm thickness for the stress measurement. Platinum layers that were 100 nm thick were RF sputter deposited on both sides of the wafer to nullify the effect of the Pt on the stress behavior of the PZT films. Two different PZT 20/80 films deposited on platinum coated MgO were analyzed. The amorphous, dried films were heated at 100 cm to crystallization temperatures of 500 ^{o}C or 650 ^{o}C,

respectively, for a soak time of 30 min. For stress measurements of PZT films on Si, Pt was RF sputter deposited onto the Si substrates at 500 ^{o}C to enhance adhesion. Because of electrode stack interactions, which affected the stress measurements, Ti interlayers were not used. The Si substrate was also approximately 75 mm thick to permit accurate stress measurements. A PZT 53/47 film deposited on Si was monitored for stress versus thermal history behavior. While multiple crystallite orientations were evidenced by X-ray diffraction for all three of the films, PZT films deposited on platinized MgO were essentially bimodal (111) and (100) crystallite orientation and the PZT film deposited on platinized Si had a degree of preferential (111) orientation.

4. Results and Discussion

We have previously demonstrated [1] that rhombohedrally distorted PZT 60/40 films of similar crystallite orientation (highly (111) oriented) have vastly different electrical properties when deposited on platinized Si or platinized sapphire substrates. The remanent polarization of the film on the sapphire substrate was 40.6 ± 3.8 μC/cm^2, while the remanent polarization of the PZT 60/40 film on Si was 20.2 ± 1.9 μC/cm^2. This substantial change in remanent polarization also is observed for tetragonally distorted PZT 40/60 films. Figure 1 shows the measured remanent polarization of PZT 40/60 films versus the thermal coefficient of expansion (TCE) of 4 different substrates upon which they were deposited. Each substrate was approximately 1 mm thick.

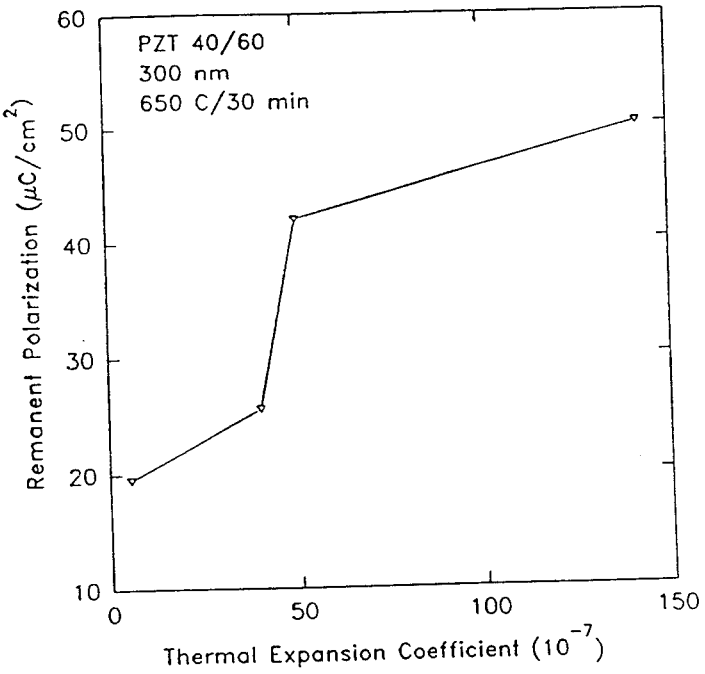


Figure 1. Remanent polarization of PZT 40 / 60 films as a function of the thermal coefficient of expansion of the underlying platinum coated substrate.

The thermal expansion coefficient in the temperature range of 400 ^{o}C to 600 ^{o}C was used, since we later show that this temperature range is critical for determining 90^{o} domain assemblages in PZT thin films. The remanent polarization montonically decreases as the thermal expansion coefficient of the substrate decreases. Substrates with lower thermal expansion coefficient will have tendency to put the PZT film in tension at the Curie point. The change in remanent polarization is substantial for these otherwise identically processed films, ranging from less than 20 $\mu C/cm^2$ to 50 $\mu C/cm^2$. It is the objective of the remainder of this paper to determine the cause of these substantial changes.

Our approach will be to postulate the reasons for the above behavior and then in subsequent paragraphs present supporting evidence for the postulations. Implicit in our discussion is that all PZT films are single phase perovskite. No second phases exist. Further, all films consist of columnar grains that extend from the bottom electrode to the top of the film. Among the features of a PZT film that have the strongest impact on dielectric properties are crystallite orientation and 90^{o} domain assemblages. Previously [15], we showed that remanent polarization systematically increased with the degree of (001) crystallite orientation for PZT 40/60 films deposited on platinized MgO substrates and crystallized at 650^{o}C. The values of remanent polarization were in quantitative agreement with values calculated from the volume fraction of different crystallites. We demonstrate in this paper that 90^{o} domain orientation and assemblage is largely controlled by the stress at the transformation temperature. Because these 90^{o} domains are not electrically reversible, their orientation and assemblage has a substantial influence on the the values of remanent polarization that are measured. If a majority of the 90^{o} domains were electrically reversible, as in large grain bulk ceramics [8], the original orientation and assemblage of these 90^{o} domains would have little impact on the remanent polarization values of the films. We show that this is not the case. We assume that all 180^{o} domains are electrically switchable. Our postulates can be summarized as follows:

1) While crystallite orientation is determined by substrate lattice parameter at the growth temperature for topotactical films, many factors influence the volume fraction of a given crystallite for nontopotactical films.

2) Transformation stress is a dominant factor in the genesis of 90^{o} domain assemblages.

3) Grain size can suppress 90^{o} domain formation: No 90^{o} domains are observed in grains less than 0.1 μm, single 90^{o} bands are observed in grains ranging from 0.2 μm to 1 μm, and for grain sizes greater than 1 μm multiple 90^{o} lamellae are observed.

The previous paragraph describes the statics of 90^{o} ferroelectric domains in PZT thin films. Our assumptions for domain dynamics in PZT thin films are very simple. All 180^{o} domains are electrical switchable, no 90^{o} domains are electrically reversible. We postulate that all 180^{o} domains switch, since highly (001) oriented PZT films fabricated by sol-gel [8] (PZT 40/60 on MgO) have remanent polarization values close to single crystal values. For hypothetical PZT 40/60 single crystals, the remanent polarization values are estimated to be in the range of 65 to 68 $\mu C/cm^2$. The aforementioned (001) oriented films had measured remanent polarization values of approximately 60 $\mu C/cm^2$. The only way to explain such high values of remanent

polarization is that essentially all of the 180° domains are electrically reversible. One would expect that all 90° domains in these films would also switch; however, for these highly oriented sol-gel films with grain size on the order of 0.1 μm, X-ray diffraction and TEM analyses indicate ittle or no evidence of 90° domain formation. We will verify the assumption that the electrical switching of 90° domains, in those films in which they form, is severely limited later in this paper.

Figure 2 shows the stress versus thermal history of two otherwise identically processed PZT 20/80 films, deposited on Pt//MgO substrates, that were crystallized at 500 °C and 650°C, respectively. Both films were heated at 10 °C/min, were approximately 300 nm thick, and were deposited on a 100 nm thick Pt // 75 μm thick MgO substrate structure. Stress was monitored via wafer curvature using a laser reflectance technique described previously [14]. The spin deposited films, which are dried at 300 °C using a hot plate, are amorphous and have a tensile stress of approximately 150 MPA. Upon heating from 300 °C, PZT film tension decreases because the thermal coefficient of expansion of the amorphous film is higher than that of the underlying MgO substrate. The PZT film stress abruptly becomes more tensile as the pyrochlore phase crystallizes at approximately 450 °C. At 500 °C, perovskite crystallization occurs and the tensile stress in the PZT film further increases. During the 30 min soak at 500 °C, the film tensile stress increases slightly due to further densification and conversion of remanent pyrochlore phases to perovskite.

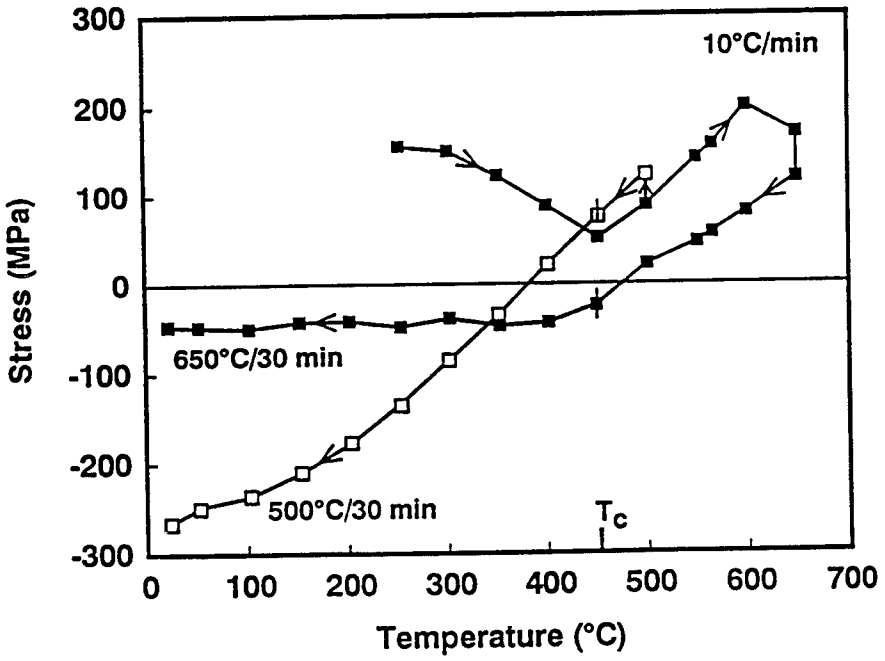


Figure 2. Stress versus thermal history behavior of two otherwise dentically processed PZT 20 / 80 thin films crystallized for 30 min at 500 °C and 650 °C, respectively.

The film stress upon cooling through the transformation temperature is a major factor in the determination of 90° configurations in PZT thin films. As the PZT 20/80 film crystallized at 500 °C cools, the PZT film tensile stress decreases, since the TCE of the PZT paraelectric state (10 X 10-6) is less than that of the MgO substrate (14 X 10-6). Importantly, the PZT film is still under tension as it cools through the transformation temperature. Thus, there is a force that favors elongation of the PZT unit cell in the plane of the film, and it is expected that the PZT film becomes preferentially a-domain oriented when it is under tension at the Curie point. That is, the c-axes of the tetragonal unit cells, being larger than the a axes, are preferentially aligned in the plane of the film. Upon cooling below the transformation temperature, the PZT film stress switches sign and becomes highly compressive. If the PZT film is preferentially a-domain oriented, high compression is expected, considering the change in a and c lattice parameters with temperature. The a lattice parameter decreases with decreasing temperature, while the c lattice parameter increases with decreasing temperature, the magnitude of the c parameter change being larger than the a parameter change. Both a and c lattice parameters are in the plane of the a-domain film, complicating a quantitative analysis. However, the in-plane TCE for an a- domain film should be less than that for the MgO substrate and considerable compressive stress should develop in the PZT film as it cools to ambient, as observed.

The stress behavior of the PZT 20/80 film that is crystallized at 650 °C is substantially different than that for the film crystallized at 500 °C. Upon cooling to the transformation temperature (450 °C), PZT film tensile stress decreases and becomes compressive, in reasonable quantitative agreement with the TCE mismatch between substrate and the paraelectric perovskite phase. At the Curie point, the film is under compression and highly c- domain oriented films are obtained. The compression favors the smaller a lattice parameters rather than the c lattice parameter being in the film plane. A preferential c-domain film that contains a majority of a lattice parameters in the film plane should have a higher TCE than a preferential a-domain film as it cools below the Curie point. Thus, as the c-domain film cools to ambient, it should develop less compressive stress than the a-domain film, which was crystallized at 500 °C, as shown in Figure 2.

Nonelastic behavior is observed above 600 °C for the PZT 20/80 film deposited on an MgO substrate. Upon heating the film from 500 °C to 600 °C, PZT film tensile stress increases, in semiquantitative agreement with the TCE mismatch between the substrate and the film. Above 600 °C, linear behavior is no longer observed and stress relaxation occurs. Stress relaxation and associated decrease in tension of the film continues during the 30 min soak at 650 °C. Among the possible causes of the mechanical relaxation are the following:

(1) Nabarro-Herring creep in the PZT thin film,
(2) plastic deformation of the Pt film,
(3) creep in the MgO, and
(4) interfacial film slippage between the MgO and Pt.

From our work on the stress behavior of PZT films deposited on Si substrates where severe nonelastic behavior was not observed, mechanisms 3 and 4 are most likely at the present time. Davidge [16] has reported plastic deformation in MgO for temperatures as low as ambient, although stress levels of approximately 100 MPa would be required for our case.

An experiment in which the percentage of a and c domains are monitored by X-ray diffraction for PZT 20/80 films crystallized at three different temperatures, provides strong support for the transformation stress - 90° domain formation concept. The PZT 20/80 films were deposited directly on MgO and crystallized at the following temperatures: 500 °C, 550 °C, and 650 °C. No Pt interlayer was used so that large grain (greater than 1 μm) PZT films would be obtained, which result in clear separation of (100) and (001) diffraction peaks. From Fig. 3, the film crystallized at 500 °C is highly a domain oriented, while the film crystallized at 650°C is highly c domain oriented. If complete strain relaxation of the PZT 20/80 films were to occur at the crystallization temperatures, from Fig. 2, it would be expected that the high TCE of MgO would cause the film to be in compression as it is cooled through the Curie Point and a high degree of c-domain orientation would result. However, there is residual tensile stress in the films after crystallization as shown in Fig. 2. The film crystallized at 500 °C is in tension as it cools through the Curie point, despite the high TCE of the MgO substrate, and preferential a-domain (100) orientation results. Conversely, the film crystallized at 650 °C is under compression as it cools through the Curie point and preferential c-domain orientation occurs. Interestingly, the 500 °C film is under far greater compressive stress at ambient than the 650 °C. This result strongly suggests that the film stress at the transformation temperature, rather than the ambient film stress, is the dominant factor that influences 90° domain formation in these chemically prepared PZT thin films.

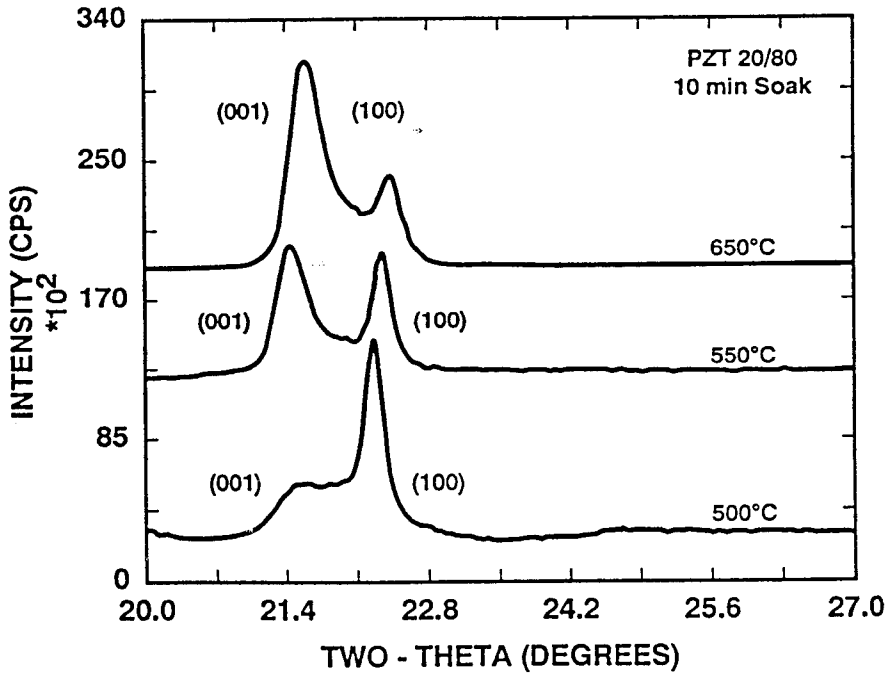


Figure 3. X - ray diffraction patterns of three otherwise identically processed PZT 20/80 thin films crystallized at 500 °C, 550 °C and 600 °C, respectively [1].

From the previous stress experiments and microstructural characterization of our PZT films we have drawn a schematic diagram, shown in Fig. 4, depicting the 90° domain orientation on an individual crystallite basis for a film in tension at the Curie point and a film in compression at the Curie point. The polarization vector is coincident with the c crystallographic direction in a given domain. Consider the crystallites at the far left of each film that have cubic (100) orientation above the Curie point. The (100) crystallite that cools through the transformation temperature in compression will have the polarization vector perpendicular to the film plane. The maximum single crystal remanent polarization will be obtained from this crystallite. For the film that is in tension at the Curie point, the polarization vector will lie in the plane of the film and the polarization measured in the major film plane will be zero. If we now consider the case of the cubic (110) crystallite, as it cools through the Curie point under tension it will remain (110) oriented with respect to the major film plane. The polarization vector will be in the plane of the film, and the measured polarization will be zero for this crystallite. Conversely, if the cubic (110) crystallite is cooled through the Curie point under compression, it becomes (101) oriented and the polarization vector is at an angle of 45° to the major film plane. Thus, the polarization contribution from the (101) crystallite will be 70.7% of the single crystal value.

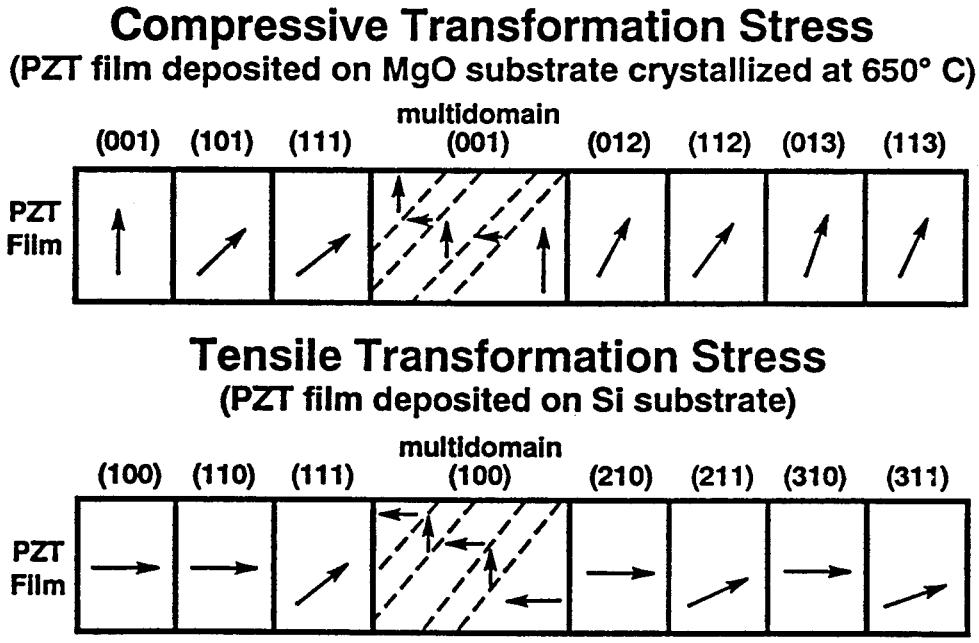


Figure 4. Schematic diagram of 90° domain assemblage and polarization vector orientations for PZT thin film under a) compressive and b) tensile stress at the transformation temperature.

Similar treatments can be considered for all the other crystallite orientations and the contribution of each crystallite to the macroscopic remanent polarization in terms of the fraction of the single crystal remanent polarization can be calculated. An interesting case is that of the (111) crystallites. The orientation of the polarization vector is independent of the stress at the Curie point. Macroscopically, a (111) oriented film deposited on Si should have the same remanent polarization as a (111) oriented film deposited on MgO, 57.7% of the single crystal value. From our transformation stress concept, the highest polarization achievable for a fine grain, chemically prepared PZT film deposited on Si would be for all crystallites having (111) orientation. For a final example, consider the case of the (211) crystallite (tension) for which the angle of the polarization vector with respect to the major film plane is 73.2°; whereas, for a (112) crystallite (compression) the angle is 26.4°. Thus, polarization contributions of 29% and 90% of the single crystal values would be expected for a-domain versus c-domain crystallites.

An important consideration for many PZT films is the effect of grain size on 90° domain formation. In Fig. 4, we show a large (100) crystallite (0.5 μm), for which our TEM results indicate that some 90° domain lamellae will be formed as the film cools through the Curie point. For the large grain under compressive stress, a significant volume percent of the grain is a-domain oriented, unlike smaller grains which have zero volume percent a-domains. It is obvious that a lower contribution to the macroscopic polarization on a volume percent basis will be obtained from the larger crystallite. Conversely, for the 0.5 μm PZT crystallite in tension, a portion is c-domain oriented; thus, this large grain will have a greater remanent polarization contribution than its fine grain counterpart that is in tension at the Curie point. The above analysis indicates that fine grain PZT films deposited on Si and MgO substrates and crystallized at 650 °C will have a larger difference in measured remanent polarizations, than similarly processed large grain PZT films.

In an effort to rigorously test our transformation stress - 90° domain concept, we have devised an experimental matrix consisting of four PZT 40/60 thin films. Two films each were deposited on platinum coated MgO and Si substrates and crystallization temperatures of 550 °C and 650 °C were used. From our transformation stress concept, we predict the following electrical and structural property relationships. The two films deposited on Si will be in tension at the Curie point and structurally we anticipate that the film will exhibit a-domain behavior. That is the integrated intensity of the (100), (110), (210), (211), etc. X-ray diffraction peaks will be substantially greater than the (001), (101), (012), (112), etc. diffraction peaks. Based on single crystal behavior of 4mm simple perovskites, one would expect that the PZT 40/60 films deposited on Si will have low values of remanent polarization, but a high value of low field dielectric constant. The film crystallized at 650°C and deposited on Pt coated MgO is expected to have a high degree of c-domain behavior. Integrated intensities of the (001), (101), (012) and (211) diffraction peaks are projected to be substantially larger than their (100), (110), (210) and (211) counterparts. Larger remanent polarization and lower low field dielectric constants are expected to be measured than for the case of the Si substrates. The final film crystallized at 550 °C on platinized MgO is expected to show a mixture of c and a domain behavior and thus have intermediate polarization and low field dielectric constant values.

Structurally, the four PZT 40/60 films are in fair agreement with our transformation stress concept. X-ray diffraction patterns of the PZT 40/60 films crystallized at 650 °C

are shown in Fig. 5. The film deposited on Si is in tension at the transformation temperature and exhibits a-domain behavior. The integrated intensities of the (100), (110), (200), (210) and (211) diffraction peaks are considerably greater than their (001), (101), (002), (012), and (112) counterparts. Conversely, the PZT 40/60 film deposited on MgO is in compression near the Curie point and exhibits c- domain behavior. The integrated intensities of the (001), (101), (012) and (112) diffraction peaks are considerably less than their (100), (110), (210), and (211) counterparts. Thus crystallites of all orientations are affected by the transformation stress in a consistent matter.

The PZT 40/60 thin film crystallized at 550 ^{o}C has different percentages of a and c-domains than originally postulated. Instead of approximately 50% each of a and c-domains this film consisted of entirely c-domains. Our previous observation for equal a and c domain populations was for a PZT 20/80 film deposited directly on MgO. The lattice parameter mismatch between substrate (Pt) and PZT film is most likely the primary reason [9] for the decrease in a-domain population. Since the Pt lattice parameter is less than that of the PZT film it will favor compression of the PZT film at the Curie point and thus a-domain formation. Phase evolution as a function of temperature for films of the two different stoichiometries and the TCE mismatch associated with the different paraelectric phases are other reasons for the difference in domain populations.

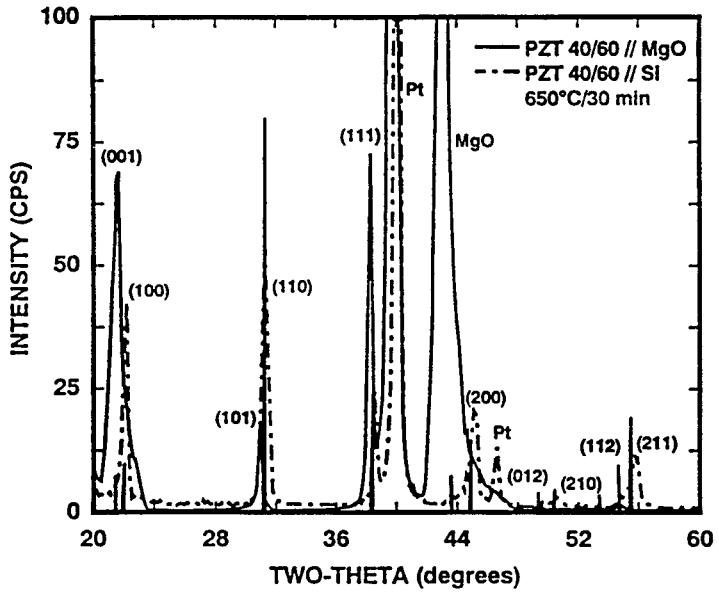


Figure 5. X-ray diffraction patterns of PZT 40/60 films with multiple crystallite orientations deposited on Pt coated wafers of silicon and MgO.

We present electrical properties from two sets of four films: (1) new films with good electrical properties, but with grain size variation between films, and (2) films from aged solutions which do not have as good electrical properties, but all have similar grain size (0.7 μm to 1.0 μm). Table 1 shows the electrical properties and orientation results from the new films. The top electrodes of all films were annealed at 550 ^{o}C for 30 min in air. For films crystallized at 550 ^{o}C, the film on Si has a lower remanent polarization (24.3

$\mu C/cm^2$ compared to 37.7 $\mu C/cm^2$), but a higher dielectric constant (1014 compared to 726) than the PZT 40/60 film deposited on Si. For PZT 40/60 films crystallized at 650°C, similar behavior is observed. The remanent polarization is less (32.2 $\mu C/cm^2$ compared to 50 $\mu C/cm^2$) and the dielectric constant more (1024 compared to 400) for the film deposited on Si compared to deposition on MgO. The film deposited on Pt//MgO and crystallized at 650 °C had a bimodal (111) and (100) crystallite orientation. Nonetheless, the correlation with the transformation stress model considering the integrated intensities of the (002) to the (200) diffraction peaks is consistent. The fact that the dielectric constant of the films deposited on Si is greater than those films deposited on MgO strongly argues against the loss of Pb on Si causing the formation of second phases.

TABLE 1. Electrical Property - structure relationships of new PZT 40/60 films

Film Description	Pr ($\mu C/cm^2$)	k (10 kHz)	(002):(200)
550°C - Si	24.3	1014	1:4
550°C - MgO	37.7	726	4.4:1
650°C - Si	32.2	1027	1:4
650°C - MgO	50.0	400	20:1

A factor that is not consistent in the first set of four PZT 40/60 films is grain size. For example, the film crystallized at 550 °C on MgO has a grain size of 0.7 mm, but the film deposited on Si and crystallized at 550 °C has a grain size of 0.1 mm. To obtain films of similar grain size, we aged our second set of films on substrates for 1 month and crystallized the four films under the same conditions as the first set (see Table 2). All four films of the second set had similar grain size, 0.7 to 1.0 mm. We postulate that a similar grain size is obtained for all films, since limited topotactical relationships develop between film and substrate compared to the first set. Thus, less constrainment of lateral PZT grain growth occurs due to the underlying fine grain Pt films, for this case of limited epitaxy. Consistent with this hypothesis, a more random crystallite orientation was developed in the second set of films. While the PZT films deposited on MgO substrates were essentially randomly oriented, the films deposited on Si were preferentially (111) oriented but contained a significant number of other crystallite orientations.

TABLE 2. Electrical property - structure relationships of aged PZT 40/60 films

Film Description	Pr ($\mu C/cm^2$)	k (10 kHz)	(101):(110)
550°C - Si	13.2	473	0:13
550°C - MgO	18.2	360	14:2
650°C - Si	22.1	676	0:14
650°C - MgO	29.8	411	17:2

The PZT 40/60 films deposited on Si had higher dielectric constants and lower remanent polarizations than their counterparts deposited on MgO. The film deposited on Si at 550 °C had a low resistivity (10^6 ohm-cm) compared to resistivity values greater than 10^{10} ohm-cm for the other films. The remanent polarization value for the 550 °C-Si film was obtained by subtracting out the charge contribution from charge transport due to the low resistivity. The integrated intensities of the (101):(110) peaks are consistent with the transformation stress concept; the ratio being greater than 1 for the films deposited on MgO and less than 1 for the films deposited on Si. These films have worse electrical properties than expected for single phase perovskite films; thus, it is likely that a second phase is present in these films that is not ferroelectric. While this violates our original premise that the PZT films be single phase perovskite, the relationships predicted from the transformation stress concept still hold.

A significant premise to our transformation stress concept is that electrical switching of 90° domains is quite limited in PZT thin films. We have performed X-ray diffraction analysis on a 0.8 μm thick PZT 40/60 film deposited on a platinized Si substrate as a function of applied electric field. The X-ray diffraction traces for 4 different field conditions are shown in Fig. 6. A top Pt electrode of 4 cm^2 area and 0.1 μm thickness was deposited, which allowed the X-ray beam to only sample the top electrode area. As expected, the as deposited sample exhibited a- domain behavior, as typified by the large (200) to (002) peak intensity ratios. Application of +12 volts resulted in little change to the (200) to (002) peak intensity. If significant 90° domain switching occurred, a large change in (200) to (002) peak height ratio would be expected. A remanent polarization of approximately 25 $\mu C/cm^2$ was measured for this voltage level, after the X-ray diffraction measurement. Returning the voltage to zero volts, the positive remanent polarization state, did little to change the X-ray diffraction pattern. Similarly, applying -12 volts, which should put the film in the negative remanent polarization state, there was little change in the ratio of (200) to (002) peak heighths.

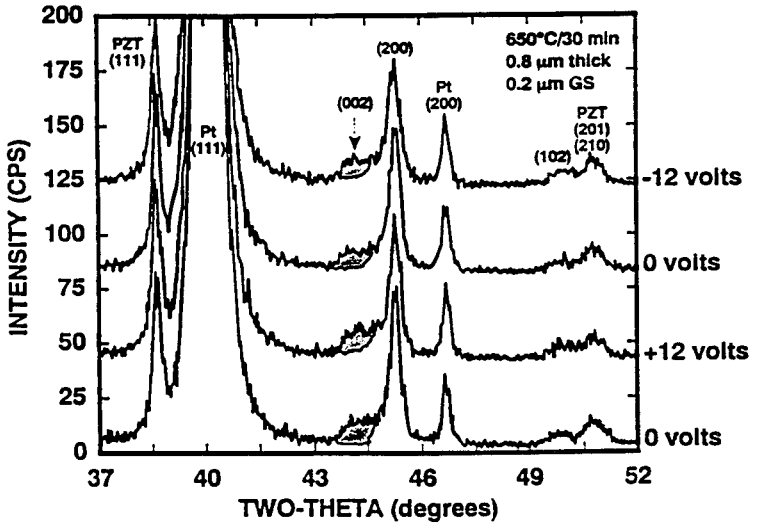


Figure 6. X-ray diffraction patterns of a PZT 40/60 film for different applied field levels.

Grain size - 90° domain relationships for our chemically prepared PZT 40/60 films are similar to those observed in bulk tetragonally distorted ceramics. Previously [18] we have shown ferroelectric domain patterns for PZT 20/80 and PZT 40/60 thin films as a function of grain size. A cross- sectional TEM of a highly oriented (001) PZT 40/60 film deposited on platinized MgO shows no evidence of 90° domains for 0.1 μm grain size films. The grain substructure that is observed in 30% of the grains does not contain diffraction contrast along (110) planes (the 90° domain twin plane). We have observed single domain lamellae in 0.2 μm grains for a PZT 20/80 film deposited directly on MgO and crystallized at 475 °C for 20 min. As grain size is increased to 1 μm, for PZT 20/80 films deposited directly on MgO and crystallized at 500 °C for 4 min, interpenetrating lamellae result in square- net domain configurations. These domain configurations in the (100) oriented grains although not identical, appear similar, to square-net domain configurations observed19 in single crystal $BaTiO_3$. For randomly oriented crystallites of approximately 5 μm dimensions that were obtained for PZT 30/70 films deposited on RuO_2 coated Si substrates and crystallized at 550 °C for 30 min, complex 90° domain patterns are also observed. While the 90° domain patterns do not have the regularity of the domain patterns of the PZT films deposited directly on MgO substrates, due to random crystallite orientation, there is significant interaction of 90° domain lamallae. In several instances, square net patterns do appear to form in order to minimize stress. These analyses provide the basis for our assumptions of the change in 90° domain configurations with grain size in chemically prepared PZT thin films.

5. Conclusions

We have determined the relationships among crystallite orientation, domain orientation and electrical properties for a series of chemically prepared PZT 40/60 thin films that exhibited multiple crystallite orientations. Because the substrate lattice parameter and the cooling rate through the transformation temperature were held constant in this study, the thermal coefficient of expansion of the substrate was a major factor in determining the 90° domain orientation of the films. PZT films deposited on low TCE substrates, such as, silicon were preferentially a-domain oriented. PZT films deposited on high TCE substrates, such as, MgO were preferentially c-domain oriented. PZT 40/60 films that were a-domain oriented had lower remanent polarizations and higher dielectric constants than films that were c-domain oriented. The larger low field dielectric constant for the a-domain films argues against the presence of nonperovskite phases as the cause of the electrical property relationships for these films. We have directly shown that electrical switching of 90° domains is very limited for PZT 40/60 films of approximately 0.2 μm grain size. Grain size - 90° domain relationships for PZT thin films were somewhat similar to those in bulk ferroelectrics, as there appears to be a critical grain size below which no 90° domain formation occurred.

6. Acknowledgements

The authors would like to acknowledge support of this work performed at Sandia National Laboratories by the U.S. Department of Energy under contract # DE-ACO4-94AL85000. The authors also gratefully acknowledge enlightening technical discussions with Jim Speck, Angus Kingon, R. Ramesh, Gordon Pike, Bill Warren, Ed Beauchamp, Jill Glass, and David Clarke. We also acknowledge the technical contributions of Dave Goodnow, Diana Lamppa and Mary Gonzales.

7. References

1. Tuttle, B.A., Voigt, J.A., Garino, T.J., Goodnow, D.C., Schwartz, R.W., Lamppa, D.L., Headley, T.J. and Eatough, M.O. (1992), *Proc. of the Eighth Int. Symp. on Appl. of Ferroelectrics*, Liu, M., Safari, A., Kingon, A. and Haertling, G. (ed.), pp. 344.
2. Kingon, A.I. (1993), DARPA Program Review, February 3, Washington, DC. 3. Speck, J., Seifert, A., Pompe, W. and Ramesh, R.J. (1994), *Appl. Phys.* **76** [1], 477.
4. Gaswami, A.K., Buessem, W.R., and Cross, L.E. (1966), *J. Am. Ceram. Soc.* **491**, 33.
5. King, G. and Goo, E.K. (1990), *J. Am. Ceram. Soc.* **73** [6], 1534.
6. Demczyk, B.G. and Rai, R.S. (1990), *J. Am. Ceram. Soc.* **73** [3], 615.
7. Arlt, G. (1990), *Ferroelectrics* **104**, 217.
8. Arlt, G. and .Sasko, P. (1980), *J. Appl. Phys.* **51**, 4956.
9. Speck, J., Pompe, W. (1994), *J. Appl. Phys.* **76** [1], 466.
10. Kwak, B.S. and Erbil, A., Wilkens, B.J., Budai, J.D., Chisholm, M.F. and Boatner, L.A. (1992), *Phys. Rev. Lett.* **68** [25], 3733.
11. Amin, A. and Newnham, R.E. (1988), *Powder Diffraction* **3** [1], 23.
12. Yi, G., Wu, S. and Sayer, M. (1988), *J. Appl. Phys.* **64** [5], 2717.
13. Schwartz, R.W., Bunker, B.C., Dimos, D.B., Assink, R.A., Tuttle, B.A., Tallant, D.R. and Weinstock, I.A. (1993), *Proc. of 3rd Int. Symp. on Ferroelectrics , pp.* 535.
14. Garino, T.J. and Harrington, M. (1992), *Ferroelectric Thin Films II, MRS Symposium Proceedings*, Vol. **243**, Kingon, A.I., Myers, E., and Tuttle, B. (eds.) , 341.
15. Tuttle, B.A., Voigt, J.A., Goodnow, D.C., Lamppa, D.L., Headley, T.J., Eatough, M.O., Zender, G., Nasby, R.D. and Rodgers, S.M. (1993), *J. Am. Ceram. Soc.* **76** [6], 1537.
16. Davidge, R.W. (1986), *Mechanical Behavior of Ceramics*, Cambridge University Press, 16-17, pp. 91.
17. Tuttle, B.A., Voigt, J.A., Headley, T.J., Potter, B.G., Dimos, D., Schwartz, R.W., Dugger, M.T., Michael, J., Nasby, R.D. and Goodnow, D.C. 1993), *Proc. of Eighth International Meeting on Ferroelectricity*, August 8-11, Gaithersburg, MD.
18. Fosbergh, R. (1949), *Phys. Rev.* **76** [1], 1187.

CHARACTERIZATION OF SOL-GEL $Pb(Zr_xTi_{1-x})O_3$ THIN FILM CAPACITORS WITH HYBRID (Pt, RuO_2) ELECTRODES

H.N. AL-SHAREEF, [1] O. AUCIELLO [1,2] AND A.I. KINGON[1]
1. *Department of Materials Science and Engineering, North Carolina State University, Raleigh, NC 27695, USA*
2. *MCNC, Electronics Technology Division, Research Triangle Park, NC 27709-2889, USA*

ABSTRACT. $Pb(Zr_xTi_{1-x})O_3$ (PZT) thin film capacitors with RuO_2 electrodes exhibit excellent polarization fatigue characteristics, but they have rather high leakage currents (typically 10^{-3} A/cm^2 at 1 Volt). On the other hand, PZT capacitors with Pt electrodes have low leakage currents (typically less than 10^{-9} A/cm^2 at 1 Volt), but they undergo severe polarization fatigue. We have developed new (Pt, RuO_2) hybrid electrodes which result in PZT capacitors that combine the excellent fatigue behavior of RuO_2/PZT/RuO_2 capacitors with the low leakage currents of Pt/PZT/Pt capacitors. The hybrid electrodes studied were of two main types: one type consisted of a Pt/RuO_2 or RuO_2/Pt double layer while the other consisted of a Pt-RuO_2 co-deposited layer. Each hybrid electrode was used as a bottom electrode to produce PZT capacitors with RuO_2/PZT/hybrid electrode heterostructures. Use of some hybrid electrodes resulted in capacitors with negligible fatigue up to 10^{11} switching cycles and a leakage current two to four orders of magnitude lower than those observed on RuO_2/PZT/RuO_2 capacitors. In addition, the capacitors with hybrid electrodes showed very small retention loss.

1. Introduction

Lead zirconate titanate, $Pb(Zr_xTi_{1-x})O_3$ or PZT, ferroelectric thin film capacitors have been studied over the past few years as candidates for use in nonvolatile memories. The PZT capacitors are normally fabricated using either metal or oxide electrodes. The most commonly used metal electrode has been Pt, while the most commonly used oxide electrodes have been RuO_2 and $La_{1-x}Sr_xCoO_3$[1-7]. However, in both cases, the PZT capacitors have drawbacks which can hamper their use in nonvolatile memories. For example, while Pt/PZT/Pt capacitors have low leakage current and relatively good dielectric breakdown properties, they undergo a severe polarization fatigue problem upon repeated switching. On the other hand, oxide/PZT/oxide heterostructures have excellent resistance to polarization fatigue, but they usually have high leakage currents and are more susceptible to dielectric breakdown. Researchers have attempted to improve the

O. Auciello and R. Waser (eds.), Science and Technology of Electroceramic Thin Films, 133-146.
© 1995 *Kluwer Academic Publishers. Printed in the Netherlands.*

fatigue characteristics of Pt/PZT/Pt capacitors using various approaches. These included donor doping of the $Pb(Zr_xTi_{1-x})O_3$ films [8,9], changing the Zr/Ti ratio[10,11], and growth of epitaxial PZT thin films[3]. Unfortunately, only marginal improvement in the polarization fatigue of Pt/PZT/Pt capacitors could be achieved.

There were also attempts to reduce the leakage current of PZT films grown on oxide electrodes. These included donor doping of the PZT films with elements such as La^{3+} [12] and, in the case of RuO_2, annealing the bottom RuO_2 electrode prior to PZT film deposition [13]. These methods have resulted in some improvement of the leakage characteristics of oxide/PZT/oxide capacitors. An alternative approach which our group has also been developing is the use of hybrid (Pt,RuO_2) electrodes which is the subject of this paper. Use of some of these hybrid electrodes resulted in PZT thin film capacitors which combine the excellent fatigue characteristics of RuO_2/PZT/RuO_2 capacitors with the good leakage current characteristics of Pt/PZT/Pt capacitors. The presence of RuO_2 in the hybrid electrode results in the good resistance of PZT capacitors to polarization fatigue. On the other hand, the presence of Pt in the hybrid electrodes results in lowering the leakage currents of PZT capacitors grown on hybrid (Pt,RuO_2) electrodes. In this paper the types of hybrid electrodes used and their effect on the electrical properties of sol-gel derived PZT thin film capacitors are discussed.

2. Experimental

Five capacitor types were prepared for this study. Three of the capacitors had hybrid (Pt,RuO_2) bottom electrodes, namely, RuO_2/PZT/Pt/RuO_2/MgO, RuO_2/PZT/RuO_2/Pt/MgO and RuO_2/PZT/(Pt-RuO_2)/MgO. A schematic of these three capacitors is shown in Fig.1. The other two capacitors, which are included for comparison, had similar top and bottom electrodes: Pt/PZT/Pt/MgO and RuO_2/PZT/RuO_2/MgO. Details of the Pt and RuO_2 deposition conditions can be found elsewhere[14]. In the case of the RuO_2/PZT/Pt/RuO_2/MgO capacitor, shown in Fig.1(a), a Pt interlayer (100Å thick) was deposited on the bottom RuO_2 electrode, prior to PZT growth, both by ion beam sputter-deposition (at 400°C) and by magnetron sputter-deposition (at room temperature). In the case of the RuO_2/PZT/RuO_2/Pt/MgO capacitor, Fig. 1(b), a 200Å RuO_2 interlayer was deposited by ion beam sputter-deposition at 400°C on the Pt bottom electrode prior to PZT film growth. For the RuO_2/PZT/(Pt-RuO_2)/MgO capacitor, Fig. 1(c), the bottom electrode was a co-deposited Pt-RuO_2 layer. The Pt-RuO_2 layer was grown using ion beam sputter-deposition at 400-500°C. The sputtering target consisted of both Pt and Ru metals. The thin Pt/RuO_2, thin RuO_2/Pt and the co-deposited (Pt-RuO_2) bottom electrodes will be referred to as "hybrid (Pt,RuO_2) electrodes" in this paper.

PZT thin films (0.2-0.25 mm thick) were subsequently deposited on the Pt, RuO_2, and the hybrid bottom electrodes using a spin-on sol-gel process described elsewhere[15]. The solution used to make the PZT films for this study had a Zr/Ti ratio of 53/47 and a 5mol% excess Pb to compensate for lead loss during annealing. Each film was formed by multilayer deposition, with each layer initially heat treated at 300°C for 5 minutes in air. The films were finally crystallized by annealing at 700°C for 10 minutes in air. For all capacitors, except the Pt/PZT/Pt/MgO capacitor, RuO_2 top electrodes were deposited on the PZT films using ion beam sputter-deposition. The top electrodes were

patterned using standard photolithographic techniques and ion beam etching (500 eV, 8 mA Ar^+ ion beam). After patterning of the top electrodes, the entire capacitor stack was annealed at 550°C for 10 minutes in air.

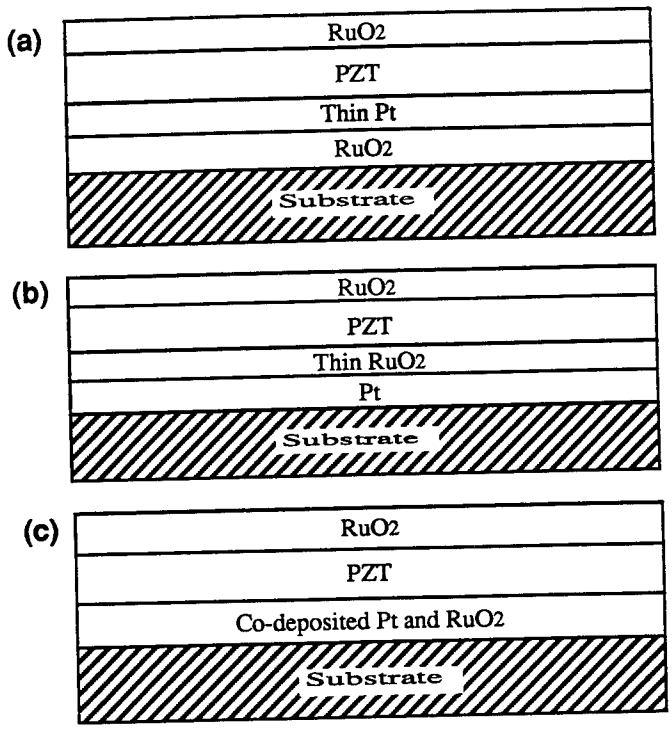


Figure 1. Schematic of three PZT capacitors with the hybrid bottom electrodes: (a) thin Pt/RuO_2 (b) thin RuO_2/Pt and (c) co-deposited Pt-RuO_2 layer.

Hysteresis, fatigue, and retention tests were performed on the capacitors using the RT66A ferroelectric tester from Radiant Technologies (Albuquerque, NM). In the hysteresis tests, two measurements were made. First, a hysteresis loop was measured using a triangular wave form. Second, a pulse polarization measurement was performed. During the pulse polarization test, 5 triangular pulses (each 2ms in width) were applied to the capacitor and several parameters were measured including $\pm P^*$ and $\pm P^\wedge$. The switched polarization (P^*) was measured after subjecting the capacitor to two triangular pulses of opposite polarity, while the non-switched polarization ($P^\wedge$) was measured after subjecting the capacitor to two triangular pulses of the same polarity. The difference between the switched and non-switched polarization (P^*-$P^\wedge$) is the net switched charge and is the most relevant parameter in ferroelectric memory applications.

The fatigue tests were performed using a square wave with an amplitude of 3-5 Volts and a frequency of 500 kHz. The square wave was produced by a function generator externally connected to the RT66A tester. The fatigue tests were carried out by continuously cycling the PZT capacitor using the externally applied square pulse.

The cycling was periodically interrupted and a pulse polarization measurement was made. The retention tests were performed by first applying a write pulse (8.6 ms in width) to the capacitor to store a given logic state. After waiting for selected periods of time, a read pulse was applied to the capacitor. The switched polarization (P*r) was measured by using write and read pulses of opposite polarity, while the non-switched polarization (P^r) was measured by using write and read pulses of the same polarity.

The DC electrical current was measured using a Keithley 617 programmable electrometer. X-ray diffraction was used to determine the phases present in the films and their orientation. Rutherford backscattering spectrometry (RBS) was used to measure film thickness.

3. Results and Discussion

3.1. HYSTERSIS, FATIGUE, AND DC LEAKAGE

3.1.1. *Pt/PZT/Pt and RuO_2/PZT/RuO_2 Capacitors*

Before the properties of PZT capacitors with hybrid (Pt,RuO_2) electrodes are discussed, it is useful to present first the typical electrical characteristics of Pt/PZT/Pt and RuO_2/PZT/RuO_2 capacitors. The fatigue and DC leakage characteristics of typical Pt/PZT/Pt/MgO and RuO_2/PZT/RuO_2/MgO capacitors are shown in Figs. 2 and 3, respectively. Notice that the difference between the switched and non-switched polarizations (P*-P^) decays by nearly 95% after $3x10^{10}$ cycles in the case of the capacitor with Pt electrodes (the Pt/PZT/Pt/MgO capacitors have in some cases shown only 50% drop in (P*-P^), but most samples typically show more than 90% drop). In comparison, the (P*-P^) value of the RuO_2/PZT/RuO_2/MgO capacitor remains essentially constant up to $4x10^{10}$ switching cycles. While the capacitor with RuO_2 electrodes has superior fatigue, it has much higher leakage current than the Pt/PZT/Pt/MgO capacitor as shown in Fig. 3. Notice that the RuO_2/PZT/RuO_2/MgO capacitor has a leakage current that is several orders of magnitude higher than the Pt/PZT/Pt/MgO capacitor. This is also reflected in the hysteresis loops of both capacitors shown in Fig. 4. The Pt/PZT/Pt/MgO capacitor has a square and well saturated loop with a remanent and saturation polarization of 40 and 50 $\mu C/cm^2$, respectively. The high polarization values are expected since these films are grown on MgO single crystals, and they are very highly oriented. In comparison, the hysteresis loop of the RuO_2/PZT/RuO_2/MgO capacitor is characteristic of a leaky capacitor. The polarization values shown are abnormally high because during a hysteresis loop measurement the RT66A ferroelectric tester measures the charge collected on an integrating capacitor and converts it to a polarization value; the charge due to leakage also collects on the integrating capacitor and is therefore included in calculating the polarization.

The leakage current of PZT thin films grown by our sol-gel process on RuO_2 electrodes were previously shown to be bulk controlled[16]. Although not detected by x-ray diffraction, TEM has shown a second phase to be present in PZT thin films grown on RuO_2[17]. Preliminary results suggest that this second phase may be a conductive pyrochlore-type lead ruthenate ($Pb_2Ru_2O_{7-x}$) phase. However, more work is needed to confirm this preliminary finding. Thus, to reduce the leakage current of PZT films grown on RuO_2, it was necessary to eliminate this second phase. We have developed two

methods which eliminate or reduce the second phase, resulting in higher resistivities (lower leakage currents) of RuO_2/PZT/RuO_2/MgO capacitors. The first method is a high temperature anneal of the RuO_2 bottom electrode prior to PZT deposition and was discussed in an earlier paper[13]. The second approach is the use of hybrid (Pt,RuO_2) electrodes, discussed in this paper.

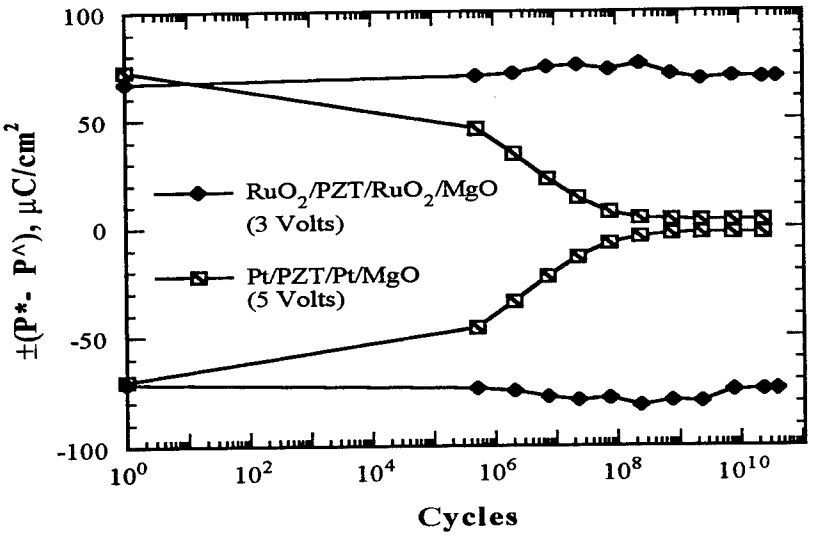


Figure 2. Fatigue curves of Pt/PZT/Pt/MgO and RuO_2/PZT/RuO_2/MgO capacitors. The fatigue tests were performed at 500 kHz.

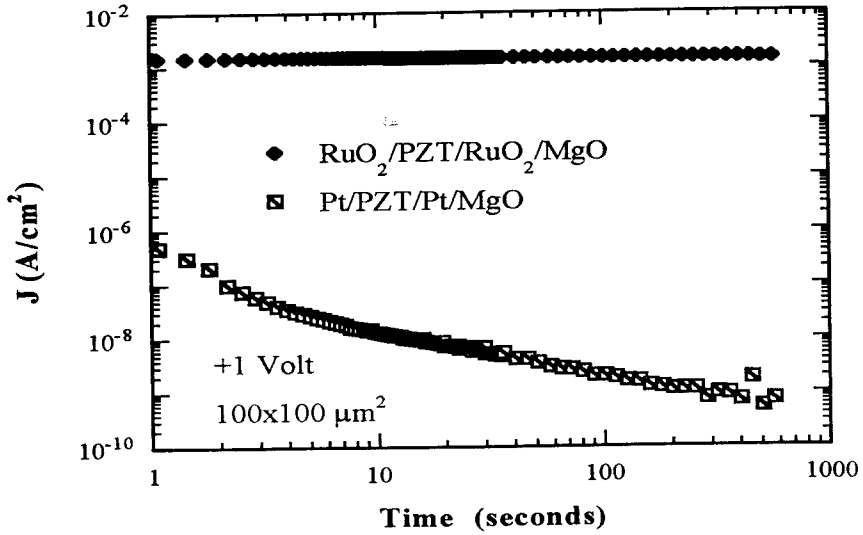


Figure 3. Time dependence of the DC electrical current of Pt/PZT/Pt/MgO and RuO_2/PZT/RuO_2/MgO capacitors.

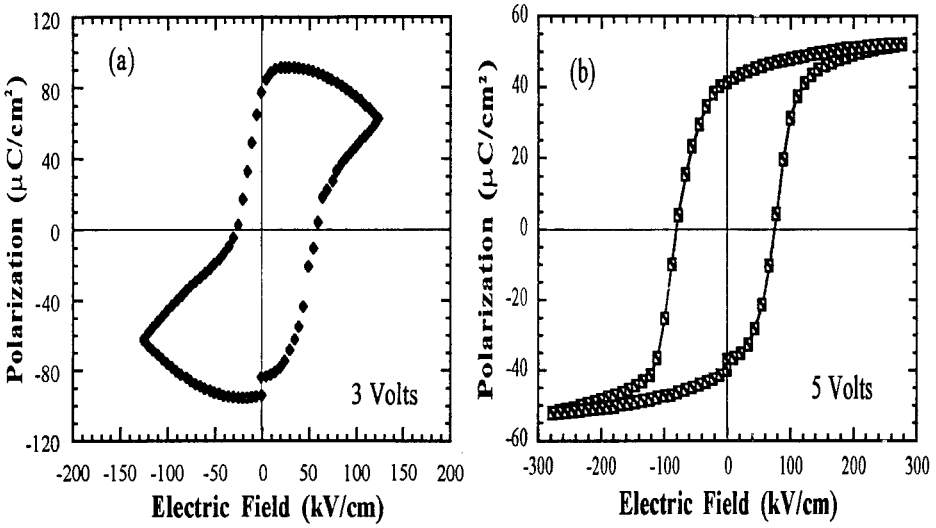


Figure 4. Hysteresis loops of (a) RuO_2/PZT/RuO_2/MgO and (b) Pt/PZT/Pt/MgO capacitors.

3.1.2. *PZT Capacitors with Hybrid Electrodes*

The hybrid (Pt,RuO_2) electrode concept was developed based on the observation that nucleation of single phase perovskite PZT films is easier to achieve on Pt than on RuO_2 electrodes[17]. PZT films grown on Pt were characterized by a high nucleation site density and were phase-pure perovskite. In comparison, the films grown on RuO_2 were characterized by a low nucleation site density and contained a non-ferroelectric conductive second phase[17]. Thus, by combining Pt and RuO_2 into one bottom electrode (hence the term hybrid electrode), one can enhance nucleation and crystallization of perovskite PZT, thereby eliminating the second phase and reducing the leakage current of the capacitors. If the amount of Pt in the hybrid electrode is properly controlled, the excellent resistance to fatigue can also be maintained.

Three hybrid electrode types were evaluated. The first consisted of a thin Pt layer on a bottom RuO_2 electrode; the second consisted of a thin RuO_2 layer on a bottom Pt electrode; the third was a co-deposited (Pt-RuO_2) layer used as a bottom electrode. A schematic of the cross section of PZT capacitors grown on these three hybrid electrode types was shown in Fig.1. The electrical properties (hysteresis, DC leakage, and fatigue) of PZT capacitors grown by the sol-gel process on these three hybrid electrodes are shown in Figs. 5-7. The fatigue and leakage behavior of the Pt/PZT/Pt/MgO and RuO_2/PZT//RuO_2/MgO are included in Figs. 6 and 7 to facilitate comparison.

Two PZT capacitors with the RuO_2/PZT/100ÅPt/RuO_2/MgO heterostructures, Fig. 1(a), were tested. One had a Pt interlayer produced by magnetron sputter-deposition at room temperature, while the other had a Pt interlayer produced by ion beam sputter-deposition at 400°C. Capacitors of this type typically had a remanent polarization of about 35-40 $\mu C/cm^2$ and they were fully switched at 3-4 Volts. A typical hysteresis loop

is included in Fig. 5. Notice that due to the asymmetry of the loop along the field axis, the actual remanent polarization value (+Pr) appears to be smaller than it actually is. This asymmetry results because the top and bottom electrodes are different, and the bottom electrode is usually exposed to higher temperatures (during film deposition) than the top one. Fig. 6 shows that the RuO_2/PZT/100ÅPt/RuO_2/MgO capacitor (with Pt interlayer deposited by magnetron sputtering at room temperature) has two orders of magnitude lower leakage current than does the typical RuO_2/PZT/RuO_2/MgO capacitor. In comparison, Fig.6 also shows that the RuO_2/PZT/100ÅPt/RuO_2/MgO capacitor (with Pt interlayer deposited by ion beam sputtering at 400°C) has four orders of magnitude lower leakage current than does the RuO_2/PZT/RuO_2/MgO capacitor. This reduction in leakage current is achieved without compromising the excellent fatigue behavior usually observed on RuO_2/PZT/RuO_2 capacitors without a Pt interlayer. As can be seen in Fig. 7, both RuO_2/PZT/100ÅPt/RuO_2/MgO capacitors show negligible fatigue up to $3x10^{10}$ cycles.

The above data show that using a thin Pt interlayer (100Å) between the PZT film and the bottom RuO_2 electrode reduces the leakage current of PZT capacitors while maintaining an excellent resistance to polarization fatigue. To understand why this occurs, an x-ray diffraction pattern of a PZT film grown on 100ÅPt/RuO_2/MgO is shown in Fig. 8. Notice that the PZT film has preferred (111) and (101) orientations. A PZT film deposited by our sol-gel process directly on RuO_2/MgO (without the Pt interlayer) is always highly (101) oriented (only the (101) reflection is observed). Moreover, the thin Pt interlayer deposited on RuO_2/MgO is highly (111) oriented. Thus, the presence of both (101) and (111) preferred orientations in the PZT film grown on 100ÅPt/RuO_2/MgO suggests that both Pt and RuO_2 control nucleation and hence orientation of the perovskite PZT phase. This implies that Pt coverage of the RuO_2/MgO surface is incomplete and that the PZT film is in contact with both Pt and RuO_2 in the bottom electrode. That is why the RuO_2/PZT/100ÅPt/RuO_2/MgO capacitor properties combine those of the PZT/Pt/MgO and PZT/RuO_2/MgO capacitors.

The capacitors with the 100Å Pt interlayer deposited at room temperature by magnetron sputtering usually have higher leakage current and better fatigue than the capacitors with the 100Å Pt interlayer deposited by ion beam sputter-deposition at 400°C. The Pt films grown by ion beam sputtering (at 400°C) are more dense than those grown by magnetron sputter-deposition (at room temperature)[18]. Therefore, more RuO_2 is expected to be in contact with the PZT film in the case of the capacitors with the 100Å Pt interlayer grown at room temperature. That is why the properties of the RuO_2/PZT/100ÅPt/RuO_2/MgO capacitor (with room temperature deposited Pt interlayer) are closer to those of RuO_2/PZT/RuO_2/MgO capacitors.

TEM observation has revealed no apparent second phases in PZT films grown on 100ÅPt/RuO_2 hybrid electrodes. The presence of the Pt interlayer appears to have increased the nucleation site density and enhanced crystallization of single phase perovskite PZT.

The second hybrid electrode type consisted of a thin RuO_2 layer on a Pt bottom electrode. PZT capacitors with this hybrid electrode type had an RuO_2/PZT/200ÅRuO_2/Pt/MgO heterostructure as shown in Fig. 1(b). Fig. 5 shows that this capacitor type has a remanent polarization of about 40 $\mu C/cm^2$ and it is well saturated at 4 Volts. The leakage current and fatigue behavior of this capacitor type are

shown in Fig. 6 and Fig. 7, respectively. Fig. 6 shows that this capacitor type has a leakage current of about $5x10^{-8}$ A/cm^2 (at 1 Volt). This is nearly five orders of magnitude lower than the leakage current of a typical RuO_2/PZT/RuO_2/MgO capacitor. The fatigue curve of this capacitor type (RuO_2/PZT/200ÅRuO_2/Pt/MgO) shows about 50% drop in the magnitude of (P*-P^) after $3x10^{10}$ switching cycles. This is shown in Fig. 7. However, it can be seen that the magnitude of (P*-P^) is beginning to level off to a value of 35 μC/cm^2.

The x-ray diffraction pattern of a PZT film grown on 200ÅRuO_2/Pt/MgO shows that the PZT film is predominantly (001) oriented. Since a PZT film grown on Pt/MgO is always (001) oriented, it can be concluded that nucleation of perovskite PZT on the 200ÅRuO_2/Pt/MgO is mainly controlled by Pt. This also implies that RuO_2 coverage of the surface of the Pt bottom electrode is incomplete. These observations are consistent with the fatigue and leakage current behavior of this capacitor type. It is possible to improve the fatigue of this capacitor type by increasing the thickness of the RuO_2 interlayer. We are currently investigating this hypothesis.

The third hybrid electrode type consisted of a Pt-RuO_2 co-deposited layer. The co-deposited layer is formed by sputtering a target that consists of both Pt and Ru metals. The Pt-RuO_2 layer was used as a bottom electrode to produce RuO_2/PZT/Pt-RuO_2/MgO capacitors as shown in Fig. 1(c).

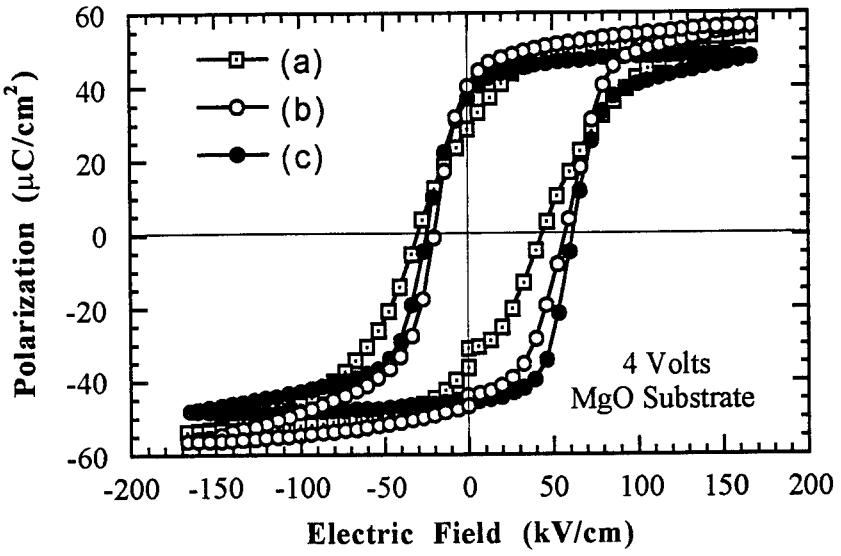


Figure 5. Hysteresis loops of: (a) RuO_2/PZT/100Å Pt/RuO_2 (Pt grown at 400°C); (b) RuO_2/PZT/200ÅRuO_2/Pt/RuO_2 and (c) RuO_2/PZT/(Pt-RuO_2)/RuO_2 capacitors.

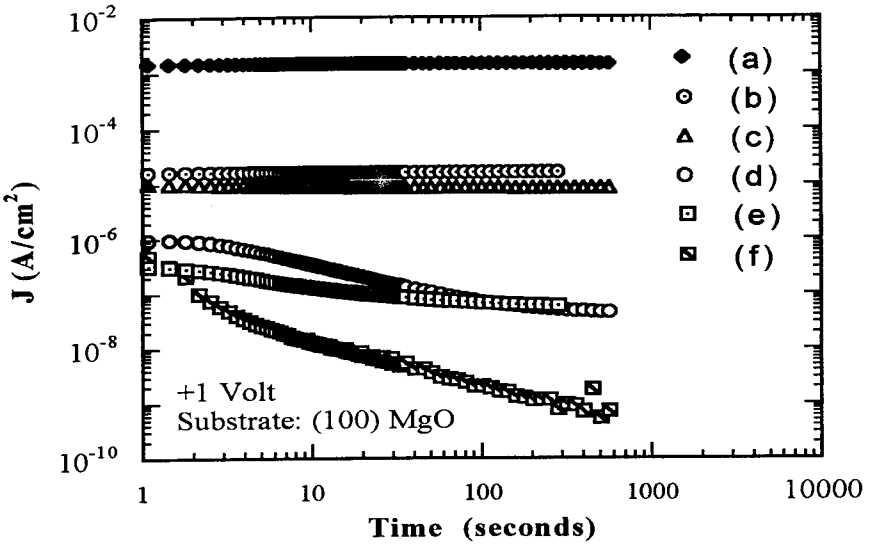


Figure 6. I-t curves of the capacitors: (a) RuO_2/PZT/RuO_2; (b) RuO_2/PZT/(Pt-RuO_2); (c) RuO_2/PZT/100ÅPt/RuO_2 (Pt grown at RT); (d) RuO_2/PZT/200ÅRuO_2/Pt/RuO_2; (e) RuO_2/PZT/100ÅPt/RuO_2 (Pt grown at 400°C) ; and (f) Pt/PZT/Pt.

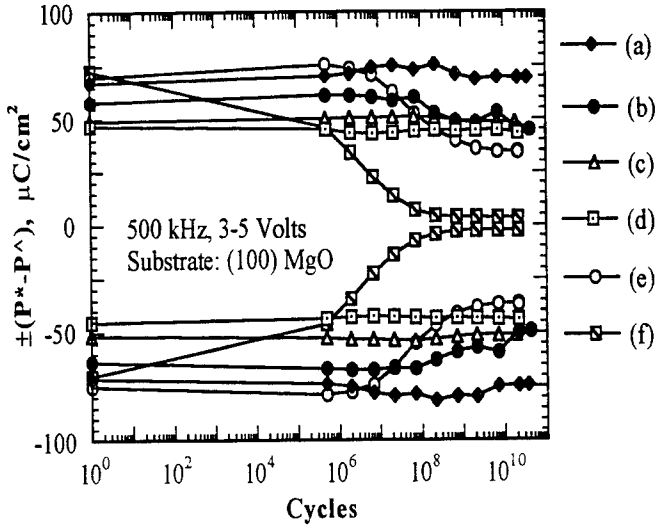


Figure 7. Fatigue curves of the capacitors: (a) RuO_2/PZT/RuO_2; (b) RuO_2/PZT/(Pt-RuO_2)/RuO_2; (c) RuO_2/PZT/100ÅPt/RuO_2 (Pt grown at RT); (d) RuO_2/PZT/100ÅPt/RuO_2 (Pt grown at 400°C) ; (e) RuO_2/PZT/200ÅRuO_2/Pt/RuO_2; and (f) Pt/PZT/Pt.

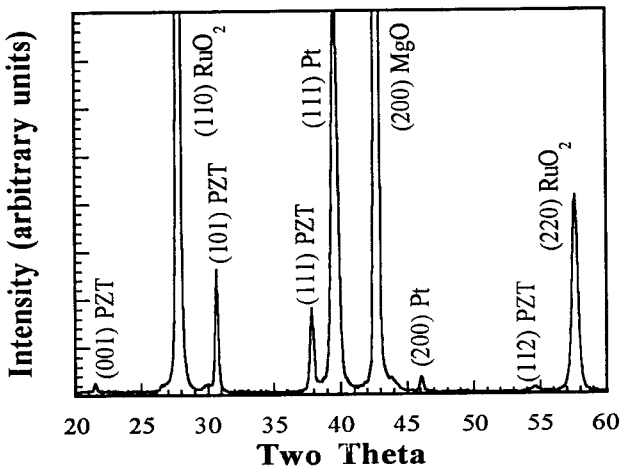


Figure 8. X - ray diffraction pattern of a PZT thin film grown on 100ÅPt/RuO_2/MgO. The Pt interlayer was deposited at 400°C.

The electrical properties of such capacitors were dependent on the composition of the Pt-RuO_2 co-deposited layer. For a Pt-RuO_2 layer with 50 atomic%Pt (determined by RBS), the properties are also shown in Figs. 5-7. It can bee seen, From Fig. 5, that this capacitor type has a remanent polarization of 40 $\mu C/cm^2$. Similarly to the other loops shown in Fig. 5, the loop is shifted along the field axis. This is most likely related to differences between the top and bottom film/electrode interfaces. As seen in Fig. 6, this capacitor has a leakage current that is two orders of magnitude lower than the leakage current of a typical RuO_2/PZT/RuO_2/MgO capacitor. Fig. 7 shows that this capacitor type has good fatigue behavior, where (P*-P^) decays by about 20% after $5x10^{10}$ switching cycles. It should be added here that when a Pt-RuO_2 layer with 80 atomic% Pt was used as a bottom electrode in an RuO_2/PZT/Pt-RuO_2/MgO capacitor, the value of (P*-P^) dropped by 70% after $3x10^{10}$ cycles; the leakage current of such capacitor was less than 10^{-9} A/cm^2 (at 1 Volt)[19].

The x-ray diffraction pattern of PZT films grown on Pt-RuO_2 co-deposited layers show both (001) and (101) reflections, suggesting that both Pt and RuO_2 control nucleation and orientation of the PZT film. Higher Pt content in the Pt-RuO_2 bottom electrode resulted in higher degree of (001) orientation, lower leakage current, and worse fatigue of the PZT capacitors.

The above results show that there is a trade-off between the resistance to polarization fatigue and resistivity or leakage current level of PZT capacitors. Therefore, one has to manipulate the thicknesses of the Pt and RuO_2 interlayers (in the case of the Pt/RuO_2 and RuO_2/Pt hybrid electrodes) and the Pt-RuO_2 composition (in the case of the co-deposited hybrid electrodes) to achieve the optimum leakage current and fatigue of PZT capacitors.

3.2. RETENTION TESTING

During a retention test the decay in stored charge (polarization) of a capacitor which has already been stored in a "1" or "0" logic state is measured as a function of time. The retention tests were performed by applying a write pulse (V_W) to the capacitor, waiting for a specified period of time, and then applying a read pulse (V_r) to measure the retained polarization. During the retention tests, both switched (P*r) and non-switched (P^r) polarizations were measured as a function of time. To measure the switched polarization the write and read pulses were of opposite polarity. To measure the non-switched polarization, the write and read pulses were of the same polarity.

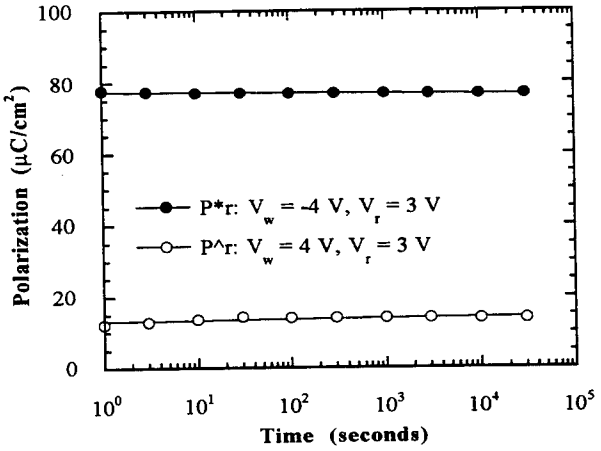


Figure 9. Retention curves of an RuO_2/PZT/100ÅPt/RuO_2/MgO capacitor showing the decay of the two logic states 1 (P*r) and 0 (P^r) with time. The 100Å Pt interlayer was deposited at room temperature.

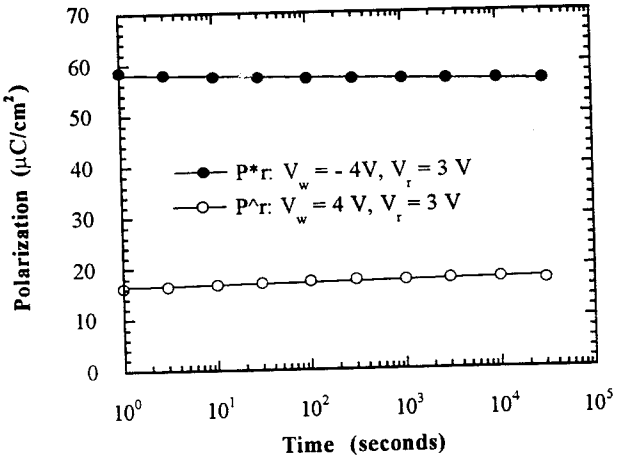


Figure 10. Retention curves of an RuO_2/PZT/100ÅPt/RuO_2/MgO capacitor showing the decay of the two logic states 1 (P*r) and 0 (P^r) with time. The 100Å Pt interlayer was deposited at 400°C.

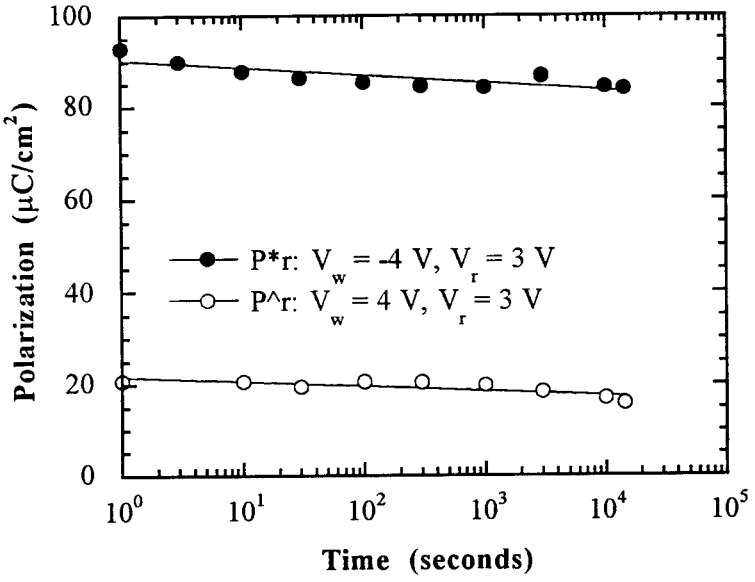


Figure 11. Retention curves of an RuO_2/PZT/200ÅRuO2/Pt/MgO capacitor showing decay of the two logic states 1 (P*r) and 0 (P^r) with time.

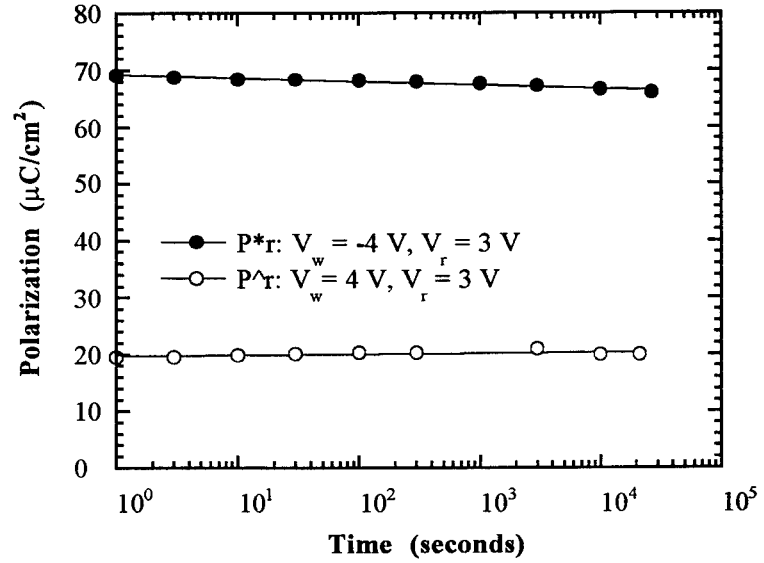


Figure 12. Retention curves of an RuO_2/PZT/Pt-RuO_2/MgO capacitor showing the decay of the two logic states 1 (P*r) and 0 (P^r) with time.

The difference (P*r-P^r) is a measure of the ability to distinguish between the two logic states of the capacitor. A retention failure is said to have occurred when the difference (P*r-P^r) falls below a certain value, which is typically taken as 1-2$\mu C/cm^2$. Using this criterion we have shown that our Pt/PZT/Pt and RuO_2/PZT/RuO_2 capacitors have a retention life-time which could be extrapolated to more than a 100 years (assuming a logarithmic decay with time continues)[19]. Results of retention tests done on PZT capacitors with hybrid bottom electrodes are shown in Figs. 9-12. As shown in these figures, all capacitors with the hybrid electrodes undergo negligible retention loss. If the decay of the polarization is assumed to continue at the rate shown in Figs. 9-12, then all samples are expected to retain 85 to 93% of their initial stored charge after a 100 years. Therefore, retention loss in these capacitors does not pose any concern in terms of their viability for use in non-volatile ferroelectric memories.

4. Conclusions

Three types of (Pt,RuO_2) hybrid electrodes were evaluated as replacement for the bottom RuO_2 electrode in RuO_2/PZT/RuO_2 capacitors. Each hybrid electrode type was evaluated in terms of its effect on the leakage current, polarization fatigue, and retention loss of PZT capacitors as compared to RuO_2/PZT/RuO_2 capacitors. It was shown that using hybrid electrodes can result in PZT capacitors with leakage currents two to four orders of magnitude lower than those of a typical RuO_2/PZT/RuO_2 capacitor. This reduction in leakage current is achieved while at the same time maintaining the excellent resistance to polarization fatigue characteristic of the RuO_2/PZT/RuO_2 capacitors. In addition, it was shown that all capacitors with hybrid electrodes have negligible retention loss.

5. Acknowledgments

The authors would like to thank Dr. D. J. Lichtenwalner and Mr. K. R. Bellur for their useful comments. Support for this work was provided by ARPA (Advanced Research Projects Agency) under contract No. N00014-93-1-0591.

6. References

1. Ramesh, R., Chan, W.K., Wilkens, B., Gilchrist, H., Sands, T., Tarascon, J.M., Keramidas, V.G., Fork, D.K., Lee, J., and Safari, A. (1992), *Appl. Phys. Lett.* **61**, 1537.
2. Bernstein, S.D., Wong, T.Y., Kisler, Y., and Tustison, R.W. (1992), *J. Mater. Res.* **8**, 12.
3. Bellur, K.R., Al-Shareef, H.N., Rou, S.H., Gifford, K.D., Auciello, O., and Kingon, A.I. (1992), *Proceedings of The Eighth International Symposium on Applications of Ferroelectrics*, IEEE publication No. **92CH3080-9**, pp. 448.
4. Vijay, D.P., Kwok, C.K., Pan, W., and Desu, S.B. (1992), *Proceedings of The Eighth International Symposium on Applications of Ferroelectrics*, IEEE publication No. **92CH3080-9**, 408.

5. Dat, R., Lichtenwalner, D.J., Auciello, O., and Kingon, A.I. (1994), *Appl. Phys. Lett.* **64**, 2673.
6. Eom, C. B., Van Dover, R. B., Phillips, J. M., Werder, D. J., Marshal, J. H., Chen, C. H., Cava, R.J., Fleming, R. M., and Fork, D. K. (1993), *Appl. Phys. Lett.* **63**, 2570.
7. Auciello, O., Gifford, K. D., and Kingon, A. I. 1994, *Appl. Phys. Lett.* **64**, 2873.
8. Watanabe, H., Mihara, T., Yoshimori, H., and Paz de Araujo, C. A. (1992), *Proceedings of the Fourth International Symposium on Integrated Ferroelectrics* pp. 346 .
9. Chen, J., Harmer, M. P., and Smyth, D. M. (1992), *Proceedings of the Eighth International Symposium on Applications of Ferroelectrics*, IEEE No. **92CH3080-9**, 111.
10. Al-Shareef, H. N., Bellur, K. R., Auciello, O., and Kingon, A. I. (1994), *Thin Solid Films* (in press).
11. Teowee, G., Boulton, J., Orr, M., Baertlein, C., Wade, R., Birnie, D. P. III, and Uhlmann, D.R. (1993), *MRS Symp. Proc.* **310**, pp. 423.
12. Ramesh, private communication (1994).
13. Al-Shareef, H. N., Bellur, K. R., Auciello, O., and Kingon, A. I. (1994),*Thin Solid Films* (in press).
14. Al-Shareef, H.N., Gifford, K.D., Rou, S.H., Hren, P.D., Auciello, O., and Kingon, A.I. (1993), *Integrated Ferroelectrics* **3**, 321.
15. Schwartz, R. W., Assink, R.A., and Headley, T.J., *Mat. Res. Soc. Symp.* **243**, pp. 245.
16. Chen, X., Kingon, A. I., Al-Shareef, H. N., and Bellur, K. R. (1994), *Ferroelectrics* (in press).
17. Al-Shareef, H.N., Bellur, K. R., Auciello, O., and Kingon, A.I. (1993), *Ferroelectrics* (in press).
18. Hren, P.D., Rou, S. H., Al-Shareef, H. N., Ameen, M.S. , Auciello, O., and Kingon, A. I. (1992), *Integrated Ferroelectrics* **2** , 311.
19. Al-Shareef, H. N., Bellur, K. R., Auciello, O., and Kingon, A. I. (1994), *Integrated Ferroelectrics* (in press).

ORGANICALLY MODIFIED SOL-GEL PRECURSORS FOR FERROELECTRIC DEPOSITION BY SPIN COATING

P. GAUCHER, J. HECTOR AND J. C. KURFISS
THOMSON CSF/LCR,
Domaine de Corbeville,
91404 ORSAY CEDEX,
FRANCE

ABSTRACT. The classical sol-gel process can only be used with dilute precursors because of the high reactivity of the alkoxides towards hydrolysis. Thin film deposition using this colloidal sols require several deposition steps for achieving thicknesses close to 0.5 μm or more. The synthesis of a solution containing an organic resin and the inorganic complex alkoxide allows the deposition of thick layers in a single step. This prevents from contamination effects during the process and from structured layers in the final ceramic film. The solution preparation is described for PZT and PLZT and the mechanism of film crystallization is demonstrated, in relation with the bottom electrode, by using the techniques of thermogravimetry (TGA) and atomic force microscopy (AFM). Finally, ferroelectric and pyroelectric measurements of ferroelectric capacitors are presented.

1. Introduction

The sol-gel coating processes have been historically first developed for obtaining amorphous films for optical applications (antireflective coating) or for microelectronics (SOG or Spin On Glass for interlayer dielectrics). In these cases, the influence of the substrate is slight and the transformation from the gel to the glass during heating is mainly a combustion of the remaining organic ligands.

The use of the sol-gel technique for making crystalline films is more recent and involves a new phenomenon : crystallization on a substrate from an amorphous state. Although this technique seems very different from the vacuum deposition techniques like sputtering, CVD or pulsed laser deposition, there are nevertheless some common features:
- the crystallinity and texture of the film are strongly dependent on the crystal structure of the substrate (or underlayer): lattice parameters and thermal expansion coefficients matching, surface defects, ...

- the quality of the interface is dependent on the substrate (or underlayer) chemistry : reactivity of the substrate surface with the deposited phase constituents, diffusion coefficients...

- the lattice energy has to be brought to the system, either thermally or by a physical way, because the initial state is a disordered one (gas or liquid phase, plasma, particle beam...).

O. Auciello and R. Waser (eds.), Science and Technology of Electroceramic Thin Films, 147-156.
© 1995 *Kluwer Academic Publishers. Printed in the Netherlands.*

Regarding the last point, the sol-gel technique has a real advantage: the final lattice of the oxide is preformed in the precursor solution. The oligomers formed by hydrolysis have already the metal oxygen bonds with the proper coordination that they will have in the crystalline oxide [1]. The additional energy necessary for achieving the 3D lattice is then lower. That is why the energetic budget can be low : rapid thermal annealing (RTA) can be used, which is not detrimental for the underlying structures.

The ideal sol-gel precursor would be then the oxide in colloidal form. Unfortunately, unless for the ferroelectric lead based compositions, it is impossible to get a stable sol able to gellify on the spin coater and not in the beaker. For that reason, some chelating agents are added (or even used as the solvent) to decrease the hydrolysis rate, like acetylaceton (acac) [2], acetic acid [3] or methoxyethanol [4]. The resulting compromise is then : good stability but low viscosity and then very low thickness, or more viscous sols but unreproducibility and too fast gellation during spin coating. To solve this problem, we have developed a precursor which combines high viscosity with high stability.

2. Precursor Synthesis

2.1. CONCEPTS AND METHODOLOGY

Two different approaches are taken by the "spin coaters" :

- the sol-gel approach : one tries to get as possible a complex alkoxide (with oxygen bonding between the different metal atoms) and to eliminate all the organics during the drying, in the form of alcohols, esters... The rheological properties of the sol : wetting, viscosity... and of its reactivity (use of glove bags) are not a priority. This technique is good for making powders, but for thin films, only very dilute solutions can be used.

- the MOD approach : the physical properties of the solution are outlined : one looks for high viscosities, high concentrations, and a suitable behavior on spin coating. In order not to be disturbed by the chemistry, no water is added and an hydrophobic solvent can even be used. The solution will in any case transform finally in the desired oxide.

Figure 1 shows the increase of viscosity by adding the hydrophobic and more viscous (12 cst)) 2-ethyl hexanol solvent to butanol for a PZT solution stabilized with acac.

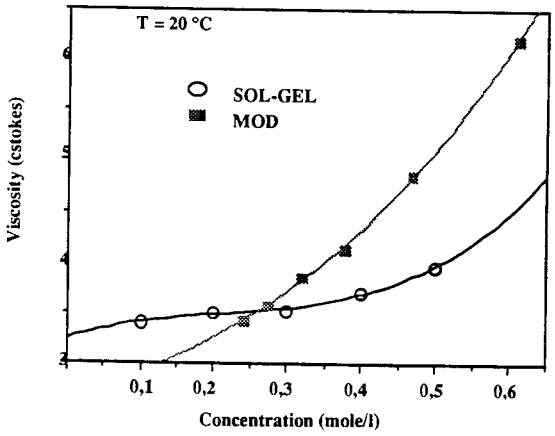


Figure 1. Comparison of viscosities between sol-gel and MOD process.

Another property we are looking for is the ability of the film to dry without cracking or stresses. Again here, the MOD can be better than the sol-gel, because of the slower gellation rate : in sol-gel, the gellation is obtained by hydrolysis and can happen even at low concentration ; the evaporation of a large quantity of solvent is then difficult. In MOD, the gellation is obtained by the evaporation of the solvent which begins then within a more compliant film. The MOD film can accommodate to the substrate and release stresses during the drying, contrary to the sol-gel film which is very stiff and has a tendency to crack. This is illustrated in Fig. 2 :

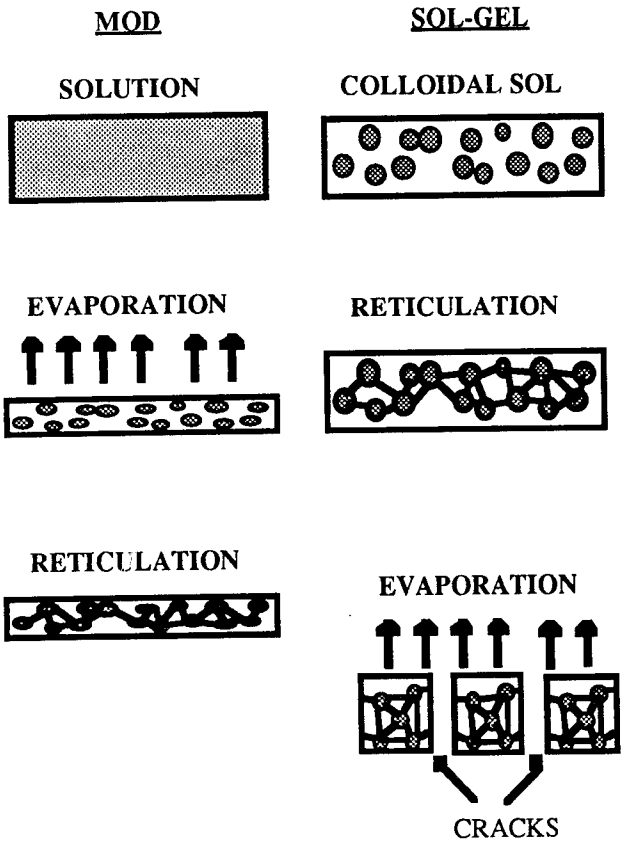


Figure 2 . Drying behavior of MOD and sol-gel solutions.

So, if we want to optimize both the chemical properties and the rheological and drying properties of the solution, it is necessary to combine the two methods. That is what we have done with our process.

2.2. SOLUTION PROCESSING

The idea [5] is to prepare two solutions : the first one (solution A) is an acac modified sol-gel precursor, where the lead is introduced as 2 ethyl hexanoate, La as nitrate, Ti and Zr as alkoxides. Ti and Zr can be dissolved only in presence of the lead salt by a reaction leading to a complex alkoxide which is soluble in the solvent. A viscous hydrophobic solvent is used : the 2-ethyl hexanol, pure or with butanol to decrease the viscosity. After addition of acac, a clear 0.5 M solution is obtained, with a relative stability : it can be used as it is for spin coating, but its viscosity changes slowly within a few weeks, and its behavior during spin coating is not optimized.

A second solution B is based on a tertiary amine which involves 4 nitrogens in a heterocyclic system: the HMTA or HexaMethyleneTetrAmine. In solution in acetic acid, this organic base can react with acac to give a red resin with high viscosity and good wetting properties.

When B is reacted with A at about 110 °C, the organic resin forms by taking off the acac from the A solution, whose mineral oligomers are now encapsulated in the organic network. Despite the suppression of the acac from the mineral phase, the solution is very stable and no evolution of the viscosity or properties has been observed during several months. The supposed free alkoxides oligomers regenerated during the reaction between acac and HMTA are unable to polymerize thoroughly because of the presence of the organic resin which screens the oligomers toward polycondensation. So we have the double advantage of a sol-gel type oligomer and of a rheological organic system.

The chart of the process is shown in Fig. 3. The kinematic viscosity obtained for a 0.5 M solution can be up to 30 cst, comparable to that of a photoresist used in microlithography. With such high viscosities, a thickness of 1 micron of PLZT can be obtained with a single deposition step at 4000 rpm, along with a good uniformity of the film on a 4 inch wafer. If we want to lower the thickness (for example for low voltage switching in memories), the viscosity is decreased by addition of butanol.

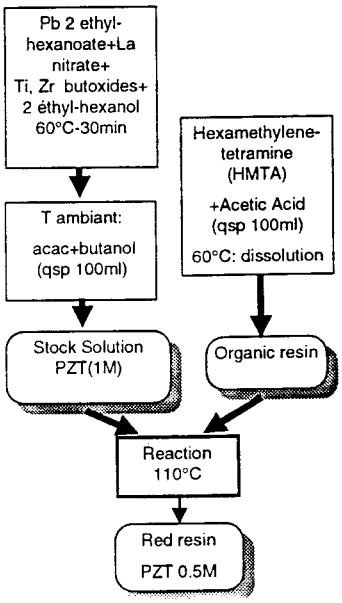


Figure 3. Thomson process for ferroelectric P(L)ZT precursors.

3. Crystallization and Densification of the Phase

3.1. PRECURSOR DECOMPOSITION

Thermogravimetric analysis (TGA) was used for studying the transformation of the precursor to the oxide. The precursor was first dried at 110 °C to eliminate all uncomplexed solvents by evaporation. The residue was then placed in a Perkin-Elmer TGA 7 system and heated at 20 °C/min. The Decomposition curve is shown in Fig. 4.

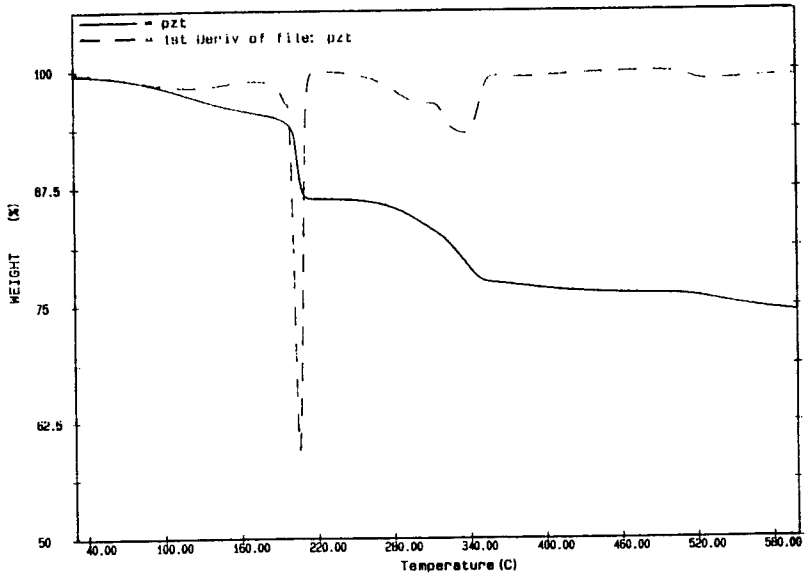


Figure 4. Thermogravimetric analysis of the dried precursor.

There are two steps for the decomposition: an abrupt one, near 200 °C that could correspond to the decomposition of the oligomer, and a more progressive one near 340 °C that could correspond to the burning of the organic resin. The total weight loss does not exceed 25% and is achieved below 350 °C. So the pyrolysis can be done at this temperature.

3.2. PEROVSKITE NUCLEATION AND GROWTH

The Atomic Force Microscopy (AFM) technique has been used to investigate the growth mechanism of the perovskite phase by varying the thickness of the film. We have used a moderately viscous solution (18 cst) that gives a thickness of 120 nm for each deposition step. Higher thicknesses have been obtained by successive deposition steps with an intermediate pyrolysis at 350 °C.

The topographic images are shown in Fig. 5. The dark regions are deeper than the bright ones. The thinner film seems homogeneous with small grains bounded into clusters 0.5 μm wide in some places. With 2 depositions, the clusters become larger (about 1 μm) but they are still separated by dark regions of lower thickness. The clusters merge for 3 depositions and this is the thickness where the roughness is the lowest (Fig.

6). When the thickness is still increased (4 depositions), the growth direction becomes perpendicular to the film and no more clusters are visible. The roughness increases then again. The optimum thickness, concerning the uniformity and roughness of the film, is then 360 nm.

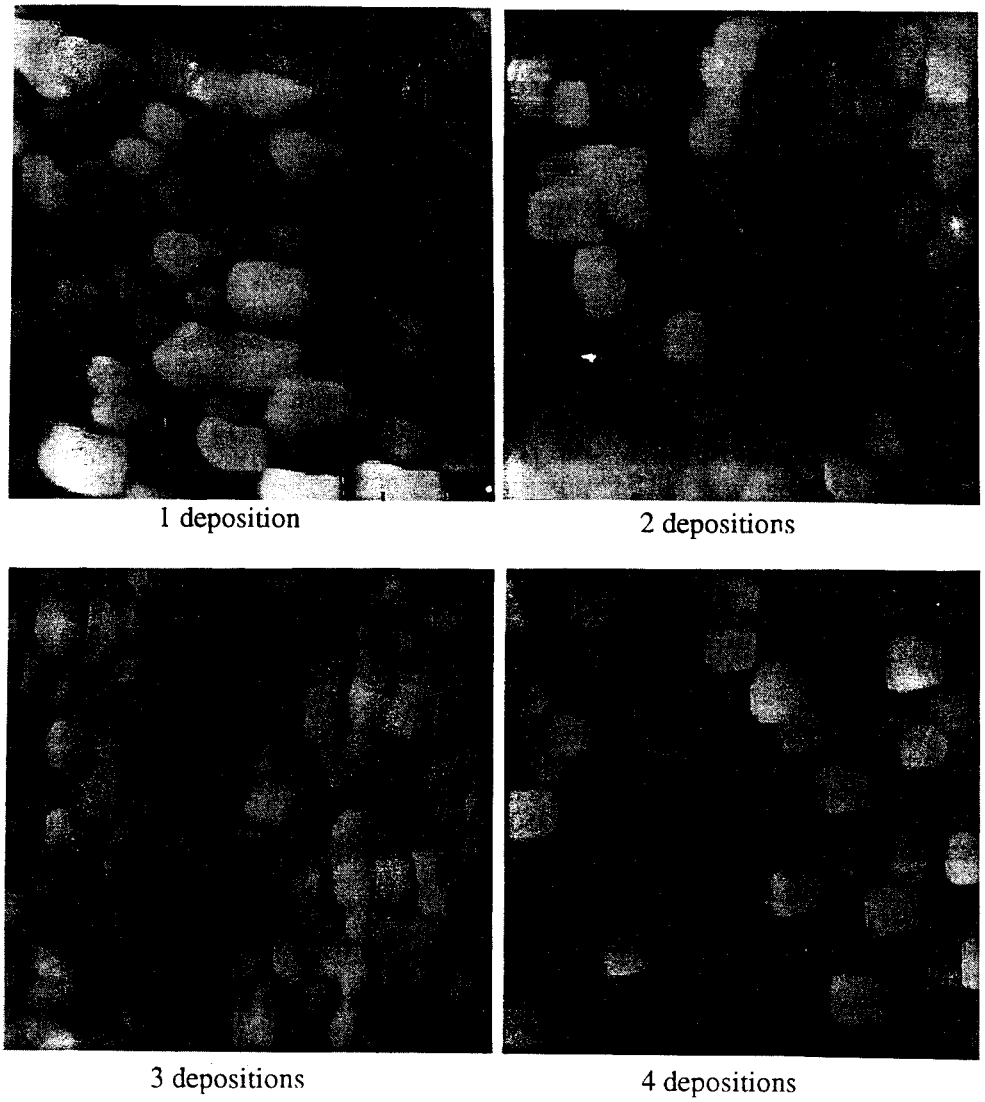


Figure 5. Atomic Force Microscopy of the surface (magnification: 1 cm = 0.2 μm).

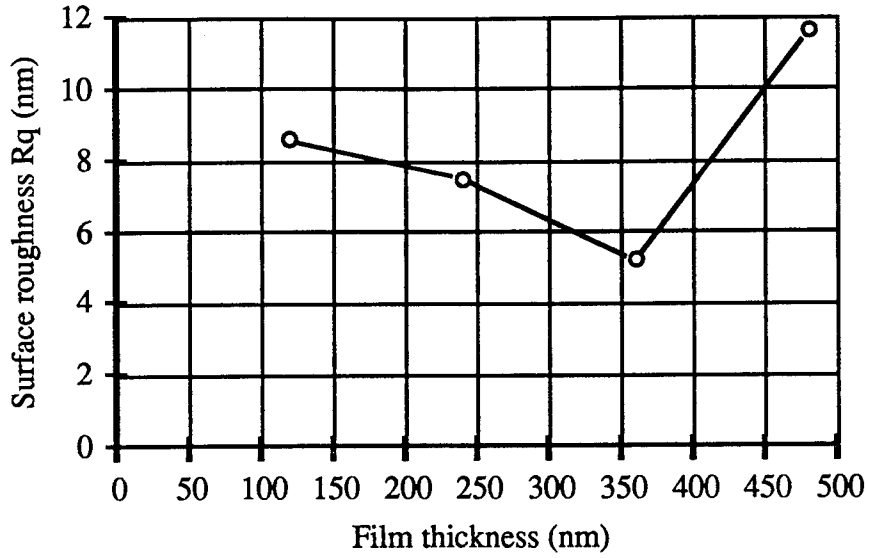


Figure 6. Variation of surface roughness with film thickness showing an optimum for 350 nm.

In another paper, we have demonstrated [6] that the clusters are formed by nucleation from a lead titanate germ followed by lateral growth (Fig. 7), until they merge, giving a fully crystallized film. The AFM technique confirms this assumption.

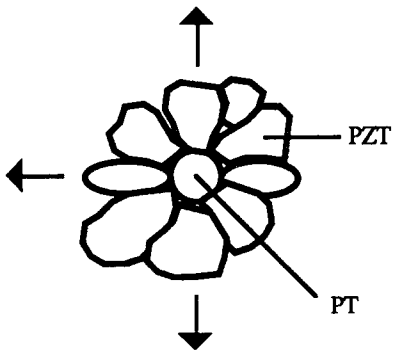


Figure 7. Schematic representation of the lateral growth of a rosette

4. Electrical Measurements

4.1. HYSTERESIS OF THE POLARIZATION

The material obtained with a single deposition step has been measured by the method of Sawyer-Tower [7] for checking the ferroelectricity. The measurement is made at 1 kHz with single sine periods of increasing amplitude (nested loops). The polarization is measured with a 12 bits digital oscilloscope (Nicolet 310) driven by a GPIB interface on a Macintosh II (National Instruments NB-GPIB card with Labview software).

The hysteresis nested loops are shown in Fig. 8, for a single deposition PZT unpatterned film, with top electrodes of 50 X 50 μm^2. The hysteresis begins at about 5V and the remanent polarization is almost 30 $\mu C/cm^2$ under 10V.

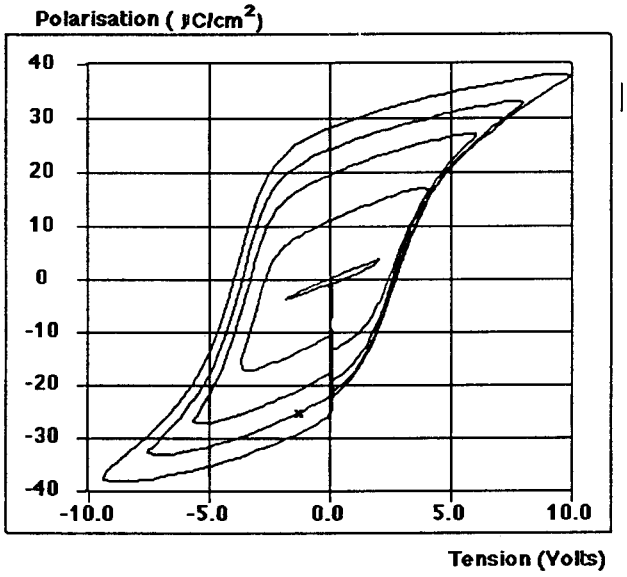


Figure 8. Nested hysteresis loop of the material at 1 kHz.

These results show that the film has a reasonably good quality.

4.2. PYROELECTRIC CURRENT

The measurement was made by the method of Byer and Boundy [8]. The wafer is heated by a hot chuck driven by a PID regulator giving a quasi linear temperature ramp. The current, within 10^{-12} and 3 x 10^{-10} A, is measured with a Keithley 487 picoammeter with GPIB interface which allows to read the data with the Macintosh. The pyroelectric coefficient is derived from the formula:

$$p = \frac{dP_s}{dT} = \frac{1}{S}.i(T).\ \frac{1}{\frac{dT}{dt}}$$

where the temperature ramp dT/dt is computed for each temperature with Labview to correct the deviation from the linearity. S is the surface of the sensitive element (0.4 X 0.4 mm^2). The sample is poled by cooling from 100 °C to RT under 40V. During the first heating cycle, the current measured corresponds to a very high pyroelectric coefficient (larger than 10. 10^{-4} C/m^2 K) as seen in Fig. 9. But during the second and third heating cycle, the calculated coefficient is about 2. 10^{-4} C/m^2 K. This value is assumed to be the true value of the coefficient ; the value deduced from the first measurement is probably due to some TSC (Thermally Stimulated Currents) arising from trapped charges in the interfaces during the poling treatment. These trapped charges are created during the poling process and are no more existing during the second and third heating treatment.

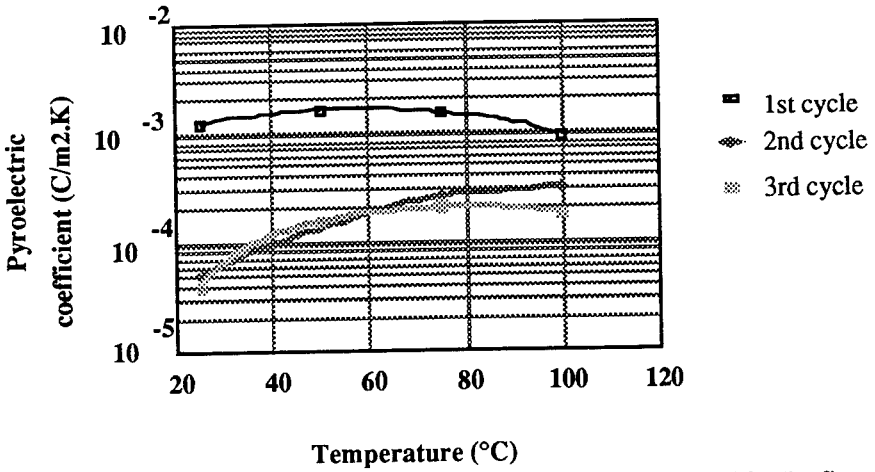


Figure 9. Pyroelectric coefficient after poling under 40V at 100 °C. The first temperature cycle shows mainly TSC (thermally Stimulated Currents). The second and third cycle shows the true (reversible) coefficient.

5. Conclusions

The modified sol-gel process described here allows to make PZT thin films suitable for memory or pyroelectric applications with a single deposition step. The obtained precursor combines the advantages of the classical sol-gel precursors (transformation in the perovskite phase with a low weight loss and a low thermal budget), and that of a good resin for spin coating (high viscosity and good wetting properties). The optimum uniformity of the film nevertheless depends on the nucleation growth mechanism of the amorphous film, which is strongly dependent on the substrate. The rosettes, primarily formed from germs of the perovskite phase, have to merge within the amorphous phase in order to give the final grains of the ceramic.

6. References

1. Gaucher, P., Faure, S. P., Barboux, P. (1991), *Euroceramics II*, Augsbourg (Germany), 3 pp. 2351.

2. Faure, S. P., Barboux, P., Gaucher, P., Livage, J. (1992), *Journal of Material Chemistry*, **2** (7), 713.
3. Yi, G., Wu, Z., Sayer, M. (1988), *J. Appl. Phys*, **64** (5), 2717.
4. Dekleva, T. W., Hayes, J. M., Cross, L. E., Geoffroy, G. (1988), *J. Amer. Ceram. Soc.*, **71 (5)**, C280.
5. Valente, I., Faure, S. P., Gaucher, P., Livage, J. (1989), *French Patent* No. 89 15174). THOMSON CSF.
6. Faure, S. P., Hector, J., Gaucher, P., Ganne, J. P. (1993), *J. Phys III*, (in press).
7. Lines, M. E., Glass, A. M. (1977), *Principles and Applications of Ferroelectrics and Related Materials*, Clarendon Press, Oxford, pp. 102.
8. Byer, R. L., Roundy, C. B. (1972), *Ferroelectrics*, **3**, 333.

PREPARATION AND PROPERTIES OF CALCIUM MODIFIED LEAD TITANATE THIN FILMS

M.L. CALZADA, F. CARMONA, R. SIRERA AND B. JIMENEZ
Instituto de Ciencia de Materiales de Madrid (CSIC),C/ Serrano 144, Madrid, Spain.

ABSTRACT. A chemical process is described in detail for the preparation of Ca-modified lead titanate films. Crystallinity, microstructure and ferroelectric properties are reported for different thermal treatments.

1. Introduction

Many research groups are studying thin films based on $PbTiO_3$ compositions, aiming at piezoelectric and pyroelectric sensing devices [1].

Pure lead titanate films have undesirable mechanical properties due to tensions developed while cooling, in the cubic to tetragonal transition phase.
But if part of the Pb^{2+} ions are replaced by ions of the same valence and smaller size, as for instance Ca^{2+}, the tetragonal distortion of the perovskite is lower than in the case of pure lead titanate. Higher mechanical stability is thus obtained after thermal treatment [2], and this shows up in the final properties of the films.

There are many methods, both physical and chemical, for the preparation of thin films [3]. Chemical methods, such as sol-gel processes, have the advantage of requiring less costly equipment than physical methods, and also make possible a better control of composition. However, these processes require the preparation of precursor solutions containing all the ions involved, and this is more difficult for multicomponent systems.

The common route, used for obtaining thin films based on $PbTiO_3$ from metal alkoxides [4], presents some problems when one wants to introduce appreciable amounts (> 8%) of modifier cations for the replacement of Pb^{2+} in the perovskite. On the other hand, these alkoxides are highly reactive with water, and a rigorous control of hydrolysis and condensation reactions is therefore required.

Alcoholic solutions of metal alkoxides, partially hydrolyzed with small amounts of water, are used for the preparation of oxides thin films by spin or dip coating [5]. In these systems, the amount of water seems to be critical for the production of homogeneous films: an excess of water produces gelation or precipitation in the solution; a deficiency of water leads to discontinuous or inhomogeneous films.

Some authors have shown that glycols and ethanolamines prevent the precipitation of oxides from alcoholic solutions of metal alkoxides [6]. The
addition of this type of compounds to precursor solutions thus allows to add water in excess, and to obtain homogeneous solutions with the adequate viscosity to permit

O. Auciello and R. Waser (eds.), Science and Technology of Electroceramic Thin Films, 157-166.
© 1995 *Kluwer Academic Publishers. Printed in the Netherlands.*

deposition by spin or dip coating. Furthermore, it facilitates the addition of inorganic salts to solutions, and therefore the preparation of multicomponent systems [7].

In this paper a study is made of a process, based on the use of glycols as solvents, for the obtainment of stable precursor solutions of modified lead titanates.

These solutions have been applied to the deposition by spin coating of ferroelectric thin films of $Pb_{0.76}Ca_{0.24}TiO_3$.

2. Experimental methods

2.1. PREPARATION OF SOLUTIONS

Lead acetate trihydrate, $Pb(OOCCH_3)_2.3H_20$, was heat-dissolved in 1,3-propanediol, $HO(CH)_20H$, with a molar ratio Pb(II)/diol = 0.76 / 5. The solution was then maintained refluxing for one hour at ~110 °C. After cooling to 80°C, titanium di-isopropoxide bis-acetylacetonate, $Ti(OC_3H_7)_2(CH_3COCHCOCH_3)_2$, was added in a molar ratio of Pb(II)/Ti(IV) = 0.76 / 1. This mixture was refluxed at = 135 °C in air for 8 hours so as to promote the reaction of the components. By products of reaction were then distilled. The volume of the distilled liquid amounted to 80 % of the volume of all 2-propanol (free or otherwise) present in the solution. The temperature of the distilled vapors during this stage was ~80 °C. Stable solutions thus obtained (hereafter referred to as PT), showed densities of # 1.42 $g.cm^{-3}$ and TiO_2 and PbO molarity of ~1.54 M (Fig. 1).

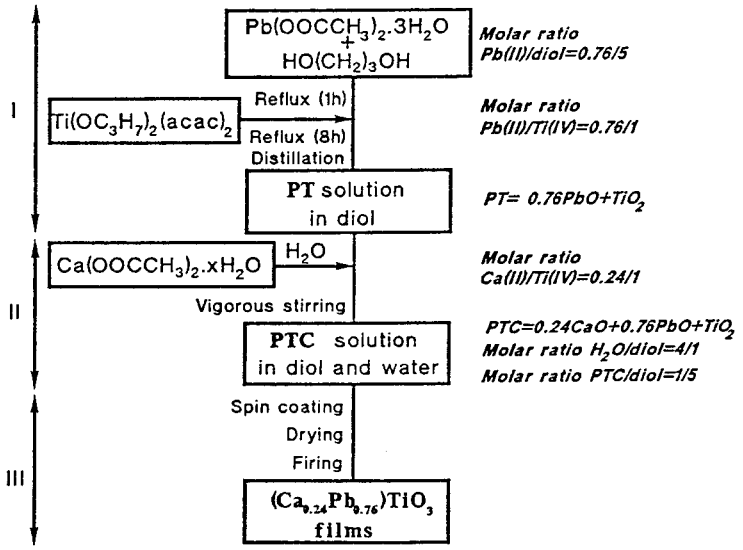


Figure 1. Chemical process for the preparation of Ca-modified lead titanate thin films.

An aqueous solution of calcium acetate, $Ca(OOCCH_3)_2.xH_2O$, was added to the PT solution with molar ratios Ca(II)/Ti(IV) = 0.24 / 1 and H_2O / diol = 4 / 1. After

vigorous agitation, a yellow stable solution was obtained (hereafter referred to as PTC) with density ~1.33 $g.cm^{-3}$ and $Pb_{0.76}Ca_{0.24}TiO_3$ molarity of ~0.94 M.

Aliquots of PT and PTC and of the distilled liquid were analyzed by infrared (IR) spectroscopy. Thermogravimetric analysis (TG and DTG) and differential thermal analysis (DTA) were carried out on solid samples of the solutions PT and PTC, dried at 100 °C for 12 hours.

2.2. DEPOSITION AND THERMAL TREATMENT

Silicon wafers (100) were sputtered with an antidiffusive layer of TiO_2 of about 500 Å thickness. Over this layer a platinum bottom electrode of ~1500 Å was deposited, also by sputtering.

PTC solutions were deposited by spin coating over these Pt / TiO_2 / Si substrates, at a speed of 2000 rpm for 45 sec. The films were dried at 350 °C for 60 sec. on a hot plate. This deposition process was carried out in a class 100 clean room.

As-deposited films are amorphous and have to be thermally treated so as to achieve the crystallization of the perovskite. Two types of treatment were used. One, which we call conventional, consists of heating at 10 $°C.min^{-1}$ up to the desired temperature (> or = 500 °C), maintaining for 1 hour, and furnace-cooling down to room temperature. The other, which we call rapid-heating, consists of putting the sample directly into the furnace, previously stabilized at the desired temperature (> or = 500 °C), maintaining for a short time (~10 min), and air-quenching it back to room temperature.

2.3. STRUCTURE ANALYSIS

The nature of the crystalline phases developed in the films was studied by X-ray diffraction (XRD), using a LiF flat monochromator between sample and detector and following a grazing angle method with an incident angle of a = 1°.

Thicknesses were measured on micrographs of cross sections obtained by scanning electron microscopy (SEM). Surface micrographs were used to study microstructure and to evaluate the quality of the films as such (cracks, pores, etc...).

2.4. MEASUREMENT OF ELECTRIC PROPERTIES

Gold or platinum top electrodes of 0.5 mm diameter, were deposited by sputtering.

Electric properties were studied using a Radiant TR66A device, with which loops were traced with maximum fields progressively higher up to ~4×10^5 $V.cm^{-1}$.

Apart from the aspect of the loops, which may be misleading, due mainly to undesirable conduction effects, films were rated by the degree of commutation achieved. This was measured by the quantity P_r^*-$P_r^\wedge$, where P_r^* and $P_r^\wedge$ are remanence values obtained as a response to the pulses applied after describing each loop.

3. Results and Discussion

3.1. PREPARATION AND PHYSICO - CHEMICAL CHARACTERIZATION OF PRECURSOR SOLUTIONS

The preparation of $Pb_{0.76}Ca_{0.24}TiO_3$ thin films is thus carried out by a diol based sol-gel process for the preparation of an intermediate solution (PT) with a molar ratio Pb(II)/Ti(IV) = 0.76 / 1. The modifying cation Ca(II) is added to the system as an aqueous solution of calcium acetate, using molar ratios Ca(II)/Ti(IV) = 0.24 / 1 and H_2O / diol = 4 / 1. During this addition, gelation of PT takes place when the ratio H_2O / diol is 6 / 1. However, this gel redissolves in excess water, so that H_2O / diol = 4 / 1 leads to stable solutions of PTC of density 1.33 $g.cm^{-3}$ and molarity 0.94 M in $Pb_{0.76}Ca_{0.24}TiO_3$.

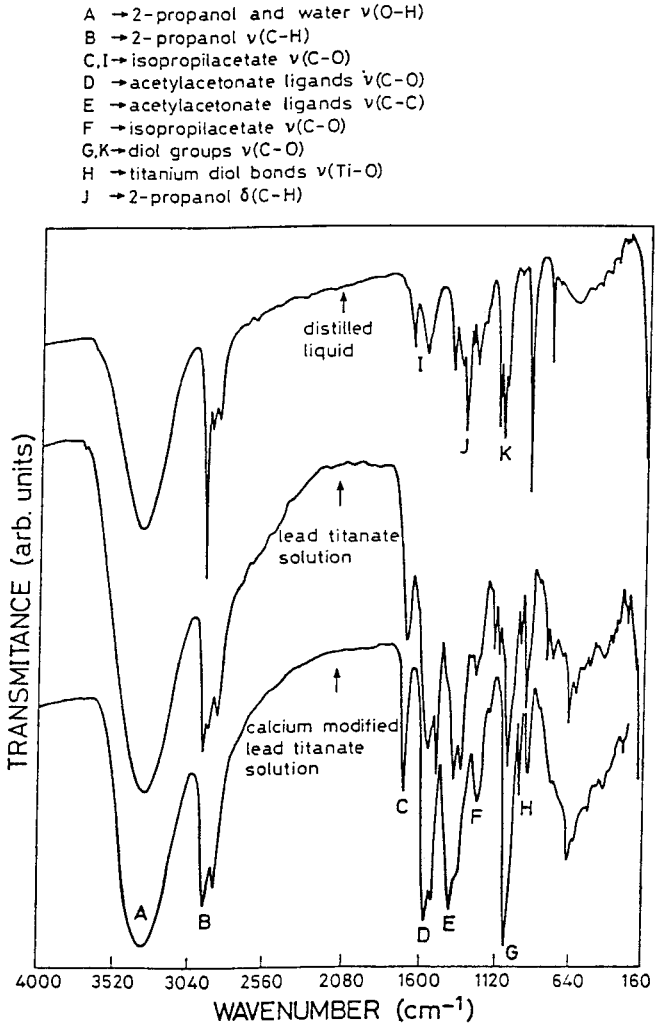


Figure 2. IR analysis of the distilled liquid, PT solution and PTC solution.

Synthesis reaction implies the distillation of byproducts before the preparation of the PT solution (see Fig. 1). The distilled liquid shows a slightly acid pH of ~ 5.4, and consists mainly of acetic acid, water and isopropyl acetate, as can be seen in the IR spectrum of Fig.2(a). IR spectra of solutions PT and PTC are very similar (Figs.2(b) and 2(c)), both showing titanium-acetylacetonate and metal-oxygen links, probably due to the formation of bonds between titanium ions and the diol used as solvent [8]. Further analysis, by IR spectroscopy and nuclear magnetic resonance, to be published elsewhere [9], show the formation of polymeric structures in PT solutions, in which the titanium ion acts with coordination index VI, and remains linked to the acetylacetonate chelating agent from the precursor $Ti(OC_3H_7)_2(CH_3COCHCOCH_3)_2$. The interchange reaction with the solvent, that takes place during the synthesis of PT solutions, produces new titanium-diol bonds (Fig.2 (b)). The addition of calcium acetate dissolved in water to the PT solution produces condensation and, hence, gelation. However, an excess of water leads to the re-solution of the gel. The solubility in water of gel-like compounds formed by titanium and polyhydroxialcohols has been reported by other authors [10,11]. In these compounds the titanium ion can work with indexes IV or VI and, in the case of dihydroxialcohols, these are linked to the titanium acting as unidentate ligand or chelating agent.

Thermal analysis, TG and DTA, of the amorphous materials obtained after drying solutions PT and PTC at 100 °C show a different thermal evolution in each case. In the PT system the elimination of organic compounds takes place in several stages (Fig.3(a)). The main combustion of organics shows off by the exothermic peak at =316 °C that has an associated weight loss of = 14.27%. At higher temperatures there are more exothermic peaks (478 °C and 512 °C) together with a weight loss of =4.25%. A similar evolution, with the elimination of organic remains at high temperatures (2400 °C) has also been observed by other authors in the lead titanate-zirconate system (PZT) when the precursors are prepared by a sol-gel method based on glycols [12].

However, the thermal evolution of the PTC solution is more simple (Fig. 3(b)). Neither weight losses nor chemical transformations are observed over 400 °C by TG and DTA. Organic compounds are eliminated at temperatures between 200 °C and 400 °C, where the main weight losses (#21.08%) are recorded. These are coincidental with exothermic reactions (see DTA) produced by the combustion of the organics. The small weight loss (=5.68%) at temperatures ~200 °C is due to the elimination of water and free alcohol.

This difference in behavior between systems PT and PTC is due to the formation of inorganic polymers with cross-links of different lengths. Although the IR spectra of both solutions are very similar, it seems evident that the addition of calcium acetate in aqueous solution to system PT, for the production of PTC solution in stage II (Fig.1), favours the rupture of inorganic polymer chains developed in solution PT during stage I [13].

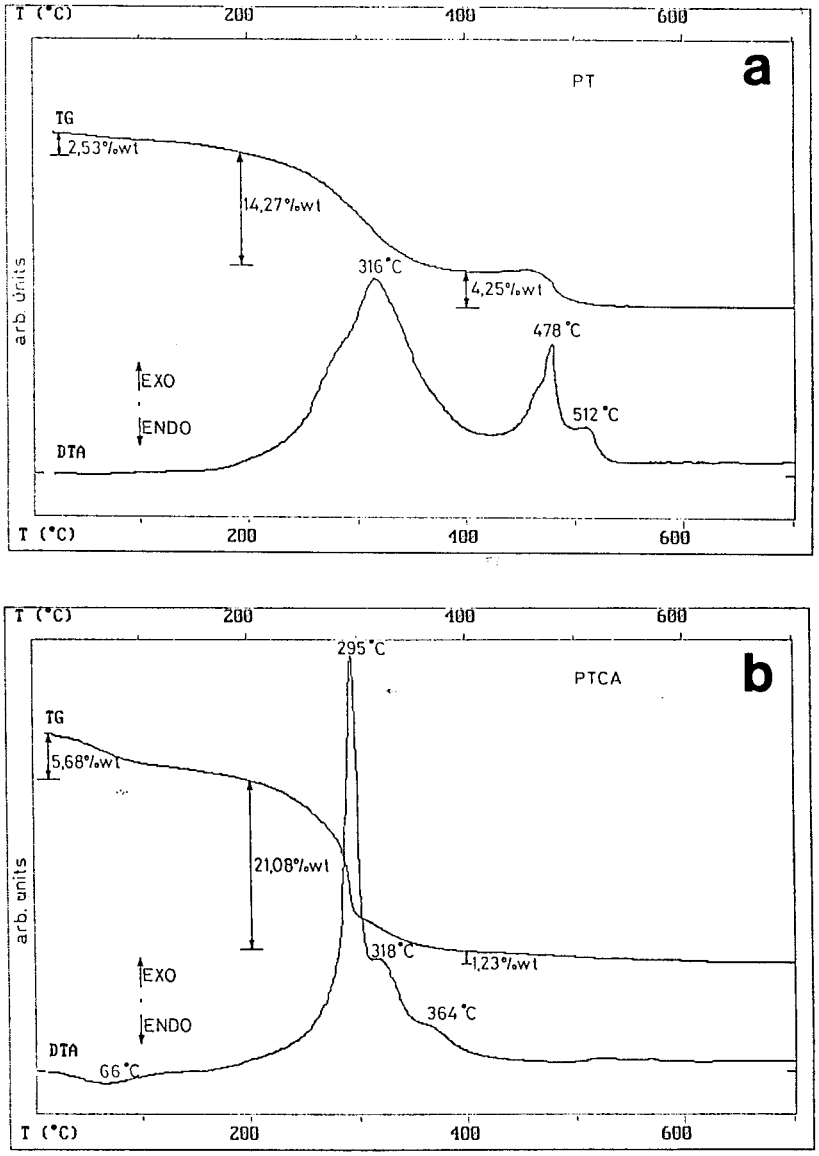


Figure 3. Thermal analysis of a) PT gels and b) PTC gels.

3.2. DIFFRACTOMETRY AND MICROSTRUCTURAL ANALYSIS

Solutions of PTC, deposited on $Pt/TiO_2/Si$ substrates and dried at 350 °C for 1 minute, show an amorphous structure observed by XRD. Thermal treatment of these films leads to the formation of crystalline phases, so that films treated at 550 °C already show a perovskite phase with tetragonal distortion C / a = 1.034 (Fig. 4(a)). This crystalline

phase improves at higher temperatures. Between 650 °C and 700 °C, the tetragonal distortion becomes c / a = 1.038, next to the expected value for the composition $Pb_{0.76}Ca_{0.24}TiO_3$. In all cases there are small amounts of pyrochlore phases together with the perovskite one.

Figure 4 (b) shows XRD spectra of films obtained at 650 °C (6, 12, 18, 24 and 48 min.). In these cases, tetragonal distortion (c / a = 1.025) is below the expected value. At the same time, the pyrochlore phase seems to be present in smaller amounts such as other authors have pointed out [14].

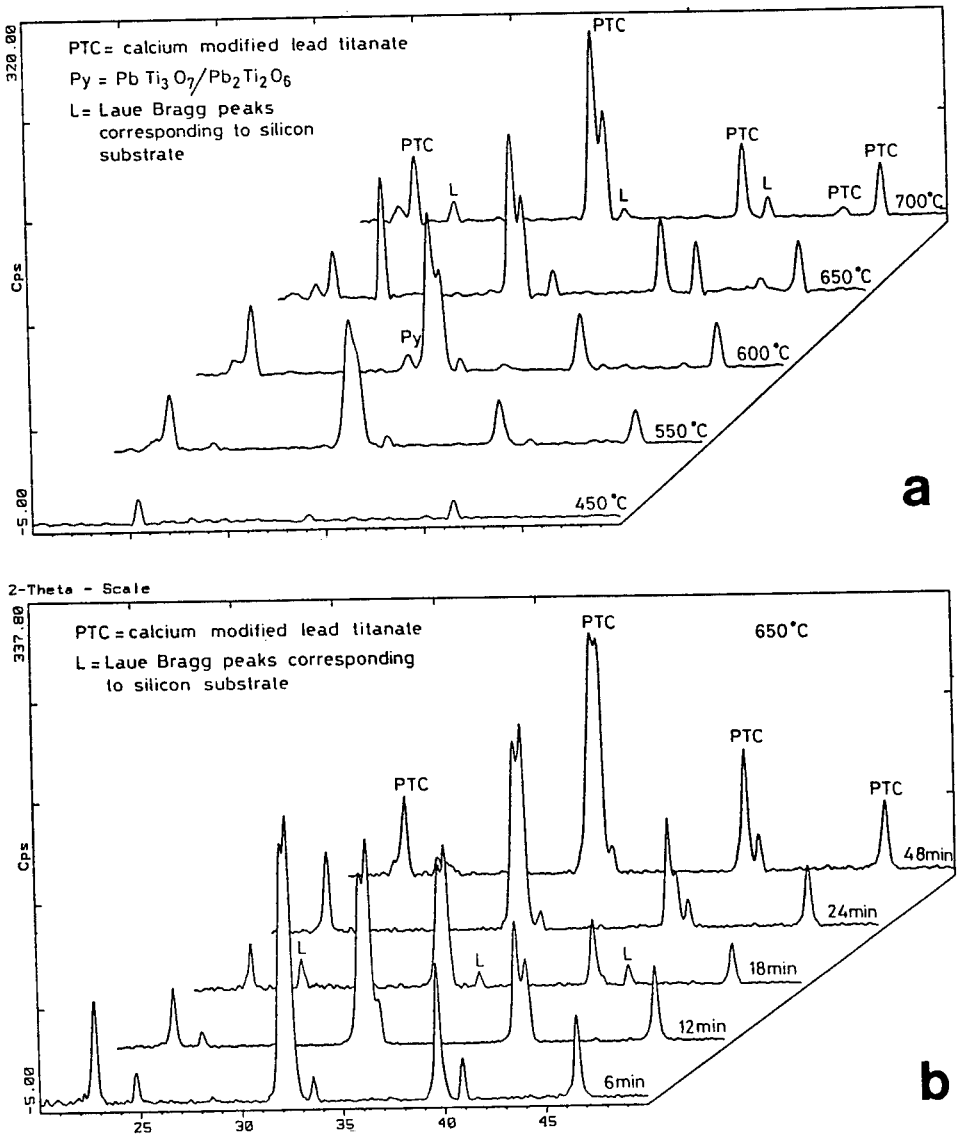


Figure 4. X-ray patterns of a) films obtained after annealing at different temperatures for 1 hour and b) films receiving rapid heating treatments.

In Fig.5, we have a micrograph showing the thickness of a film (~ 0.5 μm), obtained by a single deposition and a single thermal treatment. In Fig.6, we have microstructures representative of films obtained by conventional and rapid heating treatments, respectively. Grain sizes in films obtained by the former (~ 0.2 μm) are higher than in films obtained by the latter (~ 0.1 μm). The difference in grain size, and the possible existence a not completely crystallized phase in films obtained by a rapid-heating treatment, may be the reason for the differences in tetragonal distortion values.

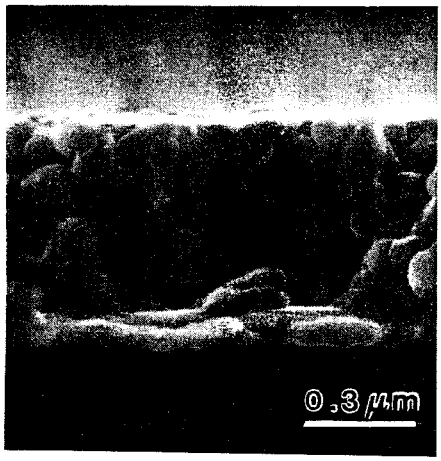


Figure 5. Cross-section of a calcium modified lead titanate film.

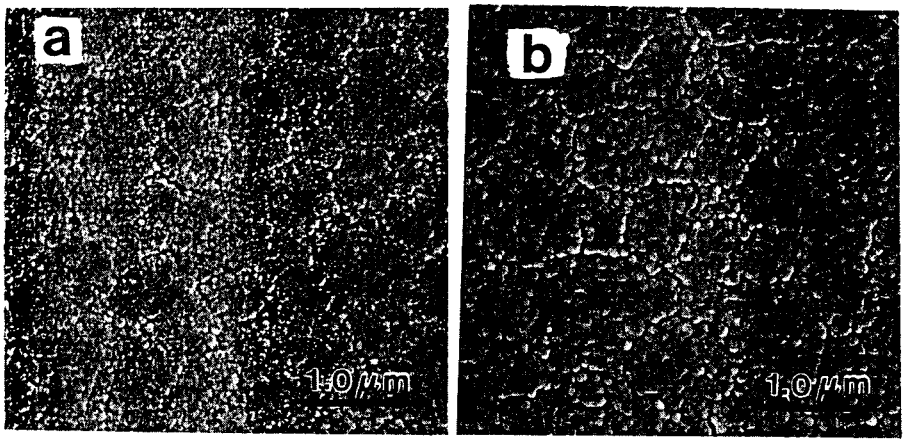


Figure 6. Micrographs of calcium modified lead titanate films: a) rapid heating treatment at 650 °C / 12 min, b) conventional treatment at 700 °C / 1 h.

3.3. ELECTRICAL MEASUREMENTS

Figure 7 shows characteristic loops of films obtained by a conventional heat treatment (700 °C / 1 h), and a rapid heat treatment (650 °C / 12 min). Remanence and coercivity

values are P_r=6 μC.cm^{-2} and E_c=140 kV.cm^{-1}, with a bias field of some 55 kV.cm^{-1}, in the first case; and P_r = 10 μC.cm^{-2} and E_c = 120 kV.cm^{-1}, with a bias field of 11 kV. cm^{-1}, in the rapid-heating case.

The degree of commutation, as measured by the quantity P_r^* - $P_r^\wedge$ is also higher in the second case (10.9 μC.cm^{-2} against 6.3 μC.cm^{-2}).

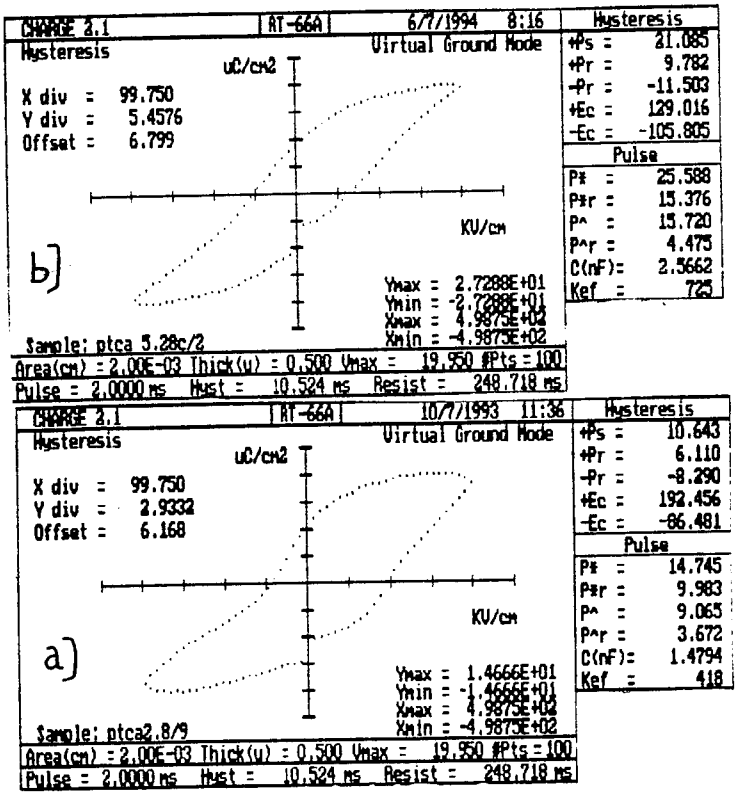


Figure 7. Hysteresis loops of calcium modified lead titanate films: a) conventional thermal treatment at 700 °C / 1 h and b) rapid heating treatment at 650 °C / 12 min.

4. Conclusions

A wet chemical process has been established for the preparation of modified lead titanate precursor solutions. This process is based on the use of modified titanium alkoxides and diols as solvents. During synthesis, an interchange reaction between the titanium alkoxide and the diol produces the formation of polymeric structures in the precursor solutions.

Films, deposited from the solution by spin coating, are amorphous, and have to be thermally treated so as to obtain perovskite structure with the desire properties.

Crystallinity and microstructures of the films are a function of the thermal treatment used. Conventional treatments lead to tetragonal distortions (c / a) next to expected values, and grain sizes of about 0.2 μm. Films receiving rapid- heating treatments show

values of c / a lower than expected, and grain sizes of ~ 0.1 μm. Amounts of pyrochlores seem to be much lower in the second case.

Ferroelectric properties of films were similar for both types of treatments, but polarization and commutation values were higher when rapid-heating was used.

5. Acknowledgements

The authors acknowledge the support of the Spanish Projects Mat91-422 (CICYT) and C120/91 (CAM).

6. References

1. Paz de Araujo, C.A. and Taylor, G.W., (1991), *Integrated Ferroelectrics* **116**, 215.
2. Jimenez, B., Mendiola, J., Alemany, C., Del Olmo, L., Pardo, L., Maurer, E., Calzada, M.L., De Frutos, J., Gonzalez, A.M. and Fandino, M.C.(1988), *Ferroelectrics* **87**, 97.
3. Sheppard, L.M., (1992), *Ceram. Bull.* **71** (1), 85.
4. Yi, G. and Sayer, M. (1991), *Ceram. Bull.*, **70** (7), 1173.
5. Xu, Y. and Mackenzie, J.D., (1992), *Integrated Ferroelectrics* **1** (1), 17.
6. Takahashi, Y., Matsuoka, Y., Yamaguchi, K., Matsuki, M. and Kobayashi, K. (1990), *J. Mater. Sci.* **25**, 3960.
7. Takahashi, Y., Niwa, K., Kobayahsi, K. and Matsuki, M. (1987), *J. Ceram. Soc. Jpn. Inter. Ed.* **95**, 890.
8. Reeves, R.E. and Mazzeno, Jr.L.W. (1954), *J. Am. Chem. Soc.* **76**, 2533.
9. Calzada, M.L., Sirera, R., Carmona, F. and Jimenez, B., *J . Am. Ceram. Soc* . (in press) .
10. Bostwick, C.O. (1953), *U.S.Patent No.* 2,643,262.
11. Booge, J.E. and Hugh, C.G. (1949), *U.S.Patent No.* 2,468,916.
12. Livage, C., Safari, A. and Klein, L.C., *J. Sol-Gel Sci. Techn.* (in press).
13. Mazdiyasni, K.S. (1982), *Ceram. Int.* **8** (2), 42.
14. Mansour, S.A., Binford, D.A. and Vest, R.W. (1992), *Integrated Ferroelectrics* **1** (1), 43.

MICROSTRUCTURE OF LEAD TITANATE-BASED THIN FILMS

L. PARDO, J. RICOTE AND
M.L. CALZADA
Instituto de Ciencia de Materiales (A).
Serrano, 144. 28006 - Madrid, Spain

ABSTRACT. The microstructure of lead titanate thin films prepared by spin-coating from a diol-based sol-gel process is studied and related to the thermal evolution of the gels. This evolution is explained in terms of the carbon content of the diol used in the preparation of the precursor solutions. The potential applications of the films as piroelectric detectors and substrates for surface acoustic waves are discussed.

1. Introduction

Lead titanate ceramics modified with calcium [1] and lanthanides [2] have been widely used and studied as bulk ultrasonic transducers due to their high electromechanical anysotropy. Their applications extend also to devices such as IR detectors for gas sensors [3] and substrates for SAW devices [4]. These compositions have been also tested more recently as thin films and their electrooptic [5,6], pyroelectric [7-11] and piezoelectric [12,13] properties have been proven to be interesting for such applications.

There is a very broad range of thin film preparation techniques which have already been used for the preparation of ferroelectric thin films [13,14] (sputtering, chemical vapor deposition (CVD), laser ablation, etc.). Chemical techniques have the advantage of producing homogeneous, large area thin films providing excellent stoichiometric control. These characteristics are desirable for sensor applications. However, randomly oriented polycrystalline films are usually obtained by these techniques, making necessary the poling step for the use of their ferroelectric properties in IR sensors and SAW devices.

In the last few years, the deposition of amorphous films by spin or dip coating of sol-gel precursor solutions onto substrates, and subsequent thermal treatment, have experienced important developments. Additionally, sol-gel methods have recently [15,16] achieved some success in the attainment of films with preferred orientation. Attempts to obtain preferential orientation of the films can be carried out by study of the effects of various parameters, such as the chemistry of the precursor solutions, the hydrolysis and condensation reactions, the aging of the solutions, the bottom electrodes and substrates and the thermal treatments of the amorphous films. This constitutes a recent expanding topic of research.

Highly c-axis oriented and epitaxial thin films of pure $PbTiO_3$ and, also, La and Ca-modified compositions have been obtained by rf-magnetron sputtering [5-12, 17]. However, to date, attempts to obtain 18 mol % La-modified lead titanate [18] films, and more recently, in the range from 5 to 30 mol % [19], by sol-gel method resulted in pseudocubic structures with low polarization switching. To the authors knowledge, Ca or

O. Auciello and R. Waser (eds.), Science and Technology of Electroceramic Thin Films, 167-175.
© 1995 *Kluwer Academic Publishers. Printed in the Netherlands.*

other Lanthanide modified $PbTiO_3$ compositions have not been processed by sol-gel methods, despite of the evidence of their practical interest in the mentioned applications.

This work presents the preparation and microstructural analysis of pure and Ca and Sm-modified lead titanate ferroelectric thin films by a sol-gel process using different diol solvents. Computer aided image analysis has been used in combination with scanning electron microscopy (SEM) to study the microstructures of the films. This combination constitutes a powerful tool for microstructural characterization in material science. It allows the quantification of complex microstructural features leading to a better understanding of the processing parameters dependence of the microstructure.

2. Experimental Procedure.

2.1. Thin Film Preparation

Stable precursor solutions based on lead titanate were prepared by reacting lead (II) acetate trihydrate, $Pb(OOCCH_3)_2.3H_20$, and titanium di-isopropoxide bis-acetylacetonate, $Ti(OC_3\ H_7\ )_2\ (CH_3COCHCOCH_3\ )_2$, in dihydroxyalcohols, of general formula $HOC_nH_{2n}OH$, with n=3,4 and 5. This process is as an extension of the diol based sol-gel method reported in [20] for n=3.

Lead acetate was dissolved in the selected diol at molar ratio of 5 to 1 of diol to lead in the preparation of precursor solutions of pure $PbTiO_3$ films. These solutions were heated to 125°C under reflux conditions for 1 h. Titanium di-isopropoxide bis-acetylacetonate was added to the solution that was refluxed from 4 to 8 h in air. Modifier cations were added to the system as water or diol-dissolved salts [21]. Calcium acetate, $Ca(OOCCH_3)_2.xH_2O$ was used in the preparation of $Pb_{0.76}\ Ca_{0.24}\ TiO_3$ thin films, herein after called PTCA films, using molar ratios Pb(II)/diol = 0.76 / 5 and H_2O / diol = 4.5 / 1. Samarium acetate, $Sm(OOCCH_3)_3.3H_2O$, and samarium acetylacetonate, $Sm(CH_3COCHCOCH_3)_3$, were used for the preparation of $Pb_{0.88}Sm_{0.08}TiO_3$ films, PTSA and PTS films respectively. Here, the molar ratios were Pb(II) / diol = 0.88 / 5, and H_2O/diol = 3/1 when the samarium acetate is used.

The byproducts of the reaction were continuously distilled until stock solutions with concentrations higher than 1 M were obtained. In this way, three different solutions with the three diols as solvents: 1,3-propanediol (system I), 1,4-butanediol (system II) and 1, 5-pentanediol (system III), were prepared. The solutions were diluted to a concentration of 0.7 M by adding 2-propanol, $(CH_3)_2CHOH$.

PTCA, PTSA and PTS films were prepared from system I solutions, whereas PT films were prepared from the three systems. Films were prepared by spin-coating the diluted solutions onto (100) oriented silicon substrates at 2000 rpm for 45 seconds. Modified lead titanate films were prepared onto passivated and platinized silicon substrates (Si / TiO_2 / Pt), whereas $PbTiO_3$ films were prepared onto both platinized (PTP film) and non-platinized (PT films) silicon substrates. After drying the amorphous films on a hot plate at 350 °C for 1 minute, the lead titanate based films were crystallized by annealing at 600-700 °C, with heating and cooling rates of 10 °C / min. Annealing took place in air with soak times of 5 and 60 minutes. The studied films were obtained by a single deposition process.

Thermogravimetry (TG) and differential thermal analysis (DTA) and grazing incidence X-Ray Diffraction (XRD) techniques were used to determine the decomposition and

transformation temperatures of the xerogels obtained from the solutions after drying at 100 °C for 12 h [22,23].

2.2. MICROSTRUCTURAL CHARACTERIZATION

The gold coated thin film samples were analyzed by scanning electron microscopy (SEM) to determine their thickness and characterize their microstructures. SEM micrographs were taken on random locations of the surface of the sample. A significant number of grains or clusters, from 600 to 2000, was measured in each film in order to obtain reliable distributions.

Figure 1 summarizes the process of computer aided analysis of the SEM images in the microstructural characterization of the films.

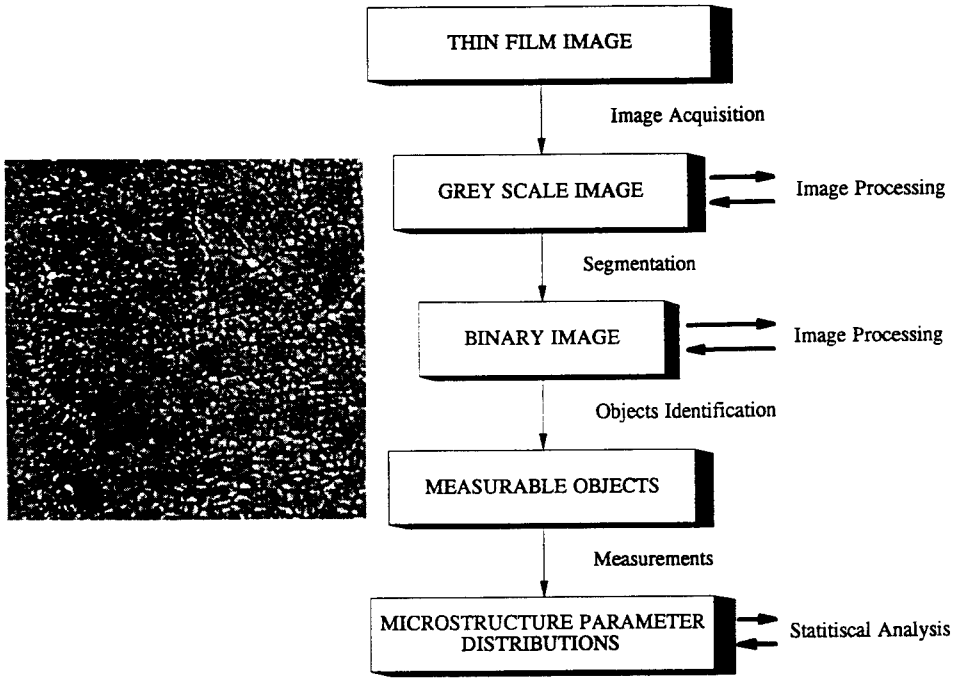


Figure 1. Flux diagram of the computer aided analysis of a thin film image.

Images were digitized using a scanner (Model JX600, Sharp) connected to a frame grabber board which analyzes images of 512 x 512 pixels. For the magnification of the examined micrographs, the pixel size was of the order of 5 x 5 nm. Semiautomatic image processing and measurements were carried out using software based on IMCO10-KAT386 system (Kontron Elektronik GMBH, 1990). Grain or cluster areas were measured. The diameter equivalent to a circular shape ($D = (4\ A / \pi)^{1/2}$) was chosen to characterize the grain or cluster size. The experimental data were analyzed with commercially available statistical software to determine by a graphic method whether the size distributions were

Gaussian or log-normal. When a linear fitting of the grain or cluster size versus the cumulative frequency, represented on a probability scale, is found, distributions are Gaussian. When linear fitting is found for the cumulative frequency of the logarithm of the measured parameter, distributions are log-normal. The mean value and standard deviation of the measured parameters were obtained after fitting the experimental data to a distribution function [24].

3. Experimental Results.

The TG analysis [22] of the pure lead titanate xerogels obtained from the precursor solutions of systems I, II and III shows an increase in the total weight loss from 16.75 to 18.50% as the content of carbon in the diol increases from n = 3 to 5. The DTA curves of the three xerogels have shown [22] the appearance of two additional exothermal peaks for systems II and III, which indicates that the decomposition and transformation reactions are similar, but differ in several aspects, from those of system I.

Pyrochlore phases are formed in all the lead titanate based xerogels when treated at temperatures above 400 °C, but they disappear at temperatures above 700 °C. Figure 2(a) shows the XRD pattern of powder from the Sm-modified lead titanate xerogel, prepared from system I and treated at 700 °C-1 h, in which a unique perovskite type structure is observed.

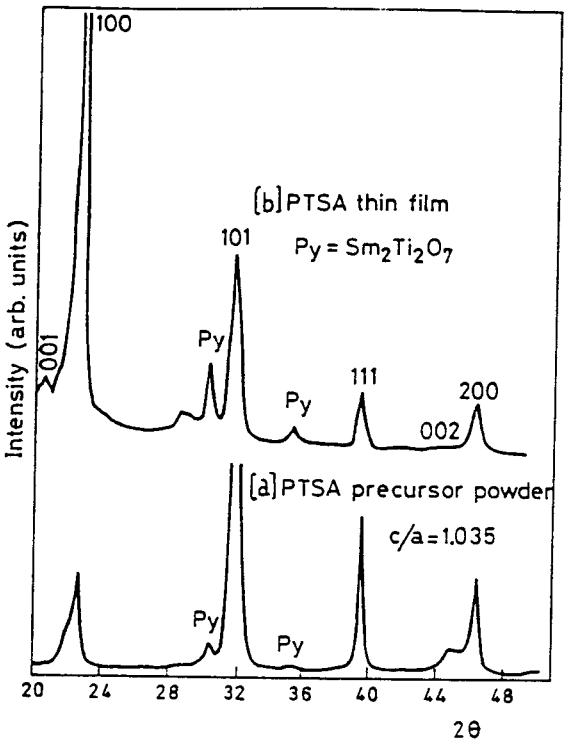


Figure 2. DRX patterns of: (a) PTSA powder and (b) a PTSA thin film.

The XRD patterns of the annealed $PbTiO_3$ films prepared onto silicon, platinized or not, showed the perovskite type structure, with a tetragonal distortion of c / a = (1.057 ± 0.002), and an insignificant amount of pyrochlore phase. Figure 3 shows the XRD pattern of (a) PTP and (b) PTCA films, prepared from system I and annealed at 700 °C during 1 h. The thermal behavior of the PTCA films is similar to the PT and PTP films, showing, after treatment at 700 °C, a perovskite type structure of c /a = (1.035 ± 0.002) with a minimum content of pyrochlore. However, Figure 2(b) shows the XRD pattern of the PTSA film in which, in addition to the presence of a pyrochlore phase, which is absent from the pattern of the thermally treated xerogel (Figure 2 (a)), a strong preferential orientation in the [100] direction can be observed. A similar XRD pattern was observed for the PTS films as well.

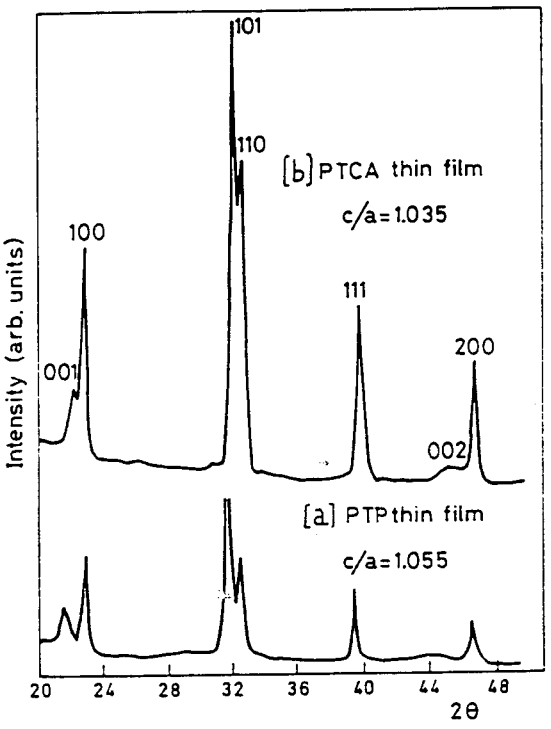


Figure 3. DRX patterns of: (a) PTP and (b) PTCA thin films.

SEM micrographs indicate that all the films are crack-free and show a film thickness of 0.5 to 0.7 μm. Figure 4 shows the SEM micrographs of (a) PTP, (b) PTCA, (c) PTS and (d) PTSA films prepared from system I and annealed at 700 °C during 1 h. Whereas PTP and PTCA show similar dense and homogeneous microstructure, both PTSA and PTS films show a microstructure consisting of large grains (~ 3 μm) surrounded by a fine grained (~ 0.05 μm) porous phase.

For pure lead titanate, PT, thin films prepared from solution of systems II and III, clusters or associations of grains with well-defined boundaries were observed [22] in the SEM micrographs of the surfaces. These closed boundaries that limit the clusters were not

observed at this length scale in system I. The grains inside the clusters are in intermediate sintering stages, leading, as the annealing time increases, to larger grains.

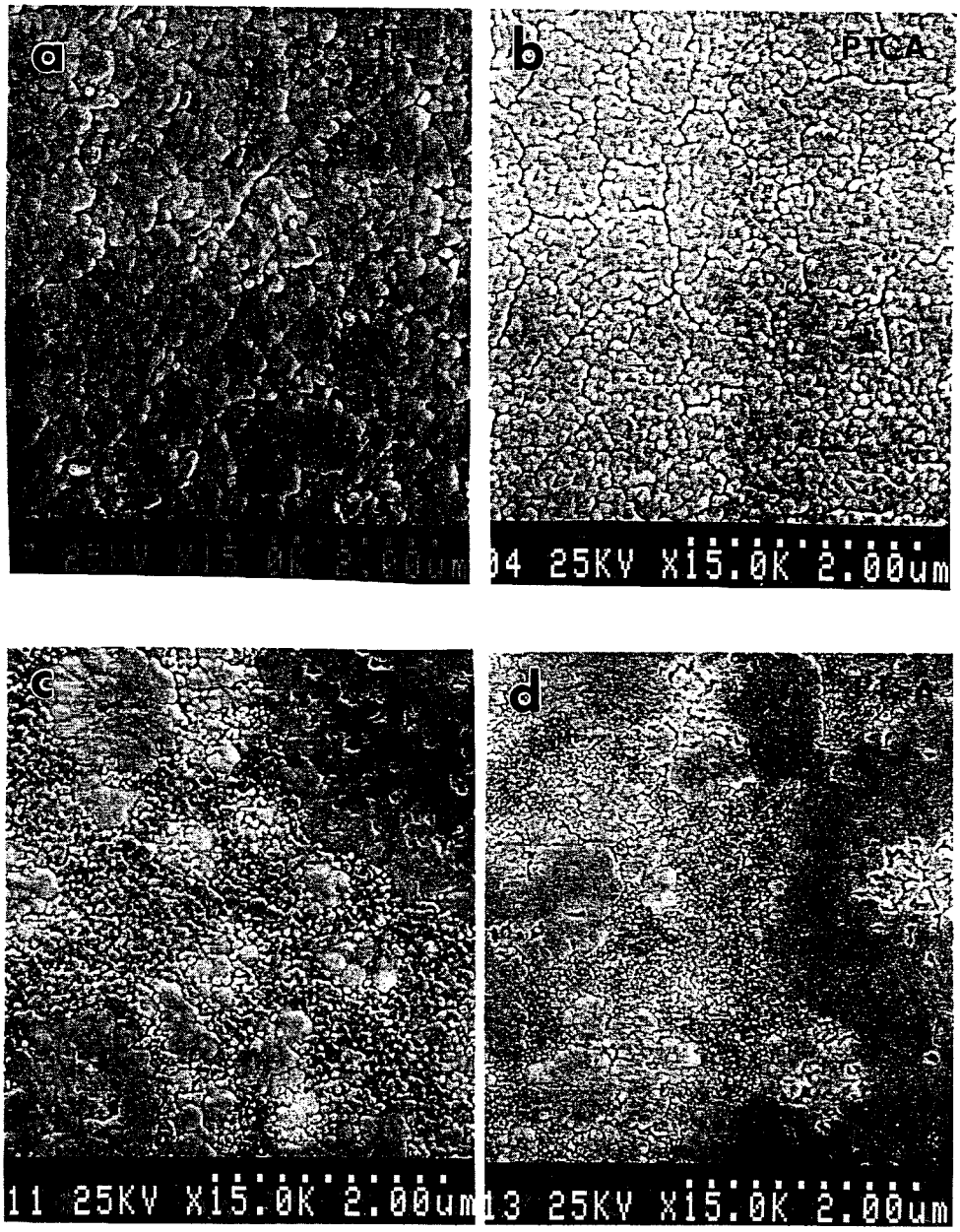


Figure 4. SEM micrographs of thin films prepared from System I annealing 700 °C - 1 h.

The processed image of a film from system I, annealed during 5 min., shows a homogeneous microstructure. On the other hand, the microstructures corresponding to films from systems II and III are inhomogeneous, showing the aspect which characterizes a microstructure in a stage of abnormal grain growth or secondary recrystallization.

The evolution of grain size distributions for thin films of system I, from 5 to 60 min. soak times, show the characteristic behavior of a normal grain growth process with an increase of the grain size mean value from 0.067 to 0.099 μm without a change in the shape of the distribution. The grain size distributions for systems II and III are log-normal. They show an increase of the mean value from 5 to 60 min. soak times. This change is from 0.073 to 0.129 μm in system II and from 0.100 to 0.131 μm in system III. The increase of the mean value is accompanied by a change in the shape towards a higher asymmetry to larger grain sizes. This shows that in both systems the number of recrystallized clusters, which give rise to the largest grains, is higher the higher the soak time. This evolution is characteristic of the secondary recrystallization process. The cluster size distributions are similar for the films of systems II and III. They show a slight increase in the mean value, from 0.626 to 0.680 μm in system II and from 0.565 to 0.647 μm in system III, with increasing soak time. The degree of recrystallization of the clusters is higher in system III than in system II. This gives rise to higher upper limits in the measured intervals of grain size: 0.814 and 0.956 μm in system III compared with 0.317 and 0.676 μm in system II, for 5 and 60 min. soak times respectively.

4. Discussion

PTP and PTCA thin film differences in grain size are in accordance with previously reported results in Ca-modified PZT films [25] and, also, in Ca and La- modified lead titanate ceramics [26,27], showing a reduction in grain size in modifications with increasing Ca content. PTSA and PTS microstructures are similar to that reported for PZT [28,29] and La-modified lead titanate [19] sol-gel films. Comparing SEM with XRD results, the fine grained phase can be ascribed to the pyrochlore phase, whereas the large grains are highly a-axis oriented perovskite phase. The appearance of these two phases can be due to the chemistry, namely the remanence of OAC groups, and to the aging of the solutions [29]. These results suggest that the appearance of this microstructure is also a composition sensitive effect. In the study to minimize the pyrochlore phase, the computer aided image analysis technique can determine very precisely the relative areas of both phases as a function of the annealing conditions of the films. This study is in progress and could determine if both phases are crystallized simultaneously from the amorphous matrix or if the pyrochlore phase appears first and the perovskite is a result of transformation from this phase at higher temperature.

Two types of microstructures have been found for pure lead titanate thin films prepared from system I, II and III, which reveals a processing dependence of the microstructure. This can be explained by the results of TG and DTA of the xerogels. The films prepared by spin-coating the precursor solutions release energy during the annealing process, as the transformation from gel to polycrystalline material takes place. This energy increases with the complexity of the polymeric species contained in the gel and, therefore, with the length of the carbon chain of the diol used as solvent. The different internal energies add to the external thermal energy, which is supplied to the systems when annealing under the same conditions of time and temperature. The increasing total

energy acting during the annealing of the films causes the development of increasingly advanced grain growth stages.

5. Conclusions

The feasibility of Ca and Sm-modified lead titanate based thin film preparation by a diol based sol-gel route has been demonstrated. Ca^{2+}-modified thin films show finer grain size microstructures than the pure $PbTiO_3$ films and both have homogeneous microstructures. Sm^{3+}-modified lead titanate films show two phases. A perovskite phase, corresponding to large (001) oriented grains, and a pyrochlore phases of nanometer scale grain size. Similarities of this microstructure are found with that reported in literature for La^{3+}-modified lead titanate films. A combination of SEM and computer aided image analysis provided a detailed microstructural characterization of the pure lead titanate films. The dependence of the microstructure on the diol solvent type was ascribed to differences in the thermal behavior of the corresponding gels. Results evidenced the strong dependence of the film microstructure on the chemistry of the precursor solutions.

6. Acknowledgments

This work was supported by Spanish Projects MAT91-422 (CICYT) and C120/91 (CAM) and was declared of technical interest by the CE COST 514 action on Ferroelectric Ceramic Thin Films.

7. References

1. Yamashita, Y., Yokoyama, K., Honda, H. and Takahashi, T. (1981), *Jap. J. Appl. Phys.* **20**, 183.
2. Ito, Y., Nagatsuma, K., Takeuchi, H. and Jyomura, S. (1981), *J. Appl. Phys.* **52**(7), 4479 .
3. de Frutos, J., Lopez, F. and Jimenez, B. (1992), *Proc. ISAF' 92*. p.36 .
4. Millar, C.E., Wolny, W.W., Pardo, L., Ricote, J., Sirera, R., Feuillard, G. and Lethiecq, M. (1993), *Proc. of the Third Meeting of the ECS*. vol.**2**, pp. 187.
5. Adachi, H., Kawaguchi, T., Kitanabe, M. and Wasa, K. (1983), *Jap. J. Appl. Phys.* **22**, Suppl. 22-2, 11.
6. Adachi, H., Mitsuyu, T., Yamazaki, O. and Wasa, K. (1985), *Jap. J. Appl. Phys.* **24**, Supp. 24-3, 13.
7. Ijima, K., Kawashima, S. and Ueda, I. (1985), *Jap. J. Appl. Phys.* **24**, Suppl 24-2, 482 .
8. Yamaka, E., Watanabe, H., Kimura, H., Kanaya, H. and Ohkuma, H. (1988), *J. Vac. Sci. Technol.* **A 6** (5), 2921.
9. Takayama, R., Tomih, Y., Iijima, K. and Ueda, I. (1987), *J. Appl. Phys.* **61** (1), 411.
10. Ye, C., Tamagawa, T. and Polla, D.L. (1991), *J. Appl. Phys.* **70** (10), 5538.
11. Polla, D.L., Ye, C. and Tamagawa, T. (1991), *Appl. Phys. Lett.* **59** (27), 3539 .

12. Adachi, H., Mitsuyu, T. and Wasa, K. (1985), *Jap. J. Appl. Phys.* **24**, *Suppl. 24-1*, 121.
13. Mansingh, A. (1990), *Ferroelectrics* **102**, 69 .
14. Swartz, S.L. and Wood, V.E. *Cond. Matter News* **1** (5), 4.
15. Tani, T., Xu, Z. and Payne, D. (1993), *Mat. Res. Soc. Symp. Proc.* **310**, 269.
16. Kushida, K., Udayakumar, K.R., Krupanindi, S.B. and Cross, L.E. (1993), *J. Am. Cer. Soc.* **76** (5), 1345.
17. Adachi, H., Mitsuyu, T., Yamazaki, O. and Wasa, K. J. (1986), *Appl. Phys.* **60** (2), 736.
18. Shimizu, Y., Udayakumar, K.R. and Cross, L.E. (1991), *J. Am. Cer. Soc.* **74** (12), 3023.
19. Ho, J.C., Lin, I.N. and Liu, K.S. (1994), *J. Mat. Sci.* **29**, 1884 .
20. Phillips, N.J., Calzada, M.L. and Milne, S.J. (1992), *J. Non-Cryst. Sol.* **147-148**, 285.
21. Sirera, R., Calzada, M.L., Carmona, F. and Jimenez, B. (1994), *J. Mat. Sci.* (in press).
22. Pardo, L., Calzada, M.L., Milne, S.J., Ricote, J. and Jimenez, B (1994), (in press).
23. Calzada, M.L. and Sirera, R. (1994) "Synthesis of multicomponents solutions for the crystallization of lead titanate based perowskites" (internal report).
24. Kurtz, S.K. and Carpay, F.M.A. (1980), *J. Appl. Phys.* **51** (11), 5745.
25. Huffman, M. and Schuele, P.J. (1993), *Ferroelectrics* **143**, 251.
26. Yamamoto, T., Igarashi, H., Okazaki, K. (1985), *Ceram. Intl.* **11** (3), 75.
27. Yamamoto, T., Igarashi, H., Okazaki, K. (1983), *J. Am. Cer. Soc.* **66** (5), 363.
28. Calzada, M.L. and Milne, S.J. (1993), *J. Mat. Sci. Lett*, 12, 1221.
29. Lakerrnan, C.D.E. and Payne D. A. (1992), *J. Am. Cer. Soc.* **75** (11), 3091.

STOICHIOMETRY AND PHASE STRUCTURE OF SOL-GEL-DERIVED PZT-BASED THIN FILMS

M. KOSEC,[1] Y. HUANG,[2] E. SATO,[3]
A. BELL,[2] N. SETTER,[2] G. DRAŽIČ,[1]
S. BERNIK[1] AND T. BELTRAM[1]

1. *University of Ljubljana, "Jožef Stefan" Institute, Jamova 39, 61000 Ljubljana, Slovenia*
2. *Laboratoire de Céramique, Ecole Polytechnique Federale de Lausanne, MX-Ecublens, CH - 1015 Lausanne, Switzerland*
3. *on leave from the Institute of Space Astronautical Science, 3-1-1, Joshinodai Sagamihara 229, Japan*

ABSTRACT. $PbTiO_3$ thin films with different amounts of excess lead oxide in the precursor solutions were prepared by the sol-gel process and spin coating. The composition, crystal structure and microstructure of films annealed at different temperatures were studied. The crystal structure and chemical composition of coexisting phases that crystallize from highly lead deficient PLZT amorphous layers were analyzed. The results are correlated with the available phase - equilibrium data in this system.

1. Introduction

The family of PZT based ceramic materials, whose most important members are $PbTiO_3$, $Pb(Zr,Ti)O_3$, $(Pb, La)(Zr, Ti)O_3$, is probably unique in possessing a variety of properties that can be utilized in electronic devices [1, 2]. The diversity of applications broadens further when these materials are in the form of thin films. Among others, devices such as non-volatile memories, pyroelectric sensors, piezoelectric SAW devices, microactuators, and electrooptic modulators have been demonstrated, and many other applications are still foreseen [3]. It is well known that the chemical composition with respect to lead content, Zr/Ti ratio and the type and amount of dopants plays a major role in tailoring the characteristics of bulk ceramics for certain applications. While the basic composition with reference to the Zr/Ti ratio and the type and amount of dopant is governed by the batch composition, the amount of PbO in the final product is mainly controlled by the thermal treatment, because of its high vapor pressure at the sintering temperature of 1100-1300 °C [4, 5]. Lowering the processing temperature of PZT - based materials in the form of thin films to 500-700 °C thermodynamically favors the possibility of better compositional control. On the other hand, scaling down the size of elements to the submicron thickness increases the surface to volume ratio and kinetically favours the reduction of the overall PbO content in the film during heat treatment. The most important consequences of lead loss is a stabilization of the parasitic pyrochlore phase

O. Auciello and R. Waser (eds.), Science and Technology of Electroceramic Thin Films, 177-186.
© 1995 *Kluwer Academic Publishers. Printed in the Netherlands.*

that is PbO deficient compared to the perovskite phase. How the desired stoichiometry can be maintained depends on the thin film processing methods.

To compensate for lead loss during sol-gel processing an excess of lead oxide is usually introduced into the precursor solution of $PbTiO_3$ [6] PZT [7-11] and PLZT [12,13]. However, there have been only a few studies on the lead losses in PZT based thin films.

Tuttle et al [7] reported that the optimum amount of excess PbO in PZT was about 5 %. At this precursor solution composition, the pyrochlore phase content in films was minimized, resulting in improved ferroelectric properties of films.

Klee et al [9] and Reaney et al [10] found that the Pb(Zr,Ti) ratio of PZT films decreased by 10 mol % from that of the solutions after annealing at 700 °C, independently of the amount of the excess PbO in the precursor solution. The final properties were again critically dependent on the amount of PbO excess.

On the other hand, the work of Huang et al [14] showed there to be little effect of excess PbO additions on the dielectric and pyroelectric properties of sol-gel prepared $PbTiO_3$ films annealed at 700 °C. This suggests that the PbO loss behavior of $PbTiO_3$ is different from that of PZT. Therefore the present authors studied the PbO losses of $PbTiO_3$ films processed at different temperatures first [15]. After that the influence of over- stoichiometry in the precursor solution on the microstructure of the annealed films was studied. In the first part of the paper the correlation between excess PbO in the precursor solution and chemical composition, crystal structure and microstructure are summarized and further discussed.

As mentioned above, the loss of PbO from PZT and PLZT, respectively, results in the appearance of a pyrochlore phase that is lead deficient and commonly rich in Zr as compared to the perovskite phase [12,16]. Detailed TEM-EDXS analyses of PLZT were therefore undertaken to follow quantitatively the composition and structure of the coexisting perovskite and pyrochlore phases in sol-gel derived PLZT films. The results are discussed in the second part of the paper.

2. Experimental

2.1. $PbTiO_3$ FILMS

Precursor stock solutions were prepared from lead-acetate trihydrate and titanium iso-propoxide in a solvent of 2-methoxyethanol. Three kinds of solution with a nominal excess of PbO of 5, 15 and 25 mol % were used. After refluxing and vacuum distillation, 4 vol % of formamide was added to the solution [14].

Gel layers were deposited by spin casting at 3000 rpm for 30 s onto silicon substrates, which had previously been coated with SiO_2/Ta/Pt layers of thickness 1000, 10 and 100 nm, respectively. After each layer deposition, the gel was dried and partially crystallized by placing on a hot plate at a temperature of 500 °C for 30 s, a process referred to as pyrolysis. This procedure was repeated to produce a film of 10 layers with a total thickness of 500 nm after crystallization. Final annealing was carried out at temperatures between 550 and 750 °C for 1 min, with a heating rate of 50 °C/s using a rapid heating module in flowing oxygen.

The precursor solution was analyzed by the ICP method. Pb/Ti ratios, calculated as PbO/TiO_2 molar ratios of thin films, were measured by electron probe microanalysis

(EPMA, SX50, Camera, France) with an accelerating voltage of 8 kV using Ti(K)α and Pb(M)α peaks on carbon coated films. A $PbTiO_3$ single crystal was used as a standard under these conditions. The Proza curves indicate that all of the X-rays come from the inside of the film; in fact, no Pt(M) peaks were observed in the spectra. The Pb/Ti ratio of the single crystal was itself determined at 20 kV using Ti(K) and Pb(L) peaks against Ti metal and PbS standards.

The films were analyzed by an X-ray diffraction apparatus (XRD, D500, Siemens, Germany) equipped with a secondary beam monochromator (Cu Kα1, Kα2 radiation). The surface microstructure of the films was analyzed by a Jeol JXA 840A scanning electron microscope. Samples were coated with Gold. The equivalent spherical diameter was measured by point analysis [17].

2.2. PLZT FILMS

PLZT 9.5/65/35 films were prepared using lead-acetate trihydrate, lanthanum acetate hydrate, titanium iso- propoxide and zirconium n-propoxide in 2-methoxyethanol solution. Details of the sol synthesis have been reported elsewhere [18]. An excess of lead oxide was omitted.

The complex precursor solution was partly hydrolyzed by adding drop-wise a mixture of water, acetic acid and methoxyethanol at room temperature. The amount of water corresponded to $r_v = 2.5$. Thin films were prepared by solution spin-coating on Si(100)/Pt and MgO(100) substrates. Three coatings were used and after each coating the film was pyrolyzed at 400 °C for 30 min. The samples were fired between 5 min and 1 hour at temperatures in the range between 500 and 850 °C and examined by scanning (Jeol 840A) and transmission electron microscopy (Jeol 2000 FX, operated at 200 kV). The chemical composition of the phases was determined using a Link AN-10000 EDXS system with a UTW detector connected to the TEM. The Cliff-Lorimer method and absorption corrections were used for quantitative analysis of Pb, La, Zr and Ti. The concentration of oxygen was determined from the stoichiometry. As a standard, a thin foil of hot-pressed PLZT (9.5/65/35) ceramic synthesized from the oxides was used. Plan view TEM specimens were prepared by mechanical thinning, dimpling and ion milling from the side of the samples opposite to the film with 4 keV argon ions. The contamination present on the thin film was removed by short ion milling from the film side. A cross-section of the thin film was prepared using a Gatan cross-sectional TEM specimen preparation kit.

3. Results and Discussion

3.1. $PbTiO_3$ FILMS

In order to follow the influence of excess PbO on the composition and crystallization of $PbTiO_3$ films, precursor solutions with 5, 15, 25 mol % excess PbO were synthesized. The Pb/Ti ratios in the precursor solutions were checked by ICP analysis. The results obtained were 1.08 for the solution with 5 mol % excess PbO, 1.15 for the solution with 15 mol % excess PbO and 1.25 for the solution with 25 mol % excess PbO.

The results of EPMA analysis of $PbTiO_3$ films thermally treated at different temperatures are presented in Fig. 1.

The Pb/Ti ratio of the dried samples was found to be 1.05 for the sample with 5 mol % excess PbO, 1.15 for the sample with 15 mol % excess PbO and 1.22 for the sample with 25 mol % PbO excess. The results are consistent with those found by ICP.

Films start to lose PbO during annealing at 600 °C for 1 min. After annealing at 700 °C for 1 min the Pb/Ti ratio of the samples approaches 1 independently of the amount of PbO in the precursor solution. Annealing at higher temperature, i.e. 750 °C for 1 min does not change the stoichiometry of the films.

Fig. 2 shows X-ray traces of selected $PbTiO_3$ films. Independent of annealing temperature and starting stoichiometry, X-ray analysis reveals only the perovskite $PbTiO_3$ phase. Neither pyrochlore nor PbO phases were detected by X-ray analysis. The additional reflections shown in Fig. 2 were identified as belonging to Ta_2O_5 originating from the Ta adhesion layer below the platinum. Oxidation takes place during heating at 700 °C.

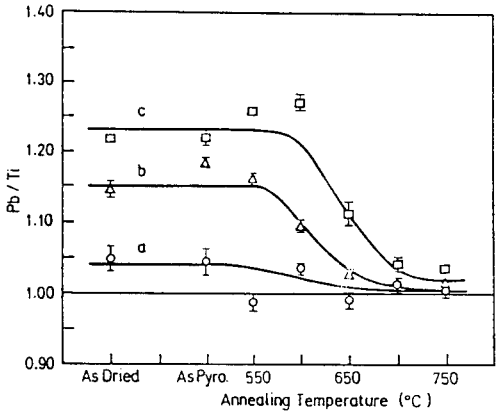


Figure 1. Composition of $PbTiO_3$ films versus temperature: a) 5 mol % excess PbO; b) 15 mol % excess PbO; c) 25 mol % excess PbO in precursor solution.

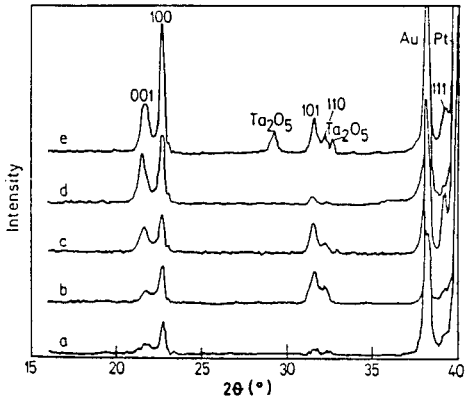


Figure 2. X - ray traces of $PbTiO_3$ film: a) pyrolyzed, 25 mol % PbO excess; b) annealed at 550 °C, 5 mol % PbO excess; c) annealed at 550 °C, 15 mol % PbO excess; d) annealed at 550 °C, 25 mol % PbO excess; e) annealed at 750 °C, 25 mol % PbO excess.

The development of a perovskite phase in films that were only pyrolyzed at 500 °C for 30 s is in agreement with published data showing that the common crystallization temperature for the perovskite phase in sol-gel prepared PT films are near 500 °C [11].

According to data for the pseudo-binary PbO-TiO_2 system [19] the solid solubility of PbO in $PbTiO_3$ is practically zero. This suggests that excess PbO in the films annealed below 700 °C might coexist as an amorphous phase, as shown for example for $Pb(Sc_{1/2}Ta_{1/2})O_3$ [20] and PZT [21].

As shown in Fig. 1 $PbTiO_3$ films reach the stoichiometric composition, and therefore the losses are only from the amorphous phase and not from the perovskite phase.

From the intensity of the X-ray lines crystallization apparently proceeds at the temperature of annealing and with a PbO excess. Films are preferentially <001> oriented as reported by Carper and Phulé [6] although the ratio of 001/100 changes neither by the annealing temperature nor by the PbO excess.

Fig. 3 shows the scanning electron micrographs of the surface of films annealed at 600 °C for 1 min and films annealed at 750 °C for 1 min.

The grain structure was first discernible in films with 5 and 15 mol % excess PbO after annealing at 600 °C for 1 min, whereas films with 25 % excess PbO annealed under the same conditions still show a non-discernible grain morphology [Fig. 3 (a), (b), (c)]. After annealing at 750 °C for 1 min (Fig. 3 (d), (e), (f)), there is a significant grain boundary growth. As expected the surface roughness and the porosity of the films increase with the amount of PbO that evaporates during annealing, as observed by EPMA analysis.

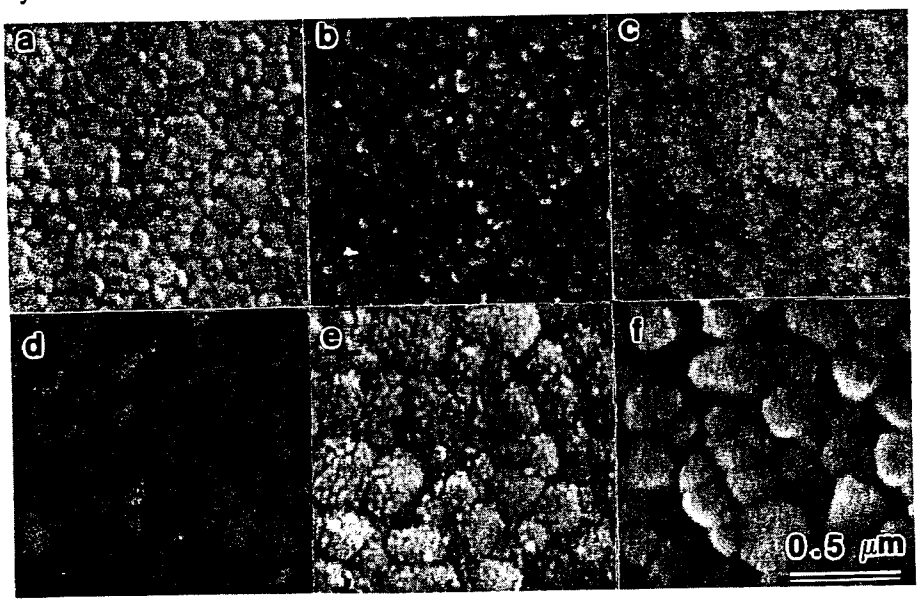


Figure 3. Scanning electron micrographs of $PbTiO_3$ films annealed at 600 °C a) with 5 mol% excess PbO, b) with 15 mol % excess PbO, c) with 25 mol % excess PbO; annealed at 750 °C, d) with 5 mol % excess PbO, e) with 15 mol % excess PbO, f) with 25 mol % excess PbO.

The equivalent spherical diameters of grains for the films annealed at different temperature are collected in Table 1.

Excess lead in the amount from 5 to 25 mol % does not influence the grain size of the $PbTiO_3$ films. There is a significant increase of grain size during annealing at 700 °C for 1 min that coincides with the stoichiometric composition of the films as found by microprobe analysis.

It seems worth discussing lead losses in $PbTiO_3$ and PZT films.

TABLE 1. Equivalent spherical grain diameter of $PbTiO_3$ films with a different amount of PbO excess annealed at different temperature.

Temperature	eq. spherical grain diameter (μm)		
(°C)	5 mol %	15 mol %	25 mol %
600	0.11	0.12	-
650	0.13	0.14	0.13
700	0.22	0.19	0.20
750	0.19	0.20	0.18

PbO losses of a PbO containing compound at a given temperature and for a fixed time are proportional to the equilibrium vapor pressure of PbO above the lead based compound.

Let us consider that the relation log p (PbO) versus (-1/T) for PbO, PZT and $PbTiO_3$ that is well investigated for high temperatures [4, 22] might be extrapolated for the thin film processing temperature. If this is the case, the equilibrium vapor pressure of PbO over $PbTiO_3$ will be 2 orders of magnitude smaller than that over PbO. Therefore when both phases coexist preferential evaporation of PbO from PbO phase is to be expected.

The $PbTiO_3$ perovskite phase starts to crystallize during pyrolysis at a sufficiently low temperature without detectable PbO loss. If a moderate temperature is applied, over-stoichiometric samples will lose PbO until stoichiometric $PbTiO_3$ is obtained. Therefore final stoichiometry will not depend on excess PbO in the precursor solution.

The crystallization temperature of PZT perovskite phase is at least 100 °C higher than that of $PbTiO_3$. At that temperature PbO losses are already significant; PbO evaporates from the whole volume, namely from the amorphous and presumably pyrochlore phase until the crystallization of the PZT phase is complete. The amount of PbO loss is therefore not dependent on the starting (over) stoichiometry. Because the equilibrium vapor pressure depends exponentially on temperature, it is obvious how important it is to lower the temperature of crystallization of the perovskite phase, as well as to exert better control over the stoichiometry of the annealed films.

3.2. PLZT FILMS

Quantitative EDXS analyses were performed on the view TEM specimens and the PbLa/ZrTi Pb/La and Zr/Ti ratios (in atom %) were calculated. For calculation, averages of at least 4 measurements on the same sample were used. The accuracy of quantitative analysis was determined on thinned PLZT (9.5/65/35) hot pressed ceramics where thin foil thickness, position of the analyzing area on the samples and counting rates and times

were varied. For all the elements examined the relative standard deviation of the measurements was less than or equal to 5 %.

The PLZT thin films samples analyzed and the ratio of the concentration of the elements in various phases (in atom %) are shown in Table 2.

TABLE 2. Composition of pyrochlore and perovskite phases of films annealed under different conditions.

Temp. (°C)/ time (min)/ substrate	phase	PbLa/ZrTi	Pb	La	Zr	Ti
Hot pressed	P	1.0	90	10	65	35
500/60/Si	A	1.0	90	10	63	37
600/60/Si	A	0.56	84	16	62	38
750/20/Si	Py	0.48	78	22	64	36
850/5/Si	Py	0.48	74	26	70	30
850/30/Si	Py	0.20	56	44	84	16
800/5/MgO	Py	0.22	61	39	87	13
850/5/Si	P	0.77	85	15	58	42
850/30/Si	P	0.71	85	15	59	41
800/5/MgO	P	0.91	89	11	58	42

A - amorphous, Py - pyrochlore, P - perovskite

After firing the thin film on a Si(100)/Pt substrate at 500 °C for 60 min, the film was amorphous with a chemical composition close to standard hot pressed PLZT (Table 2). After firing the sample on the same substrate at 600 °C for 60 min, the film was still amorphous and the PbLa/ZrTi ratio was lowered by almost one half, while the Pb/La ratio decreased with respect to the starting composition. This difference in chemical composition in the sample was explained by the evaporation of PbO, and by the reaction of PbO from the PLZT thin film with the substrate [23].

The microstructure of samples annealed at temperatures higher than 600 °C consists of perovskite rosettes surrounded by a microcrystalline pyrochlore phase (Figs. 4 (a) and (b)). The composition of the coexisting perovskite and pyrochlore phases are also given in Table 2.

The composition of the pyrochlore phases significantly differs from starting ABO_3 stoichiometry. The deviation increases with temperature and time of annealing and depends on the substrate. Depending on the annealing conditions and substrate used (see Table 2), they contain less than 50 % of A cations with respect to the starting stoichiometry A/B = 1 and approach a chemical composition with only 20 % of the original A/B ratio. Evidently such a phase contains a higher amount of La and Zr. This might be tentatively explained by the higher tendency of La and Zr to form pyrochlore [24]. The change of composition of the pyrochlore phase with annealing time was tentatively explained by solution-precipitation of pyrochlore nuclei of subcritical size

[25]. The stoichiometry of perovskite phases depends less on the annealing conditions, and generally the composition has a lower in A/B ratio and a higher in La and titanium as compared to the starting composition. The A/B ratio of perovskite phase that crystallizes on MgO, and therefore its stoichiometry, is affected by PbO loss through evaporation (no reaction with the substrate) and differs up to 10 % from the starting A/B ratio. The concentration of La is slightly increased, whereas the increase in Ti is more pronounced.

In contrast, the composition of the perovskite phase that crystallizes at 850 °C for 30 min on a Si substrate (reaction of PLZT with the substrate) is characterized by an almost 30 % A ion deficiency and a significant increase in the amount of La and Ti. Its calculated formula might be $Pb_{0.60}La_{0.11\text{-}0.29}Zr_{0.59}Ti_{0.41}O_{2.78}$. The deviation from stoichiometry is much greater than that found in bulk PLZT ceramics [26].

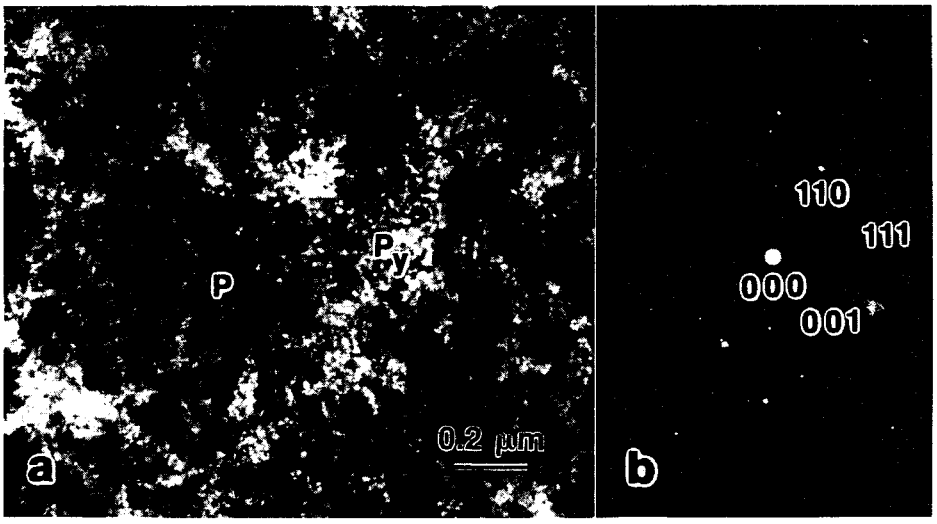


Figure 4. TEM micrograph of PLZT/850/30/Si sample. Perovskite rosette (P) are surrounded with pyrochlore (Py) particles, b) SAD of perovskite particle.

4. Conclusions

Lead losses in sol-gel-derived $PbTiO_3$ and PLZT were investigated using electron probe microanalysis and energy dispersive X-ray spectroscopy. The results were correlated with the crystallography microstructure and composition of the phases present after annealing of the samples at different temperatures.

An excess of lead oxide to the amount of 5,15, 25 mol % in the precursor solution of $PbTiO_3$ does not affect the composition of the films after annealing at 700 °C for 1 min. The composition approaches its stoichiometric value (Pb/Ti = 1). Below this temperature PbO might exist as an amorphous phase. It promotes the crystallization of the <001> preferentially oriented perovskite phase without changing the ratio of the (001) to (100) orientation. The excess of lead oxide does not influence the grain size of the thin films.

Pronounced grain growth is observed during annealing at 700 °C for 1 min, that coincides with the removal of the excess PbO.

The pyrochlore phase that coexists in lead deficient PLZT films is highly lead deficient and rich in La and Zr.

Lead deficient perovskite phases also contain an increased amount of La and a reduced amount of Zr. According to EDXS the perovskite phase can tolerate almost a 30 % deficiency of A (Pb, La) ions.

5. Acknowledgements

This work was supported by the Swiss National Electrical Engineering Programme: LESIT, and the National Research Programme of the Ministry of Science and Technology of the Republic of Slovenia.

6. References

1. Jaffe, B., Cook, W.R.Jr. and Jaffe, H. (1986), *Piezoelectric Ceramics*, Academic Press, London.
2. Haertling, G.H., (1986), *Piezoelectric and Electrooptic Ceramics, in Ceramic Materials*, E.C. Buchanan (ed), Marcel Deeker, Inc., New York, pp. 139.
3. Swartz, S.L. and Wood, V.E. (1992), *Ferroelectric Thin Films, Condensed Matter News* **1**, 4.
4. Holman, R.L. and Fulrath, R.M. (1973), *J. Appl. Phys.* **44**, 5227.
5. Kingon, AI., Terblanche, P.J., and Clark, J.B. (1985), *Mat. Sci Eng.* **71**, 391.
6. Carper, M.D. and Phulé, P.P. (1993), *Appl. Phys. Lett.* **63**,153.
7. Tuttle, B.A., Schwartz, R.W., Doughty, D.H., and Voigt, J.A. (1990), in *"Ferroelectric Thin Films"*, *Mat. Res. Soc. Symp. Proc.*, Vol. **200**, E.R. Myers and A I. Kingon (eds), Materials Research Society, Pittsburgh, pp. 159.
8. Myers, S.A. and Chapin, L.N. (1990), in *"Ferroelectric Thin Films"*, E.R. Myers and A I. Kingon (eds), *Mat. Res. Soc. Simp. Proc.*, Vol. **200**, Materials Research Society, Pittsburgh, pp. 231.
9. Klee, M., de Veirman, A., van de Weijer, P., Mackens, U., and van Hal, H. (1993), *Philips J. Res.* **47**, 263.
10. Reaney, I.M., Brooks, K, Klissurska, R., Pawlaczyk, C., and Setter, N. (in press), *J. Am. Ceram. Soc.*
11. Kwok, C.K and Desu, S.B. (1993), *J. Mater. Res.* **8**, 339.
12. No, K., Yoon, D.S., and Kim, J.M. (1993), *J. Mater. Res.* **8**, 245.
13. Chang, J.F. and Desu, S.B. (1994), *J. Mater. Res.* **9**, 955.
14. Huang, Y., Daglish, M., Reaney, I., and Bell, A. (1993), *Third Euro-Ceramics V.2.*, P. Duran and J. F. Fernandez (eds), Faenza Editrice Iberica., S.L. San Vicente, pp. 699.
15. Sato, E., Huang, Y., Kosec, M., Bell, A., and Setter, N. *(submitted to J. Appl. Phys. Lett.).*
16. Hsueh, C.C. and Mecartney, M.L. (1991), *J. Mater. Res.* **6**, 2208.
17. Underwood, E.E. (1970) , *Quantitative Stereology, Addison-Wesley Publishing Co.*, Reading, Massachusetts.
18. Beltram, T., Kosec, M., and Stavber, S. (1993), *Mat. Res Bull.* **28**, 313.

19. Phase Diagrams for Ceramists, Fig. 6425, pp. 135.

LIQUID PHASE EPITAXY OF $Na_{1-y}K_yTa_{1-x}Nb_xO_3$ ON $KTaO_3$ SUBSTRATES

Z. SITAR, R. GUTMANN, AND P. GÜNTER
ETH Zürich, Institute of Quantum Electronics
CH-8093 Zürich, HPT E4
Switzerland,

ABSTRACT. Para- and ferroelectric epitaxial layers of $Na_{1-y}K_yTa_{1-x}Nb_xO_3$ were grown from a KF-NaF–KTN solution on (100) $KTaO_3$ substrates by LPE. Lattice matching of the 5 to 30 μm thick films was achieved by adding a certain percentage of NaF to the melt. The incorporation of Na in the crystal decreased the lattice constant of the film which lead to a decrease of structural defects. Auger and XPS analyses showed that the grown films were stoichiometric, contamination free, and uniform in composition. As-grown films had a blue tint which most likely arose from oxygen deficiency. Films became transparent after annealing in oxygen atmosphere. Temperature and frequency dependence of the pyroelectric response of the in plane poled $Na_{0.1}K_{0.9}Ta_{0.55}Nb_{0.45}O_3$ layers measured by the use of a chopped laser beam revealed a maximum pyroelectric constant of 5200 $\mu As/m^2K$ at 338 K.

1. Introduction

Black body radiation of warm objects, i.e., temperature range from -30 to 100°C, occurs in the invisible infrared (IR) spectral range between 8 and 12 μm. The sensing of this radiation has became of growing interest for a wide range of applications. There exists a strong drive to find a relatively inexpensive replacement for the presently used HgCdTe technology which would not require cooling to cryogenic temperatures. Very strong contenders are detectors based on the pyroelectric materials which operate at or close to the room temperature. Pyroelectrics are not spectrally selective devices. As such, one can, with the application of a suitable filter, use the same detection system for the detection of the radiation in a broad spectral range, from x-rays to microwaves.

A pyroelectric detector can operate either in the pyroelectric or permittivity (capacitance) mode. In the first case, which utilizes the effect of falling spontaneous polarization, a stable material with a high T_C can be used. The only requirement for a successful operation is that the temperature of the material remains below T_C at all times. In the second case a material which has a transition close to the room temperature is chosen. Its temperature is stabilized with a Peltier heater/cooler close to T_C and a permanent poling voltage is applied. The advantage of the operation in this mode is highly increased sensitivity since the pyroelectric coefficient and dielectric constant

O. Auciello and R. Waser (eds.), Science and Technology of Electroceramic Thin Films, 187-199.
© 1995 *Kluwer Academic Publishers. Printed in the Netherlands.*

exhibit strong changes close to T_C. The most promising materials for the detectors operating in this mode seem to be tyrglicine sulfate (TGS) [1], $Ba_{1-x}Sr_xTiO_3$ [2, 3], different modifications of PZT [4], and $KTa_{1-x}Nb_xO_3$ [5, 6]. Properties of some ferroelectric materials relevant for pyroelectric applications with their figures of merit F_v (voltage responsivity) and F_d (noise limited figure of merit) are shown in Table 1.

TABLE 1. Properties of some ferroelectric materials relevant for pyroelectric applications.

Material	T_C [K]	F_v [cm^2/As]	F_d [$(cm^3/J)^{1/2}$]	Reference
TGS	322	3620	0.066	Herbert [7]
$BaSrTiO_3$	294	2700	0.84	Kulwicki [3]
PZT	323	5300	0.19	Lian [4]
$KTaNbO_3$	313	50000	5.0	Schubring[8]

In addition to the pyroelectric, $KTa_{1-x}Nb_xO_3$ possesses a high figure of merit also for electro-optic and nonlinear-optic applications. The combination of the two materials offers a possibility to tailor the transition temperature in the range from almost 0 ($KTaO_3$) to 691 K ($KNbO_3$) which can be used to optimize the properties for a specific application. Although both materials belong to the ABO_3 materials with the perovskite structure they show with the regard to structural phase transitions different behavior. $KTaO_3$ belongs to the cubic class (at least above 2 K), whereas $KNbO_3$ exhibits the classical sequence of 3 ferroelectric phase transitions between cubic (691 K), tetragonal (498 K), orthorhombic (263 K), and rhombohedral phases.

The existence of several phase transitions makes the heteroepitaxy of $KTa_{1-x}Nb_xO_3$ difficult. Respective thin films have been grown by rf-sputtering on Si and Pt substrates [9], by laser ablation on $SrTiO_3$ [10], by liquid phase epitaxy on $KTaO_3$ [11], and by sol-gel technique [12].

In the present paper we report on the liquid phase epitaxy of para- and ferroelectric KTN layers from dilute KF-KTN solutions. The following sections describe the growth procedures used for the deposition of $KTa_{1-x}Nb_xO_3$ thin films and the results of various structural, chemical, and electrical analyses performed after the growth.

2. Experimental Procedures

2.1. GROWTH APPARATUS

We performed the LPE growth experiments in an in-house built three zone resistively heated oven able to reach a temperature of 1500 K and a stability of better than 0.1 K. The length of the growth zone was 25 cm. The 65 cm^3 Pt crucible had a 14 cm long neck to protect oven from corrosive vapors. It was imbedded in an Inconel block in order to increase the thermal mass and to avoid its deformation at higher temperatures and upon

cooldown. The whole assembly was mounted onto a vertical ceramic rod connected on the other side to a linear-rotary motion mechanism. This arrangement allowed the experiments in the accelerated crucible rotation mode which improved the mixing of materials. A Pt tube reinforced from the inside with an Inconel rod served as the substrate holder. It allowed a continuous rotation up to 900 rpm and was connected to a motorized precision lowering and hoisting mechanism. All crucial parts of the system were protected from overheating by watercooled jackets. All vapors emerging from the hot zone were removed by a controlled airflow.

2.2. SUBSTRATES

The selection of lattice matched substrates suitable for the growth of $KTa_{1-x}Nb_xO_3$ is narrow, and $KTaO_3$, which retains its cubic structure over the whole range of temperatures and has a lattice mismatch with the cubic and tetragonal phases of $KTa_{1-x}Nb_xO_3$ of less than 0.25%, seems to be the best choice. As such, all thin films were grown on $KTaO_3$ substrates. In order to determine the most suitable growth plane for the epitaxy we performed initial growth experiments on $KTaO_3$ spheres, which allowed the examination and evaluation of the growth on different planes at the same time, and continued our work on |X| cm^2 (100) oriented wafers. Prior to growth the substrates were cleaned in solvents (alcohol, acetone) and as a last step dipped into an HF solution.

2.3. THIN FILM GROWTH

The melt was prepared from ceramic $KTa_{1-x}Nb_xO_3$ and KF. KF was found to be an excellent solvent for the concentrations of oxide material lower than 8 mol%. The dissolution started already at 1120 K but to obtain a homogeneous melt the crucible was superheated to 1370 K with a dwell time of about one hour at this temperature. So prepared melt was cooled down to the deposition temperature at a rate of 1-2 K/min. After a stabilization time of about 20 min a preheated rotating $KTaO_3$ substrate mounted with a Pt wire was dipped into the supercooled solution (supercooling in the excess of 100 K was achieved quite regularly). The growth process was stopped after 5-30 min by the quick removal of the sample from the melt. The obtained films were post growth annealed in an oxygen atmosphere at 1220 K for 20 hrs. Table 2 summarizes the important parameters used for the thin film growth.

From the diagram of the phase transitions for the $KNbO_3$ - $KTaO_3$ solid solution system [13] it is evident that, in the view of good epitaxy, the use of $KTaO_3$ substrates restricts the growth of ferroelectric $KTa_{1-x}Nb_xO_3$ layers to the tetragonal phase. Practically, this means that the x value in the films should not exceed 0.6. According to the $KNbO_3$ - $KTaO_3$ phase diagram [14] this corresponds to a maximum concentration of Nb in the melt of 0.85.

The poling of the films was done above the Curie temperature with an applied electric field of 1 kV/cm in the substrate's (110) direction. For that purpose we evaporated two golden surface electrodes separated for 5 mm and oriented with their

longer side along a (110) direction. Due to the high resistivity of the substrate all poling experiments were done by switching ferroelectric domains in-plane.

TABLE 2. Growth parameters for LPE growth of $KTa_{1-x}Nb_xO_3$ thin films.

Substrates	$KTaO_3$ - (100), (110), spheres
Solvent	KF, KF + NaF
Concentration of $KTa_{1-x}Nb_xO_3$ in the melt	3 - 8 mol%
$KTa_{1-x}Nb_xO_3$ composition in the melt	$0.68 \leq x \leq 0.85$
$KTa_{1-x}Nb_xO_3$ composition in the film	$0.19 \leq x \leq 0.47$
Maximum dissolution temperature	1370 K
Growth temperature	1150 - 1220 K
Growth rate	0.4 - 1 μm/min
Film thickness	2 - 30 μm
Annealing temperature	1220 K
Annealing time	10-20 hrs

2.4. THIN FILM ANALYSES

The grown thin films were analyzed by optical and electron microscopy, x-ray diffraction, Auger and photoelectron spectroscopy, and electrical measurements.

A Nikon optical microscope was used for the optical polarization microscopy (OPM). The instrument was used in the transmission or reflection mode and had phase contrast and differential interface contrast capabilities.

The x-ray diffraction (XRD) measurements were done using the $Cu_{K\alpha 1}$ line (0.15405 nm). All precision measurements were done around the (400) peak using the peak from the $KTaO_3$ substrate (a_S = 0.39885 nm) as internal standard. The lattice mismatch was calculated from the relative position of the film peaks with respect to the substrate peak.

For the Auger electron spectroscopy (AES) measurements a Perkin-Elmer PHI–4300 high resolution scanning Auger system was used. The analysis was performed at a primary beam energy of 5 keV and at a typical beam current of about 300 nA. Samples were cleaned with a 4.5 keV Ar^+ beam. Line scans and maps were recorded in the normalized 3-point method (signal height/background intensity) to correct for topographical effects. In order to avoid the effects of preferential sputtering the depth profiles were obtained by scanning the primary beam over an angle-lapped sample.

The photoelectron spectroscopy (XPS) measurements were performed with a Perkin-Elmer PHI 5400 small spot XPS instrument. Mg x-ray source operated at 400 W and 15 kV. The spectrometer was calibrated with Cu (2p) and Au (4d, 4f) standards with an accuracy of ± 0.2 eV. Experimental curve fitting was carried out by a least squares

procedure. All measurements were done at the room temperature and ultra high vacuum conditions.

Pyroelectric measurements were performed on as-grown and poled thin films. During the measurements the samples were thermally stabilized in a small oven with a Peltier heating/cooling element. Typical heating and cooling rates were 1-2 K/min. The pyroelectric signal at different frequencies was obtained by the use of a chopped laser beam with a wavelength of 632 nm and an average power of 2.5 mW. The voltage drop over a shunt resistor of 1 MW was recorded with a lock-in amplifier.

3. Experimental Results and Discussion

3.1. SCANNING ELECTRON MICROSCOPY

The SEM images obtained from the $KTa_{1-x}Nb_xO_3$ thin films grown on a 7 mm diameter $KTaO_3$ sphere are shown in Fig. 1. Images in Fig. 1 were obtained from (100), (110), and (111) faces, respectively.

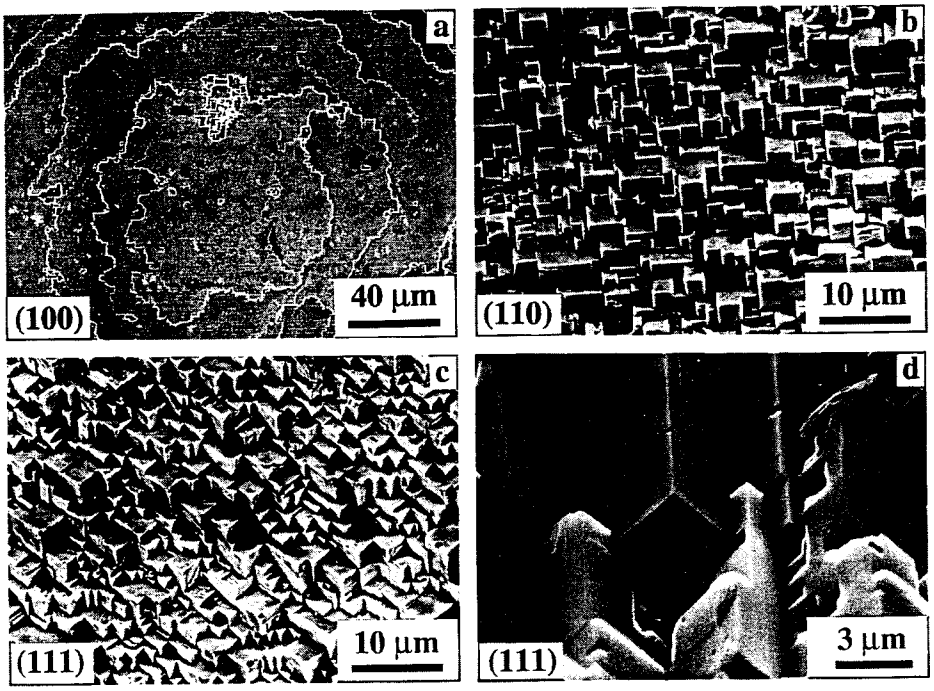


Figure 1. SEM images of $KTa_{1-x}Nb_xO_3$ thin films grown on (100), (110), and (111) planes of $KTaO_3$. Figure 1(d) shows a magnification of the growth habits on a (110) surface.

The growth on (100) faces was uniform and flat over a large area while the growth on the other two faces exhibited very strong facetting and an inhomogeneous growth. The rational for the observed behavior is that the growth planes with lower indices have a higher packing density and, therefore, generally show in an equilibrium system lower growth rates allowing enough time for the lateral rearrangements and in-plane bonding. Higher index planes, which may have no in-plane bonding vectors, allow higher growth rates resulting in entrapped cavities and nonuniform substrate coverage. A magnification of the growth habits on a (110) growth plane is shown in Figure 1(d). This image shows clearly the {100} growth facets as well as the holes which became entrapped during the growth process. The polishing of the resulting films lead to the removal of the growth facets but the polished surface remained covered with pits and pinholes of various sizes which remained present until the film was completely removed.

The center of the inner circle of Figure 1(a), which does not show any growth steps, represent the growth exactly on (100) plane while a distance away from the center represents a certain degree of missorientation. From the size of the central circle we measured the maximum substrate missorientation allowing the growth of flat stepless films to be about 30'.

Films thinner than 0.5 μm were normally not continuous and showed isolated or connected growth islands. Thicker films (>5 μm) grown on (100) $KTaO_3$ substrates were generally of a good crystalline quality and transparent but with a blue tint. The blue coloration disappeared after the annealing in oxygen atmosphere. This indicates that the as-grown films were oxygen deficient and that the blue coloration most probably arose from the oxygen vacancies.

3.2. OPTICAL MICROSCOPY

Despite the apparently good lattice match between $KTaO_3$ and tetragonal $KTa_{1-x}Nb_xO_3$, the grown thin films showed a high defect density emerging from the heteroepitaxial interface. As observed from OPM and transmission electron microscopy most of the defects were misfit dislocations, stacking faults, and twins arranged in arrays along in-plane [100] directions forming a characteristic crosshatched defect pattern as seen in Figure 2(a). This results showed the necessity for the improvement of the lattice matching if we wanted to improve the quality of films.

Small adjustments in the lattice parameter can usually be achieved by the growth of a graded buffer layer, or by the doping of the substrate or overgrowth with a suitable dopant. Considering our experimental conditions the most efficient approach to reduce the mismatch for para- and tetragonal ferroelectric $KTa_{1-x}Nb_xO_3$ ($0.29 \leq x \leq 0.45$) was to dope the layer with an appropriate ion. Taking into account that the lattice constant of $KTa_{1-x}Nb_xO_3$ is larger than that of $KTaO_3$ (0.17 % for $x = 0.29$) and that the specific physical behavior of ABO_3 type ferroelectrics depends mainly on the interactions within the BO_6 octahedron, the lattice matching appeared to be possible by doping the layer with a smaller A^+ ion, i.e. Na^+. This was successfully achieved by replacing a part of KF solvent by NaF (up to 20 mol%), leading to the growth of $K_{1-y}Na_yTa_{1-x}Nb_xO_3$ layers.

Figure 2 shows OPM images obtained from thin films of $K_{1-y}Na_yTa_{0.71}Nb_{0.29}O_3$ grown with different concentrations of NaF in the melt. Images 2(a), 2(b), and 2(c) correspond to a concentration of NaF of 0, 5, and 20 mol%, respectively. The atomic concentration of Na in the films was slightly lower than the corresponding concentration in the melt. The sequence of images (a-c) shows clearly that the incorporation of small amounts of Na drastically decreased the defect density due to better lattice matching. Since the addition of Na decreases the lattice parameter of the overgrowth the layers should at some point (when the lattice parameter of the overgrowth becomes smaller than that of substrate) undergo a transition from the compressive to tensile stress. The relief of the compressive stress will result in a defect pattern as observed in Figures 2(a) and 2(b). The average distance between the defect lines can be used as a semiquantitative measure for the lattice mismatch if the films are of the same thickness. For films grown with 10 and 15 mol% of NaF in the melt the defect contrast disappeared, indicating good lattice matching. However, films grown with 20 mol% of Na had evidently already a smaller lattice parameter than the substrate, resulting in the relief of tensile stress by cracking of the layer, as observed in Fig. 2(c).

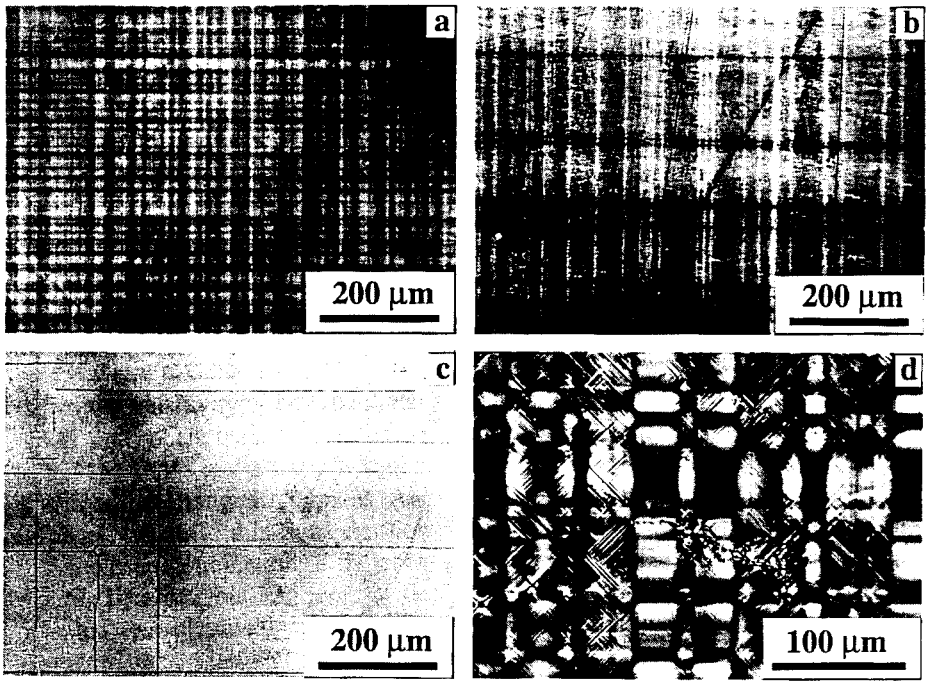


Figure 2. OPM images showing the defect density obtained from thin films of $K_{1-y}Na_yTa_{0.71}Nb_{0.29}O_3$ with the following y values: (a) - 0.00, (b) - 0.045, and (c) - 0.195. (d) shows the ferroelectric domains nucleating on defect lines.

Figure 2(d) shows a similar defect pattern at a higher magnification obtained from a $KTa_{0.55}Nb_{0.45}O_3$ film. In addition to the characteristic defect pattern seen in images 2(a) and 2(b) one can clearly distinguish also the formation of ferroelectric domains. It appears that they nucleate at the defect lines. Very few domains cross the defect lines, hence, they act as some kind of barriers for the domain propagation. This behavior may indicate that the medium range order at these lines is heavily disturbed or almost nonexistent.

3.3. X-RAY DIFFRACTION STUDIES

XRD studies confirmed the semiquantitative results obtained by OPM. The width of the (400) film peak decreased with the increasing content of Na from 4.3 to about 1.5', indicating a decrease in the defect density. The width of the substrate (400) peak was normally between 1.0 and 1.3'.

In order to determine the difference in the vertical lattice parameter between paraelectric thin films and the substrate, we examined in detail (400) reflections. Figure 3 shows a detailed 2θ scan for three different concentrations of Na in the $K_{1-y}Na_yTa_{0.71}Nb_{0.29}O_3$ thin films. Both, the substrate and film (400) peaks are present. The measurements shown in Fig. 3 were performed on the samples grown from the melt with 5, 10, and 15 mol% of NaF which resulted in y values of 0.045, 0.090, and 0.144, respectively. From the positions of the film (400) peaks with respect to the substrate (400) reflection one can say that the solutions containing less than 10 mol% of NaF produced films with a larger lattice parameter than that of substrate while melts with more than 15 mol% of NaF produced films with smaller lattice parameters. These results agree completely with the defect features observed by OPM.

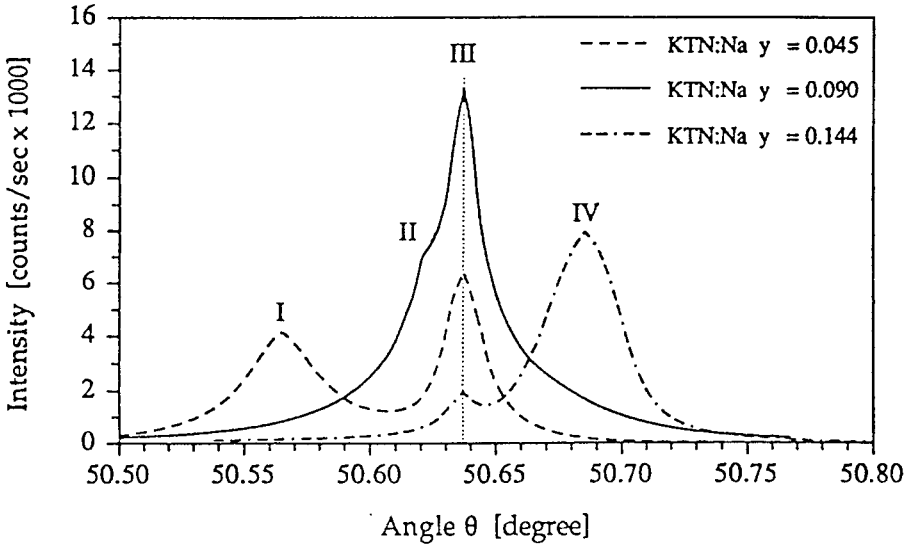


Figure 3. (400) reflections from $KTaO_3$ substrate (III) and $K_{1-y}Na_yTa_{0.71}Nb_{0.29}O_3$ thin films for three different y values (I, II, IV).

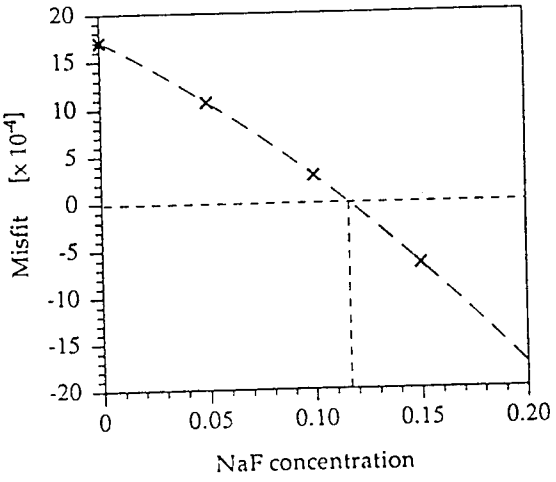


Figure 4. Lattice mismatch of $K_{1-y}Na_yTa_{0.71}Nb_{0.29}O_3$ thin films with $KTaO_3$ substrate as a function of NaF concentration in the melt.

From these measurement we were able to determine the exact Na content which lead to perfectly lattice matched $K_{1-y}Na_yTa_{0.71}Nb_{0.29}O_3$thin films on $KTaO_3$ substrates. Figure 4 shows the measured lattice mismatch as a function of NaF concentration in the melt. From the polynomial fit of the experimental data we obtained for the solution leading to the perfect lattice matching a value for NaF concentration of 11.5%.

3.4. X-RAY PHOTOELECTRON AND AUGER ELECTRON CHARACTERIZATION

XPS and Auger studies showed that the produced layers had the nominal $KTa_{1-x}Nb_xO_3$ composition. No impurities other than small amounts of F (up to 0.8%) were detected within the sensitivity of both methods (typically 0.5%). The annealing of the samples in an O_2 atmosphere resulted in a substantial decrease of the fluorine signal (30-40%), and a slight increase in the oxygen signal (~1%). The concentrations of all other elements remained unchanged. Typical Auger and XPS survey spectra obtained from $KTa_{0.71}Nb_{0.29}O_3$ thin films are shown in Figs. 5 and 6.

A closer examination of the chemical states of the elements in as-grown blue and annealed transparent samples by detailed XPS scans of different elemental peaks revealed two chemical states of K in the blue samples. Pure metallic K shows a characteristic 2p doublet peak (3/2, 1/2) at binding energies of 294.4 and 297.2 eV, respectively [15]. In an oxidized state these two peaks shift to a lower binding energy. Hence, if K in both states is present in the same sample one observes two contributions to the electron spectrum as seen in Fig. 7. This spectrum shows clearly four partially overlapping peaks. As labeled, the doublet at the lower binding energy corresponds to the oxidized K usually observed in $KTa_{1-x}Nb_xO_3$ samples, while the doublet at the higher binding energy corresponds to more metallic K. The shift between the two

doublets was measured to be 1.25 eV. As calculated from the Gaussian curve fitting the metallic K amounted to almost 50% of the total amount of K in the sample.

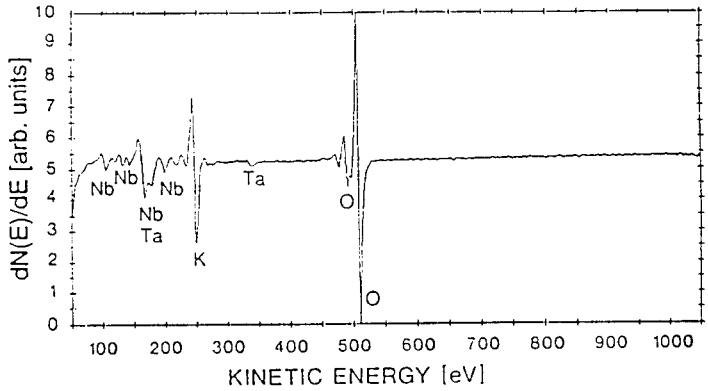


Figure 5. Auger survey spectrum of an sputter-cleaned $KTa_{0.71}Nb_{0.29}O_3$ layer showing presence of only O, Ta, Nb, and K.

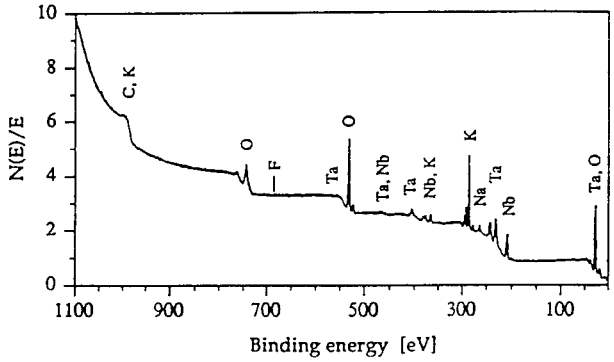


Figure 6. XPS survey spectrum of the same film as in Figure 5. Detailed scans around the binding energy of 686 eV revealed the presence of some fluorine.

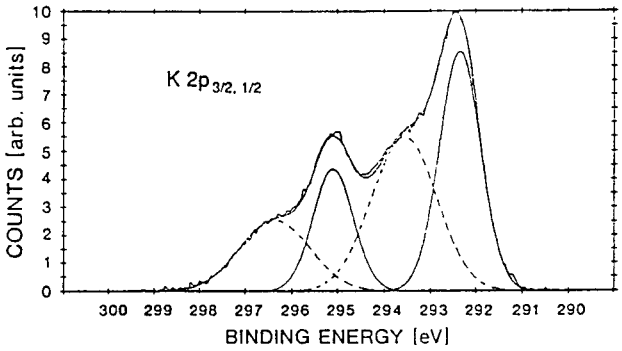


Figure 7. Detailed scan of the K 2p doubled obtained from an as-grown bluish $KTa_{1-x}Nb_xO_3$ thin film.

The reason for the broadness of the peaks arising from the metallic K compared to the other two peaks is at the moment not clear. We suspect that it arises from a not very well defined chemical state of K or from K in two or more similar chemical states. It is interesting that the evidence for the presence of the metallic K disappeared upon the annealing of the samples. This indicated that the blue coloration of as-grown samples arose from the oxygen vacancies which formed relatively deep levels and acted as color centers.

Auger depth profile shown in Fig. 8 was obtained from the surface of an angle lapped sample at 2°. Starting on the substrate, the primary electron beam was scanned across the surface in the steps of 0.5 μm and at each point the Auger signal was collected. This allowed a depth resolution of about 20 nm. The spectrum exhibited a sharp transition from the substrate to $KTa_{1-x}Nb_xO_3$ film. The main features that changed at the interface were signals from Ta and Nb while the signals from the other two elements obtained on both sides of the interface showed little difference. From this and from the other such scans made in different directions across the angle lapped surface we did not observe any changes in the magnitude of different elemental signals. This indicated that the grown films were compositionally homogeneous and stoichiometric across the whole thickness.

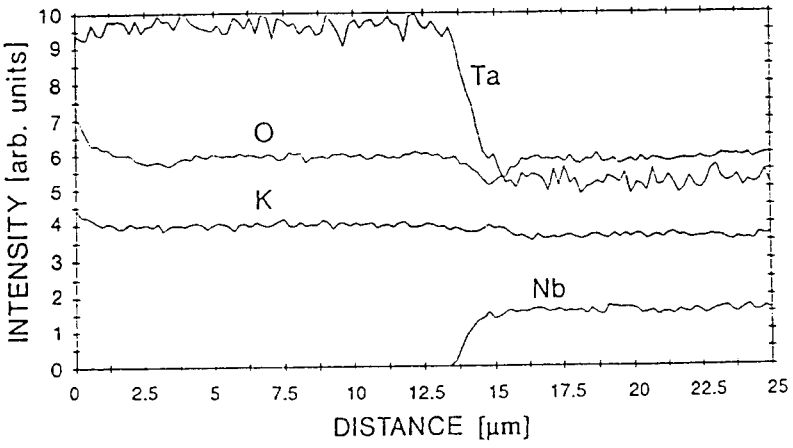


Figure 8. Auger depth profile obtained from an angle - lapped $KTa_{0.71}Nb_{0.29}O_3$ thin film. The depth resolution was about 20 nm.

3.5. PYROELECTRIC MEASUREMENTS

The pyroelectric response was measured on poled $KTa_{1-x}Nb_xO_3$ thin films. Figure 9 shows a temperature dependence of the pyroelectric signal at 200 Hz. The heating curve showed a steady increase of the pyroelectric signal as the temperature approached to the Curie point. Beyond T_C the pyroelectric response rapidly decayed and disappeared. No signal was measured on the cooling curve once the sample was heated above the

transition temperature. The pyroelectric signal reappeared after the samples were repoled. The temperature of the maximum pyroelectric effect agreed very well with the transition temperature calculated from the stoichiometry and obtained from the permittivity measurements. The maximum pyroelectric response of a $KTa_{0.55}Nb_{0.45}O_3$ thin film was measured at 338 K. This response corresponded to a pyroelectric coefficient of 5200 $\mu As/m^2K$.

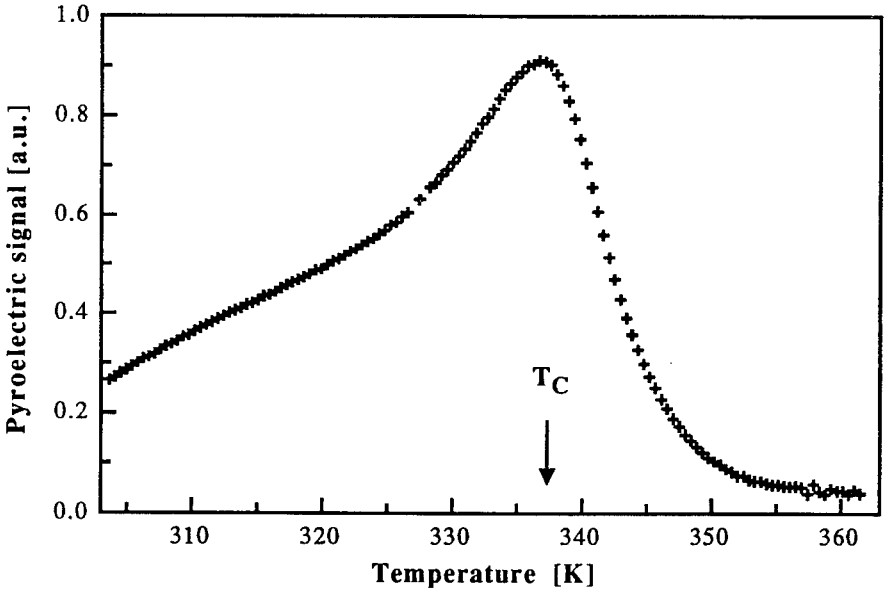


Figure 9. Temperature dependence of the pyroelectric response of a $KTa_{0.55}Nb_{0.45}O_3$ thin film at 200 Hz.

4. Summary

We successfully grew $KTa_{1-x}Nb_xO_3$ thin films on $KTaO_3$ substrates. Films grown on (100) oriented substrates were smooth while films grown on (110) and (111) faces showed strong facetting and inhomogeneous growth. Structural defects arising from the lattice mismatch between the substrate and films were eliminated by partial replacement of K with Na that reduced film's lattice parameter. The replacement of 11% of KF by NaF in the melt lead to perfectly lattice matched thin films. Chemical analyses showed that the grown films were stoichiometric and chemically homogeneous throughout the thickness. As-grown films were slightly oxygen deficient which resulted in a blue tint and the observation of some metallic K in the films by XPS. No impurities other than small amounts of fluorine were detected. Poled films showed a strong pyroelectric response which reached a maximum at the transition temperature.

5. Acknowledgments

This work was supported by the Swiss Priority Program LESIT and Swiss National Science Foundation (NFP 13: Micro- and Optoelectronics).

6. References

1. Anderson, T.W. (1992) *Proceedings of the SPIE* **1689**, 153.
2. Whatmore, R.W., Osbond, P.C., and Schorrocks, N.M. (1987), *Ferroelectrics* **76**, 351.
3. Kulwicki, B.M., Amin, A., Beratan, H.R., and Hanson, C.M. (1992), *Proceedings of the Eight IEEE International Symposium on Applications of Ferroelectrics*, IEEE, pp. 1.
4. Lian, J., Okumura, N., Adachi, M., Shiosaki, T., and Kawabata, A. (1990), *Proceedings of the Seventh IEEE International Symposium on Applications of Ferroelectrics*, IEEE, pp. 383.
5. Gutmann, R., Hulliger, J., and Reusser, E. (1992), *J. Crystal Growth* **126**, 578.
6. Stafsudd, O.M., and Pines, M.Y. (1972) , *J. Opt. Soc. Am.* **62**, 1153.
7. Herbert, J.M. (1982), *Ferroelectric transducers and sensors* 266.
8. Schubring, N.W., Mantese, J.V., Micheli, A.L., Catalan, A.B., and Lopez, R.J. (1992), *Phys. Rev. Lett.* **68**, 1778.
9. Fukami, T., and Tsuchiya, H. (1977), *Electr. Eng. Jpn.* **97**, 12.
10. Yilmaz, S., Venkatesan, T., and Gerhard-Multhaupt, R. (1991), *Appl. Phys. Lett.* **58**, 2479.
11. Bohac, P., and Kaufmann, H. (1986), *Electron. Lett.* **23**, 861.
12. Wu, E., Chen, K.C., and Mackenzie, J.D. (1984), *MRS Symp. Proc.* **32**, 169.
13. Triebwasser, S. (1959), *Phys. Rev.* **114**, 63.
14. Reisman, A., Triebwasser, S., and Holtzberg, F. (1955), *J. Am. Cer. Soc.* **77**, 4228.
15. Perkin-Elmer (1992), *Handbook of X-ray Photoelectron Spectroscopy*, Perkin-Elmer Corporation.

PULSE SWITCHING CHARACTERIZATION OF FERROELECTRIC THIN FILMS

P.K. LARSEN, R. CUPPENS AND G.J.M. DORMANS
Philips Research Laboratories,
Prof. Holstlaan 4, 5656 AA Eindhoven,
The Netherlands

ABSTRACT. This paper describes pulse methods applied in the characterization of ferroelectric thin films with emphasis on non-volatile memory applications. The basic experimental set-up is described. The circuit response time is analyzed and further investigated using circuit simulation with an electrical equivalent model of the ferroelectric capacitor as well as a linear capacitor. Transient measurements of $Pb(Zr_xTi_{1-x})O_3$ capacitors show that the physical switching time is smaller than the minimum circuit response time of 500 ps. Standard measurements including studies of the influence of pulse amplitude and width, fatigue and retention are described. Finally, the switching of a ferroelectric capacitor in a configuration similar to that of a memory cell is investigated. It is shown that the size of the ferroelectric capacitor in relation to the bitline capacitance is of major importance for its operating conditions.

1. Introduction

Ferroelectric thin films have a basic property, a remanent electric polarization, which can be applied for non-volatile information storage. If the ferroelectric film is situated between two electrodes, the polarization can be directed by applying a voltage pulse (i.e. an electric field) of proper polarity and amplitude across the capacitor. In a memory such as a ferroelectric random access memory (FERAM) the capacitor will be exposed to a large number of read and write pulses. The amplitudes and widths of such pulses have to be compatible with standard integrated circuit (IC) requirements. This means that the capacitor must be switchable with low voltages, which for a supply voltage (V_{IC}) of nominal 3.3 V, will be of the order of 2 V [1]. The time available to write or read (the pulse width) depends on the application. At present, volatile memories such as dynamic RAMs (DRAMs) are produced with access times of 100 ns and the trends are towards access times of $\leq$ 50 ns. Here the access time is defined as the time from addressing to output of the memory data. For a FERAM, the read operation is destructive, i.e. both a read and write operation has to be performed within the cycle time. In some cases other logic operations have to be carried out as well within this time. Therefore the pulse width has to be limited to less than 50% of the access time, perhaps 25%. This shows that switching within 10-25 ns must be possible for high speed applications.

O. Auciello and R. Waser (eds.), Science and Technology of Electroceramic Thin Films, 201-221.
© 1995 *Kluwer Academic Publishers. Printed in the Netherlands.*

There are some other important requirements necessary for high density FERAMs. The amount of charge released during a read operation should be sufficient to be detected. Typically, this level will be of the order of 10^{-13} C (100 mV over 1 pF). Since the released net charge $\Delta Q = 2P_rA_{FE}$, where P_r is the remanent polarization and A_{FE} is the capacitor area, it is clear that future IC generations will put strong demands on the amount of polarization. The highest density is obtained with the smallest A_{FE}, which is determined by processing rules. For instance, in a 0.25 μm process generation with A_{FE} = 0.4 μm^2 a P_r = 12.5 $\mu C/cm^2$ is required as a minimum. The endurance (i.e. the number (N) of polarization reversals (or switchings)) should at best be virtually unlimited. The decrease of polarization with N is usually termed fatigue. Ferroelectric capacitors can now be prepared with sufficient quality to allow more than 10^{12} polarization reversals [2]. This means that testing becomes a time problem unless high speed testing or testing under accelerating conditions are used. Other points to consider include retention (aging), dependence on temperature and (in)sensitivity to disturbing pulses.

The electrical properties of polycrystalline ferroelectric thin films depend on (micro)structural and compositional properties of the films. Thin film optimization normally includes analytical and structural investigations and standard electrical characterizations such as measurements of hysteresis loop, capacitance, DC conductivity and perhaps low frequency pulse switching measurements. However, this is not enough for an optimization for memory applications. The transient switching process depends critically on the film microstructure [3] and cannot be predicted on the basis of low frequency measurements. Optimization therefore requires measurements on the timescale of memory applications (say 10-100 ns). A basic understanding of the switching behaviour is further necessary. Most work has been devoted to switching in single crystals [4]. The validity of models of switching occurring by nucleation and growth of opposite polarity domains [5,6] is questionable for thin polycrystalline ferroelectric films. The observation of switching times in the ns to sub-ns range for $Pb(Zr_xTi_{1-x})O_3$ (PZT) films of thicknesses ranging from 0.1-0.4 μm [3,7] indicates that the switching can be caused by an almost simultaneous reorientation of all dipoles when the electric field is applied [8].

In this paper, fast pulse switching characterization of ferroelectric thin films will be covered. First the experimental techniques and procedures will be treated. Using circuit simulation methods it is possible to give a reliable interpretation of experimental results and separate between instrumental and physical (switching) effects. Studies of the transient switching process of polycrystalline ferroelectric thin film capacitors will be discussed. Subsequently standard pulse switching investigations will be described. Finally studies of the switching of memory cells will be presented.

2. Experimental

2.1. DEFINITIONS

The properties relevant for memory applications can be visualized by means of a hysteresis loop of the polarization versus voltage (or electric field). In Fig. 1, a loop is shown. P_{r+} and P_{r-} are the positive and negative remanent polarizations, respectively, and V_{c+} and V_{c-} the coercive voltages. We prefer to describe the loop by the applied voltage since the electric field in the ferroelectric film does not have to be directly determined by

the applied voltage and film thickness due to the presence of blocking layers [9]. The saturation voltages (in Fig. 1 at about ± 2 V) are the minimum voltage levels required to obtain a maximum remanent polarization. They are only well defined for square shaped hysteresis loops, but not for slim loops. It is therefore more relevant for switching applications to know the values of the saturation voltages than the coercive voltages. In Fig. 1, the switching and non-switching polarization changes caused by the onset of a positive pulse, ΔP_S and ΔP_{ns}, respectively, are indicated by the dashed lines. The latter is non-remanent, i.e. of dielectric nature and will be denoted P_{diel}. The switched and non-switched polarizations can be calculated by

$$\Delta P_S = P_{r-} + P_{r+} + P_{diel} = 2P_r + P_{diel} \quad (1)$$

$$\Delta P_{ns} = P_{diel} \quad (2)$$

with $P_r = (P_{r+} + P_{r-})/2$. The total polarization $P_t = P_r + P_{diel}$ is normally termed the saturation polarization for higher voltages. Often, changes on a short time scale, for instance below 1 sec, are referred to as transient effects and those on a longer time scale, for instance from 1 s to 10 years, as aging. For memory applications, one would like to know the complete time dependence, i.e. from 100 ns to 10 years. A separation of such changes into transient and aging effects is arbitrary and in fact not necessary. Of course, these effects should be small. Other factors influencing the values of P_r and P_{diel} are experimental conditions (pulse width, pulse amplitude) as well as time (retention, aging), temperature and the state of fatigue.

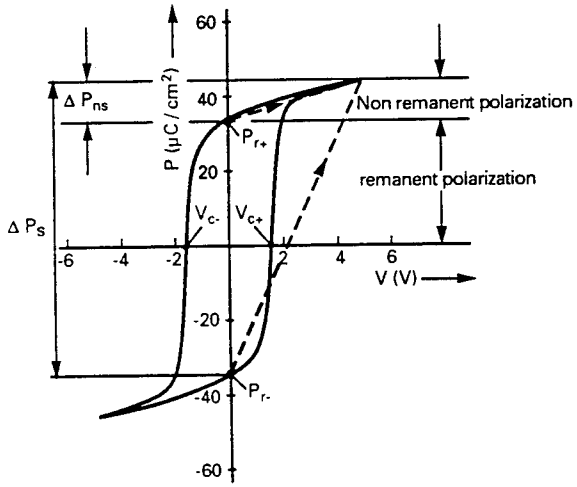


Figure 1. Hysteresis loop of a ferroelectric thin film capacitor showing polarization versus voltage. The dashed lines indicate the switched and non-switched polarization changes caused by a positive voltage pulse.

In Fig. 2, a pulse sequence useful for testing purposes is shown. It consists of a single write pulse, here negative (pulse 1), and two consecutive read pulses (2 and 3) which can be used to probe ΔP_S and ΔP_{nS}, respectively. All pulses can in principle have either polarity. The width, pulse amplitudes, delays and the period of the pulse sequence as indicated in the figure will be used and specified later in the paper. For some tests a double read pulse is not needed.

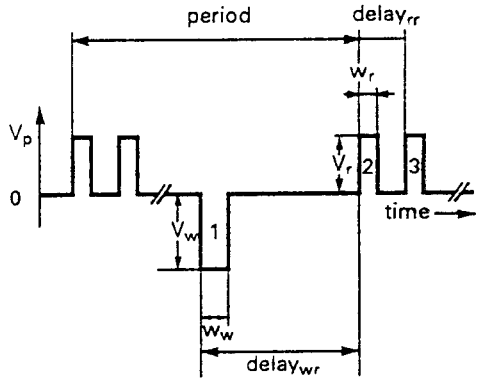


Figure 2. Pulse sequence with definition of adjustable parameters.

2.2 ELECTRICAL CIRCUITS AND SWITCHING CONDITIONS

2.2.1.*Circuit Lay-out*

Figure 3 shows a schematic representation of the circuit for switching measurements in the nanosecond range [3,7]. The three main elements are the pulse generator, the probing circuit and the signal analyzer which are connected with coaxial transmission lines. In the inset, two possible configurations of the probing circuit are shown. In circuit (a) the resistor R_1 (= Z_0) serves as an impedance match to the transmission line coming from the pulse generator. This ensures that reflection from the probe circuit back towards the generator only occurs during times where the ferroelectric capacitor (C_{FE}) is being charged or discharged. Such reflection can be minimized by maximizing the impedance consisting of C_{FE} in series with the measuring resistor R, i.e. by making C_{FE} as small as possible. This is important if the pulse generator is sensitive to the reflected signal, for instance if it cannot absorb the reflected signal. The circuit (b) configuration is open ended after the charging of C_{FE} has occurred and the pulse amplitude is that of an open circuit. There is no impedance match and therefore always a significant reflection towards the signal generator.

2.2.2. *Pulse Signal*

We will shortly discuss a few aspects of the pulse signal related to measurements of the characteristics of the ferroelectric switching behaviour.

- Pulse amplitude: Although the pulse amplitude in memory applications is smaller than 5 V, higher values are often required, for instance for investigations of thickness

dependences, accelerated fatigue tests and the influence of amplitude on the transient switching behaviour.

- Pulse width: Switching within 10 to 100 ns is desired. This gives a lower limit for the pulse width of e.g. 5-10 ns. If slow transient switching components are present, the investigation of the pulse width dependence over a broad range, e.g. up to ms, is desired.
- Pulse risetime (τ_r): Should be much smaller than the width. For investigations of the transient switching process it must be smaller than (the unknown) physical switching time (values down to 350 ps have been observed [3]).
- Pulse period: Should range from 1 s down to 10-100 ns for high speed fatigue tests. Single pulse testing (only read) is necessary for retention measurements.

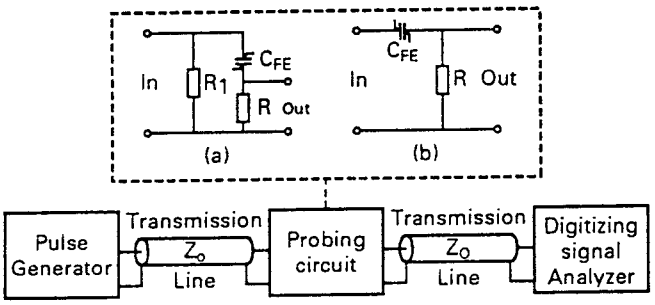


Figure 3. Schematic diagram of the circuit for pulse measurements. The inset shows two configurations of the probe circuit.

No commercial pulse generators exist having all the properties described above. Very fast pulse generators with sub-ns risetime have limitations in pulse width and period and may only provide single pulses. Versatile equipment, for instance HP 8160 signal generators, have limitations in pulse amplitude (5 V in 50 Ω), risetime (≥ 1 ns) and cannot provide double bipolar pulses. A solution to the requirements, except to a very fast risetime, is to add and/or amplify different pulse signals. Reflection problems arising from impedance mismatch can be avoided by using the transmission line between the pulse generator and the probing circuit as a delay line (delay = 5 ns/m).

2.2.3.*The Analyzing System*

The analyzing system should have a bandwidth (BW) which is sufficiently large to resolve the leading edge of the fast pulse. The corresponding risetime (τ_a) of the analyzing system can be approached by 0.38/BW.

The output signal (Out) of the probing device is being transmitted into an impedance matched transmission line terminated by a signal analyzer. Therefore there will be no reflection back to the probing circuit. The effective measuring resistance R' is the parallel impedance of R and Z_0, where Z_0 = 50 Ω is the impedance of the transmission line/signal analyzer.

2.2.4. *Equivalent Diagram and Experimental Resolution*

The experimental response time or resolution (τ_{exp}) is determined by two factors. One is given by the instrumental limit of the equipment (τ_i) and the other by the circuit load (τ_{load}), determined by the actual circuit elements. The total experimental response time can be expressed as:

$$\tau_{exp} = \sqrt{(\tau_i^2 + \tau_{load}^2)} = \sqrt{(\tau_r^2 + \tau_a^2 + \tau_{load}^2)} \qquad (3)$$

In order to measure the transient switching process of a ferroelectric capacitor by applying voltage pulses it is necessary that $\tau_{exp} << \tau_{phys}$ where τ_{phys} is a characteristic time describing the physical switching process (we assume here for simplicity that there is only one time constant). A further analysis of τ_{exp} can be made on the basis of the simplified equivalent scheme shown in Fig. 4.

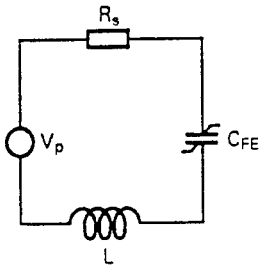


Figure 4. Equivalent diagram of the probe circuit (see Fig. 3).

Here R_s is the effective series resistance as seen from the ferroelectric capacitor C_{FE} (i.e. $R_s = R_g/R_1 + R'$, where R_g is the impedance of the pulse generator). L is the parasitic circuit inductance. There might also be some parasitic capacitance which can be included as an extra linear term in C_{FE}. The diagram of Fig. 4 is in fact a series "LRC" circuit, but with a strongly non-linear capacitor. This cannot be treated analytically. Numerical studies can be made with circuit simulation and they will be described in the following section. However, it is possible to make good estimates of the circuit behaviour and obtain reasonable values for τ_{load} and therefore τ_{exp} on the basis of the switched charges (ΔQ_S or ΔQ_{nS}) and the pulse voltage V_p. This is done by replacing the ferroelectric capacitor with a linear capacitor (C_{lin}) which is required to have a charge equal to ΔQ_S or ΔQ_{ns} at V_p, i.e.

$$C_{lin} = \Delta P A_{FE}/V_p \qquad (4)$$

where $\Delta P = \Delta P_s$ or ΔP_{ns} for the switching and non-switching case, respectively. The circuit can now be analyzed using standard circuit theory.

For large values of C_{lin}, where $(R_s/2L)^2 > 1/LC_{lin}$, one has the quasi static range. Here R_s is the total series resistance. The time from the current maximum (~ current onset) to 10% of the maximum is here taken as the circuit response time τ_{RC}, i.e.

$$\tau_{RC} \sim 2.3\, R_s\, \Delta P A_{FE}/V_P \qquad (5)$$

For small values of C_{lin} where $(R_s/2L)^2 < 1/LC_{lin}$ the circuit is in the oscillatory range with damped oscillations. These oscillations limit the time resolution. Here half a period can be taken as an appropriate measure of the circuit depending response time, denoted as τ_{LC}. This time is given by

$$\tau_{LC} \sim \pi \sqrt{(L \Delta P A_{FE}/V_p)} \qquad (6)$$

The total experimental resolution will be given by Eq.(3) with the value of τ_{load} calculated by Eq.(5) or (6), depending on the value of C. The parameter L can be measured by replacing C_{FE} with a linear capacitor [3]. The behaviour discussed above will be verified via circuit simulations which will be treated in the next subsection.

2.3. MODELLING AND VERIFICATION

In section 2.2., the switching limitations of the measuring set-up were calculated based on analytical expressions. The equivalent capacitor was calculated by Eq.(4). Ferroelectric capacitors show strong voltage dependent switching behaviour. To study the influence of the non-linearity of the switching of ferroelectric capacitors, the previously discussed behaviour was verified via a simulation of the measuring system with a circuit simulator, commonly used for the design of integrated circuits. For this study, an in-house built simulator, called "PSTAR", was used, but similar results can be obtained with other simulation programs, e.g. "SPICE". Only the flexibility to implement the different components of the measuring set-up, like ferroelectric capacitors, pulse generators, coaxial transmission lines or the signal analyzer can be influenced by the choice of the simulator. In the next section we will discuss first the modelling of the different components in the measuring set-up. The following subsections will deal with the results of the simulations and the influence of the voltage dependent nature of ferroelectric capacitors on the experimental resolution of the measuring system.

2.3.1. *Simulation Models*

Circuit simulators that are extensively used in the design of integrated circuits have very good models to describe the classical components like resistors, capacitors, inductance's, MOS and bipolar transistors. These basic components can be used to emulate more complex functions like pulse generators, coaxial transmission lines and signal analyzers. It is very hard to construct with these basic components a model for a ferroelectric capacitor. The availability of models describing in an accurate way the electrical behaviour of ferroelectric capacitors under various conditions is of crucial importance for the design

of ferroelectric memories. The model used for this study does not meet all these criteria, but describes the ferroelectric behaviour accurately enough to allow the study of the influence of the non-linear nature of the ferroelectric capacitor on the experimental resolution. The implemented model was based on a mathematical model for ferroelectric capacitors [10]. For the modelling it was assumed that the ferroelectric material switches immediately after applying the voltage. So no physical switching time limitations were included.

The pulse generator was implemented with a time controlled current source, feeding its current in the load and in a 50 Ω parallel resistor. The pulse voltage is controlled by determining the maximum current the source can deliver. In this case the total load resistance will be 25 Ω (50 Ω in the generator in parallel with the 50 Ω of the input resistance of the probing circuit). The rise and fall times of the pulse is controlled via the on or off switching time of the current source. The coaxial transmission lines were simulated as a ladder network of inductances and capacitors. Even for fast switching the number of sections has to be chosen large enough (about 10 sections per cm coax) to approach the real electrical behaviour. The probing set-up was implemented as discussed in the previous section (Fig. 3). The parasitic inductance of 10 nH was allocated to the probes. So, two 5 nH inductors were added in series with each terminal connection for the ferroelectric capacitor. The signal analyzer was simulated by a 50 Ω resistor in parallel with an RC network to simulate the finite response of the analyzer.

2.3.2. *Verification*

In Fig. 5, the system resolution, τ_{exp}, is shown as function of the capacitor value as well as a function of the area of the ferroelectric capacitor. The calculation was carried out using Eqs. (3-5) assuming typical values of ΔP and V_p. It should be noted that other values of ΔP and V_p change τ_{RC} and τ_{LC} and therefore τ_{exp}. An instrumental resolution τ_i = 480 ps, corresponding to the measurements in section 3, is indicated. Furthermore, points of the curve given in Fig. 5 were simulated with different capacitors (open circles). The switching time was measured from the onset of the current pulse (10% of maximum) to the end of the pulse (10% of maximum (RC) or the minimum (LC)). For a linear capacitor of 20 pF, it was not clear which definition of the minimal switching time has to be chosen: that of the RC or that of the LC region. Both gave different results. In the figure both values are indicated.

Until now, only a linear capacitor was considered. In reality the switched as well as the non switched behaviour of ferroelectric capacitors can be described by strong voltage dependent capacitors. Fig. 6 illustrates the difference is switching behaviour between a linear capacitor and a ferroelectric capacitor. The linear capacitor was calculated to switch the same charge as the ferroelectric capacitor (Eq.(4)). In the figure the switching behaviour of ferroelectric capacitors with two different areas were compared with the behaviour of the calculated equivalent linear capacitor.

The difference in switching between the ferroelectric and the linear capacitor can be interpreted by considering the differential capacitor during the switching (or the slope of the hysteresis loop). In the switching region itself this capacitor is larger than the equivalent linear one and thus will switch slower (see Fig. 6). At the end of the switching the differential capacitor is smaller and will switch faster. This explains the differences in the switching behaviour but it also has to be clear that the shape of the curves strongly depends on the voltage dependence of the switched charge. This effect can be evaluated by the hysteresis curve, provided that only fast switching components are present.

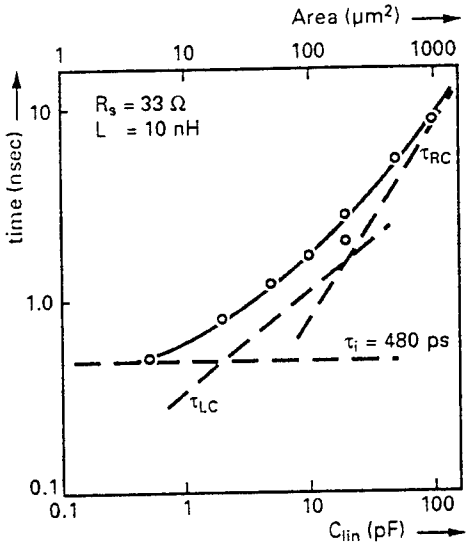


Figure 5. Simulated (circles) and calculated (dashed lines) circuit response times as a function of C_{lin} and A_{FE}, setting $\Delta P = 50\ \mu C/cm^2$ and V_P=5V.

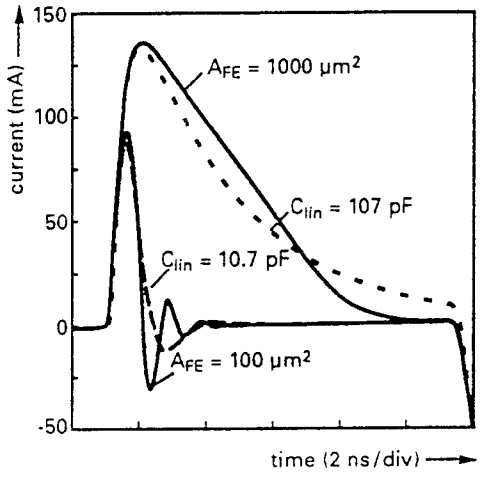


Figure 6. The switching response of two ferroelectric capacitors (1000 μm^2 and 100 μm^2) compared with the behaviour of the equivalent linear capacitors.

This simulation experiment shows that the interpretation of the results of fast switching experiments on ferroelectric capacitors have to be done very careful, since the measured switching time can be caused by the measuring set-up. Which part of the measured time is caused by the set-up strongly depends on the non-linearity of the charge to be switched. Here a good electrical model of a ferroelectric capacitor, implemented in a circuit simulator, can contribute to separate the intrinsic switching time from the set-up related components. All measured switching times that approach the experimental time resolution have to be considered as caused by the measuring set-up rather than to be allocated to physical effects.

3. Transient Switching Results

The transient switching behaviour of the ferroelectric thin film capacitor is very important for memory applications. As discussed in Section 1 the speed of switching should be compatible with device requirements. Understanding of the detailed switching process is required for optimization and lifetime predictions.

Early studies of switching in ferroelectric materials were mainly carried out on single crystals of large thicknesses compared to the submicron thicknesses considered for memory applications. A recent review was given by Stadler [4]. More recent work on films of submicron thicknesses has been carried out by various groups, reporting partly conflicting results. Scott et al. reported for sputter deposited PZT films (x=0.54) switching times in the range from 10-100 ns [11], while results of our group on sol-gel deposited PZT films indicated switching times at or below 2 ns [3,7]. It is a question how the experimental data have to be interpreted. For instance, the observation reported in ref.(12) that the switching time is proportional to the amount of switched charge can just be explained on the basis of Eq.(5). The decrease of switching time with increasing temperature observed in ref.(11) can be related to a decrease of polarization with temperature which gives rise to a decrease of switching time (see Eq.(5)). Also voltage dependencies might be explained as circuit effects. This strongly indicates that these results are circuit related and do not represent the intrinsic switching process. Measurements therefore should clarify that circuit effects are properly accounted for.

In Fig. 7, we present measurements of ferroelectric capacitors of different areas. The capacitors were prepared with Pt bottom and top electrodes. The PZT film (x=0.51) of 0.2 μm thickness was deposited by OMCVD [13]. The capacitors are parts of a fully processed test module described by Dormans et al. [14]. The measurements were carried out using a model 405B pulse generator (Picosecond Pulse Labs) for the generation of the read pulses and a digitizing signal analyzer (Tektronics model 600) detection system. The risetime of the leading edge is 300 ps and the bandwidth of the detection system is 1 GHz. This gives an instrumental resolution of 480 ps. The pulse fall time is considerably larger, about 800 ps, and the negative (dielectric) pulse caused by the trailing edge is therefore broad compared to the non-switching (dielectric) peak at the onset. The pulse amplitudes of both the write and the read pulses were 5.25 V. The pulse widths were 100 ns for the write pulse and 10 ns for the read pulses. The delays write-read and read-read were both 10 μs and the period 50 ms.

Figure 7 shows that the switching time decreases with decreasing area. An analysis of the results leads to response times which are in close agreement with the calculated values of τ_{exp} using τ_i = 480 ps, as presented in Fig. 5. This means that from these results it

is not possible to determine a switching time, besides that it is smaller than about 500 ps.

The switched and non-switched charges can be determined by integrating the current from the onset of the pulse over the pulse width, i.e. to the onset of the negative part of the signal in Fig. 7. It is found that both the switched charge (ΔQ_s) and the non-switched charge (ΔQ_{ns}) are proportional to the capacitor area (shown in the inset for ΔQ_s) These proportionalities mean that ΔP_s and ΔP_{ns} are independent of the capacitor area. The values are 51 $\mu C/cm^2$ and 24 $\mu C/cm^2$, respectively. Using Eqs. (1) and (2) one gets P_r = 13.5 $\mu C/cm^2$ and P_{diel} = 24 $\mu C/cm^2$. It is interesting to compare these results with results from hysteresis measurements. Using a 5 V amplitude and a frequency of 1 kHz (sinusoidal waves) the values are P_r = 32.5 $\mu C/cm^2$ and P_{diel} = 14.5 $\mu C/cm^2$. The short pulses used for the experiments described above seem therefore only able to switch a fraction of the available polarization. There must therefore be components of the polarization which have different response times. For memory applications only the fast components are of interest and evaluation of the suitability of ferroelectric capacitors should therefore be done on basis of pulse and not hysteresis measurements.

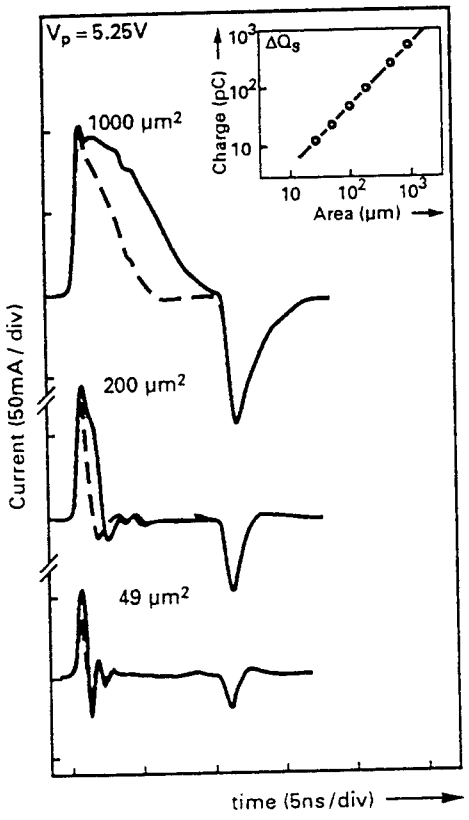


Figure 7. Switched (solid line) and non-switched (broken line) transient currents for ferroelectric capacitors of different areas. The inset shows the dependence of the switching charge ΔQ_S on A_{FE}.

If, for the fast switching component with a switching time < 500 ps, the switching speed is supposed to be determined by the propagation of domain walls across the film, this speed is larger than 400 m/s. Previously published measurements gave a switching speed of about 1 Km/s [3]. Both values are considerably larger than would be expected from domain wall mobilities (2×10^{-7} to 4×10^{-6} m^2/Vs) measured for single crystal $PbTiO_3$ [15]. Using these mobilities and the present field of ~ 260 kV/cm, the minimum switching time is = 2 ns. However, although the results therefore seem to point towards bulk switching, more clear data are required for a real understanding of the fast switching process.

4. Standard Pulse Measurements

In Section 3, it was shown that the polarization reversal can be a very fast process which makes the measurements of the switching kinetics difficult due to instrumental resolution requirements. Secondly, in order to avoid circuit load effects, measurements on small ferroelectric capacitors have to be carried out. Therefore, in practice, relatively little work is done on this type of characterization.

By integrating the pulse response signal the switched and non-switched charges ΔQ_s and ΔQ_{ns} (or ΔP_s and ΔP_{ns}) can be determined. This can be carried out as function of various parameters, considered as important for the functioning of the ferroelectric capacitor. Here, different types of such characterizations will be described.

4.1. POLARIZATION VERSUS PULSE AMPLITUDE

The dependence of the remanent and the total polarization on the pulse amplitude provides information which is comparable to that obtained from hysteresis measurements. It can be obtained from the switched and non-switched polarizations (see Section 2). In Fig. 8, measurements are shown for a capacitor with an OMCVD grown PZT film of thickness 0.3 μm. The capacitor is part of a test device including CMOS and ferroelectric test structures [14]. After the structuring of the capacitors by dry etching techniques, the wafer was given an anneal (500°C, 5 min, O_2) which improves the ferroelectric properties. It is seen that at $V_p = 2$ V there is a considerable difference between ΔP_s and ΔP_{ns}, i.e., the capacitor can be partly switched at this voltage. The figure also shows results for a capacitor after a back-end processing, i.e. after the deposition of insulation layers over the capacitor, contacting and making bond pads. This leads to a reduction of the switchable polarization and to the need for higher voltages for switching.

This type of characterization is also well suited to investigate poling effects. In some cases one finds that the response to a first pulse is different (smaller ΔP_s) from the response to later pulses. Such a poling effect is unwanted in a memory where the first write pulse should bring the capacitor into the desired state. For instance, the anneal treatment described above can reduce poling effects drastically [16].

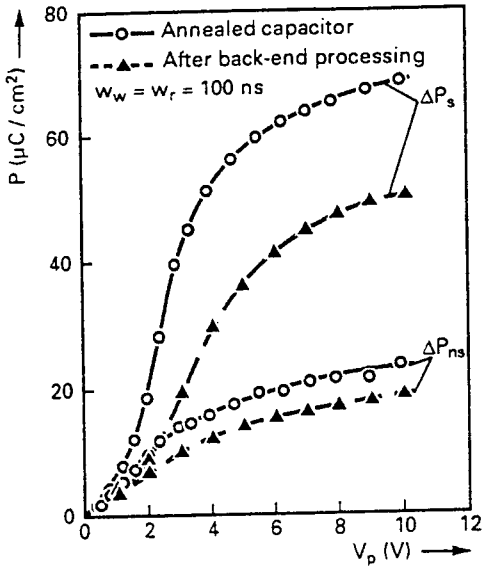


Figure 8. ΔP_s and ΔP_{ns} as function of V_p for a 2000 μm^2 ferroelectric capacitor for an annealed and a fully processed capacitor.

4.2. PULSE WIDTH DEPENDENCE

In many cases a discrepancy is found between the values of polarization determined by hysteresis measurements and by pulse measurements with higher values obtained for the former method. The two types of measurements are carried out in different time domains, i.e. typically in the frequency range 100 Hz to 1 kHz for hysteresis measurements while pulse measurements apply pulse widths in ranges from e.g. 10 ns to 10 μs. These differences indicate a time dependent polarization reversal process. In this section we discuss how pulse measurements can be used to get information on the time distribution of the switching process and its possible causes.

In pulse measurements, we have to separate between what is being switched and what is being measured. In general, a transient response signal of a width which approximately is given by Eq.(5) is being observed. After some time which can correspond to a few times τ_{RC} the signal amplitude has decreased into the noise level. It has therefore little sense to integrate the response signal further. A long tail of low amplitude, buried in noise, will not be measured. However, the amount of polarization being switched depends on the widths of the write and read pulses. If the time distribution of the switching is wide, the amount of switched polarization clearly depends on the pulse widths, i.e. for a read pulse on the width of the preceding write pulse. It thus appears that a larger switched polarization, due to longer pulse widths, is reflected in the measured signal even with a relatively short integration time.

Typical results are shown in Fig. 9. Here ΔP_s and ΔP_{ns} are displayed as function of the pulse width ($w_r = w_w$) for two differently prepared ferroelectric capacitors. One was

deposited by OMCVD and the other by spin-coating (sol-gel) [17]. The integration time was kept constant for the different widths and it is of the order of the smallest width in each case. It is seen that the non-switched polarization does not depend on the width. This is as expected since this is a dielectric term. For the switched polarization the pulse width dependence is relatively large for the sol-gel film and an extrapolation towards short pulse widths shows that the difference between ΔP_s and ΔP_{ns} at a pulse width of 10 ns is almost negligible. Therefore, the capacitor with the sol-gel PZT film is not suited for memory applications. The OMCVD prepared film also shows a width dependence but this is relatively small and it is seen that for a width of 10 ns the difference between ΔP_s and ΔP_{ns} is still large. Only a small part of the reversible polarization has a wide time distribution for the OMCVD film. For other OMCVD prepared PZT films we have observed an absence of slow switching components corresponding to similar polarization values determined by hysteresis and pulse measurements.

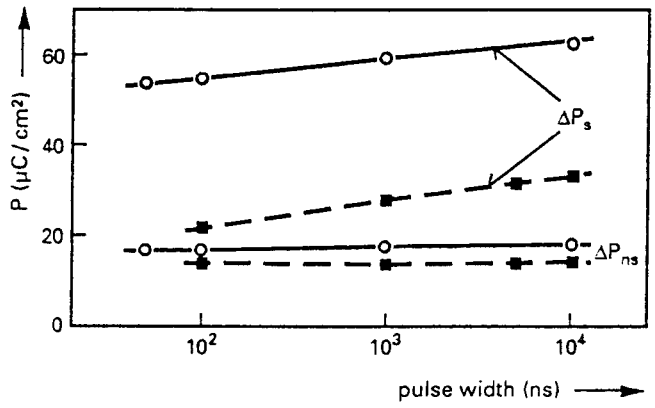


Figure 9. Pulse width dependence of ΔP_s and ΔP_{ns} for ferroelectric capacitors prepared by OMCVD (open circles) and by sol-gel (filled squares). $A_{FE} = 2000\ \mu m^2$, $V_w = V_r = 5$ V and $w_w = w_r$.

The different time dependencies can be related to different microstructures. With OMCVD, the polycrystalline PZT films are deposited in a continuous way yielding columnar grains. Ferroelectric domains here extend from the bottom to the top electrode and switching can be accomplished with charge redistribution only at the electrodes. The speed of this is determined by circuit effects (load) and by the physical switching time. On the other hand, the sol-gel films are formed by subsequent conversion of amorphous layers to crystalline layers. This means that there will be fewer columnar grains and more internal grain boundaries for these electrodes than for OMCVD films. Switching will therefore require charge redistribution at the internal grain boundaries. Due to a limited conductivity, this takes time and therefore a wide time distribution might be observed. Clearly, one of the key points to fast switching is an optimized microstructure.

In addition to the influence of microstructure on the time distribution there might be a dependence on the electrode/PZT interface and/or stress. This is observed by comparing

as prepared and fully processed ferroelectric capacitors. Results for the two capacitors discussed in the preceding subsection show a wider time distribution for the processed than for the as prepared capacitor [14].

4.3. ENDURANCE AND RETENTION

Endurance and retention studies are common types of measurements in the characterization of ferroelectric capacitors for memory applications. These topics will therefore be discussed very briefly.

4.3.1. *Endurance*

The ability to withstand a large number of polarization reversals is of major importance for memory applications. The degradation of the ferroelectric properties caused by repeated switchings, called fatigue, is found to depend on material properties (ferroelectric film, electrodes) as well as the test conditions (pulse amplitude and width).

Studies of fatigue are in principle straightforward by using cycles of single pulses of alternating polarity interrupted by measurements of ΔP_s and ΔP_{ns}. So far there is no standardization of such measurements and widely different parameters are applied. Clearly, it is needed that the measurements should be realistic with respect to the applications and should allow to test the limits. Since endurances in excess of 10^{12} cycles can be obtained with proper materials (PZT films and RuO_2 electrodes), it is needed to apply high frequency testing in the range 10-100 MHz to have an acceptable measuring time. This requires small loads, i.e. small capacitors, and a small pulse width dependence. The endurance is often seen to decrease with increasing pulse amplitude and accelerated testing at higher amplitudes might be possible. However, an understanding of the causes of fatigue in each specific case is then needed. The improvement in endurance by orders of magnitude obtained by changing the electrodes from Pt to oxidic types demonstrates the large importance of the electrode/ferroelectric film interface.

4.3.2. *Retention*

The ability to keep the polarization with time is also very essential for non-volatile memory applications. This can be investigated by using a write pulse and after a delay use a single read pulse. If the polarities of the read and write pulses are opposite or the same, ΔP_s and ΔP_{ns} are measured, respectively. Experimental results indicate that retention will not be a problem and a 10 years retention is specified for existing ferroelectric memory products [18].

4.4. INFLUENCE OF DISTURBING SIGNALS

The continuing trends in reduction of device dimensions means that stray or parasitic capacitances on the chip will become of increasing importance as ferroelectric capacitors in non-selected cells will be exposed to disturbing signals.The influence of such disturbing signals can be studied by applying these between a write and a read pulse. Such a study has been carried out with PZT capacitors [19]. It was shown that the sensitivity to disturbing pulses is strongly related to the shape of the hysteresis curve which again is related to the composition. In contrast to a Zr-rich film (x=0.71) having a slim hysteresis

loop, a Ti-rich film (x=0.36) with a square shaped loop showed little sensitivity to disturbing pulses, e.g.10^9 disturbing pulses of an amplitude of 1.2 V did not decrease the polarization measured at V_p = 5 V.

5. Memory Switching Studies

The pulse switching characterization techniques described so far have been based on a circuit (Fig. 3 circuit (a)) which allows a precise definition of the pulse amplitude applied to the ferroelectric capacitor as well as precise measurements of polarization changes, i.e. a good characterization of the capacitor. In memories, a different circuit from that discussed above is applied and this can have large consequences for the manner in which the ferroelectric capacitor is being switched. In this section, the operation of a ferroelectric capacitor in an environment which is closely related to an operation mode in a ferroelectric memory matrix will be described and discussed.

In Fig. 10a the schematic of a one transistor/one capacitor (1T/1C) memory cell is shown. By proper pulsing the plate, the wordline (WL) and the bitline (BL), the ferroelectric capacitor (C_{FE}) can be written and read. For instance, a read can be carried out by rising the potential of the plate and at the same time connecting the ferroelectric capacitor and the bitline via the wordline signal. The released charge will then flow to the bitline having a capacitance C_{BL}. This causes a voltage on the bitline which can be detected, providing the information of the state of C_{FE} before the read operation.

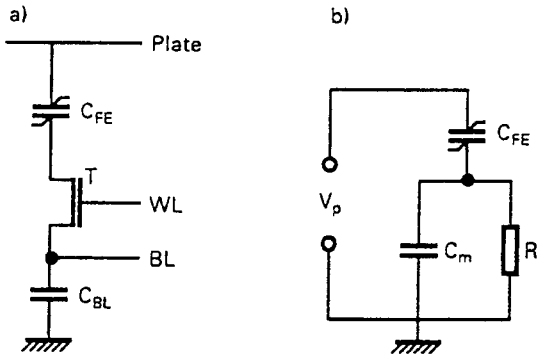


Figure 10. (a) Schematic of a one transistor/one capacitor memory cell.
(b) Pulse switching set-up.

In Fig. 10b, a measuring circuit is shown which is used to simulate the circuit of Fig. 10a. Here, a capacitor in series with C_{FE} simulates the bitline capacitance. The time dependent voltage is measured with an analyzer having an high input impedance. The load therefore consists of a parallel circuit of a capacitor (C_m) and a resistor (R). The presence of the resistor means that a voltage across C_m will decay with a time constant determined by the value of RC_m. This time constant should be much larger than the times at which

voltages are measured in the switching studies. The values of R and C_m were 1 MΩ and 275 pF, respectively, corresponding to a time constant of 275 μs.

In Fig. 11, results of pulse measurements are shown for capacitors of various areas. The capacitors were prepared with OMCVD grown PZT films (x = 0.44, d = 0.22 μm) and Pt electrodes. The figure shows for the different capacitors the voltage (V_C) across the capacitor C_m as function of time for the case of two consecutive read pulses, following a previous write pulse of opposite polarity. It is seen that there is a large difference between the measurements for the different ferroelectric capacitors in terms of the ratio between the voltage across C_m during and after the read pulses.

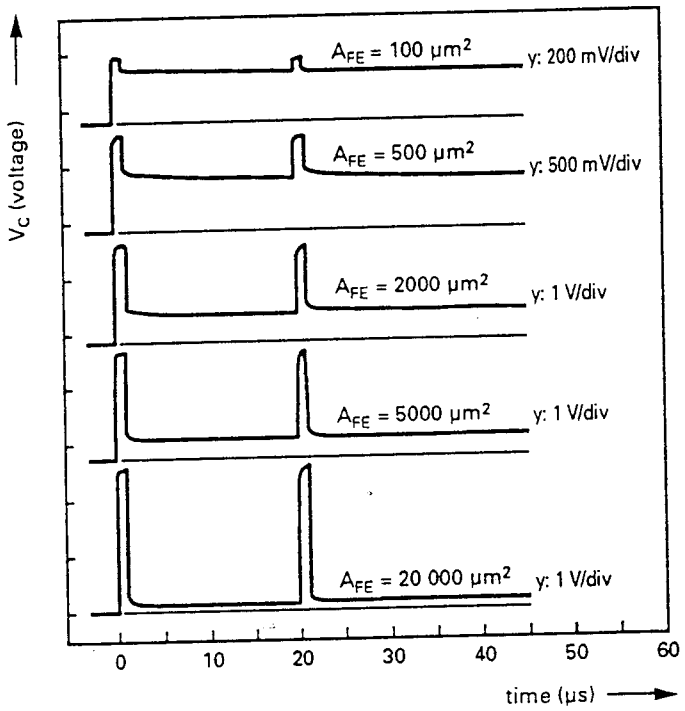


Figure 11. The voltage V_C versus time for PZT capacitors of varying areas, for a pulse sequence defined by: $V_w = -3V$, $V_r = 3V$, $w_w = w_r = 1\mu s$, $delay_{wr} = 50$ ms, $delay_{rr} = 20$ μs.

We first discuss the behaviour for relatively small capacitors. During the first read pulse with onset at zero time the polarization is reversed with a release of charge equal to $\Delta P_s A_{FE}$ where ΔP_s is given by Eq. (1). The charge on C_m (Q_c) during the first read pulse is therefore, assuming that the charge was zero before the read pulse: $Q_c = (2P_r+P_{diel})A_{FE}$. After termination of the 1st read pulse the dielectric term vanishes. There will be a voltage V_{FE} across C_{FE}, with $V_{FE} = -V_C$, since V_p is zero. Therefore $Q_c = 2P_rA_{FE}$ in this time range. The 2nd read pulse leads to an increase in Q_c determined by

$P_{diel}A_{FE}$. From the measured voltages for the smallest capacitor used in the investigation reported here (A_{FE} = 49 μm^2), we derive P_r = 28.5 $\mu C/cm^2$ and P_{diel} = 13.5 $\mu C/cm^2$ for pulses of 3 V. This is in good agreement with standard pulse measurements and with hysteresis measurements (i.e. negligible width dependence).

Turning to the larger capacitor areas, the released charge increases and this leads to an increased voltage drop across C_m, which reduces the voltage across the ferroelectric capacitor ($V_{FE} = V_p - V_C$) during the read pulse. This effect is shown in Fig. 12. For the 49 μm^2 capacitor, V_{FE} is close to V_p and ΔP_s is as expected. For the larger capacitors, V_{FE} is reduced and this leads to a reduction (A = 500 μm^2) and even a decrease (A_{FE} = 2000 μm^2) in ΔP_s.

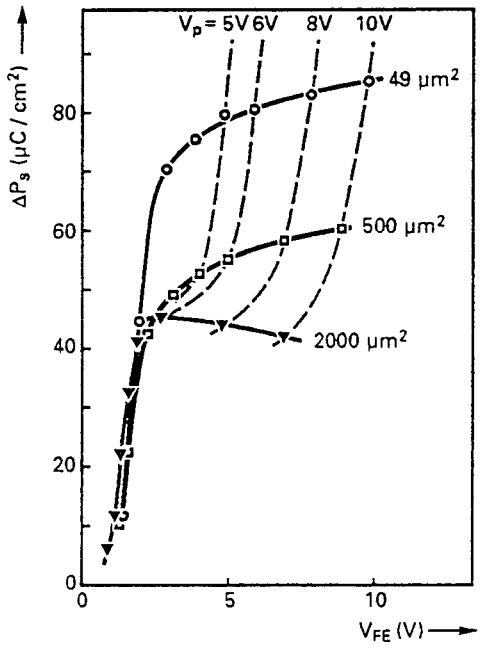


Figure 12. Polarization change as a function of V_{FE} (= V_p - V_C) during the read pulse for three capacitor areas.

In Fig. 13, the voltage across C_m after termination of the read pulse is shown as a function of V_{FE} for three pulse amplitudes. The charge on C_m (or V_C) increases first less than proportionally with area, due to the reduction in V_{FE} during the read pulse, as shown above, and then decreases. These results indicate that the required minimum voltage of, e.g. 100 mV, can be obtained for a large range of capacitor areas.

A detailed understanding of all the observations described above is difficult to obtain since it requires very detailed information about polarization versus voltage, back-switching effects, etc. We will consider here a simplified case on the basis of the hysteresis loop shown in Fig. 14.

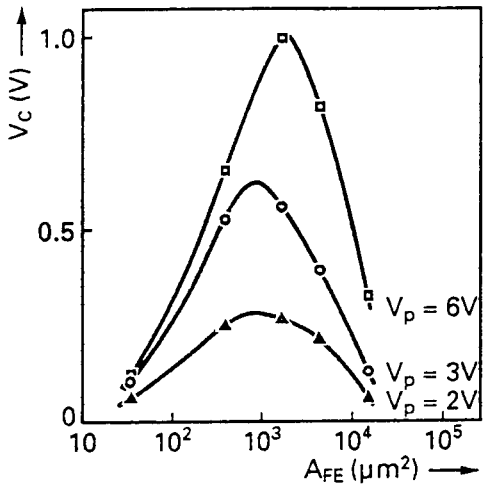


Figure 13. The voltage V_C versus A_{FE} after termination of the 1st read pulse.

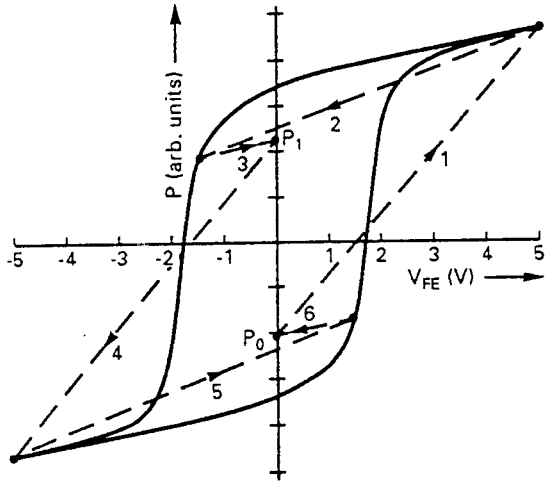


Figure 14. Hysteresis loop indicating the changes in polarization for the case of back-switching due to the charge on the capacitor C_m.

We assume that the polarization before the read pulse is P_o. The read pulse changes the polarization as indicated by line 1. If A_{FE} is not sufficiently small, V_{FE} can be markedly smaller than V_p. This reduces the switched polarization, while the ferroelectric capacitor is partially switched. Next, the pulse is terminated and due to the charge on C_m, V_{FE} will become negative (line 2). When this back-switching voltage is made zero by reset or by waiting sufficient time (RC_m discharge, Fig. 10b), the polarization becomes P_1. A

similar scheme can then begin with a following pulse of opposite polarity as shown in Fig. 14. Consequently, the value for P_r derived from these measurements approximately equals $(P_1-P_o)/2$ which is smaller than P_r. It should be noted that in a memory circuit the situation for writing is different, since potentials then are fixed (opposed to the situation during reading). In short, there are two main reasons for the observed switching behaviour: (i) Reduction of V_{FE} during switching, and (ii) back-switching effects.

There are several further points to comment on. If we scale the capacitor C_m from 275 pF to the value of a typical bitline capacitor, e.g. 1 pF, and the ferroelectric capacitors by the same factor, the areas varying from 49 to 20000 μm^2 will scale to values between 0.18 and 73 μm^2. Thus, the polarization characteristics are in principle sufficient for submicron sized capacitors if the properties are scalable down to this level. This depends on points as grain sizes and etching techniques. At present, more realistic minimum capacitor areas will be in the range from about 2 μm^2 (0.5 μm process technology) to 10 μm^2 (1 μm technology) and its is clear that if C_{BL} is not increased, the effects discussed above (partial switching due to reduction of V_{FE} and back-switching) will play important roles and have to be taken into account. An additional point is that the reduction of V_{FE} and of the polarization being switched can lead to strong improvement of the endurance. Comparisons between measurements of the endurance of a structured capacitor using standard test procedures (circuit (b) in Fig. 10) and a 1T/1C memory cell, with C_{BL} = 2 pF and A_{FE} = 25 and 49 μm^2, showed improvement of more than 4 orders of magnitude (10^8 and $>10^{12}$ cycles, respectively) for a pulse voltage of 5 V [14].

6. Conclusions

The pulse switching techniques described in the first part of this paper have shown to be well founded on the basis of analytical as well as simulation results. In general, circuit effects dominate the measurements of switching times and the physical switching time of PZT capacitors was not measurable within the time resolution of 500 ps. Progress in this area requires more advanced measuring techniques than the present ones together with very small loads (e.g. with A_{FE} down to 1-10 μm^2) to limit circuit effects. It was further demonstrated that pulse characterization methods are adequate to investigate ferroelectric properties under conditions comparable to those needed for ferroelectric memories.

The application of a second pulse measuring technique which is based on a circuit resembling that of a 1T/1C memory cell reveals that partial switching as well as back-switching effects can play major roles in a memory circuit. They have to be taken into account in circuit modelling. For a general characterization of ferroelectric properties this method is not suitable.

7. Acknowledgements

We thank our colleagues J. Dikken, R. Janssen, M. de Keijser, G. Spierings, D. Taylor, M. Ulenaers and P.J. v. Veldhoven for discussions and technical assistance. Part of this work has been carried out under the FELMAS project. The support of the European Commission is greatfully acknowledged.

8. References

1 Larsen, P.K., Spierings, G.A.C.M., Cuppens, R., and Dormans, G.J.M. (1993), *Microelectr. Eng.* **22**, 53.

2. Ramesh, R., Lee, J., Sands, T., Keramidas, V.G., and Auciello O. (1994), *Appl. Phys. Lett.* **64**, 2511.

3. Larsen, P.K., Kampschoer, G.L.M., van der Mark, M.B., Klee, M. (1992), *Symp. Proc. ISAF'92*, IEEE **92CH3080-9**, p. 217.

4. Stadler, H.L. (1992), *Ferroelectrics* **137**, 373.

5. Ishibachi, Y., and Takagi, Y. (1971), *J. Phys. Soc. Japan* **31**, 506.

6. Duiker, H.M., and Beale, P.D. (1990), *Phys. Rev.* **B41**, 490.

7. Larsen, P.K., Kampschoer, G.L.M., Ulenaers, M.J.E., Spierings, G.A.C.M., and Cuppens, R. (1991), *Appl. Phys. Lett.* **59**, 611.

8. Messenger, G.C. (1988), *IEEE Trans. Nuc. Sci.* **36**,1461.

9. Larsen, P.K., Dormans, G.J.M., Taylor, D.J., and van Veldhoven, P.J. (1994), *J. Appl. Phys.* **76**, 2405.

10. Miller, S.L., Nasby, R.D., Schwank, J.R., Rogers, M.S. (1990), *J. Appl. Phys.* **68**, 6463.

11. Scott, J.F., Kammerdiner, L., Parris, M., Traynor, S., Ottenbacher, V., Shawabkeh, A., and Oliver, W.F. (1988), *J. App. Phys.* **64**, 787.

12. Scott, J.F., Pouligny, B., Dimmler, K., Parris, M., Butler, D., and Eaton, S. (1987), *J. Appl. Phys.* **62**, 4510.

13. de Keijser, M., van Veldhoven, P.J., and Dormans, G.J.M. (1993), *Mat. Res. Symp. Proc.* **310**, 223.

14. Dormans, G.J.M., Larsen, P.K., Spierings, G.A.C.M., Dikken, J., Ulenaers, Cuppens, R., Taylor, D.J., and Verhaar, R.D.J. (1994), *Integrated Ferroelectrics* (in press).

15. Fesenko, E.G., Semenchev, A.F., and Gavrilyatchenko, V.G. (1976), *Ferroelectrics* **13**, 471.

16. Taylor, D.J., Larsen, P.K., Dormans, G.J.M., and De Veirman, A.E.M. (1994), *Integrated Ferroelectrics* (in press).

17. We are indebted to Dr. J.S. Obhi for the use of his sol-gel films.

18. Ramtron (March 1993) Specialty Memory Products, Catalog.

19. Taylor, D.J., Larsen, P.K., and Cuppens, R. (1994), *Appl. Phys. Lett.* **64**, 1392.

POLARIZATION, CONDUCTION, AND BREAKDOWN IN NON-FERROELECTRIC PEROVSKITE THIN FILMS

R. WASER
Institut für Werkstoffe der
Elektrotechnik (IWE)
RWTH Aachen University
of Technology
52056 Aachen, Germany

ABSTRACT. A review is presented of the research on conduction and breakdown of dielectric perovskites performed in recent years. Recent experimental and theoretical work on polarization processes, electrode effects on leakage current and I-V characteristics are discussed. Also, recent data on dc voltage-induced, long term resistance degradation is presented. The discussion is based on experimental work on titanate films including MIM (metal-insulator-metal) systems.

1. Introduction

The majority of integrated electroceramic devices proposed and developed in recent years such as ferroelectric memories, integrated capacitors, pyroelectric IR sensors, piezoelectric microactuators are designed to operate under dc or pulse dc electrical load. In general, the desired properties of dielectric thin films under voltage stimulation are:

O fast dielectric response

O low leakage / low loss

O long life time

These three features are of crucial importance for the quality and the reliability of the devices. For some applications such as ULSI DRAMs, it is required to study the signal response of the films in the time regime from nanoseconds for high-speed charging to weeks or months in life test experiments. Consequently, in order to cover all three features, the investigations may have to cover up to 15 orders of magnitude in time.

Due to the practical importance and the scientific challenge of this subject, a range of studies were carried out on the conduction and breakdown of dielectric perovskite-type thin films in the last years. For references see, e. g., [1-9] . In these studies, often the current-voltage (I-V) behavior is emphasized and aspects such as process-property relationships [7,9], possible mechanisms of the conductivity enhancement under high field [1-3,5,6,9], models for the origin of the breakdown [2,4,8] are described. In addition, the influence of the host material is studied by comparing, e. g. Pb(Ti, Zr)O_3 (PZT) films and

O. Auciello and R. Waser (eds.), Science and Technology of Electroceramic Thin Films, 223-248.
© 1995 *Kluwer Academic Publishers. Printed in the Netherlands.*

$(Ba,Sr)TiO_3$ (BST) films [4,8]. In our contribution to this field [2], we studied the influence of the microstructure on the polarization and leakage behavior of $SrTiO_3$ samples by comparing single crystals, conventional ceramics, and ceramic thin films of the same composition.

In the present paper, additional findings and ideas on the polarization process, electrode effects on the leakage current and the I-V characteristics, as well as recent data on the dc voltage-induced, long-term resistance degradation are presented. The discussion will be carried out regarding the experimental titanate film devices as MIM systems (i. e. Metal - Insulator film - Metal systems) which are determined by the bulk of the film and by the electrode interfaces.

2. General Material Properties of Titanate Thin-Films

2.1. MICROSTRUCTURE

Depending on the deposition technique, the deposited material, the substrate and its surface, the pretreatment, and on the deposition parameters, electroceramic thin films show a broad spectrum of different microstructures. As two extreme cases, epitaxial films on the one hand and very fine-grained, polycrystalline films on the other hand are observed. The epitaxy in the first case is usually limited in lateral dimensions giving rise to grain boundaries running across the thickness of the films (Figure 1 (a)). If the lateral extensions of the grains are small, the microstructure appears to be columnar. In fine-grained films, large-angle grain boundaries of random distribution are found. Average grain sizes in the range between 10 nm and 100 nm are typically observed in these polycrystalline films (Figure 1 (b)). The thermodynamic and kinetic conditions under which the different microstructures are obtained have been reviewed comprehensively by Lange [10].

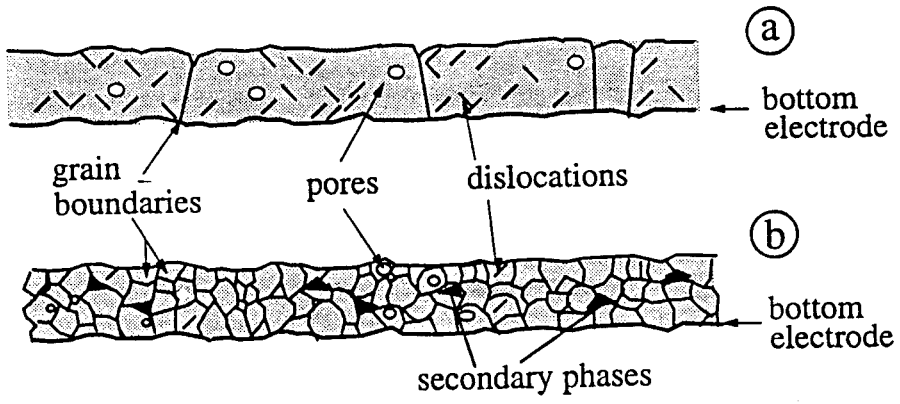


Figure 1. Sketch of possible thin film microstructures illustrated in cross - sections. Two extreme cases are shown: (a) partially epitaxial films and (b) fine - grained, polycrystalline films.

In the present paper, sol-gel prepared titanate films of the fine-grained, polycrystalline type are employed. In real films, additional microstructural features such as intergranular and intragranular pores, dislocations as well as secondary or amorphous phases at triple points (wedges) between grains are often present in varying extent as illustrated in Fig. 1.

2.2. DEFECT CHEMISTRY

The high temperature defect chemistry of regular alkaline earth titanate crystals is governed by a Schottky disorder, i. e. vacancies on anion and on cation sites. The oxygen vacancies, Vö, are positively charged relative to the regular lattice and, hence, act as donor-type native defects. They are relatively mobile ionic defects, showing a mobility of approximately $\mu_{V_O} = 2 \times 10^{-9}$ cm^2/Vs at 500 K and an activation energy of the motion of approximately 1 eV [11]. Cation vacancies are acceptor-type native defects and must be regarded as virtually immobile. Heterovalent cations may be substitutionally accommodated on alkaline earth sites or Ti sites and act as foreign dopants. Donors (including oxygen vacancies) show shallow energy levels, while acceptor states are located deep in the band gap (Fig. 2(a)). The Fermi energy and consequently the concentrations of electronic charge carriers, electrons and holes, are determined by the oxygen partial pressure during the formation of the crystal lattice and the annealing as well as by the types and concentrations of the foreign dopants. Under reducing atmospheres, native or foreign donors are compensated by electrons resulting in n-type semiconducting ceramics. Under oxidizing atmospheres, insulating ceramics are obtained which have to be considered as autocompensated semiconductors with minority electron and hole concentrations. In this autocompensation regime, foreign donor doped titanates are compensated by cation vacancies, while foreign acceptor doped titanates are compensated by oxygen vacancies. Nominally undoped titanate crystals and ceramics are usually governed by an unknown concentration of acceptor-type impurities. Therefore, slightly acceptor-doped titanates represent better defined model systems and they are used in the present study.

The band-gap of $SrTiO_3$ decreases with increasing temperatures according to $W_G(T) = 3.3$ eV - $(6 \times 10^{-4}$ eV/K)T [12]. After annealing in oxidizing atmospheres, the Fermi energy in acceptor-doped titanates is below the mid-gap level (Fig. 2 (a)). Hence, the residual conduction in these materials shows a p-type electronic contribution in addition to the ionic contribution due to mobile oxygen vacancies. As shown for Ni acceptor doped $SrTiO_3$ ceramics in Ref. [11] , the ionic and p-type contributions are comparable in magnitude. The electron mobility in $SrTiO_3$ is slightly temperature dependent and it is decreasing from approximately 6 cm^2/Vs at 300 K [13, 14] to approximately 0.23 cm^2/Vs at 1223 K [15]. Following the arguments in Refs. [16] and [15], a hole mobility $\mu_p = 0.5\ \mu_n$ is assumed. These mobility data indicate a transport mechanism in the intermediate range between a real band conduction and a polaron hopping conduction. Further details on the defect chemistry of titanates can be seen, for example, in Refs. [16-18]. A recent review is presented in Ref. [19].

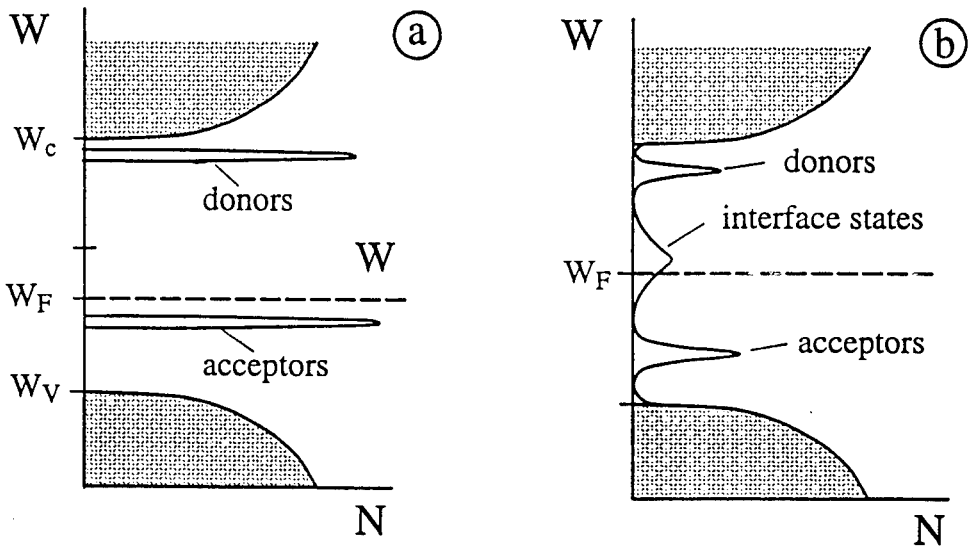


Figure 2. Band diagram for autocompensated alkaline earth titanates. The energy W is plotted vs. the density of states N. (a) Situation in the bulk, i. e. in the unperturbed crystal lattice. For the Fermi level W_F shown in the diagram, an acceptor-doped titanate annealed under oxidizing atmospheres is assumed. (b) Situation at interfaces, e. g. grain boundaries. In comparison to the bulk, the donor and acceptor state distribution is broadened and additional interface states are present. The distribution of these interface states is given as an illustrating example. The exact real distribution is not yet known.

2.3. INTERFACE STATES

Surfaces and grain boundaries (GB) introduce additional electronic states in the band gap due to the disruption of the periodical crystal lattice. In the case of acceptor-doped titanates, these are mainly positively charged (i. e. donor-type) states which lead to an up-shift of the Fermi level (Fig. 2 (b)) and, hence, to a down bending of the bands (Fig. 3 (a)). The resulting depletion space charge layers at the interfaces are of approximately 100 nm thickness (Fig.3 (b)) [20]. In Ref. [20], we comprehensively discuss the GB space charge layer in acceptor-doped $SrTiO_3$ ceramics. The depletion space charge layer at the electrode interface of an acceptor-doped $SrTiO_3$ single crystal is briefly described in Ref. [2]. In thin films, the surface states and - especially in ultra-fine grained ceramics - the GB states obviously lead to a complete depletion as suggested in Ref. [2]. Additional non-equilibrium point defects and extended defects have to be assumed in the thin films, frozen-in due to the low crystallization temperature during the processing.

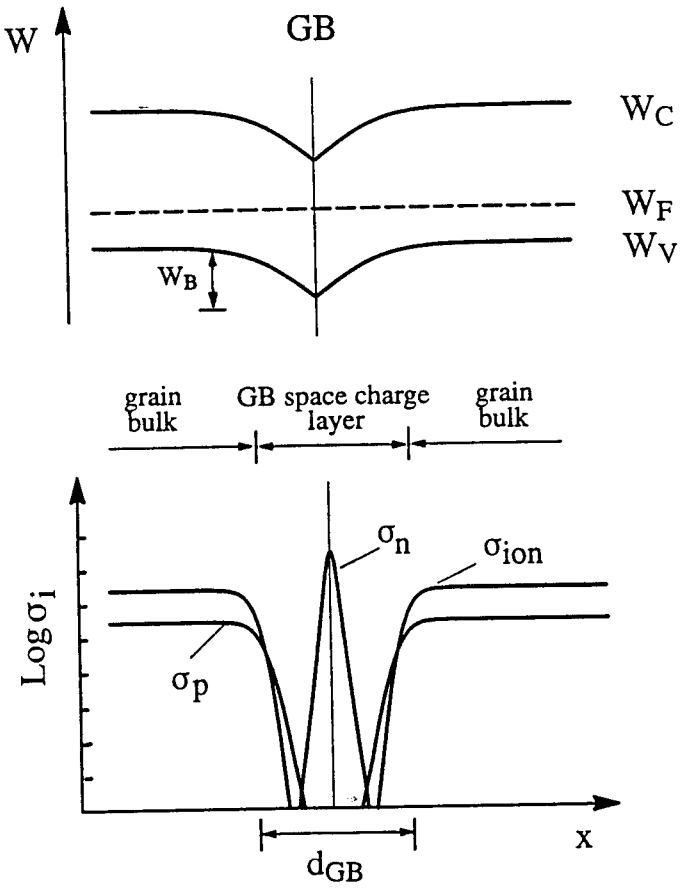


Figure 3. Sketch of (a) the energy band profile W(x) and (b) the conductivitiy profile $\sigma(x)$ across a grain boundary in acceptor doped titanate ceramics. d_{GB} denotes the width of the depletion space charge layer.

3. Experimental

This Section is dedicated to discussing the measuring technique used by the author's research group and introduces some semantic definitions on the charge transport processes and time regimes.

3.1. VOLTAGE STEP TECHNIQUE

A complete impedance analysis of dielectric thin films requires challenging measuring techniques. This is caused by the extremely broad time regime to be covered and the very large dynamic range of currents of more than ten orders of magnitude. As in preceding papers, a voltage step technique is employed for the impedance analysis. The principle of the voltage stimulation is sketched in Fig. 4.

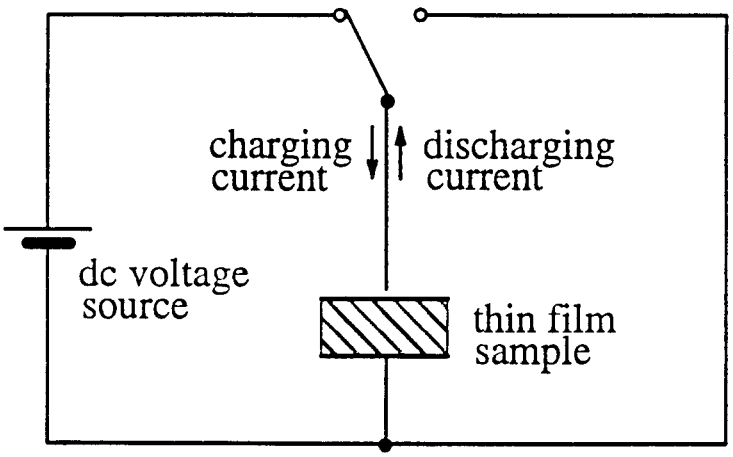


Figure 4. Sketch of the measuring principle for the dc voltage step stimulation of a dielectric thin film sample. The switch is used to select between the charging process (left position) and the discharging process (right position). The directions of the charging and discharging currents are indicated.

The signal shape of the voltage stimulation and of the current response are shown in Fig. 5. Our analysis comprises both, the charging process after applying the voltage V and the discharging process after short-circuiting. The current response for both processes is illustrated in Fig. 5 (b) on a log | I | vs. log t plot. Without referring yet to the underlying process, the current observed during the charging process empirically consists of two contributions, a polarization current, I_P, and a leakage current, I_L. The charge stored in the system described by the integral $\int I_P dt$ is usually regained as the integral of the depolarization current $\int I_D dt$ during the discharge process. Often, the time evolution of I_P and I_D is identical with reverse sign,

$$I_P(t) = - I_D(t) \qquad (1)$$

as expected for linear dielectric systems (i.e., systems with a linear polarization - field relationship). Strictly, the relation is only true for infinitely long charging times. In practical applications, it is sufficient to carry out the charging process at least one order of magnitude longer than the discharging process. It should be noted that in films with ferroelectric contributions to the polarization process, deviation from relation (1) may be observed [9]. The leakage current curve I_L-t is determined by the difference of the total current I-t and the polarization current I_P-t during the charging process. Because of relation (1), it is experimentally easy to reveal I_L-t from the charging and the discharging responses according to

$$I_L(t) = I(t) - |I_D(t)| \qquad (2)$$

for linear dielectric systems.

In order to refer to both, I_P and I_D, the term relaxation current I_R will be used throughout the text as opposed to the leakage current I_L. The time regime of dominating relaxation currents is usually named the transitory regime. The time regime of dominating leakage currents during the charging process will consequently be named the leakage regime. The same indices will be used for the current density, J, which is used throughout the text.

3.2. EQUIVALENT NETWORK

The current response sketched in Fig. 5 (b) may be formally translated into a (simplified) equivalent network shown in Fig. (6).

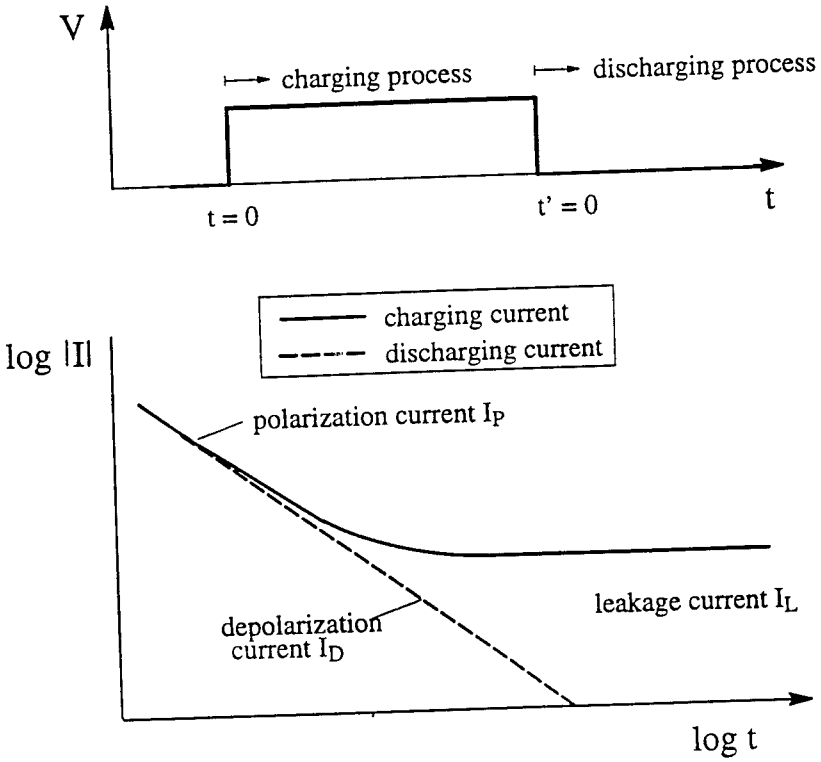


Figure 5. The signal forms of the dc voltage step (a) and a current response (b) for a charging period starting at t = 0 and a discharging period starting at t'= 0 are sketched. The current response of a typical dielectric ceramic thin film is shown unsigned on a log — log scale.

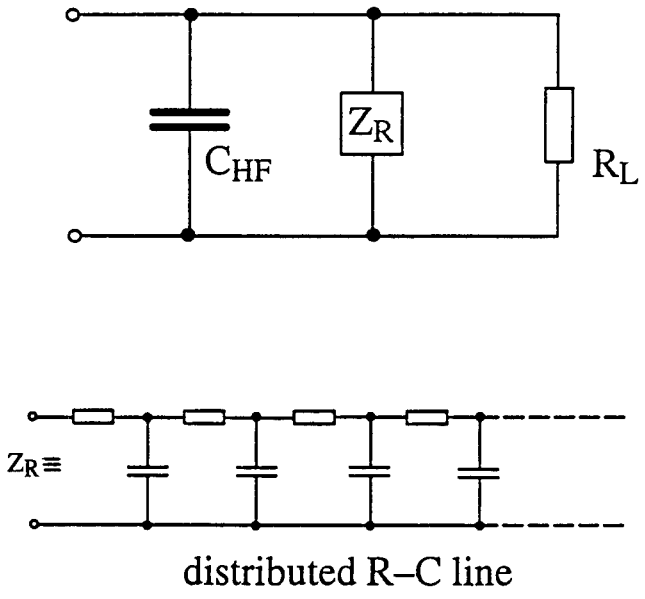


Figure 6. Electrical equivalent network of a dielectric titanate thin film device showing impedance contributions of the high-frequency capacity C_{HF} the dielectric relaxation Z_R, and the voltage-dependent insulation resistance R_L. The relaxation element Z_R represents a distributed R-C line.

The following network elements can be distinguished:

- The element C_{HF} represents the high - frequency capacitance of the thin film device. For paraelectric ceramics, it is given by the capacitance in the microwave and far infrared region. C_{HF} is immediately charged upon the application of the voltage step at $t = 0$. At $t' = 0$, C_{HF} is immediately discharged. Because it does not show any impact on the current signal at times $t > 0$, this element is disregarded in the present paper.

- The relaxation currents I_R in the transitory regime may be considered as being caused by a distributed R-C line. The slope of the I_R-t curve on the log - log scale (Fig. 5 (b)) is determined by the sequence of the R_n and the C_n with n being the order number in the distributed R-C line.

- The network element R_L represents the insulation resistance of the thin film devices. It determines the leakage current and usually exhibits a strong voltage dependence.

As said previously, the equivalent network shown in Fig. 6 is simplified. For instance, the finite conductivity of the electrodes introduces a (small) serial resistance and the electrode geometry gives rise to (small) inductances. In addition, the network elements

could be further elaborated and detailed if more information were available. For the time being, however, the network appropriately represents the typical features of the current response of dielectric titanate films and, hence, will be employed for starting the formal discussion in this paper.

3.3. I-V MEASUREMENTS

Figure 5 (b) indicates an experimental problem which is frequently encountered in determining the "true" leakage current. Obviously, the polarization current I_p must decay to a value comparable to the leakage current I_L, before the latter can be resolved with a sufficient precision. Due to the different temperature dependencies of I_p and I_L, the change-over time between the transitory regime and the leakage regime increases with decreasing temperature. In Ref. [2], we extrapolated a change-over time of up to many hours for good (i. e. low-leaky) $SrTiO_3$ thin films at room temperature. Similarly long measuring change-over times are reported for PZT thin films with Pt electrodes at room temperature [21]. This time is independent of the magnitude of the voltage step as long as the voltage does not affect the magnitude of R_L. Using the voltage-step technique, a new I-t measurement (preferably using a virgin sample dot) is needed for every data point in the I_L-V curve. To avoid uncomfortably long measuring times, most of the studies presented in this paper are conducted at elevated temperatures.

As an alternative to the voltage-step method, a voltage-ramp technique may be used for the impedance study. However, a simple analysis of the network response to a voltage ramp shows that the same time must elapse before the small signal value of the leakage current can be determined. For PZT films at room temperature, Hu and Krupanidhi convincingly demonstrated the orders of magnitude error in I_L which is made if an inadequately fast voltage ramp is employed [9]. In contrast to the interpretation in Ref. [9], the author considers this effect significant since the temperature dependencies of relaxation currents and leakage currents are completely different (see below). These dependencies, however, contain valuable information to elucidate the charge transport mechanisms. Another example for the fact that ramp tests lead to dramatic artifacts is given by Scott et al. [22]. In this paper, an apparent negative different resistivity at moderate fields observed in PZT films is found to be due to I(V) curves recorded with too fast ramps.

Abrupt changes in the activation energy over large temperature ranges (as reported e. g. in Ref. [23]) may possibly be caused simply by an unnoticed transition between the relaxation current dominated regime and the leakage current dominated regime.

3.4. LONG-TERM BEHAVIOR

A dc voltage stress applied to titanate thin films for long times frequently gives rise to a degradation of the insulation resistance, R_L. The resulting current increase is often so pronounced that the degradation finally leads into a fatal breakdown event. Figure 7 is an extended version of Fig. 5 (b) and comprises the time regimes until the breakdown event. It should be noted that at high temperature and high voltages, the leakage regime may vanish by an overlapping of the transitory regime and the degradation regime. Since the degradation is (at least partially) irreversible, it does not make sense to record and evaluate the discharging process in the case of degradation.

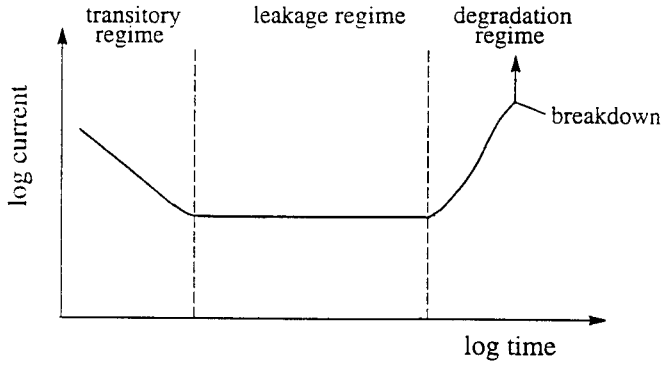


Figure 7. Sketch of the current response of dielectric titanate thin films upon a voltage - step stimulation. The initial transitory regime, the intermediate leakage regime, and the long - term degradation regime are shown.

In the present paper, the typical dc voltage-induced resistance degradation will be described on an empirical basis only. There may be an overlap with an effect known as the time-dependent dielectric breakdown (TDDB) [21] which is usually characterized by a sudden current increase after long time of low leakage.

4. Dielectric Relaxation in the Transitory Regime

4.1. RESULTS

Figure 8 shows the polarization current density $J_P(t)$ and the depolarization current density $J_D(t)$ for a $SrTiO_3$ film with a Pt bottom cathode determined at different temperatures.

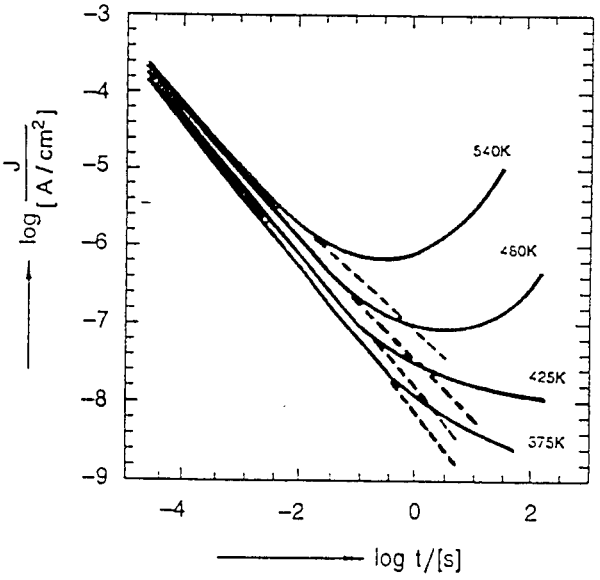


Figure 8. Current density J vs. time t for a $SrTiO_3$ thin film of 230 nm thickness upon a voltage - step stimulation of 1.0 V for different temperatures. The charging and discharging processes are shown as averaged schematic curves.

The relaxation currents can be described by the empirical Curie - von Schweidler law (sometimes called "universal dynamic response") [24, 25, 26],

$$J_R(t) \alpha t^{-n} \quad (3)$$

where the exponent n changes from approximately 0.93 at T = 375 K to approximately 0.77 at 540 K. For some films, a change in the exponent during the time evolution is observed as well.

The influence of the applied voltage on the relaxation currents was investigated in the range from 0.05 V to 8 V, corresponding to electrical fields E of 2 kV/cm to 350 kV/cm. Within this range, the relaxation currents show no deviation from a linear behavior.

The influence of the type of electrode metal and of the voltage polarity was studied for the selection of metals listed in Section (5.1.). For elucidating the mechanism of the dielectric relaxation, it is of great significance that no dependence of the relaxation currents on the metal and on the polarity was observed.

4.2. DISCUSSION ON THE NATURE OF THE CURIE - VON SCHWEIDLER BEHAVIOR

A wide spectrum of structurally disordered solids, both crystalline and glassy, extending from good insulators to fast ionic conducting electrolytes, shows the phenomenon of relaxation currents which follow the Curie - von Schweidler law, Eq. (3). This "universal" behavior has been traced back to few very different mechanisms:

- **Injection model**
  For thin films of a good insulator such as SiO_2, electrons injected from the metal cathode may get trapped and generate a negative space charge region in front of the cathode [27]. The formation of this space charge subsequently lowers the electric field at the cathode and, hence, reduces the injection current according to Eq. (3).

- **Many-body interaction model**
  The hopping motion of a charged particle will always affect the motion of all neighboring charges. As shown theoretically by Dissado and Hill [28], the charge transport is correlated due to the many-body interaction between the charges leading to Curie - von Schweidler type equations. For solid electrolytes with high ionic charge carrier concentrations, a similar model was derived and excellently fitted to the experimental data by Funke [29].

- **Distribution of Relaxation Times (DRT) model**
  As known from textbooks and illustrated in Fig. 9, a superposition of Debye - type relaxations, $J \alpha \exp(-t/\tau)$, with a (large) distribution of relaxation times, τ, unequivocally leads to Curie - von Schweidler type equations. The exponent n is determined by the specific distribution of the individual Debye - type processes. This distribution may be caused by a variation in a charge transport barrier (e. g. at the grain boundaries). Only a relatively small variation is required for the energy barrier to obtain a spectrum of relaxation times over many orders of magnitude [30].

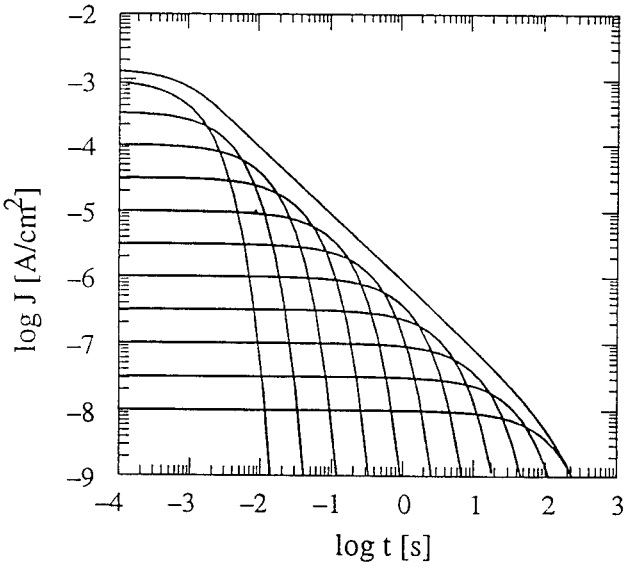


Figure 9. Curie - von Schweidler type relaxation obtained by a superposition of Debye-type relaxations.

For $SrTiO_3$ thin films, the injection model appears to be unlikely for two reasons. Firstly, the dielectric relaxation of the titanate films clearly is a bulk phenomenon which is independent of the electrode metal. As will be described in Section (5.2.), the electron emission properties of the metals used in this study are extremely different. Since the injection model relies on electron emission from the cathode as the first step, a significant influence of the electrode metal would be expected - in contrast to our findings. Secondly, during the discharging process, the emptying of the traps would happen randomly towards both electrodes. Consequently, no - or at least only a very small - depolarization current, $|I_D| < |I_p|$, would be expected - in contrast to our findings.

In principle, the hopping of the polaron-type electronic carriers as well as of the ionic carriers may be correlated to a certain extent. Therefore, the many-body interaction model cannot be discarded at first glance. However, there are two indications which render the dominance of this mechanism less likely. First, the correlation of the charge motion would be possible in conventional bulk ceramics in a similar manner as in the thin films. Yet, for conventional acceptor-doped $SrTiO_3$ ceramics, a Debye-type relaxation was observed and fully explained by a grain - grain boundary Maxwell-Wagner polarization [20]. Second, the temperature dependence (Fig. 8) is different to what is expected from the correlation model [31].

Let us consider the DRT model. As described in Section 2.3., an energy band bending and the formation of a depletion space charge layer of width d_{GB} is observed at interfaces in acceptor-doped titanate ceramics due to donor-type interface states. In Ref. [2], we proposed a complete carrier depletion in polycrystalline films and a distributed spectrum of local conductivities because the grain size, d_{gr} is below d_{GB}. To look into more details, this also means that the extent of the band bending will start to depend on the distance, d_{gr}. Hence, because of the natural variation of the grain sizes in a given film,

the energy barrier W_B will show a scatter in its height across the thin film. This is exactly what is required by the DRT model.

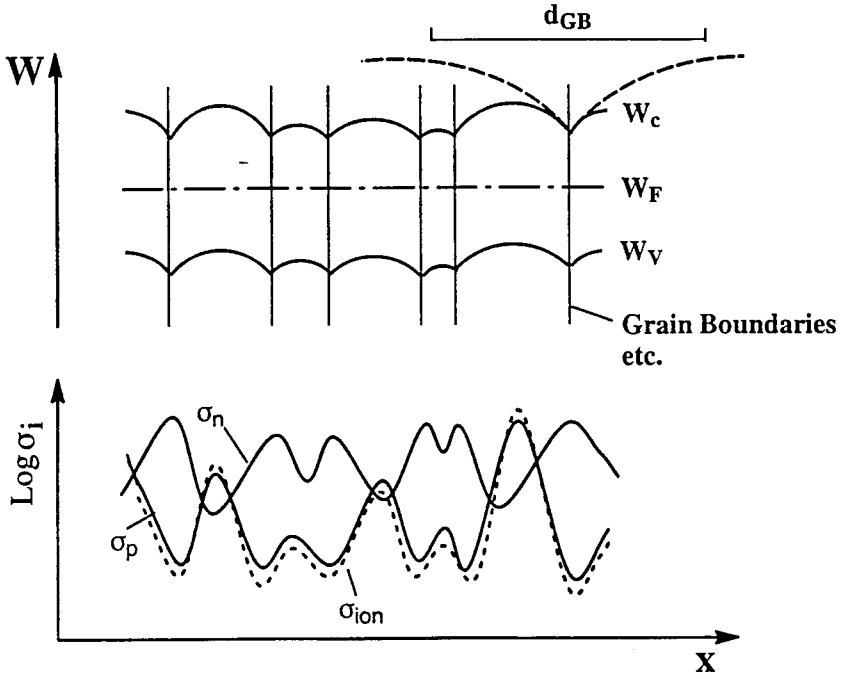


Figure 10. Sketch of (a) the band profile and (b) the conductivity profile for nanocrystalline acceptor - doped $SrTiO_3$ thin films. (·····) electronic conductivity. (———) ionic conductivity. This qualitative illustration is based on simulation results for single grain boundaries [32].

In Fig. 10, a sketch of the band profile and the conductivity profile is given. The range of barrier heights can be extracted from the temperature dependence of our $J_{D(t)}$ in Fig. 8, replotted in an Arrhenius diagram in Fig. 11.

The fastest process at t = 100 µs shows the smallest activation energy W_A of 0.110 eV, while the process at t = 1 s is activated by W_A = 0.245 eV. As previously said, these activation energies can be regarded in first approximation as the barrier height for the local charge transport leading to a *space charge polarization*. Similar activation energies are reported for the transitory regime in PZT films (e. g. 0.33-0.36 eV [33], 0.2 eV [34], 0.22 eV [7]). In both thin film material systems, PZT and $SrTiO_3$, these values are very much lower than the activation energy in the leakage regime (see Section 5). Based on this temperature dependence and the finding that the relaxation current is a bulk phenomenon of the titanate films independent of the electrode metal, the author considers the local charge redistribution process according to the DRT model as the dominant mechanism. In addition, due to the low activation energies, the relaxing carriers are obviously of electronic nature. The only mobile ionic species in $SrTiO_3$ are oxygen vacancies which show an activation energy of 1.0 eV for the migration in the crystal

lattice as mentioned in Section 2.2. This value is so high that oxygen vacancies are unlikely responsible for the dielectric relaxation.

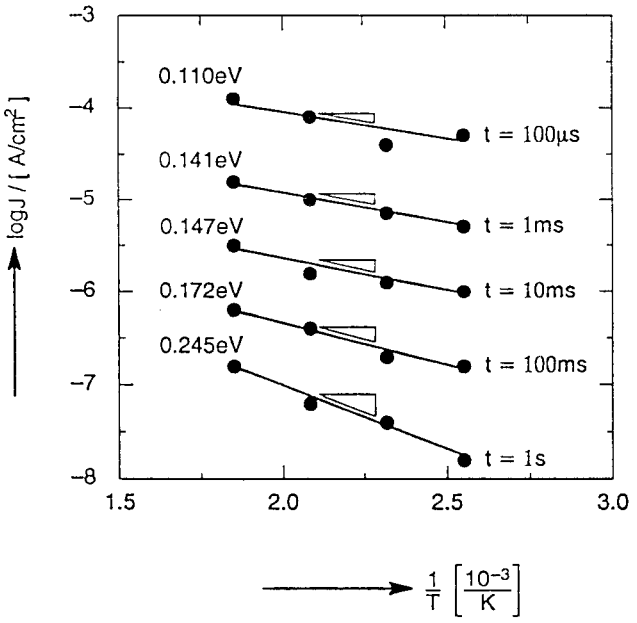


Figure 11. Log current density J vs. reciprocal temperature 1/T for the relaxation currents of acceptor-doped $SrTiO_3$ thin films.

Columnar epitaxial films (Fig. 1 (b)) show a Curie - von Schweidler behavior despite their different microstructure. First, to our experience, even high quality films incorporate sufficient artifacts (e. g. micropores, dislocations, non-equilibrium point defects) to generate a relatively high density of statistically distributed extended defect states throughout the film. This effect can easily lead to a situation similar to Fig. 10. Second, the effect may be due to the surface states which cause depletion space charge layers extending through the complete films if the thickness is not too large. For acceptor-doped $SrTiO_3$ single crystals, we found distinct depletion space charge layers at the electrode interfaces. By numerical simulation it can be shown that a Curie - von Schweidler behavior is revealed if the single crystal become thin enough to overlap the depletion layers (e. g. to obtain a completely depleted, single crystalline film) [35]. Hence, the Curie - von Schweidler behavior also can be explained for perfect films without artifacts.

Anodically formed Al_2O_3 films represent an interesting comparison to titanate films. In Al_2O_3 films, the Curie - von Schweidler law is observed over approximately 10 decades of time with a slope $n \sim 1$ and almost independent of the temperature. The dielectric relaxation can also be explained by a DRT caused by a distribution of energy barriers. The dominant mobile carriers in these Al_2O_3 films are protons incorporated during film formation in aqueous electrolytes. As elegantly proofed by Kliem, the experimental findings can be explained by a *tunneling* of the protons through the energy barriers [30].

5. Leakage Regime

5.1. RESULTS

In this Section, results for the influence of several parameters on the leakage current are presented. An emphasis is put on the electrode contacts. A variety of different materials and deposition methods have been used to produce top electrode contacts for this study. In all cases, the bottom electrode was Pt with a thickness of 70 nm deposited by sputtering. The selection of electrode contacts is listed in Table 1.

The voltage polarity dependence of the J-t results was tested for a film of 230 nm dielectric thickness with two different top electrodes, Pt and NiCr/Au, respectively. The bottom electrode was Pt. It was observed that only NiCr/Au as the negative electrode (cathode) resulted in relatively high leakage currents.

TABLE 1. Selection of electrode materials and deposition techniques used in this study. In the case of NiCr alloy and Yb, respectively, the metals were used as adhesive layers underneath an Au layer. In the last two cases, in contrast, Au is used as a protective layer on top of Al and Ti contact.

Metal electrode	Deposition technique	Thickness
Pt bottom	sputtering	70 nm
Pt top	e–beam evaporation	200 nm
Pt top	sputtering	100 nm
Pd top	e–beam evaporation	100 nm
$SrRuO_3$ top	laser ablation	200 nm
Au top	thermal evaporation	200 nm
NiCr/Au top	thermal evaporation	40/200 nm
Yb/Au top	laser ablation	60/200 nm
Al/Au top	thermal evaporation	200/40 nm
Ti/Au top	thermal evaporation	200/40 nm

In the case of a Pt cathode, the leakage currents are low (and equal within the experimental scatter), independent of Pt being the top or bottom electrode. This result unequivocally shows that only the cathode determines the leakage behavior of thin titanate films. The polarization and depolarization currents are found to be independent of the polarity and the electrode metals within the experimental scatter for all combinations of Table 1. This finding was used in Section (4.) for explaining the dielectric relaxation as a film bulk mechanism.

In Figure 12, the J-t curves for a variety of cathode materials are presented. Towards long times, all curves show increasing slopes indicating the onset of a slight resistance degradation. This is due to the relatively strong temperature and field stress and will be

treated in Section (6.). Tests at lower fields have proofed that the degradation onset can be shifted to times much greater than 10^4 s revealing a very extended leakage regime [36].

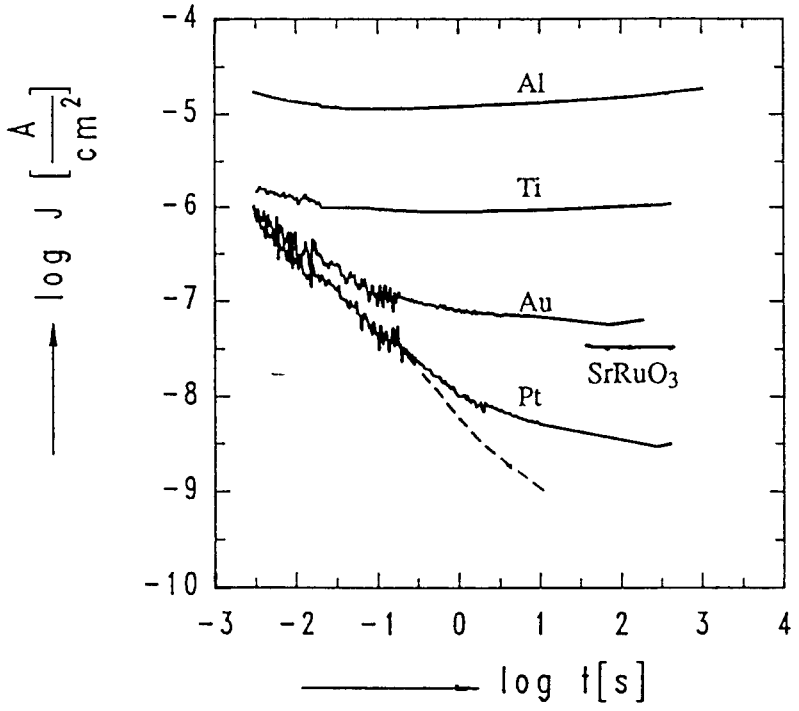


Figure 12. Current density J vs. time t for 0.1 at % Ni - doped $SrTiO_3$ films at 425 K and 0.2 V. Comparison of different top electrode materials as cathodes. All films have Pt bottom electrodes. Film thickness: 230 nm (for Al, Ti, Au, Pt electrodes), 660 nm (for $SrRuO_3$ electrode). Only one representative depolarization current curve is shown (dashed), because these curves are the same within the experimental scatter.

The $SrRuO_3$ top electrode was only available on films of different thickness. The corresponding measurements were recorded at the same voltage and the results are included in Fig. 12 for an - at least semi-quantitative - comparison with the other cathode materials. First data on W, Au, Pt electrodes measured at room temperature were reported by J. F. Scott et al. [8]. They semi-quantitatively agree with the data shown in Fig. 12. A detailed comparison, however, is impossible since no temperature and field analysis was performed in the study of Scott et al.

The impact of the temperature on the J-t characteristic is illustrated in Fig. 13 for two cathode metals of very different leakage behavior, Al and Pt. Because of this difference, a temperature interval from 300 K to 425 K was selected for Al while a range from 425 K to 535 K was chosen for Pt.

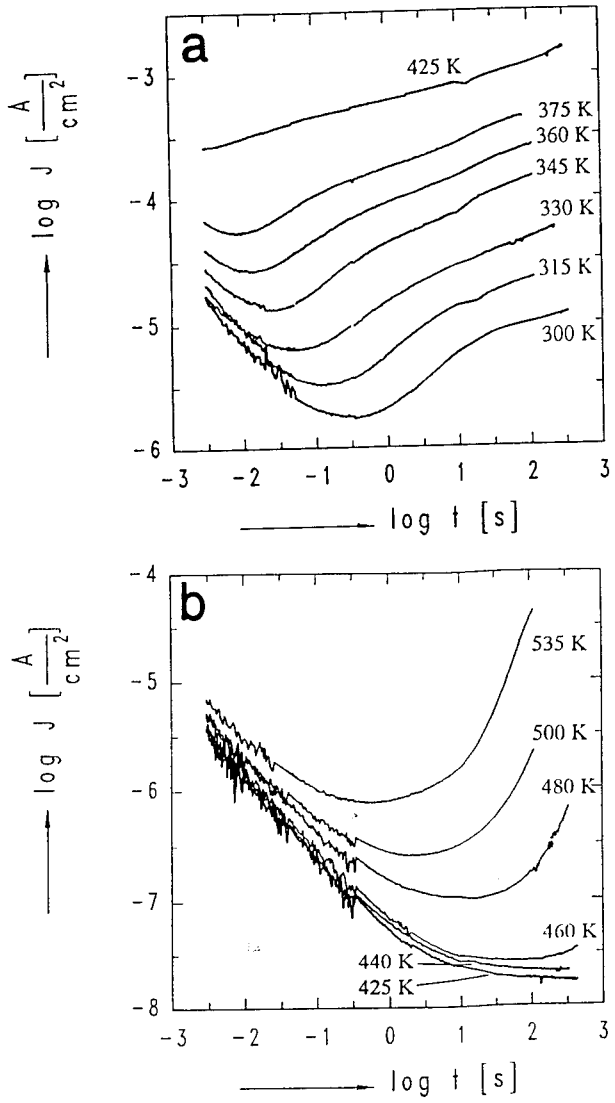


Figure 13. Temperature dependence of the current density J vs. time t curves for two 0.1 at% Ni - doped $SrTiO_3$ films. (a) Al cathodes, film thickness: 370 nm, voltage: 1.24 V; (b) Pt cathodes, deposited by e - beam deposition, film thickness: 230 nm, voltage: 1.0 V.

To give an example of the voltage influence on the leakage, the current density - field ratio, J/E, is shown as a function of time for voltages from 0.03 V to 2 V applied to a film with an Al cathode (Fig. 14). The J/E presentation reveals the data in conductivity units and displays the curves in the regime of a linear J - E relation (ohmic regime) on top of each other. This has the benefit that a deviation from the linear behavior can be recognized more easily. In the present example, J/E starts to increase for increasing voltages above a voltage greater than approximately 0.2 V, indicating a super-ohmic leakage enhancement.

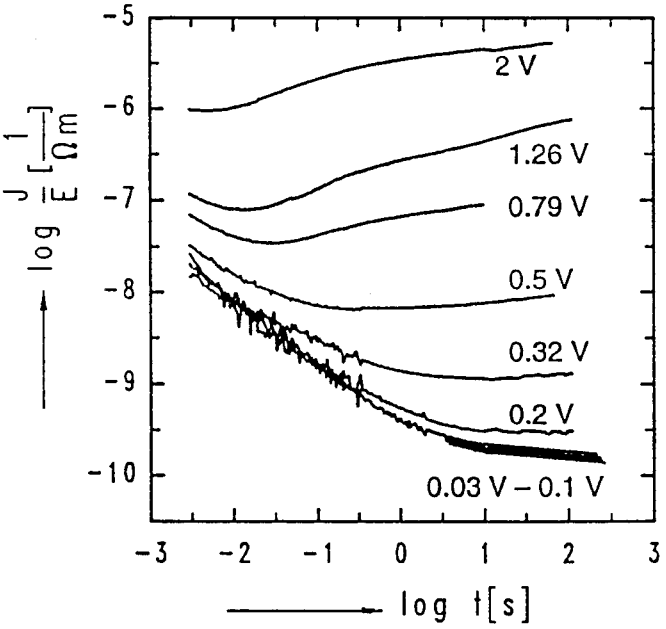


Figure 14. Voltage dependence of the leakage for a 0. 1 at % Ni-doped $SrTiO_3$ film of 370 nm thickness with Al cathodes at 360 K. Plot of the current density - field ratio J/E vs. the time t.

The complete J-V behavior is exhibited in Fig. 15 for Pt, Pd, Al, and Ti cathodes. The high-field slopes in Fig. 15 are roughly in the range between 4 and 6. Hence, there is no indication for space charge limited currents which would imply a slope of 3. A detailed analysis supporting a Schottky emission model is given in Section 5.2.

As an immediate consequence of the results, the leakage and, hence, the overall film resistance have to be regarded as primarily determined by the electrode-film interface and is found to vary over many orders of magnitude depending on the type of metal. For increasing film thicknesses, however, it is evident that the relative impact of the film bulk resistance on the overall film resistance must increase. In order to investigate the influence of the film thickness, two cathode metals of very different leakage behavior, NiCr/Au and Pt, were studied for a relatively thin film (230 nm) and a thick film (2400 nm). For the thick film, the ratio between the leakage currents for the different types of electrodes were found to be significantly smaller than for the thin film.

In order to obtain a first impression concerning the influence of the ceramic thin film processing on the leakage behavior, films made along two different modified sol/gel routes, the hexanoate route and the acetate route (see Ref. [37] for corresponding PZT films), were compared. Although the microstructure and the average grain size are different, no significant effect of the preparation route on the leakage currents was found as long as the cathode metals were kept identical. This, again, emphasizes the dominant importance of the cathodic contact for the leakage behavior.

Two methods of electrode deposition were tested for Pt. No significant differences in the J-t and the J-V characteristics were found for Pt electrodes deposited by sputtering on the one hand, and by electron beam evaporation on the other hand. Further details of this study on the leakage regime will be given in a forthcoming paper [38].

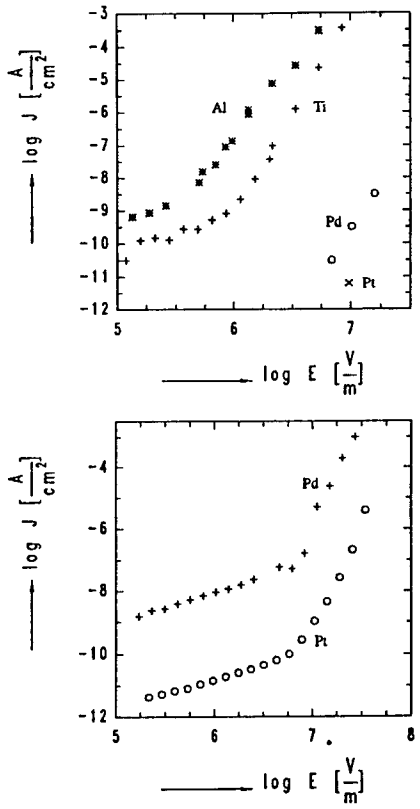


Figure 15. Current - field characteristics of 0.1 at % Ni-doped $SrTiO_3$ films with different cathodes. (a) Film at 360 K with Al, Ti, Pd and Pt cathodes; (b) Film at 440 K with Pd and Pt cathodes.

5.2. DISCUSSION ON THE NATURE OF THE ELECTRODE CONTACT AND THE LEAKAGE CURRENTS

In general, the leakage current through a MIM system is determined by the bulk of the film and by the electrode interfaces. Often, one of the contributions is highly dominating. Several limiting cases are known under which simplified mechanistic models are applicable:

- **Tunneling**
  Electrons may tunnel through barriers which are sufficiently thin (usually < 10 nm) and energetically high [39]. Typical configurations are very thin films of high band gap insulators such as Al_2O_3 and SiO_2 between metal or semiconductor electrodes. Injection into a thick film or bulk insulator may take place through the interface barrier by tunneling under very high fields (Fowler-Nordheim emission).

O **Space Charge Limited Currents (SCLC)**
In the case of flat-band or *enrichment* space charge contacts, SCLCs according to

$$J_L(V) \alpha V^2 / d^3 \qquad (4)$$

are observed above a critical onset voltage, where d denotes the film thickness. Many modifications of this relationship are discussed in the literature depending on the specific MIM system. The onset voltage strongly depends on the trap density in the film.

O **Poole-Frenkel Effect**
The conductivity of films which show hopping conduction of electronic carriers may be determined by an equilibrium between an absorption and an emission of free carriers by traps. High electric fields in the films disturb this equilibrium and shift it towards larger free carrier densities. Obviously, the Poole-Frenkel effect is a typical bulk effect.

O **Thermionic Emission**
Whenever there is a (not too thin) energy barrier W_B for an electron transfer, obviously the charge carriers need sufficient thermal energy to overcome the barrier. The temperature dependence of this thermionic emission is given by

$$J_L = A^* T^2 \exp(- W_B / kT) \qquad (5)$$

A* denotes the effective Richardson constant for the emission from the metal into the insulator. The field dependence for a charge transport from a metal into or across an insulator is determined by the Schottky effect. This is based on the fact that charges in the insulator close to the interface induce mirror charges in the metal and, hence, lead to a field dependent decrease of the barrier height, ΔW. Consequently, the zero - field barrier height W_B in Eq. (5) has to be replaced by $W_B - \Delta W$ with

$$\Delta W = e_0^{3/2} \sqrt{(E / 4 \pi \varepsilon_r \varepsilon_0)} \qquad (6)$$

ε_r denotes the permittivity of the titanate film.

Using this (simplified) terminology for the charge transfer mechanism, the experimental results and additional information from the literature will be used to obtain a deeper insight into the processes. Emphasis will be put on the influence of the electrode metal, the temperature and film thickness effect, and especially on the non-linear voltage dependence, J_L-V.

Tunneling of carriers through the entire titanate film can certainly be excluded as the dominant charge transfer process in the MIM systems considered here due to the large film thickness. In addition, the author regards tunneling through parts of the film e. g. energy barriers at grain boundaries (as suggested in Ref. [9]) as unlikely as well. Even for real semiconducting ceramics with insulating grain boundaries (e. g. ZnO varistor ceramics), an early tunneling model [40] is meanwhile succeeded by an improved non-tunneling model [41]. In the perovskite-type thin films, the situation is even much less favorable

for tunneling across grain boundaries than in bulk ceramics as will be quantitatively discussed in Ref. [38].

In Section (5.1), the very pronounced dependence of the leakage current density J on the type of cathode metal was shown. This strong influence of the cathodic metal/titanate interface renders those mechanisms as less likely which assume a dominant contribution of the film bulk to the overall resistance of the MIM system, i. e. the SCLC model and the Poole-Frenkel effect. As stated, the anode metal does not exhibit an effect on the leakage. Hence, the hole injection at the anode can be disregarded as a significant process.

The *temperature dependence*, in addition, can be used to discriminate between models. For checking the thermionic emission, Fig. 16 comprises the results for different metals in a $\ln(J/T^2)$ vs. 1/T plot according to Eq. (5). The curves unequivocally show the dependence anticipated for a thermionic emission. The barrier heights W_B can be calculated from the slope of the curves using Eq. (5). As shown in Fig. 17, there is a reasonable correlation with the work functions W_W [42].

In judging the quality of this correlation, it should be taken into account that the work function of clean metal surfaces in vacuum are certainly different from the real work function of the metals in contact with titanate thin films. In addition, sub-monolayer amounts of impurities at the interface may alter the data.

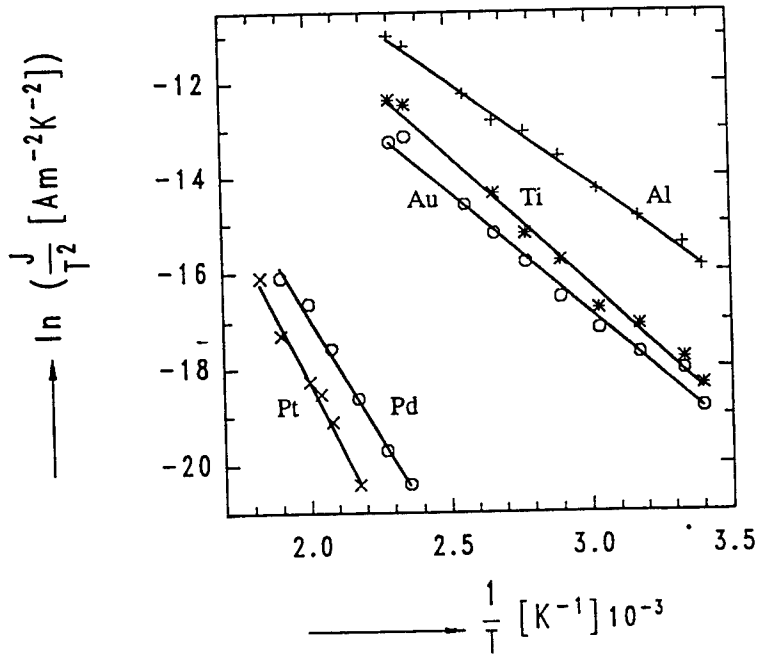


Figure 16. Temperature dependence of the leakage current density for 0.1 at % Ni - doped $SrTiO_3$ films. Al, Au, and Ti cathodes: film thickness = 370 nm, voltage = 1.26 V; Pt cathode: film thickness = 230 nm, voltage = 1.0 V; Pd cathode: film thickness = 460 nm, voltage = 1.57 V.

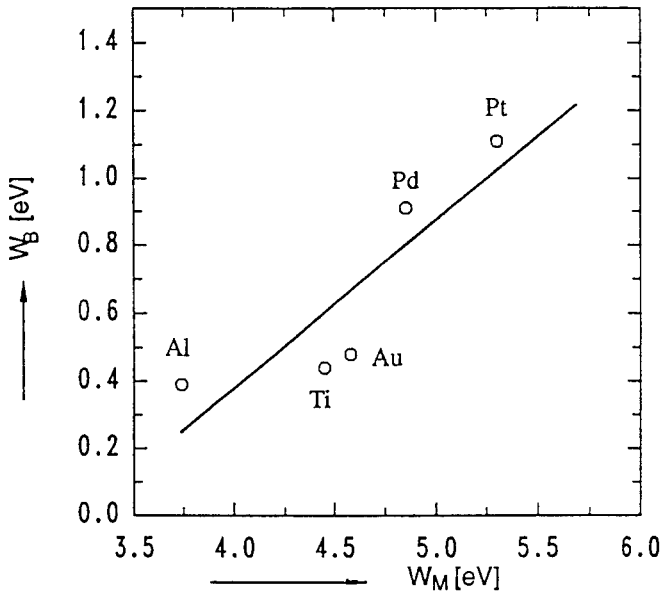


Figure 17. Barrier height W_B at the cathode contact of Ni-doped $SrTiO_3$ films vs. the work function W_M of the cathode metal.

The field dependence of the Schottky emission reveals a linear dependence between $\ln(J_L)$ and $\sqrt{E}$ according to Eqs. (5) and (6). As shown in Fig. 18, for four different metals curves are obtained which deviate only slightly from a straight line. The different slopes are due to the two different measuring temperatures. Using the effective Richardson constants from the study of the temperature dependence, the barrier heights W_B can be calculated from the ordinate values in the plot [38]. The barrier values obtained are slightly different from the data shown in Fig. 17, but they show the same trend.

A comparable correlation between the breakdown field and the metal work function was found by Scott et al. [8]. Obviously, this finding has the same origin, since impact thermal breakdown was confirmed as the dominant mechanism. Hence, the high-field leakage current density seems to be determining the breakdown. Therefore, the temperature and field dependence of the leakage current density on the one hand and the breakdown field on the other hand, both are supposed to show the same correlation to the work function of the metals.

Obviously, the data satisfyingly fit the Schottky emission model with respect to both, the temperature and the field dependence. This supports our early judgment that the leakage current across $SrTiO_3$ thin films is caused by an electron emission over a distributed Schottky barrier [2]. In this Ref., the conclusions are based on a comprehensive comparison of single crystals, ceramics, and thin film devices of the same titanate composition. However, the author emphasizes his opinion that the field dependence J_L-E alone is insufficient to qualify the model mechanism. This is due to the simplified assumptions of all models mentioned above. For example, the specific (and usually unknown) density of state distributions for interface states or traps in the films are completely ignored. Therefore, additional independent effects such as the influence of

different types of metal electrodes, the polarity, and the temperature dependence have been studied.

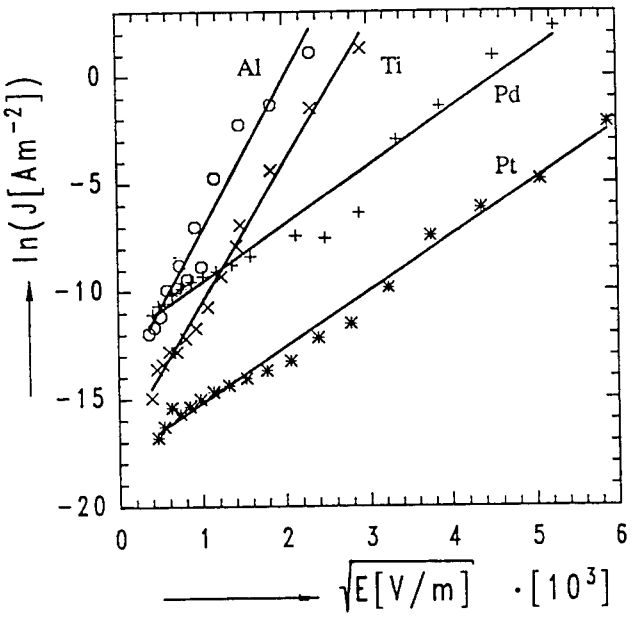


Figure 18. Field dependence of the leakage current density for 0.1 at % Ni-doped $SrTiO_3$ films with different cathodes. Pt cathode: d = 230 nm, T = 440 K; Pd cathode: d = 460 nm, T = 440 K; Ti cathode: d = 370 nm, T = 360 K; Al cathode: d = 370nm, T = 360K; (d denotes the titanate film thickness)

6. Resistance Degradation Under dc Voltage Stress

Different empirical breakdown effects of perovskite-type thin films are reported in the literature, such as the instantaneous breakdown, the time dependent dielectric breakdown (TDDB), and the resistance degradation. This section will empirically describe the resistance degradation as the process which is characterized by being (1) dc voltage-induced, (2) a long-term material wear-out effect, and (3) a slow, non-instantaneous leakage current increase. As a subsequent process, the leakage current either stabilizes at a high level or thermal runaway (thermal breakdown, see Fig. 7) takes place. A similar ac voltage-induced process can be described as a superposition of (non-symmetric) pulse dc processes with alternating polarities.

Figure 19 shows the degradation of a $SrTiO_3$ thin film in a current-time diagram on a log-log scale using the electric field as a parameter. The approximate onset of the degradation is indicated by arrows. Obviously, the degradation sets in at shorter times as the field is increased. As shown in a preliminary study [43], the onset time decreases with decreasing film thickness at constant field. The temperature dependence of the onset time

found in the study suggests a thermally activated process with an activation energy of 0.8 to 1.2 eV depending on the films.

The phenomenon of dc voltage-induced resistance degradation is known for undoped and acceptor-doped titanate ceramics since many decades [44, 45]. In the case of single crystals and coarse-grained ceramics, its mechanism may be regarded as relatively well understood in terms of a quantitative model based on the defect chemistry and transport properties of titanates [46]. The model is based on the mixed electronic-ionic conduction of the material. The electrodes have to be considered as (at least partially) blocking for the ionic (i. e. oxygen vacancy) transfer. Due to this blocking effect, a de-mixing with respect to the oxygen vacancy concentration between cathode and anode takes place. In the extended anodic region, the oxygen vacancy concentration decreases and, as consequence of the local defect chemistry, the p-conduction increases. In the cathodic region, the oxygen vacancies pile-up and the titanate becomes n-conducting. In total, a p-n junction is electrochemically induced. This junction is biased in forward direction leading to the observed over-all degradation of the insulation resistance. For thin films, the microscopic mechanism certainly may be distinctly different. For example, an oxygen depletion along the grain boundaries may take place as known for ZnO varistor ceramics and n-doped $BaTiO_3$ PTC thermistor ceramics. Alternatively, the cathodic interface which controls the leakage currents as shown in Section (5.2.) may become electrochemically deteriorated.

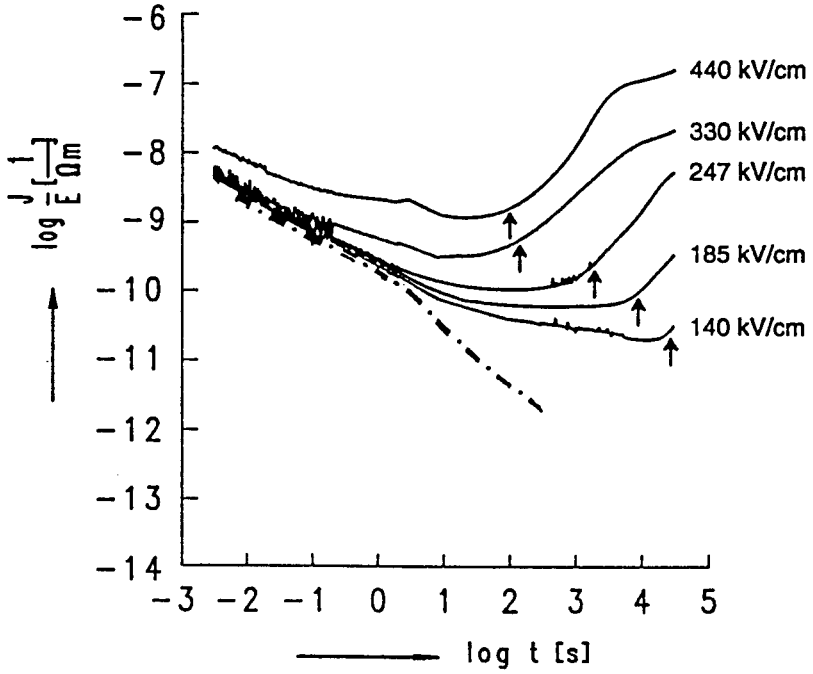


Figure 19. Field dependence of the resistance degradation for a 0.1 at Ni - doped $SrTiO_3$ film of 370 nm thickness with Pt cathodes 425 K - Plot of the current density - field ratio J / E vs. the time t. The arrows semi-quantitatively indicate the onset times of the degradation. The dash-dotted line indicates the depolarization curve for the low-field response.

7. References

1. Scott, J. F., Paz de Araujo, C. A., Melnick, B. M., McMillan, L. D. and Zuleeg, R. (1991), *J. Appl. Phys.* **70**, 382.
2. Waser, R. and Klee, M. (1992), *Integrated Ferroelectrics* **2**, 23.
3. Moazzami, R., Hu, C. and Shepherd, W. H. (1992), *IEEE Trans. Elec. Dev.* **39**, 2044.
4. Scott, J. F., Melnick, B. M., McMillan, L. D. and Paz de Araujo, C. A. (1993), *Integrated Ferroelectrics* **3**, 129.
5. Chen, X., Kingon, A. I., Mantese, L., Auciello, O. and Hsieh, K. Y. (1993), *Integrated Ferroelectrics* **3**, 259.
6. Desu, S. (1993), *Proc. of the 8th IMF, Gaithersburg, submitted to Ferroelectrics.*
7. Wouters, D. J., Willems, G., Groeseneken, G., Maes, H. E. and Brooks, K. (1994), *Proc. of the 6th ISIF, submitted to Integratede Ferroelectrics.*
8. Scott, J. F., Azuma, M., Paz de Araujo, C. A., McMillan, L. D., Scott, M. C. and Roberts, T. (1994), *Integrated Ferroelectrics* **4**, 61.
9. Hu, H. and Krupanidhi, S. B. (1994), *J. Mater. Res.* **9**,1484.
10. Lange, F. F., (1994), Proceedings of the ELECTROCERAMICS IV Conference, Augustinus Verlag, Aachen, Germany, 1223.
11. Waser, R. (1991), *J. Am. Ceram. Soc.* **74**,1934.
12. Bieger, T., Maier, J. and Waser, R. (1991), *Solid State Ionics* **53-56**, 578.
13. Tufte, O. N. and Chapman, P. W. (1967), *Phys. Rev.* **B 35**, 4360.
14. Gerthsen, P., Hardtl, K. H. and Csillaq, A. (1972), *Phys. Status Solidi* **A 13**, 127.
15. Choi, G. M., Tuller, H. L. and Goldschrnidt, D. (1986), *Phys. Rev.* **B 34**, 6972.
16. Chan, N. H., Sharma, R. K. and Smyth, D. M. (1981), *J. Am. Ceram. Soc.* **64**, 556.
17. Chan, N. H. and Smyth, D. M., (1976), *J. Electrochem. Soc.* **123**, 1584.
18. Daniels, J., Hardtl, K. H., Hennings, D., and Wernicke, R. (1976), *Philips Res. Rep.* **31**, 489.
19. Waser, R. and Smyth, D. M., (1994), *Integrated Ferroelectrics*, in Scott, J. F., (ed.) Gordon and Breach (in press).
20. Vollmann, M., and Waser, R., (1994), *J. Am. Ceram. Soc.* **77**, 235.
21. Chen, X., Kingon, A. I., Bellur, K., and Auciello, O., *Integrated Ferroelectrics* (accepted for publication).
22. Scott, J. F., Melnick, B. M., Cuchiaro, J. D., Zuleeg, R., Paz de Araujo, C. A., McMillan, L. D. and Scott, M. C. (1994), *Integrated Ferroelectrics* **4**, 85.
23. Melnick, B. M., Scott, J. F., Paz de Araujo, C. A., and McMillan, L. D., (1992), Ferroelectrics **135**, 163.
24. Kohlrausch, R. (1854), *Pogg. Ann.* **91**, 56 and 179.
25. Curie, J. (1889), *Ann. Chim. Phys.* **18** 203.
26. Schweidler, E. V. (1907), *Ann. Phys.* **24**, 711.
27. Wolters, D. R. and Zegers-van Duynhoven, A. T. A. (1988), in: Devine, R. A. B., The Physics and Technology of Amorphous SiO_2, Plenum Press, 391.
28. Dissado, L. A., and Hill, R. M., (1981), *J. Mat. Sci.* **16**,1410.
29. Funke, K. (1993), *Prog. Solid St. Chem.* **22**, 111.
30. Kliem, H. (1989), *IEEE Transactions on Electrical Insulation* **24**,185.
31. Jonscher, A. K. (1983), *Dielectric Relaxation in Solids*, Chap. 8.4, Chelsea Dielectrics Press London.

32. Hagenbeck, R., *Diploma thesis, Institut filr Werkstoffe IWE, RWTH Aachen University of Technology*, 1993.
33. Chen, X., Kingon, A. I. and Auciello, O. (1992), *Proc. 8th ISAF*, 229.
34. Moazzammi, R. (1992), *Proc. IEDM ,10.7.1-10.7.3, IEEE*, Piscataway.
35. Hagenbeck, R., unpublished results.
36. Antpohler, W. (1994), *Diploma thesis, Institut für Werkstoffe IWE, RWTH Aachen University of Technology.*
37. Klee, M., Eusemann, R., Waser, R., Brand, W. and van Hal, H., (1992), *J. Appl. Phys.* **72**,1566.
38. Antpöhler, W., Dietz, G., Klee, M. and Waser, R. (to be published).
39. Sze, S. M. (1981), *Physics of Semiconductor Devices, 2nd Edition*, John Wiley and Sons, New York.
40. Mahan, G. D., Levinson, L. M., and Philipp, H. R. (1979), *J. Appl. Phys.* **50**, 2799.
41. Blatter, G. and Greuter, F. (1986), *Phys. Rev.* **B33**, 3952; *Phys. Rev.* **B 34**, 8555.
42. Landolt-Bornstein (1959), *"Zahlenwerte und Funktionen", Springer*; H. Borchen, "Metallkunde", de Gruyter, 1963; S. M. Szw, see Ref. [39].
43. Schafer, B. (1994), *Diploma thesis, Institut für Werkstoffe IWE, RWTH Aachen University of Technology.*
44. Bunting,E.N.,Shelton,G.R., Creamer, A.S. and Jaffe, B.(1950), *J.Res. Natl. Bur. Stand.* **47**,15.
45. Lehovec, K. and Shirn, G. A., (1962), *J. Appl. Phys.* **33**, 2036.
46. R.Waser, T. Baiatu und K. H. Hardtl (1990), *J. Am. Ceram. Soc.* **73**,1645.

ANOMALOUS LOGARITHMIC DEPENDENCES IN D.C. BREAKDOWN OF FERROELECTRIC THIN FILMS

J. F. SCOTT
Faculty of Applied Science
Royal Melbourne Institute of Technology
Melbourne, Victoria 3001, Australia

ABSTRACT. Two heretofore unexplained logarithmic dependences are empirically observed for breakdown phenomena in ferroelectric thin films: 1.) The breakdown field E_B is inversely proportional to the log of the electrode area A [e.g., in pure strontium titanate Matsubara et al. report (Mat. Res. Sym. Proc. 243, 281 (1992)) E_B = 80 MV/m for A = 10^{-2} μm^2; 170 MV/m at A = 10^{-3}; and 270 MV/m at A = 10^{-4}]. 2.) The breakdown time t_B varies also logarithmically upon applied field: log t_B = B/E (here B is a constant and the validity range is for E from 70 to 120 MV/m).

2. Introduction

Neumann and Arlt have presented a theory [1] in which the breakdown time varies exactly as the reciprocal of the applied electric field in ferroelectric thick films:

$$t_B = B/E \tag{1}$$

where B is a constant independent of E but possibly dependent upon other parameters (temperature, ramp rate, electrode material, etc.):

$$B = (E_B \varepsilon_0 \varepsilon_r \tau^{-1}) \exp (E_a/kT) \tag{2}$$

where ε denotes dielectric permittivity of free space and of the medium; E_a is an activation energy; τ is an RC relaxation time determined by the capacitance of the grain boundary and the electrical resistance of the grains (hence dependent upon grain size). This relationship is empirically satisfied [2] in lead zirconate titanate (PZT) between 50 and 100 MV/m. It is based upon a model of breakdown at grain boundaries in fine-grained ceramic films. At higher fields it fails, and a slower dependence is observed in some PZT and BST (barium strontium titanate) data [3-5].

Over a limited range of field E the breakdown time t_B can be approximated either as

$$\log t_B = B/E \tag{3a}$$

or as

O. Auciello and R. Waser (eds.), Science and Technology of Electroceramic Thin Films, 249-259.
© 1995 *Kluwer Academic Publishers. Printed in the Netherlands.*

$$\log t_B = B_0 - B_1 E \qquad (3b)$$

Eqs. (3a) and (3b) have no theoretical justification in the literature, and a purpose of the present note is to suggest one. The $e^{1/E}$ form of Eq. (3) is not amenable to small-E approximations. However, it may be useful to consider the large-E expansion of t_B.

The second unexplained logarithmic dependence arises not with breakdown time t_B, but with breakdown field E_B. Both BST and pure strontium titanate qualitatively display [5, 6] a slow decrease in breakdown field with increasing electrode cross-sectional area. For BST, increasing the area by x 10 gives [5] approximately a 10% reduction in E_B. For $SrTiO_3$, decreasing the electrode area A from $10^{-2}\ \mu m^2$ to 10^{-3} to 10^{-4} increases the observed breakdown field [6] from 80 MV/m to 170 MV/m to 270 MV/m, a logarithmic dependence of approximate form

$$E_B = a/(\log A) \qquad (4a)$$

with a = (85±5) MV/m if A is measured in μm^2, or alternatively,

$$E_B = a_0 - a_1 \log A \qquad (4b)$$

This Eq. (4) is reminiscent of the connected-void breakdown model of Gerson and Marshall [7], whose failure mechanism depends simply on the odds of finding a shorting path (shorting for a given, specified field) between electrodes; in the simplest case this may appear to be linearly proportional to cross-sectional area of electrodes:

$$E_B = a'/A \qquad (5)$$

(i.e., if the area is doubled, the odds of finding such a short are exactly twice as great).

Thus the two problems encountered (breakdown time dependence upon field and breakdown field dependence upon electrode area) are analogous in that the simplest theories (Eqs. (1) and (5)) predict linear dependences, whereas the observed dependences (Eqs. (3) and (4)) are slower, involving logarithmic dependences.

3. Theoretical Approach

3.1. BREAKDOWN TIMES

The time calculated by Neumann and Arlt is actually the time after the field is applied at which irreversible voltage-driven degradation of the grain boundaries begins. It is not the point at which the film specimen is shorted. The latter is the true breakdown time and may depend in a complicated way upon the former. The difference between these two parameters will depend upon the microscopic model assumed for enhanced conduction. We assume that in the materials of interest this entails oxygen vacancy diffusion [8,9]. The rate-limiting step is further supposed to involve this diffusion. Desu and Yoo have provided a good discussion of alternative microscopic models (grain boundary models, reduction models, models emphasizing changes in potential barriers, etc.) [10].

For vacancy conduction the ionic current is related to the applied field as

$$J = s\,E \tag{6}$$

where the conductivity is

$$s = (Ce^2\nu / 6\,a\,k\,T) \exp\,[-(E_j + F/2)] \tag{7}$$

Here a is a lattice constant; e, electron charge; k, Boltzmann's constant; T, absolute temperature; ν, an attempt or "jump" frequency; C is related to entropy change; E_j is the energy to make a jump; and F is the energy to form a vacancy.

It is well known [11] that Eqs. (6) and (7) yields Ohm's Law only in the case that $aeE << kT$. For large electric fields the current instead increases exponentially with field strength E. In our case, $aeE = 3 \times 10^{-10}$ m x 1.6×10^{-19} C x 10^8 V/m = 4.8×10^{-21} J, which is slightly larger than $kT = 4 \times 10^{-21}$ J. Thus

$$J = (q / t) = D\,e^{aE} \tag{8}$$

whence

$$(q / t_B) = D\,e^{aE}, \tag{9}$$

and

$$\log t_B = B_0 - B_1 E \tag{10}$$

where

$$B_0 = \log q - \log D;\; B_1 = a \tag{11}$$

Hence Eq. (3b) is derived. Its validity is shown experimentally in Fig. 1.

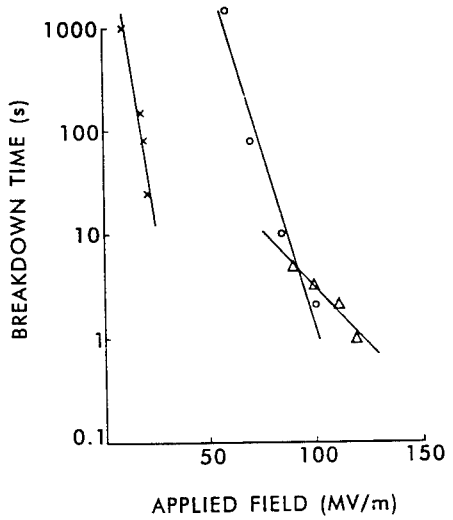


Figure 1. Breakdown time t_B versus applied electric field E for several ferroelectrics. The straight line fits confirm eq. (10). Open circles: BST (Ref. 5); crosses: PZT (Refs. 4, 49); triangles: BST (Ref. 2).

3.2. BREAKDOWN FIELDS

The assumption of Gerson and Marshall is that the void distribution is random with respect to both depth and planar location in the dielectric. This predicts a power-law dependence of breakdown field upon thickness (as $d^{-0.39}$). It does not predict a simple linear inverse proportionality between electrode area and breakdown field; the argument leading to Eq. (5) is specious. In the Gerson-Marshall theory we can assume a Gaussian distribution of distances between connected (shorting) voids that will provide breakdown at a certain field. However, unless we also know (or assume) the distribution of short-able void pathways as a function of field, this information is insufficient to solve the problem posed. Let us also assume that there is, as a function of field E, an exponential distribution of connected void pathways that will short.

$$n(E) = n_0 e^{+a(T)E/kT} \tag{12}$$

(a contains the temperature dependence but, n.b., is not simply proportional to 1/QT). The distribution of these pathways radially from the center of the electrode (assumed circular) is

$$n(r) = r^2 n(E) \tag{13}$$

We are interested in the probability of finding at least one short as a function of E and r. So, setting at breakdown ($E = E_B$):

$$1 = n_0 r^2 e^{+aE} \tag{14}$$

we find that

$$e^{+aE} = n_0^{-1} r^{-2} \tag{15}$$

or

$$E_B = a_0 - a_1 \log r^2 = a_0 - a_1 \log A \tag{16}$$

so that as the electrode area gets larger, the breakdown field E_B decreases logarithmically. QED. This is shown experimentally in Fig. 2.

4. Conclusion

The inverse logarithmic dependence of breakdown time upon applied field previously shown experimentally is found to result from oxygen vacancy conduction in the high-field regime in which Ohm's Law is replaced with an exponential conduction. This regime is valid for $aeE \geq kT$, which for ferroelectric oxides at room temperature is approximately 0.8 MV/cm.

The inverse logarithmic dependence of breakdown field upon electrode area previously found empirically is shown to result rigorously from the Gerson-Marshall theory of connected voids if the voids are assumed to have an exponential dependence of electrical failure upon applied field.

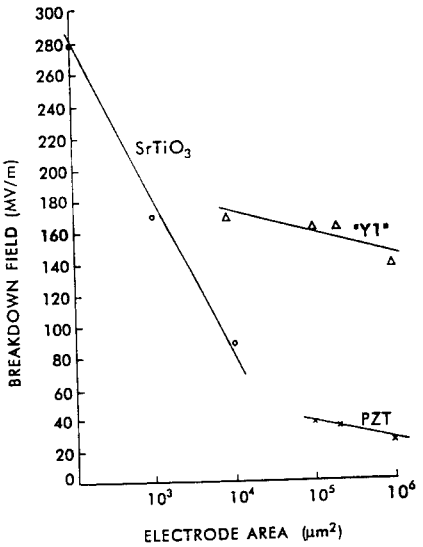


Figure 2. Breakdown field E versus electrode area A for several ferroelectrics. Straight lines confirm eq. (16). Crosses: PZT (Ref. 29); open circles: strontium titanate (Refs. 6, 49); triangles: "Y1" (Ref. 5). "Y1" designates the $SrBi_2Ta_2O_9$ family.

5. Breakdown and Leakage in Constrained Geometries

In this section we extend our earlier work on d.c. leakage current and breakdown mechanisms in thin (50-350 nm) ferroelectric films for DRAM capacitors to the case where at least one lateral dimension is comparable to film thickness. This does not become important for DRAM geometries until 1 Gb densities, but it is of more immediate concern for true ferroelectric RAMs (in which the ferroelectric film is deposited in the gate region, where its polarization alters the source-drain current). Here the submicron gate width is typically of the same magnitude as the film thickness in existing laboratory devices.

In two earlier papers [5,12], we developed in some detail the theories and experimental evidence for d.c. leakage currents I(T,E,d) in ferroelectric thin films of lead zirconate-titanate (PZT) and barium-strontium titanate (BST). Special attention was paid to space-charge-limited current phenomena. We had shown earlier [13] that in PZT the dependences of current upon field E and thickness d were in accord with standard theories [14-16] of such space charge limited currents; in particular, Eq. (17) below was satisfied over a wide range of experimental parameters:

$$I(V, d) \sim e\, m\, V^2 / d^3, \tag{17}$$

where e and m are respectively the dielectric constant and majority carrier (hole) mobility in the ferroelectrics used. This V^2/d^3 dependence is in fact a classic "signature" for space charge limited currents; but the purpose of the present paper is to investigate the situation(s) in which, due to confined lateral dimensions of the capacitor, Eq. (17) fails and must be replaced by

$$I'(V, d) \sim e\, m\, V^2 / d^2. \tag{18}$$

The initial studies of these effects due to lateral confinement were by Polke et al. [17,18] and Guerst [19].

Guerst's calculation was done only for the trap-free, perfect insulator. In that case the more exact result is

$$I'(V, d) = (2/\pi)\, e\, m\, V^2 / d^2, \tag{19}$$

compared with the three-dimensional result in the same physical approximations of

$$I(V, d) = (9 / 8)\, e\, m\, V^2 / d^3. \tag{20}$$

Note that in Eqs. (18) and (19) above I' is in units of current per unit width (A/m), whereas in Eqs. (17) and (20) I is in units of current per unit area (A/m^2).

To our knowledge, the extension of Guerst's work to incorporate both surface and bulk traps has not been published. A physical argument has been given by Rose [20] that provides some direction in the general case: He points out that for space charge injection into a long needle or platelet, most of the lines of force emanating from the cathode leave the dielectric before reaching the anode. If we denote by x the fraction of injected charge that remains untrapped and carries current,

$$I \sim x\, v\, C\, V / d, \tag{21}$$

where we assume

$$I = Q\, v / d \tag{22}$$

and

$$Q = C\, V \tag{23}$$

Then , assuming the carrier velocity

$$v = \mu E = \mu\, V / d \tag{24}$$

gives

$$I \sim \mu\ x\, C\, V^2 / d^2 \tag{25}$$

as in Eq. (19), within a factor of order unity.

Before leaving this introductory theoretical section, it is worth pointing out that other confined geometries give other qualitatively different I(V) characteristics. For example, point contact electrodes give

$$I \sim V^{3/2} \tag{26}$$

both experimentally and theoretically [21]. No one has verified such a dependence in high-dielectric oxides yet, although much of the early work in the ferroelectric thin-film field involved gold dots flash- evaporated as top electrodes. The Westinghouse group also used Hg-dot electrodes to contact their initial $BaMgF_4$ FETs, later switching to Al-dots [22]; if small in radius, these electrodes should probably satisfy Eq. (10) above.

There are few if any RAM geometries in which this situation should obtain for real commercial devices, however.

For the trap-free insulator case, Eq.26 is more precisely

$$I = 1.04\,\pi\,(\varepsilon\,\varepsilon_0\,n_0)^{1/2}\,\mu\,V^{3/2} \qquad (27)$$

which, for realistic ferroelectric (p-type BST) parameters $\varepsilon = 800$, $\mu = 0.1\ cm^2/(Vs)$, is numerically equal to

$$I = 2.15\,V^{3/2}\,n\,A \qquad (28)$$

when V is given in volts. This relationship will begin at a voltage threshold below which Ohm's law is valid, characterized by a trapping energy eV with V approximately 1 Volt. Note that the units in Eq.28 are nA, not nA/cm^2, since the electrode area is approximated as a point contact. For an applied voltage of 4V, the current I predicted in BST, assuming all n_0 holes are untrapped, is 13 nA, which is experimentally a reasonable result.

Related two-dimensional confined-geometry problems, involving both electron and holes as carriers, rather than the single-carrier problems discussed above, were addressed initially by Robinson [23] and by many authors subsequently.

5.1. EXPERIMENT

We have attempted to measure leakage currents in ferroelectric thin films as functions of voltage and thickness in confined geometry devices (prototypes of ULSI DRAMs and true FE-gate ferroelectric FETs). In this section we describe the experimental problems and existing data..

Prior to our own work [5, 12] the most detailed studies of the size dependence of electrical parameters such as spontaneous polarization and coercive field for ferroelectric perovskites were the PZT studies of Faure et al. [24]. They found, as an unexplained surprise, that the polarization increased about 30% as capacitor (or electrode) area decreased from 10^6 to $10^2\ \mu m^2$. Faure et al. [24] believe that fringing fields were not a factor in these experiments, although a priori that is the most apparent explanation. An asymmetric size effect (different for +V or -V applied voltages) was also observed and attributed to different top (gold) and bottom (platinum) electrodes; but it is not clear why this asymmetry disappeared for small electrode areas. For negative voltages the coercive voltage dropped remarkably (from 4V to 1V across 300 nm) as electrode area increased from 80 μm^2 to $1.4 \times 10^8\ \mu m^2$. This effect was tentatively attributed to pyrochlore-phase rosettes near or overlapping the electrodes. (The idea was that sufficiently small electrodes could lie entirely within or between rosettes.) Unfortunately, no leakage current data were included in the interesting results summarized in this reference. However, Bernacki [25] has provided a convincing, quantitative model relating polarization and leakage current magnitudes in PZT; in it he calculates the effect of increasing the Schottky barrier height at the metal electrode-dielectric interface and points out that Pt has an unusually large work function that plays a role in low-leakage current Pt/PZT/metal devices. The same argument has been used by the present authors [5, 12], based on the very early (1935-37) work of Von Hippel. In each case it was concluded that Pt would exhibit the lowest leakage current on M/PZT/M capacitors at a

given voltage, whereas low-work-function metals such as Al or Ag would have the worst (greatest) leakage currents.

It is important wherever possible to verify the models used to characterize current-voltage relationships via independent tests. For example, we verified the model of space-charge limited currents in PZT, first evidenced [26] by a V^2-dependence, by also demonstrating a d^{-3} thickness dependence (as was first done in semi-conductors by Zuleeg and Muller in 1964 [27]). [It is interesting to note that Zuleeg coauthored the first semi-conductor study and also the first ferroelectric insulator study, nearly 30 years apart.] Similarly, the very rapid, nearly vertical, nonlinear dependence of current upon voltage in the first 0.5 V applied in BST [5] may arise from field-induced emptying of filled traps, from impact ionization of filled traps, or other microscopic mechanisms. We have seen evidence elsewhere that for injected electron currents some anode materials break down through field emission at high voltages and begin copious injection of holes. Complicated double injection processes are possible in ferroelectric thin films and were first reported for barium titanate by Cox and Tredgold [28]. Optical studies and studies of current transients can complement the information obtained in more conventional I(V) measurements.

5.1.1. *Experiments on Small Capacitors for ULSI DRAMs*

Data on leakage current density J for PZT versus electrode area A are given by Chen et al. [29] for A = 1.0 - 40.0 x 10^5 μm^2 and for BST by Matsubara et al. [30] from A = 10^2 - 10^4 μm^2. The work by Chen et al. appears compatible with our theoretical Eq.16 in the present paper; but in neither case are the electrode areas sufficiently small to provide a test of Eq. (19).

5.1.2. *Data on Ferroelectric FETs (field-effect transistors with ferroelectric gates)*

Lampe et al. [31] have given source-drain currents for different voltages for ferroelectric FETs employing bismuth titanate or barium magnesium tetrafluoride but have not published gate currents versus voltage with which Eq.19 could be compared. Rabson's group [32] gives gate current J_G for lithium niobate FETs of 34 pA at a gate voltage of 1.0V, but only for a large area (625 μm^2) gate, for which Eq. (19) is not applicable. Kalkur et al. [33] show space-charge limited currents in pure lead titanate-film FETs at fields greater than 350 kV/m but give data for only A = 10^4 μm^2 films, which is also too large an area for the present considerations.

Despite the lack of suitable test data in the open literature, we emphasize here that existing large (256 kb) arrays of very small (2 x 2 μm) capacitors are quite suitable for the requisite leakage current measurements; however, in order to get measurably large currents, the cells would have to be measured in parallel.

5.2. APPLICATIONS

We tend to think of space-charge limited currents in ferroelectric thin films as a nuisance for DRAM or FET applications. However, it is useful to remind ourselves that there is a long history of fabricating devices based upon these phenomena. Using asymmetric electrodes with one ohmic and one blocking, researchers first made diodes with rectification ratios of 10^6 or better in the 1960s with evaporated thin films (Dressner and Shallcross [34] and Zuleeg and Muller [27]). Thin-film solid-state triode amplifiers were made from evaporated thin films by Weimer [35] and by Zuleeg [36]. Because the triode

work was with CdS films (available only as n-type) back-biased junctions could not be employed; instead, Weimer used an FET configuration with evaporated SiO as the gate insulator. Ruppel and Smith [37] achieved a transconductance of 10^{-5} mhos in a high-impedance 10^{11} ohm single-crystal device, but with very poor bandwidth (10 kHz upper limit). Wright [38] provided early discussions of the technical problems of poor frequency response due to low mobility and carrier trapping, both of which are exacerbated in perovskite oxide ferroelectric films, compared with II-VI semiconductors. Nevertheless, it might be interesting to reexamine such diode and triode devices as part of modern integrated circuits in which the ferroelectric thin films are used as passive capacitors. By utilizing asymmetric top- and bottom-electrodes in DRAM capacitors, one can intentionally convert the passive capacitors into diodes with good rectification ratios or even triodes with gain. Clever designers may find these possibilities intriguing. (Many ferroelectric RAM designs already employ dissimilar top and bottom electrode metals: McDonnell-Douglas used [39] Au (top) and Pt (bottom) on its GaAs/PZT RAM, with NiAuGe contacts; and NEC [35] uses Al/TiN (top) and Pt/Ti (bottom) on its strontium titanate DRAM. But these choices are dictated by processing temperatures at each step, not by the desire to have one electrode blocking and one ohmic.)

6. Evidence for Space-Charge Limited Currents (SCLCs) in Ferroelectric Thin Films

The discussions above are all contingent on space-charge limited currents dominating the I(V) characteristics of ferroelectric thin films. Since this has been a sometimes controversial issue, let us review the supporting data: The clearest evidence for space-charge limited currents in PZT films was first given by Scott et al. [26, 40]. Equally clear and convincing data were given by Wu and Sayer [41], who show a distinct break from a linear (ohmic) I(V) relationship to a quadratic one at approximately 1.0V. Other groups reporting SCLC in PZT include Hu and Krupanidhi [42], and Vijay et al. [43]. Published reports of Schottky I(V) behavior in PZT include that of Chen et al. [44] and a few specimens in Ref. 5. In BST Hu and Krupanidhi report SCLC, whereas Waser and Klee [45], Yamaguchi et al. [46], and Scott et al. [5] report Schottky-like behavior. In pure strontium titanate, Peng et al. [47] report SCLC, but Waser and Klee report [48] Schottky I(V).

All of the above citations involve I(V) evidence. I versus thickness d data are more scanty. Melnick et al. [13] showed a clear d^{-3} current dependence; a d^{-n} dependence with n approximately equal to 2 can be inferred from the data of Vijay et al. [43] for E greater than 20 MV/m. Peng et al. [47] observe the onset of SCLC at 10 MV/m, at which field leakage current density J varies approximately as d^{-3} (as d varies from 0.7 to 0.3 μm, J varies from 5.8 to 46 mA/cm^2; within uncertainties, this is the inverse-cube dependence predicted for space-charge-limited currents).

7. References

1. Neumann, H. and Arlt, G. (1986), *Proc. Int. Sym. Appl. Ferroelec., IEEE*, Piscataway, NJ, p. 357. See also the earlier empirical work by Minford, W. J. (1982), *IEEE Trans. CHMT* **5**, pp. 297.

2. Melnick, B.M., Araujo, C.A., McMillan, L.D., Carver, D.A. and Scott, J. F. (1991), *Ferroelectrics* **116**, 79.
3. Sudhama, C., Carrano, J.C., Parker, L.H.,, Chikarmane, V., Lee, J. C., Tasch, A. F., Miller, W., Abt, N. and Shepherd, W. H. (1990), *MRS Conf. Proc.* **200**, pp. 331.
4. Carrano, J. C., Sudhama, C., Lee, J., Tasch, A., and Miller, W. (1989), *IEDM Conf. Proc.* , pp.255.
5. Scott, J. F., Azuma, M., Paz de Araujo, C. A., McMillan, L. D., Scott, M. C., andT. Roberts, T. (1994) Integ. Ferroelectrics 4, 61.
6. Matsubara, S., Sakuma, T., Yamamichi, S., Yamaguchi, H., and Miyasaka, Y. (1990), Mat. Res. Soc. Sym. Proc. 200, 243; (1992) 243, 281.
7. Gerson, R. and Marshall, T. C. (1959), *J. Appl. Phys.* **30**, 1650.
8. Lehovec, K. and Shirn, G. A. (1962), *J. Appl. Phys.* **33**, 2036 ; Lee, H. Y. and Burton, L. C. (1986), *IEEE Trans. CHMT* **9**, pp. 469 .
9. Waser, R., Baiatu, T. and Hardtl, K.-H. (1990), *J. Am. Ceram. Soc.* **73**, 1645; **73**, 1654; **73**, 1663; Scott, J. F., Araujo, C. A., Melnick, B. M., McMillan, L. D. and Zuleeg, R. (1991), *J. Appl. Phys.* **70**, 382.
10. Desu , S. B. and Yoo, I. K. (1992), *Proc. 4th Int. Sym. Integ. Ferroelec.*, Monterey, CA, pp. 640-656; Desu, S.B. and Yoo, I.K. ((1993), *Integrated Ferroelectrics* **3**, 2.
11. Dekker, A. J. (1957), *Solid State Physics* , Prentice-Hall, Englewood Cliffs, NJ, pp.169.
12. Scott, J. F., Melnick, B. M., Paz de Araujo, C. A. and McMillan, L. D. (1993), Integrated Ferroelectric **3**, 225.
13. Melnick,B. M., Scott,J. F., Paz de Araujo, C. A. and McMillan, L. D. (1992), *Ferroelectrics* **135**, 163.
14. Lampert, M. A. and Mark, P., (1970), *Current Injection in Solids*, Academic, New York.
15. Hamann, C., Burghardt, B. and Frauenheim, T. (1988), *Electrical Conduction Mechanisms in Solids*, (VEB Publishing Co., Berlin.
16. Tredgold, R. H. (1966), *Space Charge Conduction in Solids*, Elsevier, Amsterdam.
17. Pulke, M., Stuke, J. and Vinaricky, E. (1963), *Phys. Stat. Sol.* **3**, 1885.
18. Pulke, M. (1964), *Phys. Stat. Sol.* **5**, 279.
19. Guerst, J. A. (1966), *Phys. Stat. Sol.* **15**, 107.
20. Rose, A. (1951), *RCA Rev.* **12**, 362.
21. Lampert, M. A., Many, A. and P. Mark, P. (1964), *Phys. Rev.* **135**, A1444; Ref.4, pp.176-9; see also Spangenberg, K. R. (1948), *Vacuum Tubes*, Ch.8, McGraw-Hill, New York, for a derivation of the $I \sim V^{3/2}$ law for point contacts in vacuum (he shows that the exact electrode shape, provided it is not pathological, is unimportant).
22. Sinharoy, S., Buhay, H., Francombe, M. H., Takei, W. J., Doyle, N. J., Rieger, J. H., Lampe, D. R. and Stepke, E. (1991), J. *Vac. Sci. Technol.* **A9**, 409; Sinharoy, S., Lampe, D. R., Buhay, H. and Francombe, M. H. (1992), *Integ.rated Ferroelectric* **2**, 377; Lampe, D. R., Adams, D. A., Sinharoy, S. and Buhay, H. (1993) (in press).
23. Robinson, B. (1969), *cited in Ref.14.*
24. Faure, S. P., Gaucher, P., and Ganne, J. P. (1992), *Mat. Res. Soc. Symp. Proc.* **243**, pp. 129.
25. Bernacki, S. E. (1992), *Ibid.*, **243**, 135.

26. Scott, J. F., Araujo, C. A., Melnick, B. M., McMillan, L. D. and Zuleeg, R. (1991), *J. Appl. Phys.* **70**, 382.
27. Zuleeg, R. and Muller, R. S. (1964), *Sol. St. Electron.* **7**, 575.
28. Cox, G. A. and R. H. Tredgold, R. H. (1963), *Phys. Lett.* **4**, 199.
29. Chen, J., Udayakumar, K. R., Brooks, K. G. and Cross, L. E. (1992), *Mat. Res. Soc. Symp. Proc.* **243**, 361.
30. Matsubara, S., Miyazaki, S., Sakuma, T. and Miyasaka, Y. (1993), *Mat. Res. Soc. Symp. Proc.* **243**, 281.
31. Lampe, D. R., Adams, D. A., Sinharoy, S. and Buhay, H. (1992), *Proc. 4th Int. Sym. Integ. Ferroelec.* (Monterey), pp.99, Integrated Ferroelectrics (in press)
32. Smith, E. B., Lin, H., Rost, T. A. and T. Rabson (1992), Ibid., pp. 124.
33. Kalkur, T. S. (1992), Ibid., p.336.
34. Dresner, J. and Shallcroft, F. V. (1962), *Sol. St. Electron.* **5**, 305.
35. Wiemer, P. K. (1961), *IRE Trans. Elec. Dev.* **8**, 423.
36. Zuleeg, R. (1963), *Sol. St. Electron.* **6**, 193.
37. Ruppel , W. and Smith, R. W. (1959), *RCA Rev.* **20**, 702.
38. Wright, G. T. (1962), *Sol. St. Electron.* **5**, 117; (1964) *Ibid.* **7**, 167.
39. Wu, S.-Y. and Geideman, W. A. (1992), *Integrated Ferroelectrics* **2**, 105; Sanchez, L. E., Naik, I. K., Watanabe, S. H., Leybovich, I. S., Madok, J. H. and Wu, S.-Y. (1992), *Ibid.* **2**, 231.
40. Scott, J. F., Melnick, B. M., Araujo, C. A., McMillan, L. D., and Zuleeg, R. (1992), Integ.rated Ferroelectrics **2**, 173.
41. Melnick, B. M., Scott, J. F., Paz de Araujo, C. A. and McMillan, L. D. (1992), *Ferroelectrics* **135**, 163.
42. Wu, Z. and Sayer M. (1993), *Proc. 8th Int. Symp. Appl. Ferroelec.* , IEEE, New York, pp. 244.
43. Hu, H. and Krupanidhi, S. B. (1993), *Ibid.*, pp. 440.
44. Vijay, D. F., Kwok, C. K., Pan, W., Yoo, I. K. and Desu, S. B. (1993), *Ibid.*, pp. 408.
45. Chen, X., Kingon, A. I., Gifford, K. D., Al-Shareed, H. N., Auciello, O., Hsieh, K. Y. and Rou, S. M. (1994), *Integrated Ferroelectrics* (in press).
46. Yamaguchi, H., Matsubara, S., Takemura, K. and Miyasaki, Y. (1992), *Ref.42*, pp.258.
47. Peng, C. J., Hu, H. and Krupanidhi, S. B. (1992), *Ibid.* , pp. 305.
48. Waser, R. and Klee, M. (1992), *Integrated Ferroelectrics* **2**, 23.
49. Sudhama, D., Carrano, J. C., Parker, L. H., Chikarme, V., Lee, J. C., Tasch, A. F., Miller, W., Abt, N. and Shepherd, W. H. (1990), *Mat. Res. Soc. Symp. Proc.* **200**, 331.

THE SHAPE OF THE HYSTERESIS CURVE OF FERROELECTRIC SINGLE CRYSTALS AND CERAMICS

G. ARLT
Aachen University of Technology, Templergraben 55, 52056 Aachen, Germany

ABSTRACT. A variety of intrinsic and extrinsic effects cause the shear and the shift of the hysteresis curve. The magnitude of the shear and of the shift can be calculated with the help of an electrostatic model. Any inhomogeneity of the spontaneous polarization and of the dielectric constant situated either as surface layer or as spherical or elliptical inclusion in the ferroelectric can be treated by this model.

1. Introduction

In magnetic materials the hysteresis loop has found attention by many scientists. Several books [1, 2] have been devoted to the understanding and to the theoretical simulation of general hysteresis curves. In ferroelectric research these curves have not been discussed thoroughly. Very recently some investigations were published [3,4]. It is well known that a mono-domain single crystal has a hysteresis loop with parallelogram-like shape where the switching is represented by almost vertical lines which intersect the abscissa (the field axis) at the coercive field strength. In this case the slope of the more or less straight lines through the point of remanent polarization on the ordinate is a quantity which is proportional to the dielectric constant for large signals. A multi-domain single crystal switches in a similar way, however, in various steps between the two remanent polarizations. Different domains or groups of domains in this case have more or less different coercive field strengths. In ceramics all crystallites normally are multi-domain grains. If a distribution of the coercive field strength is attributed to this ceramic a hysteresis curve with rounded edges is the result [5]. We have investigated the influence on the hysteresis loop caused by inhomogeneities of the spontaneous polarization and of the dielectric constant in the ferroelectric [6]. The inhomogeneities may be caused by a second phase or by intrinsic effects. The inhomogeneity can be ferroelectric or non-ferroelectric. The results are presented in Section 2.

O. Auciello and R. Waser (eds.), Science and Technology of Electroceramic Thin Films, 261-267.
© 1995 *Kluwer Academic Publishers. Printed in the Netherlands.*

2. Shear and Shift of the Loop and the Change of the Coercive Field by Electrostatic Fields

The measured hysteresis curve $D_2(E_2) = \varepsilon_0\varepsilon_2 E_2 + P_2(E_2)$ contains the large signal dielectric constant ε_2 given by the slope of the extremities of the curve. The curves treated here are the polarization hysteresis curves $P_2(E_2)$ resulting from the measured curves by subtracting the dielectric term. The coercive field E_{CP} of this curve is somewhat larger than that of the measured curve.

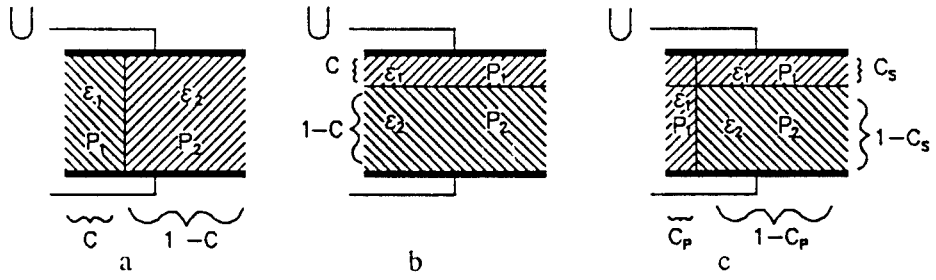


Figure 1. a, b, c are schematics of equivalent circuits for a ferroelectric layer consisting of two phases.

We apply an interface layer of a second phase or of a modified ferroelectric with polarization P_1 and dielectric constant ε_1 between the ferroelectric material with ε_2 and P_2 parameters and the metallic electrode. The electric field E_2 in the ferroelectric layer can then be calculated by using the equivalent circuit shown in Fig. 1(b) and is given by:

$$E_2 = \{1 - \frac{c\,(\varepsilon_2 - \varepsilon_1)}{B_1}\}\, E_0 + - \frac{c\,P_2}{\varepsilon_0\, B_1} + \frac{c\,P_1}{\varepsilon_0\, B_1} \qquad (1)$$

Here E_0 denotes the externally applied field, c is the volume fraction of the modified material and B_1 in the denominator represents the term

$$B_1 = \varepsilon_1 + c\,(\varepsilon_2 - \varepsilon_1) \qquad (2)$$

The three terms on the right side of Eq.(1) are abbreviated as follows

$$E_2 = K_2 E_0 + E_{2sh} + E_{2ib} \qquad (3)$$

and will be discussed with the help of Fig. 2. With and without external fields: two additional fields will exist in the ferroelectric matrix. One is a negative field E_{2sh}, which is proportional to the polarization P_2 in the ferroelectric. It is represented by the straight line in Fig. 2 (b). The other is the field E_{2ib} which is independent of the polarization of the ferroelectric material if the layer is of a non-ferroelectric polar phase. In modified materials the polarization P can be a function of P_2. For simplicity the general discussion

will concentrate on inhomogeneities being second phases. In order to counterbalance one of these two built-in fields we have to apply an external field with opposite sign.

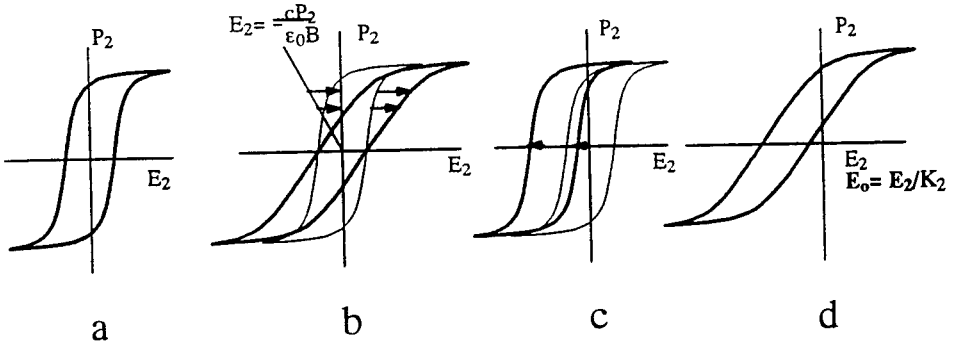


Figure 2. a) pure hysteresis curve, b) shear, c) shift and d) scaling of the field axis.

The procedure to derive the modified hysteresis curves is as follows. Fig. 2 (b) shows the shear of the polarization hysteresis curve by adding the vectors of E_2 to both sides of the loop. (Shearing the hysteresis curve is a well known method used for hysteresis curves of magnetic materials which have an air gap). The area between the ordinate and the sheared hysteresis curve represents essentially the reversible electric energy stored in the dielectric layer and in the ferroelectric..

The offset of the hysteresis curve shown in Fig. 2 (c) is the neutralization of the internal bias field E_{2ib}, caused by the polarization P_1 of the thin layer of the second phase. This shift only is present when the second layer has a polarization P_1. In most cases of defect phases this polarization is zero, therefore most second phases do not cause internal bias fields. Any kind of second phase, however can cause a shear. Finally, the E axis has to be scaled by the factor $1 / K_2$ as given by the first term in Eq. (3) and shown for shear and shift in Fig. 2 (d). One result of this scaling is an increase of the coercive field E_{CP} if $\varepsilon_1 < \varepsilon_2$.

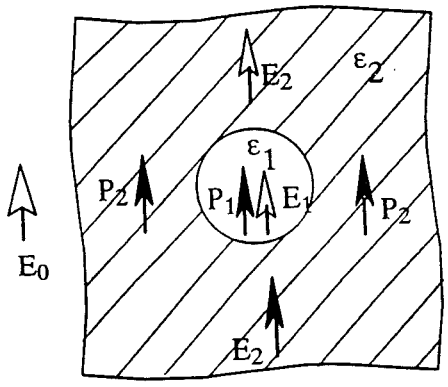


Figure 3. A spherical inclusion in the ferroelectric.

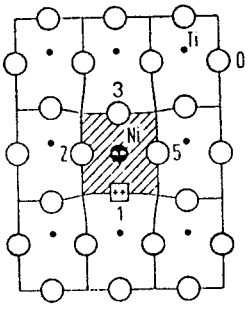


Figure 4. Non-ferroelectric inclusion.

Next, we consider a ferroelectric material having spherical inclusions of a second phase (with properties ε_1, and P_1) instead of the interface layer as shown in Fig. 3. In this case the equivalent circuit which has to be used to calculate E_2 is that shown in Fig. 1(c) with appropriate volume fractions c_s and c_p, for series and parallel placing. It is a combination of those shown in Figs. 1 (a) and 1(b) as is derived in our recent manuscript [6]. The result (its derivation is not repeated here) is the same as Eq. (1). However, the denominator B_1 (subscript: layer) (2) has to be replaced by B_{si}, which is given by:

$$B_{si} = 2\,\varepsilon_2 + \varepsilon_1 + c\,(\varepsilon_2 - \varepsilon_1) \qquad (4)$$

(subscript: spherical inclusion). Due to the first term, this denominator is larger than that of the layer. When the inclusions are ellipsoidally shaped with the depolarization factor N, or when the ferroelectric matrix is anisotropic with isotropic spherical inclusions, the denominator term becomes (subscript: ellipsoidal inclusions):

$$B_{ei} = (\,1 / N - 1)\,\varepsilon_2 + \varepsilon_1 + c\,(\varepsilon_2 - \varepsilon_1) \qquad (5)$$

N in anisotropic ferroelectrics is the depolarization factor of a fictitious ellipsoid with axes a $/\sqrt{\varepsilon_a}$ along the x and y coordinates and a $/\sqrt{\varepsilon_c}$ along the c coordinate.

The procedure to correct the hysteresis curve by shear, shift and change of scale remains the same as in the case of the layer. The effects are smaller due to the larger denominators. Eq. (1) modified by the denominators (4) or (5) are approximations which should be used for small volume fractions c only. In this case, the necessary scaling of the P_2 axis by the factor (1-c) can be neglected.

The ferroelectric materials are regarded as insulators; however, they have a final conductivity which will cause the electric fields in or around the layer or the inclusions to be screened. In this case, the effects described with Eq. (1) do not appear, disregarding which denominator is introduced. The screening by free carriers is less pronounced or even non existent when the inclusions are small. This is the case with thin film ceramics and with most kinds of point defects which are introduced e.g. by doping. In Ni-doped $BaTiO_3$, the Ni ions replace the Ti ions. For electric neutrality, lattice cells containing a Ni ion will attract and take in an oxygen vacancy as shown in Fig. 4. This lattice cell certainly is not ferroelectric, but it has a strong polarization due to the large dipole moment caused by the associated defect. This defect cell can cause an internal bias field as discussed previously [7]. Thus, lattice cells with defects represent small inclusions which are not screened by free carriers. A cubic lattice cell is approximated by a spherical inclusion, a tetragonal lattice cell by an ellipsoidal inclusion.

3. Examples

Fig. 5 shows two measured hysteresis curves of ceramic $BaTiO_3$. The slanted curve (dashed) has been measured on a fine grained sample with the grain size of about 2 μm, the other curve corresponds to a coarse grained material having a grain size of about 50 μm. Both curves represent static hysteresis curves. They were measured point by point by a special method [8] which allows every point to relax for about 20 minutes before being measured. The large signal dielectric constant of the coarse and fine grained samples

are 1650 and 2000 respectively. After subtracting the dielectric term, the $P_2(E_2)$ hysteresis curves are obtained (not shown here).

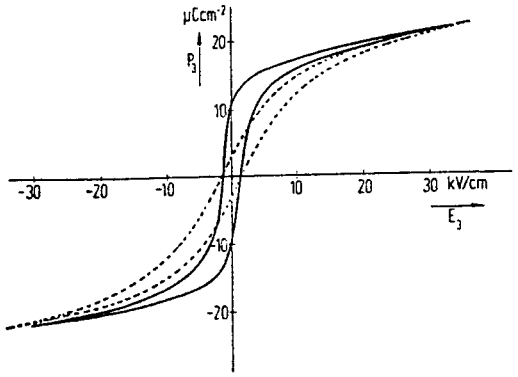


Figure 5. Hysteresis loops of coarse and fine grained barium titanate.

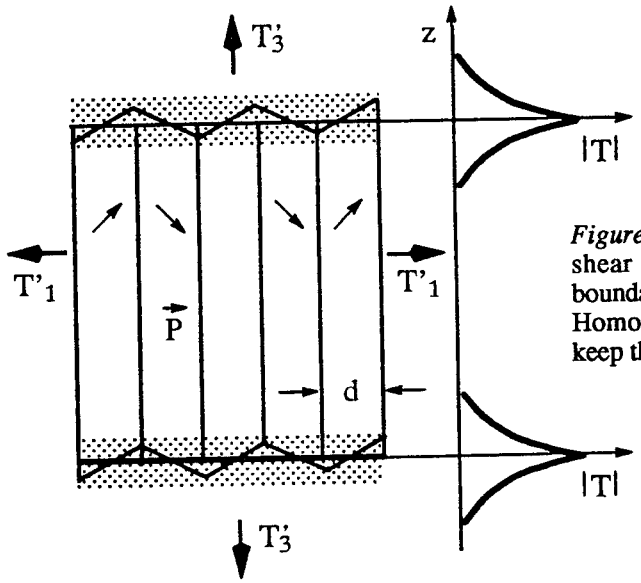


Figure 6. The twinned grain. The shear stress T exists near the boundaries only (shadowed region). Homogeneous stresses as shown keep the grain with a cubic shape.

The curve for the fine grain ferroelectric has a larger coercive field E_{CP} than the curve for the coarse grain material. The remaining final slope of the left and right side of the body of the loops are caused by shear due to second phases or modified material. It is not possible to distinguish whether the second phase or the modified material is built-in as an interface layer or as small inclusions or as thin layers enclosing the grains. From quantitative comparison with Eq. (1), using the denominator B_{si} or B_1, we find the volume fraction c of the second phase. i) In the coarse grained material, there is about 1.4% of spherical inclusions if we assume $\varepsilon_1 \approx 10$ and $\varepsilon_1 \approx 1650$. In the case of an

interface layer with $\varepsilon_1 \approx 10$, the volume fraction of this layer phase would be two decades smaller. The effective polarization P_1 of the inhomogeneities is zero because no shift was observed. ii) The fine grained ceramic exhibits a much stronger shear effect. Whether this is due to inclusions or to an interface layer, it can not be deduced from the curve. The fact that the large signal dielectric constant in the fine grained ceramic is larger than that in the coarse grained material indicates that the modifying material has a higher dielectric constant than the ferroelectric. Spherical inclusions of a second phase modify the dielectric constant to be [9,6]:

$$\varepsilon_{mix} = \varepsilon_2 \{ 1 - \frac{3\, c\, (\varepsilon_2 - \varepsilon_1)}{B_{si}} \} \qquad (6)$$

Small inclusions or interface layers having a low dielectric constant would decrease the dielectric constant of the material drastically. Thus, a second phase with low dielectric constant cannot explain both observations: the high dielectric constant and the shear. The fine grained ceramic was plain and did not contain substantial amounts of other phases. It is known from investigations of the domain configuration [10, 11] that the ferroelectric material near and in grain boundaries is exposed to very high alternating shear stresses. The stresses are of the kind to modify the ferroelectric to a state which is comparable to the state near the Curie temperature. Thus the dielectric constant in these layers is substantially higher than that inside the grains and the spontaneous polarization is reduced. The corresponding equations for intergranular layers are not yet worked out. Supposing that we have in the boundaries $\varepsilon_1 \approx 4\, \varepsilon_2$ we can derive from Eq. (6) that the volume fraction of the spherical inclusions would be about $c \approx 13$ %. The spontaneous polarization of the coarse grained ceramic is about 18 $\mu C/cm^2$ and that of the fine grained is about 17 $\mu C/cm^2$, which indicates $c \approx 6\%$. The shear field at the level $P_2 = 10\ \mu C/cm^2$ in the slanted curve is about 5.7 kV/cm. This can not be explained by spherical inclusions. Possibly, the interpretation as intergranular layers can explain the large shear. Examples for the shift of the hysteresis curve have been given in our manuscript [6] When the inclusions are concentrated near the electrode i.e. when there is a gradient of c along the z axis, shear and shift are the same as with homogeneous distribution. When, however, the concentration of the inclusions is inhomogeneous over the area of the sample a sheared hysteresis curve results which is more curved due to the broadening of the distribution of coercive fields.

4. Conclusions

An analysis of hysteresis curves: shift and shear, large signal dielectric constant and change of coercive field by defects can give useful information about the properties of the defects which are built-in. A low remanence indicates not necessarily a low degree of polarization. In a sheared curve, it indicates a good polarization which is counteracted by an electric built-in field. The high dielectric constants together with the remarkable shear in fine grained $BaTiO_3$ ceramics support a formerly given explanation [10] for this effect. All effects discussed above are of electrostatic origin, they do not include effects which are caused by the interaction of defects with the ferroelectric properties of the material.

5. References

1. Mayergoyz, I.D. (1991), *Mathematical Models of Hysteresis*, Springer Verlag, New York.
2. Krasnosel'ski, M.A. and Pokrovskii, A.V. (1989), *Systems with Hysteresis*, Springer Verlag, New York
3. Brennan, C. J. (1992), *Ferroelectrics* **132**, 245.
4. Pan, W., Sun, S. and Fuierer, P. (1993), *J. Appl. Phys.* **74**, 1256.
5. Neumann, H.and Arlt, G. (1987), *Proc. IEEE Ultrasonics Symp.*, pp. 671.
6. Robels, U., Calderwood, H.J. and Arlt, G. (1994), submitted to *J. Appl.Phys.*
7. Arlt, G. and Neumann, H. (1988), *Ferroelectrics* **87**, 109.
8. Sasko, P. (1980), *Kompensation der Polarisationsladung in der Bariumtitanat Keramik, Thesis*, RWTH Aachen , 52056 Aachen, Germany.
9. Bottger, C.J .F. (1978), *Theory of Electric Polarization*, Elsevier Scientific Publ., Amsterdam Vol. 2, pp. 176.
10. Arlt, G. (1990), *Ferroelectrics* **104**, 217.
11. Arlt, G. (1 990), *J. Mater.Sci.* **25**, 2655.

FAST TRANSIENT MEASUREMENTS ON ELECTROCERAMIC THIN FILMS

G.W. DIETZ, M. SCHUMACHER AND R. WASER
Institut für Werkstoffe der Elektrotechnik II,
Aachen University of Technology,
Germany

ABSTRACT. The principle of transient impedance measurement is described as a tool to obtain polarization currents for very short times in ferroelectric films. The method is based on applying a voltage step onto a sample and detecting the current response when the voltage is turned on and off respectively. Polarization and depolarization currents were measured for $SrTiO_3$ thin films. The results are discussed in relation to the Curie-von Schweidler law.

1. Introduction

If a voltage step is applied to electroceramic thin films, their polarization currents, $Ip(t)$, often follow the Curie - von Schweidler law, $Ip(t) \alpha t^{-\alpha}$ [1]. While these currents may be covered to a certain extent by the contributions of the dc conductivity, the depolarization currents after turning off the voltage abate with the $t^{-\alpha}$ law for many decades of time [2]. To clarify the physical reason for this behavior, it is of great importance to find the limits of the time interval within which the Curie - von Schweidler law holds.

The measurement of polarization currents to very short times requires one to apply a voltage step of variable amplitude to the sample within the shortest possible time. For the measurement of depolarization currents the sample has to be shorted within the same short time. The main problem with the current detection is to satisfy the contradictory requirements of high bandwidth and high gain of the amplifier. In order to restrict the recorded period of time not too much, it is necessary to employ at least two separate amplifiers, each optimized for its specific purpose. In dealing with high frequencies and high gain at the same time the performance of the connections between the different components is not trivial also. The whole measurement set-up has to be shielded against noise carefully and even the transmission of the amplified signals has to be carried out considering high frequency requirements.

O. Auciello and R. Waser (eds.), Science and Technology of Electroceramic Thin Films, 269-277.
© 1995 *Kluwer Academic Publishers. Printed in the Netherlands.*

2. Set-up for Fast Transient Measurements on Electroceramic Thin Films

As mentioned in the introduction, the principle of transient impedance measurements on thin films is based on switching a voltage step onto a sample and detecting the current response when the voltage is turned on and off respectively. Figure 1 shows a schematic of the measurement set-up .

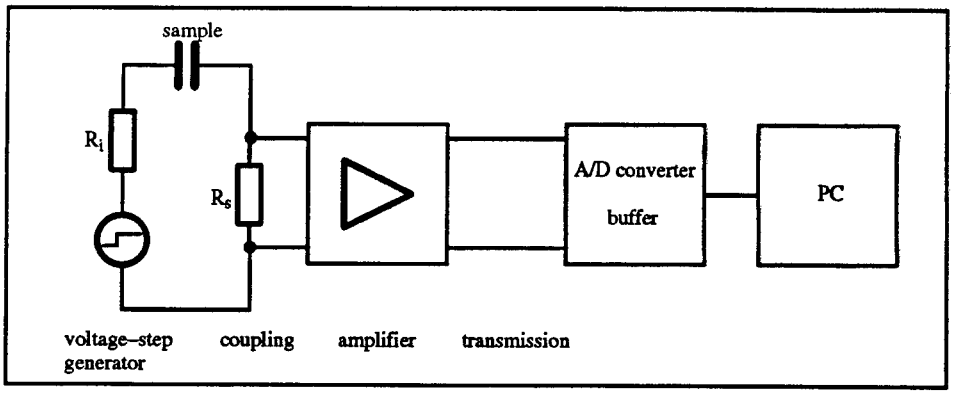


Figure 1. Principle of the measurement set-up.

2.1. AVOIDING STRAY INDUCTANCES

The coupling of voltage generator, sample and amplifier causes unavoidable stray inductances. Physical inductances cannot be avoided completely. It is only possible to minimize their influence. The sample capacitance together with these inductances form a system capable of oscillation. The rapid rise of the observed currents may easily stimulate such a resonant circuit. Resistors damp the oscillations, but for various reasons they are not allowed to have high values. The resistance of the voltage source must be small to facilitate high slew rates with capacitive loads, and the shunt must be chosen as small as possible to avoid any influence on the measured current. Therefore it remains of prime importance to minimize the inductances. Firts consider the mechanics of the set-up. To reduce the current path length the distance between the sample on the one hand and the voltage step generator and the amplifier on the other has to be very small. Our measuring head is conceived in a way that it can be put in direct contact with the sample without any cable connections outside. For more compactness, SMD technology is used. These means that the total distance between sample and input stage of the amplifier was reduced to less than 10 cm. Further measures to reduce the inductances concern the circuit layout. Again short lines are important. A second requirement is to carry the back and forth lines parallel and close together. Although the inductances can be minimized by using close parallel lines, this arrangement raises the capacitive coupling. Therefore a compromise has to be found.

2.2. VOLTAGE STEP GENERATOR

In order to achieve rise and fall times of the generated voltage step far below one microsecond, fast MOSFET switches are employed. Because of its geometrical structure, a MOSFET has an input capacitance that has to be recharged with every switching [3]. The duration of this recharging influences the attainable switching time decisively. Therefore, the control of MOSFETs requires drivers with low resistivities that are capable to emit or take high currents for short times. Because the voltage step has to be switched onto the sample but also the sample has to be shorted after the voltage is turned off, two MOSFETs in push-pull operation are used. Fig. 2 shows the principle of this so called Totem-Pole circuit.

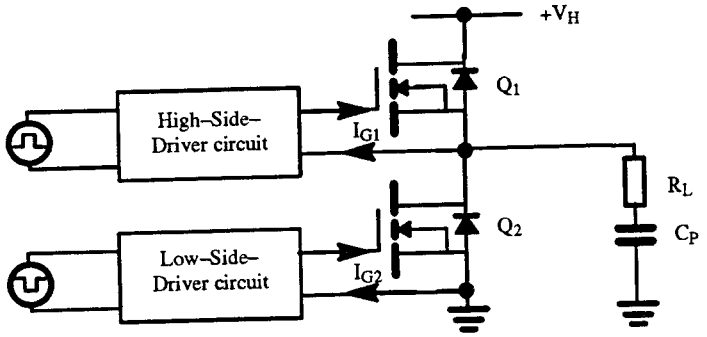


Figure 2. Totem-Pole circuit.

Each of the MOSFETs has its own driver circuit. When the MOSFET Q_1 is conducting, its source potential is nearly V_H. To ensure that the gate source voltage of Q_1 stays higher than the gate threshold voltage, the high-side-driver circuit needs its own voltage-supply that is separated galvanically from the voltage to switch, V_H. Therefore the control of this driver circuit is carried out via potential matching. Furthermore, this concept guaranties that gate currents, caused by the charging and discharging of the gate capacities, do not flow through the sample, but instead back into the drivers, as shown in Fig. 2. Drivers for two MOSFETs are offered as integrated circuits for power applications [4]. They comprise a voltage matching already and allow a simple construction of the voltage generator. With this kind of concept, i.e. a Totem-Pole circuit, driven by an integrated driver-device, that is provided by two separated voltage supplies, we are able to realize rise times of 5 V in 50 ns. Fig. 3 shows a test signal, generated with an ohmic load.

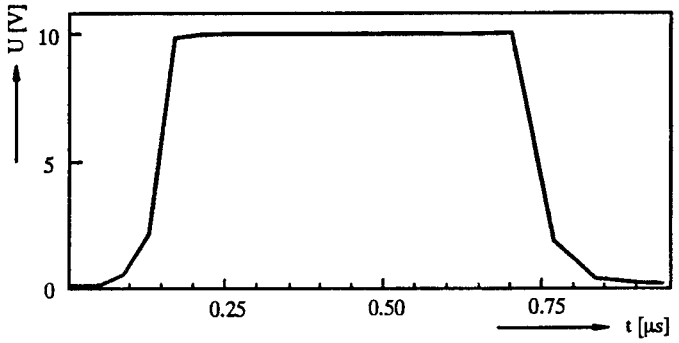
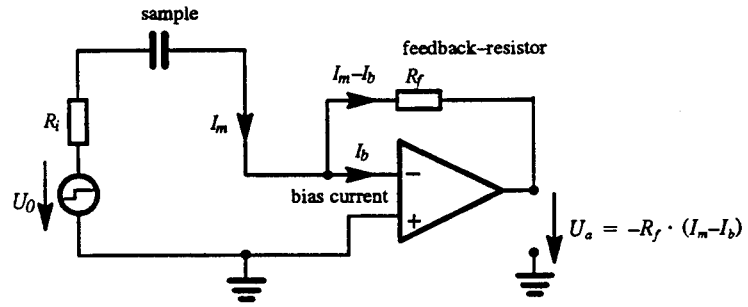


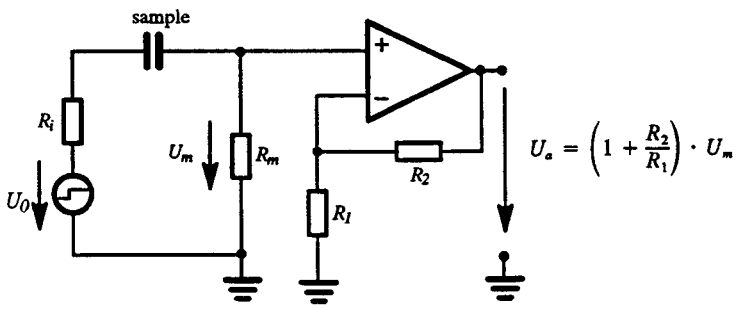
Figure 3. Voltage step with ohmic load (R = 100 Ω).

2.3. CURRENT DETECTION AT VERY SHORT TIMES

For precise current measurements, two different methods of amplifying are generally applied, namely, the feedback method with the advantage of an extremely low internal resistance (see Fig. 4 (a)) and the shunt method showed in Fig. 4 (b) [5].



a) Feedback method



b) Shunt method

Figure 4. Methods used for precise current measurements: (a) Feedback method, b) Shunt method

Measuring currents through capacitive loads at very short times, the feedback method has one crucial disadvantage. Since the currents to be measured are expected to be quite low, the loop gain of the amplifier must be high. Therefore, the current peak arising from the capacitive sample at short times causes an overload of the operational amplifier. Dimensioning the circuit for a current/voltage conversion of 0.2 V /1 µA the operational amplifier in feedback configuration would be in overload saturation for some 100 µs.

Using the shunt method, the gain is adjusted by the external resistor network consisting of R_1 and R_2. The relation between input- and output-voltage given in Fig. 4 (b) is not valid for all frequencies, however, because the differential gain A_D of a non-ideal operational amplifier decreases with increasing frequencies (Fig. 5). The total gain can be reduced with a suitable external network and the bandwidth of the closed-loop voltage gain A can be enhanced by means of reverse feedback.

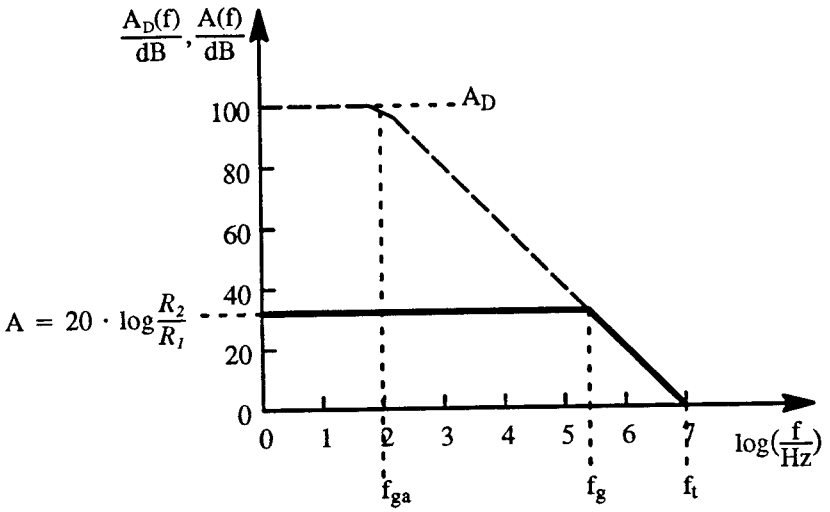


Figure 5. Enhancement of bandwidth by means of reverse feedback.

Using the shunt method, the capacitive current peak will force the operational amplifier to saturate, too. But assuming the gain as 0.2 V /1 µA again, the duration of the overload will be much less than 1 µs (dependent on the values of voltage step amplitude and sample capacitance).

To avoid the overload of the input amplifier completely, the gain had to be adapted to the maximum voltage amplitude of the operational amplifier. By doing so, the dynamical range would be limited drastically. For this reason, making use of the shunt method, a short overload time of the operational amplifier is accepted, to preserve high gain. In order to prevent further delay, the operational amplifier has to be selected for a small overload recovery time. The typical overload recovery time of the operational amplifier we use in our circuit is 1 ns, measured after 30 times overdrive. With this device, a bandwidth of 70 MHz could be realized. Figure 6 shows the overdrive behavior of the current response after applying a voltage step of 10 V on a combination of a resistor and an air capacitor,

in comparison with the calculated shape. The theoretical saturation time, t_{sat}, is about 754 ns.

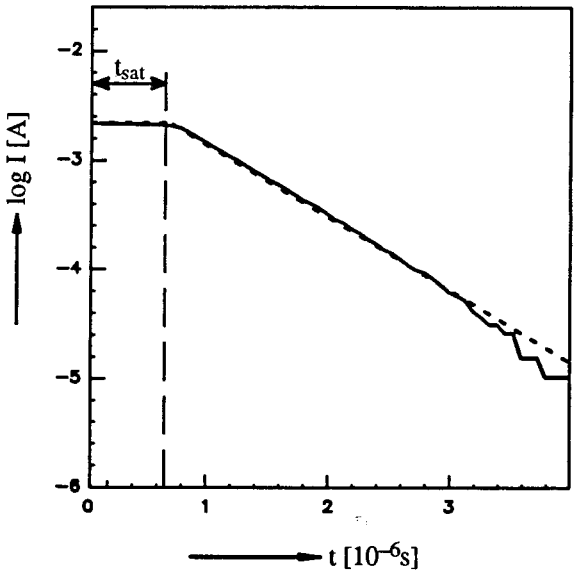


Figure 6. Current response after applying a voltage step on a resistor - air capacitor combination, with R = 1150 Ω, C = 5OO pF and V = 10 V
_____ measured curve; - - - - - - - calculated curve.

2.4. CURRENT DETECTION IN THE UPPER SHORT TIME REGIME

For times longer than 10 µs, the problem of overload is not problematic any more. But, now as before a relative high bandwidth has to be guaranteed. Contemporary low input offset currents and low noise are very important for measuring the rapidly decreasing currents with high accuracy. To satisfy the demands for this time regime, a two-stage amplifier is designed. Its operational principle is shown in Fig. 7.

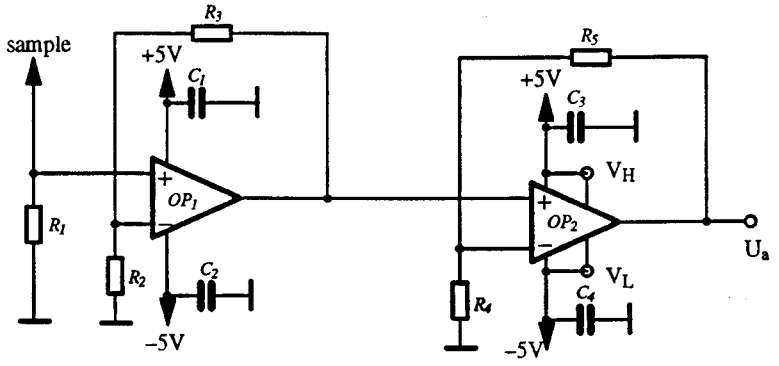


Figure 7. Principle of the two-stage amplifier for the upper short time regime. The ratio R_3/R_2 is 55.56, the ratio R_5/R_4 is 100.

The pre-amplifier is used in the shunt-mode. Its input-offset currents are smaller than 5 pA and the settling time is below 400 ns. To obtain an amplifier bandwidth of 2 MHz, the amplification of the first stage is limited to 55. The second stage is just an impedance converter and raises the total amplification of the system to 5700. With this concept, currents as small as 50 nA are measurable using far less than a millisecond measuring time. Nevertheless, the input-resistance of this current-to-voltage converter is just below 300 Ω. Figure 8 shows polarization- and depolarization-currents in the upper short time regime after applying a voltage of 10 V on a serial network of a resistor and an air capacitor. Calculated points are inserted for comparison.

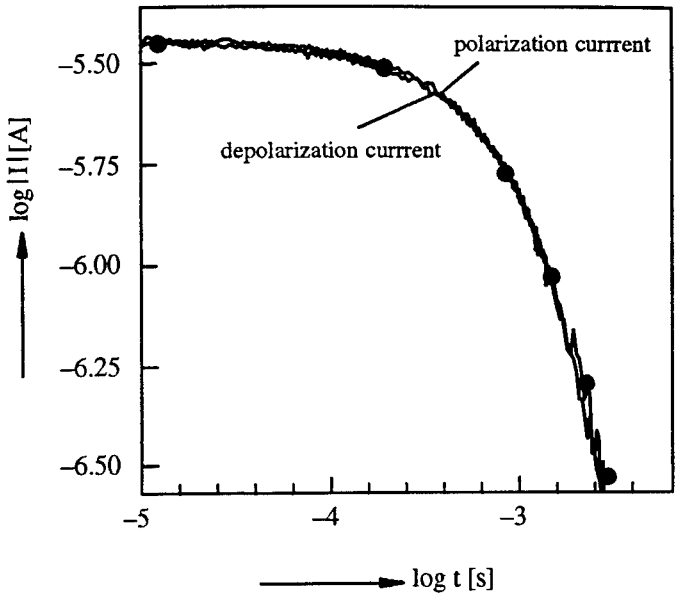


Figure 8. Log - Log plot of the polarization and depolarization currents (unsigned) vs. time after applying a voltage step of 10 V to a resistor - air capacitor combination, with R = 2.7 MΩ, C = 500 pF. The inserted points (•) are calculated values.

3. Measurements on Acceptor-Doped $SrTiO_3$ Thin Films

In this Section, some results of measurements on $SrTiO_3$ thin films are shown. In Fig. 9, the polarization and depolarization currents of a 370 nm thick sample are presented. In the middle time interval, the digitizer produced large quantization noise. Therefore, these data are removed from the diagram and replaced by a dashed line for better clarity. For times smaller than 10^{-5} s, the slope of the curves increases indicating different mechanisms for the Curie-von-Schweidler law, $I(t) \alpha\ t^{-\alpha}$. We can not explain this effect at the moment, but we found it reproducible in all our short time measurements on $SrTiO_3$ thin films. Often even three different slopes, α, can be observed in the time

period between 10^{-6} s and 10^{-3} s. An example is given in Fig. 10. The diagram shows the depolarization current of a La-doped $SrTiO_3$ thin film sample. The thickness of the specimen is 550 nm and its capacitance is 1.93 nF. A voltage step of 5 V is applied to the capacitor for 50 ms. Afterwards, the voltage is turned off and the current flow of the shortened sample is measured. Three slopes can be separated. For times shorter than 2.5 µs, the current decreases very fast. Between 2.5 µs and 30 µs, a slope of -1.5 can be observed, and for longer times finally the current falls with a slope of -0.75 which is known as a typical value from the literature [2]. Due to the temperature dependence of this process, we assume a non-ionic dielectric relaxation mechanism. Details will be reported elsewhere [6].

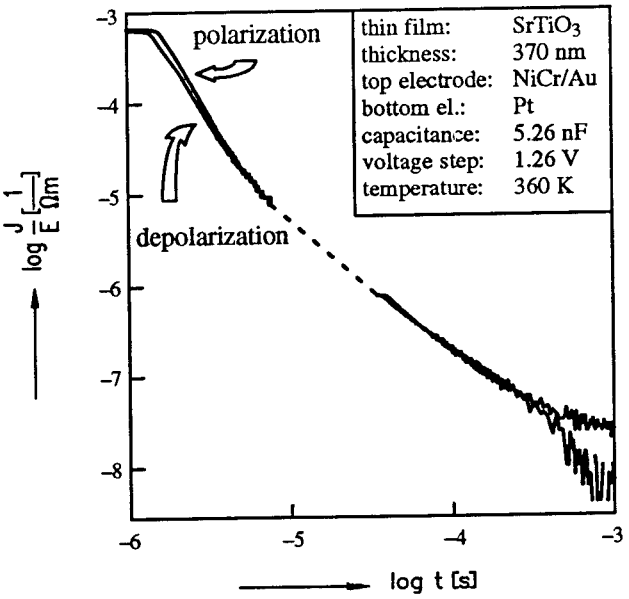


Figure 9. Unsigned current-density - field ratio \ J/E | vs. time t for the polarization and the depolarization of a $SrTiO_3$ thin film capacitor. The gap, bridged by a dashed line as a visual guide, is not covered in this specific measurement.

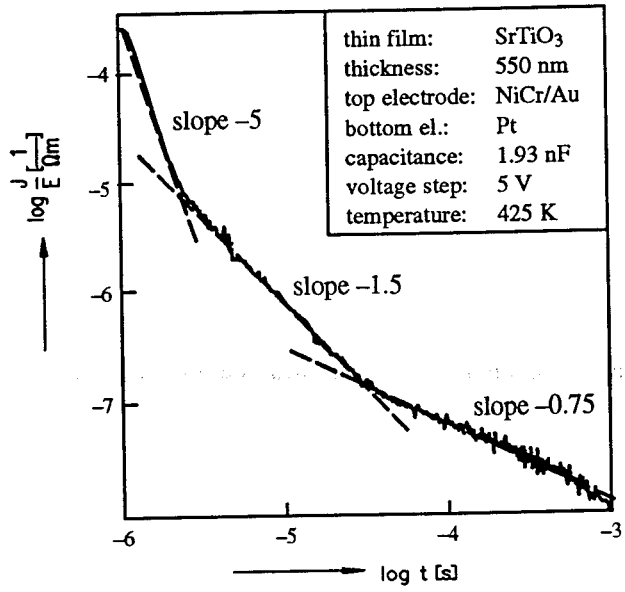


Figure 10. Depolarization current after turning off a voltage step of 5 V on a $SrTiO_3$ thin film capacitor. The dashed lines indicate the three regimes with different slopes.

Figure 11. shows a combination of a short time and a long time measurement. The graph proves that the short time measurement, realized with our self-built set-up fits well to the data recorded with a standard current amplifier (Keithley model 427) for longer times.

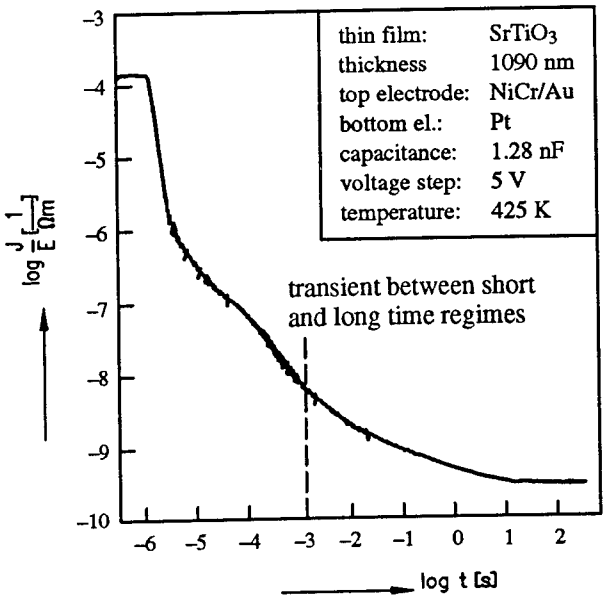


Figure 11. Polarization current applying a voltage step of 5 V on a $SrTiO_3$ thin film capacitor. The dashed line shows the crossover between the short time measurement reported in the present paper and data obtained using a current amplifier.

4. References

1. Jonscher, A.K. (1983), *Dielectric Relaxation in Solids*, Chelsea Dielectrics Press Ltd.
2. Waser, R., and Klee, M. (1992), *Integrated Ferroelectrics* **2**, 23.
3. *MOSPOWER Applications (1984)*, Siliconix Incorporated.
4. *High Voltage MOS Gate Driver IR 2110 (1990)*, International Rectifier, Data sheet PD-6.011B.
5. *Low Level Measurements* (1992), Keithley Instruments, Inc.
6. Dietz, G.W., Schumaker, R., Antpöhler, W., Waser, R. (to be published).

THE INFLUENCE OF DOPANTS ON THE LEAKAGE CURRENT IN PZT THIN-FILM FERROELECTRIC CAPACITORS

D.J. WOUTERS, G. WILLEMS, G. GROESENEKEN, H.E. MAES, K. BROOKS* AND R. KLISSURSKA*
IMEC
Kapeldreef 75, B-3001 Leuven,
Belgium
**EPFL, Lab. de Céramique*
MX-D Ecublens, Lausanne,
Switzerland

ABSTRACT. The leakage current of ferroelectric capacitors is studied in time. The ferroelectric thin film is PZT by sol-gel deposition, undoped and doped with Na or Nb. Pt is used for electrodes. Without top electrode anneal, a positive bias free carrier current is bloked by an internal diode, and ionic currents dominate. For negative bias and for samples with top electrode anneal, a free carrier current dominates. Doping influences the ionic current through change of oxygen vacancy concentration. Mechanisms limiting the free carrier conduction and a model for a capacitor is proposed.

1. Introduction

Large leakage currents flowing through a ferroelectric capacitor (FECAP) structure do adversely affect its properties. For one, they decrease the charge holding time of the high-epsilon capacitor for DRAM use. But also in ferroelectric non-volatile memories, the effect of high leakage current levels can be readily observed in a hysteresis loop measurement : (i) leakage current induces rounding of the loops, giving an over-estimation of the remanent polarization values; (ii) voltage polarity asymmetry of the leakage current results in a DC offset voltage on the integrating capacitor in the Sawyer-Tower circuit; and (iii) sometimes time dependent breakdown can be seen as a gradual opening and rounding of the loop, until complete breakdown of the FECAP has occurred.The latter effects vary depending on both the ferroelectric material treatment (e.g. annealing temperature of the sol-gel deposited film) and on the top electrode treatment (i.e. with or without anneal after the top electrode deposition). This indicates that the leakage current may be an important electrical probe of the material quality both of the ferroelectric film and of the electrode contact interfaces. Furthermore, leakage currents of FECAPs are observed to be affected by switching, indicating a possible relation between the mechanisms of fatigue and the leakage current, both of which are most probably related to the contact interfaces [1].

The DC leakage current in PZT FECAPs has been studied in detail by a number of authors [1-8]. We have recently presented a study on the time dependence of the leakage

O. Auciello and R. Waser (eds.), Science and Technology of Electroceramic Thin Films, 279-289.
© 1995 *Kluwer Academic Publishers. Printed in the Netherlands.*

current in thin-film PZT FECAP structures, focusing on the difference between samples with and without annealing after the top electrode deposition [9]. Here we will report on some new results, which are obtained using ferroelectric films with different dopants. They corroborate the former results and allow for an improved understanding.

2. Samples and Experimental Conditions

2.1. SAMPLE PREPARATION

FECAP structures have been made using Lead-Zirconate-Titanate (PZT) for the ferroelectric layer and Pt for both top and bottom electrodes. The PZT layer was deposited by sol-gel processing. Pyrolysis conditions were 350 ^{o}C, 15 sec/layer; annealing was done at 650 ^{o}C, 5min. All films have the morphotrophic boundary composition. Besides undoped films, also PZT films doped with Nb (2%) and Na (2%) have been studied.The films are 0.25-0.3 μm thick. The films are polycrystalline with a columnar grain structure, i.e. with continuous grains from bottom to top electrode. Grain sizes are of the order of 0.1-0.3 μm. Sputtered Pt was used for bottom and top electrode. On selected samples, a thermal annealing (700 ^{o}C, 5min, in O_2) has been performed after completion of the sample structure.

2.2. MEASUREMENT OF THE DC LEAKAGE CURRENT

The leakage current of the FECAP structures after the application of a DC voltage has been monitored in time from 1 to a few thousands secs, using an HP4140B pA-meter / DC voltage source. The dependence on applied voltage and sample temperature has been studied. The polarity of the applied voltage (+ or -) is referenced to the top electrode (bottom electrode grounded). A new capacitor was used for each measurement.

3. Experimental Results

3.1. MEASURED LEAKAGE CURRENTS

Fig.1. shows the time dependent leakage currents for the three different samples (undoped, Nb and Na doped), as function of bias for both positive and negative polarity (sample temperature = 150^{o}C, no annealing after the top electrode deposition). Fig.2 shows the leakage current for the Na doped sample, after an additional top electrode (TE) anneal.

3.2. GENERAL LEAKAGE CURRENT CHARACTERISTICS

The behavior of these leakage currents is in good agreement with the "general" leakage current characteristics for samples without and with annealing of the TE respectively, as reported by the authors in [9]. Indeed, we found one of the major factors influencing the way how the DC leakage current of sol-gel fabricated PZT capacitors varies with time, temperature and voltage to be the thermal treatment of the FECAP structure after deposition of the TE. So, for a general description of the behavior of the leakage current,

we have to make a distinction between samples which did and did not receive a post TE deposition anneal.

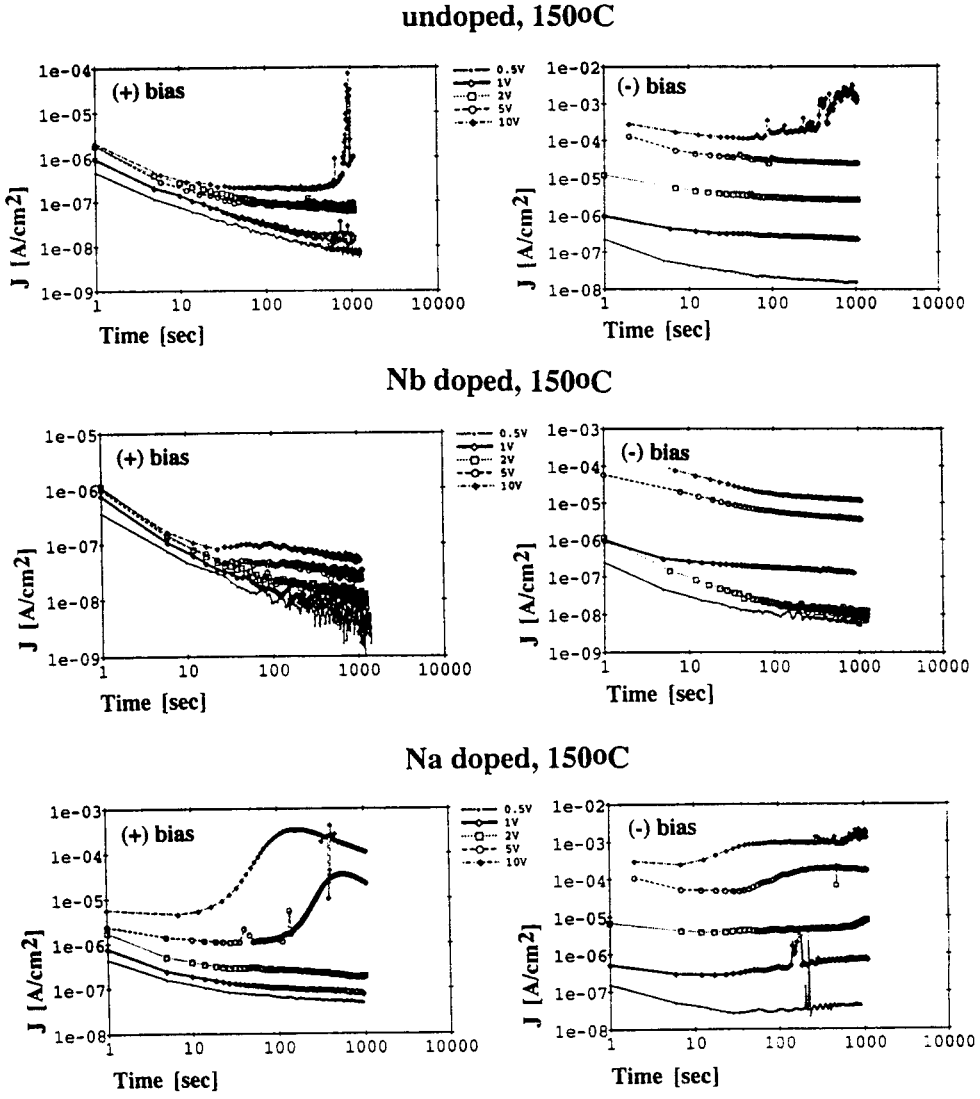


Figure 1. Leakage currents vs. time (at 150°C) for the different doped samples without anneal after the top electrode deposition, for both positive and negative voltages.

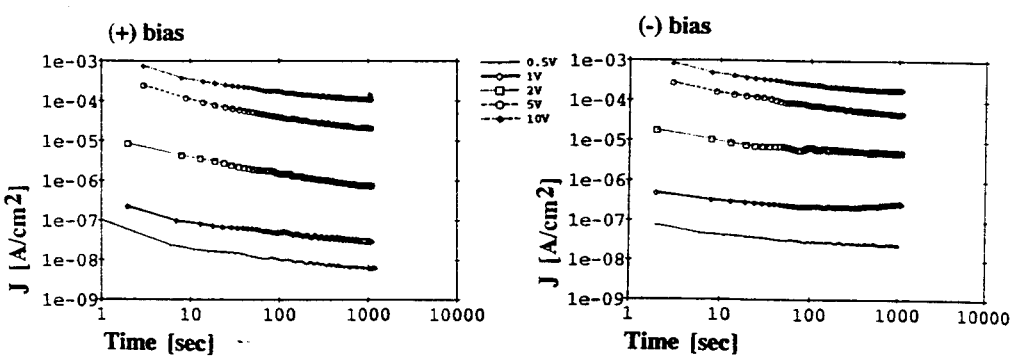


Figure 2. Leakage current vs. time (at 150°C) of Na-doped PZT sample, annealed after the top electrode deposition.

We will briefly review here these characteristics, shown schematically in Fig. 3.

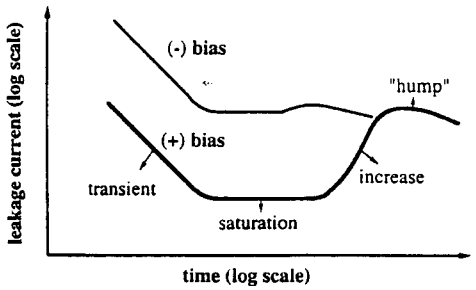


Figure 3. Leakage current characteristics vs. time (schematic) for samples without anneal after the top electrode deposition, for positive and negative voltages.

3.2.1. Without TE Anneal

The time dependent behavior can be divided into different parts or "current regimes", as has been described by a number of authors (see e.g. [4, 6, 7, 10, 12,]). We have additionally observed a large asymmetry of the currents for positive versus negative voltages. The different current regimes are most clearly distinguished for the positive voltages :

(1) a transient current regime: at short times (and/or lower sample temperatures), the current decreases in time, lineary on a logJ - logt scale. The t^{-n} time dependence of the leakage current in this transient regime can be typical for trapping, space charge redistribution in the FE film [2,11], or dielectric relaxation current [12]. So, it is not clear at all if this part of the current is a true leakage current or, on the other hand, a kind of displacement current.

(2) a saturated current regime : at longer times (and/or higher sample temperature), the current decrease saturates (on a logJ - logt scale, i.e. true saturation) to a minimum plateau value. This part of the current is generally accepted to be a real leakage current. At room temperature, even for extended times (up to a few thousand seconds) and large voltages, no saturation of the current has been observed and the current keeps decreasing in time.

(3) a current increase or resistance degradation regime : after a certain time (dependent on voltage and temperature), a steep increase of the saturated leakage current with about two orders of magnitude has been observed. We found [9] the voltage (field) and temperature dependence of this onset time to be similar to that of the resistance degradation observed in bulk ceramic titanates [10,13]. Hence, following the same model, this current increase is caused by positively charged oxygen vacancies present in the PZT film, which are mobile at higher temperatures and drift under the influence of the electric field. Near the (ion motion blocking) Pt electrode interfaces, depletion (at the anode) or accumulation (at the cathode) of oxygen vacancies results. However, changes in the oxygen vacancy concentration are locally electrically compensated by free charge carriers (electrons/holes). As a result, high hole and electron concentrations build up at the anode and at the cathode, respectively. These high carrier concentrations increase the local conductivity which may result in the higher leakage current. (Note that we form a forwardly biased p-n diode in the PZT film).

(4) after this steep current increase, a more or less gradual further decrease of the curent is observed. Between this and the former current regime, a maximum current value (current hump) occurs.

For the negative polarity, the same regions can be (though sometimes less clearly) discerned, however with following modifications :

- the current saturates at much higher current values (more or less corresponding to the current level for positive polarity after the current increase).
- only a very small current hump - if any - can be discerned (this small current increase occurs at shorter times than for the positive polarity)
- in the transient, but also in the saturated current regime, the voltage dependence is much larger than for the positive polarity.

3.2.2. With TE Anneal

In this case, the time behavior (and the high leakage current level) of the leakage current for positive voltages is similar to that for the unannealed, negative voltage case.

3.3. EFFECTS OF DOPANTS

The main effects of the different film doping which can be observed from Fig.1 are the level of the leakage curent in the saturated current regime, and the onset time of the steep current increase in the resistance degradation regime.

4. Discussion

4.1. VOLTAGE (FIELD) DEPENDENCE OF THE SATURATED PART OF THE LEAKAGE CURRENT

Figure 4 shows the field dependence of the conductivity (σ) in the saturated current regime for a Nb doped PZT FECAP, without annealing after the top electrode deposition, for positive and negative voltages (T=150 - 200 ^{o}C). For positive voltages we have Ohmic conduction, while for negative voltages, "varistor" type conductivity [2,10] is observed.

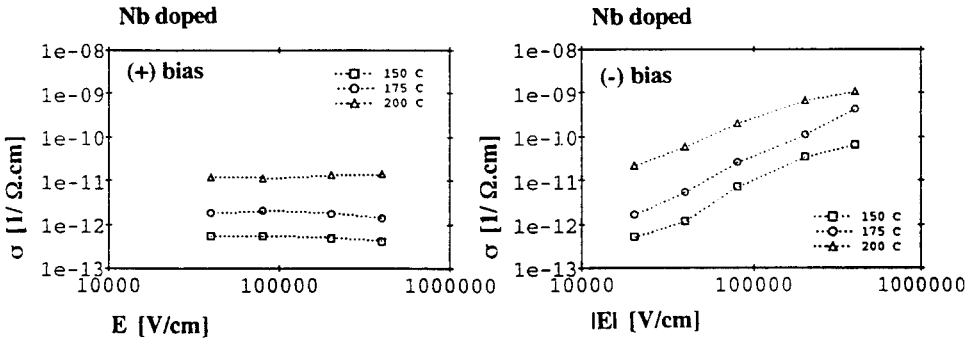


Figure 4. Conductivity vs. electric field (E = V / d) for Nb - doped FECAP, without annealing after the top electrode deposition, at different temperatures, and for (a) positive and (b) negative voltages.

Fig.5 shows the field dependent conductivity for the Na-doped sample with annealed top electrode (positive voltage). Similar varistor characteristics are obtained as for the unannealed sample under negative bias (cfr. Fig. 4).

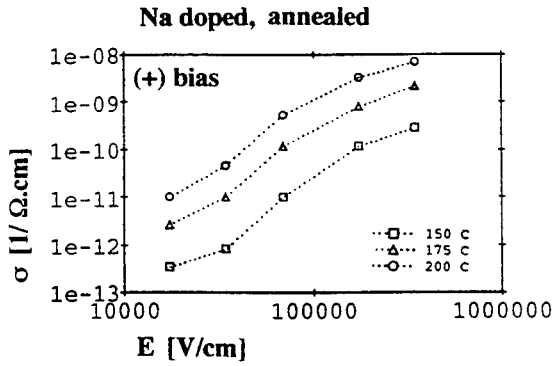


Figure 5. Conductivity vs. electric field for Na-doped FECAP, anealed after the top electrode deposition (positive bias voltage).

4.2. THE VARISTOR-TYPE CONDUCTION PROCESS

To explain the varistor type of conduction in the saturated current regime, different models such as Schottky Barrier conduction controlled by the electrode interface and Poole-Frenkel conduction out of traps in the PZT film have been proposed [2].

4.3.1. The Electrode-PZT Interface and Schottky Barrier Conduction

PZT is a wide bandgap (3.1eV) semiconductor [14]. Not intentionally doped PZT is assumed to be p-type [2]. Near the electrode interface, due to e.g. the workfunction difference between the PZT and the metal electrode (in casu Pt), band bending will occur, resulting in Ohmic or Schottky Barrier type electrical contacts, depending on the sign (and magnitude) of the workfunction difference [15], which is also dependent on the doping of the PZT film [14]. For ionic semiconductors, as $SrTiO_3$, the metal workfunction and not the interface states are indeed reported to dominate the barrier height [15].

If we assume here that, for annealed contact interfaces (as is the case for the BE in all samples and for the TE only in the samples with additional TE anneal), the p-type PZT film is depleted near the interface, the electrical contact will form a Schottky Barrier diode blocking the current from the electrode to the PZT-semiconductor. Following this model, the (annealed) FECAP structure forms two back to back diodes, and the current is limited by the reversely polarized diode at one of the interfaces, depending on the voltage polarity (which is the top interface diode for positive bias), see Fig. 6a.

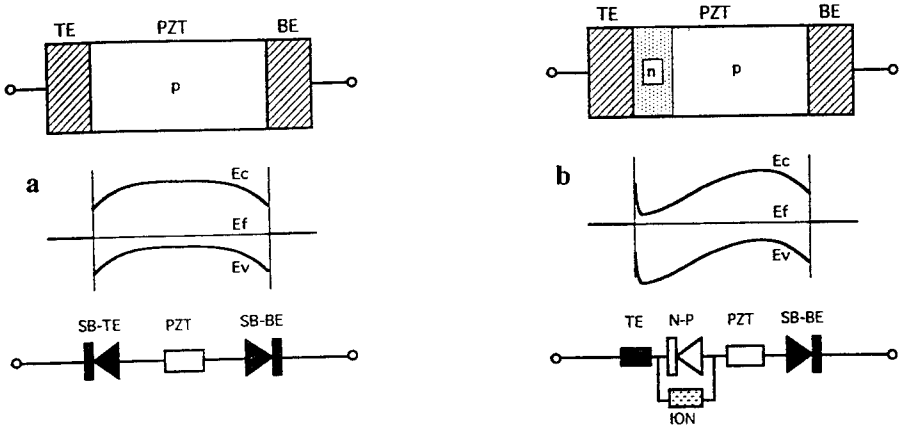


Figure 6. Equivalent electrical circuit of the FECAP (a) with and (b) without annealing after the top electrode deposition.

For the thin PZT films investigated, maximum depletion widths, however, may become larger than the total film thickness. This means that the PZT film may become fully depleted of free charge carriers (electrons or holes). Especially for the larger bias voltages over the FECAP structure, such full depletion may be expected. The occurrence of such full film depletion is important to consider as it has implications on e.g. the relation between electrical field and external voltage [15]. For a Schottky Barrier diode,

the reverse current is depending on the electrical field through the barrier lowering effect. This barrier lowering is square root depending on the electrical field in the semiconductor near the interface. For not fully depleted semiconductors, the relation between this electrical field at the interface and the appied voltage follows directly from the extension of the depletion region (the field is entirily built up from space charge in the film). This results in a square root dependence of this electrical field to the applied voltage V. Hence, the barrier lowering is related to $V^{1/4}$ (non-considering the voltage dependence of the dielectric constant [16]). However, for a fully depleted film, no additional space charge can be formed in the film by carrier depletion. Hence, electrical field variation can only be induced by charges at the electrodes. From there on, the film behaves as an ideal insulator, and the electrical field varies linearly with the applied voltage.

In a "Schottky Barrier" plot (logJ vs. $V^{1/2}$), Fig.7a, we can discern clearly two different current regimes. At high voltages (> 2V), the leakage current indeed fits an exponential dependence on $V^{1/2}$, as expected for such fully depleted or insulator type Schottky Barrier, at least at high voltages (> 2V). For the lower voltages, we found reasonable fitting both following a $V^{1/2}$ (Fig.7a) and $V^{1/4}$ dependence. Following the Schottky Barrier model, the latter may be explained by partial depletion at these lower voltages, if in combination with the (strong) voltage dependence of the static dielectric constant [16] (since the difference between fully and partial depletion only cannot explain for the observed difference in voltage dependence).

4.3.2. Other Conduction Processes

Alternatively, at least one of the current regimes (the low or high voltage current in Fig.7a) may be due to a different current conduction mechanism.

As shown in Fig.7b, also log(J /V) is linearly dependent on $V^{1/2}$ at higher voltages : this makes indeed Poole-Frenkel type conduction [15] in the PZT film (at the higher voltages) a possible candidate, too.

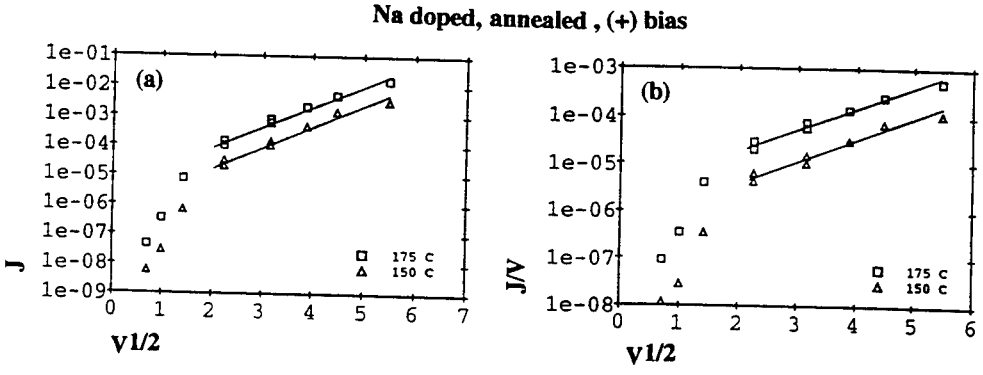


Figure 7. (a) Log(J) and (b) Log(J/V) vs. $V^{1/2}$.

It can further be remarked that the observed voltage dependence of the current in Fig.7a (logJ vs. $V^{1/2}$) is very similar to the theoretically calcultated leakage current in thin insulator films in [17], where the low voltage current is ascribed to a space charge limited current (considering free space charge out of traps in the insulator) and the high voltage region to emission-limited current (at the contact), the transition between the two conduction regimes being triggered by the onset of full depletion in the insulator film. Our experimental agreement with this theoretical model is a rather strong support of the Schottky-Barrier type of conduction at higher voltages, i.e. from the onset of full depletion, and bulk limited free space charge conduction at the lower voltages.

4.3. OHMIC CONDUCTION MECHANISM

The Ohmic conduction for the positive voltages in unannealed FECAPs maybe explained for by ionic type of conduction, i.e. motion of charged oxygen vacancies :

- in comparison with the undoped samples, the leakage current is higher for the Na doped sample and lower for the Nb doped sample. This may be expected as Na acts as an acceptor-type dopant, which is known to enhance the concentration of oxygen vacancies, while Nb acts as a donor-type dopant, reducing the number of oxygen vacancies [11].
- the temperature dependence (Fig.8) is characterized by an activation energy of 1.1eV which is typical for conduction by oxygen vacancies [12].
- Na doping, besides increasing the conductivity, also reduces the onset time for theresistance degradation regime; while Nb doping both decreases the conductivity and delays the onset of the current increase. As the onset of the current increaseregime is controlled by the oxygen vacancy motion, both effects may go together, indeed.

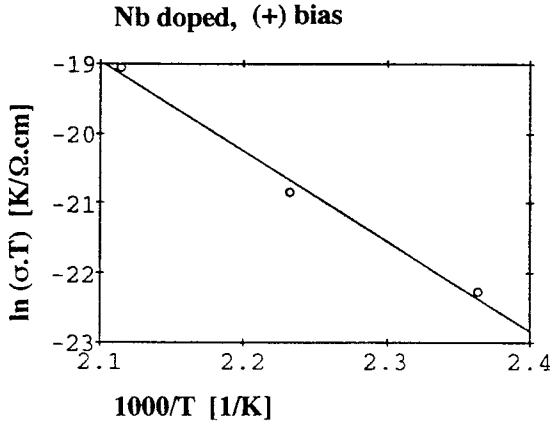


Figure 8. Temperature dependence of the conductivity , following ionic current behavior $J = V / T. \exp(-Ea/kT)$, with Ea = 1.1 eV.

4.4. POLARITY ASYMMETRY

For the unannealed contacts, we may expect a large number of crystalline defects as oxygen vacancies in the near-interface region. The resulting high positive charge may invert the PZT material in the near interface region to n-type. So we have a Pt / n-type PZT / p-type PZT structure. For the current injected from the metal side, the Pt / PZT n-type interface is conducting, but the "reverse" PZT n-p diode is blocking the free carrier transport [9].

However, this reverse n-p diode is not blocking possible oxygen vacancy motion from anode to cathode. On the contrary, the internal field of the diode will enhance such transport. So we can model the FECAP with an "ionic" resistor parallel to the reverse p-n diode (Fig. 6b). If we assume that the possible ionic conduction is much smaller than the free carrier conduction, this model can account for the observed polarity asymmetry of the leakage current : for the positive polarity (reverse diode), the ionic conduction is dominant, (but low) while for negative polarity, the diode is forwardly biased and (the relatively high) free carrier conduction occurs, however limited by another part of the FECAP structure, e.g. the back interface Schottky barrier, or by a Poole-Frenkel conduction process in the PZT film.

5. Conclusions

The study of the leakage current of PZT FECAPs with different dopants in the PZT film made an improved understanding of the different leakage current mechanisms possible. For the samples with TE anneal, leakage current is dominated by free carrier conduction processes, and possibly limited by the Schottky Barrier contacts. For the samples without TE anneal, the large polarity asymmetry of the leakage current is attributed to a p-n diode in the PZT film, caused by an inversion region induced by a high concentration of positive charge at the TE interface. For the positive polarity this diode blocks the free carrier transport, and the observed (small) leakage current is found to be of ionic nature. The doping of the film is found to primarily affect this ionic current component, through the influence of the doping on the oxygen vacancy concentration in the PZT film.

6. Acknowledgments

The authors like to thank P.Hendrickx (IMEC) for help with the measurements. Part of this work has been performed under the ESPRIT-FELMAS project.

7. References

1. Scott, J.F. et al. (1991, *J. Appl. Phys.* **70**, 382.
2. Waser, R and Klee, M. (1992), *Integrated Ferroelectrics* **2**, 23.
3. Moazammi, R. , Hu, C. and Shepherd, W.H. (1992), *IEEE Trans. on El. Dev.* **39** , 2044.
4. Yoo, I.K., Desu, S.B. and Xing, J. (1993), in *Ferroelectric Thin Films III*, Myers, E.R., Tuttle, B.A., Desu, S.B. and Larsen, P. (eds), *Mat. Res. Soc. Symp. Proc.* Vol. **310**, MRS, Pittsburgh, pp.165.

5. Chen, X., Kingon, A.I., and Auciello, O. (1992), *Proc. of the 8th ISAF Conference 1992*, IEEE, pp. 229.
6. Kingon, A.I. and Chen, X. (1994), *6th ISIF conference, Monterey (CA)*, paper 101i, to be published in *Integrated Ferroelectric.*
7. Sudhama et al. (1992), in Ferroelectric Thin Films II, Kingon, A.I., Myers, E.R., and Tuttle, B. (eds), *MRS . Soc. Symp. Proc.* Vol. **243**, MRS, Pittsburgh, pp.147.
8. Lee, J.J. and Dey, S.K. (1994), *6th ISIF Conference, Monterey (CA)*, papers 110c and 111c, to be published in *Integrated Ferroelectrics.*
9. Wouters, D.J. et al. (1994), *6th ISIF Conference, Monterey (CA)*, paper 69c, to be published in *Integrated Ferroelectrics.*
10. Waser, R. (1994), *Ferroelectric Ceramics*, Monte Verita, Birkhauser Verlag Basel, pp. 273.
11. Moulson, A.J. and Herbert, J.M. (1992), *Electroceramics*, Chapman & Hall, London.
12. Jonscher, A.K. (1983), *Dielectric Relaxation in Solids*, Chelsea Dielectrics Press, London.
13. Waser, R., Baiatu, T. and Hardtl, K.L. (1990, *J. Am. Ceram. Soc.* **73** , pp.1645.
14. Dixit, A.V., Rajopadhye, N.R. and Bhoraskar, S.V. (1986), *Journal of Material Science* **21,** 2798.
15. Sze, S.M. (1982), *Physics of semiconductor devices*, 2nd edition, John Wiley & Sons, Inc., New York.
16. The static or low frequency dielectric constant of PZT is strongly voltage dependent (cfr. slope of the hysteresis curve). It is this value of dielectric constant which determines e.g. the width of the depletion region. However, in the relation between the Schottky Barrier lowering as function of the electric field, a high frequency value has to be used (corresponding to the fast transit time of the injected electron / holes [15]). This value may differ considerably from the static value, as the ferroelectric polarization may not follow this high frequency, and as a result the voltage dependency may no longer exist, too.
17. Frank, R.I. and Simmons, J.G. (1967), *J. Appl. Phys.* **38** , 832.

PHOTO-INDUCED STORAGE AND IMPRINTING IN (Pb,La)(Zr,Ti)O_3 THIN FILMS

D. DIMOS, W. L. WARREN AND B. A. TUTTLE
Sandia National Laboratories, Albuquerque, NM, 87185-0607, USA

ABSTRACT. Pb(Zr,Ti)03 and (Pb,La)(Zr,Ti)03 thin films are shown to exhibit two distinct, but related types of photoinduced changes in their hysteresis behavior: 1) a suppression of the switchable polarization and 2) a shift of the hysteresis loop along the voltage axis. Both effects give rise to stable and reproducible hysteresis changes and, thus, either could be the basis of an optical memory. Similarly, these films can exhibit a thermally-induced suppression of the switchable polarization or a thermally-induced voltage shift. The thermally-induced voltage shift is equivalent to the imprinting effect that has been seen in ferroelectric nonvolatile memories. These phenomena can all be accounted for by trapping of charge at domain boundaries to minimize internal depolarizing fields. Whether a voltage shift or a suppression effect occurs depends on the polarization state and/or applied bias while illuminating or heating the sample. Both the photo-induced and thermally-induced hysteresis changes can be reversed by illuminating the sample under the appropriate bias. The suppression of the switchable polarization that is due to cyclic fatigue can be reversed by biasing the sample while illuminating with band-gap light, which suggests that this type of degradation is also due to simple charge trapping at domain boundaries. Finally, photo-induced experiments provide the ability to differentiate electronic and ionic contributions to hysteresis changes.

1. Introduction

Since optical memories are capable of very high information storage densities, there is great interest in developing materials for optical memory applications. Starting with the development of optically transparent (Pb,La)(Zr,Ti)O_3 (PLZT) ceramics [1], it was demonstrated that these ferroelectrics were capable of nonvolatile optical information storage [2-6]. However, these bulk ceramics required large operating voltages (> 100 V), were relatively slow (i.e., write times >> 1 s), exhibited large switching strains that could lead to cracking, and were difficult to fabricate in large areas. To overcome these difficulties, and to develop optical memories that are compatible with solid-state electronics, thin-film materials are required. Pb(Zr,Ti)O_3 (PZT) and PLZT thin films are shown to exhibit two distinct, but related types of photoinduced changes in their hysteresis behavior: 1) a suppression of the switchable polarization and 2) a shift of the hysteresis loop along the voltage axis. Both effects give rise to stable and reproducible hysteresis changes and, thus, either could be the basis of an optical memory [7-8].

O. Auciello and R. Waser (eds.), Science and Technology of Electroceramic Thin Films, 291-300.
© 1995 *Kluwer Academic Publishers. Printed in the Netherlands.*

Similar changes in the hysteresis behavior have also been reported for PZT and PLZT that have been heated to temperatures on the order of 100 °C [9, 10]. These thermally-induced changes in hysteresis behavior lead to reliability concerns for using ferroelectric thin films in nonvolatile electronic memories. The thermally-induced voltage shift is equivalent to the effect termed "imprinting", since the voltage shift reinforces one of the remanent polarization states over the opposite one. The other change in hysteresis behavior that leads to reliability problems in ferroelectric memories is due to electrical fatigue, which occurs when the ferroelectric is subjected to repeated polarization reversals.

In this paper, we describe the intrinsic photo-induced changes in the hysteresis behavior that can lead to optical storage effects in PZT and PLZT thin films. These photo-induced hysteresis changes are qualitatively accounted for by using a simple physical model based on photo-generation and subsequent trapping of charge carriers at domain boundaries. We then show that changes in the hysteresis response due to heating the films in the range of 100 °C are essentially identical to the photo-induced changes. Suppression of the switchable polarization due to cyclic fatigue can also be essentially eliminated with UV light/bias treatments, indicating that fatigue is also primarily due to electronic charge trapping. Finally, ionic migration and defect dipoles can also contribute to changes in hysteresis behavior. The technique of using UV light/bias combinations to restore shifted or suppressed hysteresis loops seems to provide the ability to differentiate the electronic and ionic contributions.

2. Experimental

PZT and PLZT films were prepared by a previously discussed sol-gel processing method [11, 12, 13]. This technique uses alkoxide and carboxylate precursors, along with methanol, acetic acid, and water as solvents. The starting solutions are fabricated by first mixing and reacting zirconium butoxide-butanol and titanium isopropoxide. Acetic acid and then methanol are added. Finally, the lead (IV) acetate and lanthanum acetate, if desired, are added and the solution is heated to ~ 85 °C to dissolve the acetates. Preparation is completed with further additions of methanol, acetic acid, and water, to yield a 0.4 M solution. The solution batches were also prepared with 5 mol % excess Pb, as compared to the stoichiometric ABO_3 formula, to compensate for Pb volatilization during the crystallization anneal.

The sol-gel derived films were deposited by spin-casting onto silicon wafer substrates. The wafers were prepared with a 500 nm oxide layer, which served as a diffusion barrier, and were electroded with a Ti (50 nm thick) adhesion layer and a Pt base electrode (~ 300 nm thick). After spin-casting each layer, the precursor film was heat-treated on a hot plate at ~ 300 °C for 5 minutes to pyrolyze organic species. The films were fired at 650 °C for 30 minutes using a 50 °C/min ramp rate to crystallize them into the perovskite phase. The resultant films were essentially single-phase perovskite and had columnar microstructures with a lateral grain size of 100-200 nm. Since individual spin-cast layers were only 90-100 nm after pyrolysis and crystallization, thicker films were obtained by depositing additional layers. A crystallization anneal was done after a maximum of four layers were deposited and pyrolyzed to avoid film cracking during the crystallization anneal.

To permit the study of photo-induced effects thin, semi-transparent Pt (10 nm) top electrodes (1-3 mm diameter) were sputter-deposited on the top of the films to establish a parallel-plate geometry. Hysteresis loops for the films were measured at room temperature

using the RT-66A ferroelectric tester (Radiant Technologies). A 200 W Oriel Hg arc lamp in combination with narrow-band interference filters was used to generate UV light for studying photo-induced effects. An Ealing optical shutter, which also triggered a voltage supply was used to control the exposure time of the arc lamp.

3. Results and Discussion

PZT and PLZT thin films exhibit two primary photo-induced changes in the hysteresis behavior. Both of these effects are reversible and reproducible and, thus, can be used to store optically-generated information [7, 8]. The first effect is a photo-induced shift of the hysteresis loop along the voltage axis, which is illustrated in Fig. 1 for a $(Pb_{0.94}La_{0.06})(Zr_{0.2}Ti_{0.8})O_3$ (PLZT 6/20/80) thin film (0.65 μm thick). The "$+V_S$" hysteresis loop was obtained by illuminating the sample with band-gap light (365 nm, 25 mW/cm^2) for 5 sec. while biasing at a saturation voltage of +10 V, where a positive voltage means that the semitransparent top electrode is biased positively with respect to the base electrode. The "$-V_S$" loop was obtained by biasing at a negative saturating voltage (-10 V) during illumination. This translation of the hysteresis response implies that illuminating the sample while biasing causes a space-charge field to be introduced in the film. The capacitor can be reversibly switched between these two stable end-point states. The difference in the polarization state at remanence for the two shifted loops can, therefore, be the basis of an optical memory.

The sign of the space-charge field is such that it reinforces the sign of the applied bias. While this result may initially appear counterinituitive, the space-charge field is of the correct sign to compensate the internal depolarizing field, as discussed below. We have verified that the sign of the space-charge field is actually driven by the sign of the polarization state by comparing the voltage shift obtained by illuminating capacitors at remanent polarization and zero bias with the shift obtained using an applied bias as in Fig. 1 [7, 8]. For films with relatively square hysteresis loops (i.e., P_r - P_s), the shift obtained at $+P_r$ ($-P_r$) is essentially the same as with $+V_s$ ($-V_s$), which demonstrated that the polarization state determines the sign of the voltage shift.

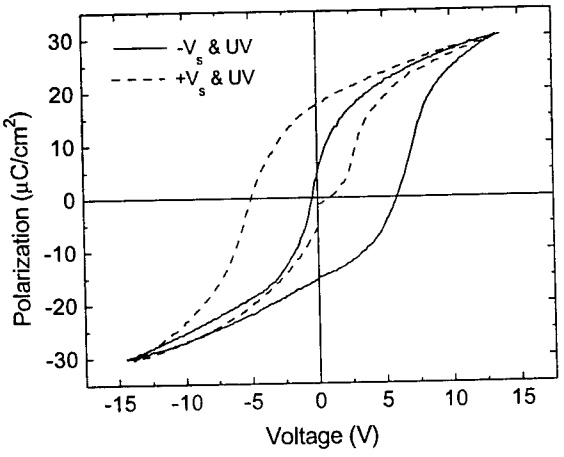


Figure 1. Hysteresis loops for a PLZT (6/20/80) film (0.65 μm thick) after optical writing with band-gap light (365 nm, I = 25 mW/cm^2) and $\pm V_S$ (± 10 V).

(0.8 μm thick). After poling the test capacitor to $-P_r$ it was illuminated with band-gap light for 10 sec. with a bias of +2.5 V, which is near the switching threshold. Under these conditions, the hysteresis response (solid line) exhibits a clear suppression of the switchable polarization at saturation and at remanence. We have previously shown that this suppression effect is optimized for biases near the switching threshold that lead to partial switching [7]. Consequently, this effect is also driven by the polarization state of the film. The initial state can be restored by illuminating while applying a saturating bias of the opposite polarity to the suppressing bias. Once again, the difference in remanent polarization between the initial or unwritten state and the suppressed or written state permits storage of optical information. In this case, it is preferable to store the information at negative remanence since the difference in remanent polarization between the unwritten and written states is greater at $-P_r$ than at $+P_r$.

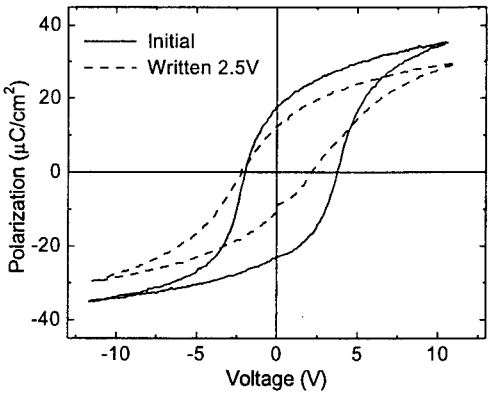


Figure 2. Hysteresis loops for a PZT 50/50 film (800 nm thick) before and after optical writing with band - gap light (365 nm, 25 mW/cm^2) at 2.5V for 5 sec.

It is worth emphasizing that the photo-induced voltage shift and the photo-induced suppression of ΔP are distinct, but related effects. The first effect is optimized by using a bias that completely switches the sample. The second effect is optimized by using a bias near the switching threshold that leads to partial switching. Qualitatively similar effects have been obtained in bulk PLZT samples, which demonstrates that these photo-induced hysteresis changes are characteristic of PZT and PLZT materials [7]. In addition, it has been recently shown that $BaTiO_3$ crystals can also exhibit a photo-induced suppression of the switchable polarization [14], which suggests that this particular effect may be common to a wide range of ferroelectric materials.

The photo-induced changes in hysteresis behavior can be qualitatively accounted for by considering the interaction between internal fields due to the polarization charge and photo-generated carriers. The situation for a fully poled thin film is schematically depicted in Fig. 3. The arrows represent the direction of the spontaneous polarization, where the arrow head is the positive end of the dipole. If the dipole charge does not terminate ideally at the electrode interfaces, an internal depolarizing field exists. Illuminating the ferroelectric with band-gap light generates electron-hole pairs which can become trapped near the interfaces to compensate the depolarizing field. This trapped charge leads to the space-charge field that causes the voltage shift. The trapped charge density can be estimated based on $Q = C\Delta V$. Typically, the observed voltage shift translates to a trapped charge density of 1-2 μC/cm^2, which means that the internally trapped charge compensates only a fairly small fraction of the remanent polarization, as expected [7].

The suppression effect can be accounted for by considering the situation that occurs during partial switching at intermediate biases. Figure 4 depicts a possible domain configuration for a film that has been partially switched to a macroscopic remanent polarization of zero. As illustrated, photo-generated charge accumulates at domain boundaries with large polarization discontinuities, which effectively "locks" the orientation of certain domains leading to a reduction in the switchable polarization. In this case, the trapped charge density can be comparable to the polarization charge so that the applied voltage is insufficient to reorient these domains. Restoration of the full hysteresis response can be accomplished by illuminating with band-gap light to generate new carriers, which recombine with the trapped charge, and a saturating bias, which subsequently reorients the previously locked domains. Since the suppression effect depends on having highly misoriented domains, the amount of suppression will depend on the possible domain configurations, which will be a function of film microstructure.

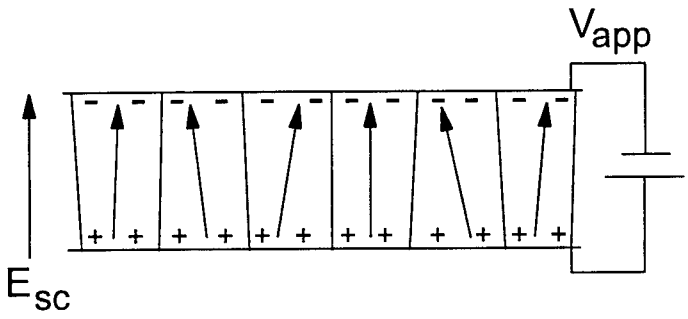


Figure 3. Schematic diagram of a columnar film that has been poled at Vs and the trapped charge that gives rise to the space-charge field.

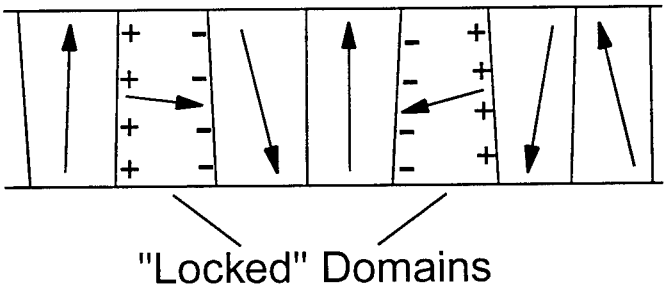


Figure 4. Schematic diagram showing a possible domain configuration for a columnar film corresponding to $P \sim 0$ and the trapped, screening charge at the domain boundaries.

A shift of the hysteresis loop along the voltage axis can also be obtained by heating the sample after poling (i.e., $-P_r$) or by using a bias that completely switches the sample

(i.e., $+V_S$). Figure 5 compares the voltage shift in a PZT 53/47 film (0.8 μm thick) obtained by illuminating with band-gap light at + 10 V for 5 sec with the shift obtained by heating at + P_r and 100 °C for 10 hours. Clearly, the photo-induced and thermally-induced voltage shifts are similar. Once again, the voltage shift implies the presence of a space-charge field due to charge trapping. In the thermally-induced case, the charge carriers are presumably due to thermal excitation of electrons and/or holes from defect levels or by injection from the electrodes rather than band-to-band excitations due to illumination. The time response for the thermal shift is slower than the photo-induced response since the concentration of thermally-generated free carriers is relatively small compared to that obtained by illumination with band-gap light. The thermally-induced voltage shift is equivalent to the imprinting effect observed in ferroelectric non-volatile memories.

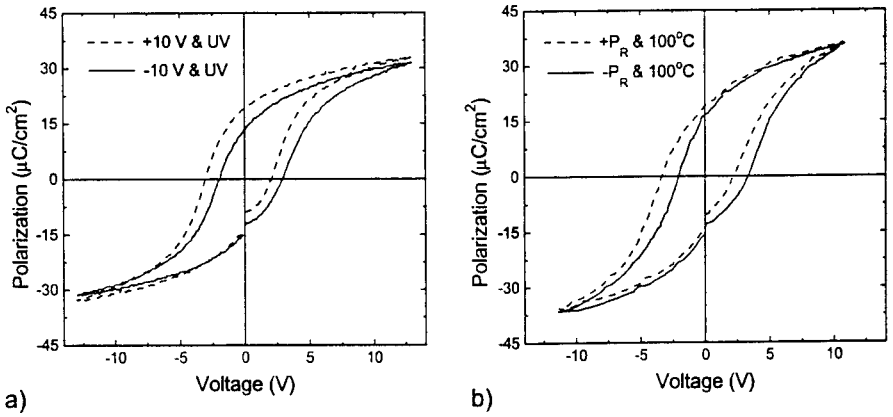


Figure 5. a) Hysteresis loops for a PZT 53/47 film (810 nm thick) illustrating a photo-induced voltage shift of ΔV = 1.04 V obtained with band-gap light and ± 10 V. b) Hysteresis loops for the same film illustrating a thermally-induced voltage shift of DV = 1.24 V obtained by heating at $+P_r$ and 100 °C for 10 hrs.

Similarly, a suppression of the switchable polarization can also be obtained by heating the sample with a bias near the switching threshold. Figures 6(a) and 6(b) compare the photo-induced and thermally-induced suppression of the switchable polarization for a PZT 40/60 film (0.5 μm) obtained by biasing at 2 V while illuminating with band-gap light or while heating the sample at 100 °C, respectively [15]. Although 2 V may not be the optimal bias for both temperatures since the coercive field is a function of temperature, both the UV/bias and thermal/bias treatments lead to qualitatively similar changes in the hysteresis response. The suppressed hysteresis loops obtained both ways can be optically restored essentially to their original state by illuminating while applying a saturating bias of the opposite polarity to the suppressing bias, as illustrated in Figs. 6(a) and 6(b). Erasure using band-gap light implies that the thermally-induced suppression of the switchable polarization can also be attributed to trapping of electrons or holes at internal domain boundaries, as previously discussed.

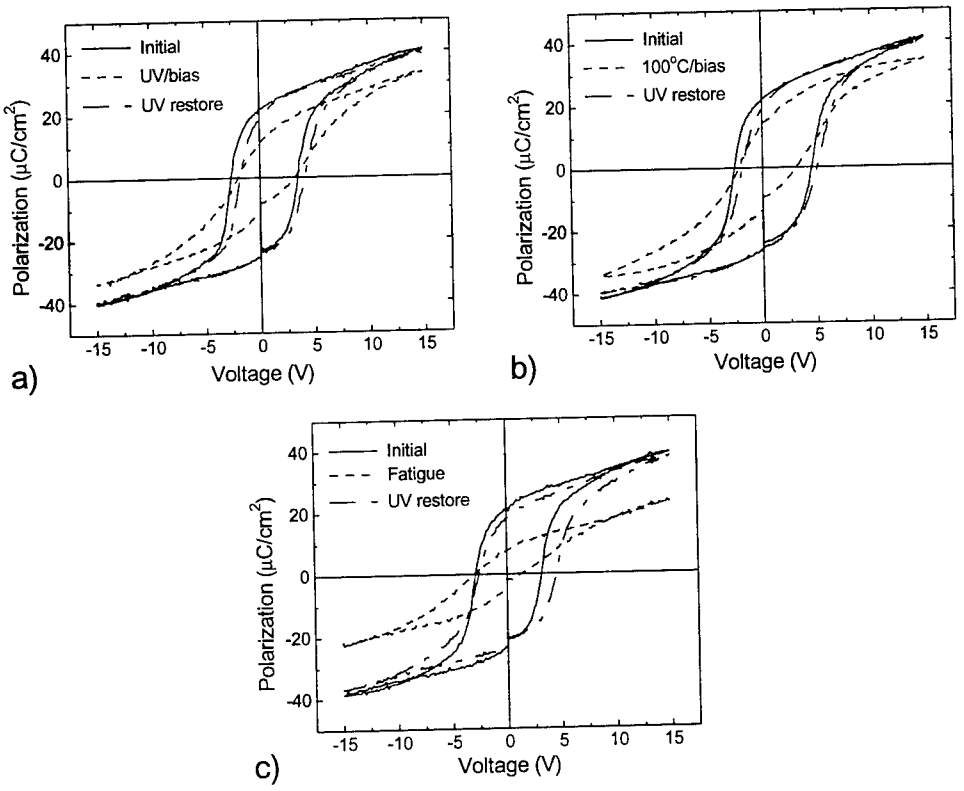


Figure 6. a) Photo-induced suppression of the switchable polarization for a PZT40/60 film (0.5 μm thick). Suppressed loop obtained by band-gap illumination with +2 V bias. UV restored loop obtained with illumination and -10 V. b) Thermally-induced suppression of the same sample with +2 V bias and heating to 100 °C. UV restoration as in (a). c) Suppression by electrical fatigue of the same sample to 3.5 x 10^8 cycles and UV restoration as in (a).

The switchable polarization in a ferroelectric film can also be significantly suppressed by repeated voltage cycling, which is known as electrical fatigue. Figure 6 (c) shows the initial hysteresis loop and the fatigued loop obtained by subjecting one of the capacitors to 3.5 x 10^8 hysteresis cycles. This figure also shows that the fatigued state can be restored almost to the initial state by illuminating with band-gap light and applying a saturating bias. In this case, restoration of the hysteresis response is essentially independent of the sign of the bias during illumination. Once again, only a minor restoration was obtained by illuminating with band-gap light without a bias or by applying a saturating bias without illumination. This result implies that electrical fatigue is also due primarily to electronic charge trapping at domain boundaries. Based on the apparent similarities between Figs. 6(a), 6(b), and 6(c), the first two suppression effects can be termed photo-induced and thermally-induced fatigue, respectively. Based on this similarity it was previously suggested that cyclic fatigue occurs primarily during the part

of the voltage cycle in which the voltage is near the switching threshold [15]. However, the mechanism for fatigue due to repeated cycling is probably more complicated than that previously described for the suppression due to partial switching with a dc bias.

While electronic charge trapping near the interfaces or at internal domain boundaries leads to changes in the hysteresis behavior, other mechanisms can contribute to hysteresis changes. Figure 7 illustrates a more complicated situation where the initial hysteresis loop of a PZT 40/60 film has been shifted towards negative voltages by annealing for 1 hr in N_2. Illuminating this sample with a bias of -15 V causes a shift in the hysteresis response back to being fairly symmetric about V=0. The photo-induced space-charge field compensates the voltage offset due to the reducing anneal. A UV / +15 V combination restores the large negative voltage shift, so that the two end-point states are a fairly symmetric hysteresis loop and one with a large offset voltage. This result implies that the nitrogen anneal creates an internal bias field that could not be eliminated by introducing photo-generated charges. Furthermore, the UV / -15 V treatment did not restore the initial hysteresis response, since the remanent polarization is also clearly suppressed. Although it should be noted that the saturated polarization is not suppressed in this case.

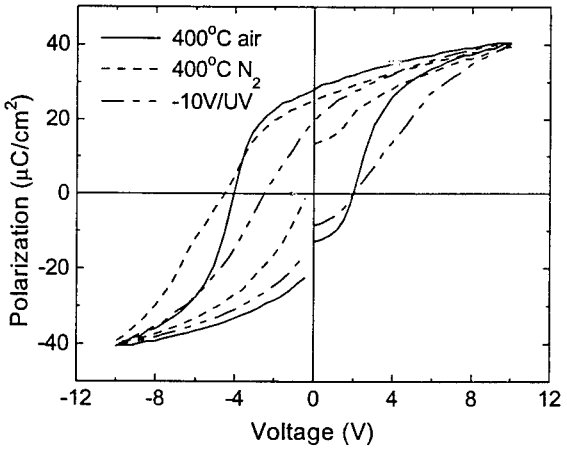


Figure 7. Hysteresis lops of PZT 40 / 60 film (0.5 μm thick) taken in the initial state, then following a 400 °C anneal in N_2 for 30 min. and then after UV restoration at - 10 V. The - 10 V restoration is the same as using + 10 V.

These results imply that the changes in the hysteresis response due to the nitrogen anneal are not simply due to electronic charge trapping, but are partly due to ionic defects. Since the reducing atmosphere anneal is critical to producing changes in the hysteresis response which cannot be optically restored, these effects are presumably due to the presence of oxygen vacancies. These vacancies can form defect dipoles with negatively charged defects, such as lead vacancies and acceptor impurities. Oriented defect dipoles can lead to internal bias fields, as observed, that would not be eliminated by introducing free carriers [16]. These results also suggest that the technique of using UV light/bias combination to restore shifted or suppressed hysteresis loops can be used to determine how much the change in hysteresis behavior is due to electronic charge trapping and how much is potentially due to ionic effects, such as the presence of defect dipoles. In fact, the

ability to separate electronic contributions to domain pinning from ionic contributions using optical restoration techniques has been demonstrated with $BaTiO_3$ single crystals [17].

4. Conclusions

PZT and PLZT thin films have been shown to exhibit two distinct, but related types of photo-induced changes in their hysteresis behavior: 1) a photo-induced suppression of the switchable polarization and 2) a photo-induced voltage shift. Both of these effects can be explained by trapping of photo-generated charge at domains boundaries to minimize internal depolarizing fields. Both effects give rise to stable and reproducible hysteresis changes and, thus, either could be used for optical storage devices, such as a read/write optical memory.

Similar changes in the hysteresis behavior are exhibited by films heated to temperatures in the range of 100 °C. The thermally-induced voltage shift is equivalent to polarization-state imprinting. The time response for the thermally-induced changes is slower than the photo-induced ones since the concentration of thermally-generated free carriers is comparatively small. The thermally-induced changes can be erased by illuminating with band-gap light and applying the appropriate bias. Consequently, the thermally-induced changes can also be attributed to trapping of electrons or holes at internal domain boundaries. Furthermore, the fatigue effect due to repeated cycling can be largely reversed by illuminating the fatigued capacitor while applying a saturation bias. This result implies that electrical fatigue is also due primarily to electronic charge trapping at domain boundaries.

However, annealing a PZT thin film in N_2 at 400 °C causes changes in the hysteresis behavior that cannot be completely erased optically. These changes are presumably due to the contribution of ionic defects, such as defect dipoles involving oxygen vacancies. The technique of using UV light/bias combinations to restore shifted or suppressed hysteresis loops appears suitable for determining how much of the change in hysteresis behavior is due to electronic charge trapping and how much is is due to ionic effects, such as the presence of oxygen vacancies and/or defect dipoles.

5. Acknowledgments

This work was performed at Sandia National Laboratories, supported by the U.S. DOE under contract #DE-AC04-94AL85000. The authors would like to thank C.H. Seager, G.E. Pike, J.A. Bullington and J.T. Evans for useful discussions. The authors also thank J. Kubas and D. Goodnow for technical assistance.

6. References

1. Haertling, G.H. and Land, C.E. (1971), *J. Am. Ceram. Soc.* **54**, 1.
2. Maldonado, J.R. and Meitzler, A.H. (1971), *Proc. IEEE* **59**, 368.
3. Land, C.E. and Smith, W.D. (1973), *Appl. Phys. Lett.* **23**, 57.

4. Maldonado, J.R., Fraser, D.B. and Meitzler, A.H. (1975), in *Advances in Image Pickup and Display*, Vol. **2**, Kazan, B. (ed.), Academic Press, New York , pp. 65.
5. Land, C.E. and Peercy, P.S. (1977), *Info. Display J.* **13**, 20.
6. Land, C.E. (1978), *Opt. Engineering* **17**, 317.
7. Dimos, D., Warren, W.L., Sinclair, M.B., Tuttle, B.A. and Schwartz, R.W. (1994), *J. Appl. Phys* .(in press).
8. Dimos, D., Warren, W.L. and Tuttle, B.A. (1993), *Mat. Res. Soc. Symp. Proc.* **310**, 87.
9. Mihara, T., Watanabe, H. and Paz de Araujo, C.A. (1993), *Jpn. J. Appl. Phys.* **32**, 4168.
10. Evans, J.T. (personal communication).
11. Schwartz, R.W., Bunker, B.C., Dimos, D., Assink, R.A., Tuttle, B.A., Tallant, D.R. and Weinstock, I.A. (1992), *Integrated Ferroelectrics* **2**, 243 .
12. Assink, R.A. and Schwartz, R.W. (1993), *Chem. of Mater.* **5**, 511.
13. Lockwood, S.J., Schwartz, R.W., Tuttle, B.A. and Thomas, E.V. (1993), *Mat. Res. Soc. Symp. Proc.* **310**, 275.
14. Warren, W.L. and Dimos, D. (1994), *Appl. Phys. Lett.* **64**.
15. Warren, W.L., Dimos, D., Tuttle, B.A., Nasby, R.D. and Pike, G.E. *Appl. Phys. Lett.*, to be published.
16. Arlt, G. and Neumann, H. (1988), *Ferroelectrics* **87**,109.
17. Warren, W.L., Dimos, D. and Smyth, D.M. *Integrated Ferroelectrics*, to be published.

DEPLETION, DEPOLARIZING EFFECTS AND SWITCHING IN FERROELECTRIC THIN FILMS

A.K. TAGANTSEV, M. LANDIVAR, E. COLLA, K. G. BROOKS AND N. SETTER
Laboratoire de Ceramique, Departement des Materiaux, Ecole Polytechnique Federale de Lausanne, Lausanne, CH 1015, Switzerland

ABSTRACT. It is demonstrated that the presence of a layer responsible for the depolarization effect in ferroelectric films can be reliably identified from the comparison of the saturation curves for P_r, P_s and E_c of the films with different thicknesses. The parameter of the hysteresis loop which is most sensitive to the presence of the passive layer is the slope of the loops at $E=E_c$. The thickness dependence of this parameter can be used for the estimation of the effective thickness of the layer.

The presence of the passive layer cannot be responsible for the thickness dependence of the coercive field observed in many experiments. Alternatively, depolarization effects can be manifested through a strong thickness dependence of the coercive field which is consistent with experimental results.

1. Introduction

Manifestations of depolarization and depletion effects in ferroelectrics have been studied for a long time[1-4]. The current intensive research of ferroelectric thin films (mainly of $PbZr_xTi_{1-x}O_3$ (PZT)) for memory applications has created a renewed interest in these effects [5-10]. In this paper, the manifestations of depolarization and depletion effects in the polarization switching of ferroelectric thin films are discussed.

It is well known that appearance of the dielectric polarization P in any sample results in the creation of depolarizing electric field which opposes the polarization. In an uncharged plate capacitor, this field is large enough to make the mono-domain ferroelectric state thermodynamically unstable. This field can be substantially compensated by the field which originates from the chargers on the capacitor plates. However, this compensation can never be complete. There are several reasons for the incomplete compensation of the depolarizing field in a ferroelectric capacitor. The simplest one is the presence of a "passive" non-switching (low-dielectric-constant) layer between the ferroelectric and the electrode. In this case, the bound charges of the ferroelectric polarization are separated from the compensating charges on the electrode. These two sets of charges form a double electric layer with a potential drop proportional

O. Auciello and R. Waser (eds.), Science and Technology of Electroceramic Thin Films, 301-314.
© 1995 *Kluwer Academic Publishers. Printed in the Netherlands.*

to the polarization. This drop is responsible for the creation of the depolarizing field even when the electrodes are at the same potential. Similar phenomena occur due to the finite thickness of the compensated charge in the electrodes [2, 7] and due to the near-by-electrode variation of the ferroelectric polarization [3]. In all of the aforementioned cases, the depolarizing field can be described by:

$$E_d = - \frac{P\ d}{\varepsilon_o\ L} \qquad (1)$$

with the effective thickness d (equivalent thickness of vacuum) being equal to d_l / ε_d, $2l_s$, or $2\xi/(1 + \delta / \xi)$ for the passive layer and the latter two cases, respectively. Here d_l, ε_d, l_s, ξ, and δ are the passive layer thickness, its relative dielectric constant, screening length of the electrode material, characteristic scale of the near-by-electrode variation of the polarization and the so called extrapolated length, respectively (Fig.1). For the case of the near-by-electrode variation of the polarization, the expression for d can be obtained using results of Ref.3 and because of some approximation made in this work it should be considered as an estimate. A more detailed discussion of the problem can be found elsewhere[11].

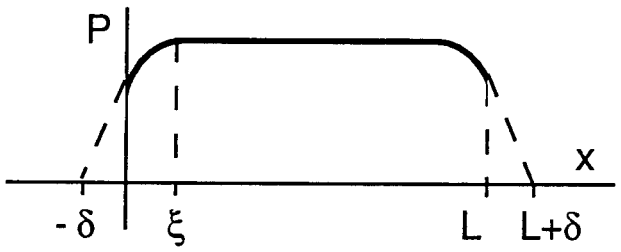


Figure 1. Schematic plot of the spatial distribution of polarization in a ferroelectric film. L, ξ and δ are the film thickness, the scale of the pre-electrode variation of the polarization and the so - called extrapolation lengths.

The depletion effect originates from the well-known fact that perovskites are often, actually, semiconductors [4] with a rather high concentration, $N_d \sim 10^{18} - 10^{20}$ cm^{-3}, of free carriers having a very low mobility. Due to the difference between the work function of the ferroelectric and the electrode material and/or due to the high concentration of surface states, a depletion layer is formed near the electrode. The experimental estimates of the thickness, W, of these layers in bulk materials, vary within the range 0.02 -0.5 μm [12-13]. In thin films, depending on the relation between the film thickness, L, and W, one deals with two cases. For L > 2W, one has two separate depletion layers near the electrodes with the gradient of the so called built-in electric field [14] in them equal to qN_d/ε (q is the electron charge and ε is the lattice dielectric constant of the ferroelectric). In this case, one finds the value of the field at the electrode to be equal to:

$$E_{bi} = \frac{q\,N_d\,W}{\varepsilon} \qquad (2)$$

If L< 2W, then the film is totally depleted and the field at the electrode is equal to:

$$E_{bi} = \frac{q N_d}{\varepsilon} \frac{L}{2} \qquad (3)$$

Let us compare the built-in and depolarizing fields for the case of totally depleted films (L < 2W) which probably holds at least for the thinnest films studied experimentally (0.1- 0.4 μm). The spatial distribution of the fields is shown in Fig. 2.

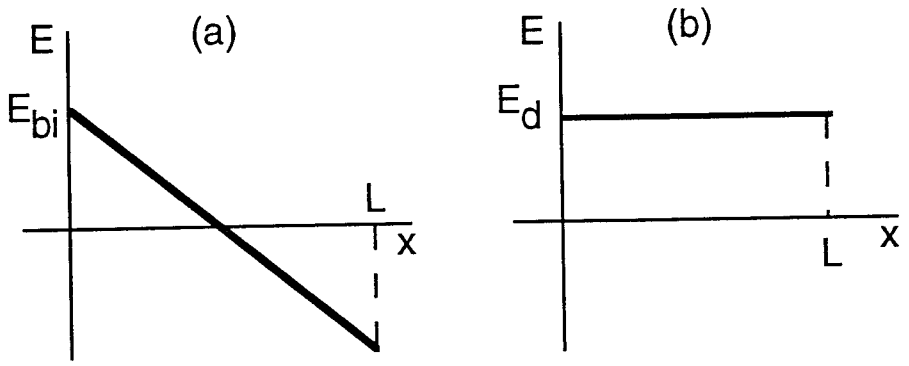


Figure 2. Spatial variation of (a) built-in and (b) depolarizing electric field.

Comparing them one should indicate:

- The built - in field is inhomogeneous, the depolarizing field is homogeneous (the details of the scale of d << L are not taken into account).
- For the case of practical interest, i.e. relatively fast switching, the built-in field can be considered as static because the time needed for substantial variations of it is of the order of the Maxwell relaxation time. The depolarizing field is dynamic, i.e. it can easily follow the variation of the polarization.
- The built - in field increases with the film thickness, whereas the depolarizing field decreases (c.f. Eqs.(1) and (3)).
- Using reasonable estimates for PZT films, of $N_d = 10^{18}$ cm^{-3}, ε= 200 Eo, L = 300 nm, P = 40 μC/cm^2, d = 0.1 nm (the doubled Thomas - Fermi length has been taken for d) one finds E_{bi} ~ 100 kV / cm, and E_d ~ 130kV / cm. These values are not high enough to make the monodomain state thermodynamically unstable but they are comparable to those of the coercive fields in PZT films. Thus one can expect a considerable influence of the depolarizing and built - in fields on the ferroelectric switching in thin films.

Let us compare their influence on switching. Not aiming to cover all of the problem, we are going to discuss some important issues of the fast switching. A discussion of the relatively slow processes can be found elsewhere, e.g. slow switching [6], retention [9].

2. Depolarizing Effect: Role of Non-Linearity and Memory

The effect of the depolarizing field on switching can be described by considering the film as a sandwich consisting of a "ferroelectric" in series with a "dielectric layer". So, the problem can be studied by using a well-known system of equations (see e.g., Ref. 5) which relate the measured polarization P and the average electric field E in the sandwich structure and the polarization P_f and the field E_f in the ferroelectric, namely:

$$\varepsilon_o E_f = \sigma - P_f \tag{4}$$

$$E (d_L + L) = \sigma d_L/\varepsilon_o\varepsilon_d + LE_f \tag{5}$$

$$P = \sigma - \varepsilon_o E \tag{6}$$

where σ is the surface charge density on the electrodes. These equations actually describe an electrical circuit containing a non-linear element with memory, because P_f is a non-linear function of E_f and this function itself is different for different maximal values of E_f on the hysteresis loop, E_{of}. Let us show that this non-linearity and memory are of key importance for a correct description of the system. To do this we consider a special case of the problem: the dependence of the coercive field of the sandwich, E_c, on $d_L/L\varepsilon_d$ for the case of a relatively thin dielectric layer, $d_L / L<<1$. Three different approximations are considered: (i) neglecting the non-linearity and memory, (ii) taking into account only non-linearity, and (iii) taking into account both non-linearity and memory. A comparison of the three results obtained reveals the role of the non-linearity and memory. This problem can be analyzed directly from the equation for the sum of the potential drops across the ferroelectric and dielectric,

$$E (d_L + L) = d_L E_L + LE_f \tag{7}$$

and the requirement that the displacement D be continuous.

$$D = D_f = D_L = \varepsilon_o \varepsilon_d E_L \tag{8}$$

where E_L, D_L, and D_f are the electric field and displacement in the dielectric and the displacement in the ferroelectric, respectively. For $d_L/L<< 1$, one readily obtains from these equations,

$$E = E_f \left(1 + \frac{d_L}{L\,\varepsilon_d}\,\frac{D_f}{E_f}\right) \tag{9}$$

2.1. NO NON-LINEARITY AND NO MEMORY

Let us use Eq.(9) to calculate the coercive field of the sandwich neglecting non-linearity and memory as it has been actually done by Merz [1] and Sakashita [15]. In this case, one substitutes the dielectric constant of the ferroelectric ε_f for the ratio D_f/E_f in Eq.(9) to find for the moment of the coercive field:

$$E_c = E_{cb}\,(1 + \frac{d_L}{L}\,\frac{\varepsilon_f}{\varepsilon_d}) \qquad (10)$$

where E_c and E_{cb} are the coercive field of the sandwich and the bulk value of the coercive field for the ferroelectric itself. This equation implies that a relatively thin dielectric layer (d_L /L<< 1) can substantially influence the coercive field of the structure because, in the case where the ratio ε_f / ε_d is large enough, the thickness dependent term in Eq.(10) can be important even for small d_L / L. A sketch of the obtained dependence is shown in Fig. 3 (a).

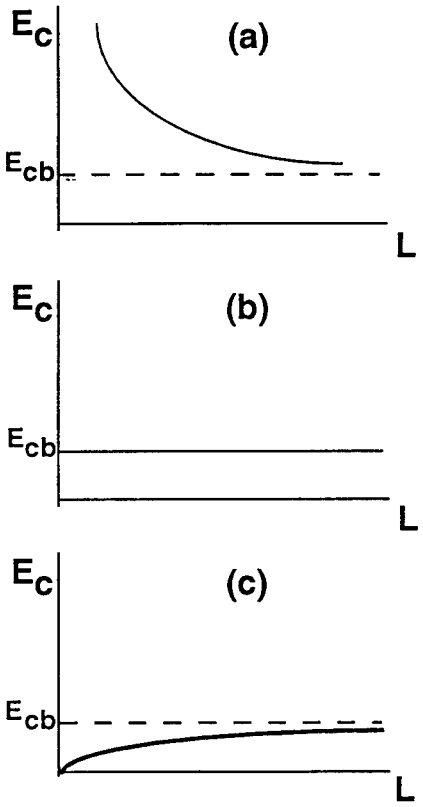


Figure 3. Schematic for the thickness (L) dependence of the coercive field of a sandwich "ferroelectric - dielectric" for a fixed thickness of the dielectric d << L: (a) -result of linear approximation, (b) -result of memory free approximation, (c) -exact result. E_{cb} stands for the bulk value of the coercive field taken at the same field.

2.2. NON-LINEARITY BUT NO MEMORY

To take into account non-linearity one should pay attention to the fact that the ratio $D_f/\varepsilon_o E_f$ is different for the different points of the hysteresis loop and calculate it at the point of interest, namely at E_c. Let as define E_c as the field at which D = 0 (using the criterion of P = 0 yields only an insignificant correction to the result). Then, due to Eq.(8), D= 0 implies D_f= 0 and D_f/E_f =0 at the coercive field point. And finally using Eq.(9) one finds:

$$E_c = E_{cb}. \qquad (11)$$

This equation implies that, for $d_L / L << 1$, the coercive field of the sandwich is independent of d_L/L, i.e. it is, for example, independent of the film thickness for a constant thickness of the thin dielectric layer. A sketch of the obtained dependence is shown in Fig. 3 (b). This result is applicable if the condition that the memory effect contribution is negligible holds. For the considered problem, that implies that the coercive field of the ferroelectric should be independent of the maximal electric field on the loop, i.e. to be in the saturated regime. It is clear that this condition cannot be met for all $d_L / L << 1$ even if the coercive field of the ferroelectric itself perfectly saturates for high fields (let us call the field at which it saturates for the ferroelectric itself E_s). Indeed, one reaches saturation in the ferroelectric part of the sandwich only if the maximal field on the loop seen by ferroelectric, E_{of}, is bigger than E_s, i.e. when the sum of maximal applied field E_o and the depolarizing one given by Eq.(l) is bigger than Es:

$$E_{of} = E_o - \frac{d_L}{L\,\varepsilon_d} P_s > E_s \qquad (12)$$

where P_S is the maximal polarization on the loop taken from the sandwich. Thus, when Eq.(12) is not met, due to insufficiently high Eo or too large (but still less than unity) value of d_L/L, one should take into account the memory effect.

2.3. NON-LINEARITY AND MEMORY

To make allowance for the memory effect one should rewrite Eq. (9) at the coercive field (with D= 0) in the following form which is more general than (11)

$$E_c = E_{cf} \qquad (13)$$

where E_{cf} is the coercive field of the loop seen by the ferroelectric. Commonly, in ferroelectrics, this field is an increasing function of E_{of} (the maximal field on the hysteresis loop seen by the ferroelectric). According the Eq.(12) E_{of} is an increasing function of the film thickness L. Taking into account these two facts one finds that, in the non-saturated regime, E_c is an increasing function of L which approaches the bulk

value of the coercive field E_{cb} on saturation. A sketch of the obtained dependence is shown in Fig. 3 (c).

Let us compare the results obtained above in the three approximation (Fig. 3). It is seen that the linear approximation is unacceptable because it gives a qualitatively wrong result. On the other hand, the result obtained by the adequate treatment of the problem looks quite surprising because everybody believes in the "rule" that a thin dielectric layer on the top of a ferroelectric can result in a substantial decrease of the voltage effectively applied to it. So one could expect a decrease of E_c with increasing L. However, looking deeper into the problem shows that there is an exception from this "rule" when the electric field is close to E_c. Near this point there exists a great difference between the differential dielectric constant $\varepsilon_f = \varepsilon_o^{-1} dD/dE$ which is large and the "average" dielectric constant $\varepsilon_a = \varepsilon_o^{-1} D/E$ which is much smaller. Although, the general idea that a thin low dielectric constant layer on top of a high dielectric constant material causes a large drop of the voltage is correct, its application to a non-linear material requires that we to specify which of the dielectric constants, ε_f or ε_a, is to be used. As it is clear from Eq. (9) it is ε_a. Thus, in the considered problem, at $E = E_c$ the ferroelectric behaves as a material with a small dielectric constant. If E_c is defined as the field at which $D = 0$ then $\varepsilon_a = 0$ and ε_a is about unity for the definition of E_c as the field at which $P = 0$.

3. Depolarizing Effect: Identification of Passive Layer

The next important question related to the passive layer is its identification from the dielectric properties of the film. Until now that has been mainly done by analyzing the thickness dependence of the coercive field. The dependence of E_c which follows Eq. (10) (see also Fig. 3 (a)) was considered as a definite sign of the presence of a passive layer (see e.g. Ref. 1, 15). However, as it has been shown above, this behavior is an artifact of the linear approximation and by no means a characteristic feature of the sandwich structure. Then the question arises as to how the passive layer can be identified.

The most sensitive parameter of the hysteresis loops to the presence of a passive layer is the slope (differential dielectric constant) at E_c. Indeed, one can easily obtain from Eqs.(4) -(6) for any point of the loop:

$$\frac{1}{\varepsilon_s} - \frac{1}{\varepsilon_f} = \frac{d}{L\,\varepsilon_d} \qquad (14)$$

where ε_s and ε_f are the differential dielectric constants on the loop taken from the sandwich and that seen by the ferroelectric. This relation enables us to estimate d_L/ε_d from the thickness dependence of $1/\varepsilon_s$ on the condition that $1/\varepsilon_f$ is independent of $d_L/L\varepsilon_d$ and that the accuracy of determining of $1/\varepsilon_s$ is high enough to trace a regular dependence of it on L. To eliminate the thickness dependence of $1/\varepsilon_f$ one should consider the saturated regime for ε_s, i.e. ε_s is independent of E_o. It is clear that, in this case, ε_f should be also independent of the maximal field on the loop seen by the ferroelectric, E_{of}. Therefore, in this case, the dependence of E_{of} on $d_L/L\varepsilon_d$ does not lead to a dependence of ε_f on $d_L/L\varepsilon_d$. As to the accuracy of determining $1/\varepsilon_s$, the best point on the loop is E_c because ε_s is maximal at this point.

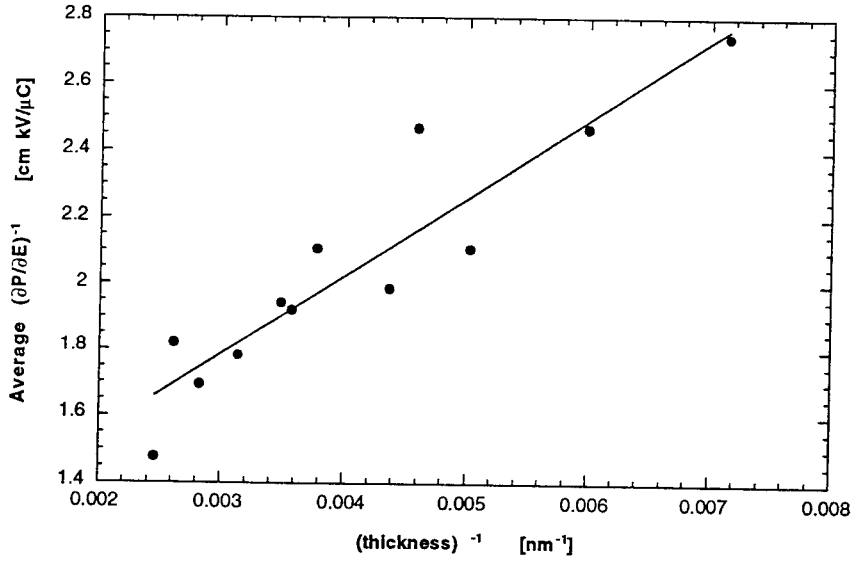


Figure 4. Dependence of inverse slope of the hysteresis loop at E_c vs. inverse thickness of the film for a set of 53/47 PZT sol-gel ferroelectric thin films. The effective thickness (equivalent thickness of vacuum) of the passive layer determined from the linear fit d = 0.02 nm.

In Fig. 4, the dependence of $(1/\varepsilon_S)$ vs. L^{-1} is shown for a set of sol-gel PZT films. The estimated effective thickness d_l/ε_d of the passive layer which can be responsible for this dependence is found to be about 0.02 nm. This value is comparable to that, 0.03 nm, estimated by Benedetto et al [9] from retention data on sol-gel PZT films. One should mention that a passive layer with such an effective thickness causes a very small variation of other parameters of the loop. For example, one can estimate the variation of the remanent polarization δP_r as

$$\delta P_r = \varepsilon_r E_d = - P_r \frac{d_L}{L} \frac{\varepsilon_r}{\varepsilon_d} \qquad (15)$$

(ε_r is the differential dielectric constant at $P = P_r$) to find $\delta P_r/P_r$ to be about 1-3% for common values of PZT film parameters.

Despite its high accuracy the method indicated above for identification of the passive layer alone cannot solve the problem because a thickness dependent tilt of the hysteresis loops can be attributed to other effects as well, e.g. to the depletion effect [16]. We believe that the most convincing way of the identification of the passive layer is to compare the saturation curves of the remanent polarization, P_r, the maximal polarization on the loop, P_s and coercive field, E_c, for samples with expected different $d_L/L\varepsilon_d$. Not going into all of the details of the analysis, which can be found elsewhere [11], below we

present the results of our computer simulations of the switching behavior of the sandwich with a real ferroelectric inside.

For this simulation we have used a set of hysteresis loops of a sol-gel PZT film as a dielectric portrait of the ferroelectric, i.e. we have numerically solved the system Eqs. (4)-(6) using the indicated set of data to find the relation between the variables P_f and E_f which enter the system. The experimental set of loops of the ferroelectric used in the calculation is shown in Fig. 5 (a) The calculated set of the loops of the sandwich for different values of the ratio $d/L = d_L/L\varepsilon_d$ is shown in Fig. 5 (b).

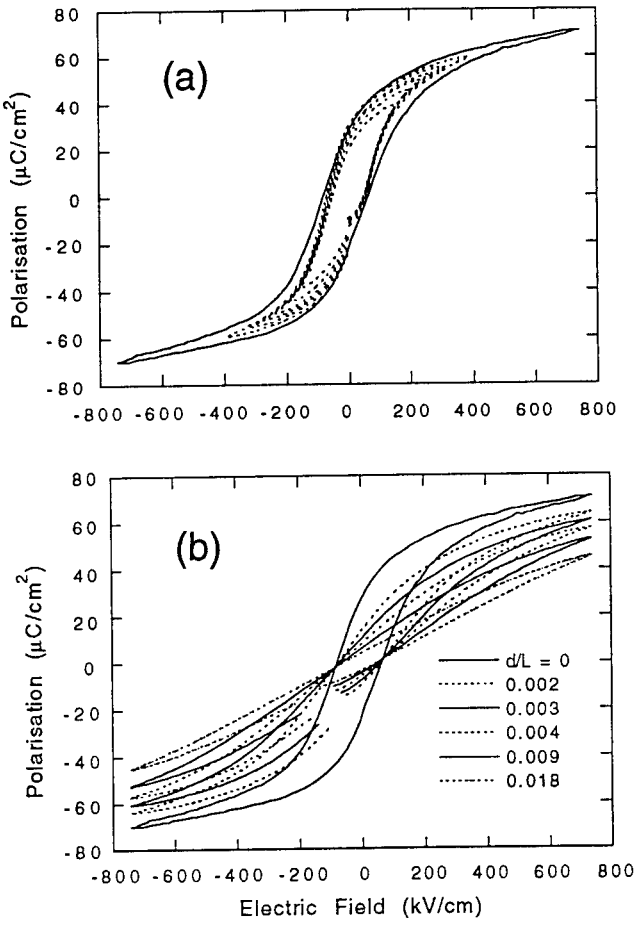


Figure 5. (a) Set of experimental hysteresis loops (not all of them are shown) for a PZT thin film taken for different maximal fields. (b) Loops for a fixed maximal field for various passive layer thicknesses in the sandwich structure "ferroelectric - passive layer" calculated using this set as a dielectric portrait of the ferroelectric.

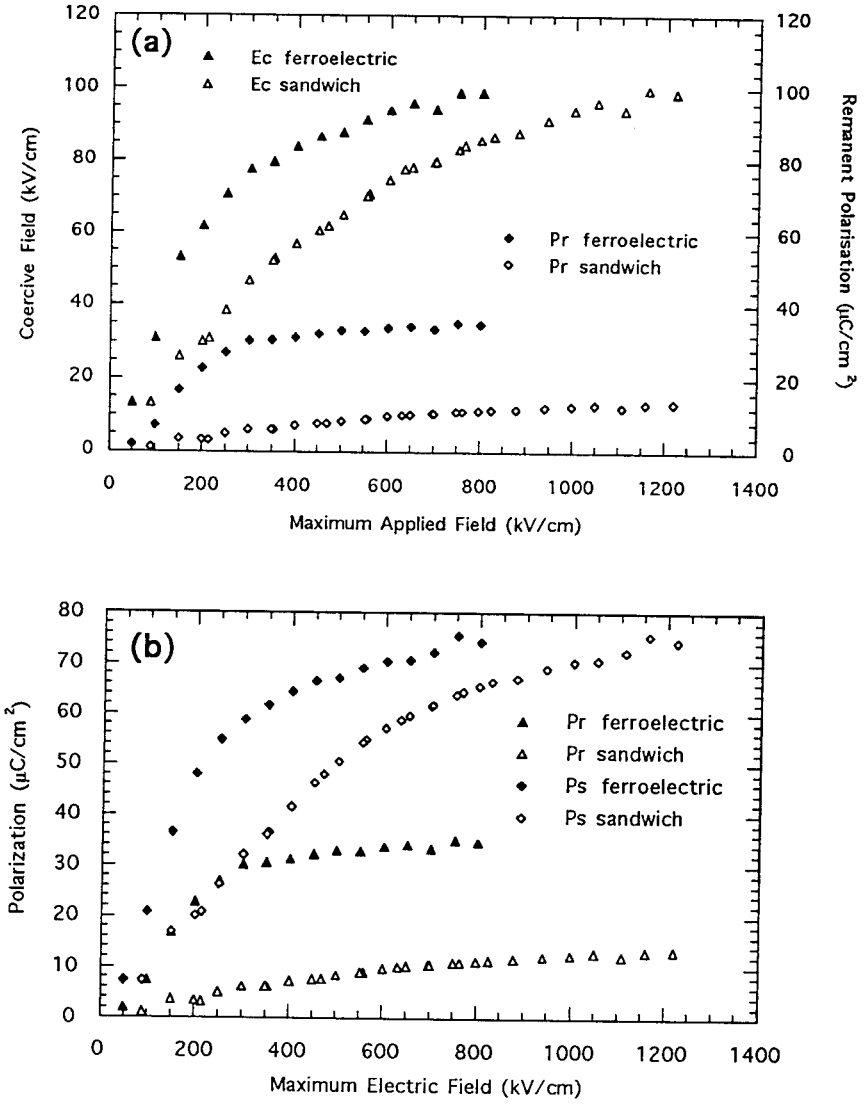


Figure 6. Saturation curves for P_s, P_r, and E_c for a ferroelectric film and the sandwich " ferroelectric-dielectric" with $d / L = 0.01$, where L and d are the ferroelectric thickness and the effective thickness (equivalent thickness of vacuum) of the dielectric.

As one can see from Fig. 5 (b), the tilt of the loops with a small decrease of the coercive field, as discussed above, is really an evident feature of the evolution of the loops with

increasing d/L. On the same lines, we have also obtained the saturation curves for P_r, P_S, and E_c of the sandwich. These curves, calculated for d/L = 0.01 together with those for the ferroelectric itself, are shown in Fig. 6.

A comparison of the curves presented in Fig. 6 reveals a qualitative difference between the saturating curves for E_c and P_s on the one hand and P_r on the other. For the first two, the effect of the passive layer is only a change of the scale along the E_o-axis (actually it is the non-linear change of the scale given by Eq. (12)) such that, in the sandwich, a bigger value of E_o is needed to reach the same values of E_c and P_s. Note that their saturated values are unaffected by the passive layer. In the case of P_r, both the field needed for its saturation and the saturated value of P_r itself are affected by the passive layer. We believe that the comparison of these curves together with the thickness dependence of the slope of the loop at E_c provide us with an effective tool for identification of the passive layer.

4. Depletion Effect

As it was shown above, the depolarizing effect arising due to a passive layer, contrary to existing opinion [1, 15], cannot result in the increase of E_C with decreasing film thicknesses observed in many experiments [17,15, 10]. The implication is that one should look for an intrinsic mechanism responsible for the observed dependence. Two explanations for this dependence recently appeared in the literature: one related to the depletion effect [10] and the other related to the surface pinning contribution [18]. One should mention that the interpretation of such kind of the dependence in terms of the size effect for the near-by-electrode nucleation [19] seems to be inconsistent in view of the results of subsequent studies of the problem [20]. The key points of Ref. 10 are discussed below to illustrate the role of the depletion effect in switching.

In characterizing ferroelectrics in terms of the coercive field, one should note the difference between two coercive fields: the coercive field for "nucleation", E_{cn}, for the near-by-electrode nucleation of new opposite domains and the coercive field for motion, E_{cm}, for the growth of the stable nuclei through the film. In general, $E_{cn} >> E_{cm}$. The reason for this inequality is that, in the case of formation of stable nuclei of opposite domains near the electrodes, one deals with elongated critical nuclei having very high energy [19], whereas in the case of the lateral domain wall motion, the nuclei providing this motion are flat (see e.g. [20] and references therein) and have substantially lower energy than the elongated ones. With the two coercive fields introduced, one reduces the description of the switching to that for the near-by-electrode nucleation of new domains of opposite sense and the growth of the stable nuclei through the film, these processes being driven by the sum of the external, E_{ext}, and built-in electric fields. One can find the value of E_{ext} needed to initiate the near-by-electrode nucleation from the condition that the sum of the built-in and external fields is equal to the coercive field for the nucleation. For the case of totally depleted films, that means (cf Eq.(3))

$$E_{cn} = E_{ext} + E_{bi};\ E_{bi} = LqN_d / 2\varepsilon \qquad (16)$$

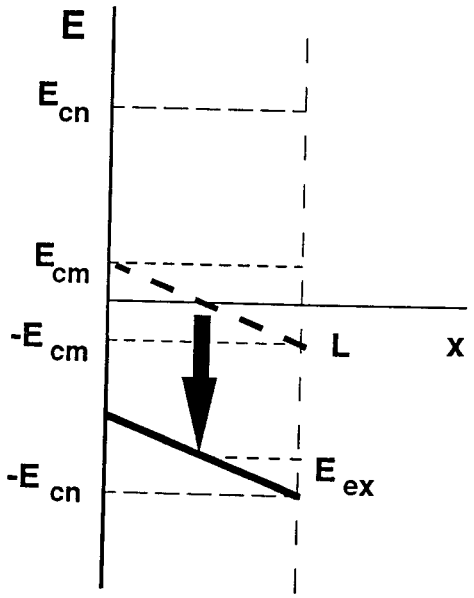


Figure 7. E(x) at the beginning of opposite nuclei formation (positively poled film). They form close to the right electrode.

The electric field distribution at this moment is shown in Fig. 7. For the case presented in this figure (note, here $2E_{bi} < E_{cn} - E_{cm}$), complete switching of the film takes place as soon as we induce the near-by-electrode nucleation. It is clear from this figure that, at the moment of nucleation, the field throughout the film is greater than the coercive field for motion, E_{cm} and therefore, this field is sufficient to switch half of the polarization using the nuclei created near the right electrode. Thus, solving Eq. (16) with respect to E_{ext} one finds the thickness dependence of the coercive field in the following form:

$$E_c = E_{cn} - AL; \quad A = N_d q / 2\varepsilon \qquad (17)$$

As is seen from Eq.(2), for the case of partial film depletion ($L > 2W$), the built-in electric field is thickness independent and also, in this case, the near-by-electrode nucleation is not sufficient to facilitate switching. All in all, now one can expect the coercive field to be thickness independent. Thus the theoretical model predicts a decreasing thickness dependence of E_c of the type shown in Fig. 8, which saturates at larger thicknesses.

As it has been shown [10] this dependence qualitatively describes the film-thickness dependence of the coercive field observed in PZT films. The fit of the experimental data for E_c with Eq.(17) also yields reasonable values for the semiconductor parameters of PZT.

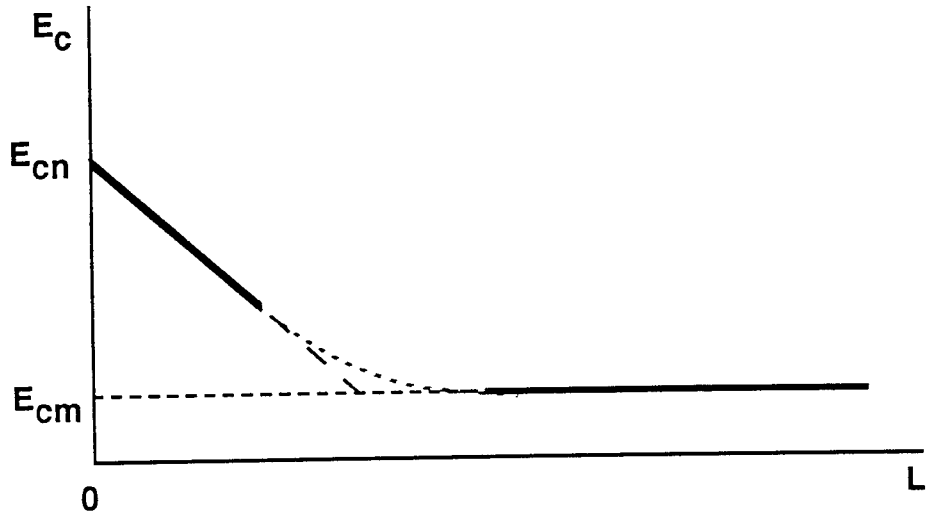


Figure 8. Predicted thickness dependence of coercive field for $qWN_d/\varepsilon > E_{cn}-E_{cm}$. Solid lines show the limiting cases of thin and thick films.

5. Conclusions

- Depletion and depolarization effects play important but quite different roles in switching.
- The presence of a layer responsible for the depolarization effect in ferroelectric films can be reliably identified from the comparison of the saturating curve for P_r, P_s and E_c of the films with the different relative thicknesses (d/L) of the layer.
- The parameter of the hysteresis loop which is the most sensitive to the presence of the passive layer is the slope of the loops at $E = E_c$. The thickness dependence of this parameter can be used for the estimation of the effective thickness (equivalent thickness of the vacuum) of the layer.
- The presence of a passive layer cannot be responsible for the thickness dependence of the coercive field observed in many experiments.
- The depletion effect can manifest itself in a strong thickness dependence of coercive field which is consistent with those observed experimentally.

6. Acknowledgments

This work was partly performed within the European ESPRIT program FELMAS. The financial support is by the Swiss Federal Office for Science and Education (OFES), and by the Swiss National Science Foundation.

7. References

1. Merz, W.J. (1956), *J. Appl. Phys.* **27**, 938.
2. Batra, I.P. and Silverman, B.D. (1979), *Sol. St. Commun.* **11**, 291.
3. Kretshmar, R. and Binde, K. (1979, *Phys. Rev.* **B 20**, 1065.
4. Fridkin, B.M. (1980), *Ferroelectric Semiconductors*, Consultants Bureau, N.Y. and London.
5. Miller, S.L., Nasby, R.D., Schwank, J.R., Rodger, M.S., and Dressendorfer, P.V. (1990), *J. Appl. Phys.* **58**, 6463.
6. Brennan, C.J. (1992), *Integrated Ferroelectrics* **2**, 73.
7. Tilley, R.D. and Zeks, B. (1992), *Ferroelectrics* **134**, 313.
8. Teowee, G. and Uhlmann, D.R. (1993), *Mat. Res. Soc. Proc.* **310**, 415.
9. Benedetto, J.M., Moore, R.A. and McLean, F.B. (1994), *J. Appl. Phys.* **75**, 460.
10. Tagantsev, A.K., Pawlaczyk, Cz., Brooks, K. and Setter, N. (1994), *Integrated Ferroelectrics* **4**, 1.
11. Tagantsev, A.K., Landivar, M. and Setter, N., *to be published.*
12. Scott J.F., Araujo, C.A., Melnick, B.M., McMillan, L.D. and Zulleeg, R. (1991), *J. Appl. Phys.* **70**, 382.
13. Waser, R. and Klee, M. (1992), *Integrated Ferroelectrics* **2**, 23.
14. Sze, S.M. (1981) *Physics of Semiconductor Devices*, Wiley, New York.
15. Sakashita, Y., Segawa, H., Tominaga, K. and Okada, M. (1993), *J. Appl. Phys.* **73**, 7
16. Tagantsev, A.K., to be published.
17. Scott, J.F., McMillan, L.D and Araujo, C.A. (1989), *Ferroelectrics* **93**, 31.
18. Lebedev, N.I. and Sigov, A.S. (1994) *Integrated Ferroelectrics* **4**, 21.
19. Kay, H.F. and Dunn (1962), *Philos. Mag.* **7**, 2027.
20. Burtsev, E.V. and Chervonobrodov, S.P. (1992), *Ferroelectrics* **126,** 293.

NONSTOICHIOMETRY, DEFECTS, AND CHARGE TRANSPORT IN PZT

M. V. RAYMOND AND D. M. SMYTH
Materials Research Center
Lehigh University
Bethlehem, PA 18015, USA

ABSTRACT. Nonstoichiometry and the resulting electrical properties for the perovskite ferroelectrics are correlated with their crystal structure and the chemical properties of the constituent atoms. In the alkaline earth titanates there is extensive hole-trapping which results in their characteristic insulating properties. There is no evidence for electron-trapping, nor for thermally-activated mobilities for either electrons or holes. The Pb-based systems behave differently because of the "inert pair" of 6s electrons on the Pb^{+2} ion. As a result, Pb^{+2} ions can act as shallow hole traps, and the hole mobility is thermally-activated. The Ti^{+4} ion appears to act as an electron trap. The presence of these intrinsic traps for electrons and holes results in transient effects following photo-excitation.

1. Introduction

The charge transport properties of crystalline inorganic compounds depend on their structure, precise composition, and the chemical properties of the constituent atoms. The structure determines the relative stabilities and the mobilities of various lattice defects that can be the products of intrinsic disorder, aliovalent doping, or nonstoichiometry. The precise composition includes both the concentration of aliovalent impurities, and deviations from the stoichiometric composition. The chemical properties of the constituent atoms, as determined by their electronic structure, establish the nature of the electronic states in the valence and conduction bands, and influence the location of various localized electronic states in the band gap, i.e. the depth of acceptor and donor levels. The nature of the electronic states also affects the electronic transport mechanism, whether thermally-activated hopping mechanisms or band conduction. Thus the charge transport properties of inorganic compounds can be rationalized, or even predicted, from some basic knowledge of structure and chemistry.

2. The Perovskite Structure

The perovskite structure is tightly packed and there is no evidence for any type of interstitial ionic defect. However, vacancies on all three lattice sites have been reported for compounds having the perovskite structure, and for the slightly distorted versions characteristic of the PZT system.

O. Auciello and R. Waser (eds.), Science and Technology of Electroceramic Thin Films, 315-325.
© 1995 *Kluwer Academic Publishers. Printed in the Netherlands.*

Oxygen vacancies are a product of chemical reduction

$$O_O \longleftrightarrow 1/2O_2 + V_O^{\cdot\cdot} + 2e' \qquad (1)$$

The defect notation is due to Kroger and Vink [1], whereby the main symbol indicates the species, with V representing a vacancy, the subscript identifies the lattice location, and the superscript indicates the charge relative to the perfect lattice. An extra positive charge, or missing negative charge, is denoted by a superscript dot, while an extra negative charge, or missing positive charge, is indicated by a superscript slash. e′ represents an electron in the conduction band. Substitutional impurity cations that have a lower ionic charge than that of the host cation they replace are called acceptor impurities, and their negative defect charge is compensated by the formation of an equivalent concentration of oxygen vacancies, e.g.

$$2PbO + Al_2O_3 \longrightarrow 2Pb_{Pb} + 2Al'_{Ti} + 5O + V_O^{\cdot\cdot} \qquad (2)$$

where Al'_{Ti} is an Al^{+3} substituted for Ti^{+4} in $PbTiO_3$.

Vacancies on the cation A site, the 12-coordinated site, can be present to accommodate an excess of the B-site cation

$$TiO_2 \longrightarrow V''_{Pb} + Ti_{Ti} + 2O_O + V_O^{\cdot\cdot} \qquad (3)$$

i.e. compositions of the type $Pb_{1-x}TiO_{3-x}$. Single-phase compositions that have an excess of A-site cations have not been observed. Cation vacancies may also be present to compensate the excess positive charge of donor impurities

$$La_2O_3 + 3TiO_2 \longrightarrow 2La^{\cdot}_{Pb} + V''_{Pb} + 3Ti_{Ti} + 9O_O \qquad (4)$$

where $La^{\cdot}_{Pb}$ is a La^{+3} substituted for Pb^{+2} in $PbTiO_3$. In the case of donor-doped $BaTiO_3$, it has been shown that Ti-vacancies are the preferred compensating defect [2,3].

Since vacancies appear to be the only possible lattice defects, the preferred type of intrinsic ionic disorder must be of the Schottky type

$$nil \longleftrightarrow V''_{Pb} + V''''_{Ti} + 3V_O^{\cdot\cdot} \qquad (5)$$

where nil represents the defect-free perfect crystal. The vacancies must be formed in stoichiometric ratio in order to maintain bulk charge neutrality. The concentrations

(activities) of these defects must then be linked by a mass-action expression under equilibrium conditions

$$[V''_{Pb}][V''''_{Ti}][V^{\cdot\cdot}_{O}]^3 = K_s(T) = K'_s \exp(-\Delta H_s)/kT \qquad (6)$$

where $K_s(T)$ is the mass-action constant, whose temperature dependence is determined by the standard enthalpy of the Schottky disorder reaction, ΔH_s. The Schottky formation enthalpy has not been determined experimentally for this structural family, but theoretical calculations give the rather high value of 2.29 eV per defect, i.e. ΔH_s = 11.45 eV [4]. This means that for readily-achieved purities, there are invariably more lattice defects present due to the naturally-occurring impurity content than to intrinsic disorder, except possibly for temperatures approaching the melting point. However, even though Eq. (5) may not represent a major source of defects, Eq. (6) still represents a valuable expression that relates the defect concentrations to one another.

The only other defect of possible importance in the perovskite-related oxides is the proton, which has been observed in these systems as a result of the up-take of water when oxygen vacancies are available

$$H_2O + V^{\cdot\cdot}_{O} + O_O \longleftrightarrow 2OH^{\cdot}_{O} \qquad (7)$$

While they have been shown to be present under equilibrium conditions, or in quenched samples [5], their possible migration under device application conditions has not been studied.

3. Chemical Properties And The Band Gap

The electronic properties of crystalline solids are closely linked to the stability of various oxidation states of the constituent atomic species. Electronic band structures are derived from the electronic states of the ions, and retain their relative stabilities. Valence bands are collective states derived from the uppermost filled electronic states of the ions, while conduction bands involve the lowest empty electronic states. In the case of ions of the main group elements with rare gas electronic structures, there is only one oxidation state achievable by normal chemical means. For example, in MgO, the valence band is made up of filled oxygen 2p states, while the conduction band is made up of the empty magnesium 3s states. Transfer of an electron from the valence band to the conduction band is closely related to the transfer of an electron from an O^{-2} ion to a Mg^{+2} ion

$$Mg^{+2} + O^{-2} \longrightarrow Mg^{+} + O^{-} \qquad (8)$$

In solid state language, this is equivalent to the ionization of an electron across the band gap, the intrinsic electronic disorder reaction

$$\text{nil} \longleftrightarrow e' + h^{\cdot} \qquad (9)$$

Where e' is an electron in the conduction band, and $h^{\cdot}$ is a hole in the valence band. The products of Eq. (8) are not stable species, so in solid MgO the transfer represented by Eq. (9) is energetically very expensive, and the band gap is large, of the order of 10 eV, and MgO is an insulator under all circumstances. As expected from the electronic structure of their ions, this is also true for CaF_2, Al_2O_3, NaCl, SrO, etc.

For transition metal elements for which the most stable oxidation states correspond to their Group number, e.g. Ti^{+4}, Nb^{+5}, W^{+6}, etc., the cations again have the rare gas electronic structure. Thus it is not possible to oxidize these cations further, but they can be reduced. TiO_2 can be chemically reduced to Ti_2O_3 and TiO, for example, and the Ti^{+3} halides are even stable in aqueous solution when protected from oxidizing atmospheres. Reduction corresponds to putting electrons back into the empty d shells of the ions. In the oxides of these elements, the valence bands are again made up of oxygen 2p states, while the conduction bands are derived from the empty d states. Putting an electron into the conduction band is equivalent to reducing the cation, an energetically feasible step. Thus the band gaps of these compounds are typically of the order of 3-4 eV. These materials can be either insulators or semiconductors, depending on their precise composition, i.e. the amount and type of dopant, or the state of nonstoichiometry. In this case, the conduction band is receptive to electrons, but the presence of holes in the valence band is still not as favorable.

For the later transition metals, the most stable oxidation states are often the lowest achievable oxidation states, and involve partial occupation of the d shells. There are just too many valence electrons to be able to ionize the atoms all the way back to the electronic structure of the preceding rare gas. Such cations as Cr^{+3}, Mn^{+2}, Fe^{+2}, Co^{+2}, and Ni^{+2} can be oxidized, but cannot be reduced. In these cases, the valence band is composed of occupied d states from the cations, and the conduction band is a combination of empty d states. Because of the ease of oxidation, the valence band is receptive to holes, while the placement of electrons in the conduction band is not favorable. This is the inverse of the situation for the earlier, reducible transition metal cations, and the band gaps are again of the order of 3-4 eV. As before, compounds of these cations can be either insulators or semiconductors, depending on the composition and equilibration. For the case of cations that can be both oxidized and reduced, e.g. Fe^{+3}, both bands are receptive to their respective carriers, and the band gaps are even more modest in magnitude.

Where do the perovskite ferroelectrics fall into this scheme? For the alkaline earth titanates (zirconates), such as $BaTiO_3$, the alkaline earth cations have only a single stable oxidation state. Ti^{+4} is reducible, but not oxidizable, and Zr^{+4} is similar but is less easily reducible. The band gap of $BaTiO_3$ is 3.4 eV [6]; band gaps in the PZT family are of similar magnitude.

4. Nonstoichiometry

For a metal oxide, nonstoichiometric compositions result from the gain or loss of oxygen relative to the stoichiometric composition. This results in a charge-balanced combination of ionic and electronic defects. The relative ease of accommodating the ionic defects

depends on the crystal structure, and for the electronic defects on the band structure, both as described above. Thus the equilibrium reduction of an oxide frequently occurs by the reaction shown in Eq. (1). A neutral oxygen atom leaves the crystal, thus preserving charge neutrality, leaving behind an unoccupied oxygen site, i.e. an oxygen vacancy, and the two electrons with which it had been combined in the form of an oxygen ion. Thus the conductivity increases with decreasing oxygen activity, $P(O_2)$, as increasing numbers of electrons are left in the material. This is seen in Fig. 1, a log-log plot of the equilibrium electrical conductivity of $BaTiO_3$ as a function of $P(O_2)$ at various temperatures [7,8]. In the range of low $P(O_2)$, the conductivity steadily increases with decreasing $P(O_2)$. Since the conduction band, made up of empty Ti 3d states, is receptive to electrons, the electrons created by reduction are free to conduct in the conduction band. This means that donor levels, including all positively-charged defect sites such as $V_O^{\cdot\cdot}$, are very shallow in $BaTiO_3$. The formation of both oxygen vacancies and electrons is relatively favorable in such compounds, the first because there are no space restrictions for the formation of anion vacancies, and the latter because of the presence of a reducible cation. Similar results can be anticipated for PZT, except that the range of $P(O_2)$ will be limited by the easy reducibility of Pb^{+2} to Pb metal.

Oxygen-excess nonstoichiometry should be energetically unfavorable in pure perovskite titanates. The potential products of oxidation are holes, and either oxygen interstitials or cation vacancies. There are no oxidizable species present, and the valence band is not very receptive to holes. There is no room in the structure for anion interstitials, and cation vacancies, particularly the highly charged $V_{Ti}^{''''}$ may not be very favorable. However, Fig. 1 shows a significant range of oxygen-excess, p-type behavior in the higher range of $P(O_2)$, i.e. the conductivity is increasing with increasing $P(O_2)$. This results from the dominant naturally-occurring impurities. The most abundant natural impurities are cations with lesser charge than that of the host cation they replace in the lattice, e.g. large monovalent cations such as Na^{+} substituted for Ba^{+2}, or small trivalant or divalent cations such as Fe^{+3}, Al^{+3}, or Mg^{+2} substituted for Ti^{+4}. These are the acceptor impurities and are compensated by oxygen vacancies as shown in Eq. (2). These extrinsic oxygen vacancies almost always exceed the concentration of any other defect in the stoichiometric composition, either intrinsic Schottky defects, Eq. (5), or intrinsic electronic disorder, Eq. (9). The availability of these unoccupied oxygen sites relieves the problem of accommodation of the excess oxygen in the lattice; they merely fill a small fraction of the extrinsic oxygen vacancies. There is still the problem of putting holes into the valence band which is derived from oxygen 2p levels in $BaTiO_3$ and analogous compounds. As a result, the major product of oxidation are holes trapped at acceptor impurities

$$2A' + V_O^{\cdot\cdot} + 1/2O_2 \longleftrightarrow 2A^x + O_O \qquad (10)$$

where A' is a generic singly-charged acceptor center, and A^x is an acceptor with a trapped hole. The p-type conduction then arises by a partial ionization of these trapped holes

$$A^x \longleftrightarrow A' + h^{\cdot} \qquad (11)$$

a process that requires an ionization energy in the range 0.5-1 eV. This is the level of ionization energy that is required to explain the insulating behavior of these compounds after they have been cooled from equilibration in the oxygen-excess, p-type region. It has been shown that with ionization energies of this magnitude, most of the holes will be trapped, even at the temperatures of equilibration [9].

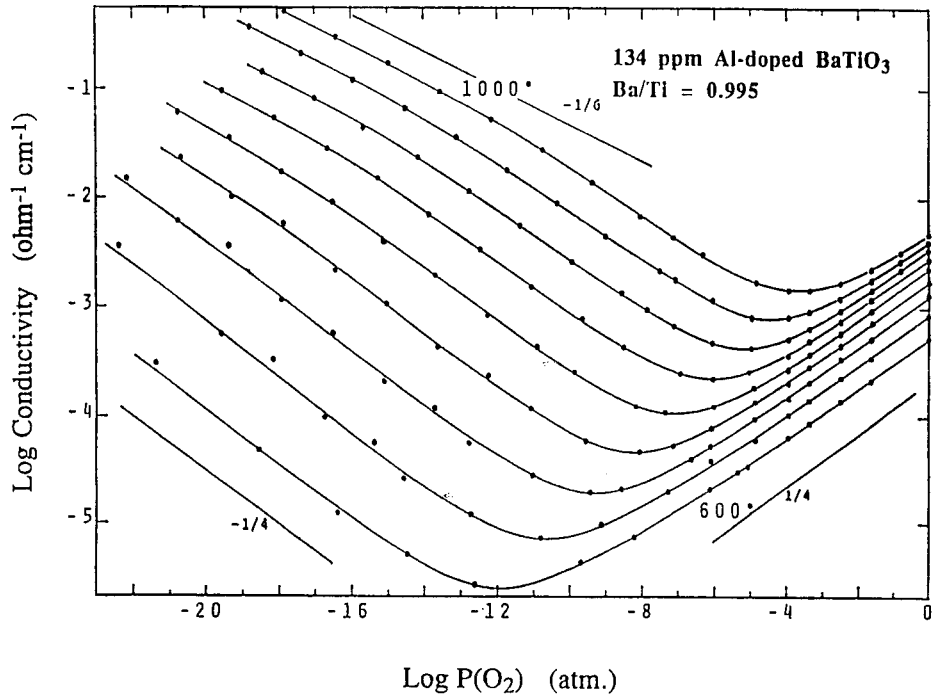


Figure 1. The equilibrium conductivity of $BaTiO_3$ as a function of $P(O_2)$. The isotherms were measured at 50 °C intervals.

Thus the presence of extrinsic oxygen vacancies as a site for excess oxygen, and of deep trapping sites that make it unnecessary to put most of the holes in an unreceptive valence band, greatly reduces the enthalpy of an otherwise unfavorable oxidation reaction. From the temperature dependences seen in Fig. 1, it is apparent that the enthalpy of oxidation of $BaTiO_3$ (0.92 eV) is substantially less than that for reduction (5.90 eV) [6]. In the latter process ionic defects are created, while for the oxidation reaction they are consumed.

The different origin and properties of the electronic states that make up the valence and conduction bands of the perovskite ferroelectrics results in a pronounced asymmetry in the room temperature electrical conductivities. Since it is energetically easy to put electrons in the conduction band, donor levels are very shallow, and the heavily reduced materials are dark-colored semiconductors. However, the only way for holes to exist in a system in which the electronic states that constitute the valence band are not receptive to holes, is for most of them to be localized at deep trapping states, the acceptor levels. Thus the oxygen-excess, p-type materials are light-colored insulators.

5. The Equilibrium Conductivity of PZT

The general appearance of the equilibrium conductivity of PZT does not differ significantly from that of its near-relatives $BaTiO_3$ and $SrTiO_3$. Conductivity for the oxygen-excess, p-type region in the $P(O_2)$ range $1\text{-}10^{-4}$ atm is shown in Fig. 2. The composition of the PZT used throughout this study is $Pb(Zr_{1/2}Ti_{1/2})O_3$. The appearance is very similar to that of $BaTiO_3$, as shown in Fig. 1, although the conductivity of the PZT is significantly higher and its temperature dependence is greater. The slopes of the Arrhenius plots of the conductivities at constant $P(O_2)$ are 0.71 eV for PZT, and 0.46 eV for $BaTiO_3$. These numbers are related to the enthalpy of the oxidation reaction to form free holes, which is the difference between the oxidation reaction to form trapped holes, Eq. (10), and twice the ionization reaction, Eq. (11). The Arrhenius slopes will also contain the temperature dependence of the hole mobility, which will be discussed later in greater detail.

$$1/2O_2 + V_O^{\cdot\cdot} \longleftrightarrow O_O + 2h^{\cdot} \qquad (12)$$

As in the case of $BaTiO_3$, the equilibrium conductivity of PZT appears to pass through a minimum value and then increase with further reduction, indicative of oxygen-deficient, n-type behavior. These data are currently being acquired and will be presented elsewhere.

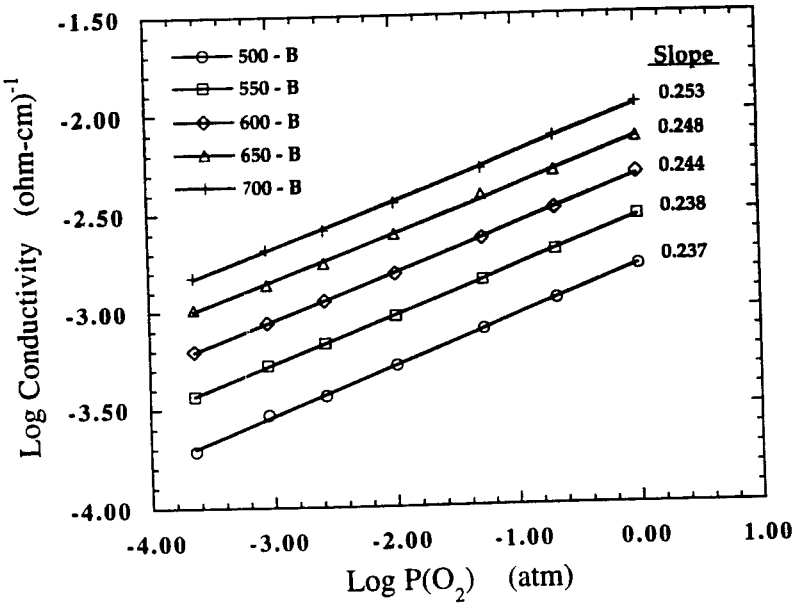


Figure 2. The equilibrium conductivity of $Pb(Zr_{1/2}Ti_{1/2})O_3$ as a function of $P(O_2)$.

6. Carrier Trapping And Mobility

The Pb-based perovskites have their own special personality, due to the specific electronic structure of the Pb^{+2} ion. While the alkaline earth cations such as Ba^{+2} and Sr^{+2} contribute very little to the electronic structure of their perovskite titanates, because of their closed-shell, inert gas structures, the Pb^{+2} ion retains its 6s electrons, the so-called "inert pair". This is a local peculiarity in that region of the Periodic Chart, shared primarily by Tl^{+1} and Bi^{+3} (as further evidence for the unique behavior of these cations, one might also note that all of these "inert pair" cations are essential ingredients of many of the high temperature superconductors).

As described earlier, there is substantial trapping of holes in the perovskite titanates, even at the equilibration temperatures. This is related to the presence of deep acceptor levels, and is essential for the insulating properties of the oxidized materials. In PZT, a trapping level of 0.7 eV has been determined, although the precise nature of the level is not known. Conversely, in the alkaline earth titanates, there is no evidence for the trapping of electrons, even at temperatures below room temperature. In spite of these similarities, the properties of PZT differ from those of the alkaline earth titanates in significant ways, especially in the vicinity of room temperature.

Important information on the different behavior of PZT has been obtained by Warren et al. by electron paramagnetic resonance (EPR) measurements on photoexcited samples [9]. After illumination with band-gap light, the PZT samples show clear EPR signals for both Pb^{+3} and Ti^{+3} centers. No comparable centers have been detected in $BaTiO_3$ or $SrTiO_3$. The centers in PZT are stable at cryogenic temperatures, but slowly decay at room temperature. Typically, the EPR signal for the Pb^{+3} center drops by about half at room temperature in about 30 minutes, while the Ti^{+3} signal has decreased by about 20% in the same period. Band calculations by Robertson show that the upper valance band states in PZT are about equally divided between O 2p and Pb 6s character [10]. In the presence of a hole, the Pb 6s states can apparently be pulled into the gap as a localized, shallow hole trap. With the trapped hole, this is the Pb^{+3} state detected by EPR. The metastability of this center suggests that it lies close to the valence band edge. Similar calculations on the Ti 3d states indicate that the electron in the Ti^{+3} center is highly localized on the Ti 3d orbital and that this trap is quite deep, at least 1 eV below the conduction band edge [10]. Each Pb^{+2} is a potential hole trap, and each Ti^{+4} is a potential electron trap in PZT. The presence of a hole trap in every unit cell precludes the free motion of holes in the valence band, and results in a thermally-activated hole mobility. Prisedsky et al. previously reported a hole mobility of 1.3×10^{-3} cm^2/V s at 600°C in PZT with an activation energy of about 0.26 eV (11). Our own more recent results are in good agreement and indicate an activation energy of 0.30 eV over the temperature range 500-700°C. The magnitudes of these activation energies are consistent with the shallow nature of the Pb^{+3} centers. One would expect the apparent ability of Ti^{+4} ions to trap electrons to lead to a similar activated mobility for electrons, but there is not yet enough information on n-type PZT to confirm that expectation. In the alkaline earth titanates electron transport is clearly not thermally-activated, nor is there any evidence for thermal-activation of the hole mobility.

It is instructive to think through the process of generation and decay of the trapped carriers, starting with the insulating ground state of the oxygen-excess, p-type material. There is an excess of holes in this state and they are almost completely localized in stable deep traps, i.e. acceptor impurities or cation vacancies with a trap depth of 0.7 eV for our samples. There are virtually no electron species in this state.

1. The excitation with band-gap light generates electrons and holes in equal numbers plus additional holes from whatever excitation occurs from the deep hole traps.

2. When the light is extinguished, the free carriers start to seek the closest available traps, and these will almost invariably be the Pb^{+2} ions for the holes, and the Ti^{+4} ions for the electrons.

3. The Pb^{+3} centers are metastable with respect to recombination with the electrons trapped as Ti^{+3} centers and to dropping into the stable, deep hole traps. The Ti^{+3} centers are metastable only with respect to recombination with the Pb^{+3} centers.

4. Since the recombination between Pb^{+3} and Ti^{+3} centers eliminates equal numbers of trapped electrons and holes, and the Pb^{+3} centers can also decay by movement of holes to the deeper traps, the Pb^{+3} centers decay at the faster rate.

5. Since the decay rate for Pb^{+3} is substantially greater than that of Ti^{+3}, it seems likely that most of the holes trapped as Pb^{+3} centers move into the deep, stable hole traps. Further decay then results from deeply trapped holes trying to recombine with deeply trapped electrons.

6. While the Ti^{+3} centers represent deeply trapped electrons, these will all ultimately disappear since there are more total hole species than electron species in the oxygen-excess, p-type material, i.e. see Step 1.

7. Unfortunately, the deeply trapped holes in the ground state of p-type PZT are not detected by EPR, so that aspect of the model cannot be directly confirmed. This has led to the suggestion that the deep traps always trap pairs of electrons, according to the "negative U" concept [12]. This assumes that a trap with one trapped hole is a deeper hole trap than an empty trap.

Our recent (and tentative) results on PZT suggest that there may be significant trapping of electrons in this material after reduction. Fig. 3 shows the conductivity of bulk PZT that has been quenched after equilibration at 700°C in various values of $P(O_2)$. The results were obtained by analysis of the ac impedance measured as a function of frequency. The long $P(O_2)$-independent plateau below 1 atm is typical of ionic conduction due to oxygen vacancies [13]. The sharp increase in bulk conductivity with decreasing $P(O_2)$ is to be expected for oxygen-deficient, n-type behavior. However, the substantial dependence of the conductivity on the temperature of measurement, i.e. the appearance of a thermally-activated conductivity, is suggestive of the ionization of trapped electrons. This is supported by the observation that the levels of conductivity are significantly less than those measured at the equilibration temperature. This behavior is consistent with a decrease in the carrier concentration with decreasing temperature, since the activation energy of about 1 eV seems much too large to be attributed to a thermally-activated mobility. However, the dependence of the n-type conductivity on the $P(O_2)$ of equilibration is much steeper than expected from conventional defect chemistry. This evidence for extensive electron-trapping in PZT is consistent with the evidence from EPR studies of photo-excited samples, and from theoretical calculations, that the Ti^{+4} ions in PZT represent rather stable electron traps in the form of Ti^{+3}.

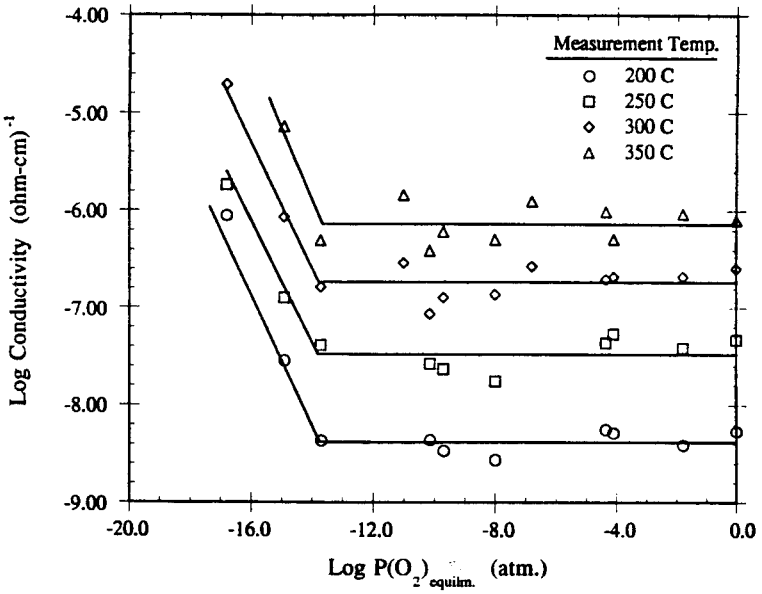


Figure 3. The AC conductivity of PZT quenched from 700°C after equilibration with various values of $P(O_2)$.

7. Conclusions

Nonstoichiometry, and the related electrical properties, can be readily explained for the alkaline earth titanates of the perovskite structure in terms of the stability of various lattice defects, and of the chemical properties of the constituent ions. There are deep, stable hole traps in these materials, due to acceptor impurity centers or cation vacancies, that result in the characteristic insulating properties of these compounds in the oxidized state. On the other hand, there is no significant trapping of electrons in these materials, and the reduced compounds are semiconductors. There is no evidence for thermally-activated mobilities for either electrons or holes.

The Pb-based systems are somewhat different because of the peculiar electronic structure of the Pb^{+2} ion with its "inert pair" of 6s electrons. These electronic states make up about half of the upper part of the valence band, and cause each Pb^{+2} ion to be a potential shallow hole trap. This results in a thermally-activated mobility for holes in PZT, with an activation energy of about 0.3 eV. It also appears that the Ti^{+4} ions can act as rather stable electron traps, perhaps as deep as 1 eV. The presence of shallow, transient hole traps in the form of Pb^{+3}, and of more stable electron traps in the form of Ti^{+3}, are specific properties of the PZT system. They may be of considerable importance in the case of optical applications for this family of compounds.

8. Acknowledgments.

The support of the Divisions of Materials Research of NSF and of ONR/ARPA is gratefully acknowledged.

9. References

1. Kroger, F. A. and Vink, H. J. (1956) in Seitz, F. and Turnbull, D. (eds.), *Solid State Physics, Vol. 3*, Academic Press, New York, pp. 307.
2. Jonker, G. H. and Havinga, E. E. (1982), *Mat. Res. Bull.* **17**, 345.
3. Chan, H. M., Harmer, M. P., and Smyth, D. M. (1986), *J. Am. Ceram. Soc.* **69 (6)**, 507.
4. Lewis, G. V. and Catlow, C. R. A. (1983), *Rad. Eff.* **73 (1-4)**, 307.
5. Waser, R. (1988), *J. Am. Ceram. Soc.* **71 (1)**, 58.
6. Chan, N.-H., Sharma, R. K., and Smyth, D. M. (1981), *J. Am. Ceram. Soc.*, **64 (9)**, 556.
7. Chan, N.-H., and Smyth, D. M. (1976), *J. Electrochem. Soc.*, **123 (10)**, 1584.
8. Smyth, D. M. (1984), *Prog. in Solid State Chem.*, **15**, 145.
9. Warren, W. L., Seager, C. H., Dimos, D., and Friebele, E. J. (1992), *Appl. Phys. Lett.*, **61**, 2530.
10. Robertson, J., Warren, W. L., Tuttle, B. A., Dimos, D., and Smyth, D. M. (1993), *Appl. Phys. Lett.*, **63 (11)**, 1519.
11. Prisedsky, V. V., Shishkovsky, V. I., and Klimov, V. V. (1978), *Ferroelectrics*, **17**, 465.
12. Watkins, G. D. (1984), *Festkorperprobleme*, **XXIV**, *Advances in Solid Physics*, pp.163.
13. Waser, R. (1991), *J. Am. Ceram. Soc.*, **74 (8)**, 1934.

X-RAY DIFFRACTION LINE PROFILE ANALYSIS OF ZnO THIN FILMS DEPOSITED ON Al-SiO_2-Si SUBSTRATES

P. SUTTA,[1] Q. JACKULIAK,[2]
V. TVAROZEK[3] AND I. NOVOTNY[3]
1. Military Academy, Department of Physics, 031 19 Liptovsky, Mikulas, Slovakia
2. Electrotechnical Faculty, Technical University of Transport and Communication, 010 00 Zilina, Slovakia
3. Department of Microelectronics, Slovak Technical University, Ilkovicova 3, 812 19 Bratislava, Slovakia

ABSTRACT. ZnO thin films have been deposited on Al-SiO_2-Si substrates by reactive sputtering. X-ray diffractometry was used to determine microstructural disorder parameters in ZnO thin films with strong preferred orientation c-axis orientation. The influence of an Al_2O_3 buffer layer on preferred c-axis orientation and microstrain of crystallites was also studied. An increase in width of diffraction peaks from omega scans were associated with systematic variation of an Al_2O_3 buffer layer technology. The microstrains showed only a small dependence on the presence of a buffer layer, but there was a definite relationship between microstrain and crystallographic direction of the films. The domain size was approximately 200 nm and it increased in a ZnO thin film deposited on an Al_2O_3 buffer layer. The next Al_2O_3 layer deposited on a ZnO layer markedly influences all investigated parameters. Apart from increasing microstrains and decreasing domain size an extensive asymmetry of the (002) diffraction line developed due to stresses with a stress gradient along the c-axis.

1. Introduction

Zinc oxide (ZnO) is a very interesting wide band gap semiconductor with hexagonal-close-packed lattice structure (a=0.325 nm, c=0.5206 nm) with one-half of the tetrahedral interstices filled. Thin films of ZnO prepared by various techniques have found many applications in semiconductor technology, in the development of new solar elements, as well as in surface acoustic wave applications due to their very good transparency in the visible region and very good piezoelectric properties.

The piezoelectric quality of ZnO films are enhanced by their high resistivity and preferential orientation of their columnar grains. Two textures of polycrystalline ZnO films are important. The c-axis in a hexagonal structure should be perpendicular [(001) orientation] or parallel [(100) orientation to the substrate.

O. Auciello and R. Waser (eds.), Science and Technology of Electroceramic Thin Films, 327-334.
© 1995 *Kluwer Academic Publishers. Printed in the Netherlands.*

The physical properties of ZnO thin films are, in addition to other factors, influenced by their structure which mainly depend on the sputtering conditions and on substrate structure. One of the appropriate methods for examining thin film structure is X-ray diffraction.

2. Experimental Procedure

In this study, a planar r.f. sputtering unit (Perkin-Elmer 2400/8L) was used for the preparation of Al, Al_2O_3 and ZnO thin films which were deposited as multilayered structures (See Fig. 1) on (100) oriented silicon wafers), which were covered by a SiO_2 layer, approximately 800 nm thick. Three targets of 203 mm in diameter (metallic Al, ceramic Al_2O_3 and ceramic ZnO) were used allowing the deposition of different thin-film structures in one sputtering run [1].

The sputtering chamber was pumped down to 2×10^{-5} Pa before admission of the gases. The sputtering gases were pure argon (99.999%) and a 25% Ar / 75% O_2 gas mixture. The silicon substrates were externally heated to 300 °C during deposition. The thickness of the sputtered aluminum lower contact layer was 100 nm. An intermediate layer of Al_2O_3, 100 nm thick, was deposited by sputtering from an Al_2O_3 target. The ZnO layers of 2.5 μm in thickness were sputtered at an r.f. power of 400 W in a 25% Ar / 75% O_2 gas, with a total gas pressure mixture of about 1.3 Pa. For electrical measurements (cross resistance), an upper aluminum contact was deposited by evaporation.

X-ray diffractometry was carried out in the automatic powder diffractometer URD-6 with Bragg-Brentano goniometer using CuKα radiation (0.154178 nm). Preliminary X-ray photographs on the film showed that all ZnO thin films were preferrably oriented in the [001] direction. Other diffraction lines observed were (102) and (103). Very weak (004) diffraction lines were also observed. Due to this fact, we have performed an omega scan of (002) diffraction lines on each sample and we have measured the diffraction profiles of the (002), (102) and (103) peaks as far as allowed by the preferred orientation.

The width and displacement of the top of the omega-scan profile against the plane normal (002) were evaluated on the base of the omega-scan curves. Diffraction profiles were corrected according to the background, and a separation of CuKα radiation into α1 and α2 components has also been made.

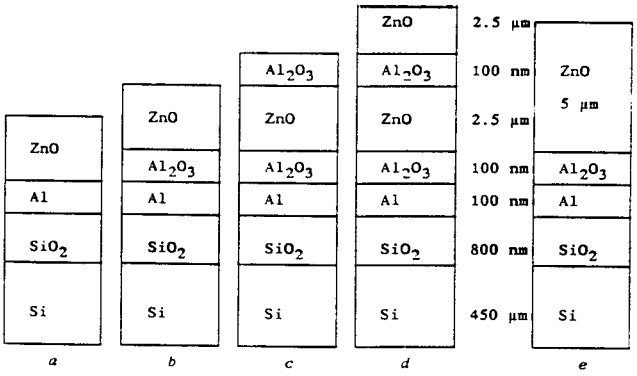


Figure 1. Schematic of the multilayered Al_2O_3 / ZnO structured films.

The method proposed by Langford [2] has been used for calculating the dimensions of the areas of coherent scattering <D> (crystallite size) and the microstrains <ε>. The chemical pure ZnO powder (99.9%) was used as an instrumental standard. Pattern decomposition was carried out by means of our program to obtain parameters defining the peak position (2θ), height (I_0) integral intensity and FWHM (full width at half maximum 2w) restricted to the $K\alpha_1$ component of the measured profile. The integral breadth β = area / I_0 was also calculated. It should be noted that line broadening studies require a good description of profile tails to reduce imprecision on breadth measurements [3].

2. Results and discussion

In all cases, X-ray diffraction measurements showed a very strong preferred orientation along the [001] direction (See Fig. 2). The characterization texture of ZnO thin films was obtained by the omega-scan. The angular distribution of crystallites for ZnO thin films deposited with various combinations of Al_2O_3 buffer layers is demonstrated in Fig. 3. The width of the omega-scan curves for the (002) diffraction line are greater than those in the case when TiN [4] and Si_3N_4 [5] buffer layers were used. The Al_2O_3 buffer layer resulted in an increase in width of the omega-scan trace (See Table 1). The next Al_2O_3 buffer layer deposited on the ZnO thin film caused a decrease in width of the omega-scan. The maximum value (17.2 degrees) was observed in the case of sample d (Si-SiO_2-Al-Al_2O_3-ZnO-Al_2O_3-ZnO). All deviations of the maximum of the omega-scan curves from the c-axis normal were negative (about -1 degree). Some X-ray diffraction data for ZnO thin films are presented in Table 1.

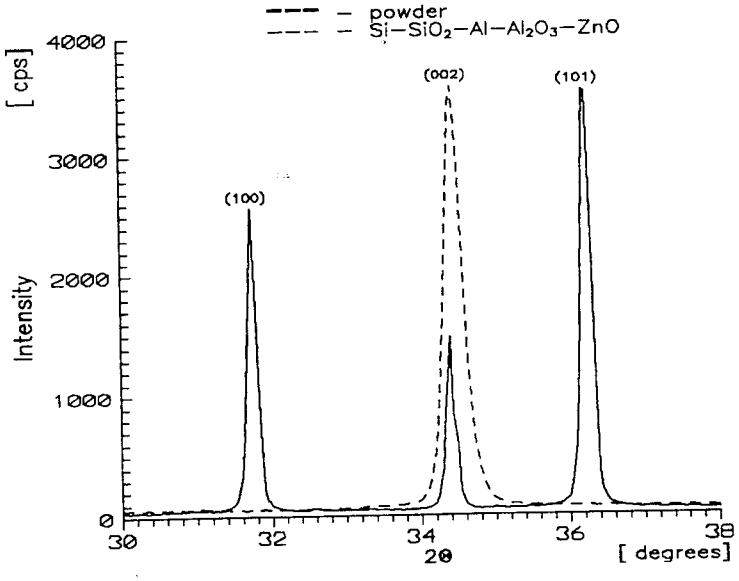


Figure 2. Diffraction patterns for a ZnO thin film and ZnO powder.

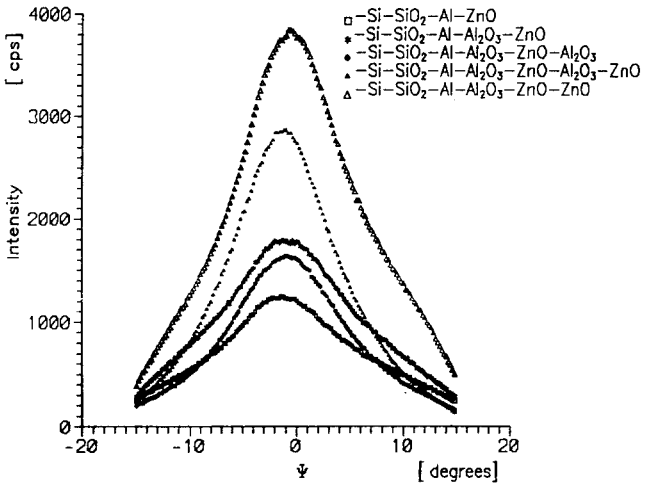


Figure 3. The influence of buffer layers on the distribution function of (002) planes of ZnO thin films obtained by the omega-scan method using a Bragg - Brentano goniometer ($\psi = \omega - \theta_{002}$).

TABLE 1. X-ray diffraction data for ZnO thin films

Parameter		Sample				
		a	*b*	*c*	*d*	*e*
Diffraction angle 2θ for (002) peak [deg]		34.48	34.48	34.43	34.43	34.46
Intensity of (002) peak [cps]		1210	2170	1540	2630	3200
Width of omega-scan of (002) peak [deg]		12.1	15.5	12.8	17.2	13.8
Deviation of maximum of the omega-scan curve from the c-axis normal [deg]		-1.5	-0.8	-0.9	-1.3	-0.7
Microstrains <ε> x10^3	(002)	1.36	1.56	1.77	1.54	1.01
	(102)	2.57	-	2.88	2.84	2.28
	(103)	2.27	1.57	2.08	2.75	1.71
Crystallite size <D> [nm]	(002)	170	400	180	175	180
	(102)	190	-	90	165	420
	(103)	235	90	130	215	145
Deviation of peak position $\delta(2\theta) = 2\theta_{TF} - 2\theta_{PVD}$ [deg]	(002)	0.02	0.02	-0.03	-0.03	0
	(102)	0.02	-	-0.02	0.01	0.01
	(103)	0.02	0.01	0	0.02	0

The dependence of the FWHM (2w) and the intensity of the peaks for the different buffer layers is demonstrated in Fig. 4.

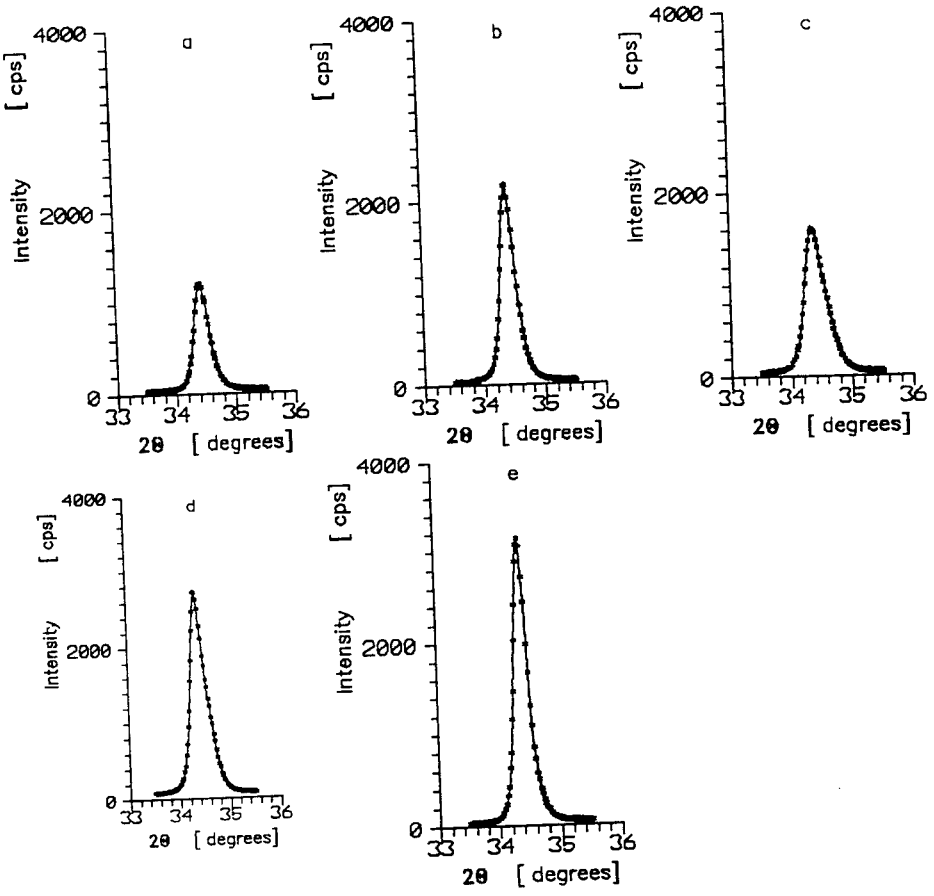


Figure 4. The influence of buffer layers on the intensity and width of the (002) diffraction lines of ZnO thin films.

Calculated values of crystallite size and microstrains are presented in Table 1. The microstrains in the [102] and [103] directions are higher than those in the main texture [001] direction. It seems that the calculated value of breadth of the diffraction line primarily caused by crystallite size includes a contribution from stacking-faults, which are most likely different for [001], [102] and [103] directions. Due to the preferred orientation of ZnO thin films, it was not possible to measure more diffraction lines to determine the stacking-fault probability [3].

The $\sin^2 \psi$ method was used to calculate residual stresses. Because of the very strong preferred orientation of the ZnO thin films, the lattice strain was determined from the (004) diffraction line. The lattice strains are given by:

$$\varepsilon_{\phi\psi}^{004} = (d_{\phi\psi}^{004} - d^{004}) / d^{004}$$

where $d_{\phi\psi}^{004}$ and d^{004} are the interplanar spacings of the (004) planes in ZnO crystallites in the stressed and stress-free state, Strains were measured with a $|\Delta\varepsilon| = 5 \times 10^{-5}$ error.

The dependence of the calculated residual stress σ on the buffer layers is presented in Table 2.

TABLE 2. Measured stress for ZnO thin films.

	Sample		
	c	*d*	*e*
$\sigma_1 + \sigma_2$ [MPa]	-416	-707	90
σ_φ [MPa]	-190	-320	68

For ZnO thin films 5 μm thick, the film stress is relatively small. The Al_2O_3 buffer layer deposited on a ZnO thin film (sample c: Si-SiO_2-Al-Al_2O_3-ZnO-Al_2O_3) caused an increase in the residual stress of the ZnO film.. The next ZnO layer deposited on Al_2O_3 (sample d: Si-SiO-Al-Al_2O_3-ZnO-Al_2O_3-ZnO) resulted in an additional increase of the residual stress. It should be noted that the gradient of stress (i.e.$\sigma_3 \neq 0$) which has been observed in samples c and d (typical asymmetry of line profile [6], Fig. 5) likely leads to a greater calculated negative tensile stress than the real value of stress [7].

In comparison with the X-ray diffraction results, the cross resistance measurement of ZnO thin films is also presented. It was measured using the constant current method (Teromet KU-106).

The cross-resistance of these thin-film structures (Table 3) is primarily determined by the resistivity of each layer. Therefore, the changes of the total cross-resistance are dependent on the presence of an intermediate Al_2O_3 layer as well as on the resistivity of the ZnO layer. These ZnO films have a columnar grain structure, which is textured in the [001] direction. One can expect to increase the cross-conductivity (along the [001] direction) with an increase of the [001] oriented grain size. The cross-resistance of ZnO films was 1.31 kΩ (Al-ZnO-Al structure - sample a). Intermediate layers (sample c) have

a direct influence on the cross-conductance, but they also have a strong influence on the anisotropic properties of the crystalline structure (Table 1). Sample e (Al-Al_2O_3-ZnO-ZnO) shows relatively low cross-resistance in comparison with sample d (Al-Al_2O_3-ZnO-Al_2O_3-ZnO structure) which is most likely caused by the higher conductivity of a double layer of ZnO, which is not interrupted by an Al_2O_3 layer.

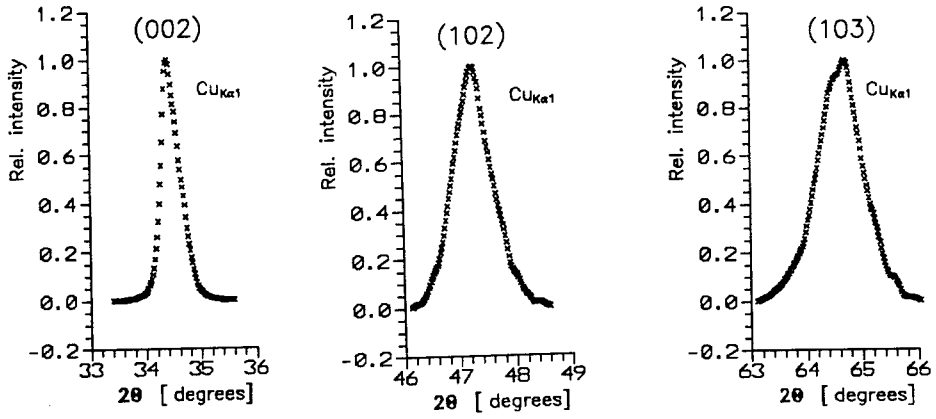


Figure 5. Line profiles of (002), (102) and (103) diffraction lines for sample c.

TABLE 3. Cross-resistance for ZnO thin films.

	Sample			
	a	*c*	*d*	*e*
Cross resistance [kΩ]	1.31	2.18	3.63	2.73

3. Conclusions

Omega-scan traces of our ZnO thin films are quite broad, being more than 10 degrees for all the examined samples. The smallest width has been observed in the sample where only a thin Al layer was deposited under the ZnO layer. Insertion of an Al_2O_3 layer between the Al and ZnO layers resulted in an increase of the omega-scan width. The next Al_2O_3 layer deposited on the ZnO thin film decreased the omega-scan width and substantially changed the (002) line profile. Taking into consideration the displacement of diffraction lines, we can assume that this asymmetry is caused by the stress gradient

in the [001] direction in the ZnO thin film. It has been observed that the stress in the ZnO thin film is present in all samples, but the gradient of this stress in the [001] direction is only caused by the Al_2O_3 layer deposited on the ZnO thin film.

Broadening of the diffraction lines is caused mainly by microdeformations. We have also observed that the changes in the lattice parameters, as well as microdeformations, depend on the direction of measurement in the ZnO film. Thus, we have determined that the ZnO thin films produced by sputter-deposition for the results reported here are considerably anisotropic.

4. References

1. Tvarozek, V., Novotny, I., Cerven, I., Kovac, T. and Lacko, T. (1992), *Sensors and Actuators* **A 30**, 123.
2. Langford, J.I. (1978), *J. Appl. Cryst.* **11**, 10.
3. Langford, J.I., Boultif, A., Auffredic, J.P. and Louer, D. (1993), *J. Appl. Cryst.* **26**, 22.
4. Sutta, P., Jackuliak, Q., Tvarozek, V. and Novotny, I. (1993), *Proc. 7th Czechoslovak Conf. on Thin Films*, Liptovsky, Mikulas, pp. 63.
5. Panwar, B.S., Bhattacharya, A.B., Nagapal, K.C. and Mall R.P. (1989), *Thin Solid Films* **168**, 291.
6. Kraus, I. and Trofimov, V.V. (1987), *Rentgenova Tenzometrie, Academia Praha.*
7. Kraus, I (1985), Uvod do Strukturni rentgenografie, Academia Praha.

ELECTRON EMISSION FROM FERROELECTRICS

H. GUNDEL
Technische Universität Berlin,
Institut für Theoretische Elektrotechnik,
Einsteinufer 17, Sekr. EN 2, D-10587 Berlin,
Germany

ABSTRACT. Electron emission from ferroelectrics has attracted much interest since the tremendous increase of the emission current in 1988 at CERN. Several potential applications as a high brightness electron source are actually under examination; but also the investigation of emission from ferroelectric thin films seem to be very promising. In order to scale down the necessary parameters from the working thick ceramic emitters to thin films, field calculations were performed. Using a real device geometry, the strong influence of the grid electrode on the electric field distribution inside and outside the ferroelectrics is shown. Based on a fundamental description of the emission mechanism, previous experimental results from ceramics are reviewed and discussed together with the results of the field calculations.

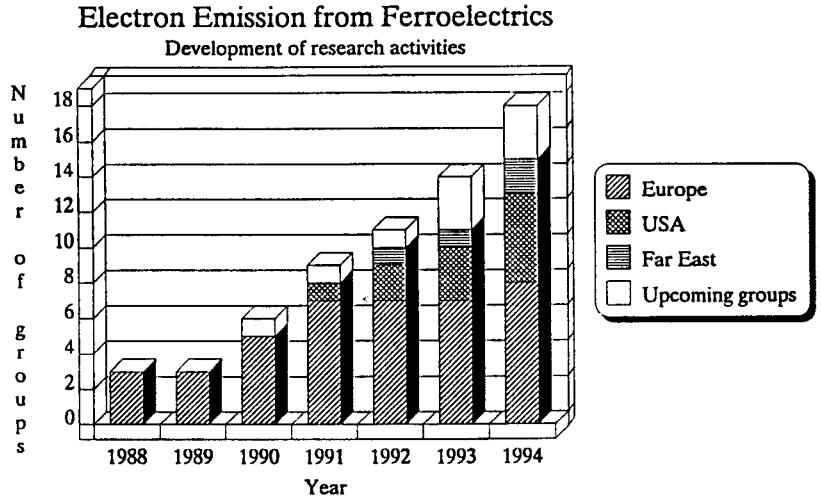
1. Introduction

Electron emission from ferroelectrics due to polarization reversal has been anticipated as early as in 1960, when the existence of a surface layer of lower permittivity than of the bulk was found in barium titanate, and the resulting electric field was calculated to be of the order of MV/cm. Consequently it has been stated "that part of the charge neutralization in the surface layer may arise from field emission process" [1]. In the following decades the (exo)electron emission phenomenon has been comprehensively investigated at various ferroelectric materials, using monodomain and multidomain single crystals and ceramics, under different conditions like atmospheric air, low pressure gas, or vacuum, and provoked by the change of spontaneous polarization due to thermal stimulation, light stimulation, alternating sinusoidal and pulsed electric fields. The rate of polarization change was rather small in those experiments and the emitted electron current did not exceed 10^{-9} A/cm^2 [2-4]. Copious electron emission has been anticipated [5,6] and occured when changing the polarization to ns-scale in PLZT, yielding emission many orders of magnitude higher than before as measured in 1988 at CERN [7,8]. Caused by the presumption of possible applications, mainly in the field of high power and accelerator technology and for vacuum microelectronics, electron emission from ferroelectrics experienced immediately reviving interest and today about 15 research groups are concerned with this phenomenon worldwide.

Together with the experimental progress, attempts to gain an improved theoretical understanding of the emission mechanism were made. More recently, the potential-energy diagram for electrons in a ferroelectric has been discussed [9-18], further developing a model of the emission mechanism that had been proposed initially in 1984 [4]. The

O. Auciello and R. Waser (eds.), Science and Technology of Electroceramic Thin Films, 335-351.
© 1995 *Kluwer Academic Publishers. Printed in the Netherlands.*

depolarizing electric field at the polar surfaces under pyroelectric conditions has been calculated [10-13]. Further conditions, including ferroelectric switching, were summarized and the dynamics of the switching process has been made visible by emission image technique [11]. A detailed analysis of the electron energy diagram, introducing dielectric surface layers and taking into account the potential barrier at the crystal-vacuum interface, was reported in 1993 where high density electron emission has been characterized as overbarrier emission of hot electrons generated due to a drastic increase of the surface layer conductivity [14]. Electron emission induced by an alternating electric field was discussed in Ref. 15 to 18. In the corresponding potential diagram, however, only the surface was considered, and it is not clearly stated whether the applied potential was taken into consideration. In all of these calculations [9-18], the ideal case of a bare ferroelectric surface (without electrode) facing the vacuum was considered with the potential's reference being separated from the ferroelectric by a vacuum gap.



Copious electron emission (1A/cm^2 and more), however, has exclusively been observed when using (partially) electroded ceramic material and when producing a strong polarization change induced by an electric field directly applied to the surface electrodes of the ferroelectric [7-9,19-40]. Therefore, additionally to a basic description of the emission mechanism, the present paper focuses on the influence of the electrode structure. Field calculations using MAFIA codes [41] have been performed which show the internal and external field distribution of an emitter and which take an electrode geometry into account as commonly used. Exemplary results from earlier investigations using thick ceramic emitters are reviewed in this context and indicate a possible way to approach electron emission from thin ferroelectric films.

2. Copious Electron Emission Induced by a Fast Change of Polarization

Ferroelectric materials are known to be macroscopically neutral although a high spontaneous polarization P_S is present which is normally screened instantaneously when the material becomes polar. The surface charge density P_S can be determined for instance by integrating the pyrocurrent generated at the surface electrodes while the material is

undergoing a transition to the non-polar phase due to heating. Thus, pyrocurrent can be considered to be a response of the ferroelectric to a disturbance of the charge equilibrium and can be characterized as a relaxation current neccessary to reach the new equilibrium state (e.g. at a higher temperature).

Let us consider a ferroelectric in its polar phase, fully covered with an electrode at one surface (rear electrode RE) and partially electroded at the opposite face (grid electrode GE). In Fig. 1a a cross-section of a part of the ferroelectric emitter is shown at the interface between the electrode and the bare material surface. Spontaneous polarization is thought to be originally oriented with the positive end ([+]) towards the grid electrode being compensated by negative charge carriers (-), and vice versa at the opposite surface, i.e. the charge at the negative end ([-]) of the representative dipole vector is compensated by a lack of electrons (o). Polarization is fully compensated and the ferroelectric appears neutral. Provided polarization is inverted fast (e.g. within 100 ns), the situation changes drastically (Fig. 1b). Underneath the electroded part of the surface a charge equilibrium can be achieved immediately by an electron flow from or to the circuit (indicated by arrows in Fig. 1b).

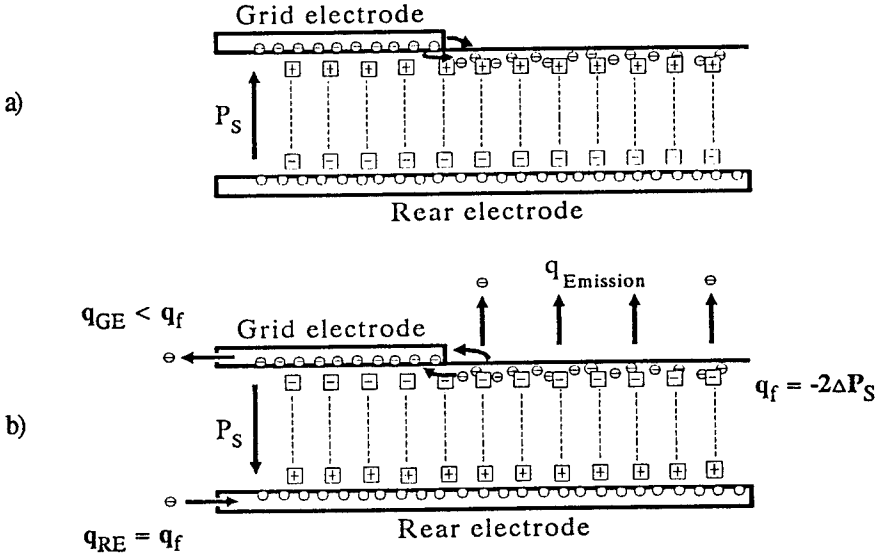


Figure 1. Electron emission induced by polarization reversal. Compensated and electronically neutral state prior to emission (a) , and emission caused by the action of a negative surface charge density q_f (b).

In the region where the ferroelectric is not covered by any electrode, however, for a transient time a surplus of negative charge $q_f = -2\Delta P_S$ is accumulated in the surface layer and results in a high potential, repulsive for electrons. They will be accelerated instantaneously and relaxation is achieved by an electron flow oriented to the vacuum. Thus emission is governed by the development in time of a repulsing potential, which raises as the amount and the speed of polarization change in the material is increased, and declines as a consequence of relaxation by emission. In Fig. 1b the ideal situation of maximum repulsing potential is shown. The relaxation currents are indicated by arrows

with the electron flow to the rear electrode q_{RE} being equal to the sum of the flow from the grid electrode q_{GE} and the emission $q_{Emission}$ to the vacuum.

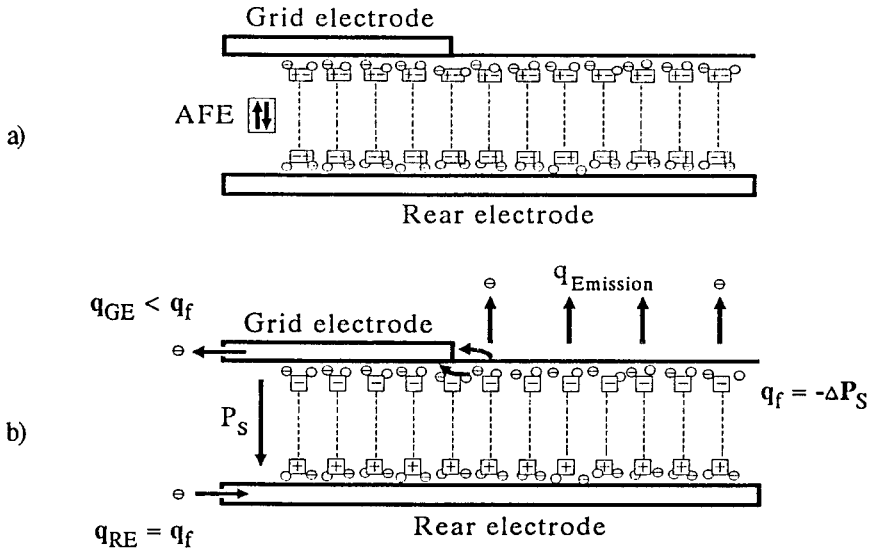


Figure 2. Electron emission induced by a transition from the antiferroelectric to the ferroelectric phase. Compensated and electronically neutral state prior to emission (a) with the antiferroelectric state indicated by [+-], and emission caused by the action of a negative surface charge density q_f (b) when the ferroelectic phase is induced.

At a ferroelectric material, assumed to be initially in its non-polar antiferroelectric phase, a similar interpretation of the mechanism of electron emission can be given (Fig. 2). The notation of the charges is the same of Fig. 1; in addition [+-] denotes the antiferroelectric structure of the lattice. The unit cell has oppositely directed dipoles with no net dipole moment, thus macroscopic polarization does not exist and again the material is neutral and at equilibrium (Fig. 2a). If, by a fast phase transition, the ferroelectric state is induced in the antiferroelectric matrix of the lattice as indicated in Fig. 2b, the condition will be similar to that discussed before. At the electroded area of the material, charge equilibrium can be achieved by a current flow from and to the electrodes. The non-compensated charge $q_f = -\Delta P_S$ underneath the free part of the material's surface again gives rise to a potential, for a transient time and repulsive for electrons, which causes emission to the vacuum. Again the sum of $q_{Emission}$ and q_{GE} has to be equal to the charge q_{RE}.

Both cases discussed above rely on a fast change of the polarization in order to minimize relaxation within the material. Appropriate ways to achieve this have been discussed earlier [5,21,29]; most reliable is the application of pulsed electric fields via electrodes, especially with respect to controlling, reproducibility, and high repetition rates. Phase transitions as well as polarization reversal may be realized at a ns-scale. When applying a negative pulse to the rear electrode, switching and phase shift will occur in a proper direction in order to achieve a negative (and for electrons) repulsing potential

at the emitting surface.

Whilst emission is consistently assumed to be a consequence of the high internal potential gradient at polarization switching, the origin of the electrons is still discussed controversely. They may be accelerated from preferable energy levels (donor states) inside the surface layer and emitted with high kinetic energy as "hot electrons" [e.g. 9,14,18] or they may be drawn from a plasma layer covering the ferroelectric surface [30]. The restoration of charge carriers after the emission process when (self-) resetting the emitter was also not investigated. Charge injection from the electrode edges via the vacuum as well as charge transport due to the (very low) conductivity in the material is possible, however, data on these processes are not available.

For the simplified model discussed in Fig. 1 and Fig. 2, it has been assumed that the change of polarization takes place homogeneously, i.e. ΔP_S is the same, no matter of whether the material is covered by an electrode or not. Actually, this is not the case since the type of material (single crystals, ceramic material), its stochiometric composition, the actual phase, the domain and grain structure, switching kinetics (domain wall motion), the geometry of the problem (dimension of the ferroelectric, shape of the electrodes), etc. are strongly involved in the emission process. While the first factors are determined once a specimen has been selected, there is a critical influence on emission due to the geometry and the external circuit parameters, which may be optimized. This is discussed in detail below.

3. The Internal and External Field Distribution of a Ferroelectric Emitter

3.1. GEOMETRY AND GENERAL ASSUMPTIONS

Up to now, most of the results have been obtained from disc-shaped cathodes, equipped with a grid electrode at the emitting surface which consists of many parallel stripes (evaporated gold or platinum) interconnected at the circumference [9]. At the opposite face normally a circular electrode is used. The scheme of a cross-section is shown in Fig. 3 indicating the geometry and the parameters that were used for the field calculations.

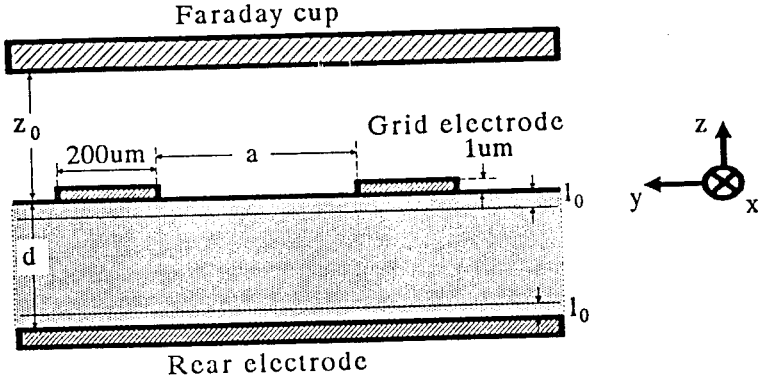


Figure 3. Scheme of a cross-section of a typical ferroelectric emitter geometry.

The spacing **a** between the single electrode stripes is 200 μm and their length in the x-direction is approximately 10 mm. Therefore in the calculations the geometry is assumed to be infinite in the x-direction, thus treating the problem as planar in the y-z-plane, and as periodic in y-direction; the dimension of the electrode stripes is constant (200 μm wide and 1 μm thick), the thickness **d** of the material (electric permittivity ε_r) is variable. The grid electrode, the rear electrode at z = -d, and the electron collector (Faraday cup) located in vacuum (ε_0) at a distance z_0 = 500 μm are thought to be ideally conducting. On both surfaces of the ferroelectric, layers of a thickness l_0 can be introduced to the model optionally. They may have different permittivity than the bulk.Most experimental data were obtained with a thickness varying from 0.1 mm to 1mm. The electron collector either was a real Faraday cup or sometimes a simple plate consisting of graphite in order to reduce secondary electron efficiency.

Under the presumption of a linear dielectric permittivity and an isotropic medium, the potential and the electric field of the arrangement have been calculated by MAFIA codes [41] which solve **MA**xwell's equations using a **F**inite **I**ntegration **A**lgorithm. Normally ferroelectric hysteresis should be taken into account, however, at high frequency switching (10 - 100 MHz) the hysteresis loop appears rather slim and is oriented flat. Thus the error that occurs when utilizing a linear dependence of the polarization **P** on the electric field **E** is much less than it would be for the case of low frequency switching. According to [42] PLZT ceramics typically have a grain size of 2 to 15 μm. With the grains being randomly oriented within the material, the assumption of isotropy for a first order approximation of the potential distribution may be justified. The Static Solver module of MAFIA provides the potential distribution $\Phi(y,z)$ or the electric field $\mathbf{E}(y,z)$ prior to any relaxation by emission or conductivity that results when a potential is applied in order to change polarization. Throughout the calculations a negative potential Φ_{RE} has been used at the rear electrode and the grid electrode is always kept to ground (Φ_{GE} = 0). The Faraday cup potential was either assumed to be at ground or was set to a positive extraction potential Φ_{FC}.

3.2. CALCULATION OF THE BASIC STRUCTURE

The electric field obtained from the MAFIA calculations is shown in Fig. 4 for different device geometries and it is represented by the length (amplitude) and direction (orientation) of arrows, normalized to a maximum arrow of each graphic. The numerical value (MAX ARROW) of the electric field is given in the figure caption. The thickness of the ferroelectric and the distance from the ferroelectric surface to the Faraday cup is 500 μm each. The ferroelectric material is assumed to have an uniform permittivity ε_r = 500, and a potential Φ_{RE} = -1 is applied. The geometries of Fig. 4a and Fig. 4b are rather simple and can be calculated analytically. In Fig. 4a the interconnecting surface between the ferroelectric and the vacuum is fully covered with an electrode and grounded. Consequently, the electric field inside the material E_i is homogeneous and can be calculated to be Φ_{RE}/d . Contrary to this, in Fig. 4b the reference to the potential Φ_{RE} is assumed to be at the Faraday cup and a bare ferroelectric surface (without electrode) is supposed to face the vacuum. For this case, the electric field inside the material $E_i = \Phi_{RE}/(\varepsilon_r+1)d$ and the field at the vacuum is $E_0 = \varepsilon_r E_i = \varepsilon_r \Phi_{RE}/(\varepsilon_r+1)d$. Due to the high permittivity of the ferroelectric, almost the whole potential drops on the vacuum and the existing field E_i is too small to be shown in Fig. 4b.

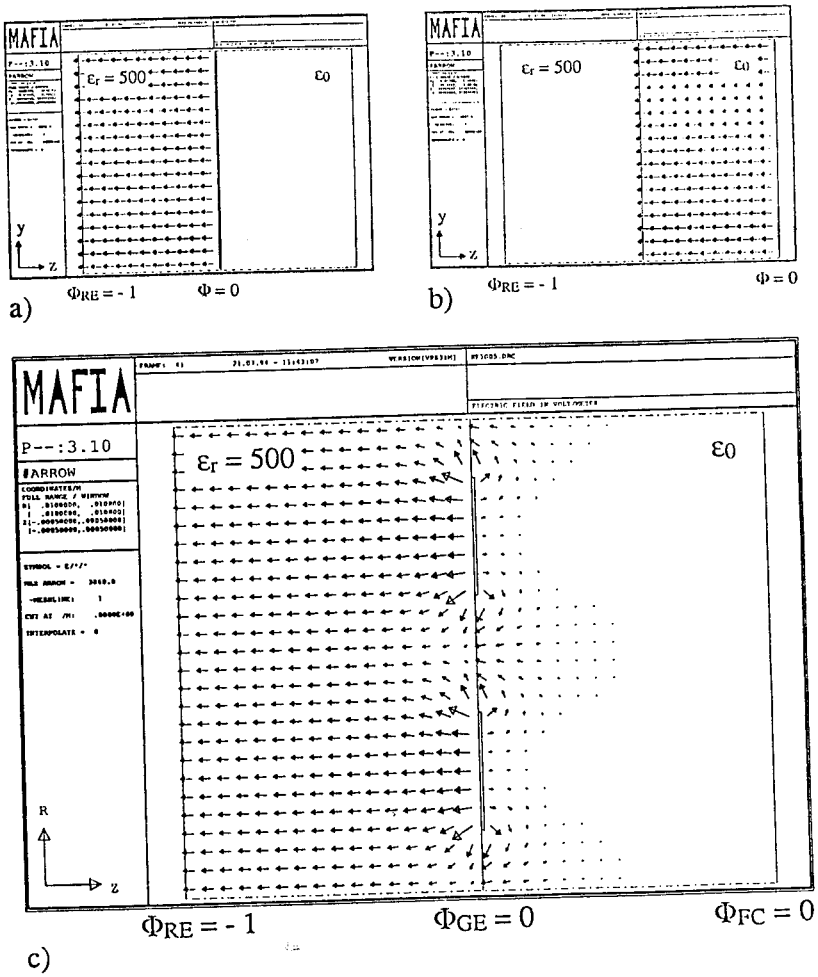


Figure 4. Electric field calculated by MAFIA for different electrode configurations: (a) Fully electroded at both surfaces. (b) without electrode where the ceramics faces vacuum; (c) with a grid electrode at the emitting surface. MAX ARROW is equal to 2000 V/m (a), 1997 V/m (b), and 3860 V/m (c); the applied potentials are indictated.

The geometry of Fig. 4c appears to be a mixture of the first two cases, approaching a fully electroded structure (Fig. 4a) or a material without an electrode at the emitting face (Fig. 4b) when the ratio a/d (spacing between the electrode stripes / thickness of the ferroelectric) is decreasing or increasing, respectively.
Several features can be recognized:
a) There is a strong electric field E_0 in vacuum between the electrode stripes which is oriented to the bare ferroelectric surface.
b) The field lines in vacuum originate either from the Faraday cup or from the grounded electrode. Therefore E_0 is strongly bent at the electrode edges and almost parallel to the z-direction between the electrodes.

c) The field inside the material E_i is oriented rather parallel to the surface at the material/vacuum interface.
d) The field E_i underneath the material's surface decreases with increasing distance to the electrode stripes.

Qualitatively, the calculations show that the electric field $\mathbf{E_i}(y,z)$ in the material is strongly non-homogeneous, particularly near the electrode edges, and up to a depth of approximately 50 µm in the material. $\mathbf{E_O}(y,z)$ is not homogeneous any more, too. For a more thorough view, the ratio a/d was changed while keeping the grid geometry constant (a = 200 µm). This enables us to determine the leakage of potential into the vacuum Φ_L for a varying thickness d of the ferroelectric. For Φ_{RE}/d = const., which corresponds to a constant electric field in case of a fully electroded material, the potential-lines are shown for a material with d = 500 µm, 100 µm, and 20 µm in Fig. 5a to Fig. 5c. The potential difference between the single lines is 10%, starting with the line nearest to the grounded Faraday cup which represents 5% of the total potential, respectively.

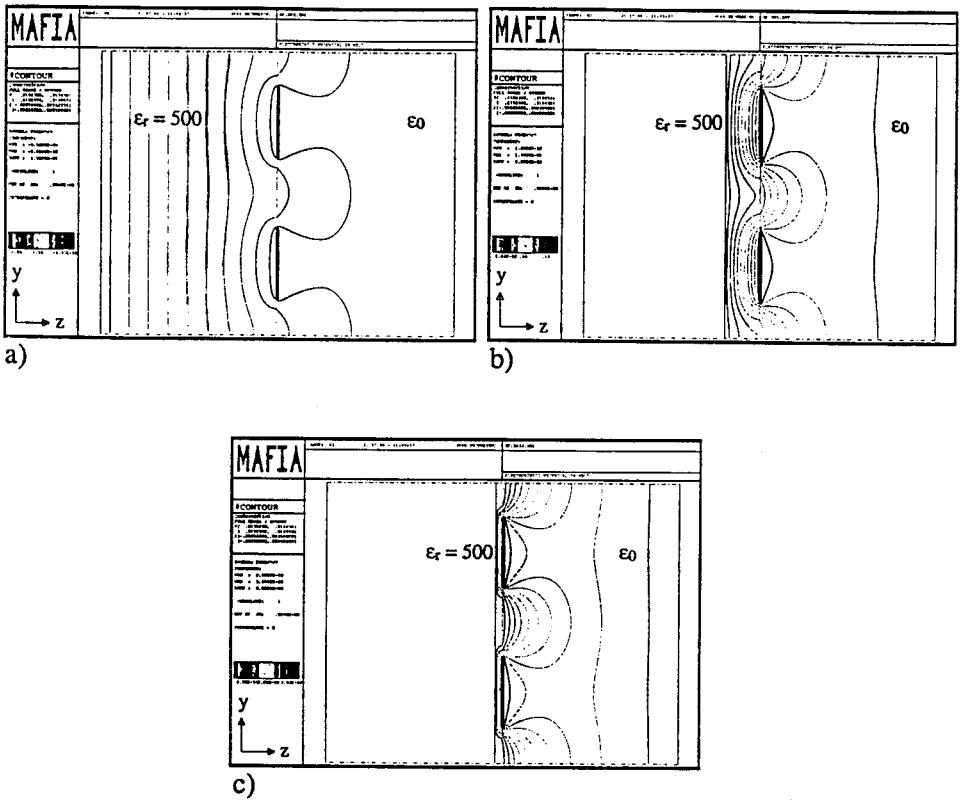


Figure 5. Potential leakage to vacuum for a material of thickness d = 500 µm (a), d = 100 µm (b), and d = 20 µm (c), at a constant grid spacing a = 200 µm. As in Fig. 4c, the grid electrode and the Faraday cup are grounded. The applied potential is Φ_{RE} = -1, -0.2, and -0.04 in Fig. 5a to 5c, respectively.

A detailed analysis of the data showed that the leakage Φ_L at the plane of symmetry in the middle of the electrode stripes increases from 18 % to 95% as the thickness d is decreased from 500 µm to 20 µm. Consequently, the electric field inside the ferroelectric is smaller than expected and even much smaller when considering the case of a large ratio a/d (compare Fig. 5c). It has been verified, however, that the field distribution (i.e. the orientation and the relative amplitudes) near to the electrode edges does not change as the material's thickness is varied. The bending of the field remains unchanged, but the absolute field (MAX ARROW) decreases by a factor of more than 3 due to the change of the ratio a/d from 0.4 to 10.

A variation of the distance z between the emitting surface and the Faraday cup almost does not affect the potential distribution for a given ratio a/d, too. The calculated electrostatic potential at the plane of symmetry between two electrode stripes is shown in Fig. 6 as a function of z and with different Faraday cup positions as a parameter (z_1 = 0.25 mm, z_2 = 0.5 mm, z_3 = 1.0 mm, and z_4 = 5 mm). The Faraday cup is thought to be ideal conducting and is grounded, respectively. Likewise in Fig. 5b, the thickness of the ceramic is 100 µm. It can be seen that the potential drop from Φ_{RE} = -0.2 to Φ = -0.15 within the ferroelectric is the same for each case, thus indicating that the electric field $E_i(y,z)$ and consequentely also the switching and the emission condition remain unchanged.

In vacuum the main part of the potential (from Φ = -0.15 to Φ = -0.05) drop within 100 µm from the ferroelectric surface, generating a nearly constant electric field at the plane of symmetry between the electrod stripes. Only at a greater distance to the emitting surface there is an influence of the Faraday cup position on the electric field distribution $E_0(y,z)$; the potential decreases more slowly with increasing position z. Even for the farest position z_4, however, at a distance further than approximately z = 1.5 mm the electric field is zero.

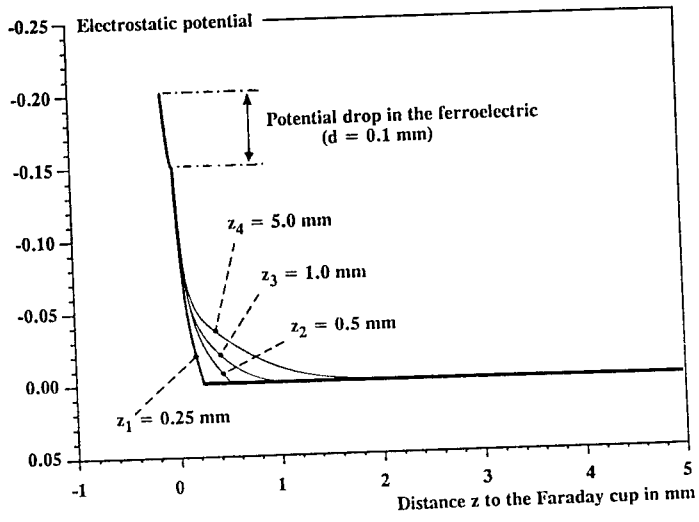


Figure 6. The electrostatic potential as a function of the distance z to the Faraday cup for the Faraday cup positions z_1 - z_4 as a parameter.

3.3. THE INFLUENCE OF AN EXTRACTION POTENTIAL

A magnified view (from Fig. 4c) of the region of the electrode edge is shown in Fig. 7a, with the visible window being 140 μm in the z-direction and 90 μm in the y-direction. The influence of an external extraction potential on the field distribution can be seen in Fig. 7b. The previously grounded Faraday cup (still located at z = 500 μm) is now excited for a potential $\Phi_{FC} = -\Phi_{RE} = 1$, which is attractive for electrons. There is an obvious change in the field distribution $E_0(y,z)$ with the field being oriented more towards the z-direction. Only very near to the electrode edge, up to a distance of approximatively 10 μm, the electric field is still bent to the electrode. It should be noted that the internal field $E_i(y,z)$ is almost unaffected by the application of the extraction potential.

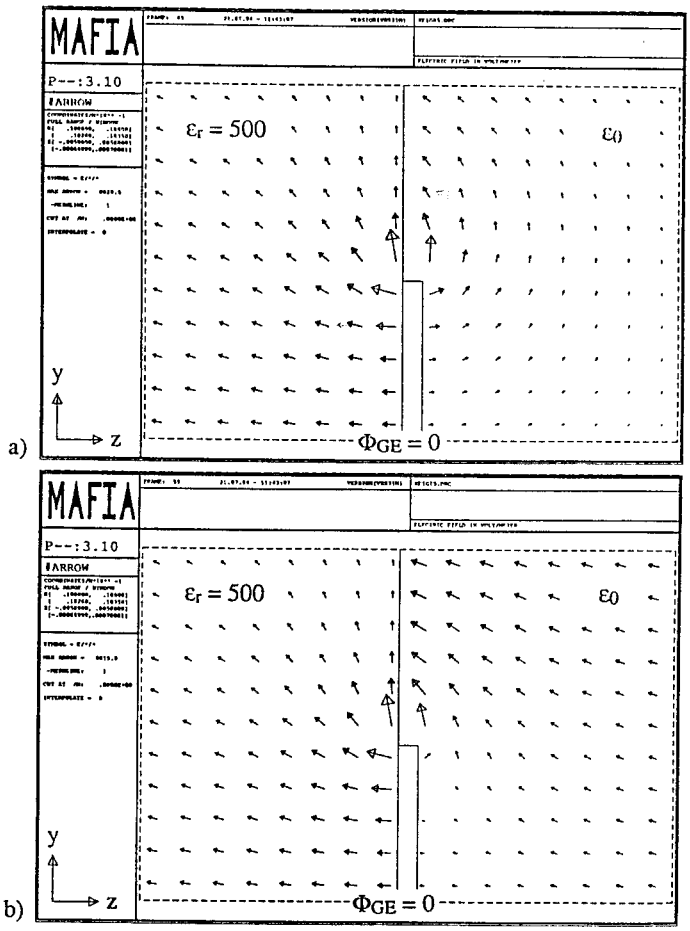


Figure 7. Magnified view of the electric field (MAX ARROW = 8020 V/m)at an electrode edge, for the same conditions of Fig. 4c (a) and with an additional extraction potential $\Phi_{FC} = 1$ applied to the Faraday cup (b). The visible window in the z-direction is ±70 μm and the Faraday cup is located at z = 500 μm.

3.4. THE INFLUENCE OF DIELECTRIC SURFACE LAYERS

Some ferroelectrics are known to have surface layers of physical properties different from the bulk material. Data, however, are not consistent and the approximated thicknesses and permittivities depend strongly on the type of measurement. For $BaTiO_3$, for example, the thickness of such a layer was determined to be approximately 10 nm to obove 20 µm according to Ref. 43 and 44. On the contrary, for PZT and PLZT materials the existence of surface layers have not yet been proven. Provided they do exist, they should be very thin and of a permittivity up to approximately 100 [45].

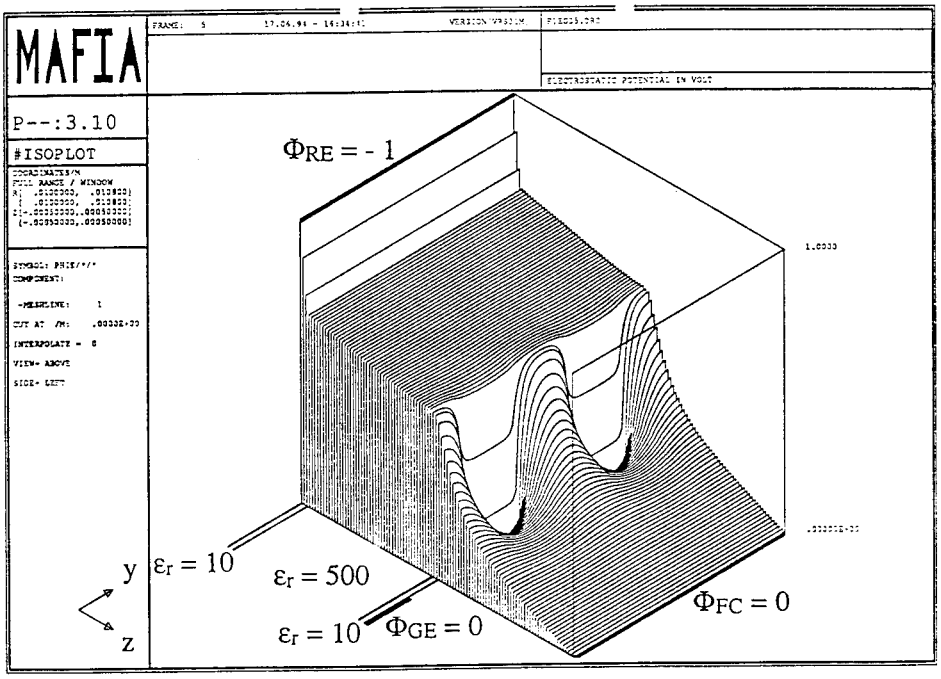


Figure 8. The negative electrostatic potential of a ferroelectric assumed to have two dielectric surface layers of 25 µm thickness with a permittivity of 10. The bulk permittivity is 500.

Dielectric surface layers have also been included in the emission models discussed in Ref. 14 and 18 in the frame of 1-dimensional potential considerations. In order to compute its possible influence on electron emission, the model was modified by introducing a layer of relative permittivity $\varepsilon_r = 10$ and of thickness $l_0 = 25$ µm at both surfaces, respectively. The thickness of the surface layers was chosen very large intentionally in order to allow for a presentation of the results in the frame of resolution of the graphics. An $\varepsilon_r = 10$ seems to be reasonable as compared to a bulk permittivity of $\varepsilon_r = 500$. At the boundary to the bulk, a jump of the relative permittivity is assumed, maintaining the normal component of the dielectric displacement constant.

The negative electrostatic potential distribution of the arrangement can be seen in Fig. 8 where the Faraday cup is set to ground. Contrary to the case of Fig. 5a, where the

electric field does not change very much through the material's thickness, there is a strong potential drop at both surface layers. Consequently, the field at the bulk is much smaller. Due to a ratio of 1 : 50 of the permittivities, the leakage of potential appears to be at the surface only. The electric field of the bulk seems to be almost homogeneous and dependens only little on the location of the grounded electrode. The highest potential gradient, of course, can be found underneath the electrode stripes and is much less in the plane of symmetry between them.

4. Discussion

4.1. FUNDAMENTAL PROPERTIES OF THE EMISSION MECHANISM

From the model of the emission process, it can be deduced that the amount of emitted charge is correlated to the rate of polarization change. This has been proven when increasing the rise time of the applied electric field [25]. Consequently, electron emission should be possible also if only part of the polarization is switched fast, too. This is in accordance to the experimental data where emission correlated to partial switching was demonstrated [35].

In Fig. 9 the switched charge is shown together with the integrated emission current for a consecutively pulsed $Pb_{0.97}Nd_{0.02}(Zr_{0.55}Ti_{0.45})O_3$ ceramic of 150 µm thickness (from Ref. 35). The applied pulse had an amplitude of Φ_{RE} = -400 V and was of 2.2 µs duration.

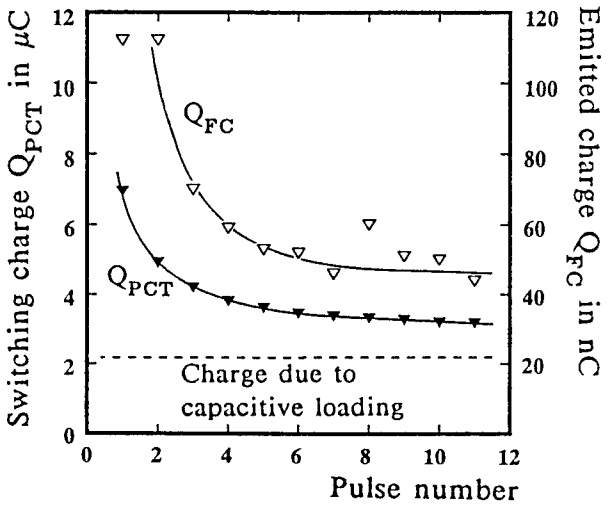


Figure 9. The switching current Q_{PCT} and the emitted charge Q_{FC} for partial switching as a function of the number of applied pulses. The charge necessary for capacitive loading is indicated by a dashed line (from Ref. 35).

Emission was obtained from 15 mm^2 bare surface within the grid electrode of 8 mm in diameter. At the first pulse the rise time of the electric field was slower due to the high capacity of the ferroelectric. This might be the reason for the smaller than expected

emitted charge, which should have been higher in accordance with the trend shown by the slope of the fittted Q_{FC} curve shown in Fig. 9. Furthermore, provided that emission is governed by the developement of the internal potential in time, an energy distribution of the electrons should exist. Qualitatively, this has been confirmed experimentally by the method of applying a counterpotential to the Faraday cup [8,9]. The energy distribution, however, has been detected only for the integrated emission current. Time resolved measurements have not yet been performed.

As the emission is induced by the polarization change inside the solid state, it should be independent from the gas pressure of the surrounding medium. This has been demonstrated from vacuum (10^{-4} Pa) up to the low pressure gas regime (1 Pa) where amplification due to charge multiplication starts [9,31].

Electron emission from ferroelectrics together with the special dielectric material properties as a function of temperature was investigated for PLZT 2/95/5 [8,9], PLZT X/65/35 (X = 7, 8, 9, 10) [22], and some special composition of $(Ba,Sr)TiO_3$ [28]. For details the reader is referred to these original publications or to review papers [21,29].

The two types of mechanisms discussed in Fig. 1 and Fig. 2 are different only in the way of achieving the neccessary polarization change. From the switching kinetics, follows directly that stable emission conditions caused by polarization inversion in a material inside its ferroelectric phase (Fig. 1) requires an active resetting from pulse to pulse. This may be achieved by applying an electric field of opposite polarity to the material and thus returning to the initial point at the hysteresis loop [33,34]. The shape and the place of the resetting field between successive pulses can be optimized in order to allow for a minimum of fatigue. Resetting may be realized automatically by keeping the rear electrode of the ferroelectric at a positive d.c. potential (U_{bias}) and pulsing it from this level to negative polarity gaining a maximum of polarization change at a lower applied electric field strength. The emitted charge per square centimeter as a function of the applied potential Φ_{RE} and U_{bias} is shown in Fig. 10 (from Ref. 34). The amount of emitted charge can be adjusted by defining the stroke at the hysteresis loop no matter where the starting point is.

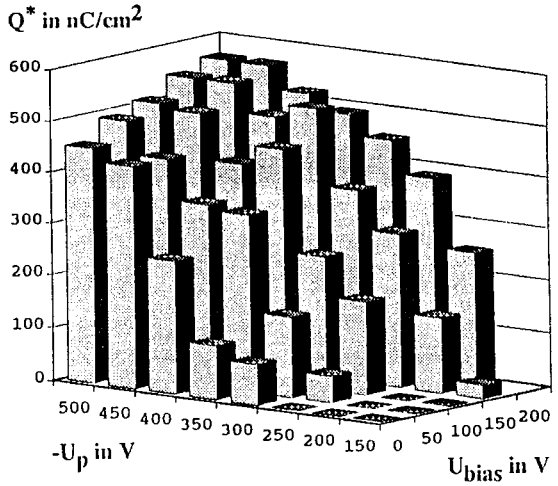


Figure 10. The emitted electron charge per square centimetre as a function of the negative voltage U_P, pulsing from a positive d.c. resetting potential U_{bias}.

Contrary to this, electron emission induced by a phase shift offers the unique advantage that an active resetting of the emitter is not neccessary between consecutive pulses. When the driving electric field is switched off, the material returns to its initial phase prior to the emission. So-called backward switching has been investigated recently [46], reporting on switching times down to 1 μs in the case of a ferroelectric - antiferroelectric transition for $(Pb,La)(Zr,Ti,Sn)O_3$ ceramics of distinct stochiometric composition. This is in accordance with the repetition rate of electron emission up to the MHz region observed for a special composition of antiferroelectric $(Pb,La)(Zr,Ti)O_3$ [25].

4.2. THE INFLUENCE OF THE ELECTRODE GRID

The phenomenological description of the emission process visualizes the important role of the structured surface electrodes of ferroelectric emitters and reveals two main features. First, surface electrodes are needed to generate strong polarization changes unless extremly high fields are applied (via vacuum) as they are used for example in RF-cavities. Second, the field bending near to the electrode edges, has to be minimized.

From the leakage out of the potential (Fig. 5) it becomes clear that for diminishing thickness of the emitter the field between the electrode stripes decreases. Thus, switching is less effective or may be even suppressed completely. Previous analyses that compared emission from samples of different thickness at a constant U_{RE}/d have to be rediscussed since the actual existing internal field is lower than assumed before. This is especially important because emission is an exponential function of the applied external field [8,9,22,28,31,32]. The observed decrease in emitted charge at constant U_{RE}/d then can be consistently explained by a smaller fraction of the bare ferroelectric surface which participates in the emission process.

From Fig. 7 it can be seen that a positive potential at the Faraday cup almost does not influence the internal field distribution of the emitter. The extraction field mainly causes orientation of the field outside the emitter near the electrode edges into z-direction. Moreover, it can be assumed that only part of the emitted electrons is measured at the Faraday cup and that there is a loss of charge to the grid electrode. In Fig. 11, the electron emission is shown as a function of the distance to the emitter and at different extraction potentials as a parameter (from Ref. 35), confirming these assumptions.

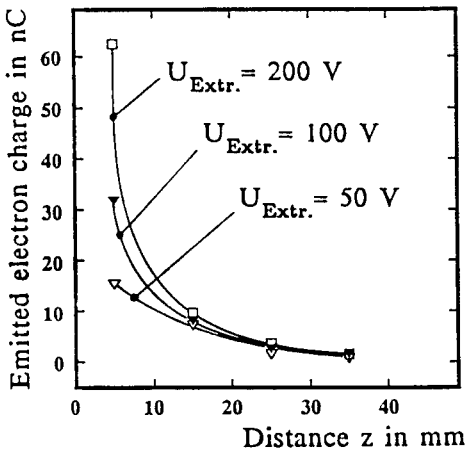


Figure 11. The emitted electron charge Q_{FC} versus the distance z to a 85 μm thick emitter (PZT) for different extraction voltage as a parameter.

At greater distance from the emitting surface there is no loss in the emitted charge any more. This has been varified by beam profile measurements [27] that showed, however, a blowing up of the pulsed electron beam. Qualitatively, this can be correlated to the total of emitted charge, the Coulomb forces within the electron bunch itself being the reason for the transversal beam divergence. Superimposed the initial electron velocity into the z direction, a characteristic beam profile has been observed [27]. Based on the principle of the emission process as discussed in Fig. 1 and 2, the non-homogeneous energy distribution that was reported in Ref. 8 and 9 can be understood.

Defining dielectric surface layers results in a weaker but almost homogeneous field in the bulk of the material and in a high potential gradient at the dielectric layers. Provided the bulk electric field is still high enough to switch polarization this could be of advantage since the material might switch through the whole volume. When considering the surplus of negative charge as being generated at the interface between the bulk and the surface layer, electrons could be better accelerated as already proposed in Ref. 14. For a smaller value of the thickness l_0, the effect, however, will be less pronounced.

4.3. THE APPLICATION OF FERROELECTRIC EMITTERS

Polarization changes that induce electron emission from ferroelectrics can be provoked by several methods, the most prosperous for technical use seem to be the utilization of pulsed electrical fields. First applications as an electron source (charge injection trigger) in high power gas switches developed for the CERN Large Hadron Collider beam dumping system prove the reliability of such ferroelectric cathodes [7,47,48]. Further applications as high brightness electron sources for different use are under examination, e.g. for high power microwave tubes, x-ray tubes, free electron lasers, and injectors for accelerators [36,38,40,49]. Particular measurements resulted in a brightness competitive to conventional cathodes [36].

The first evidence of electron emission from ferroelectric thin films was presented at the present Workshop [50]. From the field calculations discussed above the conclusion may be drawn that not only the film thickness but all dimensions should be scaled down in order to proceed to a reliable working laboratory device. Integrated circuit technology should be applied as it is used for the development of ferroelectric non-volatile memories, too. The demonstration of such a thin-film micro electron-source, operating at low voltage, without the need of high vacuum, and adressable in a matrix would have a huge impact on research and development in vacuum-microelectronics for the future.

5. Literature

1. Miller, R.C. and Savage, A. (1960), *J. Appl. Phys.* **31** (4), 662.
2. Rosenblum, B., Bräunlich, P., and Carrico, J.P. (1974), *Appl. Phys. Lett.* **25** (1), 17.
3. Biedrzycki, K. (1986), *Phys. Stat. Sol. (a)* **93**, 503.
4. Rozenman, G.I., Okhapkin, V.A., Chepelev Yu.L., and Shur, V. Ya (1984), *JETP Lett.* **39**, 477.
5. Gundel, H., Riege, H., Wilson, E. J. N., Handerek, J. and Zioutas, K. (1988), CERN PS/88-53 (AR). Also (1989), *Nucl. Instrum. Methods* A **280**, 1.
6. Gundel, H., Riege, H., Wilson, E.J.N., Handerek, J. and Zioutas, K. (1988), CERN PS/88-54 (AR). Also (1989), *Ferroelectrics* **94**, 337.

7. Gundel, H., Riege, H., Handerek, J. and Zioutas, K. (1988), CERN PS/88-70 (AR) Also (1989), *Appl. Phys. Lett.* **54** (21), 2071.
8. Gundel, H., Handerek, J., Riege, H., Wilson, E. J. N. and Zioutas, K. (1989), CERN PS/89-35 (AR). Also (1990), *Ferroelectrics* **109**, 137.
9. Gundel, H., Riege, H., Wilson, E. J. N., Handerek, J. and Zioutas, K. (1989), *Ferroelectrics* **100**, 1.
10. Rosenman, G.I., Tsedrik, M.S., Rez, I. S., Vasilevsky, S.A. and Chepelev, Yu.L. *Ferroelectrics* (1990), **110**, 113.
11. Rosenman, G.I., Malyshkina, O.V. and Chepelev, Yu.L. (1990), *Ferroelectrics* **110**, 99.
12. Rosenman, G.I. (1991), *Ferroelectrics* **118**, 451.
13. Rosenman, G.I. (1992), *Ferroelectrics* **126**, 305.
14. Rosenman, G.I. and Rez, I. (1993), *J. Appl. Phys.* **73** (4), 1904.
15. Biedrzycki, K. (1991), *Ferroelectrics* **119**, 33.
16. Biedrzycki, K. and Le Bihan, R. (1992), *Ferroelectrics* **126**, 253.
17. Biedrzycki, K., Aboura, H., Chartier, J.L. and Le Bihan, R. (1992), *Phys. Stat. Sol. (a)* **132**, 205.
18. Biedrzycki, K., Aboura, H. and Le Bihan, R. (1993), *Phys. Stat. Sol. (a)* **140**, 257.
19. Gundel, H. and Riege, H. (1990), *Appl. Phys. Lett.* **56** (16), 1532.
20. Gundel, H., Handerek, J., Kuhn, H., Riege, H. and Wilson, E.J.N. (1990), Proc. *2nd European Particle Accelerator Conference*, Nice, Edition Frontières, ISBN 2-86332-090-4 Vol. **1**, 712.
21. Proc. *Bendor Workshop on 'Short Pulse High Current Cathodes'*, Bendor 1990, Edition Frontières 1990, ISBN 2-86332-092-0, with contributions of J. Handerek (p. 73), H. Gundel (p. 305) and H. Riege (p. 323).
22. Gundel, H., Handerek, J., Riege, H. and Wilson, E. J. N. (1990), *Ferroelectrics* **110**, 183.
23. Ivanchik, I.I. (1990), *Ferroelectrics* **111**, 147.
24. Airapetov, A. Sh., Ivanchik, I.I., Lebedev, A.N., Levshin, I.V. and Tikhomirova, N.A. (1990), *Sov. Phys. Dokl.* **35** (3), 267.
25. Gundel, H., Handerek, J. and Riege, H. (1991), *J. Appl. Phys.* **69** (2), 975.
26. Ivers, J.D., Advani, R., Nation, J.A. and Schachter, L. (1991), *Proc. IEEE Particle Accelerator Conference*, San Francisco, California, USA, , Vol. **4**, pp. 2104.
27. Gundel, H., Heydari, H., Suchland, D., Schmidt, K. and Henke, H. (1992), *Proc. 3rd European Particle Accelerator Conference*, Berlin , Vol. **2**, 1023.
28. Handerek, J. and Riege, H. (1992), *Ferroelectrics* **128**, 43.
29. Gundel, H. (1992), *Integrated Ferroelectrics* **2**, 207.
30. Riege, H. (1992), *Le Vide, les Couches Minces - Suppl.* au n° **260**, 190.
31. Asano, J., Imai, T., Okuyama, M. and Hamakawa, Y. (1992), *Jpn. J. Appl. Phys.* **31**, 3098.
32. Asano, J., Okuyama, M. and Hamakawa, Y. (1993), *Jpn. J. Appl. Phys.* Vol. **32**, Pt. 1, No. 1B, 396.
33. Asano, J., Iwasaki, S., Okuyama, M. and Hamakawa, Y. (1993), *Jpn. J. Appl. Phys.* Vol. **32**, 4284.
34. Gundel, H. and Meineke, A. (1993), *Ferroelectrics* **146**, 29.
35. Gundel, H. (1993), *Technical University of Berlin, TET-Note 93/014, contributed paper to the International Symposium on Integrated Ferroelectrics*, ISIF-5, Colorado *Springs , to be published in Integrated Ferroelectrics.*

36. Jiang, B., Kirkman, G. and Reinhardt, N. (1993), *Proc. 1993 IEEE Particle Accelerator Conference*, Washington, DC, USA,
37. Ivers, J.D., Schachter, L., Nation, J.A., Kerslick, G.S. and Advani, R. (1993), *J. Appl. Phys.* **73** (6), 2667.
38. Schachter, L. , Ivers, J.D., Nation, J.A. and Kerslick, G.S. (1993) *J. Appl. Phys.* **73** (12), 8097.
39. Pleyber, G., Biedrzycki, K. and Le Bihan, R. (1993), *Ferroelectrics* **141**, 125.
40 Sampayan, S.E., Caporaso, G.J., Holmes, C.L. Lauer, E.J., Prosnitz, D., Trimble, D.O. and Westenskow, G.A. (1994), *Nucl. Instr. and Meth. A* **340**, 90.
41 MAFIA Release 3.1, The MAFIA Collaboration, (c) 1991 by T. Weiland, Darmstadt, Germany.
42. Haertling, G.H. (1987), *Ferroelectrics* **75**, 25.
43. Jona F. and Shirane, G. 1962, *Ferroelectric Crystals, Pergamon Press 44) M.E. Lines and A.M. Glass, Principles and Applications of Ferroelectric and Related Materials, Clarendon Press, Oxford 1977, ISBN 0-19-851286-4.*
45. Prof. J.F. Scott, privat communication.
46. Pan, W.Y., Gu, W.Y. and Cross, L.E. (1989), *Ferroelectrics* **99**, 185.
47. Courtois, L., Faure, P., Handerek, J. H., Riege, H. and G.H. Schröder (1992) *Proc. 3rd European Particle Accelerator Conference*, Editions Frontières, Gif-sur-Yvette Cedex, France (1992), ISBN 2-86332-115-3, vol. 2, 1597.
48. Faure, P. , Riege, H., Schröder, G.H., Handerek, J. and Courtois, L. (1993), *Proc. 9th IEEE International Pulsed Power Conference*, Albuquerque, New Mexico.
49. Cavazos, T., Shiffler, d., Wroblewski, B., Fledermannn, C., Gahl, J. and Schamiloglu, E. (1993), *Proc. 9th IEEE International Pulsed Power Conference, Albuquerque, New Mexico*
50. Auciello, O., Ray, M.A., Palmer, D., Duarte, J., and McGuire, G.E. (1994), *Appl. Phys. Lett.* (in press).

INTEGRATION OF FERROELECTRIC THIN FILMS FOR MEMORY APPLICATIONS

H. ACHARD AND H. MACE
C.E.A. / L.E.T.I. /
Technologies Avancées
CENG, 17 r. des Martyrs, Cedex 9,
38054 Grenoble, France

ABSTRACT. This review deals with the tasks involved in integrating ferroelectric thin films for memory applications. Main emphasis is put on process integration. Some of the results presented come from the European ESPRIT project called FELMAS (especially dry etching results). The compatibility of CMOS devices and ferroelectric capacitors is discussed and main issues toward the development of VLSI memories, are outlined.

1. Introduction

The field of applications for integrated ferroelectrics [1, 2] is huge. It ranges from electronic devices such as memories [3, 4], capacitors [5], pyroelectric detectors [6], piezo-electric devices [7], micro-actuators and sensors [8], to electro-optic applications [9]. One major and common issue for most of these applications is the successful integration of the relevant ferroelectric materials with the manufacturing processes of the various substrates. A number of papers have been devoted to the study of stand-alone capacitors (elaboration and electrical characterization) but there is little written information available about integration and process-related issues.

In this paper we review the tasks involved in integrating FerroElectric (FE) thin films for memory applications: FE capacitor-layers compatibility with substrate devices, FE capacitor integration processes and back-end process steps. Additionally, we mention some results obtained within the framework of the European ESPRIT project FELMAS (Ferro Electric Layers for Memory Applications and Sensors).

This review will be limited to the work performed on FE non-volatile Random Access Memory (FERAM) using typically a PZT FE capacitor (Fecap) as storage medium and integrated with silicon CMOS However, some results come from the studies on integration for high ε DRAM (volatile memories) [10, 11], because these memories can be quite similar. Integration on GaAs has been already reviewed [12] [13]. Other kinds of FE non-volatile memory devices such as: Metal / FE / Metal / Insulator / Semiconductor (MFMIS [14, 15] and Metal / FE / Semiconductor (MFS) [16], will not be considered here, although some issues are similar, because they imply additional and specific integration constraints (e.g. FE-SC compatibility).

This paper is organized as follows: the second section gives the boundary conditions of the subject, considering temperature and design, basic constraints. The third, fourth, and fifth sections deal with process-related issues; the fourth section giving more detail on the state of the art of dry etching but also on dry etching work performed in

O. Auciello and R. Waser (eds.), Science and Technology of Electroceramic Thin Films, 353-372.
© 1995 *Kluwer Academic Publishers. Printed in the Netherlands.*

FELMAS. Finally, the impact of ferroelectric integration process on CMOS devices and FE capacitors, is discussed in section six.

2. Thermal Limits and Design, Basic Constraints

2.1. TEMPERATURE CONSIDERATION

A first point of concern is the relative compatibility between CMOS and FE stack (Festack) thermal treatments [17]. On one hand, we have the standard CMOS process heat treatments; the last "high temperature" treatments applied are related to source/drain activation and PSG or BPSG flow, with thermal budgets -in standard furnace annealing- between 850 and 900°C for 30mn. Then after contact opening and aluminum metallization, the final forming gas anneal (N_2 / H_2, 450°C - 30mn) is performed below 500°C to avoid Si spiking and the formation of Al hillocks. On the other hand, formation of the PZT perovskite phase requires more than 550°C and Festack integrity can be damaged over 750°C. Consequently, the Festack preparation is usually performed between the BPSG flow and the Al metallization. This constraint could be modified through the use of refractory metallization or by using lower temperatures for PZT phase formation, thus allowing Festack deposition over metallization.

2.2. DESIGN CONSIDERATIONS

The design of a FERAM memory cell with a single transistor, single capacitor architecture (DRAM like) can be achieved in two ways [18]: either with a planar Fecap over Locos, laterally displaced from the access transistor (Fig. 1 (a), this is the main option considered in FELMAS), or with the Fecap directly on top of the drain of the transistor (Fig. 1 (b)). This second integration scheme leads, of course, to the highest packing density but mainly requires solutions to the challenging problem of direct contact between bottom electrode (BE) and Si. The 256 Kbit prototype memory recently developed by T. Sumi [19] using direct contacts, shows that this promising approach is now emerging.

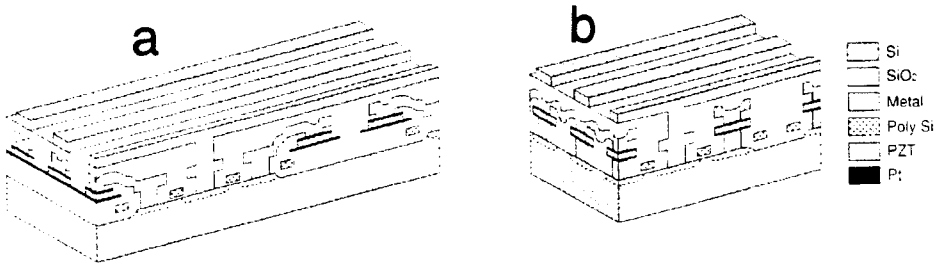


Figure 1. Ferroelectric capacities integrated with MOS transistors with two levels metallization; capacitor on field oxide (a), capacitor above drain (b).

Let us consider this direct contact integration scheme. Different options are available for the exact layout and structure of the integrated Fecap and each structure will have specific process integration issues. The structures proposed by Fazan [20] or Eimori [11] (Fig. 2), for a volatile FERAM memory cell, are similar to that needed for a non-

volatile FERAM one. On this memory cell cross section we can list the various points of concern which are developed in the following sections: Festack compatibility with CMOS, Festack patterning, back-end process steps.

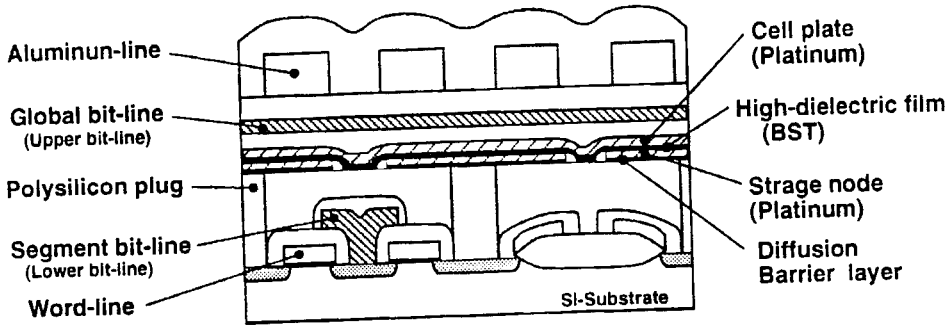


Figure 2. Schematic cross sectional view of planar stacked capacitor cell with high - dielectric constant film.

3. Festack Compatibility with CMOS

3.1. SUBSTRATE CONTAMINATION

Contamination introduced by Festack layers deposition (electrodes and PZT) can have two consequences: degradation of MOS electrical characteristics (metallic contamination) and pollution of the wafer itself (which may induce pollution of the subsequent process equipments). For example, in the FELMAS project we have measured by SIMS the lead contamination on the back side of a wafer after PZT sol-gel deposition and annealing at 700°C [21]. We have detected up to 7 at% of Pb on the Si surface and 20ppm at 60nm depth.

Clearly, pollution must be limited as much as possible to avoid CMOS degradation and to limit contamination of the back-end equipments. Nevertheless, whatever care might be taken to avoid device and equipment pollution, a dedicated back-end line is certainly unavoidable to separate front-end high temperature processes (for which pollution is unacceptable) from back-end low temperature ones. To reduce CMOS degradation, barrier layers must be considered at various interfaces to limit diffusion phenomena, as discussed in later sections.

3.2. IMPACT OF THE PZT PREPARATION METHOD ON MOS DEVICES

In the FELMAS project [21], we have evaluated the influence on MOS devices, of various PZT preparation methods having very different thermal budgets i.e. 450°C, 700°C and 750°C furnace annealing for 30mn and 650°C for 4mn (RTA). The various Festacks made (Ti \ PT \ PZT) were deposited and annealed on: Si wafers processed with polysilicon capacitors and covered with BPSG (no barrier layers were deposited between BPSG and Festack). Then, Festacks and BPSG were chemically removed, polysilicon capacitors characterized and results compared to that for reference wafers

(same process applied, but no Festack deposition). The maximum shift, from the reference value, is 15mV and the spread between extreme results is 25 mV. We observe that the thermal budget of the Festack preparation method has a very limited impact on flat-band voltages of MOS capacitors and consequently on the threshold voltages of transistors.

3.3. BOTTOM ELECTRODE INTERFACE WITH FIRST INTERLEVEL DIELECTRIC

In the direct contact option presented in Fig. 2, the BE-ILD1 (first InterLevel Dielectric) interface has a limited extension; on the contrary, it is the main interface when Fecap is over Locos (Fig. 1 (a)) . With such a structure, a study by S.L. Miller [22] shows the importance of a barrier layer at this interface. In their standard integration process, a TiO_2 barrier layer is grown between ILD1 and Fecap. When they omit this TiO_2 barrier, the DC parametric electrical characterizations e.g. threshold voltages, are not affected (Fig. 3 (b)); but time-dependent reliability electrical characteristics e.g. gate oxide breakdown field, are strongly degraded as shown on Fig. 4 (a). With the TiO_2 barrier, the TDDB results are equivalent to the CMOS reference ones. This proves that, considering their integration conditions, some diffusion occurs from Fecap towards CMOS and must be stopped to ensure MOS reliability.

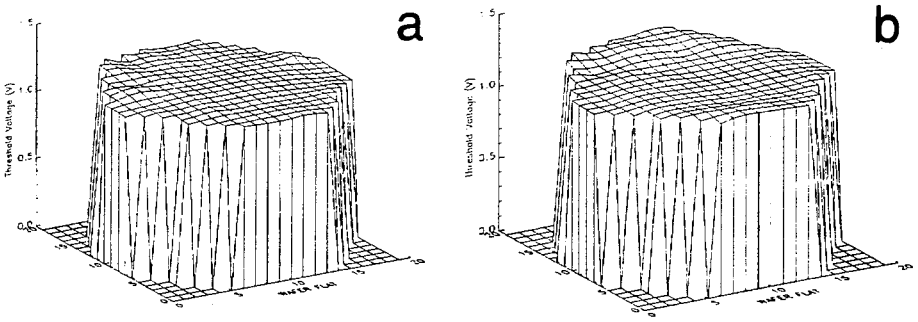


Figure 3. Map of M.O.S. threshold voltages; standard PZT integration process (a), integration process omitting TiO_2 - RuO_2 bottom electrode (b).

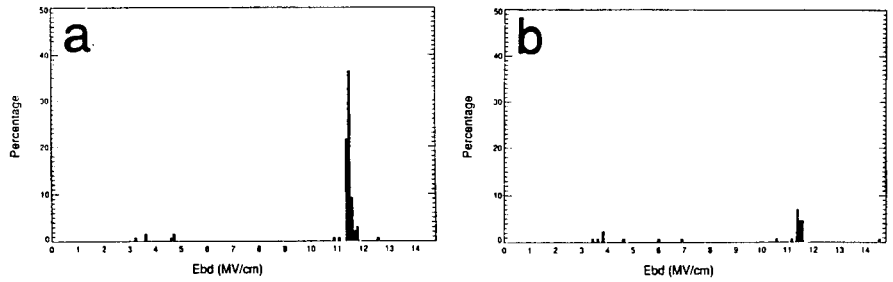


Figure 4. Distribution of MIS capacitor breakdown fields; standard PZT integration process (a), integration process omitting TiO_2 barrier layer (b).

3.4. BOTTOM ELECTRODE INTERFACE WITH SI CONTACTS

In the very large scale integration option proposed in Fig. 2, the interface stability between Fecap BE and Si contact is a key issue, along with low contact resistances. Usual conductive barrier layers between metallization (Al) and Si contacts for CMOS circuits (e.g. Ti N, Ti W) are not stable over temperatures such as 500 - 550 °C. In our VLSI option, where a planar topography is preferred for the Festack deposition (planarized contacts), the actual stacking of layers for this direct contact option is: Si junction \ barrier layer #1 \ plug material (e.g. polySi or W) \ barrier layer #2 \ BE \ PZT. This is a research subject in itself and the choice of barrier layer materials depends on the plug and BE layers chosen for this stack. Additionally barrier layer #2 must be compatible with optimized growth conditions for the Festack.

For example, a study has been performed by K. Takemura [23] on Sr Ti O_3 over Si (for high ε DRAM applications). It is shown that a Ta barrier layer (Si \ Ta \ Pt \ Sr Ti O_3) stabilizes the structure better than a Ti one up to 600 °C (Fig. 5); but contact resistances are degraded at this temperature, and are too high for circuit applications. One can note that the current evolution towards lower Festack manufacturing temperatures or thermal budgets e.g. RTA processing, could make this issue less difficult.

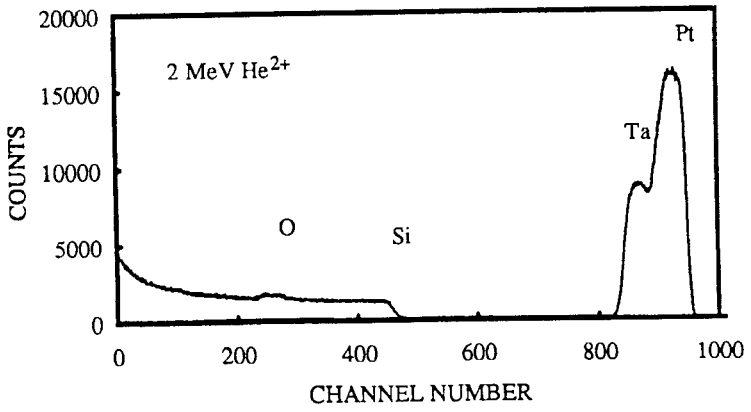


Figure 5. RBS spectrum of Pt/Ta barrier after $SrTiO_3$ thin film deposition at 600 °C.

3.5. PZT INTERFACE WITH FIRST INTERLEVEL DIELECTRIC

In the direct contact option, high packing densities are achieved because one side of the Fecap is connected directly to the access transistor (via a dedicated BE) and the other side is a common electrode for lots of memory cells in rows or columns. The dedicated BE must be patterned prior to PZT and TE depositions; consequently, beyond BE areas, PZT is in contact with ILD1. At the required thermal budgets, PZT is likely to interact with silicon dioxides (ILD1). It is possible to avoid contact between PZT and ILD1 using a structure where the overlying metallization level makes contact with the TE of each memory cell (i.e. TE and BE are dedicated to the memory cell), but this is done at the expense of packing density.

Consequently, a barrier layer at this interface has also to be considered. Recent results published by R. E. Jones [24] show that a TiO_2 layer is almost stable under annealing treatment up to 600 °C for 30mn in oxygen (Fig. 6). Additional studies would have to be performed to check if the electrical performance of underlying CMOS devices would be altered.

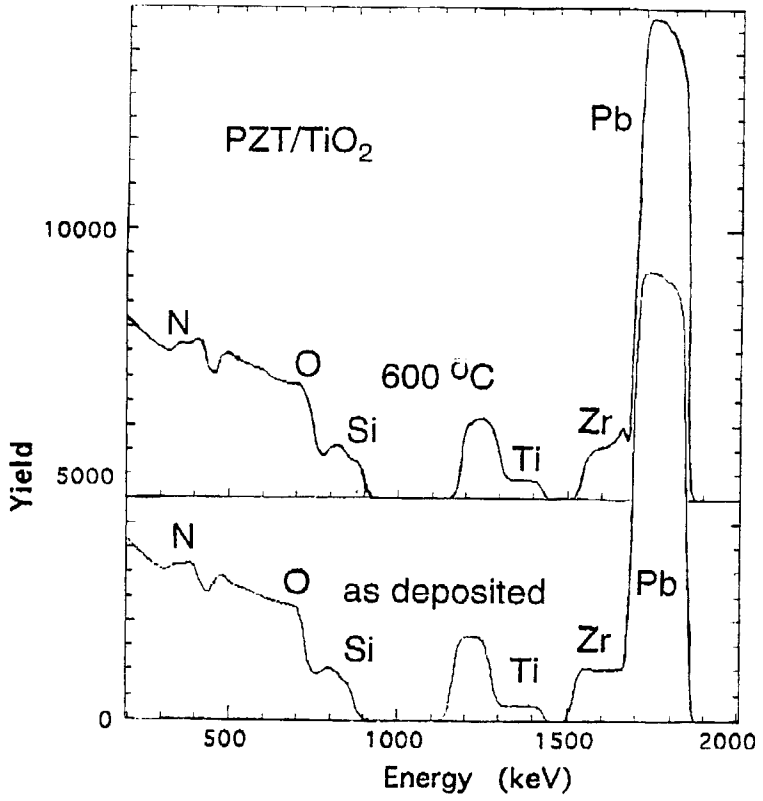


Figure 6. RBS of PZT 50 / 50 over TiO_2, as deposited and after a crystallization anneal at 600 °C for 30mn in oxygen.

4. Festack Patterning

4.1. CONFORMALITY OF FESTACK LAYERS

The surface on which PZT is to be deposited is not always planar. This can be due to: CMOS topography after reflow, contact hole topography (when they are not filled with a plug material) or even, 3D capacitor structure constraints. If the PZT deposited layer is not conformal, it will be thicker than nominal in hollow areas of the topography and thinner on top of relief [17] (Fig. 7). To remove the thicker PZT areas, when dry etching the PZT layer, an over-etching of the underlying substrate is unavoidable. This is critical if PZT is etched over silicon dioxide, as in Figure 2, because selectivity over

silicon oxide is difficult to achieve. However, even when PZT is etched selectively over a Pt BE (selectivities around 2.5 have been achieved in FELMAS), it is very difficult to find a process window allowing complete removal of the PZT residues, without damaging the Pt electrode, as shown on the micrograph presented in Fig. 8. Furthermore, this problem is amplified at the next Pt - ILD1 interface.

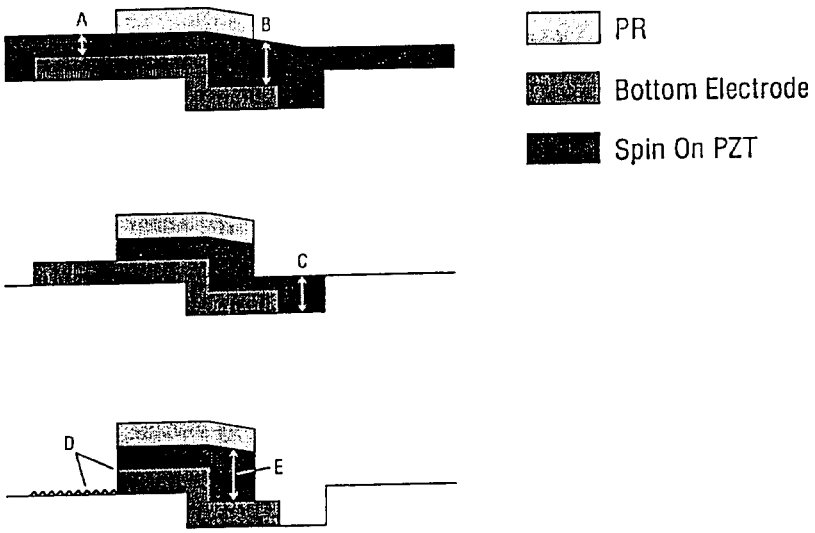


Figure 7. Scenario of process defects production when dry etching a non-conformally deposited PZT layer; as-deposited (up), PZT residues (middle), bottom electrode over-etching (down).

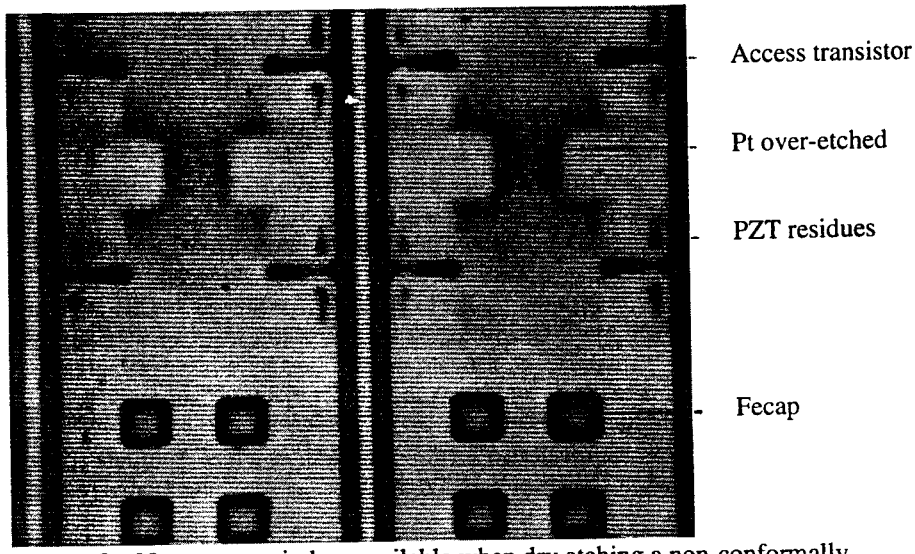


Figure 8. No process window available when dry etching a non-conformally deposited PZT sol-gel layer over Pt; the Pt layer is already over-etched whereas PZT residues still remain.

This raises the question of sol-gel method compatibility with circuit processing. If non-planar topographies are to be used below PZT, either PZT has to be deposited almost conformally or selectivity of the dry etching methods employed has to be markedly improved.

4.2. STATE OF THE ART OF FESTACK DRY ETCHING

Many different techniques have been used to pattern ferroelectric materials of the PZT family [25] (ceramics or thin films). Few of them meet all the V.L.S.I. requirements e.g. pattern resolution, anisotropy, fast etch rate, process temperature compatibility, selectivity.

Wet chemical etching has been successfully demonstrated, especially for micro-fabrication, by S. Trolier [26], P.F. Baude [27] and particularly S. Mancha [28, 29]. But undercutting, due to isotropic etching, is usually observed and obtaining micrometer patterns is almost impossible.

Laser enhanced chemical etching (T. Shiosaki [30]) and eximer laser etching (M. Eyett [31]) have also been successful but induce surface morphology degradations in the vicinity of patterns (photothermal melting) and are currently limited to pattern resolutions above ten microns.

Various kinds of ion-beam etching techniques have produced more relevant results. Standard ion-beam etching (T. Kawaguchi, [32]), is free from glow-discharge induced thermal damage e.g. composition modifications, and leaves smooth surfaces (compatibility with optical applications). Reactive ion-beam etching (RIBE) with C_2F_6 (S.H. Lee, [33]) has given higher etch rates (1,5µm/h) without degrading pattern resolution. But the most attractive option is the chemically-assisted ion-beam etching (CAIBE) studied by P.F. Baude [27], with (Xe, Cl_2) plasma. This technique provides a fast, low temperature, anisotropic etching leaving smooth surfaces; but it is not an industrial technique at the present time.

Reactive ion etching (RIE) combines the advantages of sputtering by energetic ions (anisotropy) and etching through the chemical reactivities of species produced in the plasma (selectivity, higher etching rate). Using a down-stream plasma, M.R. Poor [34] has evaluated the pure chemical contribution with CF_4 or HCl / He. He has shown that no volatile species are formed below 200 °C, that a combination of both gases enhances the etch rate and that, as expected, etching is isotropic.

Others RIE studies have evaluated the efficiency of various gas mixtures. With CF_2Cl_2 / O_2, D.P. Vijay [35] performed anisotropic etching at low pressure and low RF power. He explains that chlorine etching is an ionic phenomena, whereas fluorine etching is rather more ion enhanced. Because of the too low vapor pressures of fluorines or bromides K.Saito [36] employed CCl_4 instead and produced highly anisotropic patterns, but at reduced RF power to avoid resist damage and residues. Finally, single step etching of Pt / PZT / Pt stacks has been demonstrated by J.J. von Glabbeeck [37] with CF_4 / Ar plasma. He explains that ion bombardment (Ar) enhances the probability of chemical reaction with fluorine species.

Concerning interfaces we must also mention a problem which is often reported in integration studies: the weak adhesion usually observed between electrodes (especially noble metals) and materials in contact with it. This issue is critical when etching the Festack because it often induces delamination of the electrodes. In FELMAS it has been possible to limit its impact through the use of low substrate temperatures, thus reducing thermal expansion effects.

4.3. PZT AND PT DRY ETCHING TECHNIQUES DEVELOPED IN FELMAS

In the FELMAS project, we have developed Festack patterning techniques for the following structure: Pt (TE) / PZT / Pt-Ti (BE). The aim was to settle dry etching techniques presenting the best possible compatibility with the VLSI requirements mentioned in the previous paragraph. Much efforts have been devoted toward achieving high etch rates, resist mask compatibility and selectivity. Some of the results obtained are disclosed below (a previous study with this equipment has been published by B. Charlet [38]).

The DECR (Distributed Electronic Cyclotronic Resonance) plasma reactor was well suited for this study, due to its high plasma density and low pressure. Additionally, the chosen reactor features RF substrate biasing and substrate temperature control.
Using CF_4 chemistry, we have studied PZT and photoresist etch rates as a function of the substrate polarization i.e. RF power applied to the substrate (Fig. 9).

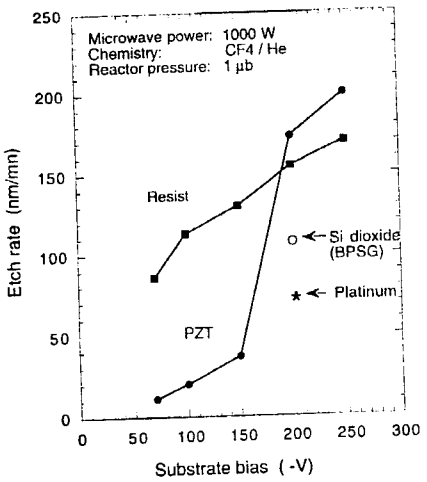


Figure 9. PZT and photoresist etch rates versus substrate polarization (DECR dry etching).

We observe that the PZT etch rate rises with bias polarization but not in a linear way. Over a bias threshold around 150V, the etch rate is strongly increased and reaches **140nm/mn** @ 200V. This effect cannot only be explained by physical sputtering, because, using pure Ar plasma, the PZT etch rate is about 10nm/mn @ 200V. At this bias voltage, the surface temperature of the wafer (pyrometric measurement) reaches 245 °C; at this temperature, pure chemical etching should be negligible, as shown by M.R. Poor [34] . Therefore, the fluorine etch mechanism is likely to be a strongly ion-assisted process. The ion bombardment induces surface effects which lower the activation energy of desorption processes and consequently increase the chemical reactivity of PZT components.

Working at rather high bias voltages (to increase the etch rate) induces, as mentioned previously, substrate temperatures over 200 °C. This is not compatible with the use of standard resist masks and may alter the FE film composition. The substrate temperature must therefore be lowered.

Using a He gas flow, as the thermal transfer medium, between the back-side of the clamped wafer and the cooled chuck we were able to control the temperature of the wafer versus the He gas pressure in the system. Under plasma, the range of achievable substrate temperatures is between 90 and 280 °C. It is necessary to make a compromise

for choosing the substrate temperature. On one hand, high temperatures increase etch rate but excessive heating can carbonize the photoresist, making it more difficult to remove with organic solvents. On the other hand, low temperatures, required for standard resist compatibility, combined with the relatively low volatility of fluoride compounds can induce redeposition of various elements during etching; this phenomena is even more critical on the edges of photoresist patterns, where the low angle impact of the ion flux allows an easier build up of redeposited material (i.e. potential residues after stripping).

In order to try to limit the formation of such residues, we added Cl_2 to the CF_4 chemistry. The evolution of the etch rates for PZT, Pt and resist are presented in Fig. 10 as a function of the Cl_2 percentage in the CF_4 / Cl_2 mixture.

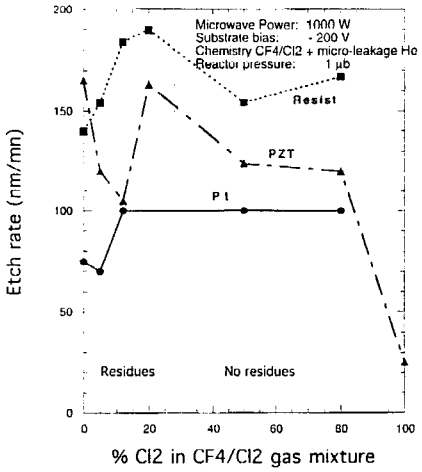


Figure 10. PZT, Pt and photoresist etch rates in a CF_4 / Cl_2 gas mixture.

We observe that PZT etch rate is high and decreases as Cl_2 is added to CF_4, as already observed in the same reactor with SF_6 / Cl_2 by B. Charlet [38]. Usually, etching rates with Cl_2 chemistry are low; surface reactions are different and their are no spontaneous etching mechanisms. The main interest of the Cl_2 addition is that it strongly limits the formation of residues, but only with percentages of injected Cl_2 above a threshold value of 20% (Cl_2 over CF_4 flow ratio). Lower etching rates with Cl_2 is a result which contrasts with previous studies in a RIE reactor [35], showing that chlorine by-products of PZT are more volatile than fluorine ones. However comparison of results in different kinds of reactors is certainly not relevant. A micrograph of an etched and stripped Fecap is shown on Fig. 11; PZT pattern edges had the same slope as resist, proving that the etching process is anisotropic.

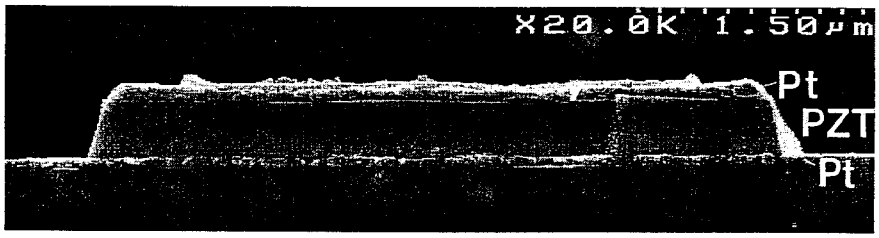


Figure 11. SEM cross-sectional view of a PZT Fecap (Pt / PZT / Pt-Ti), after DECR dry etching of Pt (top electrode) and PZT.

For Pt, the etch rate is quite high (**100nm/mn** @ 200V) and similar with Ar or Cl_2 (Fig. 10). It confirms the pure sputtering nature of the mechanism involved for this material (no chemistry or temperature assistance). The Pt etch rate is slightly lower with CF_4 chemistry. This is certainly related to a lower transfer momentum for F^+ ions compared to Ar^+ and Cl^+. Fig. 12 shows a Pt BE after dry etching.

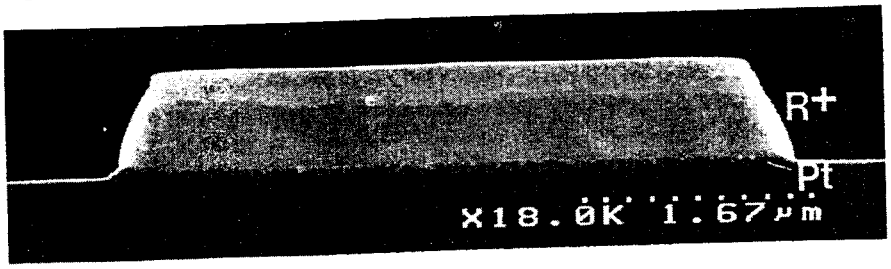


Figure 12. SEM cross-sectional view of a Pt / Ti bottom electrode over BPSG, after DECR dry etching and before resist stripping.

In conclusion we can say that dry etching techniques will meet the VLSI etching requirements, especially for resolution, even if some improvements, such as selectivity are still needed.

4.4. FECAP PROPERTIES AFTER PATTERNING

An example of Fecap electrical properties after dry etching patterning (TE and BE) of a Ti \ Pt \ PZT (OMCVD) \ Pt Festack, produced in Felmas, is given in Fig. 13. The dry etching patterning did not induce any degradation. Detailed investigations on this subject have been performed by K. Ishihara [39].

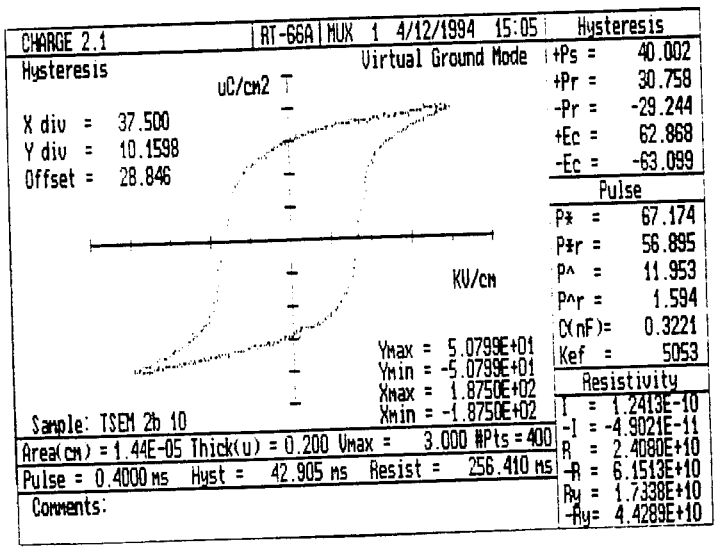


Figure 13. Hysteresis and pulse measurements @ 3V (Radiant tech. RT66A) on a Pt / PZT (OMCVD) / Pt Fecap; after TE, PZT and BE dry etching.

5. Ferroelectric Back-end Process

The back-end process consists of various process steps performed after Festack patterning, in order to complete the circuit production. The FE back-end process is mainly taken from the standard CMOS one; above all, it must provide the best possible compatibility with CMOS. This process has also to be compatible with the Fecap specificities e.g. platinum electrodes, PZT sensitivity to hydrogen. In the following paragraphs we review the successive back-end steps and develop examples about their impact on Fecap properties.

5.1. OXYGEN ANNEAL AFTER FECAP FABRICATION

Various benefits can be drawn from annealing Fecaps under oxygen after their manufacture. R. Moazzami [40] shows that such annealing increases by a factor of almost two the switched remanent polarization. This annealing also seems important in limiting the degradation induced by further back-end steps, as demonstrated by R. D. Nasby [42] on RuO_2 / PZT Fecaps: after ILD2 deposition, the remanent polarization is reduced by 20% if the Fecap was annealed under O_2 but by 85% if it was not. Finally, G.J.M. Dormans [41] observes a decrease of the coercive field (Fig. 14), and attributes this effect to a reduced thickness of the apparent non-ferroelectric interface layers between PZT and electrodes. Oxygen deficiencies, mainly at the PZT-electrode interfaces, are certainly partly compensated during this anneal and it improves the Fecap ferroelectric properties.

This outlines the importance of being able to measure with accuracy the oxygen content of PZT films [44] and, ideally, to monitor it during the integration process.

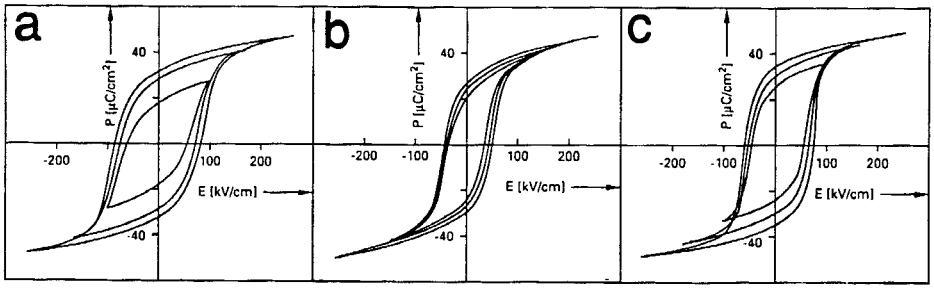


Figure 14. Hysteresis curves of 5000 μm^2 Fecaps with 300 nm OMCVD PZT, at three different stages of the processing. Immediately after their structuring (a), after an additional anneal (b) and after back-end process (c), (measurements were performed at 1 KHz @ 3V, 5V and 8V).

5.2. SECOND INTERLEVEL DIELECTRIC DEPOSITION

After patterning, capacitors are capped with the second interlevel dielectric layer (ILD2), in order to provide isolation toward the first metallization level. The second IDL should present the best possible compatibility with the back-end process and Fecap; it should have adequate dielectric properties (assuming that the thermal budget of the silicon dioxide densification treatments are not compatible), be conformal to ensure good step

coverage for metallization, avoid inducing leakage currents on Fecap edges (where ILD2 is in contact with PZT) and limit the amount of hydrogen introduced in the PZT. Among the various methods available, evaporation and sputtering are hydrogen-free but not conformal; CVD or PECVD are conformal but usually contain several percent of hydrogen. This is true for silicon oxide or silicon nitride layers but additionally Si N_X layers are usually under high stress and could modify Fecap properties through induced stress.

Comparative study of various ILD2 has been performed by B. ROD [43] and P.D. Maniar [45]. P.D. Maniar shows that CVD or sputtered ILD2 layers can both drastically reduce remanent polarization (Fig. 15), but also that "optimized" CVD or sputtered ILD2 deposition processes can be totally safe for the Fecap polarization. Details about these optimized processes are not disclosed, but one can say that they are related to process parameters such as the hydrogen content and chemistry involved, the level of stress and preparation temperature of the layer, the purity of materials involved etc. ILD2 capping can also enhance the fatigue phenomenon as shown by R. D. Nasby [42]. He observes that starting from identical remanent polarization values, after 10^{10} cycles the polarization of the Fecap covered with ILD2 is 30% lower than that of the uncapped capacitor.

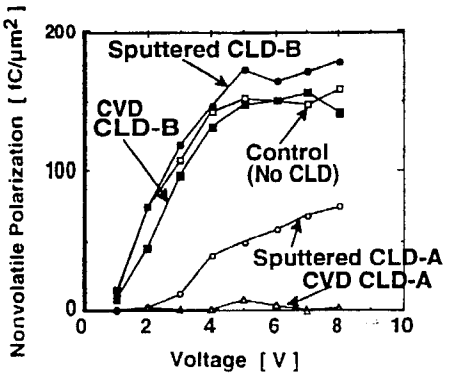


Figure 15. Comparison of different CVD and sputtered CLDs (Capacitor Level Dielectric) and their impact on non-volatile polarization. CLD-A and CLD-B refer to different processing conditions.

5.3. DRY ETCHING STEPS

After Fecap encapsulation, vias are cut through ILD2 to contact Fecap electrodes and MOS source/drains. Contacts on MOS are almost standard whereas Fecap contacts are specific, due to the electrode material (usually Pt or RuO_2). Noble metal electrodes are convenient etch stop layers for dry etching techniques but process induced damage to the Fecap are possible as reported by R. Moazzami [40] (Fig. 16). On this figure he shows that "weak" contact etch processes almost destroy remanent polarization whereas the "optimized" process does not affect it. Again, this effect is shown to be related to hydrogen-containing ambients during the dry etching.

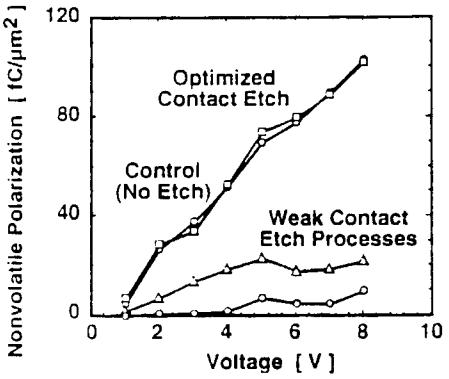


Figure 16. Comparison of different fluorine-based contact etch processes. An optimized process has been obtained in a reduced free hydrogen ambient.

Additionally, exposure of interlevel dielectric layers to dry etching plasma conditions can build up capacitively induced charges in the underlying conductive layer [46]. This phenomenon, responsible for gate-oxide degradations (TDDB) in standard CMOS processing, could also induce electrical defects in the ferroelectric capacitors [39] [40].

5.4. METALLIZATION BARRIER LAYER

First metallization after Fecap has to be compatible with both Fecap electrodes and MOS source-drains. For standard MOS processing, metallization is usually composed of an Al alloy (e.g. Al Si Cu) deposited over a barrier layer which is necessary to keep the contact stable during the final heat treatment of the circuit at 450 °C for 30mn.

A barrier layer is also compulsory for Fecap contacts as demonstrated by S. Matsubara [47] on Ba Sr Ti O_3 Fecap; with a direct Al / BST contact, Fecap breakdown voltages are drastically reduced after a 500°C N_2 anneal during 30mn, whereas with an Al / TiN / BST contact, breakdown characteristics are only slightly reduced (Fig. 17). Then metallization layer is patterned.

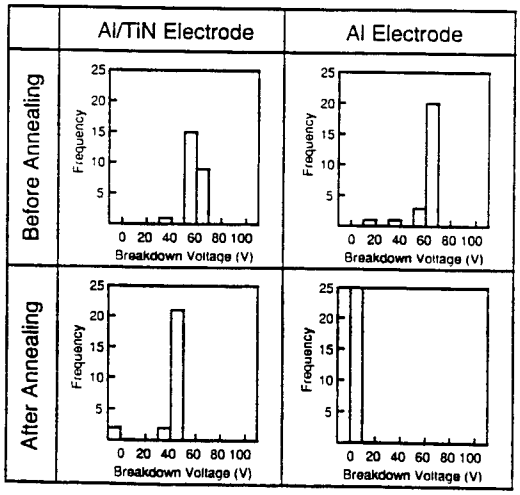


Figure 17. Distribution of BST Fecap breakdown voltages, with and without metallization barrier layer. Results are displayed before and after annealing @ 500°C, in N_2, during 30mn.

5.5. PASSIVATION COATING

The final dielectric passivation layer (usually Si O N), encapsulates the circuit, providing mechanical and chemical protection of its surface. Almost no information has been released about its compatibility with Fecap. Similarly to ILD2, hydrogen and strain induced defects may dominate. Finally, windows are opened through this passivation for wire bonding.

5.6. FORMING GAS ANNEAL

The last heat treatment applied is an annealing at 450 °C for 30mn in N_2 / H_2 ambient. This forming gas anneal is essential for CMOS. The injected hydrogen saturates Si dangling bonds at the gate oxide interface and reduces contact interfaces. Again, little information has been released about actual effect of this forming gas anneal on Fecaps after completion of the back-end process, except concerning the so-called "Y_1" FE Fecaps which are insensitive to hydrogen [48].

Results have been reported by P. D. Maniar [45] on uncapped capacitors subjected to low pressure (<5 torr) forming gas annealing up to 400°C during 20s, (Fig. 18). At this temperature, remanent polarization almost vanishes. It confirms the harmful effect of hydrogen on Fecaps. It has also been noticed that hydrogen accelerates the fatigue rate.

To ensure full compatibility of the FE back-end process with this forming gas anneal, special precautions e.g. hydrogen barrier layers to protect the Fecap, will have to be taken. Beneficial effects of hydrogen have also been noticed in the same study [45]; the leakage current of PZT capacitors is decreased by an order of magnitude after this forming gas anneal.

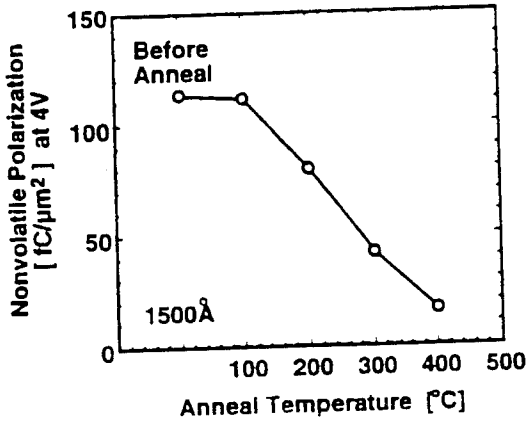


Figure 18. Impact of annealing in hydrogen containing ambients, on Fecap non-volatile polarization.

5.7. PACKAGING

Again, few details have been published about the impact of this last but by no means least, production step. D. J. Sheldon [49] has reported better data retention performance with ceramic packaged parts rather than plastic packaged ones. This is explained to be due to the baking cure step (up to 430°C) experienced by ceramic parts which might help "rejuvenate" damage done to the PZT during the fabrication process.

6. Impact of FE Integration Process on CMOS Devices and FE Capacitors

6.1. IMPACT ON CMOS DEVICES

One condition for a successful integration of FE capacitors with silicon CMOS devices is a negligible impact of the FE process involved, on those devices. Currently, no exhaustive studies have been released about CMOS reliability after FE material integration.

Difficulties to achieve compatibility is highly related to the kind of memory structure chosen. For example, the direct contact option is a very demanding goal, with respect to contamination issues for CMOS. For the Fecap over Locos option, S.L. Miller [22] has demonstrated that, considering their process, a TiO_2 barrier layer between ILD1 and B.E. was necessary to ensure good CMOS electrical properties. Other results from R. Moazzami [40] or G.J.M. Dormans [41] do not mention any barrier layers and show almost identical MOS characteristics for transistors and diodes with and without ferroelectric processing (Fig. 19). In fact, it is not relevant to compare the various results reported about impact on CMOS because each integration process is specific e.g. electrode materials and thicknesses, PZT process and thermal budget.

Feasibility of F.E. integration without damaging CMOS has been demonstrated; however, further studies are necessary and will have to be focused on CMOS reliability issues, in order to demonstrate total immunity.

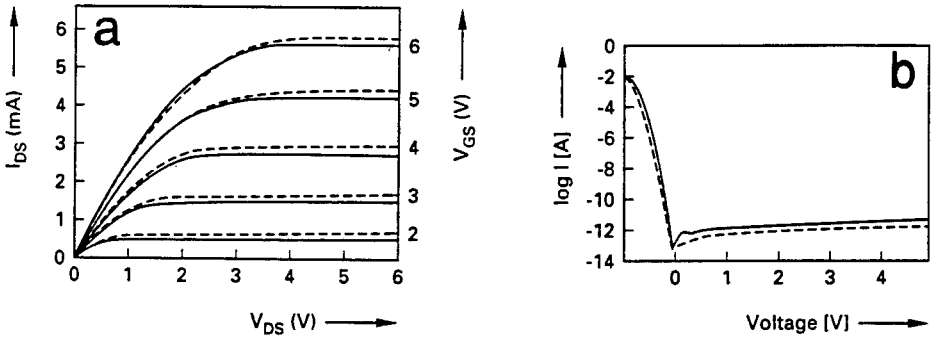


Figure 19. Representative characteristics for a 20µm long NMOS transistor (a) and a $1mm^2$ n+/p diode (b) on a wafer with (full lines) and without (dotted lines) ferroelectric processing.

6.2. IMPACT ON FE CAPACITORS

Another condition for a successful integration of FE capacitors with silicon devices is, of course, to maintain a high level of performance for the FE capacitors. Studies dealing with integration are mostly focused on this issue. For example, Dormans results [41] prove that, with an optimized FE integration process, hysteresis properties are maintained (Fig. 14). Similar results have been shown in FELMAS (Fig. 20). Regarding endurance, very good results have been reported with conventional Pt / PZT / Pt integrated capacitors by T. Sumi [19] (Fig. 21); in FELMAS [50] and by

G.J.M. Dormans [41] (Fig. 22). On this last figure, 10^{12} switching cycles are applied under 3V, while keeping sufficient detection voltage on the memory sense amplifier. Note that, at higher voltages, an even better endurance is expected. Further studies are currently being conducted with alternative electrode materials [51] e.g. metallic oxides such as RuO_2, to take advantage of less disturbed interfaces with PZT.

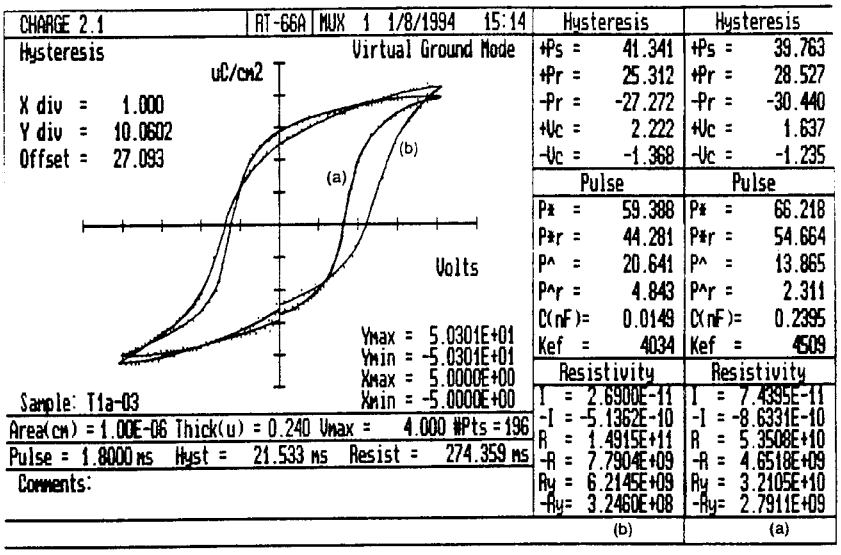


Figure 20. Hysteresis and pulse measurements @ 4V (Radiant Tech. RT66A) on a Pt / PZT (OMCVD) / Pt Fecap. a) after Fecap patterning. b) after completed back-end process.

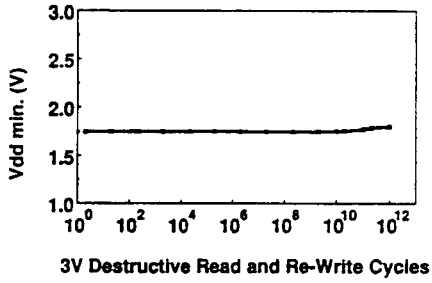


Figure 21. Endurance characteristics of a 256 kb FERAM memory cell using a Fecap with the "Y1" FE material.

Other important electrical properties of Fecaps e.g. switching dynamics [52], conduction mechanisms [53], aging [54] retention [55] are also being studied, but usually not on fully integrated capacitors. These studies are often carried out as a function of temperature [56] to understand thermally activated mechanisms and define the basis of reliability prediction models. Detailed studies have been reported by D.J. Sheldon [49] on reliability results for commercial memory products.

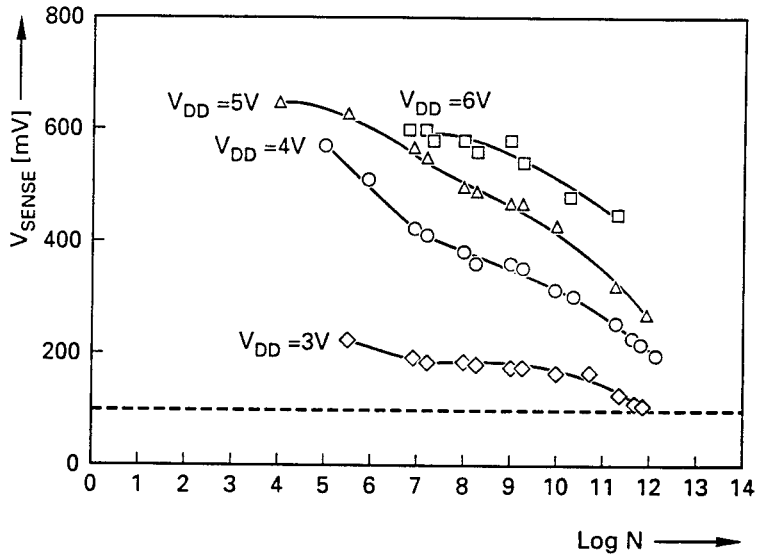


Figure 22. Fatigue at different supply voltages (V_{DD}) for a 1T / 1C cell having a 125 μm^2 Fecap with 300 nm OMCVD PZT. The dashed line at 100 mV indicates the offset voltage for the sense amplifier.

7. Conclusion

A primary goal for integrated ferroelectric memories is to optimize the FE process integration and compatibility on Si devices. Integration has already been demonstrated and we have no evidence of any critical point concerning compatibility or process integration. But the most interesting goal, which is the development of VLSI memory devices, is a very challenging one, especially for non-volatile memories. All the basic techniques required to succeed are available e.g. compatible FE material deposition methods, high performance dry etching processes, compatible back-end processes. Recent results [19] show that high integration is well advanced for volatile and non-volatile memories. However, some important issues need additional and extensive work e.g. research on basic failure mechanisms in the ferroelectric capacitor, improvement of manufacturing processes and compatibility, in depth studies on the reliability of CMOS devices and ferroelectric capacitors.

Finally, we must mention the interest for non-destructive read out (NDRO) integration schemes which are very demanding in terms of compatibility, but present an even more attractive potential as memory devices.

8. Acknowledgements

We acknowledge the contribution of FELMAS partners (under the ESPRIT project # 6137), LETI pilot lines, M. Nunez and L. Peccoud.

9. References

1. Paz de Araujo, C.A. (1991), *Ferroelectrics* **116**, 215.
2. Haertling, G.H. (1991), *J. Vac. Sci. Technol.* **A9 (3)**, 414.
3. Paz de Araujo, C.A. (1992), *MRS Symp. Proc.* **230**, pp. 277.
4. Kinney, W.I. et al. (1994), *Proc. of IEEE ISSCC*, pp. 266.
5. Krupanidhi, S.B et al. (1993), *Proc. of the 5th ISIF*, 7, *Integrated Ferroelectrics.*
6. Tossel, D.A. (1993), *Integrated Ferroelectrics* **3**, 205.
7. Wersing,W. (1993), In: *Ferroelectric Ceramics*, Setter, N. and Colla, E.L. (eds.), Birkhauser Verlag, Basel, 299.
8. Polla, D.L. (1994), *Proc. of the 6th ISIF*, 117, *Integrated Ferroelectrics* (in press).
9. Dimos, D. et al. (1993), *Proc. of the 5th ISIF*, pp. 52.
10. Lee, J. et al. (1993), *Ex. Abstracts ICSSDM*, pp. 850.
11. Eimori, T. et al. (1993), *Ex. Abstracts IEDM*, pp. 631.
12. Ueda, D. (1994), *Proc. of the 6th ISIF*, pp. 2.
13. Wu, S.Y.(1991), *Proc. 3th ISIF.*
14. Nakamura, T. (1994), *Proc. of the 6th ISIF*, pp. 4.
15. Hsu, S.T. (1991), *Proc. of the 3th ISIF.*
16. Lampe, D.R. (1993), *Proc. of the 5th ISIF*, pp. 92.
17. Kammerdiner, L. et al. (1993), *Proc. of the 5th ISIF*, pp. 1.
18. Cuppens, R. et al. (1992), *Microelectronic Engineering* **19**, 245.
19. Sumi, T. et al (1994), *Proc. of IEEE ISSCC*, 268.
20. Fazan, P.C. (1994), *Integrated Ferroelectrics* **4**, 247.
21. FELMAS (1993), *Internal Annual Report, ESPRIT Project* # 6137.
22. Miller, S.L. et al. (1993), *Proc. of the 5th ISIF*, pp. 25.
23. Takemura, K et al. (1992), *Proc. of the 4th ISIF.*
24. Jones, R.E. et al. (1994), *Proc. of the 6th ISIF*, pp. 12.
25. Fleddermann, C.B. (1994), *Proc. of the 6th ISIF.*
26. Trolier, S. et al (1986), *Proc. of the 6th IEEE ISAF*, 707.
27. Baude, P.F. (1993), *MRS Symp. Proc.* **310**, pp. 139.
28. Mancha, S. (1992), *Ferroelectrics* **135**, 131.
29. Asselanis, D. and Mancha, D. (1988) *United states Patent* Number: 4, 759, 823.
30. Shiosaki, T. et al. (1987), *Jap. J. Appl. Phys. Supplement* **26-2**, 159.
31. Eyett, M. et al. (1987), *J. Appl. .Phys .* **62**, 1511.
32. Kawaguchi, T. et al. (1984), *Applied Optics* **23 -13,** 2187.
33. Lee, S.H. et al. (February 1986), *Optical Engineering* **25 - 2**, 250.
34. Poor, M.R. et al. (1991), *M.RS Sym. Proc.* **200.**
35. Vijay, D.P. et al. (1993), J. *Electrochem. Soc.* **140 - 9**, 2635.
36. Saito, K. et al. (1992) , *Jap. J. Appl. Phys.* **31 Part 2 n°9A**, L 1260.
37. Van Glabbeek, J.J. (1993), *MRS Symp. Proc.* **310**, pp. 127.
38. Charlet, B. et al. (1993), *M.R.S Symp. Proc* **310**, pp. 363.
39. Ishihara, K. et al (1994), *Proc. of the 6th ISIF*, pp. 60.
40. Moazzami, R. et al. (1994), *Proc. VLSI Symposium.*
41. Dormans, G.J.M et al (1994), *Proc. of the 6th ISIF*, pp. 15.
42. Nasby, R.D. et al. (1994), *Proc. of the 6th ISIF*, pp. 13.
43. Rod, B. et al. (1994), *Integrated Ferroelectrics* **4**, 155.
44. Cattan, E. (1993), *J.V.ac. Sci. Technol.* **A11 (5)**, 2808.
45. Maniar, P.D. et al. (1993), *MRS Sym. Proc.* **310**, pp. 151.
46. Hirao, S. et al. (1993) , *Ex. Abstracts ICSSDM*, Makuhari, pp. 826.
47. Matsubara, S. et al (1992) , *MRS Sym. Proc.* **243.**
48. Yoshimori, H. (1993) , *Proc. of the 5th ISIF*, pp. 3.

49. Sheldon, D.J. (1994), *Proc. of the 6th ISIF*, pp. 50.
50. FELMAS (1994), *Internal Annual Report, ESPRIT Project* # 6137.
51. Lee, J. et al. (1994), *Proc. of the 6th ISIF*, pp. 125.
52. Larsen, P.K. et al. (1992), *Proc. of the ISAF, IEEE 92* CH 3080-9, 217.
53. Waser, R. (1993) , *In: Ferroelectric Ceramics,* Setter, N. and Colla, E.L. (eds.), Birkhauser Verlag, Basel, 273 .
54. Moazzami, R. (1994), *Proc. of the 6th ISIF*, pp. 47.
55. Hadnagy, T.D. (1994), *Integrated Ferroelectrics* **4,** 217.
56. Gregory, A. et al (1992), *IEEE IRPS*, **91.**

PROCESSING AND DEVICE ISSUES OF HIGH PERMITTIVITY MATERIALS FOR DRAMS

B.E. GNADE, S.R. SUMMERFELT, AND D. CRENSHAW
Semiconductor Research and Development, Texas Instruments, Inc. Dallas, Texas, USA

ABSTRACT. A review of the requirements for future generation DRAMs is presented. The current status of development of ferroelectric materials as possible high permittivity thin-films for capacitor dielectrics is reviewed. A survey of current film deposition methods identifies those techniques that are most compatible with future ULSI manufacturing constraints. We will emphasize issues associated with bottom electrode development, because we feel this is critical to the success of implementation of ferroelectric-based high permittivity materials. Electrical issues such as leakage current and reliability will be discussed briefly. Finally, suggestions for future work will be presented.

1. Introduction

Due to large and increasing demand for dynamic random access memories (DRAMs) [1] (see Fig. 1), the technology to produce higher density memories continues to drive

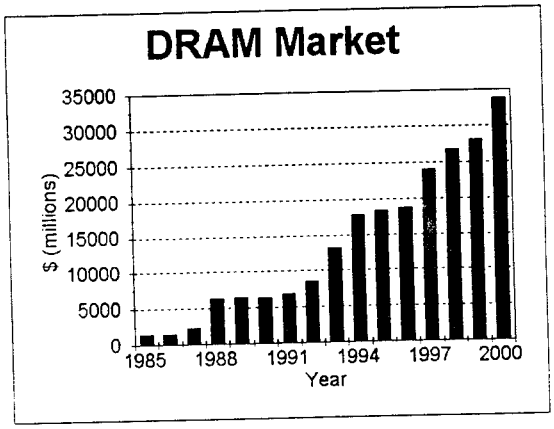


Figure 1. Projections for future DRAM growth.

O. Auciello and R. Waser (eds.), Science and Technology of Electroceramic Thin Films, 373-382.
© 1995 *Kluwer Academic Publishers. Printed in the Netherlands.*

semiconductor development. 16 Mbit DRAMs are in volume production, with 64 Mbit DRAMs projected to he available in limited quantities in 1995. A summary of operating parameters and features is listed in Table 1.

TABLE 1. Operating parameters and features of current and future DRAM generations.

	Minimum Feature Size (μm)	C/area fF/μm^2	Operating Voltage (V)	Wafer Size (mm)	Device Size (mm^2)	Year, 1 million Devices
16 Mbit	**0.6**	**25**	**3.3**	**150**	**140**	**1992**
64 Mbit	**0.35**	**30**	**3.3**	**200**	**200**	**1995**
256 Mbit	**0.25**	**55**	**2.2**	**200**	**300**	**1998**
1 Gbit	**0.18**	**100**	**1.6**	**300**	**450**	**2001**
4 Gbit	**0.15**	**140**	**1.6**	**300**	**650**	**2004**

A unique need for DRAM manufacturers is the development of a high permittivity material to be used as a capacitor dielectric. Sufficient charge storage capacity in a small area is one of the most challenging design issues for Ultra Large Scale Integration (ULSI) DRAM technology. Figure 2 shows that while the charge required per capacitor is decreasing for each new generation, the capacitor are is being reduced even faster. The minimum charge/capacitor is limited by sensitivity to single event upsets, rather than by sense amplifier operation. If we continue to use oxide-nitride-oxide (ONO) dielectrics, the

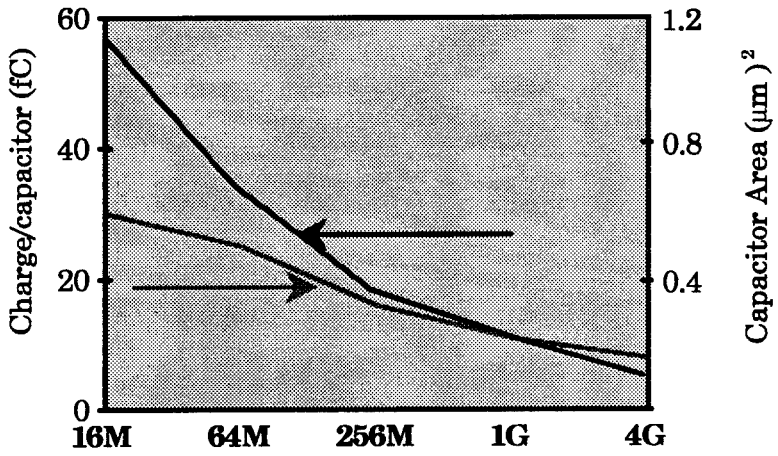


Figure 2. Charge per capacitor and capacitor area as a function of device generation.

required effective capacitor area is several times the total DRAM cell area by the time we reach 1 Gbit. In the past. charge storage capacity was increased via cell structure innovation, increasing the effective storage area beyond the amount allocated for the capacitor cell. Innovations include trench capacitors, stack capacitors (including crowns and fins), and "rugged" polycrystalline silicon to increase surface area/unit area [2]. See Fig. 3 for examples of capacitor architectures currently being investigated.

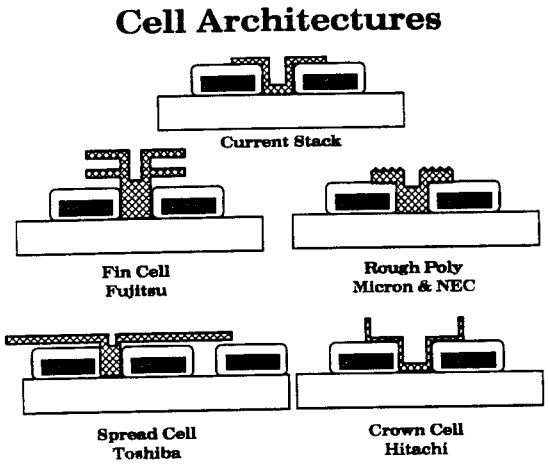


Figure 3. Alternative cell architectures that are being investigated to increase surface area per unit area in DRAM storage cells [3].

In all of these structures, an oxide-nitride (ON) or ONO composite layer serves as the capacitor dielectric. 256 Mbit DRAMs allow only 0.5 μm^2 for a capacitor that must store at least 30 fC at 2.5 V [4, 5], giving an effective capacitance requirement of > 50 $fF/\mu m^2$. It will be difficult to meet such stringent specifications if an ONO composite dielectric, with an effective dielectric constant of 6, is used.

The use of a material with a dielectric constant > SiO_2/Si_3N_4 provides an alternative to cell structure innovation for increasing capacitance/unit area (see Fig. 4). There are several moderate dielectric constant materials that have been, or are being studied as possible capacitor dielectrics. These materials are summarized in Table 2.

TABLE 2. Moderate dielectric constant materials.

Material	Reference	ε	Growth Process	Capacitance $fF/\mu m^2$
TiO_2	6	30-40	MOCVD	9.3
Ta_2O_5	7,8	25	MOCVD	13.8(20.4)
ZrO_2	9	14-28	MOCVD	9.9
Y_2O_3	10	17	Sputtering	4.7
Si_3N_4	Comparison	7	MOCVD	7-8.6

It is important to note that the important parameter is capacitance/unit area. The second parameter of interest is dielectric strength, which places a lower limit on the

thickness of the dielectric. Since $C/A = \varepsilon_0 \varepsilon / t$, where ε is the dielectric constant and t is the thickness, you can see that a large dielectric constant is useful only if the dielectric strength is large enough to allow thin films. Figure 5 shows that most linear dielectrics fall near a straight line when the dielectric constant is plotted vs. breakdown field. Ta_2O_5 (k=22) is being seriously considered by DRAM manufacturers for use at the 256 Mbit node. Ta_2O_5 layers with an effective oxide thickness (t_{eff}) below 2.5 nm have not been reported in the literature [11], suggesting that Ta_2O_5 will not be useful beyond 256 Mbit. Only when a dielectric is to the upper right of the line is it superior to SiO_2. As seen in Fig. 5, materials which currently fall above the line are thin-film ferroelectrics. The use of thin-film ferroelectrics for capacitor dielectrics was suggested in 1989 [12].

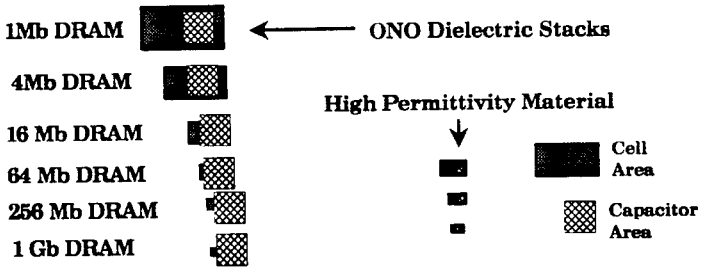


Figure 4. Capacitor area vs. cell area using a high dielectric constant material and ONO dielectric stacks.

Ferroelectric-type dielectrics are presently being investigated for use in high density DRAM. because many exhibit a dielectric constant > 250. $(Ba,Sr)TiO_3$ (BST), a perovskite ferroelectric, is a potential key material in future generation DRAMs [13]. In this paper we review the current status of the development of thin-film ferroelectric materials as high permittivity capacitor dielectrics. Fabrication issues such as film deposition and electrode requirements are addressed.

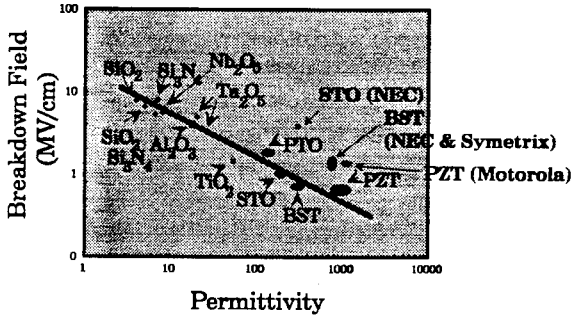


Figure 5. Breakdown field vs. permittivity of commonly studied dielectrics. Notice that thin-film ferroelectric materials are the only materials which fall substantially above the line.

3. Ferroelectric Thin-Film Capacitors

A major advantage resulting from the use of high dielectric constant ferroelectric oxides in >256 Mbit DRAMs would be the use of planar capacitors. A storage node capacitance of approximately 65 $fF/\mu m^2$ would make this possible. State-of-the-art "rugged" polycrystalline silicon with an ONO dielectric gives a maximum capacitance of 20 $fF/\mu m^2$. Current BST technology has demonstrated the material can provide > 100 $fF/\mu m^2$ [5]. Several cell architectures based on the use of a capacitor-over-bit-line (COB) cell structure with a single stacked BST capacitor have been suggested [13, 14].

3.1. FILM DEPOSITION

For ULSI applications, good step coverage and low deposition temperature are required. Stoichiometry, uniformity, and electrical properties are dependent on the deposition method [15, 16]. Roy, et al. [17] tabulated the advantages and disadvantages of nine commonly used deposition methods. Deposition and/or annealing temperatures range from 500-800 °C for thin-film deposition of BST.

Either O_2, N_2O, or O_3 is required during the deposition or anneal in order to form ferroelectric oxides using conventional deposition techniques. The use of oxidizing ambients during deposition and annealing of BST make it impossible to use silicon as the bottom electrode. The formation of any SiO_2 at the dielectric/electrode interface during deposition will dominate the capacitance, because we are trying to achieve equivalent oxide thicknesses of < 4 Å. Noble metals or conducting oxides are the most promising candidate materials for use as the bottom electrode in a BST storage node technology, giving a metal- insulator-metal (MTM) capacitor structure.

3.2. BOTTOM ELECTRODES

The choice of electrode material (both bottom and top) will strongly effect the electrical properties of the dielectric material. The bottom electrode is particularly difficult because it is present during the high temperature BST deposition in a strongly oxidizing environment. The bottom electrode/barrier must satisfy the following criteria:

- not react with BST, nor degrade its electrical properties
- remain conductive after BST deposition
- prevent the interdiffusion of silicon, BST, and oxygen
- maintain a low resistance contact to underlying silicon
- adhere to silicon and SiO_2
- maintain a stable morphology
- be manufacturable

Many of these criteria are unique to the high density DRAM application, which due to space limitations requires the capacitor to be directly connected to the underlying silicon. With MOCVD BST deposition temperatures ranging from 630-750 °C in 1-100 Torr oxygen activity [18], there are few good choices for the bottom electrode. The only metals that are thermodynamically stable under these deposition conditions are platinum and gold (see Fig. 6). Typical capacitor contact metals such as TiN, tungsten, aluminum, and polycrystalline silicon are not suitable because they react with O_2 during BST deposition to form low dielectric constant oxides. In addition, reactive metals can degrade the BST film properties by removing oxygen from the BST during or after deposition.

The leakage current measured in BST thin-film capacitors appears to be controlled by the height of the BST/electrode Schottky barrier [19, 20, 21]. Data presented by Scott at this conference on several electrode systems support this idea. Of the electrode systems currently being studied, platinum has the highest work function.

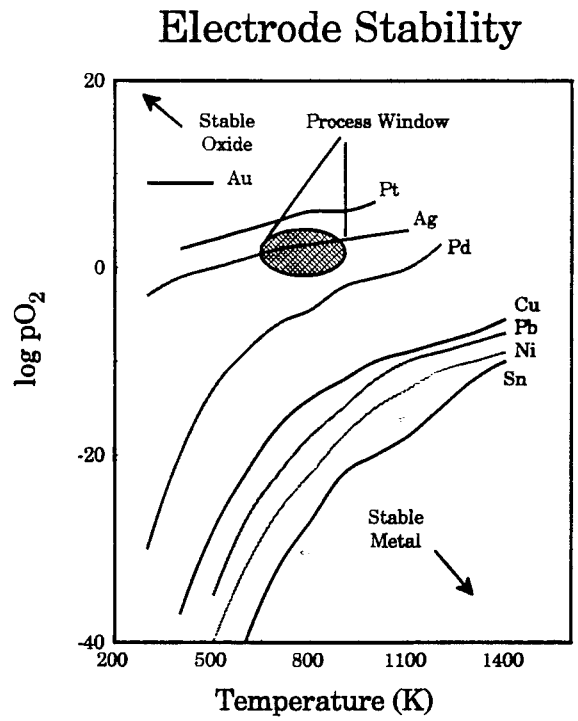


Figure 6. Stability of metals in oxygen as a function of oxygen activity and temperature. Typical deposition conditions are noted by the process window. Only metals to the upper left of the processing window are thermodynamically stable during BST deposition.

While the thermodynamic stability and high work function of platinum make it attractive as a bottom electrode material, there are two issues which must be addressed. Platinum readily reacts with silicon to form $PtSi_2$ at approximately 400 °C. The $PtSi_2$ oxidizes, forming an interfacial layer of SiO_2. Also, the oxygen diffusion rate through thin-film polycrystalline Pt is quite high [22, 23]. Because of these deficiencies, a diffusion harrier must be placed between the platinum electrode and the polycrystalline silicon plug. Fujii et al. [14] observed SiO_2 at the BST/Pt interface when Pt/Ti was used, while no SiO_2 was observed for Pt/TiN/Ti electrodes. Auger electron spectroscopy depth profiles for the two cases confirmed that TiN successfully prevented silicon from diffusing to the BST/Pt interface, while titanium did not. TiN is a commonly used barrier layer between silicon and metals such as tungsten, aluminum, and noble metals. TiN is the preferred barrier layer at this time because of its stability and its pervasive use in the semiconductor industry. The main difficulty with using TiN as the barrier layer is poor

oxidation resistance. TiN oxidizes rapidly above 500 °C and forms an interfacial layer of TiO_2 at the Pt/TiN interface [24, 25, 26].

Another possible barrier layer that has been investigated is tantalum. NEC has demonstrated good BST capacitors on Pt/Ta/Si bottom electrodes. However, the contact resistance from the platinum to the silicon substrate was large because the Ta and polycrystalline silicon oxidized during the BST deposition, due to oxygen diffusion through the Pt [27]. Another problem with this barrier is the reaction of tantalum and polycrystalline silicon to form $TaSi_2$, which can oxidize to form an interfacial layer of SiO_2.

A potential problem with platinum lower electrodes is the physical stability of the surface. Platinum has been observed to form large hillocks [28]. One explanation for the hillock formation is the differential thermal expansion ratio between Pt and Si. The platinum is under compression at temperatures above the deposition temperature, and apparently hillock formation can relieve the stress. Depositing the Pt at elevated temperatures (250-350 °C) [28] reduces hillock formation.

The temperature, time, and oxygen potential during BST deposition are critical in determining whether the bottom electrode will survive. Lowering the temperature, shortening the time, and/or decreasing the oxygen potential during the BST deposition is as important as designing a more stable bottom electrode.

The top electrode generally has less stringent requirements because it is not subjected to the BST deposition process. Due to the fact that DRAMs operate in a bipolar mode it is important to have low leakage current, or high Schottky barriers, at both interfaces. Because of this, platinum is also popular as a top electrode material. Another important factor is the cleanliness of the BST surface before platinum deposition. It has been shown that deposited $SrTiO_3$ surfaces are more reactive than single crystal $SrTiO_3$ [29]. X-ray photoelectron spectroscopy data suggest that the deposited $SrTiO_3$ surface has an appreciable amount of hydroxide on the surface even after only a short exposure (< 1 min.) to air. BST surfaces probably behave in a similar manner.

4. Electrical Properties

DRAM capacitor dielectrics have several electrical requirements; 1) dielectric constant, 2) leakage current, and 3) dielectric fatigue. The capacitance requirements were discussed in section 2. Leakage current and fatigue will be discussed below.

4.1. LEAKAGE CURRENT

The criteria for maximum allowable leakage current varies with DRAM cell design. Koyama [13] used the following specifications to arrive at a maximum allowable leakage value for a 256 Mbit DRAM: 1) refresh time = 128 ms, 2) maximum allowable charge loss per refresh cycle = 1 fC, and the storage node area = 0.5 μm^2. Using these values, a maximum leakage current at 3.3 V (or 1.6 V if half V_{cc} bias is used [30]) of 1.6×10^{-6} A/cm^2 is determined. A maximum leakage current of 1.5×10^{-7} A/cm^2 is often stated [13], allowing a 10X margin for reliability. Meeting this leakage current requirement has been difficult. The leakage current requirements highlight the importance of the correlation between dielectric constant and breakdown field.

4.2. Reliability and Dielectric Fatigue

Because the theory of conduction and breakdown mechanisms in thin-film ferroelectric materials is not yet mature, it is not certain that reliability testing methods commonly used for conventional dielectrics are valid for use on ferroelectrics [31]. Time-dependent-dielectric-breakdown (TDDB) experiments have been performed on various dielectrics. Carrano et al. [31] performed TDDB experiments on lead zirconate titanate (PZT) films and found time-to-breakdown (t_{bd}) appears to be exponentially dependent on applied field. The fact that these films are ferroelectric (not paraelectric) could indicate that TDDB results might be masked by polarization effects. Continuing this study, Sudhama et al. [32] measured a time-to-breakdown of only 2.2 months for a 200nm thick PZT film under 3 V bias.

TDDB experiments performed on BST thin films have yielded data which appear to allow more standard lifetime extrapolation methods (t_{bd} appears to be dependent on applied field). Koyama et al. [13], defining T_{50} as the time required for 50% device failure at a leakage current of 10^{-4} A/cm^2, determined T_{50} to be > 100 years under a 5 V bias voltage.

TDDB studies conducted by Fujii et al. [14] for 140 nm BST films on Pt/TiN/Ti bottom electrodes produced a similar result for 5 V bias voltage. Results reported so far for BST suggest that it is compatible with current DRAM TDDB requirements.

Dielectric fatigue is the degradation of stored charge per unit area (Q_c) under dynamic stress. Under normal DRAM operation, unipolar stressing is sufficient to make projections of film reliability. Bipolar stressing is required when half V_{cc} biasing [30] is used. PZT has been found to suffer negligible reduction in Q_c after 10^{13} cycles of unipolar stress (0-10V) with a 10 MHz square wave [32]. This result predicts a fatigue free operational lifetime of > 4 x 10^4 years. These same films were found to suffer a 25% decrease in Q_c after only 10^6 cycles of + 5 V bipolar stressing. It is apparent that fatigue is greatly accelerated in ferroelectric films by bipolar stressing. This type of fatigue is not expected to occur in paraelectric films such as BST and $SrTiO_3$ (STO), but no studies have been reported in the literature.

5. Summary

Research on ferroelectric-type dielectrics has increased rapidly in recent years due to the potential impact on ULSI DRAM technology. Possessing dielectric constants that are 100 x that of SiO_2, the use of ferroelectric thin films should allow the use of storage node capacitors that are far less complicated than today's crown and fin structures. Deposition methods which are designed for stoichiometry control, good step coverage, and process compatibility are being investigated. The deposition method strongly effects the integration of the bottom electrode material into an MIM capacitor technology. Capacitors have been fabricated with STO, BST, and PZT which meet the leakage current requirements for 256 Mbit DRAMs. TDDB experiments on BST (paraelectric) films have shown t_{bd} >100 years. PZT films have been observed to fatigue after aggressive bipolar dynamic voltage stressing.

6. References

1. The Merchant Market for DRAMs (1992), *In-Stat P9220DR* **38**.
2. Sakao, M., Kasai. N. and Ishijama, T. (1990), *IEDM* **90**, 655.
3. Fazan, P. (1994), *Integrated Ferroelectrics* **4**, 247.
4. Lee, J., Chikarmane,V. (1993), *Integrated Ferroelectrics* **3**, 113.
5. Eimori., T., Ohno, Y., Kimura, H., Matsufusa, J., Kishimura, S., Yoshida, A., Sumitani, H., Maruyama, T., Hayashide, Y., Moriizumi, K., Katayama, T., Asakura, M., Horikawa. T., Shibano, T., Itoh, H., Sato, K., Namba, K., Nishimura, T.. Satoh, S., Miyoshi, H. (1993), *IEDM* **93**, 631.
6. Rausch, N., et al. (1993), *J. Electrochemical Soc.* **140**, 145.
7. Shinriki, H., et al. (1989), *IEEE Trans. Electron Devices ED*-**36**, 328.
8. Fazan, P.C. et al. (1992), *IEDM Tech. Digest*, 263.
9. Shappir, J., et al. (1986), *IEEE Trans. Electron Devices ED*-**33**, 442.
10. Manchanda, L., et al. (1988), *IEEE Electron Dev. Lett. EDL*-**9**, 180.
11. Lo, G.Q., Kwong, D., Fazan, P.C. (1993), *IEEE Electron Del. Lett.* EDL-**14**, 216.
12. Tasch, A.F., Parker, L.H. (1989), *Proc. of the IEEE* **77**, pp. 374.
13. Koyama, K., Sakuma, T., Yamamichi, S., Watanabe, H.. Aoki, H., Ohya, S., Miyasaka, Y., Kikkawa, T. (1991), *IEDM* **91**, 823.
14. Fujii, E., Uemoto, Y., Hayashi, S., Nasu, T. (1992), *IEDM* **92**, 267.
15. Van Buskirk, P., Gardiner, R., Kirlin, P.S. (1992), *MRS Symp. Proc.*, 223.
16. Yamamichi, S., Sakuma, T., Takemura, K. Miyasaka, Y. (1991), *Jap. J. Appl. Phys.* **30**, 2193.
17. Roy, R.A., Etzold, K.F., Cuomo, J.J. (1990), *MRS Symp. Proc.*,
18. Van Buskirk, P.C., Gardiner, R., Kirlin, P.S., Nutt, S. (1992), *J. Mat. Res.* **7**, 542.
19. Brennan, C.J. (1991), MRS Proceedings, *Ferroelectrics Thin Film*
20. Brennan, C.J. (1991), *Proc. 3rd Inter. Symp. on Integrated Ferroelectrics*, 354.
21. Scott., J.F., Melnick, B.M., Araujo, C.A., McMillan, L.D., Zuleeg, R., (1991), *Proc. 3rd Inter. Symp. on Integrated Ferroelectrics*, pp. 176.
22. Grill, A., Kane, W., Viggiano, J., Brady, M., Laibowitz, R. (1992), *J. Mat. Res.* **7**, 3260.
23. Takemura, K., Matsubara, S., Sakuma, T., Yamamichi, S., Yamaguchi, H., and Miyasaka, M. (1992), *4th Int. Symp. on Integrated Ferroelectrics*, pp. 481.
24. Suni, I., Sigurd, D., Ho, K.T., Nicolet, M.-A. (1983), *J. Electrochem. Soc.* **130**, 1210.
25. Tompkins, H.G.(1991), *J. Appl. Phys.* **52**, 3876.
26. Wittmer, M., Noser, J., Melchior, H. (1981), *J. Appl. Phys.* **52**, 6659.
27. Miyasaka, Y., and Matsubara, S. (1991) *Thin Film Capacitor and Manufacturing Method Thereof*, United States Patent, 5,053,917.
28. Hren, P.D., Al-Shareef, H.N., Rou, S.H., Kingon, A.I., Buaud, P., Irene, E.A. (1992), *MRS Proceedings.*
29. Bhattacharya, P., Komeda, T., Park, K., Nishioka, Y., Summerfelt, S., Gnade, B. (1993), ECS Meeting, Fall 1993, New Orleans.
30. Kumanoya, M., Kazuyasu, F., Hideshi, M., (1985), *IEEE J. of Solid-State Circuits SC*- **20**, 909.
31. Carrano, J., Sudhama, C., Lee, J. (1989), *IEDM*, pp. 255.

32. Sudhama, C., Carrano, J.C., Parker, L.H., Chikarmane, V., Lee, J.C., Tasch, A.F., Miller, W., Shepperd, W.H. (1990), *MRS Symp. Proc.* **200**, pp. 331.

FERROELECTRIC THIN FILMS FOR CAPACITOR AND SENSOR APPLICATIONS

R. W. WHATMORE, P. KIRBY, A. PATEL, N. M. SHORROCKS, T. BLAND AND M. WALKER
GEC-Marconi Materials Technology, Caswell, Towcester, NN12 8EQ., United Kingdom

ABSTRACT. Considerable emphasis has been placed in recent years on the potential application of ferroelectric thin films, particularly those based on PZT-on-Silicon substrates to non-volatile memories. However, these materials also possess properties which make them interesting for a wide range of other applications. For example, they have high dielectric constants which can be applied to capacitor structures in analog circuits for circuit elements such as filters as well as in digital memories. The pyroelectric coefficients and figures-of-merit which can be obtained from these films are comparable with those of bulk ceramic materials, making them of interest for uncooled IR detection and thermal imaging. Likewise, the films show strong piezoelectric activity which gives them potential for passive devices such as microphones or accelerometers or active devices such as thin film resonators for filter applications. The physical (mechanical and electrical) structures which are needed to produce these kind of devices are very different from those needed to make memories. Some of these are discussed and used to derive the constraints, such as process temperatures, which must be applied to the fabrication of the ferroelectric film. The potential of the films are illustrated by the growth and electrical properties of lead zirconate titanate compositions for capacitor, IR detector and piezoelectric sensor applications. Examples of practical RF capacitor and pyroelectric device structures are given.

1. Introduction

There has been an enormous growth of interest over the last 5 years in the application of ferroelectric (F/E) thin films integrated onto Silicon IC's to non-volatile memories. This is reflected in the emphasis of the papers in the proceedings of this meeting. However, F/E materials in general have a much wider range of applications. Indeed, although bulk F/E's were examined extensively for memories in the 1950's and early 1960's [1] they are never used in that role now. Instead they are used in capacitors, piezoelectric, pyroelectric and electro-optic devices etc [2].

This paper examines the use of F/E thin films in electronic devices other than memories, including capacitors (for non-storage applications), pyroelectric infra-red detectors and piezoelectric devices. Of particular interest are the properties which can be achieved in such films under processing conditions which are compatible with

O. Auciello and R. Waser (eds.), Science and Technology of Electroceramic Thin Films, 383-397.
© 1995 *GEC Marconi Ltd. Printed in the Netherlands.*

semiconductor (Si or GaAs) IC's and the means for fabricating those films into working devices.

In this, the methodology for device fabrication is extremely important. It is contended here that it will be necessary for economic reasons to deposit the F/E layer as late as possible in the sequence of device manufacturing processes. This is because the managers of semiconductor processing facilities, be they silicon or gallium arsenide based, are necessarily very conservative in the materials they will allow into their lines because of the risk of cross-contamination. They are rightly intolerant of new or "exotic" ones such as F/E oxides. Hence, by depositing the F/E layer late in the process, the number of processing facilities which need to be dedicated to F/E-based devices, and therefore the capital and operating costs, can be minimized.

The ideal would be to put the F/E layer down only after the semiconductor device is complete and passivated. In this way, application specific integrated circuits (ASIC's) can be designed to perform the necessary signal processing functions associated with the F/E element (amplification, multiplexing, etc) and purchased from any processing foundry able to meet the performance requirements. This enables the manufacturer of the F/E-containing IC to take advantage of the processing scale of the foundry without incurring the huge capital costs of setting up a dedicated facility.

There are two main limitations which this places upon the F/E thin film process. These are the processing temperatures required during deposition to obtain the correct crystallographic phase and electrical properties and the selection of any chemical etches required for patterning the materials. It is also important to choose appropriate metals (or other conductors) or insulators for their compatibility with the semiconductor device. It would not be wise, for example, to use gold metallizations in association with silicon IC's, especially if the device is to see elevated temperatures after the gold deposition.

The limitations on temperature of F/E film growth on Si IC's emerge from the use of Al/Si metallizations. Ohmic contacts between the conducting tracks and the Si are formed at around 425°C [3]. It is generally considered that 450°C is the maximum temperature to which devices using such conductors can be exposed, and for relatively short periods of time. TiW conductors which might withstand higher temperatures have been used in some specialized Si IC processes but are not yet standard in most foundries. Similar low F/E temperatures would be required if they were to be used with GaAs monolithic microwave integrated circuits (MMIC's).

The growth of thin films of materials such as $PbTiO_3$ (PT), Pb $(Zr_xTi_{1-x})O_3$ (PZT), Pb $(Sc_{0.5}Ta_{0.5})$ O_3 (PST) and $Pb(1-3/2y)La_y)$ $(Zr_xTi_{1-x})O_3$ (PLZT) has been reported by various techniques including sol-gel [4], metal organic chemical vapor deposition (MOCVD) [5] and dual ion beam sputtering (DIBS) [6]. Generally, processing temperatures to achieve single phase perovskite material with good electrical properties have been 600 to 800 °C. A major focus in the study reported here, therefore, has been achieving these properties at lower processing temperatures. The materials chosen for the study have all been in the PZT system and the processing has concentrated on the sol-gel method. The following sections describe film processing, growth of films for capacitor applications and films for pyroelectric/piezoelectric applications.

2. Film Processing

The wet chemistry deposition processes of sol-gel and metallorganic decomposition (MOD) have developed rapidly in the last ten years [7,8]. The sol-gel process is a metal

organic processing route that can be adapted to give thin films, bulk monoliths or powders by direct precipitation. Simplicity, stoichiometric control and low cost are the primary advantages of the technique. Also, due to the wide availability of suitable precursors, it is a relatively easy process to modify compositions and to obtain complex oxide materials. In this study, titanium n-butoxide and Zirconium n-butoxide were chosen along with lead (ii) acetate and reacted according to the scheme shown in Fig. 1.

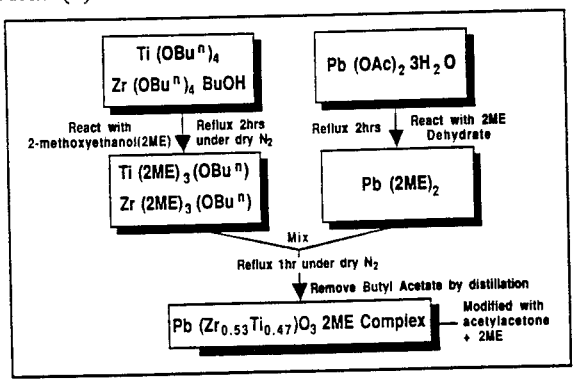


Figure 1. Process flow for PZT sol preparation.

Dilute solutions were used for deposition (typically 0.1 to 0.2 molar). While the original reason for this was to avoid cracking problems, it is considered that this has had an important effect upon processing temperatures.

Films were spin coated at 2000 rpm for 30 secs onto substrates consisting of silicon coated by e-beam evaporation with 1000Å Pt / 50Å Ti onto SiO_2. Spinning was followed by a short bake at 170°C to remove the solvent, repeating several times and then consolidating the film at temperatures close to 430-460 °C. Thicker layers were obtained by repeating the cycle. 80 layers of 0.1 molar PZT 30/70 sol gave a thickness of between 0.8 to 0.9 μm while 70 layers of 0.14 molar PZT 20/80 sol gave a thickness of 1.0 μm.

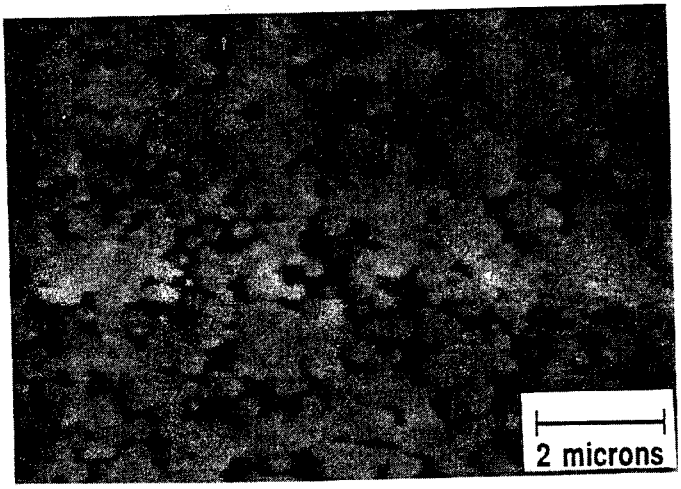


Figure 2. PZT 30/70 thin film consolidated at 430 °C showing the formation of rosettes.

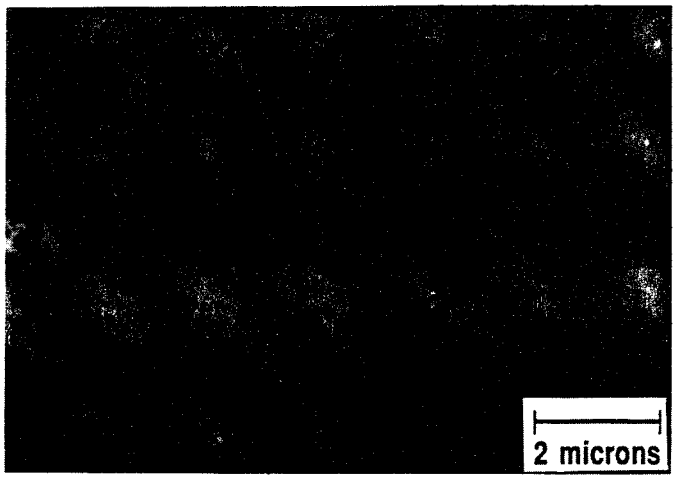


Figure 3. PZT 30/70 thin film consolidated at 460 °C showing the uniform surface formed by the merging of rosettes.

Rosette formation was observed in films processed at, or above, 430 °C. Figure 2 shows the rosettes formed on a PZT30/70 film consolidated at 430 °C. At temperatures of 460 °C or above, individual rosettes could not be observed - as shown in Fig. 3, which is the surface morphology of a PZT 30/70 film consolidated at 460 °C. One of the unique features of this process is that highly (111) preferred orientation perovskite single phase films are obtained after the consolidation step, obviating the requirement for further high temperature annealing. This is exhibited by the XRD trace shown in Fig. 4 for a 460 °C film.

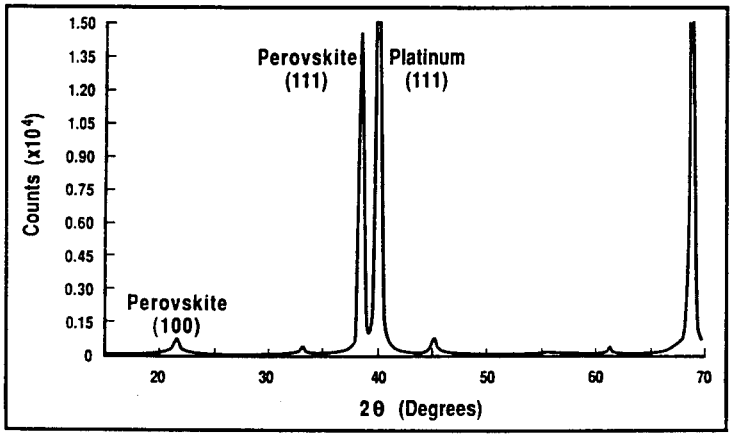


Figure 4. XRD scan for PZT 30/70 thin film showing the highly-preferred (111) film orientation and the absence of pyrochlore phase.

The minimum temperature required for the intermediate high temperature baking appears to be close to 450 °C. The amount of perovskite in the films was calculated from XRD traces such as the one shown in figure 4 vis:

$$\text{Perovskite \%} = 100 \times \frac{I_{111}(\text{Perovskite})}{(I_{111}(\text{Perovskite}) + I_{222}(\text{Pyrochlore}))}$$

Figure 5 shows the Perovskite % as a function of consolidation temperature for a PZT 30/70 film composition. 100% Perovskite is obtained for a film temperature of 445 °C. At present, this is the lowest-known processing temperature for device-worthy PZT films.

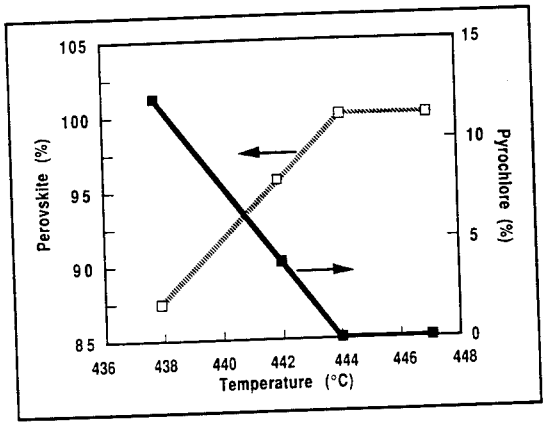


Figure 5. Showing the variation of the percentages of perovskite and pyrochlore phases in the PZT 30 / 70 films as a function of consolidation temperature.

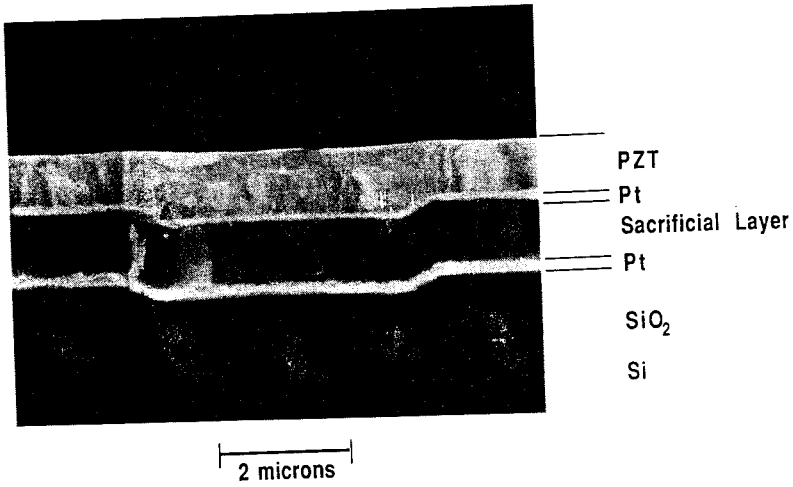


Figure 6. SEM cross-section through a PZT 30/70 film on Pt/Ti/SiO_2/Si.

The quality of the layers obtained can be seen in Fig. 6 which shows an SEM fracture surface on a standard substrate. The film is non-porous and dense with some evidence of columnar grain growth.

Figure 7 shows the planarizing effect of the PZT film when deposited onto a substrate with surface morphology, in this case a SiO_2/Si substrate bearing a patterned sacrificial layer (see section 4 below).

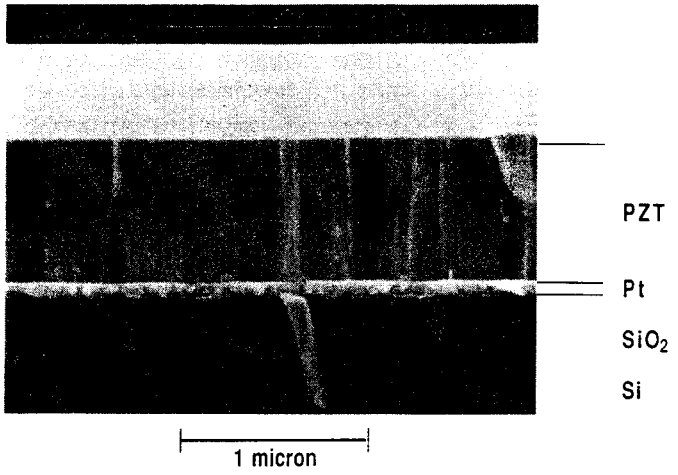


Figure 7. SEM cross section through a PZT 30 / 70 film on a structure exhibiting morphology, showing the planarizing effect of the sol-gel film.

3. F/E Thin Film Capacitors

Capacitors are used in RF circuits for tuning elements, interstage isolation and for RF bypass. The two most-commonly used dielectrics in MMIC's are Si_3N or SiO_2, with dielectric constants (e) of 6.5 and 4.0 respectively [9]. There are significant savings to be made in the areas which must be dedicated to capacitors, and hence the cost of the circuit, if the dielectric constant can be increased by using a F/E thin film. There is the potential for using F/E thin film capacitors on silicon as discrete flip-chip components on multichip modules using solder-bump interconnection techniques [10]. Finally, F/E thin films capacitors offer the ability to vary the capacitance with modest applied voltages for applications such as tunable phase shifters and filters. In this study both ferroelectric PZT 53/47 and antiferroelectric $PbZrO_3$ (PZ) films have been assessed. PZ is of particular interest because, being antiferroelectric, it possesses low loss at GHz frequencies and its ε is bias voltage invariant, while nevertheless exhibiting an interesting value (ca 100).

The basic capacitor layer structure that allows measurement at microwave frequencies is illustrated in Fig. 8. A continuous TiPt metallization is deposited over an oxide isolated silicon substrate and then a thin PZT or PZ layer is deposited over this metallization by the sol gel technique. After firing to achieve the desired ferroelectric

properties, the ferroelectric film is wet etched to expose the lower capacitor electrode and define the ferroelectric mesa.

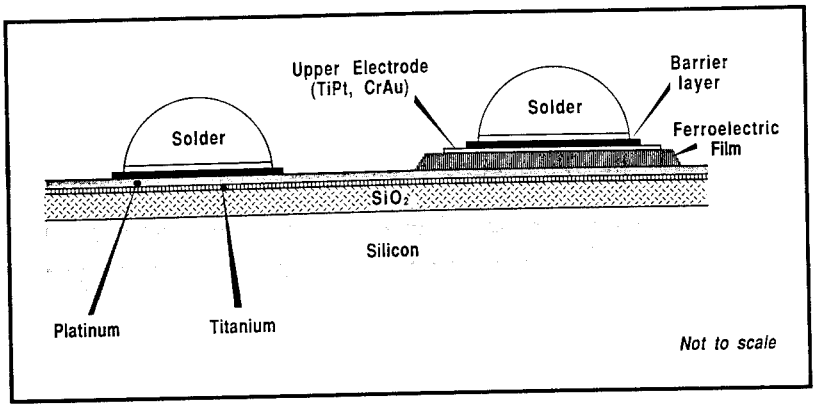


Figure 8. Schematic cross section through a PZT flip-chip capacitor.

An upper electrode of the desired area is then deposited and defined on the patterned ferroelectric film. A non-solderable barrier metallization is defined on both upper and lower electrodes to prevent subsequent interaction between the solder bump structure and the existing platinum metallization. Solder wettable metallization and solder areas are then defined over the barrier layer areas and the solder reflowed to form a well defined solder bump. The outer four solder bumps provide support for the capacitor, the inner two provide electrical connection. The thin film capacitor structure is then bonded to an alumina substrate as illustrated schematically in Fig. 9. The substrate carries coplanar striplines of 50 Ω impedance that allow RF-on-wafer measurements over the frequency range of 45 MHz to 20 GHz.

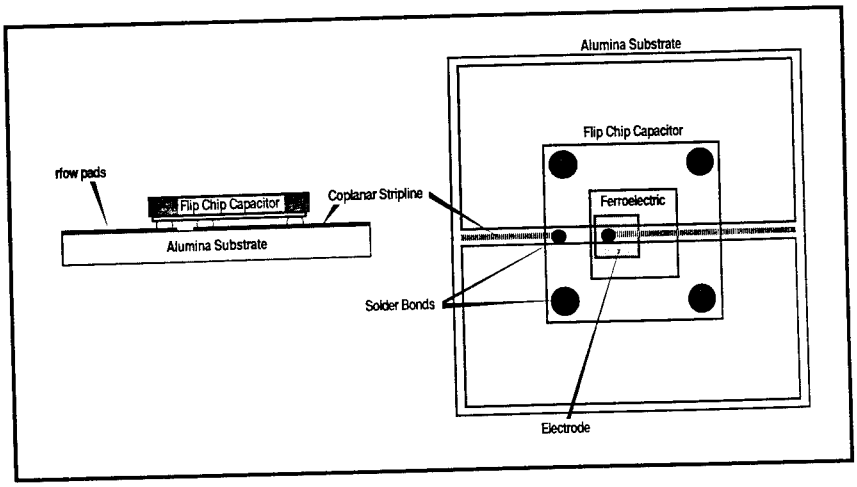


Figure 9. Flip-chip capacitor design showing alumina stripline substrate and ferroelectric, electrode and solder bond locations on flip chip capacitor structure (schematic).

A processed ferroelectric capacitor is shown in Fig. 10. The area of the electrode is 450x450 microns. This capacitor technology has been demonstrated using PZT compositions 53/47, and 100/0. Using this composition range capacitor values from less than 1 pF to 15 nF were obtained. The alumina substrates with flipped capacitors were measured using a Cascade Microtech RFOW prober. S-parameters were obtained over the 0.05 - 5.05 GHz frequency range using a HP8720 A network analyzer. In order to ascertain the capacitance and resistance of the ferroelectric capacitors two de-embedding structures were measured. A '50' ohm characteristic impedance coplanar line whose length is identical to that of the flip chip capacitor RFOW measurement structures and a structure that is flip chip bonded but did not have a ferroelectric film between the electrodes. The latter gave a measure of the external series resistance, which was large (~1.5 ohm) because of the thin metal electrodes (~ 1200 Å) used in the present study.

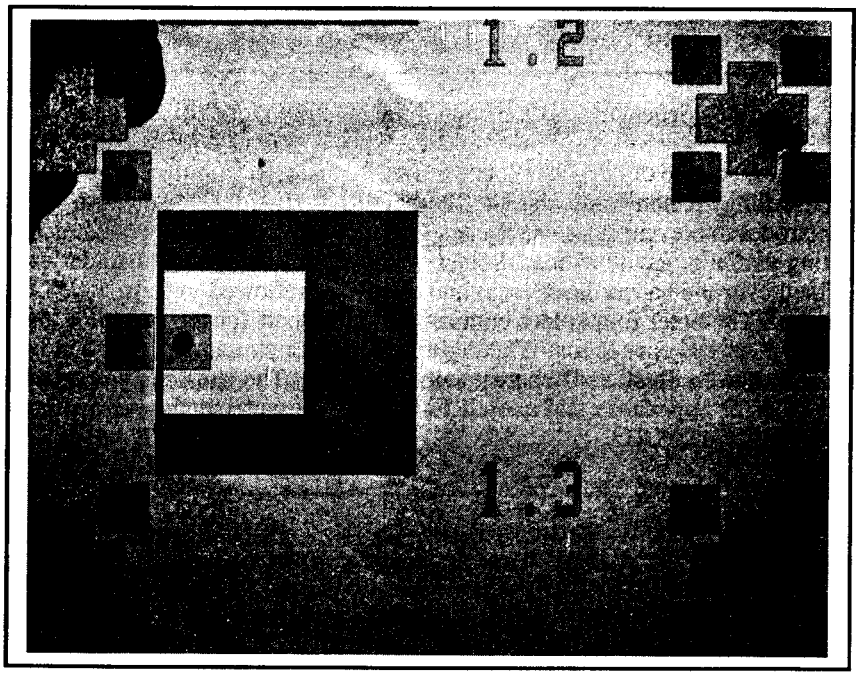


Figure 10. A single capacitor structure. The electrode area is ~ 450 x 450 μm.

Figure 11 shows the typical s-parameter data obtained from a flip chip bonded PZT capacitor structure having a 53/47 composition. There was an unexpected resonance at about 1GHz. Over the range 0.05 to 0.75 GHz, a reasonable fit to the data could be obtained with the model of Fig. 12. The capacitor is described by a series resistance RC and a capacitance, CC. C1 and C2 represent the characteristics of the input and output feedlines under the flipped component and the capacitance to ground of the capacitor's electrodes. Table 1 shows the modelled results for PZT (53/47) and PZ capacitors; the modelled capacitance values are within 10% of those measured at low frequencies using bridge techniques and correspond to ε values of 655 and 100 for the two compositions,

respectively. Tan δ values of typically 0.01 to 0.02 were obtained in the range 10^2 to 10^6 Hz for the PZ films, while the PZT 53/47 films gave values of 0.03 to 0.05 over the same range. The lower dielectric constant and loss from the PZ films is precisely what would be expected from an antiferroelectric (AFE) material compared with a ferroelectric. This is because the AFE domain walls would not be expected to be mobile under the applied AC field whereas it is known that the main source of loss in a F/E at low frequencies is due to the domain wall movement contribution. This is particularly so near the morphotropic phase boundary in PZT where the domain walls are at their most mobile. Interestingly, the PZ films exhibit a significantly higher bulk resistivity ($10^{10}\Omega$m cf 10^9 Ωm for PZT 53/47).

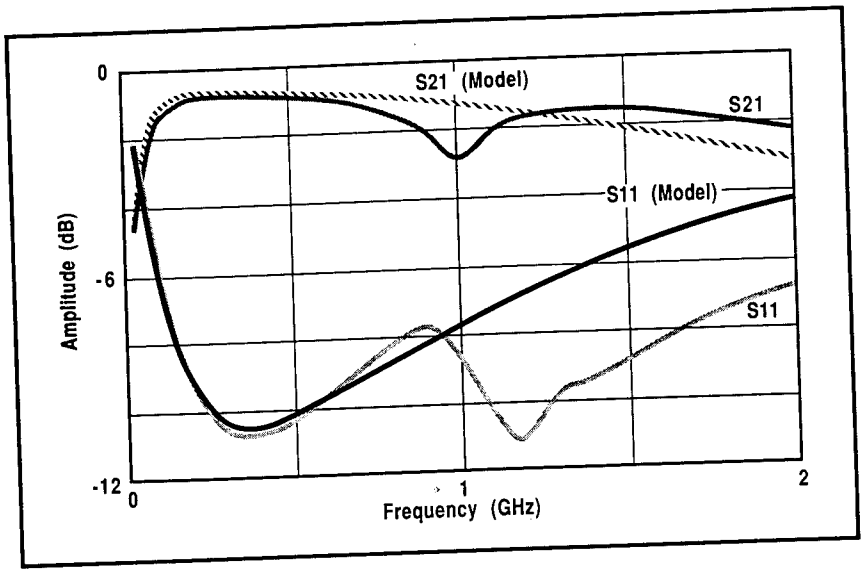


Figure 11. PZT capacitor's S-Parameter response and a model fit to it.

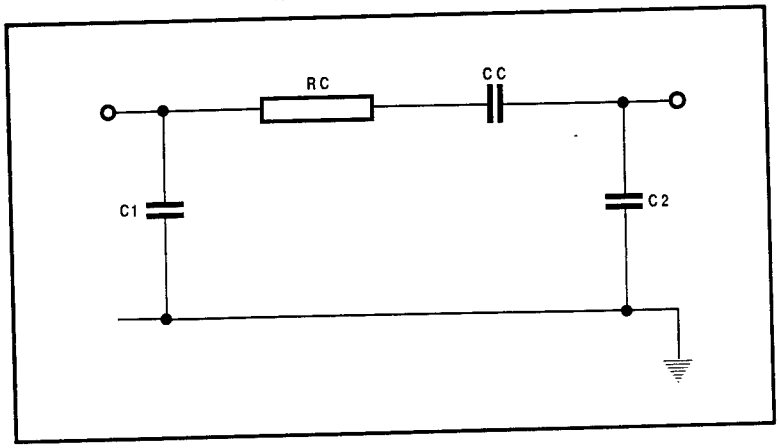


Figure 12. Low frequency capacitor model.

TABLE 1. Results obtained by modeling the PZT 53/47 and PZ chip capacitor structures over the range 0.05 to 0.75 GHz, compared with the low frequency properties.

PZT 53/47 Capacitors

High Frequency Properties					Low Frequency Properties			
Type	Capacitance(CC) (pF)	Resistance (RC) (Ohm)	C1 (pF)	C2 (pF)	Capacitance (pF) 20 KHz	ε (10^2 to 10^6 Hz)	tan δ	ρ (Ωm)
1.5	410.4	1.1	0.8	3.5	420		0.03	
3.4	22.6	3.4	0.3	2.5	23	655	to	10^9
3.5	21.3	3.7	0.4	2.5	15		0.05	
4.5	13.9	7.5	0.7	1.1	15			

PZ Capacitors

High Frequency Properties					Low Frequency Properties			
Type	Capacitance(CC) (pF)	Resistance (RC) (Ohm)	C1 (pF)	C2 (pF)	Capacitance (pF) 20 KHz	ε (10^2 to 10^6 Hz)	tan δ	ρ (Ωm)
1.4	127.8	1.5	0.5	3.5	130		0.009	
4.4	93.3	1.3	0.4	1.3	94	100	to	10^{10}
1.5	68.8	1.6	0.4	3.6	63		0.018	
3.1	20.3	2.4	0.3	2.9	22			

The change in S-parameter response of 53/47 capacitors with respect to a dc voltage placed across the component's electrodes is shown in Fig. 13. Cycling the voltage up and down revealed a hysteresis which when modeled could be assigned to a variation in the component's capacitance. With series capacitor structures it was possible to get a reversible variation from 14.1 to 4.8 with applied voltages of between 0 and 30V. By comparison, the PS capacitor varied by less than 10% from 0 to 20V applied bias.

It is considered that these results show the considerable potential of these F/E films for capacitor applications at frequencies into the Hz range.

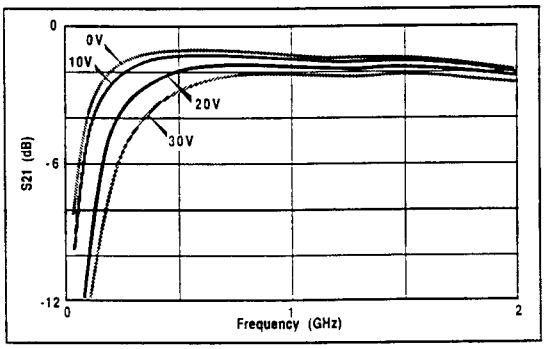


Figure 13. DC Bias voltage dependence of the capacitance of 53/47 Capacitors from 0 to 30V, measured up to 2 GHz.

4. F/E Thin Films for Pyroelectric and Piezoelectric Applications

There has been a major drive over the last 10 years to develop uncooled thermal imaging arrays based upon the pyroelectric effect which have been extensively reviewed elsewhere [11, 12]. To date, practical arrays have largely been based upon the interfacing of bulk F/E ceramic materials [13] with CMOS readout circuits using flip chip technology [10]. However, there has also been significant effort in developing techniques for integrating pyroelectric thin films directly onto silicon IC's [6].

In order to obtain good performance from a pyroelectric thermal imaging array, it is necessary to have:

(a) A good pyroelectric material with a high value of the figure-of-merit F_D, defined by:

$$F_D = \frac{p}{C_V(\varepsilon \varepsilon_0 \tan \delta)^{1/2}}$$

where p = pyroelectric coefficient; C_V = volume specific heat; ε=dielectric constant of ferroelectric; Tan δ = dielectric loss of ferroelectric

F_D is proportional to the signal-to-noise ratio of the detector when the noise is dominated by the Johnson noise associated with the detector's AC conductance [11].

(b) A low thermal conductance from the detector element to the substrate. This can best be achieved by engineering the pyroelectric element into a suspended structure of the type shown in Figure 14. The gap between the support and the substrate is filled with air (or Xe or vacuum for the highest-possible isolation). The support could be made of, for example, SiO_2, Si_3N_4 or the ferroelectric material itself (as described in section 5 below).

(c) A low noise readout circuit for the pyroelectric signal. This entails using a well-qualified silicon process for the readout chip and damaging it as little as possible in the process of making the pyroelectric array by using low process temperatures and compatible etch chemicals as discussed above.

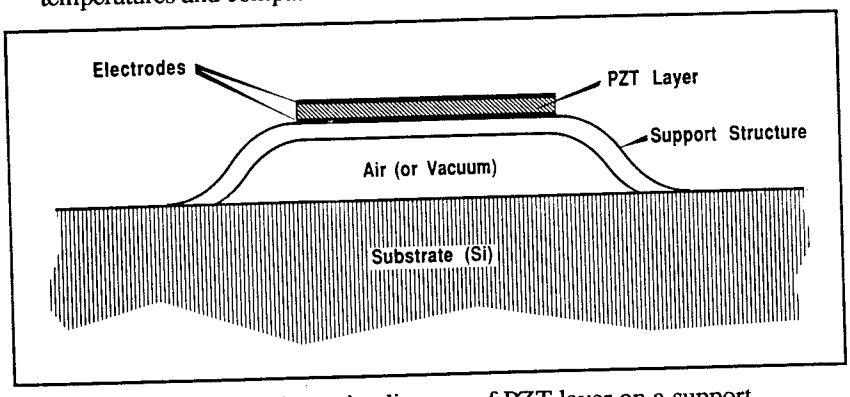


Figure 14. Schematic diagram of PZT layer on a support structure for pyroelectric or piezoelectric device applications.

The air-backed structure of the type shown in Fig. 14 could also form the basis for piezoelectric devices such as microphones or accelerometers. In this case, the important parameter to measure is the piezoelectric d_{31} coefficient.

The electrical properties of the thin films fabricated as described in Section 2 have been studied systematically, by forming test capacitors between the underlying platinum electrode and 2mm diameter chromium/gold electrodes evaporated onto the top surface. Table 2 summarizes the results obtained from (111) oriented PZT films, typically 0.8 to 1.1 μm thick. Most of the work has been done on the 30/70 composition, for which the spread in the results is noted in this table. The properties were measured both as-deposited and after poling, under a field of up to 2.5 x $10^7 Vm^{-1}$ applied for 15 minutes at 150°C.

TABLE 2. Electrical Properties of PZT Thin Films

Composition	20/80	25/75	30/70	Units
Pyroelectric Coefficient				$10^{-6}Cm^{-2}K^{-1}$
Unpoled	-50	+10	+50 - 150	
Poled	-180	-260	+220 - 280	
Permittivity				ε_o
Unpoled	290	470	450 - 550	
Poled	260	380	350 - 450	
Dielectric Loss				%
Unpoled	1.0	1.1	1.0 - 1.3	
Poled	1.1	1.0	0.8 - 1.1	
Resistivity	16	30	1 - 20	$10^{11}\Omega m$
F_D Merit Figure	1.3	1.6	1.5 - 1.7	$10^{-5}Pa^{-1/2}$

The permittivity (ε) and dielectric loss ($\tan \delta$) were measured as a function of frequency using a Wayne Kerr 6425 Multi Bridge; the 30Hz results are also given in Table 2. The pyroelectric coefficient (p) was calculated from the amplitude of the ac current produced when the film temperature was modulated at 15mHz. The resistivity was derived from the leakage current at 1V bias at 20°C, after 15 minutes settling time. Losses are significantly lower than the PZT 53/47 composition, probably because these are tetragonal materials for which the domain walls will be less mobile.

The PZT films have some pyroelectric response prior to poling, though the sign of the coefficient varied with composition. This activity defined a preferred direction for poling: except for the 25/75 composition, poling in the reverse direction gave about 30% less activity. Poling also reduced the permittivity and often the dielectric loss. Table 2 also includes the F_D merit figure, with $C_V = 2.7 \times 10^6 Jm^{-3}K^{-1}$ as the assumed volume heat capacity of the film. A value of F_D $1.7 \times 10^{-5} Pa^{-1/2}$ is similar to the values obtained in bulk ceramics of the PZT system which have not been deliberately doped to enhance F_D.

Piezoelectric measurements have been made on one film of PZT 53/47. The 0.3μm film was poled at 6V and a d_{31} piezoelectric coefficient of 6×10^{-11} CNm^{-1} was obtained. This was calculated from the voltage response of the film to bending of its substrate. This bending was achieved by accelerating a sample, in the form of an end-supported cantilever beam, at 100 to 1000 Hz on a vibration table. The response varied with the square of the distance of the electrode from the free end of the cantilever, as expected for a beam bending under its own weight. The d_{31} coefficient is about two thirds of the bulk ceramic value, as expected for a film of predominantly (111) orientation.

5. Fabrication of PZT Microbridges

As discussed above, infra-red detector elements require good thermal isolation from the underlying drive circuitry. This is achieved by making 'microbridges', which have only a few points of contact with the silicon device. The thermal isolation of the element is improved further by using a 'N' shaped design for the microbridge.

The microbridges are fabricated using the following process flow:

* Contacts are opened through passivation to metal tracks.
* A sacrificial layer is deposited and patterned with vias enclosing the contacts through passivation.
* The lower electrodes for the detector elements are deposited and patterned.
* The ferroelectric material is applied and annealed.
* A thin top electrode/absorber layer is defined by float-off photolithography and evaporation.
* The elements are defined by ion milling through the ferroelectric and lower electrode material, stopping in the sacrificial layer.
* The sacrificial layer is removed by wet etching and the completed structure is carefully dried.

This process has been used to fabricate test arrays in PZT. Figure 15 shows part of one of these arrays, with elements at 60 μm pitch. The PZT film has sufficient mechanical

strength to support itself and to withstand the rinsing and drying processes. There is some non-uniform stress in the structure, with a net tensile stress on the underside of the elements causing slight bowing.

All of the processes, including deposition and annealing of the ferroelectric film, are compatible with fully fabricated CMOS devices using conventional metallization. At no point do the devices exceed a temperature of 450^{o}C (the maximum temperature allowed with aluminium alloy tracks present) and no chemicals are used which would attack the underlying semiconductor device.

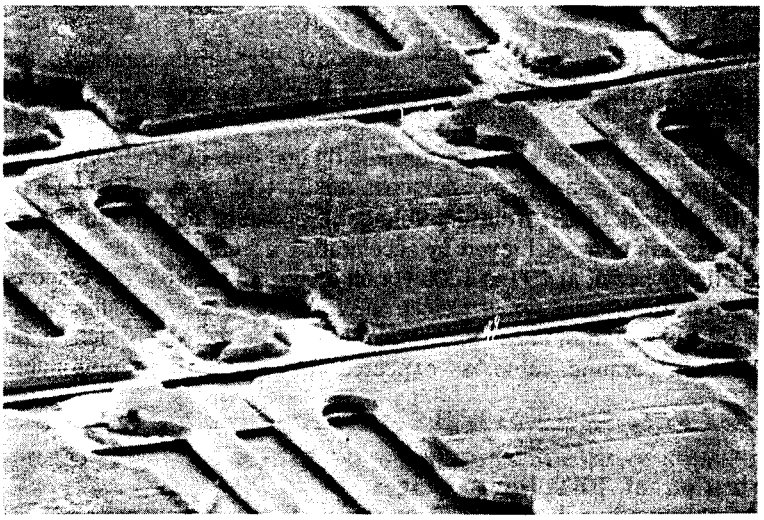


Figure 15. Fabricated array of PZT microbridges on a 60 microns pitch for IR detector elements.

6. Conclusions

The work reported here has shown that ferroelectric oxide thin films have much wider potential for application than simply non-volatile memories. The constraints imposed by the need to deposit the films onto active semiconductor devices have been analyzed and it has been shown that, even satisfying these, good dielectric, pyroelectric and piezoelectric properties can be obtained from PZT films. Examples of practical flip chip capacitor and pyroelectric device structures have been given.

7. Acknowledgement

This work has been carried out with the support of the Defence Research Agency, Malvern.

8. References

1. Campbell, D. S. (1957), *J. Brit. IRE* **17**, 385.
2. Whatmore, R. W. (1991), An Introduction to Ferroelectric Ceramics and their Applications, in P Vincenzini (ed), *Fundamentals of Ceramic Engineering*, Elsevier Applied Science, pp. 223.
3. Foster, D. J. (1991), Silicon Processing: CMOS Technology, in L. S. Miller and J. B. Mullin (eds), *Electronic Materials from Silicon to Organics*, Plenum Press pp. 173.
4. Patel, A., Shorrocks, N. M. and Whatmore, R. W. (1991), *IEEE Trans. UFFC* **38**, 672.
5. Ainger, F. W., Patel, A., Shorrocks, N. M., Trundle, C. and Whatmore, R. W. (1992), *Integrated Ferroelectrics* **1**, 363.
6. Tossell, D. A., Shorrocks, N. M. and Whatmore, R. W. (1993), *Integrated Ferroelectrics* **3**, 301.
7. Klee, M., Eisemann, R., Waser, R., Brand, W. and Van Hal, H. (1992), *J. Appl. Phys.* **72**, 1566.
8. Patel, A., Tossell, D. A, Shorrocks, N. M., Whatmore, R. W. and Watton, R. (1993), *Mat. Res. Soc. Symp. Proc.* **310**, 53.
9. Turner, J. A. (1991) High Speed Compound Semiconductor IC's in L. S. Miller and J. B. Mullin (eds). *Electronic Materials from Silicon to Organics*, Plenum Press pp. 193.
10. Pedder, D. J. (1989). Flip Chip Solder Bonding for Advanced Device Structures, *Plessey Research and Technology Research Review 1989*, pp. 69.
11. Whatmore, R. W. (1986), *Rep. Prog. Phys.* **49**, 1335.
12. Whatmore, R. W. (1991), *Ferroelectrics* **118**, 241.
13. Whatmore, R. W. Stringfellow, S. B. and Shorrocks, N. M. (1993), *Proc. SPIE Vol 2020 Infrared Technology XIX* , pp. 391.

PIEZOELECTRIC AND FERROELECTRIC DEVICES: POTENTIAL AND ISSUES

M. SAYER, D.A. BARROW, R. NOTEBOOM, E.M. GRISWOLD AND Z. WU
Department of Physics,
Queen's University,
Kingston, Ontario, K7L 3N6,
Canada

ABSTRACT. The potential applications for thin film piezoelectric and electrooptic devices are wide spread, ranging from microactuators integrated into silicon, to larger scale devices using silicon as a convenient substrate, to thin films fabricated on other substrates and in various geometries. This includes film driven structures, high frequency sensors using film technology, and interferometric devices in fiber optics. Design constraints implicit in devices and processing techniques to engineer and modify film properties are discussed.

1. Introduction

In view of the large amount of effort that has been expended recently on ferroelectric lead zirconate titanate films for non-volatile memories, it is of interest that the earliest interest in such ferroelectric films was as piezoelectric [1], pyroelectric [2] and electrooptic [3] substrates, actuators and sensors rather than as capacitor dielectrics. This paper reviews factors inherent in the design of such devices and considers how new processing knowledge and techniques may assist in their realization.

2. Piezoelectric and Electrooptic Devices

Piezoelectric thin films are important in several types of device. Figure 1 illustrates important piezoelectric applications:

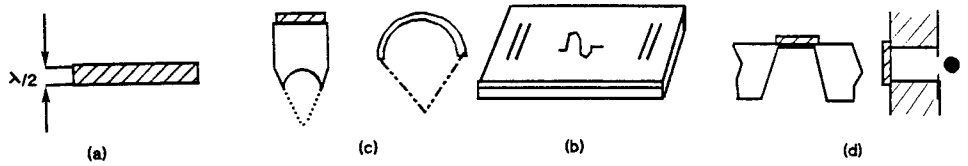


Figure 1. Devices based on piezoelectric phenomena

O. Auciello and R. Waser (eds.), Science and Technology of Electroceramic Thin Films, 399-412.
© 1995 *Kluwer Academic Publishers. Printed in the Netherlands.*

Applications include:

a) Bulk piezoelectric resonators
Thickness mode plate resonators operate at a frequency inversely related to the thickness of the resonator - Figure 1 (a). As bulk ceramics (usually lead zirconate titanate) these operate in the ultrasonic frequency range of 10-200 kHz as the primary component of ultrasonic ranging and imaging systems. The interest in thin films is primarily for higher frequency generation (50 - 500 MHZ) for ultrasonic sensors and sources for medical application [4].

b) Surface acoustic wave substrates
Specific electrode geometries can induce the propagation of surface acoustic waves on substrates - Fig. 1 (b) [5]. Since the speed of propagation of surface waves is significantly reduced compared to that for propagation in the bulk, delay lines and filter structures can be fabricated for important frequency ranges. Such filters are currently important for microwave applications such as cellular radio. While piezoelectric substrates such as lithium niobate are used for most high power SAW devices, non-piezoelectric materials such as glass or silicon can be used if a piezoelectric film such as zinc oxide or PZT is used under the electrode structure [6]. In a more recent application, surface wave generation on PZT ceramics and films underlies various designs of piezoelectric motors [71].

c) Focused high frequency ultrasound sources
Thin zinc oxide and lead zirconate titanate coatings prepared on the end of shaped quartz rods provide high frequency acoustic sources for ultrasonic imaging - Figure 1(c) [8]. The conventional technology is to use planar transducers with carefully configured and polished quartz rods. Thin film PZT on machined steel surfaces would reduce the cost of such devices significantly.

d) Mechanical strain and pressure sensors.
Piezoelectric elements are used for detection of induced strain in a range of applications. Important sensing functions in automobile electronics - for example, pre-ignition and timing sensors or in orthopedics (9) are accomplished using piezoelectric elements. The basic structure is similar to that of the actuator shown in Figure 1(a). However the sensitivity can be enhanced by forming the film on a supporting membrane - Fig. 1 (d). Such membranes can then be driven as a diaphragm actuator for a fluid flow valve [10], or to form ink droplets in an ink jet printer by flexure of the wall of a micromachined pressure chamber.

e) Positioning Sensors and Actuators
Two opportunities arising from new technologies are shown in Fig. 2. Bimorph actuators perform crucial positioning functions in scanning tunneling and atomic force microscopy - Fig. 2 (a) [11], while linear actuators in which the motion is amplified by the fabrication of stacked piezoelectric arrays or by other forms of mechanical advantage are important in positioning mirrors in optical interferometry -Fig. 2 (b).

f) Electro-optic Modulation
The large electrically induced birefringence of ferroelectrics can be used in various forms of optical gate [3,12]. These are of significant practical importance for integrated optical

modulators and switching devices for high speed communications. Two systems are possible. Figure 3 (a) shows a direct electrooptic device based on electrically induced birefringence [13], while 3 (b) illustrates an interferometer based modulator [8]. The change in optical path length in the driven arm may be induced by a number of external phenomena. An important factor in any optical device is the optical loss due to absorption or scattering. The elimination of scattering in deposited films remains technically elusive; the interferometer method in Fig. 3(b) does not perturb the optical path within the fiber.

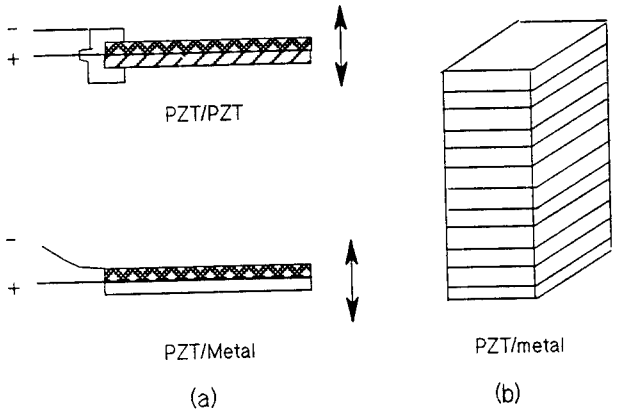


Figure 2. Piezoelectric positioning devices: a) bimorph device used in force microscopy, b) stacked arrays for mirror positioning in optical interferometry - the electrodes are not shown.

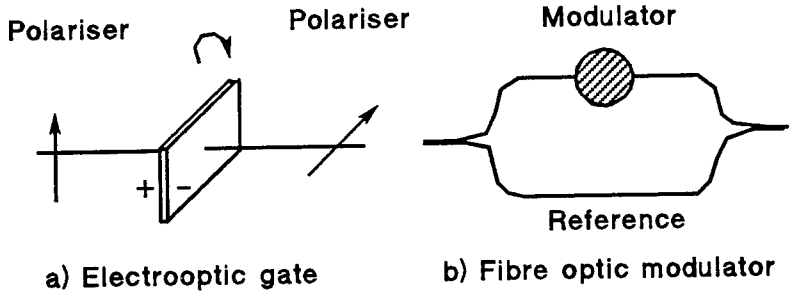


Figure 3. a) An optical gate utilizing electrically induced birefringence. b) An interferometric optical fiber modulator.

3. Transducer Design Constraints

The scale of the above devices can vary significantly. They may range from micromachined structures with dimensions of tens of microns, to large area structures of macroscopic (> cm^2) size. Films provide a number of advantages. In principle, these

include: a) simpler manufacturability of devices on complex geometries, b) the use of substrates which are easily available and which can be integrated with conventional semiconductor technology, c) the development of high sensitivity sensors and actuators in frequency ranges which are inaccessible using bulk technology.

These advantages are related to the processing ease and dimensions of thin films, and the possibility of achieving crystallographically textured forms of complex materials during processing. However, by their nature, films have small mass and are fabricated on a supporting structure. Any micromechanical or electrooptical structure involving films must therefore: a) provide adequate stimulus to the system at an acceptable driving voltage, b) be capable of being driven by conventional electronics, c) have a thermal budget for processing which does not degrade the substrate material or associated device structures, and d) have reproducible piezoelectric and mechanical properties. The fact that films are prepared on a substrate may not only affect the chemical and electrical conditions at the interface, but may also modify the piezoelectric parameters of the film itself.

In the design of film actuators factors which must be considered are:

- the absolute and relative dimensions of the film and its supporting structures
- the intrinsic magnitude of the piezoelectric coefficients
- The field distribution within the device
- the electrical impedance of the device
- the mechanical damping of supporting systems
- electromechanical fatigue under operating conditions.

These aspects of film actuation may be explored in terms of a representative device - commencing with the composite piezoelectric structure shown in Fig. 4. Under steady state non-resonant conditions, piezoelectric stress arises due to the expansion of the upper piezoelectric element when a voltage is applied. The strain is a function both of the mechanical properties of the system (piezoelectric + supporting structures) and the voltage which is actually applied to the piezoelectric.

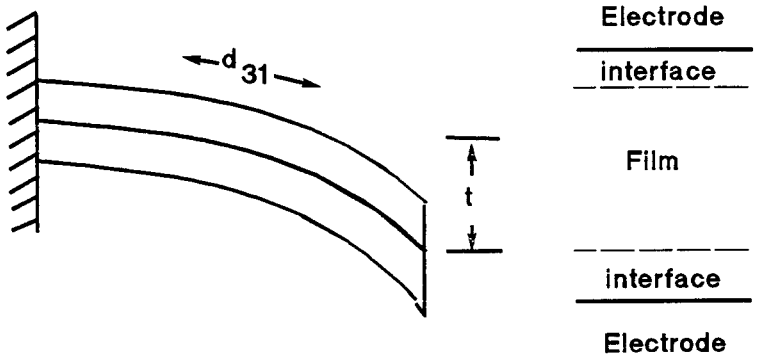


Figure 4. (a) Stress developed in planar piezoelectric film on a non-piezoelectric substrate. The maximum stress generated is calculated from $d_{31}E_Z$. (b) Local effects within the film. These include non-ferroelectric interfacial layers and internal crystallographic texture.

The strain along the length 1 of the elements dl is [14]

$$dl / l = X(k, r)\, d_{31}\, V / t_f = X(k, r)\, d_{31}\, E_z \qquad (1)$$

where t_f is the thickness of the film, k is the ratio of the Young's Modulus of the substrate to that of the film, r is the ratio of the thickness of the substrate to that of the film, and d_{31} is the piezoelectric charge coefficient.

$$X(k, r) = \frac{3kr\,(1 + r)}{1 + k^2r^4 + 2k\,[2r+3r^2+2r^3]} \qquad (2)$$

The deflection dt of the free end of a cantilever of length l is:

$$dt = Z(k, r)\, d_{31}\, L^2 \frac{V}{t_f^2} \qquad (3)$$

where:

$$Z(k,r) = \frac{1 + k^2r\,(4r + 3)}{1 + k^2r^4 + 2k\,[2r+3r^2+2r^3]} \qquad (4)$$

The functions X(k,r) and Z(k,r) include properties of the film and of the substrate. The deflection of this structure as a function of relative film thickness and various material ratios is shown in Fig. 5. The detailed behavior depends on the relative values of the mechanical moduli of the film and the substrate, but under steady state conditions, the deflection is a maximum when the piezoelectric film has a thickness of about 0.4 times that of the support. This is one guideline for the piezoelectric film thickness necessary to actuate a structure of particular dimensions.

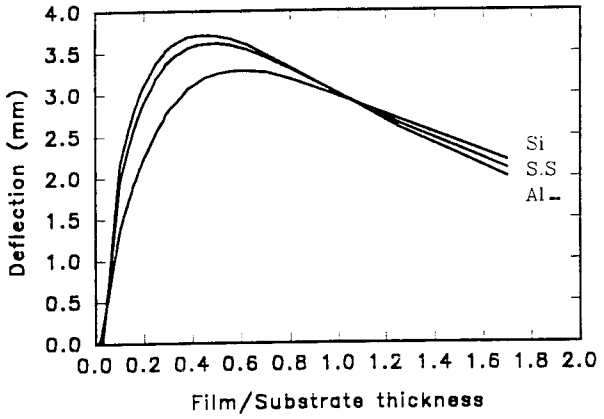


Figure 5. Induced strain in a bimorph structure 5 cm long and Al, stainless steel or Si support layer 50 μm thick as a function of the relative thickness of the piezoelectric layer. The various curves are calculated for different ratios of Young's Modulus for the film and for substrates of Al, stainless steel and Si respectively.

In non-resonant applications, the magnitude of the piezoelectric stress applied by the film to the structure, or the strain induced in the piezoelectric itself is of primary importance. The maximum achievable stress is given by the small signal piezoelectric coefficients for the bulk material, although clamping of the film properties by the substrate may reduce these values. The complexity of the piezoelectric/substrate interaction is such that unambiguous values for the coefficients can often only be extracted from the performance of devices. It may be noted that even for lead zirconate titanate the applied stresses are small - of the order of $\Delta t = \mu m/V$, and therefore large voltages must be applied to achieve appreciable strains. This implies that the electrical breakdown strength of a piezoelectric film used for device purposes must be high.

In resonant applications, the resonant frequency is set more by the dimensions of the resonating element. Depending on the boundary conditions, the resonant frequency f_{res} for a resonator corresponds to a mechanical vibrational mode having a wavelength of $\lambda/4$ or $\lambda/2$ across the defining dimension of the structure (Figure 2(b)). Since $\lambda = c/f_{res}$ where c is the velocity of sound in the material,

$$f_{res} = \frac{1}{2\, t_f} \sqrt{(1 / s_{11}\, \rho)} \qquad (5)$$

if $\lambda/2$ applies for a thickness mode resonator.

For a rectangular PZT slab 4.5 cm long, 1.5 cm wide and 0.3 cm thick, the principal length, width and thickness modes are approximately 51 kHz, 153 KHz and 760 kHz respectively; the radial mode for a 2.5 cm diameter PZT resonator is about 92 KHz. In contrast, the resonant frequency of a film thickness mode PZT resonator 23 μm thick is 100 MHz. This frequency range is of great interest for a wide range of medical imaging and non-destructive test applications. However film thicknesses of this order have been difficult to attain, being intermediate between what can be achieved easily by thinning bulk ceramic or be built up by conventional film deposition. Film deposition methods now appear to make this possible.

A specific issue for high permittivity ferroelectric films, particularly at high frequencies is the low electrical impedance of the film when it acts as a capacitor element. Very thin non-ferroelectric interfacial layers can then perturb the field distribution across the device significantly. This field distribution also depends on whether the voltage is applied as a dc voltage, a pulse voltage or in resonance. This is of particular importance if the ferroelectric film is fabricated on an electrode which has a tendency to oxidize. If the system is modeled as two capacitors in series, the two interfacial layers being lumped for convenience,

$$\frac{1}{C_T} = \frac{1}{C_1} + \frac{1}{C_2} \qquad (6)$$

In terms of the relative permittivity of the interfacial layer ε_d and of the ferroelectric ε_f respectively,

$$C_T = \frac{\varepsilon_d\ \varepsilon_f}{t_d\, \varepsilon_f + t_f\, \varepsilon_d}\ A \qquad (7)$$

$$\varepsilon = \frac{\varepsilon_d \varepsilon_f t}{t_d \varepsilon_f + t_f \varepsilon_d} \qquad (8)$$

where t_d and t_f are the thickness of the interfacial and the ferroelectric layers, and t is the total thickness. If $\varepsilon_d = 9$ and $\varepsilon_f = > 500$, a significant change in permittivity is measured for even 10 Å of interfacial film. This measurement can be sensitive to other factors. In the case of PZT films prepared on aluminum electrodes, Barrow [15] has calculated the thickness of an interfacial layer to be of the order of 1000 Å. While this appears physically unlikely due to diffusion of electrode material, it may be evidence of changes in oxygen content in the ferroelectric near the metal interface due to reduction during processing.

Finally, the electrical impedance of the transducer at the frequency of operation is of importance [16]. This sets the characteristics of the driving amplifier, and/or the output voltage of the transducer acting as a sensor. In the simplest case, at frequencies far from resonance, the transducer can be treated as a simple capacitor. To match to conventional electronics the impedance should be of the order of 50 ohms. Thus,

$$50 = \frac{1}{w C} = \frac{t}{2 \pi f \varepsilon \varepsilon_o A} \quad (\Omega) \qquad (9)$$

where C (μF) is the capacitance of the transducer. For ceramic PZT with a relative permittivity of 480, a 2.5 cm diameter, 3 mm thick disc has a radial mode resonant frequency of 92 kHz. If this disc is run at, say, 80 kHz, it has an impedance of about 2700 ohms. This provides no intrinsic problem for impedance matching. On the other hand, if a thin film having dimensions appropriate for a 100 MHz thickness mode transducer is to have an impedance of at least 50 ohms when operated at 90 kHz, its area must be considerably less - 1.9×10^{-7} m^2, or a disc of diameter 0.49 mm. This relationship between area and frequency is a significant constraint for the design of large area thin film high frequency resonators. At resonance, the transducer becomes purely resistive with a resistance much less than that calculated from eq. (9). The best piezoelectric will have high piezoelectric coefficients with as low a permittivity as possible. This is the reason that lead titanate with a permittivity of around 200 is of interest for sensor applications.

4. Processing and Materials

Advances in material processing impact the field of piezoelectric device development in a number of ways. The major difference from ferroelectric memory and capacitor development is the requirement for thicker films. Circuits, electrodes and device structures tend to be somewhat simpler, but the obvious advantages of processing methods which are compatible with silicon technology remain: -reliable mass- production, array fabrication, and integration with signal processing or driving circuits.

Device development has primarily taken advantage of a) multiple coatings applied by sol-gel processing, b) rapid thermal processing to reduce thermal budgets and control the microstructure, and c) external poling to induce piezoelectric behavior. While the

emphasis on materials has been on lead zirconate titanate (PZT), other piezoelectrics have advantages and show promise for development. These include lead titanate (low permittivity compared with PZT) and materials such as strontium barium niobate having high piezoelectric coefficients.

Issues and processes related to piezoelectric film devices include:

4.1. SOL-GEL PROCESSING

Sol-gel processes based on acetate [17] and methoxyethanol [18] solutions have been extensively explored for spin, dip and spray coating. For thick films used for devices on silicon, major problems during fabrication are those of crack propagation in the film, and simultaneous adhesion to both metallized and non-metallized substrates. This problem is illustrated in Fig. 6.

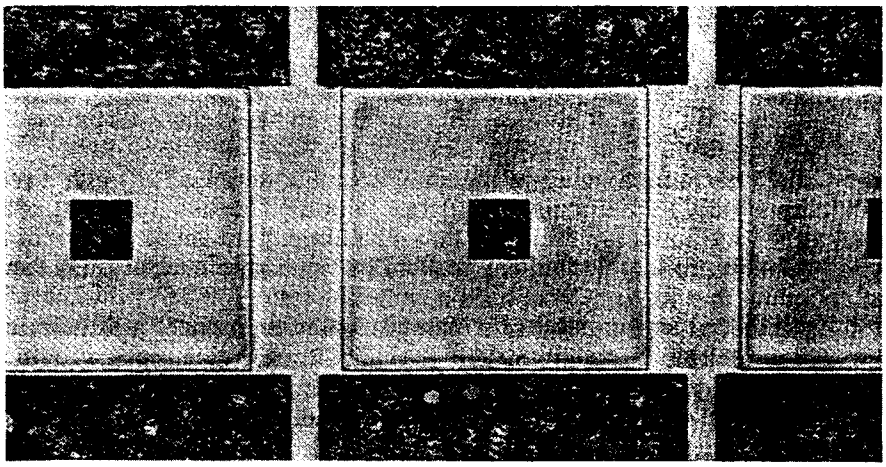


Figure 6. PZT films processed on a photolithographically patterned wafer prepared by Honeywell Technology Center, Minnesota. The PZT film shows high adhesion and integrity on an underlying Ti/Pt metallization. The film is crazed on the intervening SiO_2 buffer layer.

A solution is to fabricate the film as a blanket three layer (electrode/coating/electrode) on the metallization and pattern after deposition. This can be implemented most easily if the film is patterned before the final firing. Film thicknesses of up to 5 μm can be achieved in a single coat [19]. However, this process is difficult to reproduce. Multiple coating is easier and can be automated [20]. Using individual layers of up to 0.3 μm in thickness, up to 10 μm thick PZT films are relatively easy to achieve with high density and good piezoelectric properties. Figure 7 shows the dielectric response associated with the 280 MHz thickness mode resonance for a 9 μm thick PZT film fabricated on sheet aluminum.

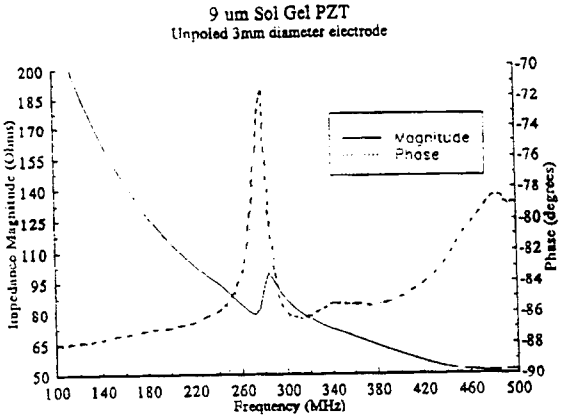


Figure 7. Magnitude and phase response associated with a thickness mode resonance in a 9 μm thick film of PZT.

In general interfacial layers are less important for the piezoelectric response than for other applications of ferroelectrics. This is partly because the external fields which are available are generally higher and the thickness of the film presents no problem for dielectric breakdown. However, the development of high Q resonators depends on a well sintered, homogeneous microstructure. More recently, sol-gel techniques have been developed to lay down even higher thicknesses per coat (3-5 μm/coat). Figure 8 shows an 18 μm thick film. While the full transducer response has yet to be measured, the action of these elements as transducers or as sensors is comparable to that of ceramics.



Figure 8. 18 μm thick PZT film using a modified sol-gel process.

4.2. STOICHIOMETRY DURING PROCESSING

High Q piezoelectric resonators require high density, homogeneous elements with carefully control of grain boundaries. In bulk ceramics this is ensured by high temperature sintering and careful control of the processing conditions. Potential problems in multiply coated films processed at intermediate temperatures and their resolution are illustrated in Fig. 9 [21]. For a film prepared from a solution of stoichiometric composition, the transmission electron micrograph in Fig. 9 (a) shows dark lines at the interface separating

successive layers denoting non-stoichiometry at the interface. A fine crystal structure may also be noted at the free surface. Glancing angle X-ray diffraction and Auger analysis showed that the interface is no longer stoichiometric and a significant proportion of the non-ferroelectric pyrochlore phase was present. However, when the film was prepared from a solution having 10% excess lead (Fig. 9 (b)), the structure crystallized entirely into the ferroelectric perovskite phase, the microstructure was more uniform, and less evidence for interfacial layers was present. This indicates that the composition plays an important role not only in sintering the film at a local level. In particular crystallization will be affected if lead is lost at the interface during processing.

4.3. RAPID THERMAL PROCESSING

Multiply-coated films prepared on platinum electrodes must be repeatably processed through both the firing and crystallization stages. Traditionally this has been accomplished by furnace annealing - in order to reduce stress on the film and substrate and to thereby minimize the probability of debonding during processing. However, rapid thermal processing (RTP) has shown significant advantages in controlling microstructure, in crystallizing films into the perovskite phase, and by reducing the thermal budget, minimizing the loss of volatile components such as lead oxide [22,23].

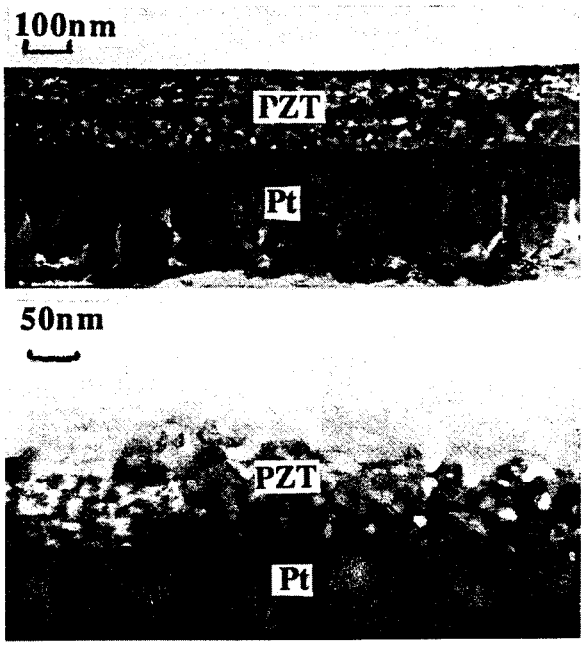


Figure 9. (a) Transmission electron micrograph of a multiply coated PZT film processed by rapid thermal annealing. The dark lines correspond to inter-layer non-stoichiometry, (b) TEM of an equivalent film processed with a higher lead composition. The interlayers have almost entirely disappeared and the film microstructure is more uniform.

RTP clearly reduces the fabrication time for multilayer coating. The effect of temperature ramp rate on crystallization is shown in Fig. 10 [22], while enhancement of the dielectric constant is shown in Fig. 11.

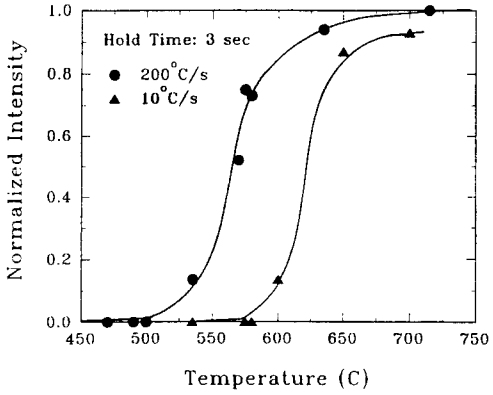


Figure 10. Degree of crystallization versus temperature ramp rate during rapid thermal processing [22].

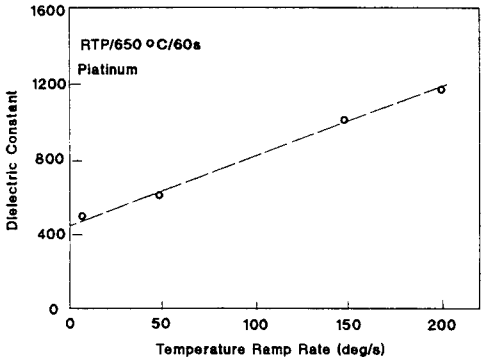


Figure 11. Dielectric constant versus temperature ramp rate for (55 / 45) PZT on platinum.

It is still not clear whether the temperature effect shown in Fig. 10 simply originates from rapid achievement at high ramp rates of a temperature at which the perovskite phase crystallizes readily with minimum loss of a critical component such as PbO. However, recent experimental [23] and theoretical studies[24] suggest that additional factors associated with nucleation and growth in a system involving a phase transition are involved. For the fabrication of thick film elements, both rapid thermal processing and careful control of film composition is important in order to densify and sintered films at the lowest achievable temperature. In the case of films containing large proportions of

grain boundary phases, RTP may be effective in maintaining the dielectric constant of the grain boundary regions at a high value.

4.3. MODIFICATION OF PZT FILMS BY DOPANTS

Most ceramic PZT is extensively doped to control and modify both the ferroelectric and dielectric properties [25]. One of the outstanding issues in film fabrication is the relative insensitivity of PZT film properties to dopants. Although some recent work has shown a change in Curie temperature, bulk conductivity and permittivity on the addition of dopants such as Nb and La [26], in general the additions have to be significantly higher than used in ceramics for the same effect. This suggests that the role of interfacial boundaries is significant in ferroelectric films.

4.4. FERROELECTRIC AND PIEZOELECTRIC FATIGUE

Piezoelectric activity in films generally involves fields significantly higher than those generated in comparable ceramics. In some cases this may be sufficient to induce reversals of the ferroelectric polarization and consequent ferroelectric fatigue. This allows the possibility of studies of fatigue processes linking the electrical and mechanical properties of ferroelectrics. Recent studies by Wu et al [27] suggest that ferroelectric fatigue associated with ferroelectric memories is linked with the generation of structural defects in the perovskite lattice. The fatigue processes have been related to an interaction between mobile domain walls and lattice defects. The process has been studied by examining the temperature dependence of hysteresis loops in non-fatigued as well as fatigued specimens, and the second involves direct measurement of lattice defects which are correlated with fatigue by a thermally stimulated current (TSC) technique. This is shown in Fig. 12.

The fatigue process induces a permanent variation in the lattice structure. The exact nature of these defects still needs clarification, but the continuous creation of lattice defects and their effect of pinning of mobile domain walls appears to be a primary fatigue mechanism in PZT. These effects of electromechanical coupling may be important in high field actuation of thin film piezoelectric devices.

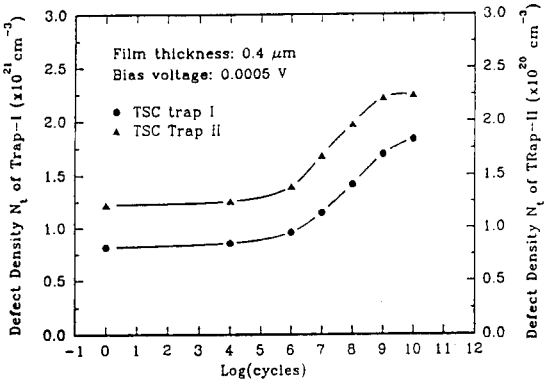


Figure 12. Evidence for the generation of trapping states associated with mechanical defects during ferroelectric hysteresis.

5. Macroscopic Devices Using Film Technology

The use of piezoelectric films to drive macroscopic structures can be illustrated using the film driven cantilever shown in Fig. 4. The cantilever was 3 cm in length and is fabricated by depositing a 10 μm thick sol-gel PZT by multiple coats on a 200 μm thick stainless steel foil. The vibrational frequency of this strip is expected to be about 4 kHz. Figure 13 (b) shows the frequency response of the system. The resonance frequency is principally set by the mechanical properties of the supporting stainless steel structure. In this case a correction has to be introduced to account for a non-piezoelectric interfacial layer created during processing. The dielectric constant of the PZT film is measured to be 300, a value which is half the expected value. When the low frequency motion is predicted from eqn.(3) with d_{31} = 80 pC/N, agreement between experiment and theory can be achieved if eqn.(3) is multiplied by a correction factor equal to the ratio of the measured dielectric constant to the expected value.

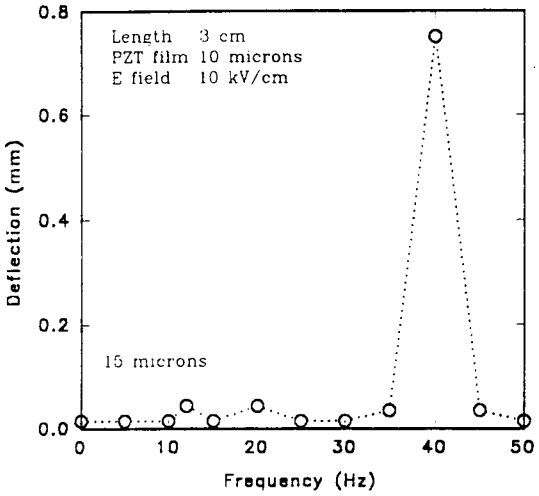


Figure 13. a) 3 cm long stainless steel strip cantilever driven using a 10 μm thick PZT film. b) amplitude vs frequency.

6. Summary and Conclusions

Processing methods for both PZT and other ferroelectrics have now advanced to the stage where reliable films of an appreciable range of thickness can be fabricated. For piezoelectric applications, electrodes and interfacial layers are less significant than for capacitor development. A new technology of both macro- and micro-machined devices is a real possibility.

7. Acknowledgments

This work was carried out with support from the Ontario Center for Materials Research and the Natural Sciences and Engineering Research Council of Canada.

8. References

1. Sayer, M.(1986) *Proc. 6th IEEEInt.Symp.Appl.Ferroelect, IEEE, Piscataway*, pp 560.
2. Ichinose, N., Hirao,Y., Nakamoto, N. and Yamashita, T. (1985), *Jap. J. Appl. Phys.* **23**, *Suppl.* **24-2**, 463.
3. Land, C.E., Butler, M.A. and Martin, S.J. (1989), *IEEE-IEDM* , 251.
4. Swartz, R.G. and Plummer, J.D. (1979), *IEEE Trans. Electron. Devices, ED-* **26**, 1921.
5. Hickernell, F.S. (1985), *IEEE Trans. Sonics and Ultrason. SU* **32**, 634.
6. Sreenivas, K., Sayer, M., Baar, D.J. and Nishioka, M. (1987), *Appl. Phys. Letts.* **52**, 709.
7. Udayakumayer, Chen, J., Brooks, K.G. , Cross, L.E. , Flynn, A.M. and Erlich, D.J. (l991), *Mat. Res. Soc. Symp. Proc.* **243**, 49.
8. Yi, G., Sayer, M., Jen, C.K., Yu, J.C.H. and Adler, E.L. (1989), *IEEE Ultrason. Symp.*, pp. 1231.
9. Adams, D., Kempson, G.E. and Swanson, S.A.V. (1978), *Med.& Biol.Eng.& Comput.* **16**, 113.
10. Binnig, G. and Smith, D.P.E. (1986), *Rev. Sci. Instrum.* **57**, 1688.
11. Polla, D.L. (1992), *Proc. 8th IEEE Int. Symp. Appl. Ferroelect., IEEE*, Piscataway.
12. Land, C.E. (1989), *J. Amer. Ceram. Soc.* **72**, 2059.
13. Adachi, H. , Kawaguchi, T. , Setsune, K., Ohji, K. and Wasa, K. (1983), *Appl. Phys. Lett.* **42**, 867.
14. Steel, M.R., Harrison, F., and Harper, P.G. (1978), *J. Phys. D: Appl. Phys.* **11**, 979.
15. Barrow, D.,Vasant Kumar, C.V.R., Pascual, R. and Sayer, M. (1992), *Mat. Res. Soc. Symp. Proc.* **243**, pp. 113.
16. Sayer, M., Vasant Kumar, C.V.R. , Barrow, D., Zou, L. and Amm, D.T. (1992), *Mat. Res. Soc. Symp. Proc.* **243**, 39.
17. Yi, G. and Sayer, M. (l991), *Ceram. Bull.* **70**, 1173.
18. Budd, K.D., Dey, S.K. and Payne, D.A. (1985), *Proc. Brit. Ceram. Soc.* **36**, 109.
19. Yi,G. and Sayer, M. (1992), *Proc. 6th IEEE Int. Symp. Appl. Ferroelect., IEEE*, Piscataway.
20. Li, K.K., Haertling, G.H. and Howng, W-Y. (1993), *Integrated Ferroelectrics* **3**, 81.
21. Griswold, E.M.,Weaver, L and Sayer, M. (1994), *Proc. 21st Annual Meeting, Microscopical Society of Canada*, Montreal, June 1994, pp. 42.
22. Wu, Z., Pascual, R., Vasant Kumar, C.V.R., Amm, D.T.and Sayer, M. (l991), *Mat. Res. Soc. Symp. Proc.* **224**, 305.
23. Hu, H., Peng, C.J. and Krupanidhi, S.B. (1993), *Thin Solid Films* **223**, 327.
24. Dang, E.K.F. and Gooding, R.J. (1994), The Role of Heating Rates and Long-Range Elastic Interaction in Determining the Crystallization Kinetics of Ceramic Thin Films.
25. Jaffe, B., Cook, W.R.Jr. and Jaffe, H. (1971), *Piezoelectric Ceramics*, Academic Press, London and New York, 1971.
26. Chang, J-F. and Desu, S.B. (1994), *J. Mat. Sci.*, in press.
27. Wu, Z., and Sayer, M.(1993), *Proc. 8th IEEE Int. Symp. Appl. Ferroelect., IEEE*, Piscataway.

INTEGRATED FERROELECTRIC MICROELECTROMECHANICAL SYSTEMS

D. L. POLLA
Department of Electrical Engineering
University of Minnesota
200 Union Street S.E. (4-178)
Minneapolis, Minnesota 55455
USA

ABSTRACT. Ferroelectric thin films have been integrated with silicon-based microelectromechanical systems, commonly called MEMS. Several thin films of the PZT family have been used in the formation of both microsensors and microactuators in processes compatible with silicon nitride, surface-micromachined, membranes and analog CMOS technology. Back-end micromachining of MEMS structures based on PZT-type electroceramic thin films is described.

Several ferroelectric MEMS examples are described including 1) cantilever beam micro-accelerometer, 2) acoustic pressure sensor, 3) uncooled pyroelectric infrared imaging array, 2) integrated acoustic sensor, 4) micro-positioner, and 5) simple cantilever flap actuators. Major issues of merging technologies with ferroelectric thin films with microelectromechanical structures and on-chip electronics are described.

1. Introduction

Microelectromechanical systems [1-5], or MEMS, continue to receive considerable research interest with extensive commercialization of products anticipated but not yet realized. The general goal of MEMS is to realize both electrical and mechanical systems on a semiconductor substrate, or chip, including microsensors, microactuators, and control electronics. This paper specifically addresses the use of electroceramic thin films with either a high piezoelectric or pyroelectric activity for MEMS applications.

Piezoelectric MEMS [6-8] are usually operated in one of two modes: sensor or actuator. When used as a sensor one usually detects a change in internal dipole moment within the piezoelectric crystal induced through either a stress or change in temperature. This change in internal dipole moment is usually detected in the form of a charge or voltage developed across a set of appropriately located electrodes surrounding the piezoelectric crystal. When used as an actuator, a voltage is applied across a set of electrodes thereby inducing a strain or deformation of the crystal. This controlled deformation is used to do work. The two operational modes are summarized in Fig. 1.

O. Auciello and R. Waser (eds.), Science and Technology of Electroceramic Thin Films, 413-426.
© 1995 *Kluwer Academic Publishers. Printed in the Netherlands.*

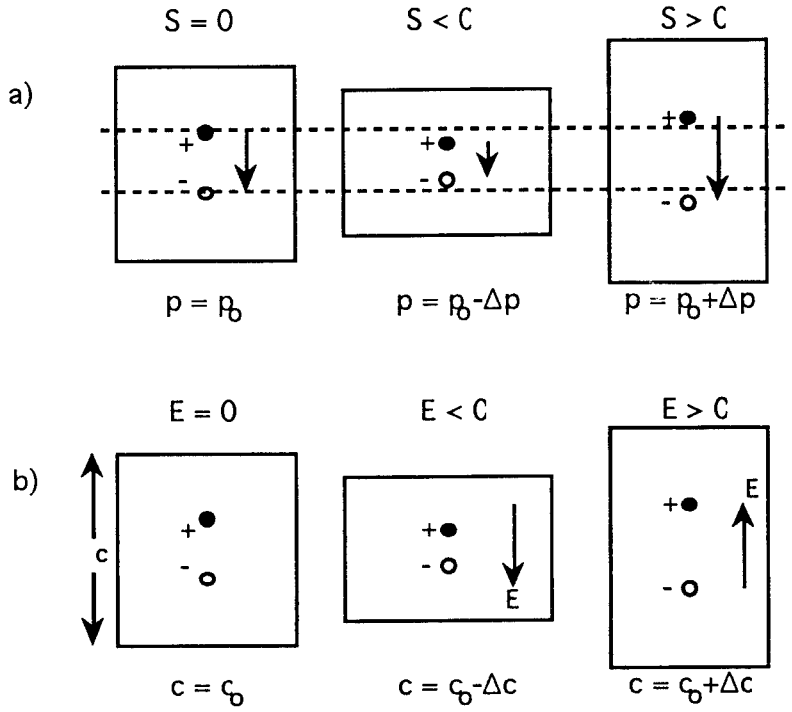


Figure 1. (a) Alteration of unit cell dipole under applied strain in direct piezoelectric effect (physical basis for microsensor operation), and (b) deformation of unit cell in response to applied electric field by converse piezoelectric effect (physical basis for microactuator operation).

There are several approaches toward realizing MEMS primarily based on silicon integrated circuit (IC) processing techniques. A specialized sequence of IC processing techniques known collectively by the term solid-state micromachining [9] is used to form mechanical structures capable of controlled motion when activated (microactuator) or predictable deformation when subject to a physical force (microsensor). This usually involves the formation of movable, constrained, or partially-constrained structures with precise dimensions set by thin film deposition, lithography, and etching. For example, cantilever microbeam accelerometers might consist of a thin film patterned in the form of a diving board elevated approximately 1 μm above the surface of a silicon wafer. Such micromachining processes which are based on the formation of additional materials on a semiconductor substrate are commonly referred to as surface-micromachining techniques.

Figure 2 shows an example of several MEMS structures formed by solid-state micromachining techniques including: a) cantilever beam piezoelectric accelerometer [10], b) piezoelectric acoustic sensor [11-12], c) pyroelectric infrared detector [13-14], and d) piezoelectric positioner [15-17]. In all cases a low residual stress silicon nitride [18] structural support is coated with a PZT-type ferroelectric thin film. The microfabrication techniques used will more completely described in Section 3. The four examples shown generally can be fabricated with lateral dimensions as large as 2 mm on

a side and active electroceramic film thicknesses of approximately 1-2 μm. The limitation for making small ferroelectric MEMS is mainly set by lithography considerations.

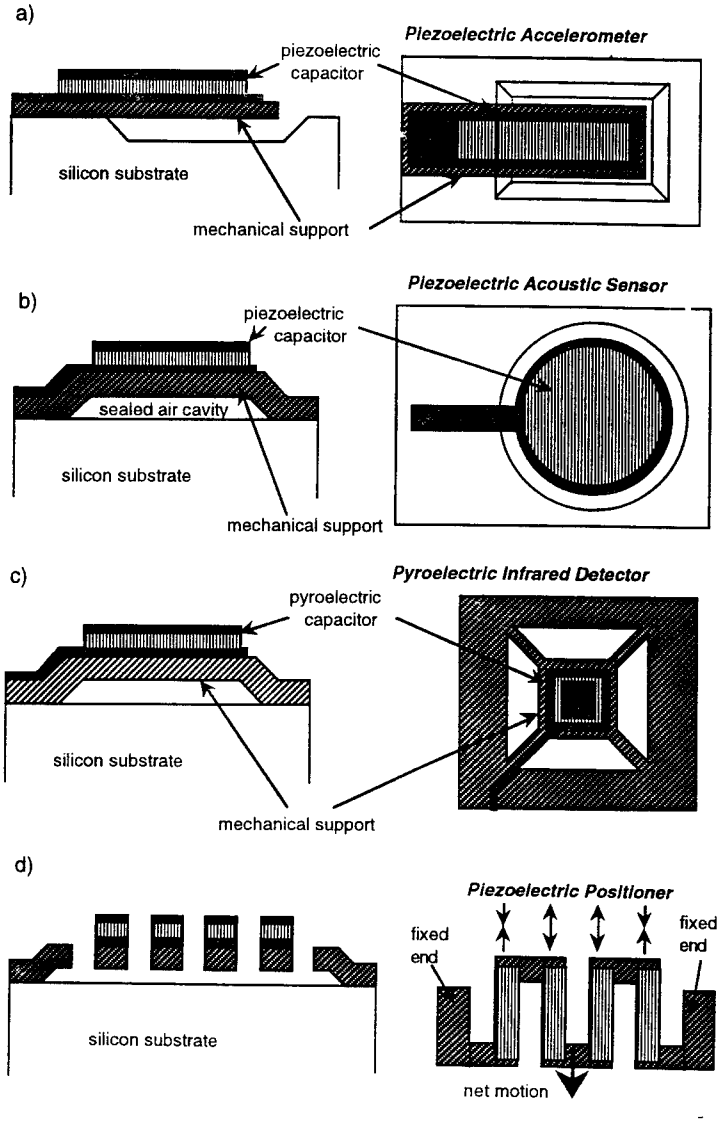


Figure 2. (a) Example of a piezoelectric cantilever microbeam accelerometer formed by surface-micromachining techniques; (b example of a piezoelectric acoustic sensor formed by surface-micromachining techniques; (c) example of a simplified low thermal mass and pyroelectric infrared detector element formed by surface-micromachining techniques; (d) example of a simplified low thermal mass and pyroelectric infrared detector element formed by surface-micromachining techniques.

2. Materials

Accurate a priori knowledge of both electrical and mechanical properties thin film properties are important to the design and resulting performance of electroceramic MEMS. This generally means that thin film processing techniques must produce good crystallinity (or polycrystallinity) and be reproducible in nature. An example of an oriented 3600 Å-thick PZT (54/46) thin film is shown in Fig. 3.

In our laboratory, we have mainly focused on the PZT system for MEMS applications. While PZT and modified-PZT formulations may not represent the best choices for all piezoelectric MEMS applications, we have tried to focus our work on this system in order to determine needed information about longer term prospects for commercialized process insertion. While more detailed materials results have been presented elsewhere, there are generally five important materials properties for common electroceramic MEMS: 1) dielectric coefficient, 2) piezoelectric coefficient, 3) pyroelectric coefficient, 4) Young's modulus, 5) intrinsic stress, and 6) noise voltage.

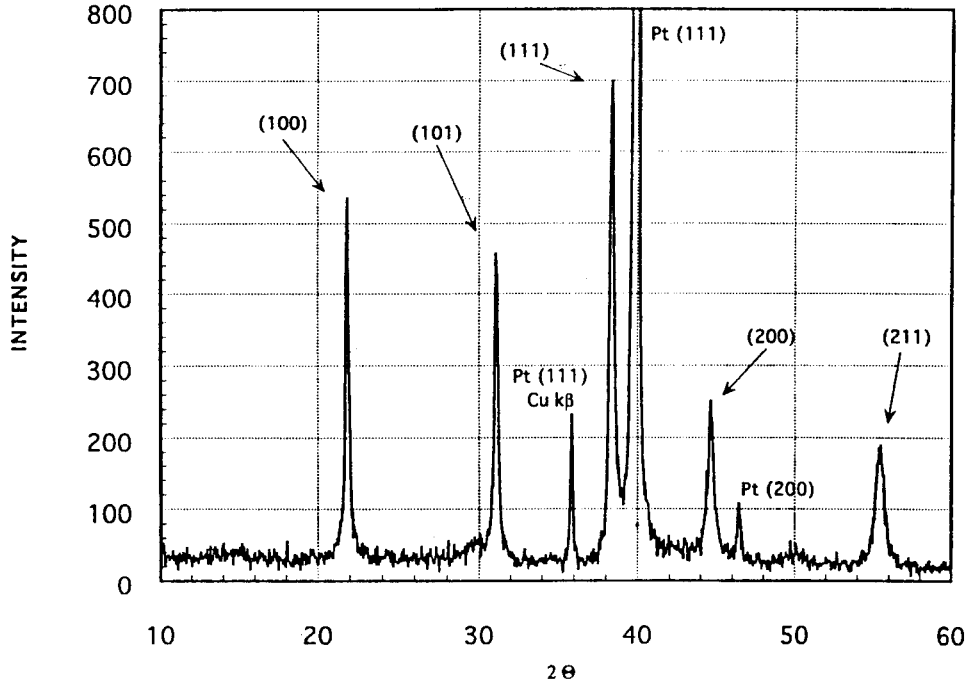


Figure 3. Typical XRD spectrum for a 3600 Å-thick PZT (54/46) thin film (Courtesy of L. Francis).

Young's modulus measurement versus PZT (54/46) film thickness is shown in Fig. 4. The measurement of Young's modulus was performed on carefully prepared PZT membranes. Force-deflection techniques were used to characterize mechanical properties [19]. Electrical noise-voltage for both PZT (54/46) and $PbTiO_3$ is shown in Fig. 5 [20].

Other relevant thin film materials data important to electroceramic MEMS is given in Table 1.

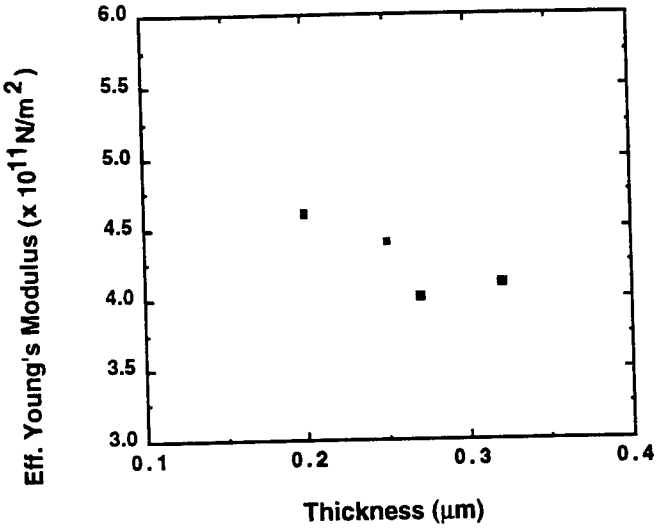


Figure 4. Young's modulus in PZT (54/46) thin films.

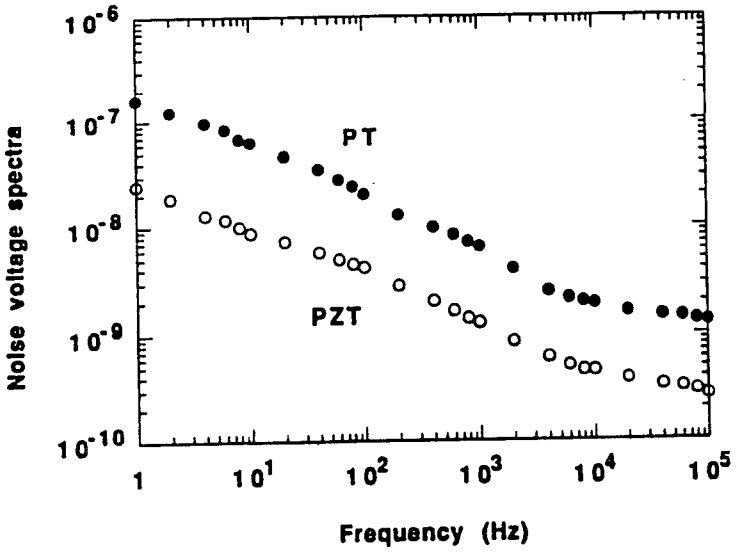


Figure 5. Noise voltage in PZT and $PbTiO_3$ microsensor capacitor structures.

TABLE 1. Summary of ferroelectric thin film properties as integrated with MEMS.

	PZT (54/46)	$PbTiO_3$	$PbZrO_3$	PLZT (9/54/46)
Piezo. Coeff. d_{33} (pC/N)	190-220	15-20	- -	200
Pyro. Coeff. * (nC/cm^2-K)	50-70	75-96	- -	65
Dielectric Const.	800-1100	80-120	100	110
Dielectric Breakdown (MV/cm)	0.6-1.0	0.5	- -	- -
Electrical Fatigue (# cycles ± 10 V)	10^{10}	- -	- -	- -
Resistivity (Ω-cm)	10^7-10^8	10^7-10^8	10^8	10^8
Loss Tangent (tan δ) x 10^{-3}	8-20	10-30	20	4
Eff. Young's Modulus E/(1-v) x 10^{11} N/m^2	4.0-4.6	4.5	- -	3.9
Intrinsic Stress x 10^8 N/m^2	2.6-6.8	2.1-5.3	- -	2.0

* includes primary plus secondary piezoelectric responses

3. Solid-State Micromachining

Solid-state micromachining is commonly viewed as an enabling technology for MEMS. In our work considerable process development has evolved both new materials and processing methods. A basic generic processing sequence is described in this section for the realization of devices similar to that of Fig. 2. Some additional process enhancements are included in this section to build better reliability into the resulting structures.

Figure 6. shows the basic generic fabrication steps for either piezoelectric accelerometers or piezoelectric flap valves. The difference lies in the detection of a voltage or application of a voltage, respectively). This fabrication sequence is briefly described.

Initially, four-inch *p*-type silicon substrates are put through a standard initial cleaning sequence. The resistivity and orientation for most surface-micromachined MEMS applications is not important. If transistors are already fabricated on the wafer, a 1.5 μm LPCVD silicon nitride encapsulation is used to protect on-chip circuitry during MEMS fabrication. Therefore our process can be considered to be a back-end IC process.

The first mask shown in Fig. 6 (a) defines the air gap, or region in which the MEMS device will be unconstrained with respect to the substrate. In Fig. 6 (b) an aluminum etch-mask is defined and recessed trenches are cut into the silicon substrate by CF_4/O_2 reactive ion etching. In many of the processes in which we have worked, final devices were destroyed by the processing due to severe topography variation. We therefore use

1.0 μm deep trenches and a planarization process to set the air gap in our MEMS structures for improved process reliability.

In Fig. 6 (d) a sacrificial layer of LPCVD PSG is deposited to form the sacrificial, or spacer layer. The thickness of the PSG is selected to be approximately twice the thickness of the trench depth. In Figs. 6 (e) and 6 (f) a planarization and etchback step is carried out to restore the flatness of the silicon surface leaving a recessed PSG region.

The structural membrane material is then deposited as shown in Fig. 6 (g). In our most recent work over the last two years we have replaced our *n*-type polycrystalline silicon structures with low-stress silicon nitride structures formed by LPCVD at 800 ^{o}C. Unlike *n*-type polycrystalline silicon which exhibits an as-deposited compressive stress, our LPCVD silicon nitride is under low tensile stress. This not only ensures flat structural membranes on which to subsequently deposit ferroelectric thin films, but also eliminates the high temperature annealing and complicated self-doping mechanisms required in PSG-polycrystalline structures.

As shown in Fig. 6 (h), the lower electrode for the PZT device is deposited. We have used sputtered Ti/Pt as the lower electrode. Cleanliness is very important and adhesion difficulties between the silicon nitride and Ti layer sometime occur. The use of approximately 1000 Å of undoped polycrystalline silicon adhesion layer (not shown) has helped to eliminate this problem while not severely changing the composite stress state of the structural support.

The ferroelectric thin film is then deposited as shown in Fig. 6 (i). In our laboratory we have investigated both sol-gel deposition and planar magnetron sputtering of PZT-type materials. To date our best results have been achieved with sol-gel materials of approximately 3500 Å-thickness in all PZT compositional ranges studied. The details of PZT sol-gel procedures have been extensively discussed elsewhere [21].

The upper electrode is next deposited as shown in Fig. 6 (j). This is also typically Ti/Pt. Patterning of the top electrode is carried out as shown in Fig. 6 (k). In most MEMS device applications it is necessary to remove the piezoelectric material in regions outside the device active area. This is carried out by ion beam milling as shown in Fig. 6 (l). Here the upper metal electrode is used as an etch mask.

After PZT definition the lower electrode is then patterned (Fig. 6 (m)) and the features of the microstructure are patterned by RIE (Fig. 6 (n)). This exposes the underlying PSG sacrificial layer.

Appropriate aluminum electrical interconnection lines and bonding pads are then patterned. A PECVD silicon nitride encapsulation layer is applied and patterned to protect the device structure as shown in Fig. 6 (o). Lateral etching of the PSG is then carried out using a 5:1 water : buffered hydrofluoric acid etch. This undercuts the region beneath the silicon nitride structural support and leaves a free standing (unconstrained) structure.

There are several important considerations in this last etching step. First, the undercutting takes place at the end of the process such that fragile free-standing microstructures are not subjected to further lithography steps. Second, we have found that the use of photoresist masking only does not adequately protect the PZT from attack by the buffered hydrofluoric acid. Third, any pinholes in the encapsulation layer usually allow the PZT to be attacked by the hydrofluoric acid. Fourth, etching chemicals and trench depths are designed such that the sacrificial etching takes approximately 10 minutes to carry out. Longer etching times require good encapsulation and selectivity between the PSG and silicon nitride membrane. The final device is shown in Fig. 6 (p).

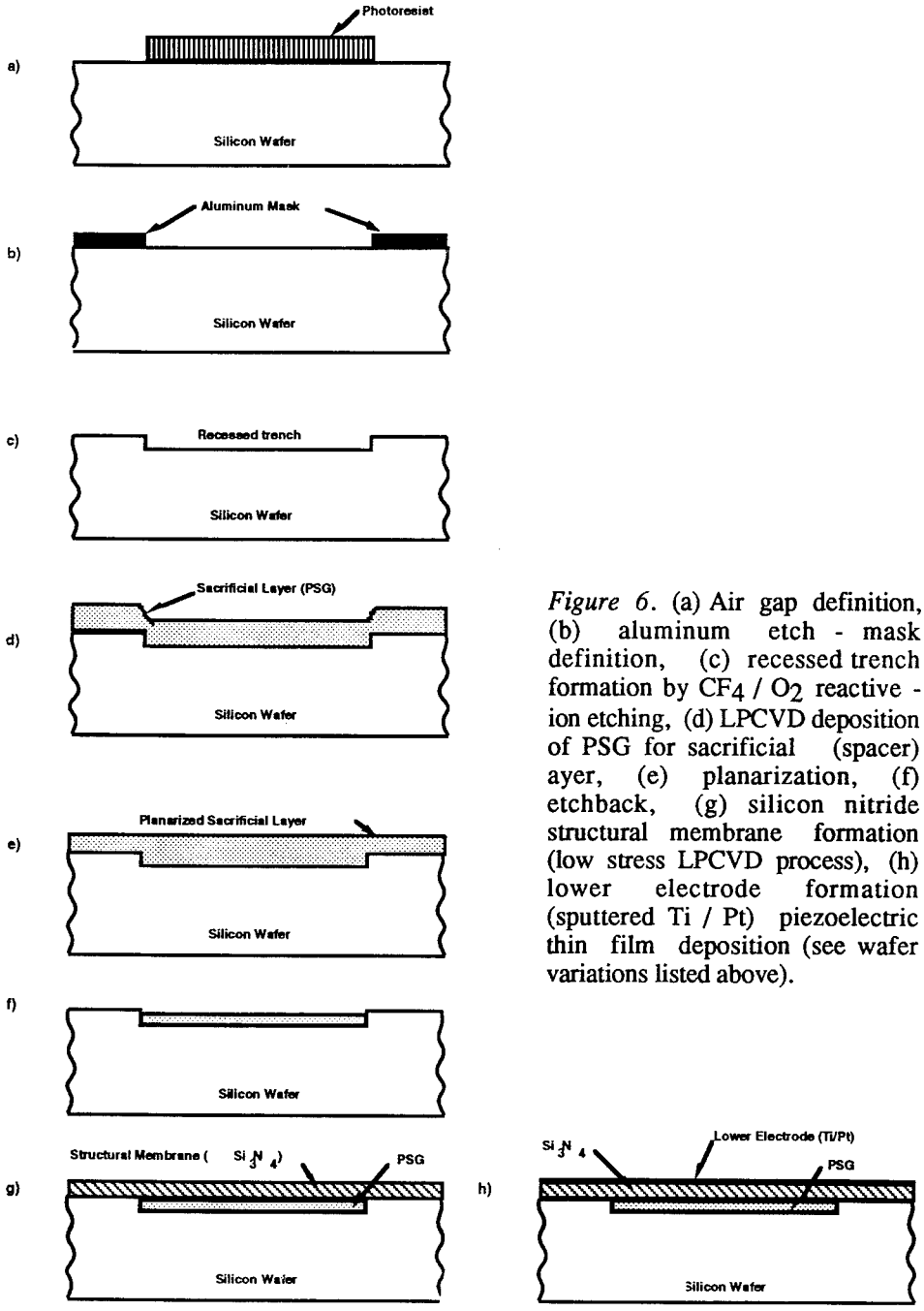


Figure 6. (a) Air gap definition, (b) aluminum etch - mask definition, (c) recessed trench formation by CF_4 / O_2 reactive - ion etching, (d) LPCVD deposition of PSG for sacrificial (spacer) ayer, (e) planarization, (f) etchback, (g) silicon nitride structural membrane formation (low stress LPCVD process), (h) lower electrode formation (sputtered Ti / Pt) piezoelectric thin film deposition (see wafer variations listed above).

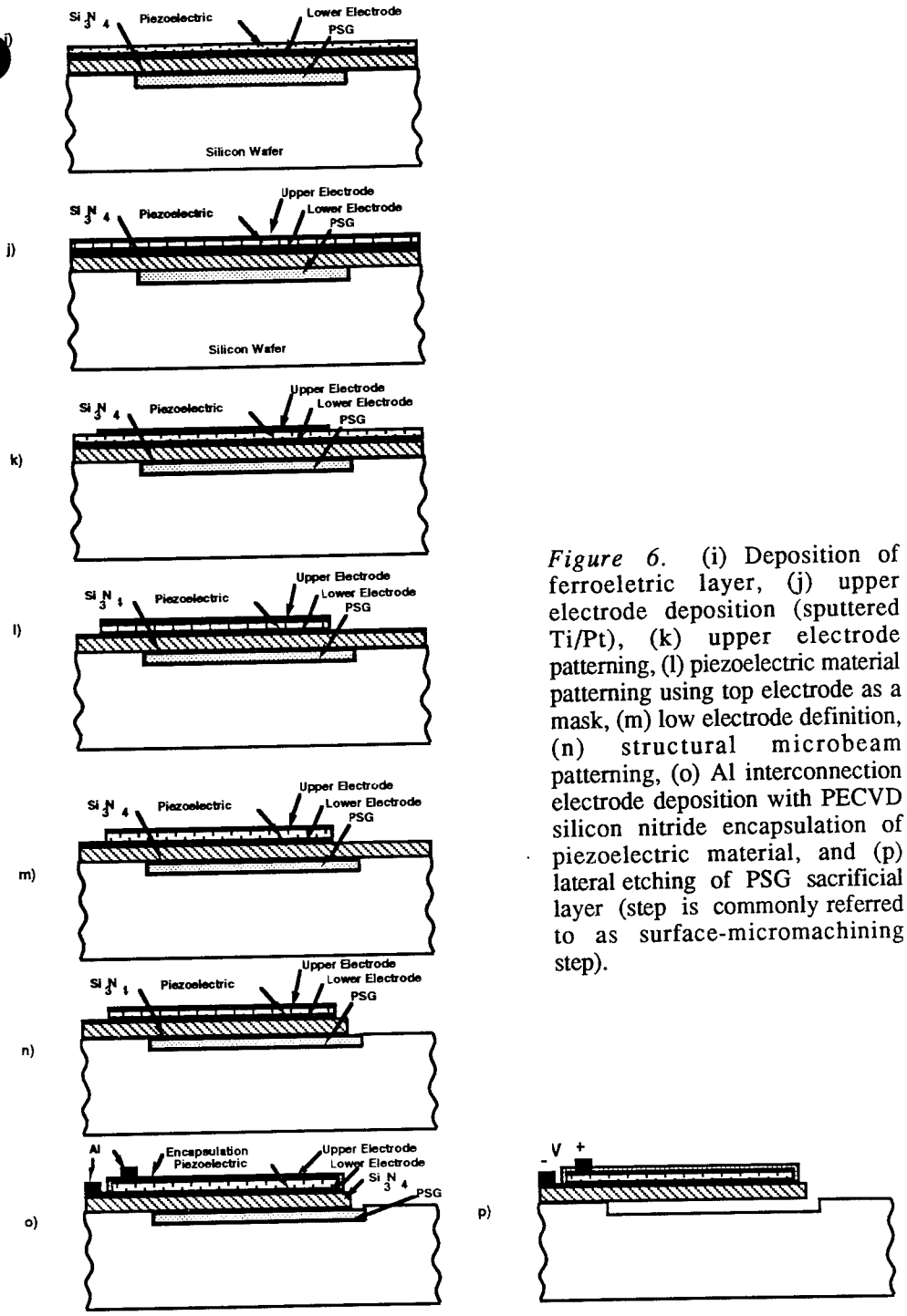


Figure 6. (i) Deposition of ferroeletric layer, (j) upper electrode deposition (sputtered Ti/Pt), (k) upper electrode patterning, (l) piezoelectric material patterning using top electrode as a mask, (m) low electrode definition, (n) structural microbeam patterning, (o) Al interconnection electrode deposition with PECVD silicon nitride encapsulation of piezoelectric material, and (p) lateral etching of PSG sacrificial layer (step is commonly referred to as surface-micromachining step).

4. Microsensors

Micromachined sensors have been formed using processing techniques similar to those presented in Fig. 6. Our most complete work has focused on three microsensor types: 1) piezoelectric acoustic pressure sensors, 2) piezoelectric cantilever beam accelerometers, and 3) pyroelectric infrared detectors. Optical photographs for these three devices are shown in Fig. 7.

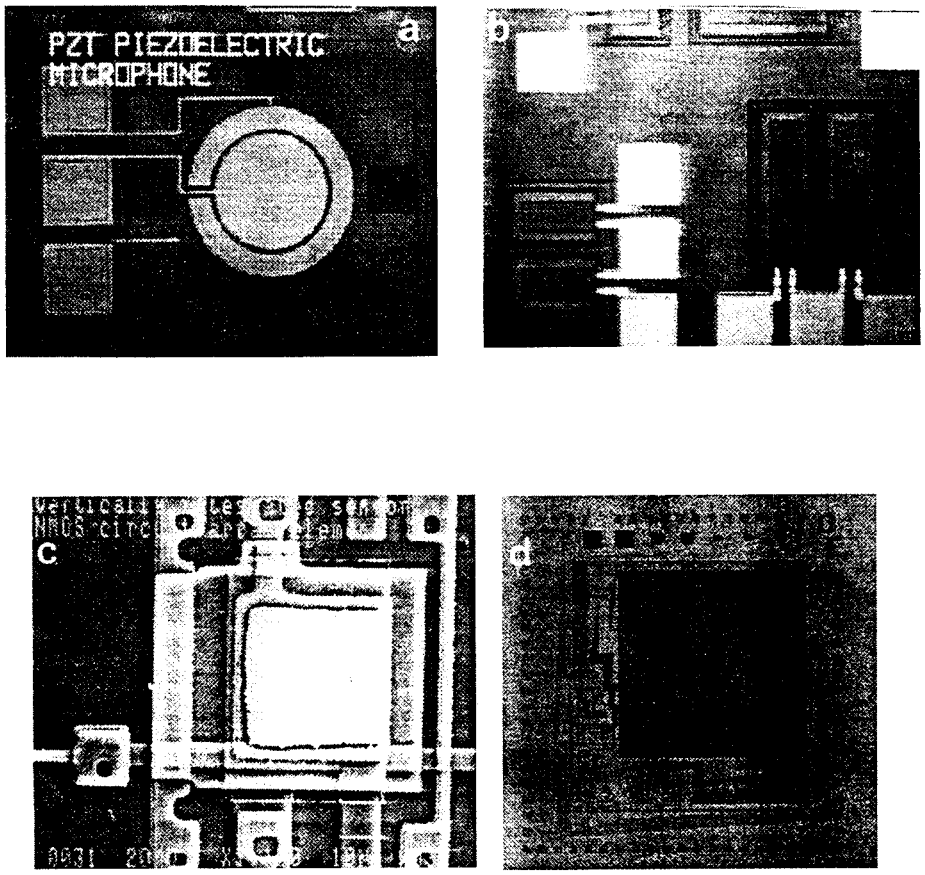


Figure 7. (a) Optical photograph of a piezoelectric acoustic microphone. The membrane diameter shown is 500 μm. (b) Optical photograph of several piezoelectric cantilever beam accelerometers. (c) SEM micrograph of a pyroelectric pixel element. (d) 64 x 64 element array with on - chip signal conditioning. A performance summary for the electroceramic microsensors fabricated by solid - state micromachining is given in Table 2.

TABLE 2. Summary of three different microsensor performance properties.

Acoustic Pressure Sensor (11)	
PZT (54/46)	
Piezoelectric Effect	
Diameter	500 μm
PZT Thickness	3400 Å
Responsivity @ 5.0 kHz	220 μV/μbar
Cantilever Beam Accelerometer (10)	
PZT (54/46)	
Piezoelectric Effect	
Length / Width	400 μm / 100 μm
PZT Thickness	3300 Å
Responsivity	4 mV/g
Infrared Detector (13, 14)	
PbTiO3	
Pyroelectric Effect	
Pixel size	40 x 40 μm^2
Thickness	3200 Å
Responsivity @ 30 Hz	2 x 10^8 cm-$Hz^{1/2}$/W

5. Microactuators

Microactuators has been fabricated based on the converse piezoelectric effect in PZT. Two technology demonstration devices based on solid-state micromachining and ferroelectric thin films have been demonstrated: 1) meanderline positioning device [17] (similar to Fig. 2d) and 2) cantilever flap valve [22, 23] (similar to Fig. 2a).

The basic piezoelectric positioning device is implemented in a geometry of N thin film piezoelectric bars connected in a meander line configuration which are mechanically in series and electrically in parallel as shown in Fig. 8. Each bar has electrodes on two opposing faces parallel to the length of the bar with electrical connection made to the terminals of a dc variable power supply. The piezoelectric polarity between bars is alternated to achieve linear expansion and linear contraction in adjacent bars. Because both ends of the meanderline are anchored to a silicon substrate, the center of the meander line experiences a forward displacement equal to N times the change in length of a single piezoelectric bar. An additive displacement is therefore obtained. The folded geometry allows substantially large displacement to be obtained on a microfabricated chip.

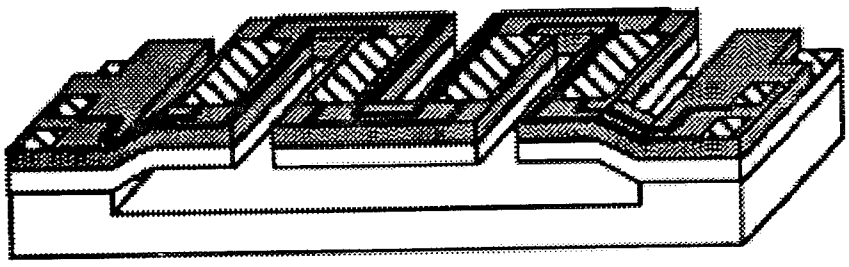


Figure 8. Cantilever meanderline actuator based on PZT thin films.

The positioning force obtained from the meanderline has been derived by Robbins, et. al. [17]. The force F_{pz} is given by

$$F_{pz} = 2\,E\,d_{31}\,w\,V$$

where V is the applied voltage, w is the width of the piezoelectric bar, d_{31} is the piezoelectric coupling constant, and E is Young's modulus. Results obtained for N=16 showed displacements of approximately 1.5 μm when actuated with 20 V.

Cantilever flaps similar to those of the cantilever microbeam accelerometer structure (see Fig. 9) have been actuated with high voltage drive electronics [22]. For the PZT piezoelectric thin films used in this work, dielectric breakdown strengths of 700 to 1000 KV/cm are commonly measured. Typical PZT thin film thicknesses in this process range from 2500 - 7000 Å depending on the intended device application. The maximum voltage which can be sustained across the PZT actuator capacitor is therefore 25 - 70 V, well within the voltage generation capability of the HVMOS drive electronics.

For a PZT-on-silicon nitride cantilever measuring 275 μm x 135 μm with active film thickness of 0.35 μm, the measured tip deflection is approximately 2 - 3 μm when actuated with 25 V. This value is approximately a factor of three lower than theoretical predictions [23].

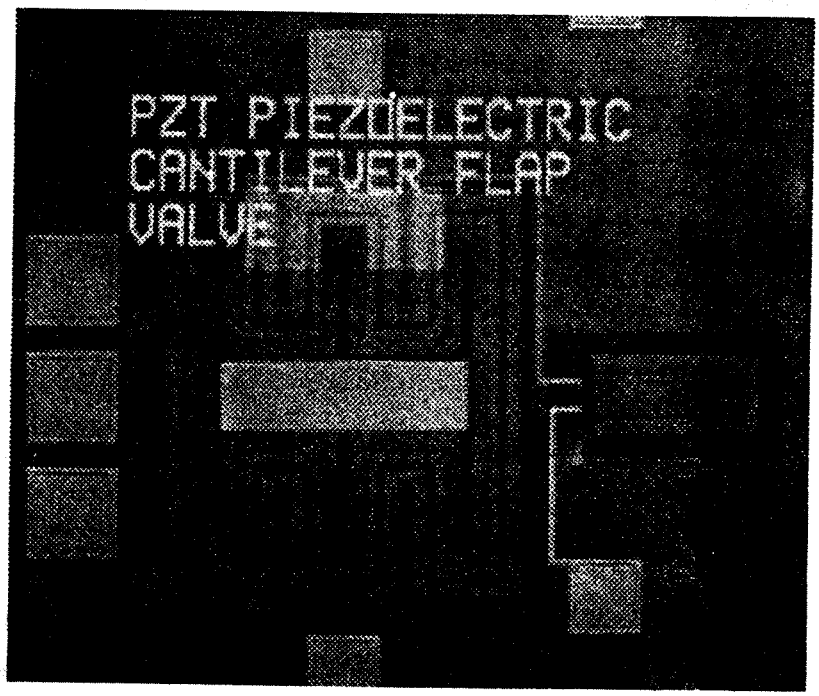


Figure 9. Piezoelectric flap valve integrated directly to an on - chip high - voltage NMOS transistor.

6. Conclusions

Piezoelectric thin films have been integrated with microelectromechanical systems consisting of surface-micromachined silicon nitride membranes. Electroceramic MEMS fabrication processes have been compatibly developed with silicon nitride membranes and on-chip MOS electronics. Both physical microsensors and microactuators have been fabricated.

Although several MEMS demonstration devices have been fabricated and tested, several processing issues still face PZT thin films. The following processing problems still represent challenges to be solved before commercializable MEMS can be realized:

1) control of electroceramic orientation
2) adhesion of electroceramic and electrodes to structural support
3) control of intrinsic stress
4) encapsulation of the electroceramic thin film during sacrificial etching
5) step coverage
6) compatibility with commercial CMOS fabrication lines

TABLE 3. Summary of piezoelectric microactuator performance.

Micro-Positioner		
	PZT (54/46)	
	Converse piezoelectric Effect	
	Number of bars	16
	Length / Width	400 µm / 100 µm
	PZT Thickness	3300 Å
	Displacement at 20 V	1.5 µm
Cantilever Flap (Valve)		
	PZT (54/46)	
	Converse piezoelectric Effect	
	Length / Width	275 µm / 135 µm
	Thickness	3500 Å
	Vertical tip displacement @ 25 V	2-3 µm

7. Acknowledgments

The author would like to acknowledge generous technical contributions from his colleagues and students: Prof. Lorraine F. Francis, Prof. Arthur G. Erdman, Prof. William P. Robbins, Dr. Chian Ping Ye, Dr. Peter J. Schiller, Mr. Paul Baude, Mr. Dan Glumac, Mr. Wika Tjhen, and Mr. Thomas Cooney.

This work was supported by the National Science Foundation, ARPA, and University of Minnesota Center for Advanced Manufacturing, Design, and Control.

Microfabrication work was carried out at the University of Minnesota Microelectronics Laboratory for Research and Education (MLRE). Materials synthesis and characterization was carried out in the University of Minnesota Center for Microelectromechanical Systems.

8. References

1. Howe, R. T., Muller, R. S., Gabriel, K. J. and Trimmer, W. S. N. (1990), *IEEE Spectrum*, pp. 29.
2. Connor, O' (1992), *Mechanical Engineering*, pp. 40.
3. Stix, G. (1992), *Scientific American* , pp. 107.
4. Muller, R. S., et. al. eds. (1990), *Microsensors, IEEE Press*, New York .
5. Interested readers will find seven (every two years) *Proceedings of the International Conference on Solid-State Sensors and Actuators*, most recently held in Yokohama, Japan, June 1993 and six *Proceedings of the IEEE Workshop on Micro Electro Mechanical Systems*, most recently held in Oiso, Japan, January 1994.
6. Polla, D. L. 1992, *Mat. Res. Soc.*, Vol. **276**, pp. 3, Spring Meeting, San Francisco, CA.
7. Flynn, A.M., Tavrow, L. S., Bart, S. F. and Brooks, R. A., Ehrlich, D. J., Udayakumar, K. R. and Cross, L. E. (1990), *EEE Ultrasonics Symposium*, Honolulu, HI, Proceedings, Vol. 3, pp. 1163.
8. Tzou and, H. S., Fukuda, T. (eds.) (1992), *Piezoelectric Smart Systems*, IEEE Press.
9. Howe, R. T. (1988,), *J. Vac. Sci. Technol.* **B6**, pp. 1809.
10. Blow, B., Polla, D. L., Harjani, R. and Tamagawa, T. (1993), *IEEE VLSI Circuits Symposium* .
11. Schiller, P., Ye, C., Tamagawa, T. and Polla, D. L. (1992), *4th International Symposium on Integrated Ferroelectrics*, Monterey, CA, Mar. .
12. Kim, E. S. and Muller, R. S. (1987), *IEEE Electron Dev. Lett.*, EDL-7, , pp. 254.
13. Ye, C., Tamagawa, T., Schiller, P. and Polla, D. L. (1992). *Sensors and Actuators A 35*, 77.
14 Pham, L. and Polla, D. L. (1994), *IEEE Trans. on Ultrasonics, Ferroelectrics, and Frequency Control*, UFFC-41 .
15. Robbins, W. P., Polla, D. L., and Glumac, D. (1991), *IEEE Trans. on Ultrasonics, Ferroelectrics, and Frequency Control*, UFFC-38, , p. 454.
16. Robbins, W. P. (1991), *IEEE Trans. on Ultrasonics, Ferroelectrics, and Frequency Control*, UFFC-38, 460.
17. Robbins, W. P., Polla, D. L., Tamagawa, T. and Glumac, D. E. (1991), *Sixth International Conference on Solid-State Sensors and Actuators*, San Francisco, CA, Technical Digest, pp. 55.
18. Polla, D. L. (1994), *Proc. 6th International Symposium on Integrated Ferroelectrics*, Monterey, CA, pp. 117.
19. Tjhen, W. , Ye, C.-P, Schiller, P., Tamagawa, T. and Polla, D. L. (1991), *3rd IEEE Workshop on Micro Electro Mechanical Systems*, Nara, Japan.
20. Ye, C. P., original data to be published.
21. Hsueh, C.-C., Tamagawa, T., Ye, C., Helgeson, A. and Polla, D. L. (1993), *Integrated Ferroelectrics* **3**, 21 .
22. Schiller, P. and Polla, D. L. (199) *Seventh International Conference on Solid-State Sensors and Actuators*, Yokohama, Japan, June 3.
23. Yan, J. (1992), "Piezoelectric Microvalves," M.S. Thesis, Department of Electrical Engineering, University of Minnesota, December

FUNDAMENTAL PROPERTIES AND SOME APPLICATIONS OF SOL-GEL CERAMIC THIN FILMS

A.S. SIGOV, [1] V.I. PETROVSKY,[1] E.F. PEVTSOV,[1] K.A. VOROTILOV,[1] AND A.S. VALEEV[2]

1. *Moscow Institute of Radio Engineering, Electronics and Automation 117454 Vernadsky Prosp., 78, Moscow, Russia*
2. *Scientific Research Institute of Molecular Electronics 103460, Moscow, Russia*

ABSTRACT. Sol-gel techniques to produce a number of perovskite thin films and to integrate thin ferroelectric layers with current technology of silicon based integrated circuits (ICs) are discussed. Some approaches to investigation of electrical properties and second optical harmonic generation as well as to modeling of physical phenomena in thin ferroelectric films are reported. Finally, some considerations are given on applications of integrated ferroelectrics.

1. Processing of PZT Memory Elements

We have studied various ferroelectric thin films (mainly PZT ceramic) and integrated structures prepared with the use of sol-gel techniques based on electro-chemical synthesis. The synthesis and the formation procedures were optimized by running a statistical check on the physical and chemical properties of the starting solutions as well as the films obtained (X-ray phase analysis, SEM, ellipsometry, second optical harmonic generation and electrophysical characteristics). Chemical aspects of the electrochemical synthesis procedure are described in detail by Yanovskaya et al [2,3]. The significant problem of preparation of PZT and other lead containing materials is the volatility of PbO during heat treatment. An excess of lead containing component is usually added to a stock solution to overcome this difficulty [4]. The effect of lead excess in solution prepared by electrochemical techniques on some properties of PZT films is illustrated in Fig. 1.

The films prepared from solutions in which lead excess was no greater than 5% and at an annealing temperature T_a=600 °C had weak ferroelectric properties due to crystallization of the pyrochlore phase under this condition.

The increase of the annealing temperature to T_a=650 °C led to the enhancement of remanent polarization, but dielectric hysteresis loops were unsaturated and nonsymmetrical. The latter effect may be connected with the primary formation of

O. Auciello and R. Waser (eds.), Science and Technology of Electroceramic Thin Films, 427-437.
© 1995 *Kluwer Academic Publishers. Printed in the Netherlands.*

pyrochlore nanocrystallites on the film surface. For lead excess in the range from 10 to 30 %, the dielectric hysteresis loop had good saturation, but the increase of Pb excess led to some decrease of remanent polarization and break-down voltage. Further increase of lead excess caused even greater degradation of film properties.

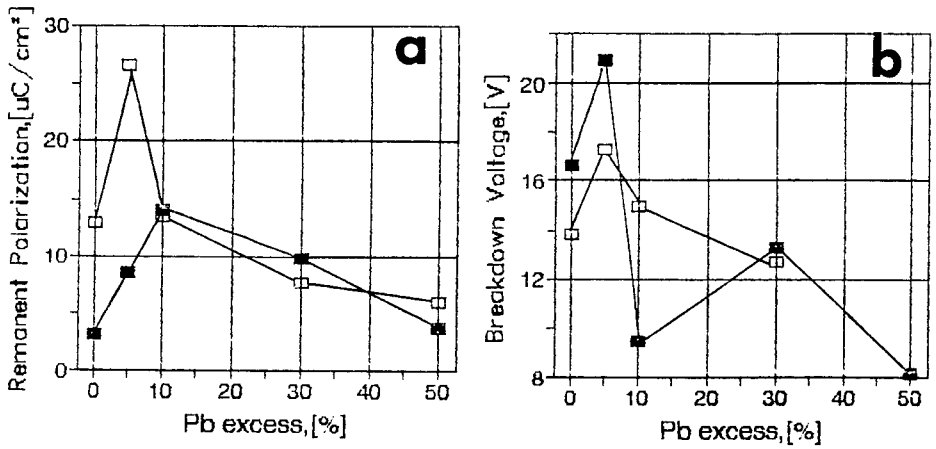


Figure 1. The effect of lead excess on remanent polarization (a) and breakdown voltage (b) of PZT films.

Along with many advantages [5-8], the integration of ferroelectric thin films with current silicon-based ICs technology involves a variety of serious complications, some of which are briefly described below:

1. Interaction of ferroelectric films with surrounding materials produces on the one hand a distortion of ferroelectric element performance, and on the other hand, a leakage and degradation of transistor structures.
2. The use of Pt electrodes causes problems related to etching and bad adhesion. A titanium sublayer is often used for adhesion improvement of bottom electrodes to silicon oxide, but it can not solve this problem completely. In addition, titania and titanium silicide produced as a result of the interaction of titanium with silicon oxide hamper processing of the bottom electrode configuration. The radio-frequency ion etching process is difficult to implement due to significant heating of the photoresist mask. Therefore, ion beam etching was used for the etching of platinum electrodes. The etching of the titanium layer is the most difficult part of the electrode processing. The main reason is that titanium oxides have much lower sputtering rate than the metal itself, whose sputtering rate is also fairly low. Typical etching rates for Pt, Ti, SiO_2, and PZT were as follows: 23-25, 12-14, 25, and 15 nm/min.
3. Processes for wet and ion beam etching of PZT films were developed. But the element sizes that went away during the wet etching process took place in two stages. In relation to the ion beam etching, the main difficulty is the nonconformal deposition of the ferroelectric layer due to the planarization of the topography relief which is inherent for layers produced by spinning.

Various processing sequences for the fabrication of PZT-based capacitors are shown in Fig. 2. The first version is a common sequence of processing steps for the production of thin film capacitors. However, the deposition of ferroelectric films after selective

etching of the bottom electrodes leads to a significant interaction of PZT with the SiO_2 layer during heat treatment, which causes serious damage to both the PZT layer and the IC elements. In the second version, the bottom electrode and ferroelectric layers are deposited first, followed by the processing used to define the ferroelectric configuration and the top electrodes (Fig. 2 (b)). However, there is a problem of survival of the bottom electrode when using ion beam etching for patterning the top electrodes. Due to the lack of etching selectivity characteristic of ion beam etching, the bottom electrode can be etched away, when patterning the top electrode, if an appropriate etch stop is not developed. In the third processing version (Fig. 2 (c)), the bottom electrode, the ferroelectric layer, and the upper electrode are successively deposited on the substrate. Subsequently, a selective etching process is used to etch the structure from the top electrode towards the bottom electrode. This processing method permits to avoid interaction of the PZT film with surrounding layers during high-temperature annealing. But in this case, high mechanical stresses in the multilayer structure may result in defects. The fourth version of processing sequence steps avoids the drawbacks of the processing sequences described above. In this fourth version, in contrast to the second one, a silicon dioxide layer is deposited by PECVD after formation of the bottom electrode and the ferroelectric layer (Fig. 2 (d)). Subsequently, a hole (via) in SiO_2 is opened in selectively to PZT and Pt. The selectivity in the plasma etching of SiO_2 with respect to PZT was about 7, but products of interaction of SiO_2 and PZT can lead to the unreproducibility of the PZT capacitor structures. In the fifth version (Fig. 2 (e)), the upper electrode is formed before SiO_2 deposition, after the etching of the ferroelectric layer and the bottom electrode. However, the fifth processing version also has some drawbacks, as the oxide film which protects transistor structures is doubly exposed to the ion-beam etching.

The description of the processing sequences presented above indicates that the integration of ferroelectric materials with IC technology can be improved provided that a better approach for the processing of ICs is found. Typical characteristics of PZT capacitor memory element prepared by sol-gel techniques are given in Table 1.

TABLE 1. Main characteristics of a PZT capacitor memory element.

Chemical composition	$Pb_{1.1}Zr_{0.52}Ti_{0.48}O_3$
Phase	Perovskite
Film thickness	0.18 - 0.25 μm
Structure	Si-SiO_2-Ti-Pt-PZT-Pt
Remanent polarization	10 - 30 $\mu C/cm^2$
Coercive voltage	0.5 - 1.5 V
Operating voltage	5 V
Breakdown voltage	> 20 V
Switching time	< 10 ns
Switching cycles	$> 10^8$

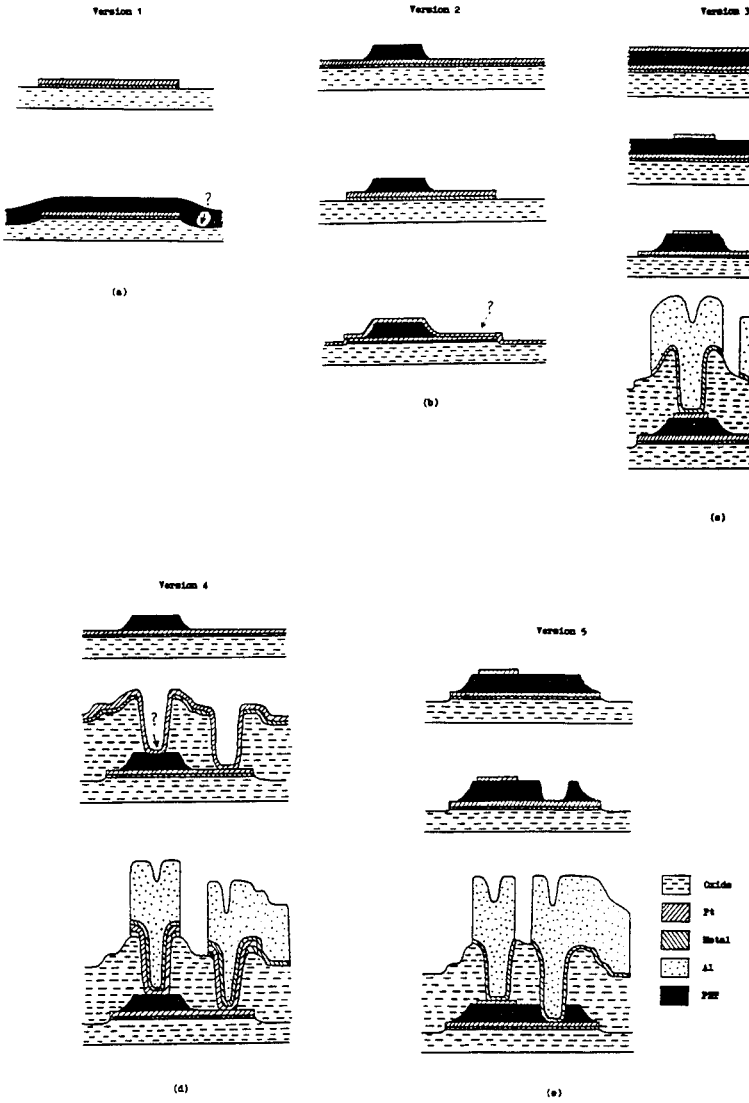


Figure 2. Various processing procedures to produce PZT-based capacitors for memories.

2. HIGH DIELECTRIC CONSTANT MATERIALS

We have investigated film processing and the properties of a number of ferroelectric perovskites: barium-strontium titanate (BST), strontium titanate-zirconate (STZ), and zirconium-tin titanate (ZST). The BST films on platinized silicon substrates had $\varepsilon = 150$ and $\tan\delta = 0.019$ at a frequency of 1 MHz, whereas the films prepared on In_2O_3 substrates had somewhat lower values of dielectric constant, probably, due to higher orientational influence of the platinum contact and a lower interaction at the interface. The increase of the heat treatment temperature of BST films up to T_a=750 °C

lead to an increase of crystallite sizes and of the dielectric constant. However, the dielectric nonlinearity is therewith enhanced (the decrease of the capacitance of a BST film prepared at T_a = 600 °C was about 0.15 percent/volt, while for the films crystallized at T_a = 750 °C this value was about 0.85 percent / volt). In contrast to BST films, the STZ films prepared on In_2O_3 substrates had a higher degree of crystallinity and higher value of the dielectric constant with lower losses (ε = 123 and tan δ = 0.014) than the films prepared on platinized silicon (ε = 81 and tan δ = 0.027). The change in capacitance of STZ films with applied voltage was very similar to the change observed for BST films (0.1- 0.7 percent/volt), but demonstrated true paraelectric behaviour (no hysteresis). The ZST films had much lower dielectric constant (e=40) than the BST and STZ ones. At the same time, they had smaller tan δ = 0.007-0.012 and dielectric constant dispersion. The capacitance of ZST films was absolutely independent of voltage. All the data discussed above and also preliminary measurements of the structures at frequencies up to several tens of MHz make it possible to consider this material as a plausible candidate in MMICs.

3. Qualitative Approaches to Ferroelectric Phenomena in Thin Films

In this section we attempt to investigate physical phenomena in ferroelectric ceramic thin films by correlating results from different experimental techniques such as Merz, Sawyer-Tower, C-V, and pyroelectric response measurements. Our study with the use of the Merz method shows that the retention characteristics provided by these techniques are very sensitive to any change in film processing procedure. Nevertheless, for the films with optimum composition, according to our viewpoint, no significant changes of the polarization charge were observed in the time range between 50 ns and 1 ms. Measurements of the dielectric hysteresis in the range from 1 Hz to 10 kHz do not reveal any frequency dependence in the charge response. From these facts it may be deduced unambiguously that polarization switching processes in our films are rather fast (< 50 ns), while other processes of charge alteration (ion drift, electric conduction, charge exchange of impurity levels, etc.) are slow enough (> 1 s). Therefore, it does not seem incorrect to consider the hysteresis loop and the C-V curve simultaneously, which allows us to separate the switchable part of the charge. In Fig. 3, one can see the hysteresis loop derivative and the C-V curve, whereas the initial hysteresis loop and the loop corresponding to the switchable part of the charge are displayed in Fig. 4 (obtained by integrating the difference in ordinates of two curves from Fig. 3). It is easily seen that the shape of the loop obtained corresponds more closely to the theoretical one for monocrystals, and the differences are probably caused by the polycrystalline nature of ferroelectric films [9]. Theoretical analysis of this issue taking into account differences in the polarization direction of crystallites resulting in a transverse electric field is now under way.

The pyroelectric properties of thin ferroelectric films were studied with the use of low-frequency sine temperature wave techniques [10]. The change in the sample temperature was maintained by a Peltier element and the pyroelectric current was registered by an electrometer. We examined both the pyroelectric effect under the influence of an external electric field that induced polarization of the film, and the stability of these properties. It was found that both the magnitude and the sign of the

pyroelectric current changed in accordance with polarization, and the values of the pyroelectric coefficient ranged from 10^{-9} to 10^{-8} C/cm^2. K). The pyroelectric response thus showed a small variation with time, corresponding to the retention data obtained by the Merz technique.

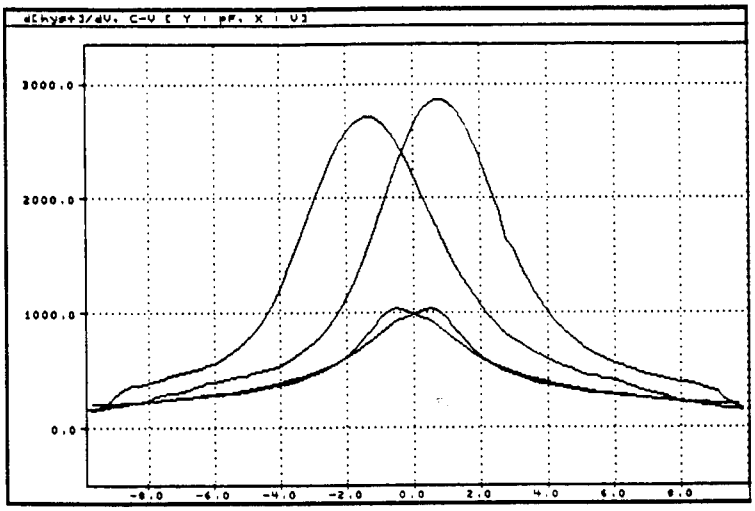


Figure 3. C - V characteristics of PZT films. The bottom curves are the measured C-V dependence, while the top curves are derivatives of the dielectric hysteresis loops.

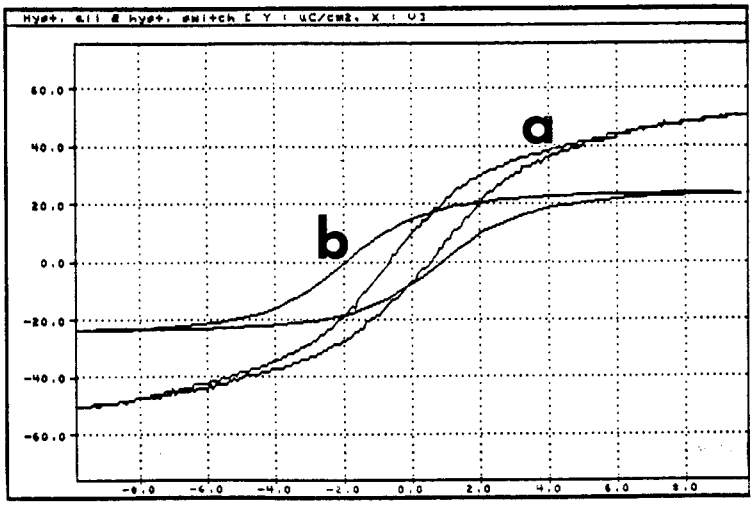


Figure 4. Dielectric hysteresis loops for PZT films: (a) directly measured loop; (b) loop reconstructed from C-V measurements.

In order to estimate the coercive field value we have considered a simple model where the coercive field was originated from the domain wall pinning by surface inhomogeneities [11]. It follows from Ref.11 that the coercive field may be estimated as

$$E_c = E_{at} (k_{at} d)^{-1} \exp (- V_o^2 / V^2) \qquad (1)$$

where

$$E_{at} = \alpha k_o^{1/2} k_{at}^{1/2} , \; v_o^2 = \alpha^2 k_o \gamma^{-1} k_{at}^{-5}, \; k_o = \beta/\alpha \qquad (2)$$

γ is the kinetic coefficient, α and β are the Landau coefficients, k_{at} is of the order of the reciprocal lattice vector, d is the film thickness, and is the random potential of the inhomogeneities. One can see the relationship $E_c \sim 1/d$ (repeatedly obtained in experiments) and a fairly non-trivial dependence of the results on the amplitude V of the inhomogeneities.

Let us now turn to evaluation of the field E_c . With $E_{at} \sim 10^7$- 10^8 V/cm and d=1 μm the pre-exponential factor is in the range 0.1 - 1.0 MV/cm. It appears to be more cumbersome to make an estimate of the potential V, because the near-surface layer of a real film has an extremely complicated structure. Nevertheless, even the simple roughness of the film surface is enough to induce the potential V. Indeed, the presence of a domain wall leads to increasing energy of the system, so the wall shall be positioned in the regions where the film thickness is less. Estimates show that in such a case we have $V \sim V_o$ even for a roughness size of the order of several lattice constants. Thus, putting $V \sim V_o$ and $d \sim 1$ μm, one has $E_c \sim 0.1$ - 1.0 MV/cm, which is closely related to the experiments.

4. Second Optical Harmonic Generation

In recent years, second optical harmonic (SOH) generation has found widespread use for the investigation of surfaces, interfaces and thin films. This generation obeys selection rules of extremely broad applicability, which are called "polarization prohibitions". These selection rules forbid the generation of the s-polarized isotropic SOH at smooth surfaces or homogeneous thin films. A violation of the rules for SOH generation could be connected only with the inhomogeneity of a thin film, but the azimuthal angular dependence of the intensity has not been clarified yet. We assume that this dependence is related to the microcrystalline structure of the films and permits in principle the estimation of the structural parameters.

The SOH generation method was applied to the study of PZT films in both ferro- and paraelectric phases as well as BST films in the paraelectric phase. The temperature dependence of the reflected SOH intensity is displayed in Fig. 5.

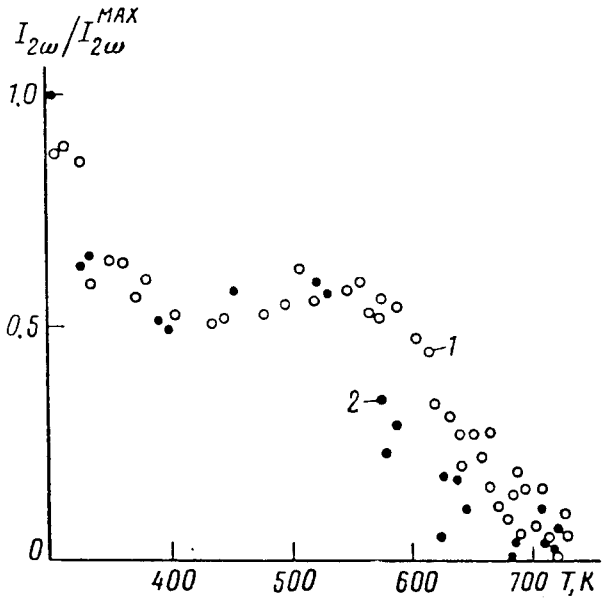


Figure 5. Temperature dependence of the normalized intensity of the reflected SOH in the case of a p - polarised pump for the s-polarized component [points 1 - (o)] and the p - polarized component [points 2 - (•)].

The initial stage of heating from 300 to 600 K is accompanied by a slight decrease in SOH intensity (apparently, a consequence of temperature-induced changes in the optical constants for the ferroelectric phase). Near 620, the SOH intensity drops sharply because of the transition to the paraelectric phase. A plateau appears in the curve at about 650 K. The curve presented in Fig. 5 is similar to that for the spontaneous polarization (i.e. the order parameter). The values of allowed p-polarized and forbidden s-polarized SOH intensities proved to be comparable. With the use of these data one can estimate [12] the mean size of microcrystallites, which is ~ 500 Å, although the local size present large fluctuations.

Some results were obtained for BST films in the paraelectric phase. We measured the intensity of allowed p-polarized reflected SOH as a function of azimuthal angle, while rotating the film around the normal to its plane, for different angles of incidence (Fig. 6). The samples with different annealing temperature had different structure and, consequently, different azimuthal dependence of SOH intensities. As an example, we display the results for the BST films prepared at annealing temperature of 600 °C. The high value of p-polarized component of the SOH intensity shows that our films possess a large component of non-linear susceptibility in the direction normal to the film surface.

A fairly small s-component of the SOH demonstrates that the samples are quite homogeneous and, in addition, the films prepared at 600 °C are rather anisotropic. Analogous measurements for the samples with annealing temperatures of 700 °C and 75C °C show that both the p- and s-polarized SOH intensities are two orders of magnitude less than for the samples described above (it is very likely that the reason is their centrosymmetric structure). The features of SOH dependence on the angle of

incidence can be interpreted in terms of linear interference of the fundamental beam in the three-layered structure (substrate-ferroelectric-air).

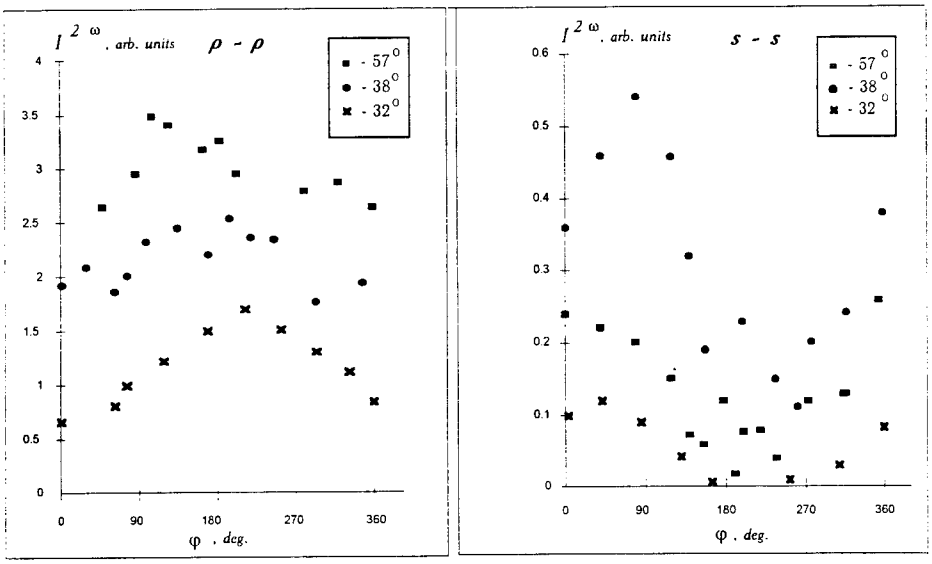


Figure 6. Azimuthal angular dependence of SOH intensity for a BST film (annealing temperature: 600 °C) for three different incidence angles. a) p-polarized SOH with p-polarized pump (p-p geometry); b) s-polarized SOH with s-polarized pump (s-s geometry).

5. Some Considerations on New Devies

The circuitry designs for ferroelectric memories should have some peculiarities due to properties of ferroelectric materials. The key feature is a very high electric energy density (a hundred times higher than in semiconductor structures), resulting in the possibility of loading a great number of storage elements onto the bus without optional amplification, thus allowing quite different specific topologies for the circuit. The methods for read in/out information in the storage element depend on ferroelectric phenomena used for storage purposes. If the film in the paraelectric phase is used for the storage, the information is stored in the form of a mobile charge, as in ordinary dynamic memories. Then, the top electrode of the storage element may be simply grounded, and the information read in/out by row-forming sensors is performed by feeding and sensing voltage at row buses after elements sampling (by feeding enable pulse to corresponding column bus). If the film in the ferroelectric phase is used for the storage, then a nonvolatile memory is realized. The information ("1" and "0") is recorded by feeding pulses of opposite polarity, so the voltage should be applied to the top electrode. For a destructive readout, after the column sampling, the sensing pulse is applied to the top electrode and reverses from "1" to "0" all elements of the column. After picking the sensing pulse off, the voltage is applied to the rows with "1" written in sampled elements, the voltage magnitude being defined by the polarization reversal charge, and the readout may be done just in the same manner as in the previous case.

The nondestructive readout may be realized by using the pyroelectric effect. When the sampled elements are heated due to a current pulse applied to the top electrode, the voltages of different polarity are applied to the row buses (the polarity reflects the polarization in sampled elements).

Another promising area for ferroelectric film applications is their integration with CCD-multiplexers for creating parallel analog processors. CCD arrays are a very important means of analog processing, first of all,
due to the possibility of simply achieving the parallel shift and addition of analog data with high accuracy (10^{-3} to 10^{-4}). The main drawback of such devices lies in the difficulty of achieving analog multiplication and in the necessity of saving a large number of factor coefficients. This drawback can be eliminated by using CCDs with ferroelectric films, which permits to save analog information very easily as a polarization state and multiplying it by the input signal with the use of the pyroelectric phenomenon.

The third line of our inquiry in the field of integrated ferroelectrics is pyroelectric heat receivers. Ferroelectric films with CCD can be also used for this purpose. The main problem lies in the necessity of maximum reduction in heat capacity and heat losses of the receiving elements. The use of suspended construction is a critical requirement in such devices. A fairly low sensitivity of pyroelectric receivers and low irradiation in the IR range requires a lot of time for signal accumulation. It can be reached only in array constructions making possible the extension of the time of signal accumulation up to the frame time.

6. Acknowledgments

The authors want to thank M. Yanovskaya and I. Obvinzeva (Physical Chemistry Institute), and also L.Solovjeva (NIPIM) for long-standing fruitful cooperation. Thanks also to the staff of the Institute for Molecular Electronics: V.Dyagilev, T.Trainis, L.Liskin, V.Sladkov, and A. Lvovich for valuable cooperation. The research described in this publication was made possible in part by the Grant N MRQOOO from the International Science Foundation .

7. References

1. Yanovskaya, M.I., Solovjeva, L.I.~ Kovsman, E.P., Obvinzeva, I.E., Vorotilov, K.A., and Turova, N.Ya. (1994), *Integrated Ferroelectrics* (in press).
2. Yanovskaya, M.I. Turova, N.Ya., Solovjeva, L.I. (1994), *Alkoxide Precursors for Ferroelectric thin films, these Proceedings*, in press .
3. Vorotilov, K.A., Yanovskaya, M.I., and Dorokhova, O. (1993), *Integrated Ferroelectrics* **3** , 33.
4. Watanabe, H., Mihara, T., Yoshimori, H., and Paz De Araujo, C.A. (1992), *Proceedings 4th Inter. Conf. Integr. Ferroelectrics*, C.A. Paz De Araujo (ed.), University of Colorado Press, 346.
5. Scott, J.F., Paz De Araujo, C.A. and McMillan, L.D. (1992), *Integrated Ferroelectrics, Condensed Matter News* **1**, 16.
6. Wu, S.Y. and Geideman, W.A. (1992), *Integrated Ferroelectrics* **2**, 105.

7. Petrovsky, V.I., Sigov, A.S. and Vorotilov, K.A. (1993), *Integrated Ferroelectrics* **3**, 59.
8. Orlova, E.V., Petrovsky, V.I., Pevtsov, E.F., Sigov, A.S. and Vorotilov, K.A. (1992), *Ferroelectrics* **134**, 365.
9. Brennan, C.J. (1992), *Ferroelectrics* **132**, 245.
10. Garn, L.E., and Sharp, E.J. (1982), *Appl. Phys. Lett.* **53**, 8974.
11. Lebedev, N.I. and Sigov, A.S. (1994), *Ferroelectrics* **4**, 21.
12. Aktsipetrov, O.A., Apukhtine, S.B., Nikulin, A.A., Vorotilov, K.A., Mishina, E.D. and Sigov, A.S. (1992), *JETP Lett.* **54**, 563.

$SrTiO_3$ THIN FILMS FOR OXYGEN SENSORS

J. GERBLINGER AND H. MEIXNER
Siemens AG, Corporate Research and Development
Otto-Hahn-Ring 6, D-81739 Munich, Germany

ABSTRACT. The gas-sensitive effect of $SrTiO_3$ is based on the fact that charged oxygen vacancies in the crystal lattice interact with oxygen molecules in the gaseous phase. The high diffusion coefficient of the oxygen vacancies explains why thin films made of strontium titanate appear to be promising candidates for use as sensor materials for high-speed oxygen sensors at high operating temperatures. A doping process developed for thin films enables acceptors and donors to be introduced specifically into the basic material. The sensor characteristic of strontium titanate can thus be optimized for different applications by the incorporation of dopants.

1. Introduction

1.1. RESISTIVE OXYGEN SENSORS

The material most frequently used at the present time for detecting oxygen at high temperatures ($T > 700°C$) is zirconium oxide. The solid electrolyte zirconium oxide is an oxygen ion conductor at the operating temperatures mentioned. This means if different oxygen partial pressures prevail on either side of the material it is possible to pick up a voltage corresponding to the difference between the oxygen partial pressures via porous electrodes. A major disadvantage of oxygen sensors based on solid electrolytes is that they are difficult or impossible to miniaturize. Oxygen sensors based on the resistive principle are considerably more compatible with microsystems. Metal oxides such as $SrTiO_3$ have an electrical conductivity which is a function of the partial pressure of the oxygen - in other words a reference volume is not needed to determine the partial pressure of the oxygen.

1.2. DEFECT MODELS FOR UNDOPED AND DOPED $SrTiO_3$

The O_2-sensitive effect of resistive oxygen sensors is based on the fact that charged oxygen vacancies in the crystal lattice interact with oxygen molecules in the gaseous phase. $SrTiO_3$ is a promising material for a high-speed oxygen sensor at high operating temperatures because of its great temperature resistance and the high diffusion coefficient of oxygen vacancies [1] .

O. Auciello and R. Waser (eds.), Science and Technology of Electroceramic Thin Films, 439-453.
© 1995 *Kluwer Academic Publishers. Printed in the Netherlands.*

The concentration of the different defects in undoped $SrTiO_3$ can be estimated by model calculations [2,3,4]. It is evident that the p-conductivity occurring in the undoped material at high oxygen partial pressures can be attributed to a certain number of strontium vacancies with a negative charge (usually V_{sr}'') and to impurity acceptors present in the material. If the oxygen partial pressure at the surface of the sensor material is lowered, a new state of thermodynamic equilibrium arises between the gaseous phase and the sensor material. Oxygen diffuses from the inside of the solid material leaving vacancies, desorbs in molecular form from the surface of the sensor and reaches the gaseous atmosphere. At high temperatures the resulting oxygen vacancies usually have a double positive charge ($V_O^{\bullet\bullet}$) i.e. they give two electrons to the conduction band and thus act as donors. As soon as the concentration of electrons exceeds that of the holes, the electrical conductivity switches from p- to n-conduction. Assuming for the sake of simplicity that oxygen vacancies occur only in double charged form $V_O^{\bullet\bullet}$ and that charged strontium vacancies and impurity acceptors can be grouped together under N_A', the requirement for charge neutrality for undoped $SrTiO_3$ can be expressed as follows:

$$n + [N_A'] = p + 2\,[V_O^{\bullet\bullet}] \qquad (1)$$

where $n = [e']$ and $p = [h^{\bullet}]$ designate the concentrations of electrons and holes respectively. With single ionized donor-type ($D^{\bullet}$) or acceptor-type (A') impurity dopants the neutrality requirement is extended to

$$n + [N_A'] + [A'] = p + 2\,[V_O^{\bullet\bullet}] + [D^{\bullet}]. \qquad (2)$$

While acceptors incorporated additionally into the bulk material are compensated like existing charged strontium vacancies or impurity acceptors, there are basically two alternative ways of compensating charges introduced into the bulk material by donors. In existing literature on n-doped titanates, it is assumed that at high oxygen partial pressures the donors incorporated are mainly compensated by ionized strontium vacancies while at low oxygen partial pressures compensation is provided via electrons [5]. The consequence of this is that the concentration of oxygen vacancies in the n-type $SrTiO_3$ is several powers of ten lower than in the undoped material. Any change in the oxygen partial pressure in the vicinity of the n-doped material also results in a new concentration of oxygen vacancies in this sensor material. Since the oxygen vacancies in the n-doped bulk material only play a subordinate role, a change in their concentration does not have any significant effect on the electrical conductivity of the material. As a result of the Schottky equilibrium

$$K_S = [V_{sr}''] * [V_O^{\bullet\bullet}], \qquad (3)$$

a change in concentration of $V_O^{\bullet\bullet}$ results in a change of [V_{Sr}'']. This fact is crucial for measured changes of conductivity since the electrical conductivity in the doped material at high oxygen partial pressures is largely determined by the strontium vacancies. Estimates in literature indicate that the equilibrium states take considerably longer to become established in the n-doped bulk materials following a change in the oxygen partial pressure in the vicinity of the material than it does in undoped material [5].

2. Manufacturing Samples

2. 1. SPUTTER TECHNOLOGY

The manufacture of $SrTiO_3$ thin films by the cathode sputtering process has become established despite the so-called "preferential sputtering" effect [6]. The sputtering process generally involves accelerating ionized argon atoms onto the surface of a target. Impact cascades triggered by the incident ions result in transfer of momentum to ions on the surface of the target.

The term preferential sputtering is used to signify that, particularly with polyatomic targets, the sputter yield varies for the individual target components because different momentum transfers are necessary for the particular target components depending on the mass of the atom concerned and its binding conditions.

In the case of $SrTiO_3$, however, it can be demonstrated that stochiometric $SrTiO_3$ films (ratio Sr/Ti = 1) can be formed by adding specific proportions of O_2 to the usual sputter gas argon [$P(Ar)/P(O_2)$ = 10/1 where P(Ar) = 8 x 10^{-3} mbar] and by optimizing the total sputter pressure P(Ar) + $P(O_2)$. Fig. 1 shows the Sr/Ti ratios of 1 µm thick $SrTiO_3$ films on Al_2O_3 substrates after annealing for 3 hours at 1100°C [7]. Rutherford backscattering RBS was the analysis method used for measuring the stoichiometric conditions shown in Fig. 1.

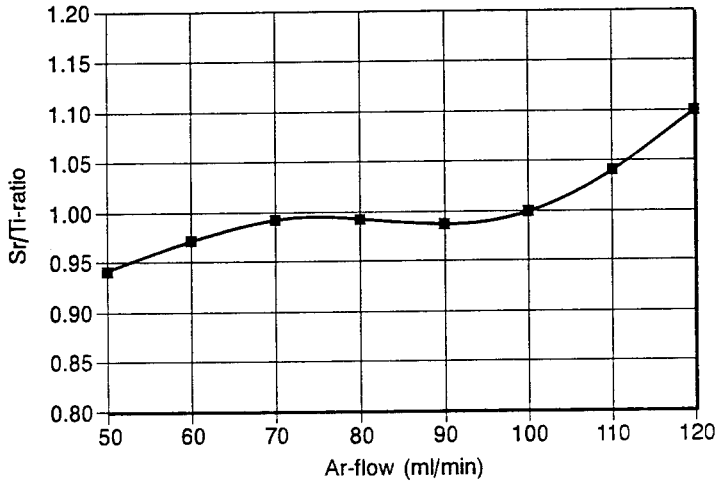


Figure 1 . Sr /Ti ratio of sputtered $SrTiO_3$ films as a function of the argon flow in the sputter chamber at a constant oxygen sputter pressure of P (O_2) = 0.8 x 10^{-3} mbar.

The lowest atomic layers of the sputtered films are not taken into account in the results shown in Fig. 1 since there was a verifiable Sr depletion in all the annealed layers in the direct vicinity of the substrate Segregation of titanium ions in the region of the substrate, preferential sputtering of titanium at the start of the sputtering process and diffusion of strontium ions into the Al_2O_3 substrate are the possible causes of the concentration of titanium there [8].

Fig. 1 illustrates that at a constant oxygen sputter pressure [$P(O_2) = 0.8 \times 10^{-3}$ mbar] the stoichiometric composition of the sputtered layers is a function of the argon sputter pressure P(Ar) or the total sputter pressure $P_{tot} = P(Ar) + P(O_2)$. A certain excess of titanium is detectable in the films at low argon flows of 50 or 60 ml/min ($P_{tot} < 10^{-2}$ mbar). It is not possible to obtain a Sr/Ti ratio of 1 with argon flows less than 70 to 90 ml/min (10^{-2} mbar $< P_{tot} < 2 \times 10^{-2}$ mbar). There is a considerable excess of zirconium in the sputtered films at higher argon flows.

2.2. SANDWICH STRUCTURES

The simplest way of producing doped $SrTiO_3$ films using the sputter process would consist in incorporating the dopants into the target material in a similar fashion to the sintering process used in the production of bulk materials. Since the extent to which dopants in particular are incorporated into the $SrTiO_3$ lattice it is not yet known, the preferential sputtering effect mentioned, produces totally undefined concentrations of dopants in the sputtered layers as they grow. Consequently a method of forming the layers has been developed, titled as "sandwich process", in order to provide defined dopant concentrations as far as this is possible (cf. Fig. 2) [9].

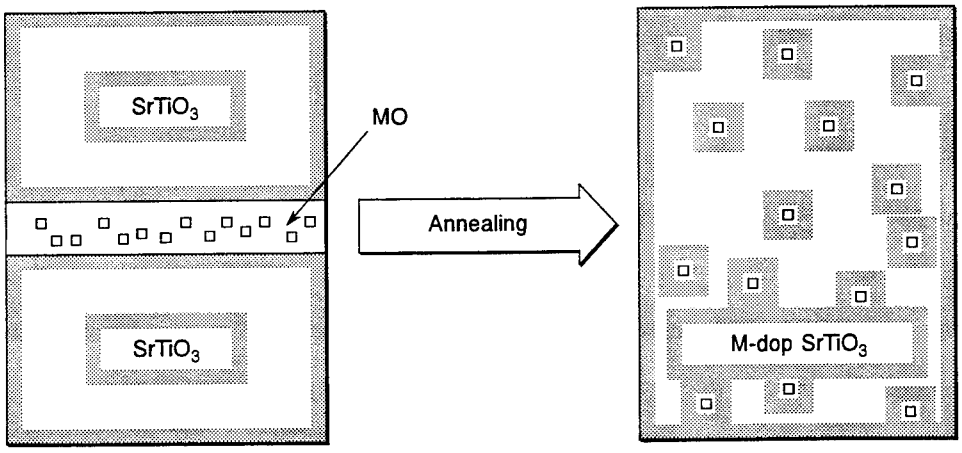


Figure 2. Schematic representation of the introduction of dopants in the "sandwich process".

3. Experimental Work

3.1. UNDOPED SrTiO3 THIN FILMS

3.1.1. *Effects of Surface Charges on the Sensor Characteristic of $SrTiO_3$ Oxygen Sensors*
The electrical conductivity σ of a sputtered, stochiometric $SrTiO_3$ film is shown in Fig. 3 as a function of the oxygen partial pressure. Comparing this characteristic with that of polycrystalline materials or even monocrystals indicates firstly that the minimum values for electrical conductivity are shifted to higher oxygen partial pressures (the p-branch of the sensor characteristic is less evident in the case of the thin films) and secondly, the electrical conductivity of thin films in the p-type region varies more as a function of temperature. Various analytical experiments have shown that the substrate material Al_2O_3 or the electrodes of screen-printed platinum used in the measurement didn't influence them [6].

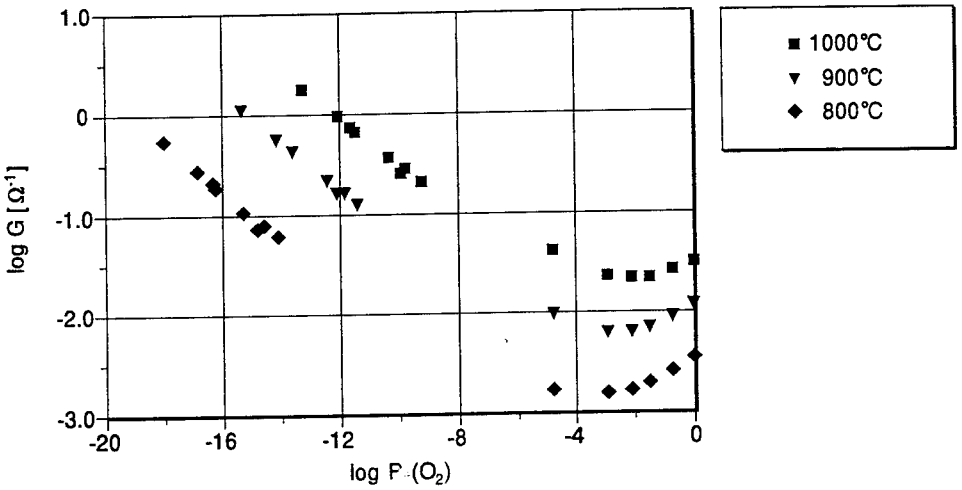


Figure 3. Sensor characteristics of a 1 µm thick stoichiometric $SrTiO_3$ thin film.

Tragut [10] has developed a model to explain the differences observed in the sensor characteristics between sputtered and polycrystalline or monocrystalline $SrTiO_3$. This model describes the influence of charge states at the grain boundaries on the conductivity behavior of $SrTiO_3$. The model works on the assumption - known from other experiments that there is a concentration of titanium at the surface of the titanate [11]. If the electron density is very low, as it is usually the case with the titanates, the d-orbitals of the titanium which are not occupied by oxygen cannot absorb electrons and thus do no longer adequately compensate the charge on the nucleus of the titanium. Considering the complex in isolation the complex appears positive. These positive surface charges result in a concentration of electrons and positively charged vacancies in the lattice (mainly Sr vacancies) in a space charge region along the grain boundary. This produces an n-type channel which is also evident in thin films in the electrical conductivity behavior. The partial conductivity of the electrons is significantly enlarged compared to that of the defect

electrons. Assuming the extent of the space charge region to be equal for monocrystals or polycrystalline bulk materials and thin films, this causes the minimum of the electrical conductivity to be shifted towards higher oxygen partial pressure as the surface/volume ratio increases. This model of the surface of $SrTiO_3$ oxygen sensors also explains the effects of other gases (CO, CH_4, H_2, CO_2 and H_2O) - the so-called cross sensitivities - on the conductivity behavior [12]. Similar charge states are presumably also present at the surfaces of other typical materials for oxygen sensors, e.g. CeO_2 [13].

3.1.2. *Effects of the Stoichiometric Composition of Sputtered Films on their Electrical Conductivity*

Considering the position of the minimum value of the electrical conductivity as a function of the oxygen partial pressure $P(O_2)$, it is apparent that at a specific sensor temperature in the range between 800°C and 1000°C the conductivity minimum is at the highest oxygen partial pressures for the stoichiometric samples (sputter pressure 10^{-2} mbar < P_{tot} < 2 x 10^{-2} mbar). The conductivity minimum moves towards lower oxygen partial pressures as the titanium and Sr excess increases [7,8].

Another main characteristic of the conductivity behavior apart from the position of the minimum values for conductivity are the slopes of the conductivity curves in the n- and p-type regions. Since the minimum values of the electrical conductivity are close to the boundary of the upper $P(O_2)$ measurement range, discussion of the slopes in the p-type region has been dispensed with. The test points in the n-type region, unlike those in the p-type region, can be approximated adequately by a single straight line. The transition of the slopes from -1/4 to -1/6 which is well known from bulk materials is never observed in the case of the sputtered thin films [7,8]. Whereas the theoretical value of -1/4 is always reached approximately with both the stoichiometric samples and the samples with Sr excess at temperatures between 800°C and 1000°C, an increasingly strong reduction in the slope is observed in the n-type region as the titanium excess increases.

The effects of the Sr/Ti ratio of the sputtered films both on the position of the minimum value of the electrical conductivity and on the slope of the sensor characteristic in the n-type region can be explained by a model divided into three different regions (cf. Fig. 4). The validity of the following examination of plausibility depends on the assumption that there must always be a certain minimum number L_{Sr} of strontium vacancies in a sputtered $SrTiO_3$ film and that it is not possible to fall below this number even if there is an excess of strontium in the films.

Region I: $P_{tot} < 10^{-2}$ mbar

In the case of titanium excess in the sputtered $SrTiO_3$ films there are so few strontium ions in the film that more strontium vacancies than necessary (L_{Sr}) occur and at the same time excess titanium is formed as TiO_2. The number of intrinsic acceptors increases due to the additional strontium vacancies (cf. Sec. 1.2.) thus enlarging the p-type region in the material. The minimum value of the electrical conductivity is at the relatively low $P(O_2)$.

The electrical conductivity σ_G of the entire film is made up of the electrical conductivities σ_{ST} and σ_{TO} of $SrTiO_3$ and TiO_2 components of the entire film, regardless whether the excess TiO_2 settles as an impurity phase around the grains or whether separate TiO_2 grains develop. This leads to

$$\sigma_G = \rho_{ST}\ \sigma_{ST} + \rho_{TO}\ \sigma_{TO} \qquad (4)$$

where ρ_{ST} and ρ_{TO} are factors representing the proportion of $SrTiO_3$ and TiO_2 respectively in the entire film. TiO_2 is a purely n-type material with a maximum slope of -1/6 whose electrical conductivity is of the same order of magnitude of that of $SrTiO_3$. Hence, the higher the proportion of ρ_{TO} of TiO_2 in the entire film, the further σ_G remains from the theoretical slope of -1/4 for $SrTiO_3$.

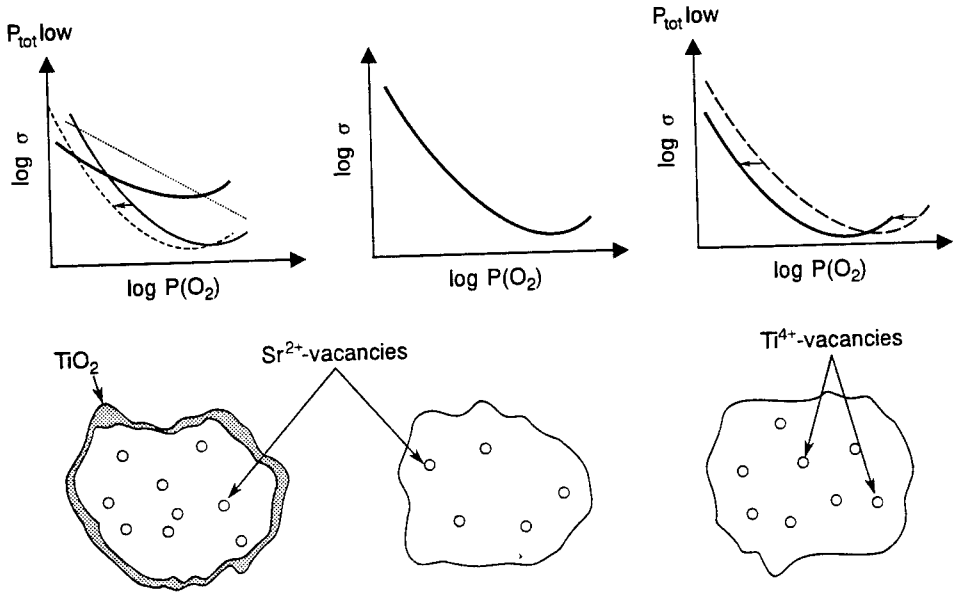


Figure 4. Schematic representation of the influence of stoichiometry on the electrical conductivity behavior of sputtered $SrTiO_3$ films.

Region II: 10^{-2} mbar < P_{tot} < 2 x 10^{-2} mbar

TiO_2 impurity phases are no longer detectable in this region. The electrical conductivity σ_G of the entire film corresponds more and more to that of $SrTiO_3$ in accordance with equation (4) (ρ_{TO} -> 0). Parallel to this, the number of Sr vacancies falls and approaches the minimum value L_{Sr}. As a result, the minimum values of the electrical conductivity in this region are considerably higher than those in region I.

Region III: P_{tot} > 2 x 10^{-2} mbar

Titanium vacancies must be produced when there is an excess of Sr in the sputtered $SrTiO_3$ films for two reasons. Firstly, because the minimum number of strontium vacancies has already been reached in region II and because unlike excessively stoichiometric bulk materials no SrO impurity phase and no compound in the form $Sr_xTi_yO_3$ (x > y) are detectable [6]. Up to four positive charges can be generated at the defect point when a titanium vacancy V_{Ti} is produced, so this kind of intrinsic acceptor has a particularly strong effect on the conductivity behavior of the sputtered films. The

minimum value of the conductivity shifts in favor of the p-type region towards lower oxygen partial pressures, even with a low number of ionized titanium vacancies. The increase in the n-type region is not, however, altered by the additional acceptors.

3.1.3. Effects of the Stoichiometric Composition of Sputtered Films on their Kinetic Behavior

A test setup which allows the oxygen partial pressure to be changed almost instantly within a few milliseconds in a measurement chamber kept to the minimum possible size was used to determine the kinetic behavior of sputtered $SrTiO_3$ films [14]. For the following experiments (also in Sec. 3.2.2. and Sec. 3.3.2.), the sensor operating times were measured in each case after changing the oxygen partial pressure from $1\,0^{-4}$ bar to 1 bar. An operating time t_{90} was selected for the sensors to allow the kinetic behavior of the films to be compared, where t_{90} is the time taken for the resistance of the sensitive film to change by 90% after the start of the change of oxygen partial pressure t ($R = R_0$).

$$t_{90} = t\,(R=R_0) - t\,(|1 - R / R_0| = 0.9) \qquad (5)$$

R_0 is the resistance of the oxygen sensitive film at the point at which the oxygen partial pressure starts to change at $P(O_2) = 10^{-4}$ bar. Samples with a film thickness of 1 µm were used for all the tests on doped and undoped $SrTiO_3$ films whose results are described in the following.

Fig. 5 shows the samples with excess titanium (argon flows 50 ml and 60 ml) and a stoichiometric sample (argon flow: 70 ml) in the Arrhenius plot as a function of the operating time t_{90}. The test results show clearly that in the temperature range up to approximately 900 °C the response times of the samples with TiO_2 impurity phases are considerably longer than those of the stoichiometric sample. Above this temperature, however, there is no longer any detectable difference in the kinetic behavior of the three samples presented. In the case of the stoichiometric sample, the test points can be approximated by a single straight line whereas with the samples with excess titanium two distinct activation energies occur. Ongoing studies have demonstrated that in the temperature range shown in Fig. 5 the diffusion of the oxygen vacancies in the crystal lattice of the stoichiometric sample is to a certain extent the step which determines the operating time. However, the mechanism which determines the kinetics in $SrTiO_3$ thin films with excess TiO_2 at temperatures below 900°C has yet to be studied. Possible causes of the inhibited interaction with the oxygen in the gaseous phase include a lower diffusion rate of the oxygen vacancies in the TiO_2 which has been observed in this temperature range or a diffusion barrier between the TiO_2 and the $SrTiO_3$ components of the entire film.

Even if the results in Fig. 6 do not appear to offer any findings worth mentioning, one point at least can be emphasized here. As the RBS analyses have shown (cf. Fig. 1), the $SrTiO_3$ thin films used for this measurement have approximately the same stoichiometric characteristics. The kinetic properties of these samples are therefore not expected to be any different. The consistency of the test results in Fig. 6 is therefore evidence of the very good reproducibility of the experiments performed.

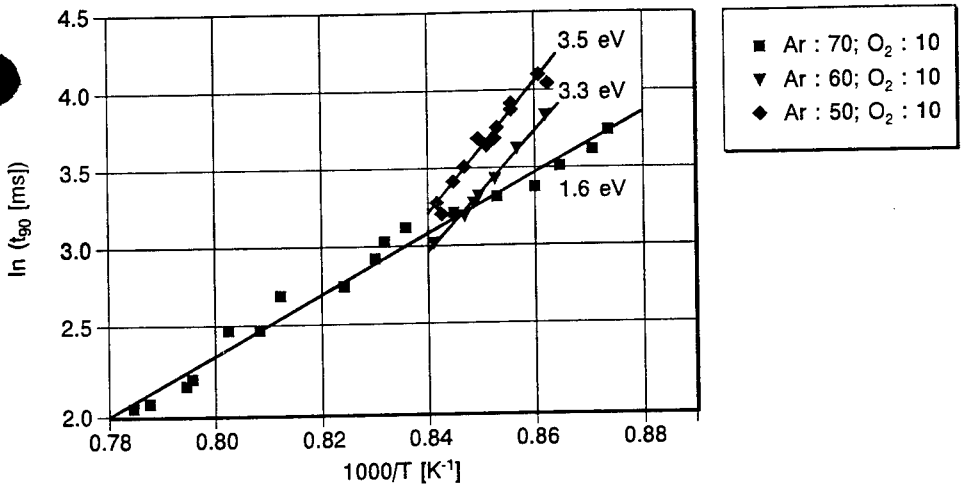


Figure 5. Influence of TiO_2 impurity phases on the operating time t_{90} of $SrTiO_3$ thin films (Arrhenius plot).

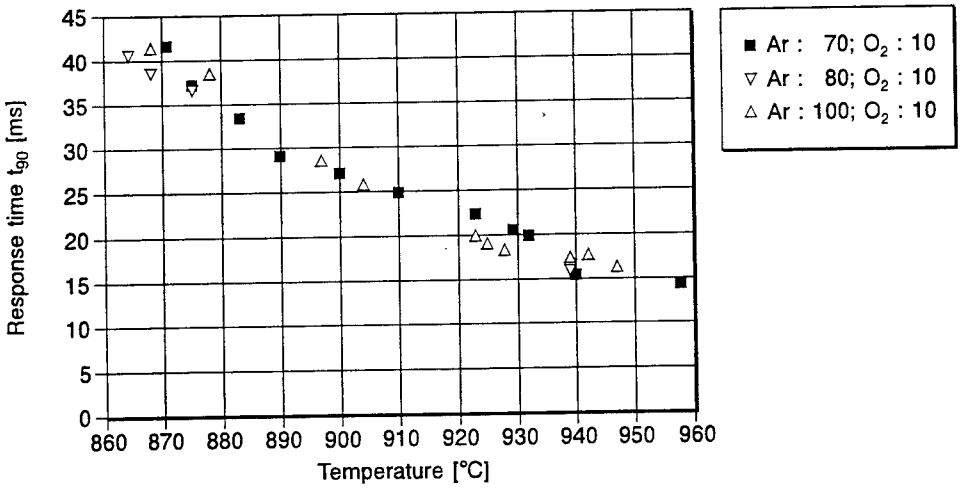


Figure 6. Operating time t_{90} of approximately stoichiometric $SrTiO_3$ thin films as a function of the sensor temperature.

As Fig.7 shows, a significant excess of strontium is necessary before there is any retarding effect on the kinetics of $SrTiO_3$ thin films.

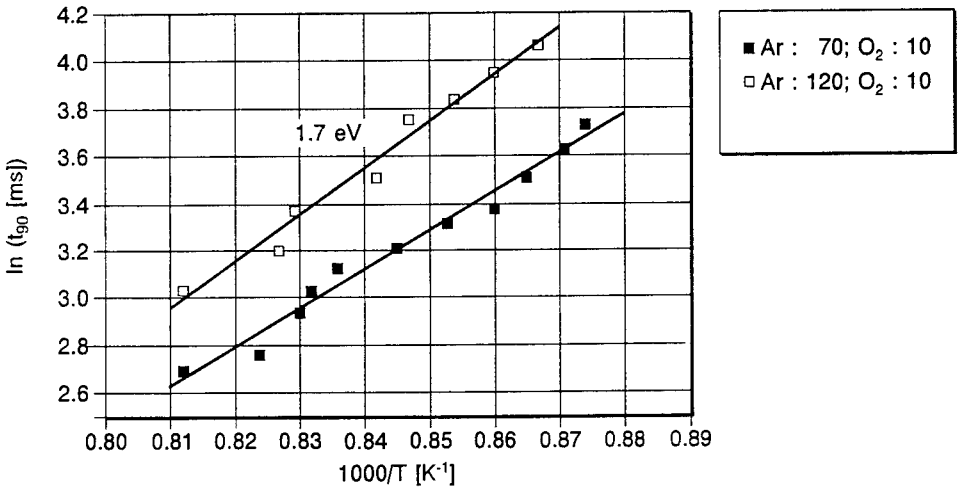


Figure 7. Influence of Sr excess on the response time t_{90} of $SrTiO_3$ thin films (Arrhenius plot)

Fig. 7 illustrates that if there is an excess of Sr in the sputtered films in the temperature range under investigation, a second process does not occur below a certain temperature as it does in the case of a titanium excess (cf. Fig. 5), but instead the volume diffusion of the oxygen vacancies is inhibited over the entire temperature range. Ionized titanium vacancies forming when there is an excess of Sr (cf. region III in Sec. 3.1.1.) could be responsible for this effect as well.

3.2. ACCEPTOR-DOPED $SrTiO_3$ FILMS

Doped $SrTiO_3$ thin films can be manufactured to the most closely defined specifications using the sandwich process described in Sec. 2.2. Although the distribution of the required dopant before and after the special annealing process (40 hours at 1100°C) can be determined by analytical experiments (e.g. secondary mass spectroscopy SIMS), it is not possible on the basis of these experiments to say whether the dopants are actually introduced into the $SrTiO_3$ crystallite and if so whether they actually act as dopants there. Investigations into the influence of dopants on the conductivity behavior of the sputtered thin films provide far more information about this [7, 8].

3.2.1. *Effects of Acceptor Dopants on the Sensor Characteristics*

Trivalent transition metals such as Al, Ga, or Fe with an ion radius of the same order of magnitude as Ti^{4+} -ions are the main candidates suitable as acceptors for $SrTiO_3$. If these transition metals are incorporated as an intermediate layer in the sandwich, the minimum value for electrical conductivity shifts towards lower oxygen partial pressures $P(O_2)_{min}$ as the concentration increases to the maximum dopant concentration 1 at.%. This is

shown in Fig. 8 for the example of Ga-doped $SrTiO_3$ films. Fig. 8, however, also shows clearly that use of a dopant concentration above about 1 at.% no longer has any noticeable influence in the form of a further shift of the minimum value for conductivity towards lower $P(O_2)min$. This conclusion also applies to Al- and Fe-doped films, regardless of whether the doping oxides used were present prior to annealing as one or more intermediate layers.

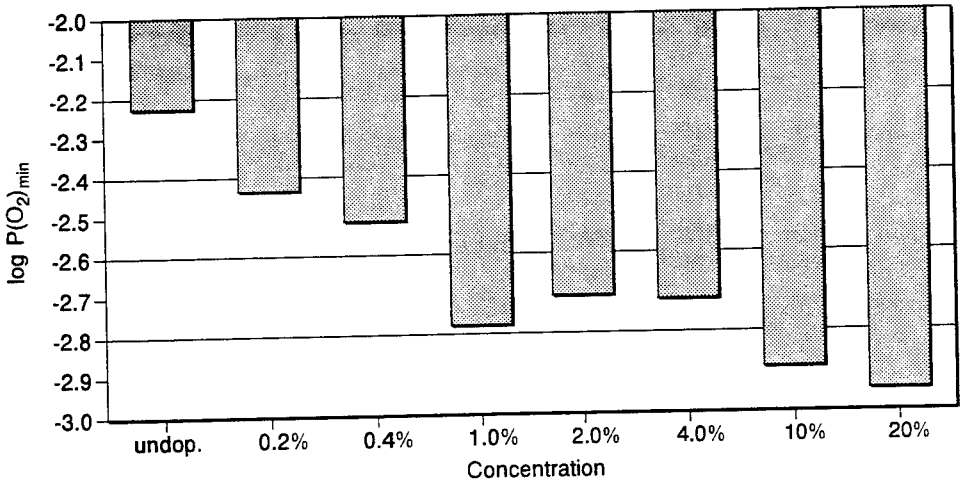


Figure 8. Position of the minimum value for conductivity $P(O_2)min$ as a function of the dopant concentration of Ga-doped $SrTiO_3$ films.

The non-incorporation of doping oxide into Al- or Ga-doped $SrTiO_3$ thin films with concentrations above 1 at.% has no further noticeable effect, whereas the excess of Fe_2O_3 results in a marked flattening of the conductivity curve in the n-type region. This is due to the fact that in contrast to Al_2O_3 or Ga_2O_3 the absolute electrical conductivity of Fe_2O_3 is of the same order of magnitude as that of $SrTiO_3$ (and comparable with that of TiO_2) so that although sputtered samples made of Fe_2O_3 are n-type at 1000°C, unlike TiO_2 they only have a maximum slope of -0.06 [8].

3.2.2. *Influences of Acceptor Dopants on the Kinetic Behavior*

The shift of the minimum value for conductivity of the acceptor-doped $SrTiO_3$ thin films has shown that when dopant concentrations of up to 1 at.% were used, at least part became incorporated in the lattice where it actually acts as an acceptor. Dopant concentrations of less than 1 at.% also reduce the operating times of sensors significantly as the ambipolar diffusion model leads us to expect [1]. This is illustrated in Fig. 9 with the example of an undoped $SrTiO_3$ thin film and a 0.4 at % Ga-doped film. The thickness of the film is in each case 1 µm. The operating times are longer when higher dopant concentrations are used. In the case of Ga-doped films with a dopant concentration of 1 at.% or 2 at.% the operating times are in the same range as the undoped material. At even higher levels of doping oxide the operating times of the doped material are far slower than

those of the undoped $SrTiO_3$. A fundamentally similar behavior is observable in Fe- and Al doped $SrTiO_3$ thin films [8].

The relatively low number of acceptors which become incorporated compared with bulk materials may possibly also be explained by the considerably greater influence of the charge states along the grain boundary in the case of thin films. This is also the reason why the ambipolar diffusion model can only be used subject to certain conditions.

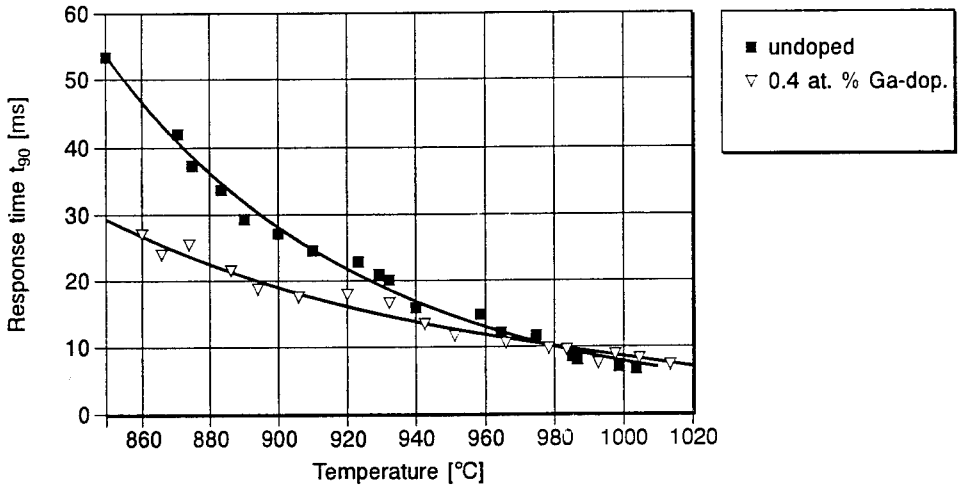


Figure 9. Comparison of the operating times for an undoped and 0.4 at.% Ga-doped $SrTiO_3$ thin film.

3.3. DONOR-DOPED $SrTiO_3$ FILMS

3.3.1. *Influences of Donor Dopants on the Sensor Characteristics*

Pentavalent or hexavalent transition metals with an ion radius of the same order of magnitude as Ti^{4+}-ions are the most suitable candidates as possible donor dopants for sputtered $SrTiO_3$ thin films. Potential doping oxides investigated to date include Ta_2O_5, Nb_2O_5 and WO_3. The reason for the choice of these doping oxides is that they are chemically stable at high temperatures especially against moisture which is not the case with the oxides of the lanthanide series (La_2O_3 or Y_2O_3), whose metal could be incorporated in an Sr position in the crystal structure. Doping of the sputtered $SrTiO_3$ films with oxides of the lanthanide series in the sandwich process would involve considerable expense - if it were possible at all.

Analytical SIMS experiments have demonstrated that acceptors could be incorporated in the $SrTiO_3$ lattice far more readily than donors in comparable concentrations. A possible reason which must be considered for this are the potential conditions at the surface of the grains of the $SrTiO_3$ bulk material described in Sec. 3.1.1.

Although it appears that is relatively difficult to introduce the donor dopants used in the sandwich process into the lattice of the bulk material it is all the more surprising that concentrations of just a few tenths of a percent are sufficient to shift the minimum value

for electrical conductivity to oxygen partial pressures of $P(O_2) > 1$ bar. Dopant concentrations of as little as approximately 1 at.% produce a linear relationship between log σ and log $P(O_2)$ with a slope of -1/4 for Ta-, Nb-, or W-doped $SrTiO_3$ films at high oxygen partial pressures.

3.3.2. *Influences of Donor Dopants on the Kinetic Behavior*
Fig. 10 shows the response time t_{90} of an undoped and a 0.15 at.% Nb-doped $SrTiO_3$ thin film (film thickness I µm in each case) as a function of temperature.

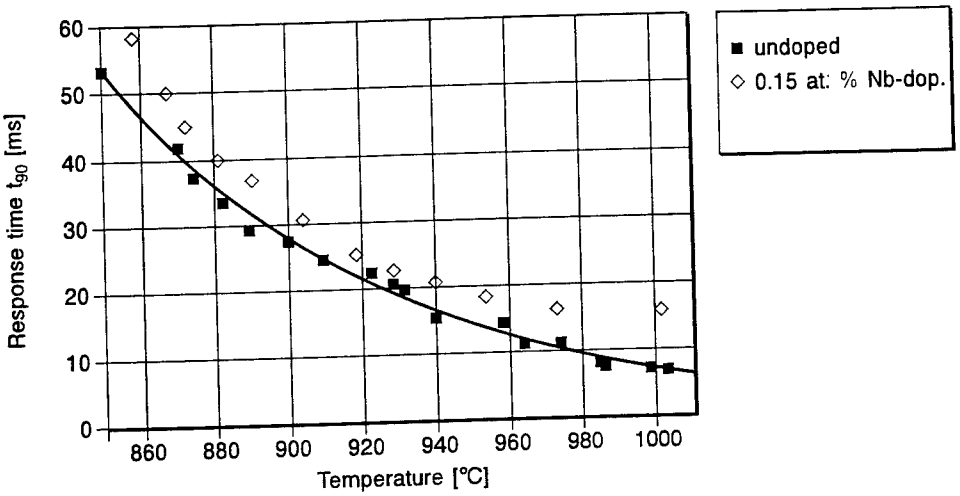


Figure 10. Comparison of the operating times for an undoped and a 0.15 at.% Nb-doped $SrTiO_3$ thin film.

The results in Fig. 10 clearly show that although the incorporation of donor ions into the bulk material $SrTiO_3$ slows down the operating times of the sensors, it does not do so to anywhere near the extent which would have been expected in view of the compensation mechanism for donor dopants which is known to occur in bulk materials (cf. Sec. 1.2.). Even with a 1 at.% Ta-doped $SrTiO_3$ film 1 µm thick and at a sensor temperature of 1000 °C the operating time after a change in the oxygen partial pressure from 10^{-4} bar to 1 bar is still less than 40 ms. From what we know of n-doped bulk materials we would have expected an operating time several powers of ten greater than that of the undoped material. As a consequence of these test results it must be assumed that essentially the same defect model applies in donor-doped $SrTiO_3$ thin films produced by the sandwich process as for undoped $SrTiO_3$ thin films.

4. Applications

4.1. TEMPERATURE-COMPENSATED OXYGEN SENSOR

The results presented in Sections 3.2. and 3.3. clearly show that the minimum value for electrical conductivity of undoped $SrTiO_3$ thin films can be shifted to lower or higher

oxygen partial pressures by the selective introduction of acceptors or donors. However, the conductivity experiments which were performed also demonstrated that - subject to the accuracy of measurement - the relationship between electrical conductivity and temperature was not altered by introducing either acceptors or donors. $SrTiO_3$ thin films, both undoped and acceptor- or donor-doped at maximum 1 at.%, have a thermal activation energy of E_A = 1.4 (+ 0.2) eV in the range 0.01 bar < $P(O_2)$ < 1 bar and 750 °C < T < 1000 °C. The sensor effect can therefore be doubled in certain oxygen partial pressure ranges by measuring the difference in resistance between a p- and an n-doped $SrTiO_3$ film and the dependency of the sensor signal on temperature can be largely eliminated. A typical field of application for sensors of this type is determining the oxygen partial pressure of industrial and small-scale furnaces.

4.2. LAMBDA PROBE

In the field of lambda sensor systems for vehicles there is an increasing demand for signal-generating probes which can be used to reduce vehicle emissions by a significant amount. Lambda sensors based on $SrTiO_3$ thin films appear to have the properties required for future probes. They have a lambda value which is an almost linear function of the sensor signal in the range around $\lambda = 1$ and they are also capable of detecting the lambda value of combustion selectively in the individual cylinders of an Otto engine at a working temperature of 1000 °C in less than 10 ms. The signals from the $SrTiO_3$ lambda probes can therefore be used to optimize combustion in each individual cylinder to give more or less the maximum degree of catalyzer conversion and hence a suitably low emission of pollutants at all times.

5. References

1. Mueller, A. and Haerdtl, K.H. (1989), *Appl. Phys.* **A 49**, 75.
2. Daniels, J., Haerdtl, K.H., Hennings, D. and Wernicke, R. (1976), *Philips Res. Rep.* **31**, 487.
3. Balachandran, U. and Eror, N.G. (1981), *Solid State Chem.* **39**, 351.
4. Chan, N.H., Sharma, R.K. and Smyth, D.M., (1992), *J. Electrochem. Soc.* **128**, 1762.
5. Wernicke, R. (1975), Ph.D. Thesis, RWTH Aachen, Germany.
6. Gerblinger, J. and Meixner, H.(1990), *J. Appl.Phys.* **67**, 7453.
7. Gerblinger, J. and Meixner, H.(l 994), *Silicates Industriels*, no. **1-2**, 31.
8. Gerblinger, J. (1991), Ph.D. Thesis, Unversity of Karlsruhe, Germany.
9. Gerblinger, J. and Meixner, H. (1992), *Sensors and Actuators* **B 6**, 231.
10. Tragut, C. (1992), Ph.D. Thesis, University of Karlsruhe, VDI-Frotschrittsberichte Reihe 8, No. 291, Dusseldorf, Germany, VDI-Verlag.
11. Chiang, Y.M. and Tagaki, T. (1990), *J. Am. Ceram. Soc.* **73, 11**, 3278.
12. Gerblinger, J., Lampe, U., Meixner. H., Perczel, I.V. and Giber, J. (1994), *Sensors and Actuators* **B18-19,** 529.
13. Lohwasser, W., Gerbinger, J., Lampe, U. and Meixner, H. (1994), J. *Appl. Phys.* **75, 8**, 3991.

14. Gerblinger, J. and Meixner, H. (1991), *Proc. of Transducers* '91, San Francisco, USA, **24.-27.06.91**, 592.
15. Gerblinger, J. and Meixner, H. (1993), *Proc. of Euro-Ceramics II*, **Vol. 3**, Augsburg, Germany, 11.-14.09. 91, 2463.

INDEX

Devices

Accelerometer 415
Area 374
Barrier Layer 367
Breakdown field 376
Capacitors 6, 12, 16, 18, 357, 369, 377, 388
Charge 374
Cell architecture 375
CMOS 356
Dielectric constant 375
DRAM Memories 355
Dry etching 362, 363, 364, 367
Electrodes 358, 377
Electrical properties 394
Electro-optic modulator 400
Fabrication procedure 420, 421
Ferroelectric Memory 81, 355, 356
High frequency 400
High permittivity 373
Hysteresis 365, 366, 370
Leakage current 379
Memory architecture 2
Microactuators 423, 424
Microbridges 395
Microelectromechanical system 413
Microsensors 422
Packaging 368
Passivation coating 368
Piezoelectric resonator 400
Pyroelectric 392
Positioning sensors 400
Pressure sensors 400
Surface acoustic wave 400
Transducer design 401
Electrostriction 616
Electro-optic 621
Ferroelectric Field Effect 609
High Frequency 574
High Permittivity 373, 376
Infrared Detector 620
Field-Effect 232-234
Magnetometer 595
Micron and Sub-Micron Patterning 568
Microwave 587

Electrical Characterization

Charge storage 38
Coercive field 31, 264
Depolarization effects 303, 306, 309
Dielectric constant 46
Dielectric response 32, 35, 36, 46, 234
Electrical Conductivity 36, 40, 112, 139, 143, 225, 240, 241, 278, 279, 317, 322 323, 326
Electron emission 337, 338, 348
Hysteresis loops 13, 58, 80, 83, 110, 111, 114, 138, 140, 142, 156, 167, 205, 220, 295, 296, 298, 299, 300, 301, 311, 265, 267, 263
Imprint 18, 19, 20, 293
Fatigue 35, 57, 59, 60, 82, 138, 139, 143, 312
Film properties 418
Interface states 228
I-V characteristics 36, 39, 41, 233
Leakage current 32, 33, 37, 239, 242 255, 281, 282, 283 284, 286
Low field region 39
Remanent polarization 31, 46, 12, 13
Retention 34, 145, 146, 217
Short term properties 12
Space charge limited conduction 39
Switching 203, 211, 212, 213, 218, 303
Time dependent dielectric breakdown 33, 34, 38, 225, 251, 252
Noise voltage 417
Young's modulus 417

Electro-optic Materials

$Na_{1-y}K_yTa_{1-x}Nb_xO_3$ 189, 191
$KTaO_3$ 189, 191

Ferroelectric Materials
$BaTiO_3$ 94, 104, 108, 109
$Bi_4Ti_{13}O_{12}$ 106, 109, 113
Materials integration 5
Perovskite 604, 605
Pb(Mg, Nb)O 101, 104, 107, 108 115
PTO 53, 101, 115, 180, 181, 183
PLZT 4, 7, 8, 9, 10, 11, 13, 14, 181, 184, 293
PZT 1, 3, 4, 5, 6, 8, 53, 55, 76, 77, 79, 80, 81, 96, 101, 104, 119 135, 136, 137, 138, 179,
$SrTiO_3$ 108, 115, 277
$SrBi_2Ta_2O_9$ 106, 109, 113

Film Characterization
AFM 154
Microscopy 325
Binding Energy 289-307
Charging Shift 288
Diffraction 164
Defects 296
Detectors 273
Dielectric constant 63, 410
Direct Recoil Spectroscopy 265-267
Dopants 410
Electron Microscope 313-316
Electron-Sample Interaction 326, 327
Electronic Structure 297
Electron Spectroscopy 283-309
ESCA analysis 197, 198
X-ray diffraction 9, 11, 12, 13, 29, 30, 56, 60, 61, 79, 102, 105, 106, 107 127, 130, 132, 144 165, 172, 173, 182 196, 329, 331, 333, 335

Film Deposition
Chemical Vapor Deposition 76
Crystalline Orientation 29
Crystallization 28
Pulsed laser ablation-deposition 1, 3, 53, 67, 69
Alkoxide precursors 87, 88, 90, 94, 96, 150, 162
Hydrolisis conditions 95
Sol-gel films 135, 149, 152, 160, 170, 179

Film Properties
Compresive Stress 128

Ion Beam Sources
Beam Formation 26
Kaufmann source 23, 28

Plasmas
Electron Cyclotron 26
ERC plasma 27, 36
Glow discharge 25, 26
Ion flux 27, 34, 36, 45
Magnetrons 27

Substrates
$LaAlO_3$ 6, 7,11, 13, 14, 15
BTO 9, 10, 11, 14, 25
LSCO 2, 4, 8, 9, 10, 11 13, 14
Pt 78, 79, 136, 137, 138
RuO_2 76, 77, 79, 81, 136 137, 138
YSZ 7, 8, 11,12
Si 11, 12, 15
SiO 10, 12, 15
$SrTiO_3$ 38
ZnO 67, 69, 329